



UNIVERSITY OF
CAMBRIDGE

A Fragment-Based Drug Discovery
Approach for the Development of
Selective Inhibitors of Protein
Kinase CK2

Sophie Louise Mitchell

Queens' College
University of Cambridge

May 2018

This dissertation is submitted for the degree of Doctor of Philosophy

A Fragment-Based Drug Discovery Approach for the Development of Selective Inhibitors of Protein Kinase CK2

Sophie Louise Mitchell, slm75@cam.ac.uk

Department of Chemistry, University of Cambridge, Lensfield Road, Cambridge, CB2 1EW, UK

Over the last twenty years, fragment-based drug discovery (FBDD) has emerged as a highly successful way to provide lead compounds for subsequent optimisation into drug candidates. Initial hits usually exhibit lower potency than those identified by more traditional techniques, such as high-throughput screening (HTS), but the optimisation phase of FBDD is highly efficient, thus providing superior lead-like compounds. The recent application of FBDD in a variety of protein kinase campaigns has successfully led to the identification of novel binding sites and highly efficient chemical ligands. This demonstrates the utility of the FBDD strategy against well-established kinase targets, where selectivity is otherwise challenging due to significant conservation of the ATP-binding site.

Protein kinase CK2 is a ubiquitously expressed and constitutively active regulator of cell growth, proliferation and apoptosis. Elevated levels of CK2 protein and activity have historically been involved in human cancer, including lung, cervical and head and neck cancer types, and its overexpression is associated with worse prognosis. A number of CK2 inhibitors are currently available displaying activity against multiple cancers in vitro and in the clinic, however these candidates target the ATP-binding site and thus display poor selectivity in kinase panel assays.

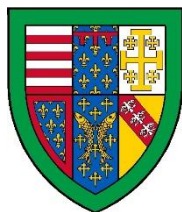
Here, the application of FBDD towards the development of potent and selective inhibitors of the catalytic α -subunit of CK2 is explored. This project exploits a novel, conserved binding site, named the α D pocket, for the generation of allosteric inhibitor molecules. Following characterisation of a previously unreported binding mode and structure-based optimisation of a potent inhibitor series, a fragment linking strategy between the lead α D-site fragment and a low-affinity pseudosubstrate peptide is investigated. This work validates the utility of FBDD towards the discovery of new binding modes and presents a first in class CK2 α allosteric inhibitor series. Furthermore, it provides the first X-ray crystal structure of protein kinase CK2 in complex with a ligand binding in the substrate-binding channel.

Declaration

This dissertation is the result of my own work. It includes nothing which is the outcome of work done in collaboration except where specifically indicated in the text. It is not substantially the same as any that I have submitted, or is being concurrently submitted, for a degree or diploma or other qualification at the University of Cambridge or any other University or similar institution. I further state that no substantial part of my dissertation has already been submitted, or is being concurrently submitted, for any such degree, diploma or other qualification at the University of Cambridge or any other University or similar institution. The length of this dissertation does not exceed the word limit prescribed by the Physics and Chemistry Degree Committee.

Sophie Mitchell

May 2018



Queens' College, University of Cambridge

Abstract

Over the last twenty years, fragment-based drug discovery (FBDD) has emerged as a highly successful way to provide lead compounds for subsequent optimisation into drug candidates. Initial hits usually exhibit lower potency than those identified by more traditional techniques, such as high-throughput screening (HTS), but the optimisation phase of FBDD is highly efficient, thus providing superior lead-like compounds. The recent application of FBDD in a variety of protein kinase campaigns has successfully led to the identification of novel binding sites and highly efficient chemical ligands. This demonstrates the utility of the FBDD strategy against well-established kinase targets, where selectivity is otherwise challenging due to significant conservation of the ATP-binding site.

Protein kinase CK2 is a ubiquitously expressed and constitutively active regulator of cell growth, proliferation and apoptosis. Elevated levels of CK2 protein and activity have historically been involved in human cancer, including lung, cervical and head and neck cancer types, and its overexpression is associated with worse prognosis. A number of CK2 inhibitors are currently available displaying activity against multiple cancers in vitro and in the clinic, however these candidates target the ATP-binding site and thus display poor selectivity in kinase panel assays.

Here, the application of FBDD towards the development of potent and selective inhibitors of the catalytic α -subunit of CK2 is explored. This project exploits a novel, conserved binding site, named the α D pocket, for the generation of allosteric inhibitor molecules. Following characterisation of a previously unreported binding mode and structure-based optimisation of a potent inhibitor series, a fragment linking strategy between the lead α D-site fragment and a low-affinity pseudosubstrate peptide is investigated. This work validates the utility of FBDD towards the discovery of new binding modes and presents a first in class CK2 α allosteric inhibitor series. Furthermore, it provides the first X-ray crystal structure of protein kinase CK2 in complex with a ligand binding in the substrate-binding channel.

Acknowledgements

First and foremost, I would like to thank Prof. David Spring for giving me the opportunity to work in his group. I could not have asked for a better PhD experience, and would not be the scientist I am today without his leadership and guidance. Professor Spring supported me throughout the highs and lows of my four years of study, and for the support he has offered me I could not be more grateful.

I would like to thank Dr. David Twigg for his help and guidance throughout my first year. Twigg supported me on a day to day basis and always made time to answer my questions. Without him I would not have found my feet in the Spring group so quickly.

I have been fortunate enough to work on an exciting and fast-paced project, with an incredibly enthusiastic and lively team. Dr. Claudia De Fusco and Jessy Iegre, you have been my rocks throughout the experience and I will forever remember the patience and support that they offered me. My thanks go to Dr. Paul Brear and Dr. Max Rossman who conducted all of the biochemical and biological testing for my compounds, and without whom this project would not have been possible.

I would also like to thank the other members of the Spring group, especially those working in lab 226, who have provided endless entertainment and encouragement throughout the years. A special mention to Dr. Jamie Stokes, Dr. Naomi Robertson and Dr. Hannah Sore, the best lab and office leaders I have ever had the pleasure of working alongside. Additionally, a strong shout out to Dr. Joe Ciardiello for his endless help with the HPLC machines. He has the patience of a saint.

Thank you to all of my proof readers: Dr. Stephen Geddis, Dr. Gabri Fumagalli, Dr. Naomi Robertson, Dr. Tommy Osberger and Josie Gaynord. I really appreciate the time you all spent to look through my work. I know it isn't an easy job, but your contributions made all the difference.

Finally, I am extremely grateful to BASF and Dr. Tobias Seiser for providing my PhD funding and coordinating my CASE-award study trip. Thank you to Queens' College for my Munro scholarship and John Collins Bursary and thank you to the Department of Chemistry for my travel grant.

Abbreviations

°C	degrees Celsius
Å	angstrom
Ac	acetyl
Akt	protein kinase B
aq.	aqueous
ATP	adenosine triphosphate
Bcl	B-cell lymphoma
BIM	Bcl-2-like protein 11
BLI	biolayer interferometry
Bn	benzyl
Bu	butyl
CAPK	cyclic (adenosine monophosphate)-dependent protein kinase
cat.	catalyst
CDK	cyclin-dependent kinase
CE	capillary electrophoresis
CK2	casein kinase 2
CLL	chronic lymphocytic leukaemia
cLogP	calculated logarithm of the octanol/water partition coefficient
cm ⁻¹	wavenumbers
conc.	concentrated
COSY	correlation spectroscopy
cryst.	crystallography
D	dimensional/aspartic acid
d	<i>D</i> -aspartic acid
Da	dalton(s)
d.b.	did not bind
dba	dibenzylideneacetone
deprot.	deprotection
d.i.	did not inhibit kinase activity
DIC	<i>N,N'</i> -diisopropylcarbodiimide
DIPEA	<i>N, N</i> -diisopropylethylamine
DME	1,2-dimethoxyethane
DMF	<i>N, N</i> -dimethylformamide

DMSO	dimethyl sulfoxide
dppf	1,1'-bis(diphenylphosphino)ferrocene
DRB	5,6-di-chloro-1-β-D-ribofuranosylbenzimidazole
Dvl	dishevelled
EC ₅₀	half maximal response concentration
eq.	equivalent(s)
ESI	electron spray ionisation
Et	ethyl
FBDD	fragment-based drug discovery
FDA	US Food and Drug Administration
Fmoc	fluorenylmethyloxycarbonyl
g	gram(s)
GI ₅₀	half maximal proliferation concentration
GPCR	G-protein coupled receptor
h	hour(s)
HATU	1-[bis(dimethylamino)methylene]-1 <i>H</i> -1,2,3-triazolo[4,5- <i>b</i>]pyridinium 3-oxid hexafluorophosphate
HBA	hydrogen bond acceptor
HBD	hydrogen bond donor
HMBC	heteronuclear multiple bond correlation
HOBt	hydroxybenzotriazole
HPLC	high performance liquid chromatography
HRMS	high resolution mass spectroscopy
HS1	hematopoietic lineage cell-specific protein 1
Hsp90	heat shock protein 90
HSQC	heteronuclear single quantum correlation
HTC	hepatoma tissue culture
HTS	high-throughput screening
Hz	hertz
<i>i</i>	iso
IC ₅₀	half maximal inhibitory concentration
IKK	IκB kinase
IP	intellectual property
IQA	5-oxo-5,6-dihydroxyindolo- [1,2-α]quinazolin-7-ylacetic acid

IR	infrared
ITC	isothermal titration calorimetry
<i>J</i>	coupling constant
JAK	Janus kinase
K_d	dissociation constant
K_i	inhibitory constant
K_M	Michaelis constant
l	litre(s)
LCMS	liquid chromatography mass spectroscopy
LE	ligand efficiency
LEF	lymphoid enhancer-binder factor
LHS	left hand side
m	milli
M	molar/methionine
<i>m/z</i>	mass to charge ratio
Me	methyl
mGlu	metabotropic glutamate
min	minute(s)
min.	minimal
m.p.	melting point
MS	mass spectrometry
MST	microscale thermophoresis
MW	molecular weight
n	nano
n.d.	no data
NMR	nuclear magnetic resonance
NS3	non-structural protein 3
Oxyma	ethyl (hydroxyimino)cynoacetate
PAINS	pan-assay interference compounds
PDB	protein data bank
PDPK	phosphoinositide-dependent protein kinase
Ph	phenyl
pH	logarithm of the reciprocal of hydrogen ion concentration
PI3K	phosphoinositide 3-kinase

Pim	Moloney murine leukaemia virus
pin	pinacol
PIP3	phosphatidylinositol 3,4,5 trisphosphate
POM	polyoxometalate
PPI	protein-protein interaction
ppm	parts per million
PTEN	phosphatase and tensin homolog deleted on chromosome 10
Py	pyridine
R	unspecified substituent
RBF	round-bottom flask
R _f	retention factor
RHS	right hand side
r.t.	room temperature
SAR	structure-activity relationship
SBDD	structure-based drug design
S-Phos	2-dicyclohexylphosphino-2',6'-dimethoxybiphenyl
SPPS	solid-phase peptide synthesis
SPR	surface plasmon resonance
STAT	signal transducers and activators of transcription
t	tertiary
TAT	trans-activator of transcription
TBB	4,5,6,7-tetrabromobenzotriazole
TCF	T-cell specific transcription factor
Tf	trifluoromethanesulfonyl (triflyl)
TFA	trifluoroacetic acid
THF	tetrahydrofuran
TIPS	triisopropyl silyl
TLC	thin layer chromatography
t _r	retention time
v/v	volume for volume
w.t.	weight
w/w	weight for weight
zm	Zea mays
δ	chemical shift

Δ	heat
ΔG	change in Gibbs free energy
μ	micro
μW	microwave
U_{max}	absorption maximum

Standard one and three letter codes are used for all amino acids.

Table of Contents

Declaration.....	i
Abstract.....	ii
Acknowledgements.....	iii
Abbreviations.....	iv
Chapter One: Introduction.....	1
1.1 Fragment-Based Drug Discovery (FBDD)	1
1.1.1 General Principles	1
1.1.2 Fragment Library Design	3
1.1.3 Biophysical Techniques	5
1.1.3.1 Ligand-Observed NMR	5
1.1.3.2 X-Ray Crystallography	6
1.1.3.3 Surface Plasmon Resonance (SPR).....	6
1.1.3.4 Isothermal Titration Calorimetry (ITC).....	6
1.1.4 Hit-to-Lead Generation	7
1.1.5 Advantages and Limitations of FBDD.....	12
1.1.6 Kinase Inhibitors and FBDD.....	14
1.2 Protein Kinase CK2	18
1.2.1 CK2 Structure	18
1.2.1.1 The Catalytic α and α' Subunits	19
1.2.1.2 The Regulatory β Subunits	22
1.2.1.3 The Tetrameric Holoenzyme $\alpha_2(\alpha')\beta_2$	23
1.2.2 CK2 as a Cancer Driver	24
1.2.2.1 Elevated CK2 Level	24
1.2.2.2 Addiction to CK2.....	25
1.2.3 CK2 Signalling and Cancer	26
1.2.4 CK2 as an Anticancer Target	28
1.2.5 CK2 Inhibitors to Date	29

1.2.5.1	ATP-Competitive Inhibitors.....	30
1.2.5.2	Alternative Site Inhibitors	32
1.2.5.2.1	CK2 α /CK2 β Subunit Interface Inhibitors.....	33
1.2.5.2.2	Polyoxometalates (POMs) Target an Alternative Exosite.....	35
1.2.5.2.3	Bisubstrate Inhibitors.....	35
1.2.6	Discovery of the α D Pocket on CK2 α	39
1.3	Project Aims	42
Chapter Two: Results and Discussion		46
2.1	Target-Oriented Fragment Library Design, Synthesis and Testing	46
2.1.1	Fragment Library Design	46
2.1.2	Fragment Library Synthesis.....	49
2.1.3	Fragment Library Screening and Biochemical Assessment.....	54
2.1.4	Analysis of the New Binding Mode	59
2.2	Structure-Based Optimisation of the New Binding Mode	62
2.2.1	Optimisation Strategy for Hit-to-Lead Generation	62
2.2.2	SBDD on Ring A	63
2.2.3	SBDD on the Amine Head Group	67
2.2.4	SBDD on Ring B.....	70
2.2.5	Negative Allosteric Mode of Action	81
2.2.5.1	Hypothesis One: Disruption of the ATP-Binding Site.....	82
2.2.5.2	Hypothesis Two: Disruption of the Substrate-Binding Site.....	84
2.2.5.3	Hypothesis Three: Transition Between the Open and Closed Forms of CK2 α	85
2.2.5.4	Experimental Evidence.....	86
2.3	α D Pocket to Substrate-Binding Channel Linking Investigation.....	89
2.3.1	Background	89
2.3.2	Project Aim and Preliminary Modelling	90
2.3.3	α D-Site Fragment Optimisation	94
2.3.4	Linker Optimisation.....	105

2.3.4.1	Optimisation Strategy and Previous Work.....	105
2.3.4.2	Development of a Peptide Linker	107
2.3.4.2.1	Initial Peptide Linker Test Set	107
2.3.4.2.2	Polyanionic Tripeptide Linkers.....	110
2.3.4.2.3	Alternative Peptide Linkers.....	116
2.3.5	Fragment Linking.....	122
Chapter Three: Conclusions and Future Work.....		125
3.1	Conclusions	125
3.2	Future Work.....	128
Chapter Four: Experimental.....		130
4.1	General Experimental	130
4.2	General Methods	132
4.2.1	General Method A : Phenol triflation	132
4.2.2	General Method B : Suzuki coupling of unhindered substrates.....	132
4.2.3	General Method C : Benzonitrile reduction.....	133
4.2.4	General Method D : Suzuki coupling of hindered substrates.....	133
4.2.5	Manual Fmoc Solid-Phase Peptide Synthesis (Fmoc-SPPS)	133
4.2.6	Microwave Fmoc Solid-Phase Peptide Synthesis (Fmoc-SPPS).....	134
4.2.7	Automated Fmoc Solid-Phase Peptide Synthesis (Fmoc-SPPS)	136
4.3	Experimental Details for Target-Oriented Fragment Library.....	136
4.4	Experimental Details for Structure-Based Optimisation of the New Binding Mode	150
4.5	Experimental Details for α D Pocket to Substrate-Binding Channel Linker Investigation ...	162
4.6	Computational Docking Procedure.....	185
4.7	Crystallisation and Screening Conditions.....	187
References		190
Appendix		209

Chapter One: Introduction

1.1 Fragment-Based Drug Discovery (FBDD)

1.1.1 General Principles

Over the last twenty years, fragment-based drug discovery (FBDD) has emerged as a highly successful way to provide lead compounds for subsequent optimisation into drug candidates.¹ To date, two FBDD-derived oncology drugs have been clinically approved²⁻⁴ and more than thirty other examples are in clinical trials^{5,6} for disease states including cancer,⁷ Alzheimer's disease⁸ and type 2 diabetes.⁹ FBDD has not only been adopted as a mainstream technique within pharma, but is also well-established within biotech and academic institutions, reliably generating high quality chemical leads against a range of targets.^{1,6,10,11}

The core concept of FBDD is the detection of low affinity fragments that bind to a biological target with well-defined interactions.¹² These low molecular weight (MW) hits can then be efficiently elaborated into larger, more potent compounds while maintaining the key binding interactions.¹² High affinity fragments derived from this process can be used to probe the biology of the target or as a lead for drug discovery.¹³

With this in mind, the FBDD process can be described in three main steps: fragment library design, fragment screening, and hit-to-lead generation. The FBDD pipeline is depicted in Figure 1, and further detail on each stage is given below and in the sections that follow.

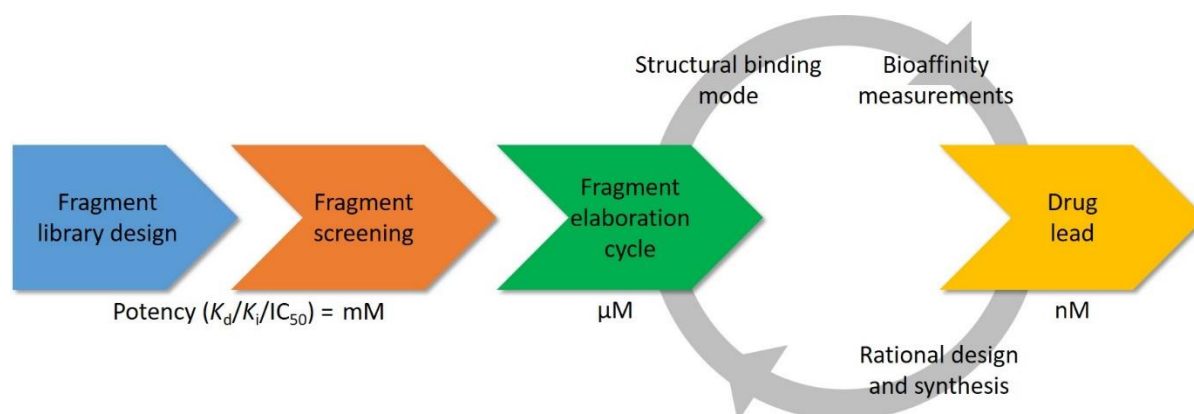


Figure 1: General workflow of the FBDD approach. After fragment library screening and hit validation, a ligand is optimised into a drug candidate by iterative cycles of rational design, chemical synthesis and affinity measurement. The relative potency at each stage is shown. K_d – dissociation constant; K_i – inhibitory constant; IC_{50} – potency.

Typically, an FBDD project begins with the design of a suitable fragment library for screening against a pre-selected target. These fragment libraries are relatively small collections (500-3000 compounds)

of diverse, low MW compounds (<300 Da) featuring 10-20 'heavy' (or non-hydrogen) atoms.⁶ Owing to the small size of fragments, biological binding affinities are in the mM range, and therefore library screening requires sensitive biophysical methods and high concentration biochemical assays.¹³ Following initial identification, a hit is validated through use of a secondary screening technique, commonly X-ray crystallography or NMR spectroscopy. These methods provide detailed structural information, thereby enabling characterisation of the fragments' binding pose.^{10,14,15} The final step involves iterative cycles of fragment elaboration, structural screening, and bio-affinity measurements to facilitate hit-to-lead generation. The use of X-ray crystallography is particularly prevalent at this stage as it provides visualisation of the protein-ligand complex, thus promoting rational structure-based drug design (SBDD).^{1,16} X-ray crystallography reveals ways to boost binding affinity whilst the chemist maintains physicochemical properties within an acceptable range¹⁷ – an underappreciated factor in drug discovery and a well-known source of attrition for small molecule drugs.¹⁸

In recent years, FBDD has proven itself as a viable alternative to more traditional drug discovery techniques, such as high-throughput screening (HTS) and virtual screening. In contrast to FBDD, HTS uses collections of millions of compounds with MW ~500 Da in search of nM range binding affinities.¹⁹ While HTS has led to many successful drug leads, more recently it has yielded fewer hits and more false positives.^{20,21} This has encouraged a transition to FBDD, which typically yields higher hit rates and has proven itself against more challenging targets for which HTS has failed, *e.g.* protein-protein interactions (PPIs).²²⁻²⁴

Furthermore, despite the lower potency of initial hits, FBDD is considered more efficient than HTS in the optimisation phase.^{10,14} Analysis suggests that FBDD generates smaller, less lipophilic hits and leads than HTS, and strict SBDD ensures every moiety of the compound contributes significantly towards binding. Figure 2 depicts the efficiency of HTS relative to FBDD hits. It emphasises that higher MW compounds, as used in HTS, adopt suboptimal binding modes with the protein target whereas fragments, as used in FBDD, engage more efficiently (Figure 2, **a** vs. **b** respectively). If multiple fragment hits are identified, then they can be combined into an optimised lead during hit-to-lead generation (Section 1.1.4).

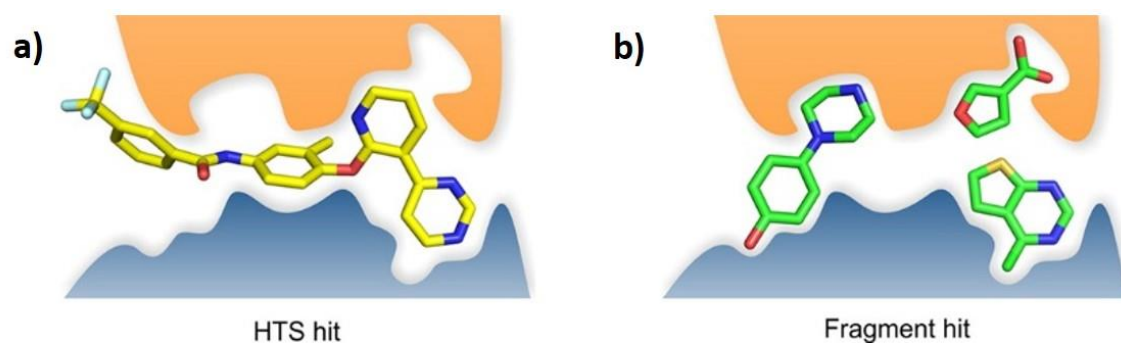


Figure 2: Diagram showing the relative efficiency of HTS vs. FBDD hits. **a)** The higher MW of an HTS hit results in binding by virtue of numerous suboptimal interactions. **b)** In contrast, fragment hits have lower MW and thus bind to the target with fewer, but more optimised, interactions. Combining multiple fragment hits can lead efficiently to a high affinity drug candidate. Reprinted with permission from Scott et al.²⁵ Copyright (2018) American Chemical Society.

The following sections consider the key components of an FBDD program in greater depth. The main advantages and limitations of the technique are highlighted and the relevance of FBDD in the development of kinase inhibitors is introduced.

1.1.2 Fragment Library Design

The outcome of an FBDD program is very much dependent on the quality of the initial fragment hits.²⁶ With this in mind, it is essential that the fragment library is carefully designed, with thorough consideration of multiple factors including fragment size, complexity and properties.²⁵

As mentioned in Section 1.1.1, most fragment libraries are small in number, just a few thousand compounds, aimed at providing a reasonable number of hits without overwhelming the screening methods.⁶ Additionally, the size of each fragment is limited to 300 Da which, in theory, provides more efficient sampling of chemical space than larger molecules.²⁷ It has been calculated that the size of chemical space increases approximately 8-fold for every heavy atom in a molecule and therefore, a diverse library of 1000 fragments, with MW 190 Da, covers chemical space in an equivalent manner to 10^{18} molecules of MW 440 Da.^{26,28} As a result, a concentrated, fragment-sized screening library should be capable of sufficiently probing the surface of multiple, varied biological targets.

Once the size and MW range of the fragment library has been determined, attention must be given to the individual members of the collection. There are five areas to consider when assessing whether a fragment is appropriate for an FBDD screening library:

1. Fragment complexity, diversity and shape

As modelled by Hann, a molecule needs to have sufficient features to make interactions with a binding site, but not so many that binding is prevented.²⁹ Therefore, a careful balance between fragment complexity and MW is required. Furthermore, diverse scaffolds with a variety of 2D and 3D shapes should improve molecular recognition against varied and challenging biological targets.²⁶

2. Physicochemical properties

In 2003, Congreve *et al.* analysed a diverse range of fragment hits from the Astex archive. They observed that the average physical properties of successful hits fell within different orders of three: MW <300 Da, hydrogen bond donors (HBDs) ≤3, hydrogen bond acceptors (HBAs) ≤3 and CLogP ≤3.³⁰ Fifteen years on, the 'Rule of Three' concept is still widely used as a guiding criteria when constructing fragment libraries. Properties commensurate with biophysical screening at high concentration, such as high aqueous solubility, are also vital in order to avoid fragment precipitation and aggregation.³¹

3. Reactive properties

Fragments bearing functional groups known to be reactive towards proteins, associated with aggregation in solution and/or the generation of false positives, should be avoided.³² These traits mean compounds can register as hits in an assay without having specific binding affinities that can be further enhanced.⁶ Some compounds can be easily recognised, *e.g.* Michael acceptors, alkyl halides and epoxides, while others can be identified by comparison to known pan-assay interference compounds (PAINS).³³

4. Fragment analogues and exit vectors

During hit optimisation, the availability of fragment analogues, either commercially or through efficient chemical synthesis, is essential.²⁶ For the latter, fragments bearing multiple exit vectors, or so-called synthetic 'handles', enable growth in 3-dimensions so that new binding interactions can be accessed.

5. Fragment quality control

Regular quality control checking must be possible for the fragments so that high concentration screening can be performed reliably.³⁴ Quality control includes checking for compound purity, stability, precipitation, aggregation and pH change.³⁵

Practitioners working carefully within these fragment library guidelines have reported multiple cases of high quality protein-hit interactions.¹ Many of these hits have then been successfully used as starting points in hit-to-lead generation.

1.1.3 Biophysical Techniques

Until recent years, conventional biophysical methods, such as differential scanning fluorimetry (DSF) and mass spectrometry (MS), have not been sufficiently sensitive to identify the modest affinity of fragments for a protein target.^{36,37} As a result, biophysical techniques compatible with the smaller size and reduced complexity of fragments have been developed.²⁶ From 2011 to 2013, a shift in screening method preference was observed (Figure 3, a). This is owed in part to the strides in technology but also to increased accessibility.³⁸ Since 2016, three biophysical techniques have dominated the majority of FBDD efforts: NMR spectroscopy - specifically ligand-observed NMR experiments, X-ray crystallography and surface plasmon resonance (SPR) (Figure 3, b).³⁹

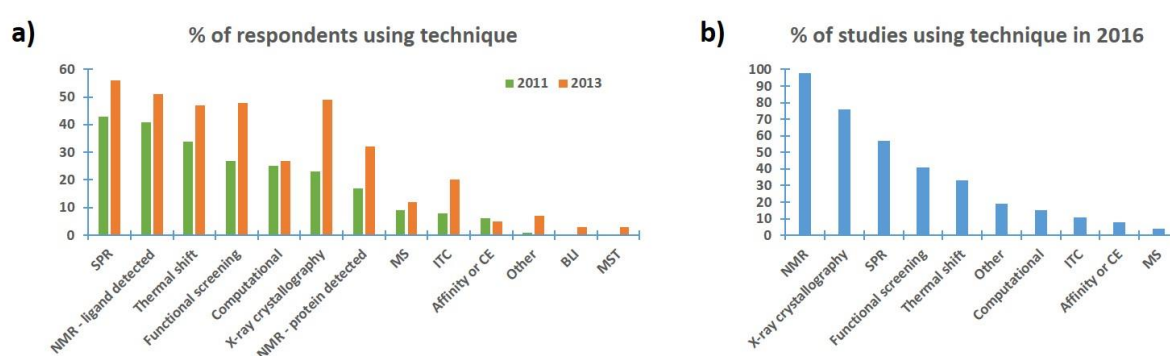


Figure 3: Biophysical techniques used for screening in FBDD programs. **a)** Poll results adapted from the blog *Practical Fragments*,³⁸ reporting a change in fragment screening techniques between the years 2011 and 2013. **b)** Analysis adapted from Swain in 2016,³⁹ in which the screening techniques in 165 published FBDD programs were considered. SPR - surface plasmon resonance; MS - mass spectrometry; ITC - isothermal titration calorimetry; CE - capillary electrophoresis; BLI - biolayer interferometry; MST - micro-scale thermophoresis.

1.1.3.1 Ligand-Observed NMR

Ligand-observed NMR utilises a combination of 1D NMR experiments to track shifts in fragment NMR peaks before and after the addition of a protein.³⁴ From this, it is possible to determine which ligands have undergone a binding event, but no information on the binding site or affinity can be derived. In practice, it is common to use three different 1D experiments - saturation transfer difference (STD),⁴⁰ water-ligand-observed gradient spectroscopy (Water-LOGSY)⁴¹ and Carr-Purcell-Meiboom-Gill relaxation dispersion (CPMG RD),⁴² and to include a competition step to differentiate between specific and non-specific binding.¹³ As this is a measurement in free solution, the solubility and stability of the fragments and protein can be evaluated for each measurement.¹³ This minimises the likelihood of false positives and negatives due to aggregation or precipitation.

1.1.3.2 X-Ray Crystallography

In the past, X-ray crystallography was generally viewed as a secondary screening technique. Following recent developments in high-throughput crystallography, it has now found common use in primary screening.⁴³ Any hits identified through this route are inherently validated for the target, and the binding pose information provides a platform for rapid and efficient SBDD.³⁵ Orthogonal assays are required for biological assessment of the fragment hits, as X-ray crystallography reveals the binding mode and not the potency of a fragment.³⁵ Nonetheless, X-ray crystallography remains a highly popular technique and is the screening concept on which the successful biotech company - Astex Pharmaceuticals - was founded.⁶

1.1.3.3 Surface Plasmon Resonance (SPR)

The key feature of SPR is immobilisation of the target protein to a sensor chip. A solution containing the fragment is then injected over the surface and the refractive index of the interface is monitored. Following a fragment binding event, the protein complex increases in mass near the sensor surface, which is detected as a change in refractive index.⁴⁴ If the ligand solubility is much higher than the dissociation constant (K_d), then titration can be used to quantify binding.⁶ However, in practise these values are often in the same range. SPR uses smaller quantities of protein than either NMR or X-ray crystallography and is a relatively rapid screening technique. The main disadvantage of SPR is that the protein can be challenging to immobilise, while retaining its binding integrity.¹³

1.1.3.4 Isothermal Titration Calorimetry (ITC)

ITC measures the thermodynamics of a protein-ligand interaction *via* observation of the heat exchange during the binding reaction.⁴⁵ Experiments are performed by titration of a ligand into a sample solution containing the protein. Following each addition, the heat released or absorbed is monitored and thermodynamic analysis then enables quantitative characterisation of the binding process.⁴⁶ Data obtained through ITC measurements include the binding constant (K_a), enthalpy (ΔH), entropy (ΔS) and Gibbs free energy of binding (ΔG) and the binding stoichiometry.^{45,47,48} In the past, the use of ITC has been limited due to a lack of sufficient sensitivity, however recent technology developments have yielded instruments capable of measuring heat effects arising from reactions involving nanomole amounts of reactants.⁴⁶ As a result, ITC has become a popular primary screening technique in FBDD.^{49,50}

While focus has been given to four of the most widely used biophysical techniques, other sensitive technologies are also successfully used in screening programs. Those gaining more widespread attention include: protein-observed NMR spectroscopy,⁵¹ thermal shift analysis (TSA),⁵² computational screening,^{53,54} and mass spectrometry (MS).^{55,56} With every method there is a risk of false positives and negatives, and therefore some FBDD programs combine two or more screening techniques and follow up on mutual hits.⁶ While this approach may reduce time wasted on promiscuous fragments, it can also lead to novel and unusual protein-ligand interactions being overlooked, and thus must be used with caution.

1.1.4 Hit-to-Lead Generation

Hit-to-lead generation uses structural biology as a starting point for rational fragment elaboration into a drug candidate.¹⁶ Most of the success stories to date have utilised a robust model of how the fragment binds, and an analysis of all published hit-to-lead examples from 2015 indicates X-ray crystallography is by far the preferred structural technology.¹ Molecular docking can also be useful in assisting SBDD at this stage.³⁵

During optimisation, ligand efficiency (LE) metrics are commonly used to judge the relative efficacy of a fragment manipulation.⁵⁷ The calculation determines the binding energy of the ligand per atom and can be calculated by converting the K_d into the Gibbs free energy (ΔG) of binding [Eqn 1] at 300K and dividing by the number of 'heavy' (*i.e.* non-hydrogen atoms) [Eqn 2].⁵⁸ Furthermore, the Gibbs free energy (ΔG) can be substituted for IC_{50} [Eqn 3].⁵⁷

$$\Delta G = -RT \cdot \ln(K_d) \quad [\text{Eqn 1}]$$

$$LE = \Delta G / N_{\text{non-hydrogen atoms}} \quad [\text{Eqn 2}]$$

$$LE = 1.4(-\log(IC_{50})) / N_{\text{non-hydrogen atoms}} \quad [\text{Eqn 3}]$$

Ligand efficiency is a way of normalizing the potency and MW of a compound to provide a useful comparison between compounds with a range of MWs and activities. This provides a guide to show whether the atoms added during a cycle of elaboration are making optimal interactions with the protein.⁵⁸ In theory, the use of LE metrics should enable the medicinal chemist to achieve an appropriate balance of physicochemical properties and binding affinity. Thereby, minimising the chance of clinical failure due to lipophilicity-related safety issues, such as lack of selectivity, poor solubility and low metabolic clearance.^{18,59} Analysis by Schultes *et al.* and Hopkins *et al.* into the LE of FBDD hits that were selected for further optimisation in 2010 and 2013 respectively, reported average starting LE of 0.38.^{57,60}

Three synthetic strategies are typically employed in hit-to-lead generation: fragment linking, growing and merging (Figure 4).¹³

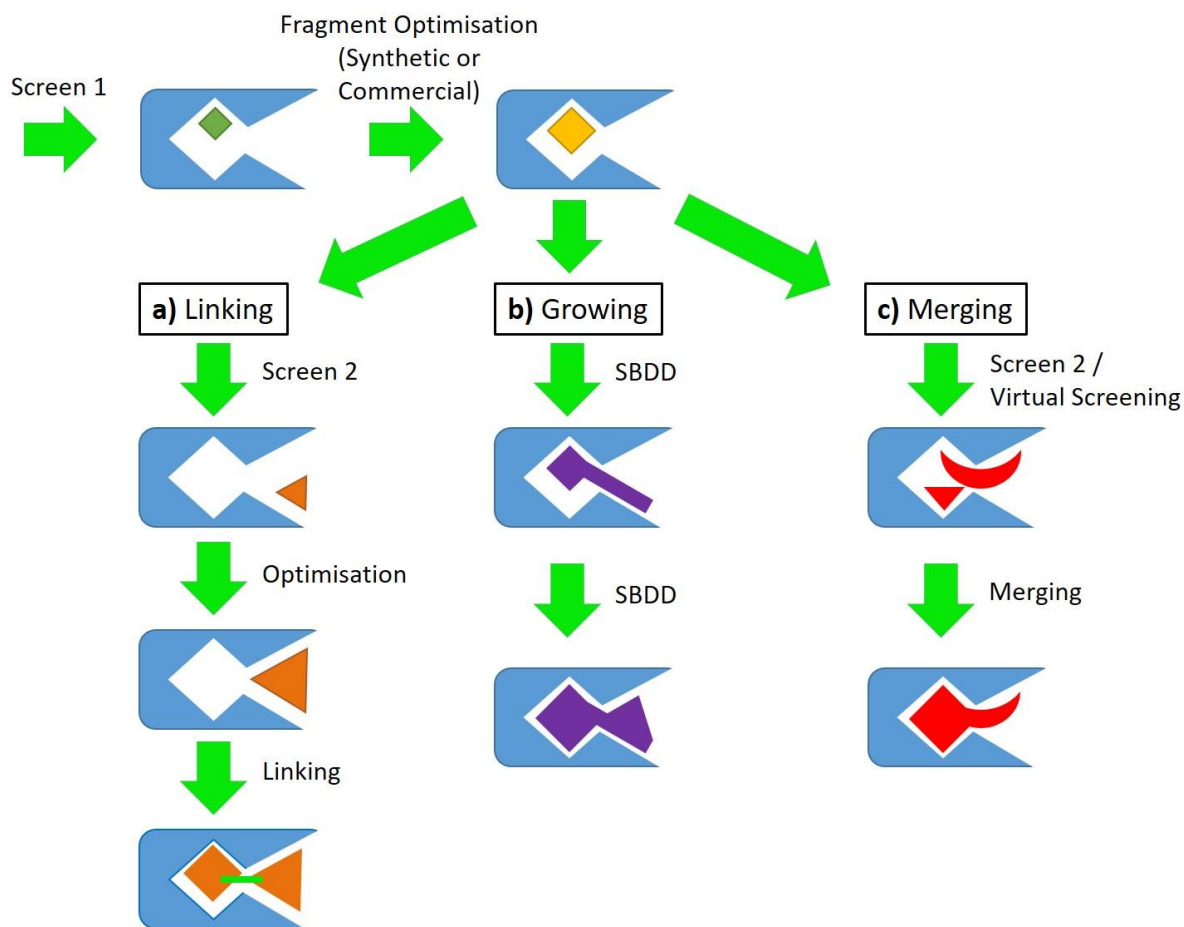


Figure 4: Strategies for fragment optimisation. **a)** Fragment linking. **b)** Fragment growing. **c)** Fragment merging. Adapted from Lamoree *et al.*,¹³ Copyright (2018), with permission from Portland Press.

In the **linking** strategy, two or more fragments binding in different regions of the pocket are linked together *via* rigid or flexible linkers (Figure 4, **a**).²⁵ The linked compound should then have a more favourable ΔG of binding than the sum of the ΔG values for the individual fragments. This is described by the concept of 'super-additivity'.^{61,62} However, in practise, fragment linking is often highly challenging as linkers can constrain the molecule too much. This results in suboptimal interactions with the target and a subsequent loss in binding affinity.¹⁵

The earliest example of fragment linking comes from Shuker *et al.* at Abbott in 1996.⁵¹ This was the first publication of an FBDD project in which a weak μM affinity hit was successfully developed into a potent nM affinity lead. Shuker *et al.*'s work is considered proof of concept for fragments in drug discovery.⁶³

The most advanced example of fragment linking also comes from workers at Abbott, with their selective Bcl-2 inhibitor ABT-199 (**5**) (Figure 5).⁴ Bcl-2 is an apoptosis regulator protein and its aberrant activity results in evasion of cell death and the development of Bcl-2-dependent tumours.⁶⁴ Studies towards this target were as follows: fragment screening by protein-observed NMR, followed by structure determination and optimisation, identified fragments **1** and **2** as inhibitors of Bcl-x_L, a prosurvival protein related to Bcl-2 (Figure 5, **a** and **b**).^{65,66} Combination of fragments **1** and **2**, before further elaboration, provided potent inhibitor **3** (Figure 5, **a** and **c**). This was further optimised to ABT-737 (**4**) (Figure 5, **a** and **d**) which entered clinical trials as a dual Bcl-x_L/Bcl-2 inhibitor.⁶⁵ Subsequent modification of ABT-737 (**4**) provided final drug candidate ABT-199 (**5**) (Figure 5, **a**). In 2016, ABT-199 (**5**) received approval by the US Food and Drug Administration (FDA) for the treatment of chronic lymphocytic leukaemia (CLL) and was released onto the market as venetoclax.⁶⁷

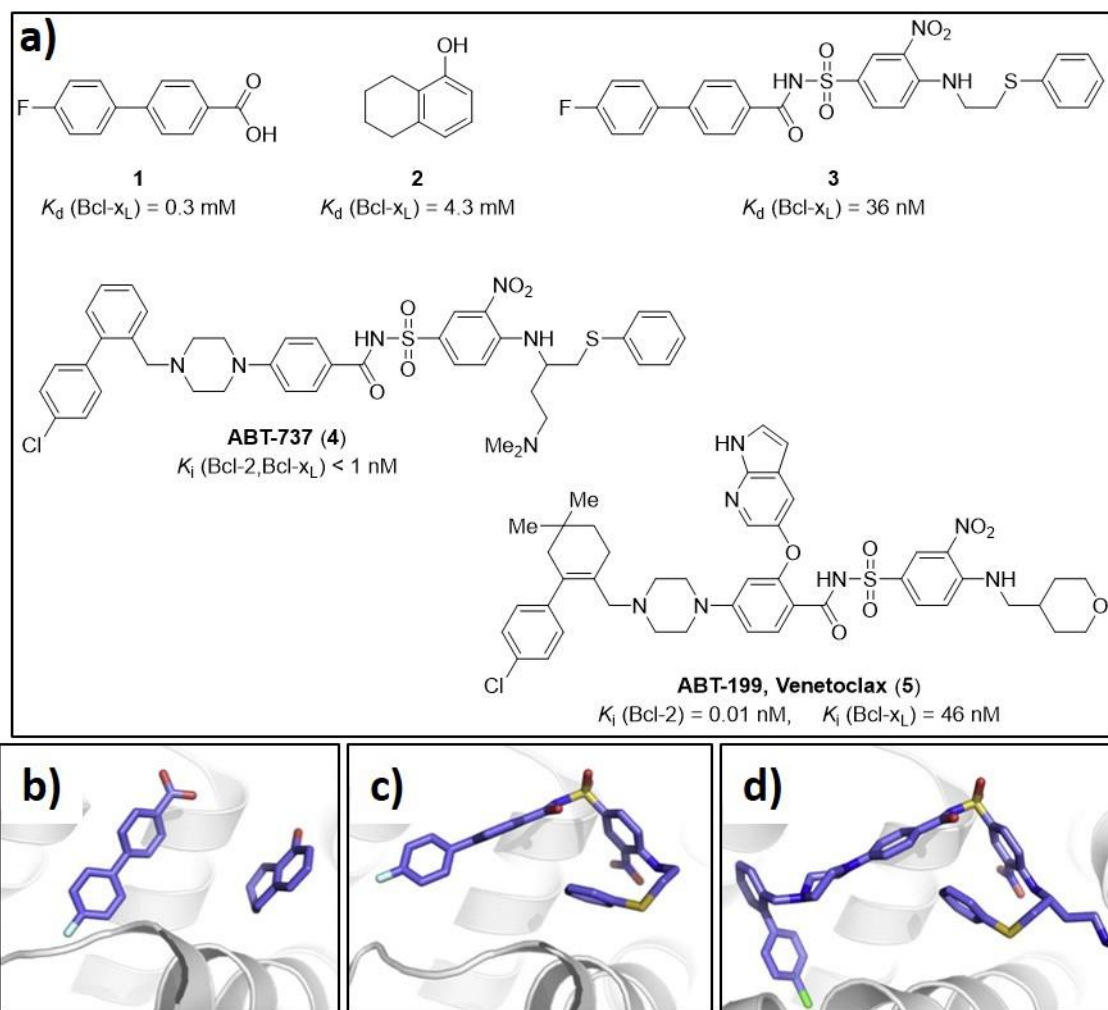


Figure 5: The discovery of ABT-199 (5, venetoclax) by fragment linking. **a)** Chemical structures of compounds tested in the development of ABT-199 (5). **b)** The ternary co-crystal structure of fragments 1 and 2 bound to Bcl-x_L (PDB: 1YSG), the relative binding positions of the two fragments shows potential for optimisation via a linking strategy. **c)** The co-crystal structure of linked-derivative 3 bound to Bcl-x_L (PDB: 1YSI). **d)** The co-crystal structure of optimised ABT-737 (4) bound to Bcl-2 (PDB: 2XYJ). Adapted from Doak *et al.*,⁶⁸ Copyright (2018), with permission from Elsevier.

The second strategy, fragment **growing**, is the most widely applied strategy and involves growing a validated hit in a stepwise fashion, picking up additional target interactions with each iteration (Figure 4, **b**).¹⁵ Structure-guided design is prevalent in this method and a modular approach to optimisation allows medicinal chemists to address specific questions such as the utility of adding a HBA/HBD or filling a small lipophilic pocket. This also highlights the importance of including synthetic handles in the design of the initial library.³¹

The most prominent example of fragment growing comes from the development of FDA-approved vemurafenib (9) by Bollag *et al.* (Figure 6).² Vemurafenib (9) is a selective inhibitor of the B-Raf V600E mutant kinase, which is a well-documented oncogene and present in almost half of all melanomas.⁶⁹

An initial hit (**6**) was identified from a biochemical screen against the kinase Pim-1 (Figure 6, **a**). X-ray crystallography validated the hit and guided the development of elaborated fragment **7** (Figure 6, **a** and **b**). Iterative rounds of SBDD grew into the back cavity of the binding pocket, identifying fragment **8** (Figure 6, **a**). At this point, fragment **8** was co-crystallised with B-Raf V600E and observed to bind the ATP-site in a similar manner to Pim-1 (Figure 6, **c**). Addition of a 4-chlorophenyl moiety provided clinical candidate vemurafenib (**9**) (Figure 6, **a** and **d**). A loss in potency between fragment **8** and lead vemurafenib (**9**) was observed (IC_{50} from 13 to 31 nM), but LE and kinase selectivity were improved. In 2011 vemurafenib (**9**) became the first drug with FBDD origins to be approved by the FDA and is currently used in the treatment of B-Raf driven melanoma.³

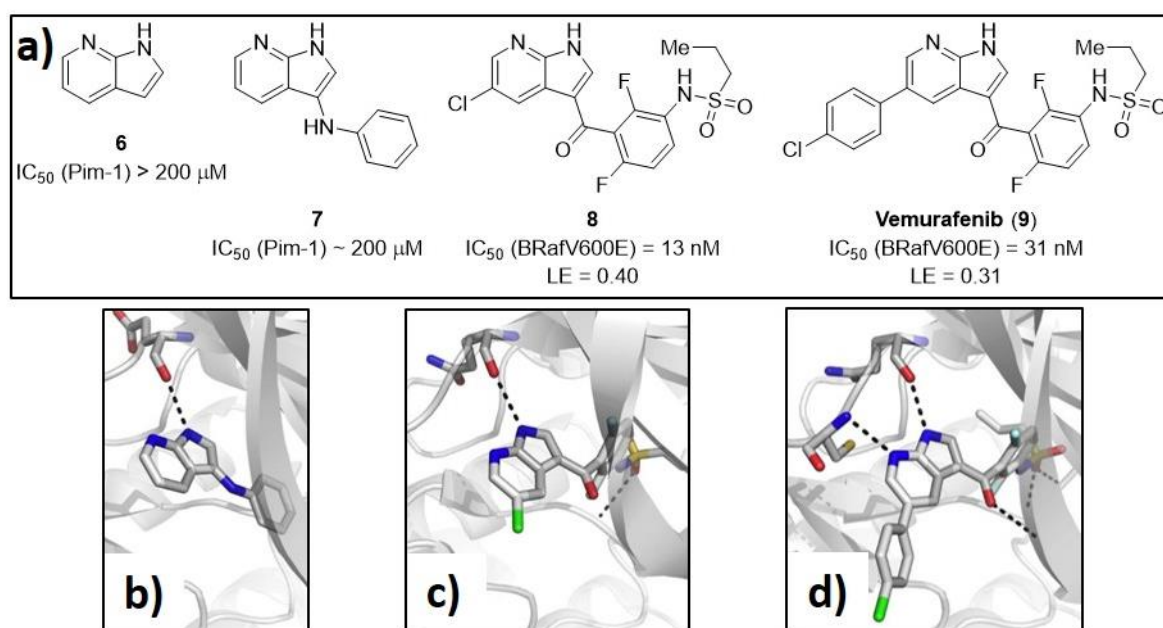


Figure 6: The discovery of vemurafenib (**9**) by fragment growing. **a)** Chemical structures of compounds tested in the development of vemurafenib (**9**). **b)** The co-crystal structure of fragment **7** bound to Pim-1 (PDB: 3C4E). **c)** The co-crystal structure of derivative **8** bound to B-Raf V600E (PDB: 3C4C). **d)** The co-crystal structure of vemurafenib (**9**) bound to B-Raf V600E (PDB: 3OG7). Dotted black lines represent polar interactions. Adapted from Doak et al.,⁶⁸ Copyright (2018), with permission from Elsevier.

Finally, fragment **merging** sees the best features of several overlapping fragments merged into a single molecule with higher potency (Figure 4, **c**).¹³ It relies on the overlay of multiple crystal structures and ambitious SBDD, therefore few successful reports of this technique exist. One example, from the Vernalis archive, shows how fragments were combined with a literature compound in the development of PDPK1-selective inhibitor **16** (Figure 7).⁷⁰ With the use of X-ray crystallography and computational docking, compound **12** was developed from fragments **10** and **11**, while species **14** was derived from **13**. Overlay of the crystal structures for **12**, **14** and literature compound **15**, suggested fragment combination to provide final product **16**. Compound **16** selectively binds PDPK1 with an IC_{50}

of 90 nM, but inhibition of the kinase did not have the desired anti-cancer effect and thus the project was terminated.⁷⁰

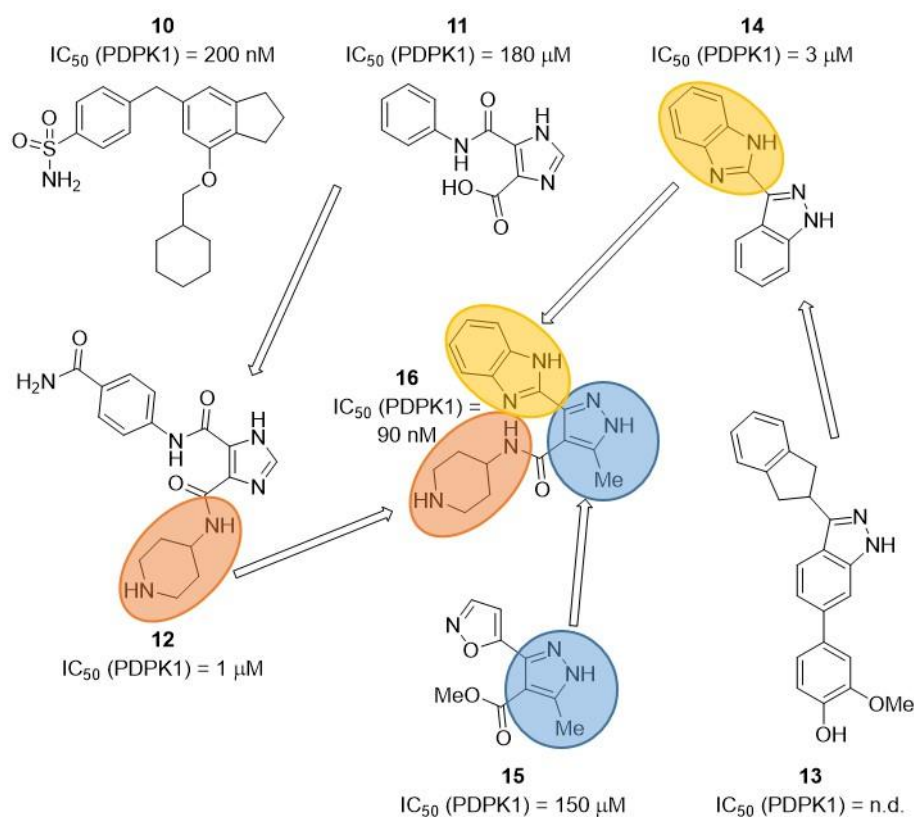


Figure 7: The discovery of protein kinase PDPK1 inhibitor **16** by fragment merging. Initial hit fragments **10**, **11** and **13** were elaborated into fragments **12** and **14**. These were combined with the core of **15** to provide final inhibitor **16**. The circled portions highlight the structural moieties preserved from each fragment during the merging process. n.d.: no data. Adapted from Hubbard,⁷⁰ Copyright (2018), with permission from the International Union of Crystallography.

FBDD projects aim to conclude the hit-to-lead phase once a collection of target-selective, lead-like compounds, with substantial potency, have been generated. These chemical tools should have physicochemical properties resembling drug candidates, rendering them suitable for progression into clinical trials.³¹

1.1.5 Advantages and Limitations of FBDD

As alluded to in the previous sections, the FBDD process has multiple advantages over traditional drug discovery. Firstly, the binding of a low MW fragment reflects a high intrinsic binding enthalpy overcoming an entropic binding penalty.^{71,72} As a result, fragments can be highly efficient ligands and better starting points for physicochemical-controlled elaboration than higher MW hits from HTS. Additionally, the reduced complexity of fragments lowers the chance of a steric group preventing binding. In turn, this leads to an increase in the number of FBDD hits and easier identification of

functional motifs that are essential for target binding.¹³ High hit rate may raise concerns of low specificity *i.e.* a fragment binding to various proteins and/or to a single protein in several ways. But specificity can be introduced during fragment optimisation, and a broad initial approach enables more thorough interrogation of target druggability²⁶ – a vital aspect for chemists investigating new and unusual binding sites and mechanisms. On this note, Saalau-Bethell *et al.* at Astex demonstrated the utility of FBDD towards the discovery of a novel allosteric binding site.⁷³ This site was positioned at the interface between two domains of the Hepatitis C viral protein NS3. Their work showcased successful fragment screening against a challenging PPI and the value of FBDD in identifying alternative modes of action.

Limitations of the current FBDD methodology have also been identified. Evaluation of several existing fragment libraries by Morley *et al.* reported limited shape diversity to the screening sets, with predominantly (hetero)aromatic-derived chemotypes.³⁶ They surmised that this ‘flatness’ might predispose the fragment library success for certain target classes, and limit its tractability against new targets that require pharmacophores with alternative substitution vectors.

Analysis by Johnson *et al.*, into the protein target class featured in FBDD projects from 2015, goes some way to supporting the hypothesis made by Morley (Figure 8).¹ Johnson *et al.* showed that previously exploited, literature-rich protein kinases and proteases were dominant among the successful targets in 2015. In contrast, emerging classes such as PPIs and membrane-bound proteins (*i.e.* GPCRs) barely featured. The preparation of fragment libraries drew on knowledge from previously successful FBDD studies, and therefore heavily featured core scaffolds known to hit existing targets. These biased libraries ultimately led to exaggerated discoveries on the same, well-documented proteins which, in agreement with Morley, interact well with planar, sp²-rich compounds.

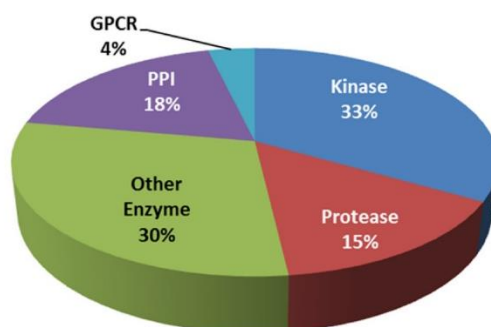


Figure 8: Protein target class analysis for 27 fragment-to-lead examples with publication year 2015. GPCR – G-protein coupled receptor; PPI – protein-protein interaction. Reprinted with permission from Johnson *et al.*¹ Copyright (2018) American Chemical Society.

A further observation by Johnson *et al.* was the reliance of FBDD practitioners on X-ray crystallography – 85% of the FBDD projects in 2015 used X-ray structural data for hit validation and optimisation.¹ Earlier work by Murray *et al.* in 2010 reported similar findings, from which they hypothesised whether the lack of a protein crystal structure had the potential to render a target off-limits.¹⁶ With this in mind, a second explanation for the lack of diversity in protein class targets was put forward by Johnson *et al.* In this analysis the ease of crystallisation of the target protein was considered.¹ They observed that the challenges of obtaining crystal structures for membrane-bound proteins, or ligands in complex with PPIs, were well documented, whereas kinase and protease targets are often readily-crystallised.^{74–77} This provides an alternative explanation for the distribution reported in Figure 8.

Despite the above limitations – with respect to library diversity and target crystallisation, encouraging FBDD progress has recently been reported for multiple PPIs and one membrane protein.^{78–82} Of greatest note is FDA-approved venetoclax (**5**) (Section 1.1.4), which acts to disrupt the PPI between Bcl-2 and BIM, instigating apoptosis in the treatment of chronic lymphocytic leukaemia (CLL).⁴ Additionally, Christopher *et al.* at Heptares published a promising membrane protein example in 2015.⁸² They demonstrated the use of biochemical assays and X-ray crystallography for the development of an advanced, lead-like modulator of the mGlu₅ receptor. mGlu₅ is a member of the metabotropic glutamate receptor family, and modulates synaptic transmission in response to the neurotransmitter glutamate.⁸³ Dysfunction in this signalling is linked to numerous disorders including Parkinson's disease,⁸⁴ neuropathic pain,⁸⁵ anxiety⁸⁶ and depression.⁸⁷

To summarise, low affinity fragment hits can be found for most targets, including those that fail in HTS.⁸⁸ As X-ray crystallography techniques continue to develop,⁴³ and attention is given towards fragment libraries with greater three-dimensionality,³⁶ further success against these previously 'undruggable' targets is expected.

1.1.6 Kinase Inhibitors and FBDD

Protein kinases catalyse the transfer of the terminal phosphate group of adenosine triphosphate (ATP) onto an amino acid residue, commonly serine, threonine or tyrosine, within a polypeptide chain.⁸⁹ Their activity is vital in the mediation of intracellular signalling and as such, they are deemed key regulators of cellular processes.⁹⁰ Aberrant kinase activity has been linked to a large number of disease states including cancer and inflammation as well as metabolic, autoimmune and neurological conditions.^{91–93} As a result, protein kinases are considered one of the most important target classes in modern drug discovery.⁹⁰ Research into the 'druggable kinome' (*i.e.* members of the kinome related to human disease and susceptible to modulation by drugs) has identified more than 150 potential

kinase targets to date.⁹⁴ As of March 2017, a total of 32 kinase inhibitors had been approved by the FDA and more than 1000 clinical studies were ongoing.⁹³

Despite the aforementioned value of exploiting protein kinases in disease therapy, a number of key challenges exist.⁹⁵ All kinases utilise ATP as a cofactor and as a result, the ATP-binding site has been thoroughly investigated and forms the basis for the majority of kinase inhibitor projects.^{96,97} However, drugs with ATP-site competitive modalities are rife with well-documented difficulties:

1. Competition with ATP

Inhibitors must outcompete mM levels of intracellular ATP in order to bind the kinase target.⁹⁵

2. Protein kinase selectivity

There are over 500 human protein kinases, all of which bind ATP in a similar manner, thereby presenting an obvious selectivity challenge when designing inhibitors of just one kinase.⁹²

3. Physicochemical properties

The ATP-binding site is relatively flat and lined on two sides with hydrophobic residues. Therefore, unless care is taken, inhibitors that are lipophilic and sp²-rich are produced – characteristics with poor prognosis in clinical trials due to lack of selectivity, poor solubility and low metabolic clearance.^{59,98}

4. Intellectual property (IP)

The last 20 years has seen an intense interest in kinases by the pharma industry, with the majority of lead-candidates mimicking the adenine group of ATP. As a result, the IP around this template is highly congested.^{95,99}

However, despite these difficulties, it is important to note that some ATP-site competitive kinase inhibitors are remarkably selective for individual kinases when *in vitro*.^{100,101} The high observed potency of these inhibitors can be best explained by the Cheng-Prusoff equation [Eqn 1].¹⁰² This states that a drug IC₅₀ value (concentration of drug at which 50% of the kinase activity is inhibited) depends on the intrinsic affinity of the inhibitor (the dissociation constant, K_d) as well as the competition from intracellular ATP (governed by the [ATP], usually 1-5 mM,¹⁰³ and the $K_{m, ATP}$).¹⁰⁰

$$IC_{50} = K_d(1 + [ATP]/K_{m, ATP}) \quad [\text{Eqn 1}]$$

Thus, the Cheng-Prusoff equation establishes that the affinity of the kinase target for ATP (expressed as $K_{m, ATP}$) is critical in determining the potency of an ATP-site competitive inhibitor. This means that inhibitors with similar intrinsic affinities (K_d values) against multiple kinases *in vivo* will more potently

inhibit kinases with higher $K_{m, ATP}$ values when in cells.¹⁰¹ Therefore, superior selectivity *in vitro* can sometimes be observed for drugs targeting kinases that display weaker competition with ATP.

Returning to the difficulties outlined previously, the application of FBDD in the search for kinase inhibitors has become of great interest. Screening diverse fragment libraries provides the potential for novel scaffold and mechanism discovery. This works in new IP space and offers the opportunity of developing inhibitors that bind to alternative positions on the protein. Careful hit elaboration allows control over physicochemical properties⁹⁵ and the wealth of available kinase structural data accelerates the optimisation step, affording clinically acceptable lead compounds in a timely manner.⁹⁹ To highlight the uptake of FBDD by kinase practitioners, Johnson *et al.* analysed all fragment-to-lead projects from 2015. They found that protein kinases constituted the largest target class (Figure 8).¹ Furthermore, in 2016 over one third of FBDD candidates in clinical trials were kinase inhibitors.⁵ Finally, as summarised in Section 1.1.4, vemurafenib (**9**) was the first FDA-approved drug with origins in FBDD and is a potent and selective kinase inhibitor.²

However, even with the dawn of FBDD, development of kinase inhibitors displaying modalities distinct from the ATP-binding site remains a significant challenge.⁹⁵ To date, very few examples of allosteric kinase inhibitors exist in the literature, but in 2011 two interesting fragment-based approaches were reported (Figure 9 and Figure 10).^{104,105}

The first, from Pollack *et al.*, used SPR to screen a diverse fragment library against protein kinase p38 α .¹⁰⁴ This led to the identification of a novel lipid binding pocket (Figure 9). X-ray crystallography of hit fragment **17** in complex with p38 α verified the binding position and subsequent SBDD improved binding affinity tenfold. Overlay of ligand-protein X-ray crystal structures with the Apo and active forms of p38 α suggested an allosteric mechanism of action for the inhibitor series. Their work continues towards the synthesis of more potent analogues.

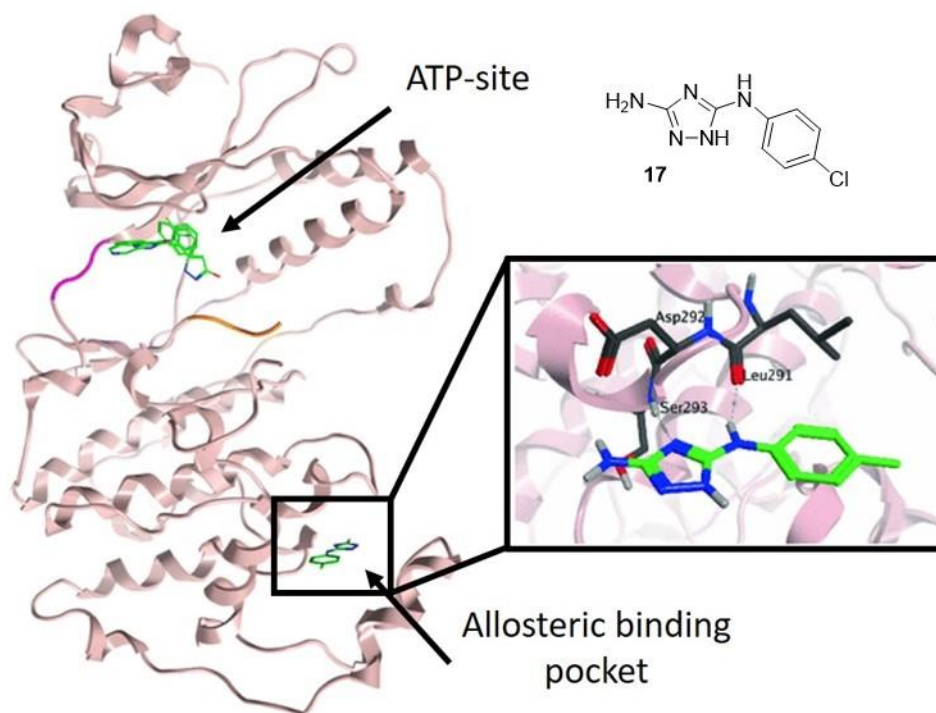


Figure 9: Discovery of an allosteric binding pocket on protein kinase p38 α . Position of the allosteric pocket relative to the ATP-binding site is shown. An enlargement of the binding mode for hit fragment **17** (green) is featured and key p38 α residues are highlighted (black). Adapted from Pollack *et al.*,¹⁰⁴ with permission from Springer, Copyright (2018).

The second example comes from Betzi *et al.* who utilised X-ray crystallographic screening to identify an allosteric site on protein kinase CDK2 (Figure 10). When hit fragment **18** binds in this pocket, the C-helix undergoes a conformational change and the ATP-binding site is reduced in size. As a result, the crucial interaction between CDK2 and cyclin A is disrupted and CDK2 kinase activity is lost. Their work on elaborating initial hit **18** is ongoing.

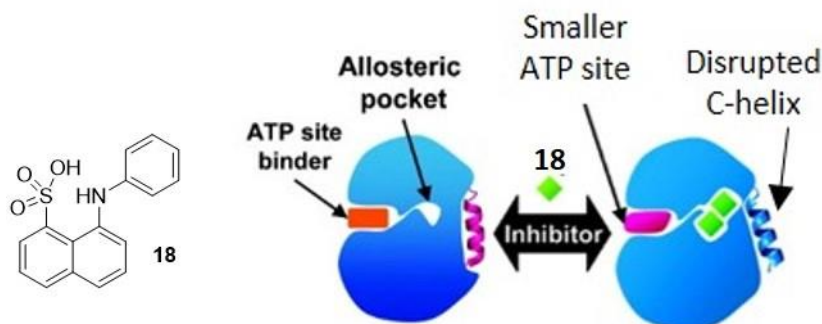


Figure 10: Discovery of an allosteric binding pocket on protein kinase CDK2. Position of the allosteric pocket relative to the ATP-binding site is shown. Upon binding allosteric inhibitor **18** (green diamond) the C-helix conformation is disrupted (purple to blue helix) and becomes incompatible for cyclin A association. The ATP-binding site is also reduced in size (orange to purple rectangle). Adapted with permission from Betzi *et al.*¹⁰⁵ Copyright (2018) American Chemical Society.

In conclusion, the successful approval of vemurafenib (**9**), and the emergence of allosteric kinase inhibitors, validates the power of FBDD in the identification of efficient fragments and new binding pockets. Continued work in this area should facilitate the development of novel kinase modulators with properties superior to traditional ATP-site competitive drugs.

1.2 Protein Kinase CK2

Protein kinase CK2 is a ubiquitous serine/threonine kinase that is highly conserved in eukaryotic cells.¹⁰⁶ Since its discovery in 1954,¹⁰⁷ over 600 substrates modulated by CK2 phosphorylation have been identified.¹⁰⁸ CK2 interacts with diverse and essential cellular pathways including cell growth,¹⁰⁶ proliferation,¹⁰⁹ survival,¹¹⁰ morphology¹¹¹ and transformation.¹¹² Furthermore, its role in signalling pathway activation,¹¹³ angiogenesis,^{114,115} embryonic development¹¹⁶ and circadian rhythm¹¹⁷ is well documented. Extensive research into CK2 signalling has established a definitive link between increased expression/activity and disease states such as cancer,¹¹² cardiac hypertrophy,¹¹⁸ multiple sclerosis¹¹⁹ and inflammation.¹²⁰ Additionally, in contrast to the majority of eukaryotic kinases, CK2 is constitutively active, *i.e.* active in the absence of phosphorylation and/or specific stimuli.¹⁰⁶

The breadth of CK2 impact on cellular machinery has given it the status of a ‘master regulator’ within the cell,¹²¹ and the last twenty years have seen increased interest in the development of chemical modulators for this kinase.¹²² The following section reviews the structure of CK2, before its role in cancer is examined and its targeting in cancer therapy is considered. An overview of published CK2 inhibitors is given and the therapeutic potential of a novel binding site, discovered by FBDD, is introduced.

1.2.1 CK2 Structure

The CK2 holoenzyme is a tetramer comprising two catalytic alpha subunits (α and α') supported on a regulatory beta (β) subunit dimer (Figure 11).¹²³ The most stable form of the protein is in its tetrameric complex. However, studies show the widespread presence, and full kinase activity, of CK2 α and α' subunit monomers within cells.^{124,125} Crystal structures of the holoenzyme¹²⁶ and individual subunits^{127,128} have been published and over 70 structures of CK2 in complex with its inhibitors have been deposited in the protein data bank (PDB).¹⁰⁸ Structural analysis of these crystals revealed CK2 conserves most of the major structural motifs reported for all kinases (*i.e.* the P-loop, substrate binding site, catalytic loop and activation loop). Furthermore, comparison of all known CK2 primary sequences suggests CK2 α and α' are well conserved within eukaryotes.¹²³ The CK2 β subunit primary

sequence is similarly well conserved in higher eukaryotes, but two homologues have been identified in yeast and three in *Arabidopsis thaliana*.^{123,129–131}

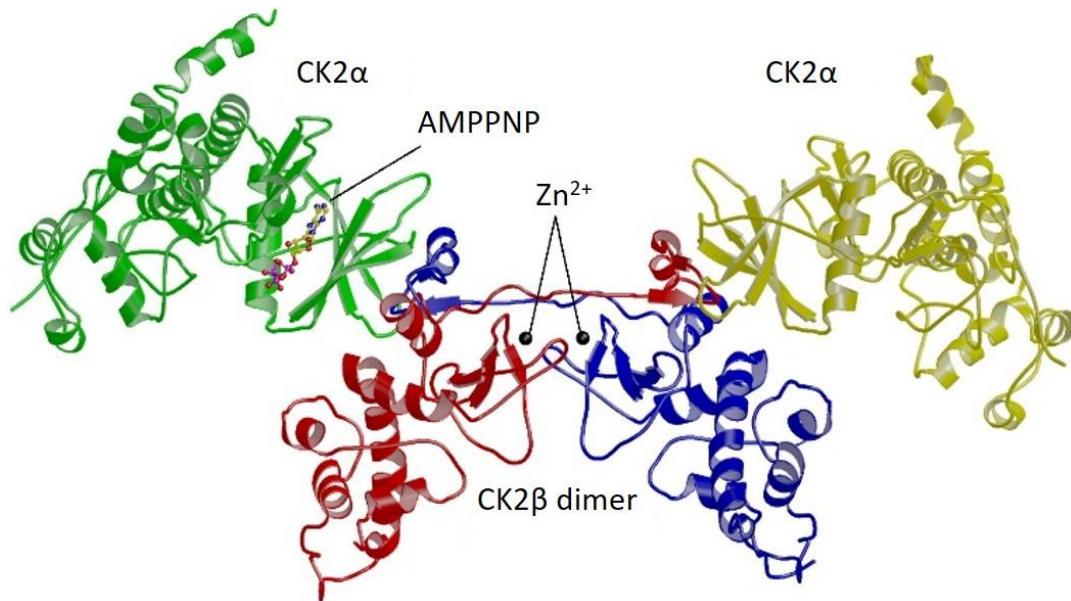


Figure 11: Overview of human CK2 holoenzyme complex (PDB: 1JWH). The tetramer consists of two CK2 α catalytic subunits (green and yellow) and a CK2 β regulatory dimer (red and blue). A molecule of AMPPNP is shown in the ATP-binding site of one CK2 α subunit and two Zn²⁺ ions are shown in the CK2 β dimerization region. Reprinted from Niefind et al.,¹³² Copyright (2018), with permission from Elsevier.

1.2.1.1 The Catalytic α and α' Subunits

The catalytic subunits are responsible for binding ATP and the substrate, and catalysing the phosphorylation event.¹²⁸ In mammals, the CK2 catalytic subunit is composed of two genes, CK2 α (CSNK2A1) and CK2 α' (CSNK2A2), which share 75% sequence similarity.^{123,133} Of the two, the CK2 α protein has broader and higher-level tissue expression, but specific roles for the two isoforms have not yet been established.^{134–136}

Drawing from all known crystallographic information, the architecture of the CK2 α -subunits can be described by two main topological determinants (Figure 12). The first is the *N*-terminal domain, also known as the '*N*-lobe', and includes β strands 1-5 in an antiparallel arrangement and the α C helix. The second is the *C*-terminal domain, also known as the '*C*-lobe', and is dominated by an α -helical fold (helices α D-N) featuring two small double-stranded β -sheets (β 6-9).^{128,137} The two lobes are connected by a short loop, called the '*hinge region*' (Glu114-Asn118), which is the basis for the ATP-binding site.^{128,137} Overall, this is a typical kinase fold structure.¹³⁸

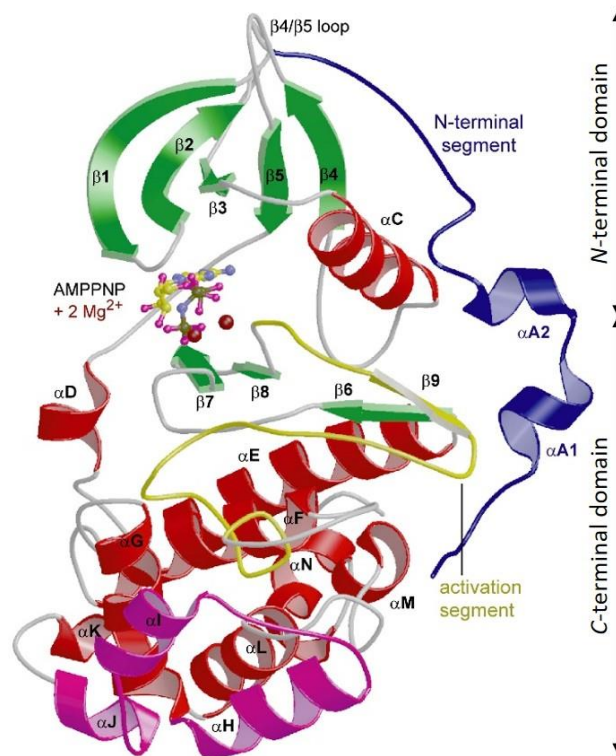


Figure 12: Overview of *Zea mays* catalytic subunit, CK2 α , with AMPPNP and Mg $^{2+}$ ions occupying the ATP-binding site (PDB: 1LP4). The key structural features of the subunit are labelled and the short loop between $\beta 5$ and αD represents the hinge region. Reprinted from Niefind et al.,¹³² Copyright (2018), with permission from Elsevier.

The catalytic subunits are both related to the CMGC group kinase subfamily, named after the initials of some members including cyclin-dependent kinases (CDKs), mitogen-activated protein kinases (MAPKs), glycogen synthase kinases (GSKs) and CDK-like kinases. This group has a diversity of functions in cell cycle control, growth and stress response, cell signalling, splicing and metabolism.¹³⁹ However, the α and α' subunits display some sequence characteristics unique to CK2.¹²³ Most notable are three differences:

1. High concentration of basic residues around the substrate-binding channel

In contrast to the rest of the CMGC kinase class, CK2 is characterised by an acidophilic substrate recognition site. In particular, helix αC (Lys74-Arg80)¹⁴⁰⁻¹⁴² and residues Lys49¹⁴³ and His160¹⁴⁴ are acidic in all other kinases within the CMGC family. In CK2, these residues are important for the recognition of substrates at the $n+3$, $n+2$ and $n-2$ positions respectively (Figure 13, **b**). Additionally, the activation segment of CK2 (Figure 13, **a**) hosts an unusual basic triplet (Arg191, Arg195 and Lys198), responsible for the recognition of the substrate at position $n+1$ (Figure 13, **b**).¹⁴² In line with these observations, CK2 substrates are characterised by multiple acidic residues surrounding the phosphoacceptor amino acid.¹⁴⁵

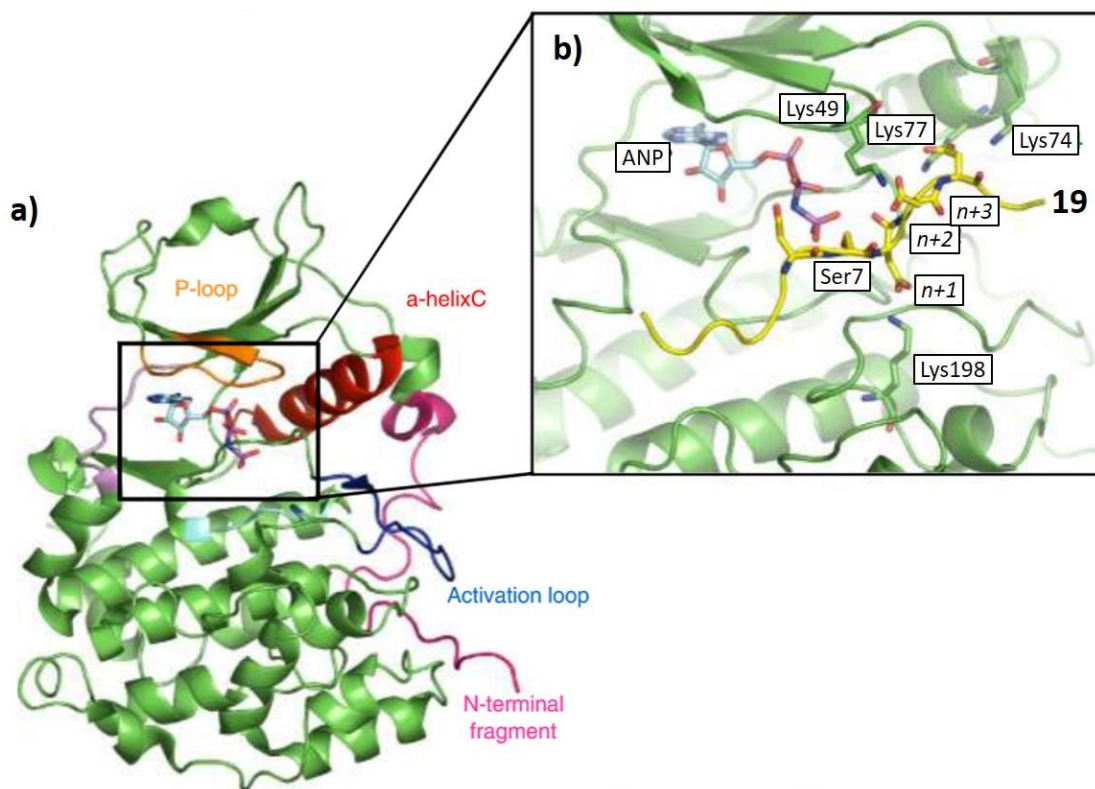


Figure 13: Representation of CK2 α with an enlargement of the substrate binding region. **a)** Human CK2 α (green) with typical kinase subdomains highlighted and ANP (blue) occupying the ATP-binding site (PDB: 1JWH). **b)** CK2 α substrate binding channel (green) with substrate mimic **19** (yellow) modelled. The most important protein-peptide interactions are highlighted. Adapted from Cozza *et al.*,¹²³ Copyright (2018), with permission from John Wiley and Sons.

In 1994, Marin *et al.* developed a CK2-selective dodecapeptide substrate mimic (sequence: RRRADDSDDDD, **19**).¹⁴⁶ Point-mutation studies in both the protein¹⁴² and peptide¹⁴³ corroborated the sequence binding position as the substrate channel (modelled in Figure 13, **b**). However, to date, CK2 has not successfully been crystallised with the peptide, or a genuine substrate, so this has not been unambiguously verified.¹⁴⁵ Peptide **19** demonstrates the ability of CK2 to recognise and bind highly acidic substrates (considered in greater depth in Results and Discussion, Section 2.3).

2. Absence of a regulatory phosphorylation site in the substrate recognition domain

Both catalytic subunits lack the common phosphorylation mechanism by which other members of the class downregulate the substrate-binding site activity.¹²³ Absence of this reputed phosphorylation site, either a threonine or tyrosine in the substrate recognition domain, contributes to the observed constitutive activity of CK2.

3. Absence of a regulatory phosphorylation site in the activation loop

Neither catalytic subunit presents any serine or threonine residues in the activation loop (Asp175-Tyr188) and no phosphorylation event near this region has ever been reported.¹²³ In contrast, all other

CMGC and eukaryotic serine/threonine kinases require phosphorylation of this loop to promote a transition from the inactive to active state.¹³⁹ This transition promotes maximal enzyme activity. In the case of CK2, which is always in its active state, it has been shown that the unusual position of the *N*-terminal domain is instead essential.¹⁴⁷ This blocks the activation loop in an open, and consequently active, conformation.

1.2.1.2 The Regulatory β Subunits

Within the CK2 tetrameric complex, the regulatory subunit dimer, $(CK2\beta)_2$, acts as a central scaffold,¹⁴⁵ alters CK2 substrate specificity¹⁴⁸ and modulates kinase activity.^{149,150} CK2 β is encoded by the gene CSNK2B and is ubiquitous in the eukaryotic kingdom.¹²³ It ranges in size from 26 - 46 kDa and bears no sequence similarity with any other known proteins except the stellate protein from *Drosophila melanogaster*.¹⁵¹

The primary sequence of CK2 β presents an interesting distribution of acidic and basic residues located at the *N*- and *C*-terminals respectively (Figure 14, **a**).¹⁵² X-ray crystallographic data and biochemical experiments have clarified the structures and functions of these regions. The *N*-terminal domain has an α -helical fold and is involved in the negative regulation of CK2 activity.¹⁵³ The *C*-terminal domain contains β sheets 1-5, two α -helices and a zinc-binding site. It is responsible for the positive regulation of CK2, β - β dimerization, association with the α -subunit and preservation against unfolding and proteolysis.¹⁵⁴

The Zn²⁺-binding motif (residues 105-161, *C*-terminal) provides a highly efficient dimerization interface for the CK2 β subunits (Figure 14, **b**). First, multiple hydrophobic interactions are formed between the zinc-finger motifs of two CK2 β monomers. This pulls the two subunits into close contact. Then, the CK2 β tail of each monomer, consisting a small two-stranded antiparallel β -sheet (β_4/β_5), crosses the dimer interface to nestle against the second CK2 β unit. This sets the stage for two CK2 α subunits to associate independently with the dimer.¹⁴⁵ When this happens, the β_4/β_5 segment inserts into a shallow hydrophobic groove formed by β -sheets 1-5 in the *N*-lobe of CK2 α . This PPI is 832 Å² and referred to as the CK2 α /CK2 β -subunit interface.¹²⁶

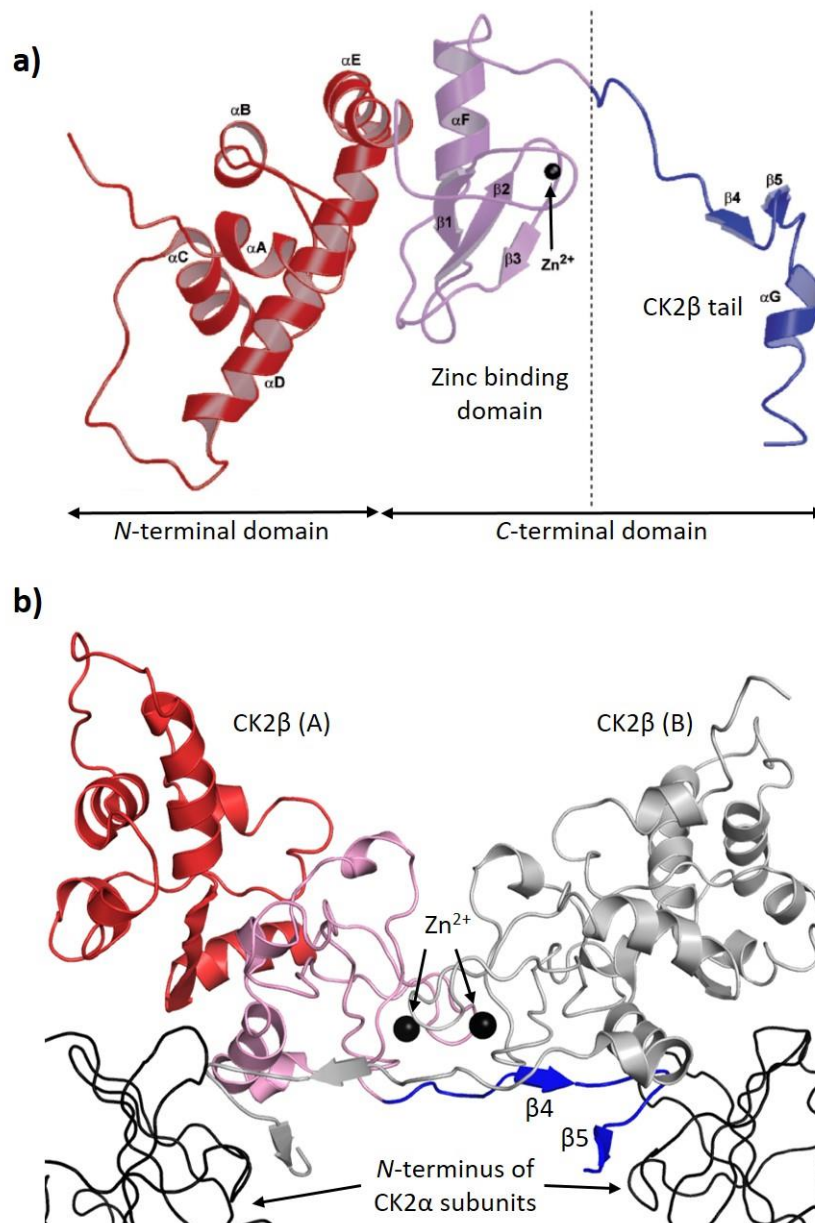


Figure 14: Regulatory subunit CK2 β , extracted from holoenzyme X-ray crystal structure (PDB: 1JWH). **a)** Architecture of CK2 β subunit with main domains, N-terminal (red) and C-terminal (purple and blue), shown. The zinc-binding site (purple) and C-terminal tail (blue) are highlighted for clarity. Reprinted from Niefind et al.¹⁴⁵ with permission from Springer, Copyright (2018). **b)** Overall ribbon presentation of a CK2 β dimer in the holoenzyme. The CK2 β monomers (A: red/purple/blue, B: grey) interact at the zinc-binding site (purple) and the CK2 β tails (blue) extend across the dimer interface to sit against the opposite monomer. The N-lobes of two CK2 α subunits are superimposed as black traces to indicate the position of the CK2 α /CK2 β interface.

1.2.1.3 The Tetrameric Holoenzyme $\alpha_2(\alpha')\beta_2$

As mentioned previously, in Section 1.2.1, protein kinase CK2 is usually isolated as a tetrameric structure, $\alpha_2(\alpha')\beta_2$ (Figure 11). The tetramer displays greater stability than individual CK2 α

monomers,¹⁵⁴ and the activity of isolated CK2 α subunits is generally lower with respect to the holoenzyme.¹⁵⁵ Some studies suggest that a transition from an isolated tetramer to an inactive multimeric form of CK2 is possible *via* electrostatic contacts. These hypothesised multimeric structures include holoenzyme dimers,¹⁵⁶ holoenzyme linear tetramers¹⁵⁷ and holoenzyme circular tetramers.¹⁵⁸

1.2.2 CK2 as a Cancer Driver

An association between CK2 and neoplasia has been known for a long time.^{159–161} In particular, a cause-effect link between abnormally elevated CK2 expression/activity and the enhancement of the tumour phenotype has been established.¹⁶² The following sections summarise the impact of raised cellular CK2 level on cancer (Figure 15) and introduce the concept of CK2 addiction in cancer cells.

1.2.2.1 Elevated CK2 Level

A striking observation is that CK2 activity is invariably more elevated in tumours than in corresponding normal tissues and cells.^{160,163} Over the years, multiple studies have shown that CK2 genes, especially CK2 α and α' , are overexpressed in many common cancer types. These include lung,¹⁶⁴ head and neck,¹⁶⁵ mammary gland,¹⁶⁶ prostate¹⁶⁷ and kidney cancers.¹⁶⁷ Furthermore, CK2 level can be used as both a diagnostic and prognostic marker.^{162,168} To demonstrate, Kaplan-Meier Plotter analysis by Ortega *et al.* found strong correlation between CK2 expression level and lower patient survival rate for lung, breast and ovarian cancer types.¹⁶⁹ Similarly, analysis into head and neck tumours by Gapany *et al.* gave the same unfavourable prognosis.¹⁷⁰

When considering the role of CK2 in healthy cells, it is hardly surprising that raised activity should have such a devastating effect. The ability of CK2 to promote cell proliferation,¹⁰⁹ growth¹⁰⁶ and survival,¹¹⁰ modulate diverse signalling pathways,¹⁷¹ enhance cellular transformation¹¹⁵ and support neovascularisation¹⁷² all provide selective advantage to a tumour, and are characteristic hallmarks of cancer.¹⁷³ The oncogenic nature of CK2 is further supported by experimental studies in mice,¹⁷⁴ whereby site-specific overexpression of CK2 leads to cancer development *via* enhanced pro-survival and anti-apoptotic signalling.^{175,176} CK2 α -subunit “knock-in” experiments also result in promoted neoplastic transformation.^{177,178}

Finally, elevated CK2 level is known to contribute toward the multi-drug resistant phenotype¹⁷⁹ – one of the major problems in the pharmacological treatment of tumours. In CK2, this counteracts the

efficacy of anti-tumour agents, most notably imatinib^{180,181} and melphalan.¹⁸² Their effectiveness is consequently restored by CK2 inhibition.

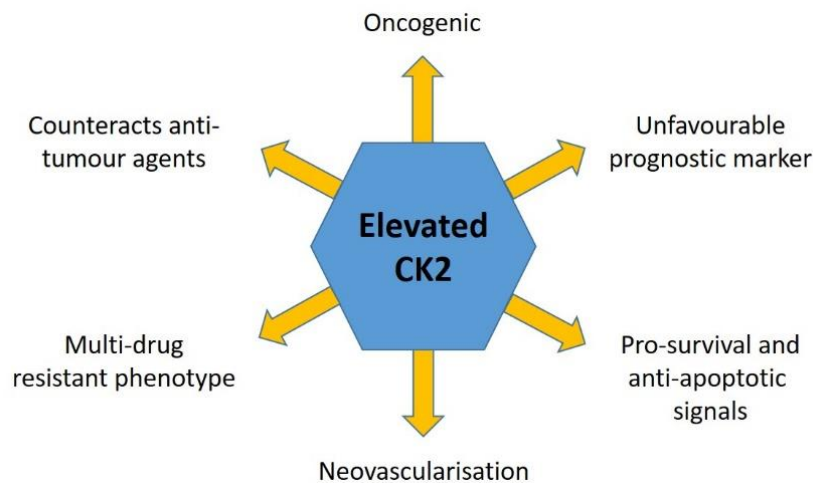


Figure 15: Summary of the effects of abnormally high CK2 level.

1.2.2.2 Addiction to CK2

The term 'addiction' was originally coined by Weinstein.¹⁸³ It was used to highlight the fact that tumour cells, enriched in a particular oncogene, may critically rely on a sustained level of this gene to a greater extent than cancer cells not overexpressing the gene. As a result, the malignant phenotype can be reverted toward normal, or apoptotic, by just lowering the level of the oncogene the tumour is addicted to. Consequently, the proteins associated with these oncogenes represent potential drug targets.¹⁸⁴

Over recent years, it has been observed that not all addictive proteins are activated by mutations to their genes. This phenomenon is now referred to as 'non-oncogene addiction'.^{184,185} It applies to situations where a protein which is not subjected to obvious mutation becomes overexpressed to a degree of causing an undue reliance on itself. Protein kinase CK2 is a pertinent example of this class.¹¹⁵ There are no gain-of-function CK2 mutants known, yet its elevated expression level is associated with a host of cancer types, and the majority of these display a reliance on it for survival.

CK2 is expressed in all cells but its level significantly differs, with higher expression levels observed in cancer cells. This suggests specific roles of CK2 in malignancies and a stricter reliance on its functionality for survival. This concept is supported by the observation that primary tumour cells treated with CK2 inhibitors are more susceptible to cell death than healthy precursor cells treated in

the same manner. This has been found for multiple myeloma,¹⁸² acute myeloid leukaemia¹⁸⁶ and T-acute lymphoblastic leukaemia cells.¹⁸⁷

In summary, CK2 may not be a *sensu stricto* 'tumour promoter' but whenever its activity is abnormally increased, a favourable cellular environment for cancer onset results. Extensive data provides evidence for elevated CK2 as a biomarker for cancer, and addiction studies reveal CK2 as necessary for cancer cell survival. Therefore, the development of potent and selective cell-permeable CK2 inhibitors, devoid of undesirable side effects, represent a valuable tool for the treatment of a wide range of oncological diseases.

1.2.3 CK2 Signalling and Cancer

The ability of CK2 to promote tumours may be largely due to its ability to regulate a broad range of signal transduction pathways. These include the NF- κ B,¹¹⁶ Wnt,¹¹⁶ PI3K/Akt,¹⁸⁸ Hedgehog¹⁸⁹ and JAK/STAT pathways.¹⁹⁰ Modulation of these signalling cascades results in cells displaying distinct liabilities, such as growth advantage, enhanced survival and dynamic adaptation to stress.¹⁹¹ Ultimately, these alterations can lead to tumorigenesis and therefore the signalling mechanisms represent avenues by which CK2 can induce cancer.

Illustrated below are three pathways in which CK2 is a multi-site regulator (Figure 16). Under healthy conditions, CK2 modulates transcriptional activity and enables regular development. When CK2 activity is elevated, the transcriptional pathways are abnormally reactivated and lead to oncogenesis.¹¹⁶

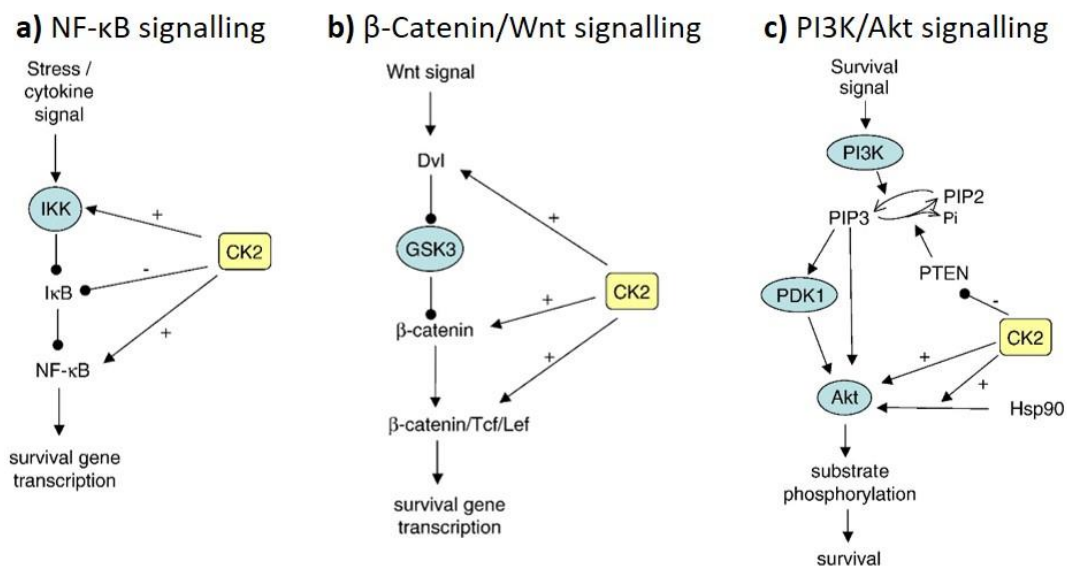


Figure 16: CK2-dependent pathways **a)** NF- κ B pathway. **b)** β -Catenin/Wnt pathway. **c)** PI3K/Akt pathway. A positive effect (+) is indicated by a normal arrow and means enhanced stability and/or activity. A negative effect (-) is indicated by a dot-arrow and means inhibition or increased degradation. Blue circles denote kinases located in 'vertical pathways' downstream from extracellular signals, while CK2 is in a yellow rectangle to show involvement in 'lateral pathways'. Reprinted from Ruzzene et al.,¹¹⁵ Copyright (2018), with permission from Elsevier.

a) NF- κ B signalling

NF- κ B normally binds to its inhibitor I κ B and is sequestered in the cytosol. Activation of kinase IKK, by stress or a cytosine signal, promotes proteolytic degradation of I κ B. This releases free NF- κ B which then translocates into the nucleus and functions as a transcription factor for anti-apoptotic and pro-proliferative genes (Figure 16, a).¹¹⁵

CK2 acts at different levels of this process. Firstly, it can phosphorylate IKK thereby promoting I κ B degradation and enabling NF- κ B signalling.¹⁹² Secondly, it can directly phosphorylate I κ B, providing an alternative pathway for promoting I κ B proteolysis.^{193,194} Finally NF- κ B itself can be phosphorylated and activated by CK2.^{195,196}

Aberrant activation of NF- κ B has been documented in several cancers including mammary gland, prostate and head and neck cancer.^{197,198} Knockdown of individual CK2 subunits also results in a decrease in NF- κ B gene expression.¹⁹⁹

b) β -Catenin/Wnt signalling

The Wnt signalling cascade regulates cell proliferation (Figure 16, b).¹¹⁵ When in the presence of Wnt, the stabilising protein dishevelled (Dvl) inhibits the 'destruction complex' associated with kinase GSK3. As a result, β -catenin is not targeted to the proteasome and its cellular level remains high. It then acts as a co-factor for transcription factors of the TCF/LEF family and promotes survival.

CK2 can affect this pathway at multiple levels: phosphorylation of Dvl, β -catenin and the β -catenin/TCF/LEF complex are all possible. This promotes their stabilisation and activates survival gene transcription.^{200,201}

Song *et al.* showed that β -catenin is upregulated in mice overexpressing CK2 α in mammary glands.²⁰⁰

c) PI3K/Akt signalling

PI3K activation leads to the phosphorylation and activation of the oncogene Akt, which has downstream anti-apoptotic effects (Figure 16, c).²⁰² The pathway is antagonised by PTEN, a phosphatase which dephosphorylates PIP3 and maintains PI3K/Akt signalling down, under resting conditions.²⁰³

In this pathway, CK2 is again a multi-site upregulator. It acts indirectly by phosphorylating PTEN and inhibiting its phosphatase ability, thus resulting in unregulated Akt-dependent signalling.²⁰⁴ It also acts directly, by phosphorylating Akt and inducing a hyper-activated state.²⁰⁵ In addition, phosphorylation of the chaperone protein Hsp90 is possible by CK2. This results in a stabilised Akt-Hsp90 association that protects Akt from dephosphorylation.²⁰⁶

Aside from the role of CK2 as a cell survival agonist, it also acts as an antagonist in the apoptotic program.¹¹⁵ Its action is most notable in the disruption of caspase-mediated cleavage. Caspases are a family of protease enzymes that play an essential role in programmed cell death.²⁰⁷ Their activation leads to controlled degradation of cellular components, and caspase deficiencies or mutations are a cause of tumour development. Analysis of the caspase cleavage consensus sequence shows significant similarity with the CK2 substrate consensus sequence.²⁰⁸ This has led to the common observation that sequence phosphorylation by CK2 hampers subsequent cleavage by caspases. This results in inhibition of apoptosis and promotes tumorigenesis. This has been recognised for Bid,²⁰⁹ Max,²¹⁰ hematopoietic lineage cell-specific protein 1 (HS1),²¹¹ presenilin,²¹² connexin 45.6²¹³ and PTEN proteins.²¹⁴

In summary, it is clear that CK2 plays a global role as a pro-survival and anti-apoptotic agent, which potently contributes to its oncogenic activity.

1.2.4 CK2 as an Anticancer Target

In developing novel avenues for effective cancer therapy, the ultimate goal is to eradicate all tumour cells in the host and achieve a complete cure of the disease.¹²¹ Thus, it is important to consider targeting a protein that is uniquely indispensable for cell survival, otherwise tumour cells will escape

cell death by recruiting an alternative pathway.^{161,215} The molecular targeting of 'non-critical' species might limit their therapeutic utility and hinder productive treatment of the disease.²¹⁶

CK2 plays a key role in many cellular processes that have been demonstrated as essential for cell survival. The knock-out of CK2 α is lethal in mice²¹⁷ and *Saccharomyces cerevisiae*,²¹⁸ while the deletion of CK2 β alleles results in abnormal development in the early stages of mouse growth.²¹⁹ Additionally, downregulation of CK2 impacts not only cell growth and proliferation, but also induces widespread apoptosis and inhibition of angiogenesis, all to the benefit of cancer cell elimination.^{114,220–223} In line with this, gene silencing targeted against CK2 provides the second most effective induction of apoptosis across the whole kinome when tested in pancreatic tumour cell lines.²²⁴ Finally, as far as the literature reports, there appear to be no redundant pathways to compensate for CK2 downregulation.^{217–219} Ultimately these findings validate CK2 as an attractive and suitable target for cancer therapy.

It is important to mention here that the ubiquitous and essential nature of CK2 functionality raises issues of host toxicity. This therefore casts doubt on its 'druggability'. However, studies show that normal cells exhibit relative resistance to apoptosis induction in response to CK2 inhibitors, compared to cancer cells. This observation suggests that malignancies may be more sensitive to CK2 modulators than healthy cells.^{220,222} The concept of cancer cell addiction to CK2 was discussed more thoroughly in Section 1.2.2.2, Addiction to CK2.

In conclusion, dysregulated CK2 activity has been identified as a key player in the development and maintenance of the cancer phenotype. Elevated CK2 level reflects the pathological status of a tumour and serves as a biomarker for cancer studies. Furthermore, it is an unfavourable prognostic marker in the clinic. Subunit knock-out studies and gene silencing have shown CK2 as an essential-for-survival cellular component, and downregulation of CK2 activity in cancer cell lines has a marked effect against the malignant state. These results validate CK2 as an anticancer target and suggest that development of potent and selective CK2 inhibitors could provide a valuable toolkit for the treatment of multiple cancer types.

1.2.5 CK2 Inhibitors to Date

The recent emergence of CK2 as a potential anticancer target has led to the development of a number of cell-permeable CK2 inhibitors.²²⁵ These inhibitors have been shown to have activity against multiple cancer types *in vitro*¹⁷¹ and one candidate, silmitasertib (**20**, formerly CX-4945), gained FDA-approved orphan drug status in January 2017.²²⁶ Silmitasertib **20** is used for the treatment of advanced

cholangiocarcinoma and is currently undergoing phase I/II clinical trials against lung, cervical and head and neck malignancies (ClinicalTrials.gov Identifier: NCT02128282).²²⁷

The majority of published CK2 inhibitors have relied on a rational structure-based approach in their design. This has been possible thanks to a wealth of multidisciplinary work bridging chemical synthesis, biological assays and X-ray crystallography.²²⁸ Furthermore, an analysis of the oncomine database revealed that the dominant CK2 α subunit is overexpressed in 5 out of the 6 most important cancer types in the United States, thereby channelling attention toward this particular portion of the protein rather than the α' or β subunits.¹⁶⁹

The following sections review the most notable CK2 inhibitors and their binding sites. ATP-competitive inhibitors are considered first, followed by a discussion regarding the need for alternative binding sites. A selected summary of successful exosite-binding inhibitors is then given.

1.2.5.1 ATP-Competitive Inhibitors

More than 40 X-ray crystal structures of CK2 α in complex with different ATP-competitive inhibitors have been deposited in the PDB.²²⁹ This has made it possible to efficiently exploit molecular docking for the proposal, analysis and corroboration of hypotheses about CK2 binding.^{230,231} As a result, the majority of published CK2 inhibitors have been rationally designed to compete at the ATP-site on CK2 α .¹²³

Structural analysis of the catalytic site of CK2 has revealed a handful of unique properties specific to CK2 over other kinases. One particular feature is that hydrogen bonding with the hinge region is not essential for binding (Figure 17, **a**). As such, the common pharmacophore for CK2 activity is instead composed of an important hydrophobic/aromatic area in the centre of the pocket (Figure 17, **b**).¹²⁴ This motif is essential and is present in all sub-micromolar inhibitors (Figure 17, **c**). It potentially accounts for the specific inhibition of CK2 by relatively small molecules.²³²

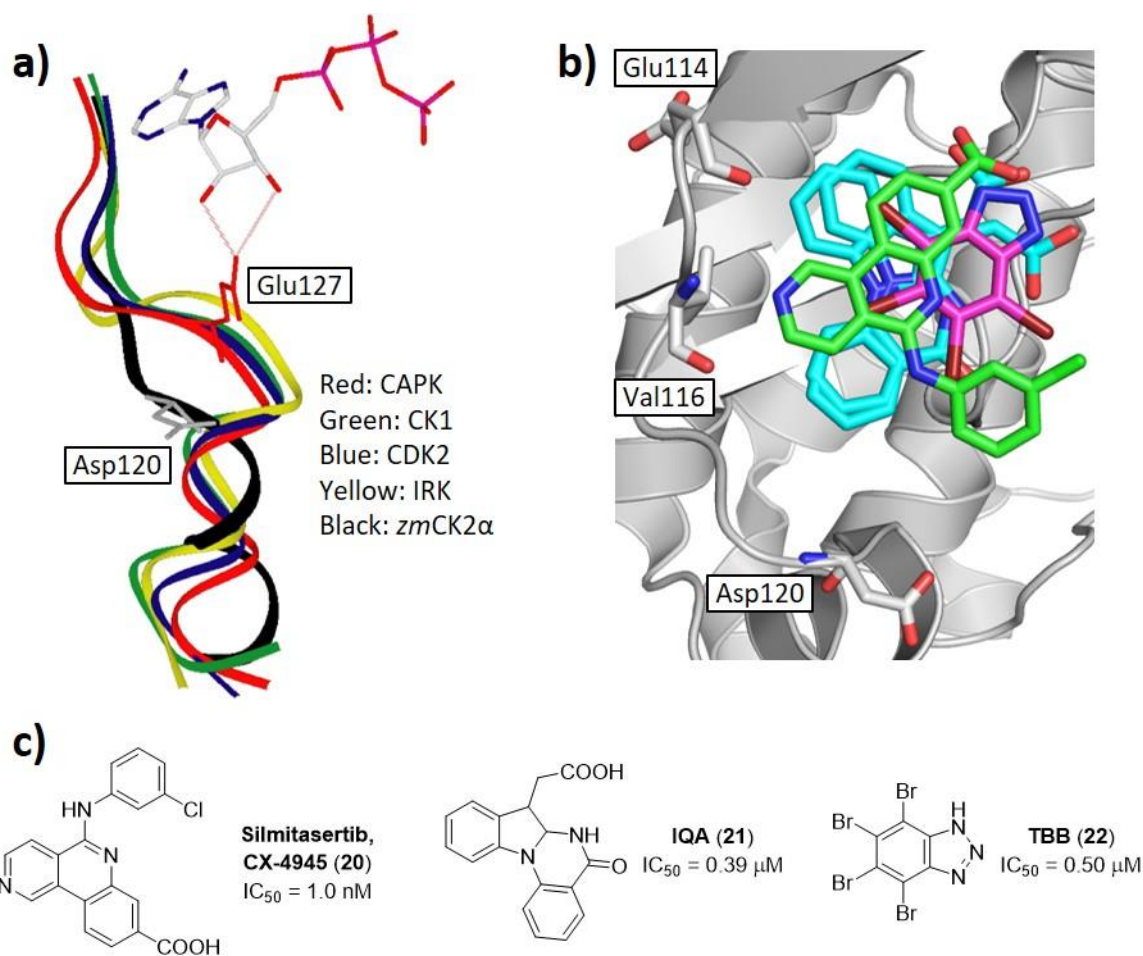


Figure 17: ATP-competitive inhibitors of CK2. **a)** *Zea mays* CK2α hinge region (black) overlaid with other eukaryotic protein kinases to demonstrate relative proximity of the protein backbone to ATP (grey). H-bonding between ATP and Glu127 (red) in CAPK is highlighted (dashed lines) and equivalent residue Asp120 (grey) in CK2α is shown in its distal position. CAPK – Cyclic-AMP Protein Kinase; CDK2 – Cyclin-Dependent Kinase 2; IRK – Insulin Receptor Kinase. Reprinted from Niefind et al.,¹³² Copyright (2018), with permission from Elsevier. **b)** Superposition of ATP-competitive CK2 inhibitors silmitasertib **20** (green) (PDB: 3PE1), IQA **21** (blue) (PDB: 1OM1) and TBB **22** (magenta) (PDB: 1J91) binding in the ATP-site without making polar interactions to the hinge region Glu114, Val116 or Asp120 (white). The aromatic cores of the three inhibitors overlap, highlighting the main CK2 pharmacophore responsible for the binding potency. **c)** Chemical structures of three prominent ATP-competitive CK2 inhibitors with corresponding IC₅₀ values.¹²³

Clinical candidate silmitasertib **20**, mentioned in Section 1.2.5, is an ATP-site competitive inhibitor and the only drug currently in human trials against CK2 (Figure 17, **c**). The inhibitor is well tolerated despite the ubiquitous role of CK2 in cellular pathways, and reports describe it as ‘highly selective’.^{233,234} However, silmitasertib **20** inhibits at least 12 other kinases with nanomolar IC₅₀ values, and is more effective against Clk2 than CK2α.^{235,236} This results in clear cellular effects that are not linked to the inhibition of CK2, such as widespread CK2α-independent alteration in alternative splicing for numerous genes, and suppression of the phosphorylation of serine/arginine-rich proteins in mammalian cells.²³⁶ In fact, multiple ATP-competitive inhibitors described as being ‘selective’ against

CK2 are also the most potent known inhibitors of other kinases. This is especially true within the DYRK, HIPK and Clk protein families.^{236,237}

The aforementioned observations highlight a common issue with ATP-site competitive inhibitors: a lack of selectivity owed to conservation of the ATP-binding site across all kinases. Furthermore, compounds that do disclose specificity for CK2, instead exhibit other physiological effects in cells. These off-target effects require further investigation, and reflect the fact that ATP-binding sites are not unique to just protein kinases.¹¹³ Off-target activity of this type limits the use of ATP-competitive drugs and impedes their development in cancer therapy. As a result, there is an increased interest in the development of alternative inhibitors that utilise more selective binding positions outside of the active site.

1.2.5.2 Alternative Site Inhibitors

The complex and multi-domain architecture of protein kinase CK2 lends itself to the discovery of alternative binding sites for novel small molecule modulators (Figure 18).²³⁸ The development of inhibitors targeting different surfaces of the kinase could avoid the shortcomings of conventional ATP-competitive inhibitors. These include poor selectivity, *in vitro* competition with a high ATP concentration and reliance on highly conserved residues in the ATP-binding site, that are susceptible to mutation.^{239,240}

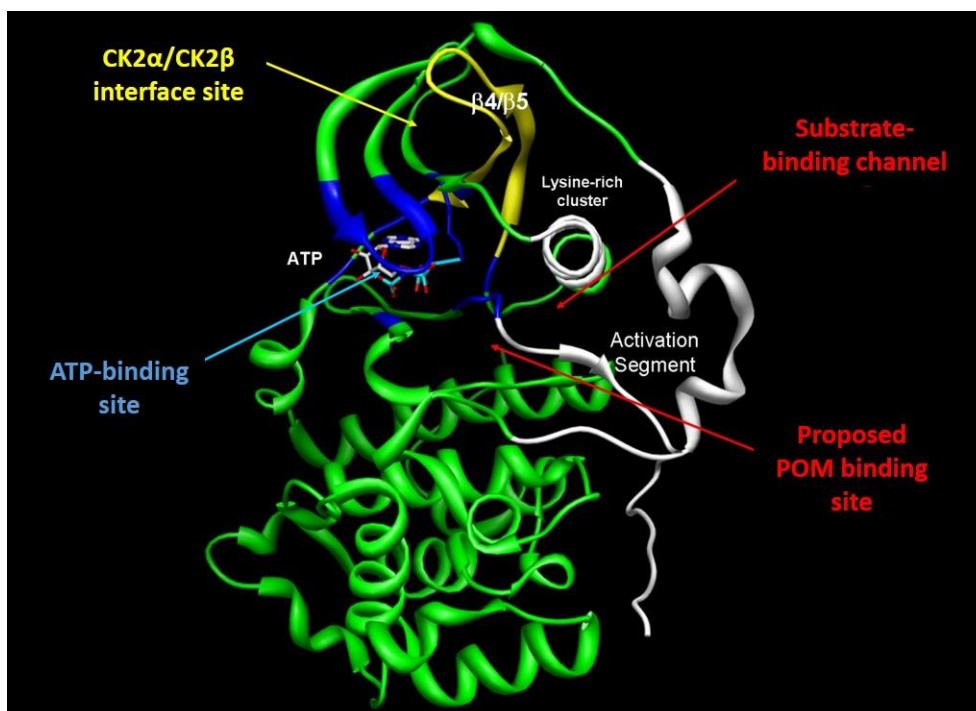


Figure 18: Representation of CK2 α illustrating the alternative surface areas targeted by new potent inhibitors. The highly conserved ATP-binding site is shown in blue with ATP (grey), key substrate recognition elements are shown in white, the CK2 α /CK2 β interface site is shown in yellow and the hypothesised binding position of the POM inhibitor series is indicated. Reprinted from Prudent *et al.*,²⁴¹ Copyright (2018), with permission from Elsevier.

One strategy is to identify and exploit a negative allosteric mode of action. Small molecules that bind allosteric pockets exert control over a protein's function by perturbing the conformation of essential enzymatic residues. This can then lead to protein activity inhibition.^{242–244} These sites represent valuable targets for drug design, but the discovery of new allosteric pockets is challenging and often occurs serendipitously by analysis of protein-ligand structural complexes.^{245,246} To date, only Raaf *et al.* have fully characterised an allosteric site on CK2 α , located at the CK2 α /CK2 β interface (Section 1.2.5.2.1).²⁴⁷ However, ongoing work by Prudent *et al.* suggests the existence of a second allosteric site (Section 1.2.5.2.2).²³⁸

Work towards other alternative inhibitors has also been published, and this includes targeting CK2 substrates,^{248,249} targeting the CK2 β subunit²⁵⁰ and the development of CK2 α bisubstrate inhibitors (Section 1.2.5.2.3).^{251,252}

1.2.5.2.1 CK2 α /CK2 β Subunit Interface Inhibitors

The crystal structure of DRB **23**, an old and relatively selective CK2 inhibitor,²⁵³ in complex with human CK2 α revealed a new binding position.²⁴⁷ It showed that DRB **23** is able to bind not only the canonical ATP pocket, but also a secondary site at the interface with CK2 β (Figure 19, a). This hydrophobic pocket

proximity of the ATP-site to the CK2 α /CK2 β pocket makes a functional connection between them likely, therefore supporting an allosteric mode of action.

More recent work by Bestgen *et al.* led to the development of a cell permeable version of Pc peptide **24**, called TAT-Pc13 (**26**) (Figure 19, **b**). This was shown to promote CK2 holoenzyme disruption within living cells, and rapidly induce caspase-independent cell death.²⁵⁶ Continued work by this group aims to utilise TAT-Pc13 **26** towards the identification of CK2 β -dependent substrates and selective ways to target them.

1.2.5.2.2 Polyoxometalates (POMs) Target an Alternative Exosite

Polyoxometalates (POMs) are a unique class of inorganic compounds that are potent inhibitors of CK2.²⁵⁷ They are complexes of early-transition metal ions and oxo ligands discovered by Prudent *et al.* through HTS of highly diverse chemical libraries. The best inhibitor reported is $K_6[P_2Mo_{18}O_{62}]$ **27** which has an IC₅₀ of 1.4 nM and displays high specificity for CK2 against a panel of 29 kinases.²⁵⁷ Steady state kinetic analysis and site-directed mutagenesis showed that POMs do not target CK2 α in the ATP- or substrate-binding sites or at the CK2 α /CK2 β interface. Biophysical experiments are underway to further decipher this unexpected inhibition mode, and Figure 18 indicates a proposed POM binding site. These non-classical kinase inhibitors may provide an exploitable allosteric mechanism, allowing the future development of potent CK2 α drugs with enhanced selectivity relative to ATP-mimetic inhibitors.²³⁸

1.2.5.2.3 Bisubstrate Inhibitors

An emerging strategy to increase the selectivity of ATP-site competitive kinase inhibitors is based on the design of so-called 'bisubstrate' (or bifunctional) inhibitors.²⁵¹ These species consist of two combined moieties, one targeted to the ATP-binding site, and the other shaped in such a way that it mimics the phosphoacceptor substrate, and therefore competes for the substrate-binding site. At variance with ATP-competitive inhibitors, which often bind with high affinity but low selectivity, and with pseudosubstrate inhibitors, which are in principle quite selective but generally bind very weakly, bisubstrate inhibitors are expected to be both very potent and selective. This is owed to the cooperative effects of their dual mode of binding. In the last decade, several successful examples of this strategy have been reported for a variety of kinases^{258,259} and now attention has turned to CK2. Unfortunately, a common feature of all reported bisubstrate inhibitor-protein complexes is the failure to determine the whole structure of the ligand by X-ray crystallography.^{260–262} Attempts often lead to

the detection of the ATP-competitive moiety and no defined electron density for the pseudosubstrate portion.

One successful CK2 bisubstrate inhibitor comes from Cozza *et al.*, where a purely ATP-competitive CK2 inhibitor – K137 **28** – was derivatized at its 3-amino position with a peptidic fragment composed of four glutamic acid residues (Figure 20, **a**).²⁵¹ The bifunctional inhibitor, K137-E4 **29**, gave an IC₅₀ value of 25 nM against the CK2 holoenzyme, which is several fold better than original ATP-site fragment **28** (IC₅₀ = 130 nM). Furthermore, K137-E4 **29** effectively demonstrated the synergistic effect of anchoring *via* inhibitor K137 **28**, as the isolated glutamic acid tetramer was originally devoid of efficacy. K137-E4 **29** was more selective than parent inhibitor K137 **28**, failing to inhibit any kinase other than CK2 in a panel of 140 kinases. In contrast, 35 kinases were inhibited more potently than CK2 by K137 **28**. Residue mutation studies and molecular docking experiments confirmed the double mode of binding for K137-E4 **29** (Figure 20, **b**).

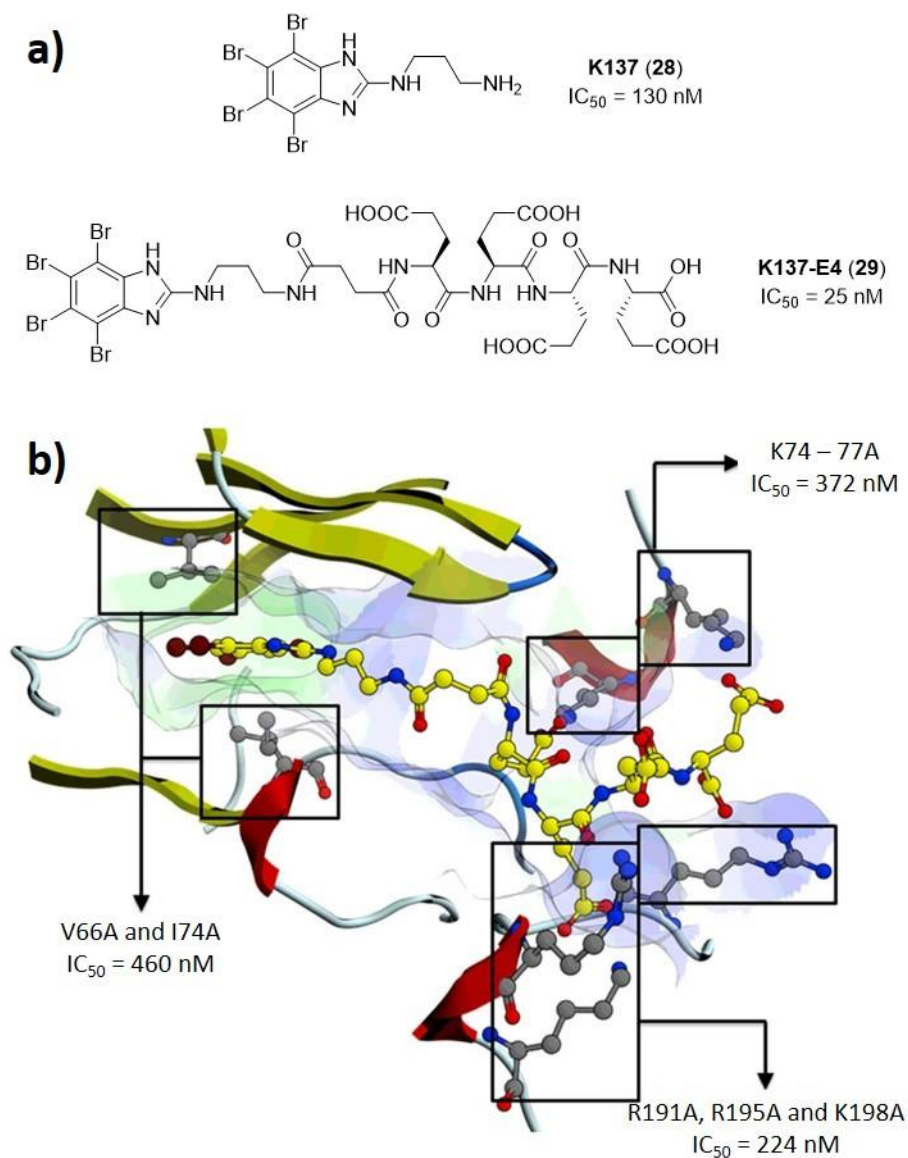


Figure 20: CK2 bisubstrate inhibitor K137-E4 **29**. **a)** Chemical structures of K137 **28** and K137-E4 **29** with IC₅₀ values against CK2 holoenzyme.²⁵¹ **b)** In silico interaction between K137-E4 **29** (yellow) and CK2α (PDB: 3Q04). Residues involved in the interaction are highlighted in grey. The IC₅₀ values of corresponding Ala mutants are indicated for comparison with that of wild-type CK2 (black box outlines). K74-77A means K74A, K75A, K76A and K77A. Reprinted from Cozza *et al.*,²⁵¹ Copyright (2018), with permission from Portland Press.

A second example of a bisubstrate inhibitor has been published by Rahnel *et al.*²⁵² Their biligand inhibitor, ARC-772 **31**, was constructed by conjugating ATB **30** with a carboxylate-rich peptoid *via* an optimised hydrophobic linker (Figure 21). ARC-772 **31** was found to bind CK2 with a *K_d* of 0.3 nM and showed remarkable CK2 inhibitory selectivity in a panel of 140 kinases – highly superior to ATB **30** alone.²⁶³ Ester prodrug, ARC-775 **32**, was efficiently taken up by HeLa cancer cells and observed to activate apoptosis marker caspase-3 with an EC₅₀ of 0.3 μM – a 20-fold lower extracellular

concentration than clinical candidate silmitasertib **20** (EC_{50} of 6.5 μ M). No discussion of the binding mode for ARC-772 **31** is reported at this time.

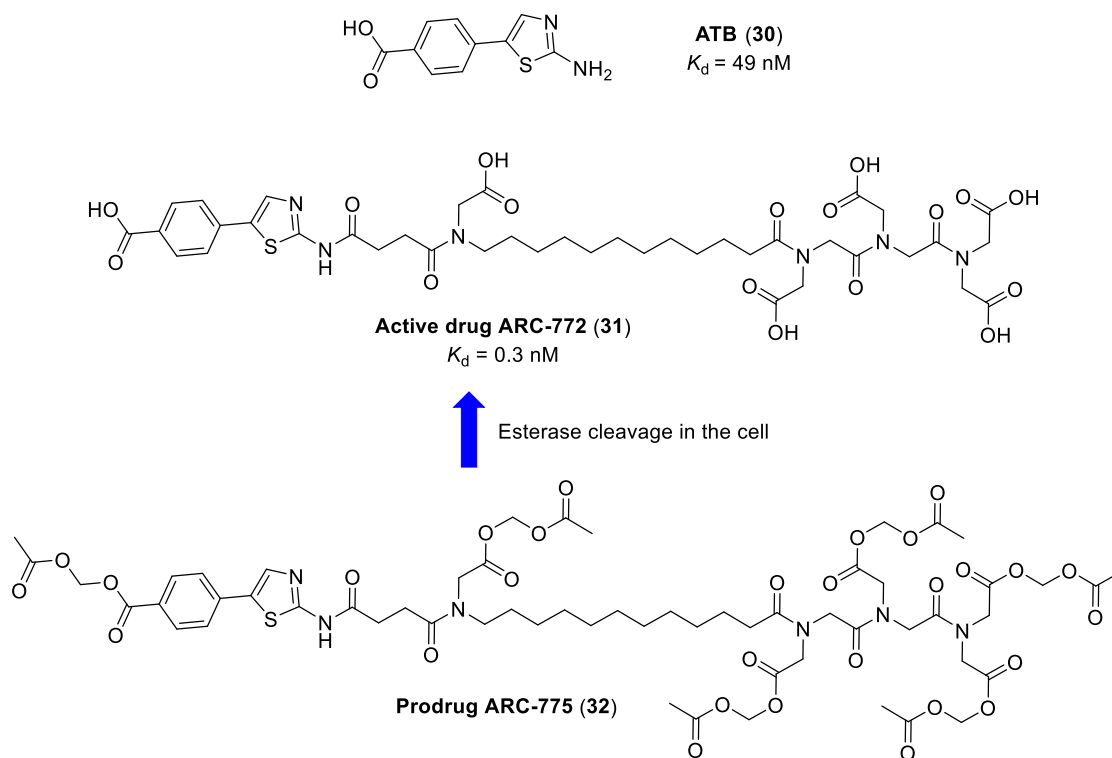


Figure 21: Chemical structures of ATP-site competitive inhibitor ATB **30**, bisubstrate inhibitor ARC-772 **31** and prodrug ARC-775 **32**. Upon penetration of the cell plasma membrane, the acetoxymethyl ester moieties on ARC-775 **32** are cleaved by esterases to release active drug ARC-772 **31**.

Results from bisubstrate inhibitors K137-E4 **29** and ARC-772 **31**, showcase the potential of this strategy in drug development against CK2. They both demonstrate how moderately potent, and quite promiscuous, ATP-competitive inhibitors can be converted into more effective, and very selective, CK2 antagonists by elaboration with pseudosubstrate moieties.

In conclusion, the design, testing and synthesis of compounds that interact differentially with the surface areas of CK2 α , outside of its catalytic cleft, has already led to the identification of new potent inhibitors.²⁴¹ Furthermore, recent crystal structure analysis across multiple kinases, including CK2, has revealed how dynamic their structures are.²⁶⁴ This has suggested that exploitable, and as of yet undiscovered, allosteric networks exist throughout each protein. HTS has proved fruitful in initial attempts to identify these binding sites and mechanisms on CK2 α ,^{255,257} but the application of FBDD could be a more efficient means of further interrogation. The use of low molecular weight fragments in initial screening, partnered with sensitive X-ray crystallography or NMR spectroscopy, could identify promising small molecules for drug development. Detection of any new inhibitor binding pocket must

be urgently followed up with full structural and biophysical characterisation, in order to understand the mechanism of action and promote SBDD towards improved drug candidates.

1.2.6 Discovery of the α D Pocket on CK2 α

A recent FBDD program by the Spring/Hyvönen group collaboration at the University of Cambridge led to the discovery of a novel binding pocket for small molecules on CK2 α , named the α D pocket.²⁶⁵ A high concentration crystallographic screen of a commercial fragment library was performed to probe the surface of CK2 α . The original aim was to screen for new allosteric inhibitors at the CK2 α /CK2 β interface.²⁶⁶ Instead, a hit (**33**) was identified that induced the opening of a previously unseen cryptic pocket close to the ATP-binding site (Figure 22, **b**). The newly identified α D pocket is located behind the α D helix (Asp120-Thr127) and is largely hydrophobic in character. This binding site is either closed or partially open in all other Apo structures of CK2 α , with either Phe121 (PDB: 3FWQ), Tyr125 (PDB: 5CVH) or Leu124 (PDB: 5CVG) occupying the pocket (Figure 22, **c**). Upon binding fragment hit **33**, the residue occupying the α D pocket is displaced, and Met225 rotates to open the bottom of the pocket. The α D helix is released from the C-lobe and adopts an open helical arrangement.

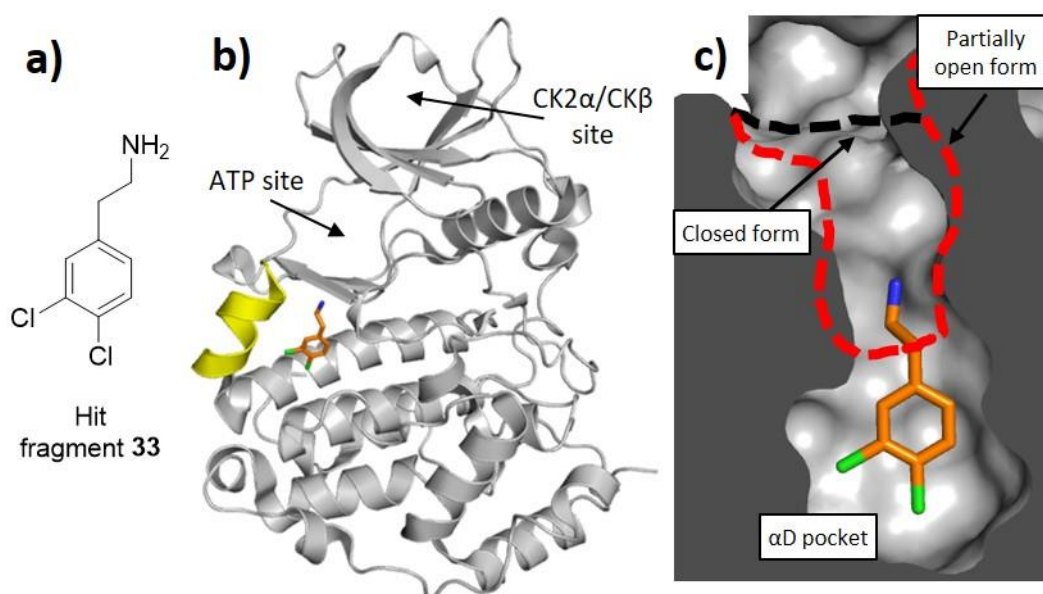


Figure 22: Discovery of the α D pocket on CK2 α . **a**) Chemical structure of hit fragment **33**. **b**) X-ray crystal structure of hit **33** (orange) in complex with CK2 α (grey) (PDB: 5CLP). The position of α D-site fragment **33** relative to other CK2 α features is shown and the α D helix is highlighted in yellow. **c**) Cross section of the α D pocket with hit **33** (orange) bound. The size of the α D pocket in the closed CK2 α structure (PDB: 3FWQ) is represented by the black dashed line and the α D pocket in the partially open CK2 α structure (PDB: 3WAR) is represented by the red dashed line.

Following hit validation, further exploration into the druggability of this site was undertaken by the Spring and Hyvönen groups.^{265,266} Elaboration of fragment **33** using SBDD led to high affinity α D-

selective binding fragment **34**, but no inhibition of CK2 α kinase activity was observed (Figure 23, **a**). A fragment-linking strategy was then proposed, whereby benzylamine fragment **34** would be linked to a low affinity ATP-site competitive inhibitor *via* an optimised flexible linker. ATP-competitive fragment **36** was identified in a high concentration crystallographic screen of a commercial fragment library, and deemed suitable for linking to α D fragment **34**. The linker approach was rationalised on the grounds that the α D-pocket appears to be a unique feature of CK2 α compared to other human kinases. Thus it could be exploited as an anchor site to deliver a weak ATP-site inhibitor selectively onto CK2 α over other kinases (Figure 23, **b** and **c**).

Efficient execution of the linking strategy, using iterative linker growth and computational modelling, led to chemical probe CAM4066 **35** (Figure 23). Linked species **35** demonstrated the highest CK2 selectivity of any reported inhibitor to date when tested against a panel of 52 kinases. A K_d of 320 nM was also recorded, which is a 1000-fold improvement on starting fragment **34**. An IC_{50} of 370 nM was reported for CAM4066 **35**, a vast improvement on original fragments **34** and **36**, as neither showed efficacy up to 500 μ M. Poor cell permeability led to the development of pro-CAM4066 **37**, a prodrug version of CAM4066 **35**, for use in cellular assays (Figure 23, **b**). When pro-CAM4066 **37** was tested against HCT116, Jurkat and A549 cancer cell lines, GI_{50} values of 9, 6 and 20 μ M respectively were reported. This profile compares well to the corresponding values for clinical candidate silmitasertib (**20**) (5, 5 and 17 μ M GI_{50} respectively).²⁶⁵

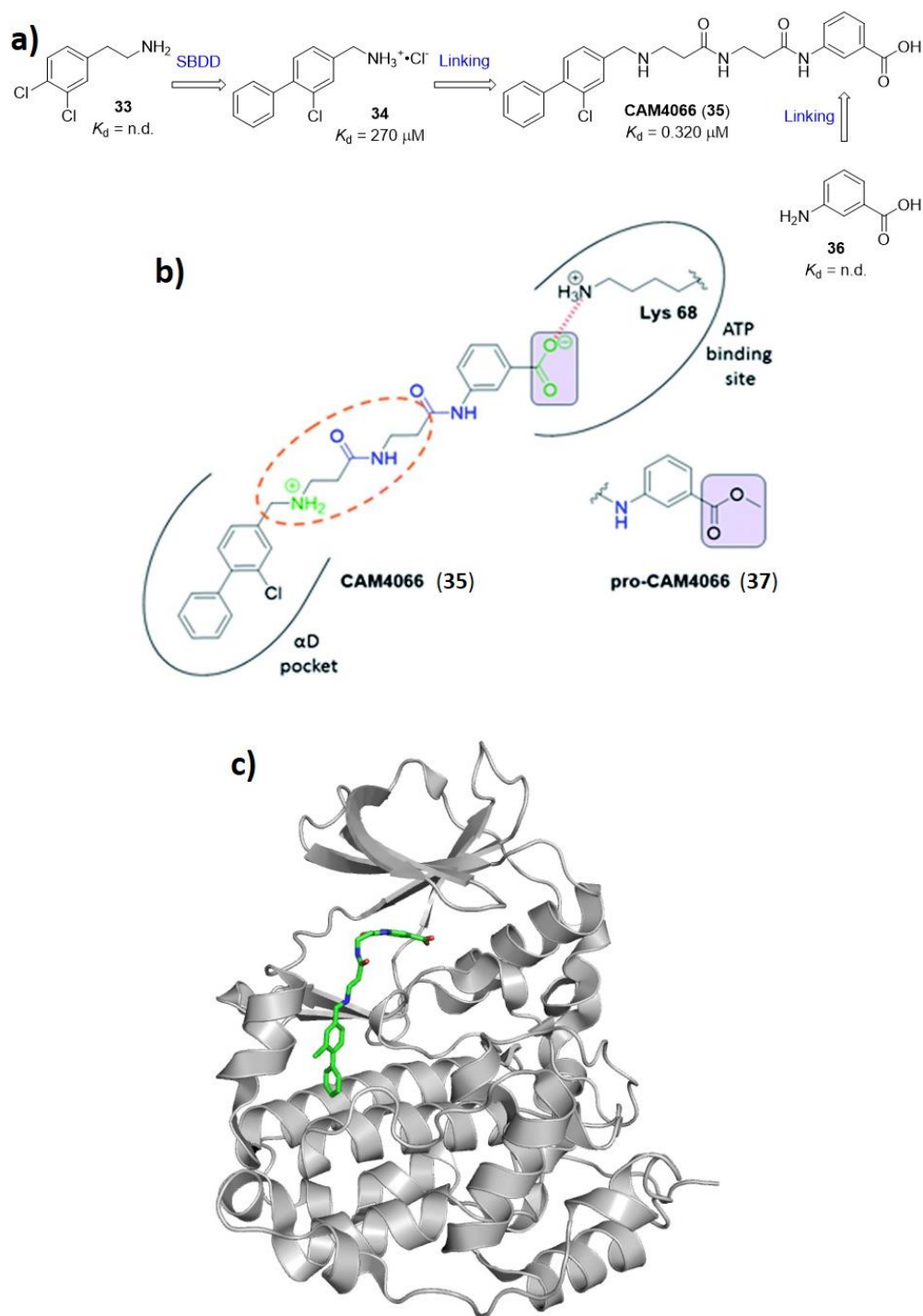


Figure 23: Development of optimised, linked inhibitor CAM4066 **35**. **a)** Chemical scheme demonstrating hit-to-lead generation of CAM4066 **35**. Hit fragment **33** was elaborated into α D-site selective binder **34** which was linked to ATP-competitive inhibitor **36** via an optimised linker to produce potent, CK2-selective inhibitor CAM4066 **35**. K_d values are reported where possible.²⁶⁵ n.d.: no data. **b)** Representation of CAM4066 **35** binding to CK2 α and structure of pro-CAM4066 **37**. Zwitterionic elements are coloured in green, amide bonds in blue and the difference between CAM4066 **35** and prodrug pro-CAM4066 **37** is highlighted by the purple box. The interaction between CAM4066 **35** and highly conserved Lys68 is shown as a red dashed line. The flexible linker is circled in orange and the α D pocket and ATP-binding site are reported as black curves. Reprinted with permission from Iegre et al.²⁶⁷ Published by the Royal Society of Chemistry. **c)** X-ray crystal structure of CAM4066 **35** (green) in complex with CK2 α (grey) (PDB:5CU4).

CAM4066 **35** provides valuable proof of concept, validating both the use of FBDD on CK2 α and the development of anchored inhibitors binding in the novel, poorly conserved α D-pocket. CAM4066 **35** is a new generation of selective CK2 α inhibitor and lays the groundwork for further elaboration into higher affinity candidates with improved pharmacokinetics. Furthermore, full characterisation of the novel α D exosite now enables easier investigation into the utility of this binding pocket for allosteric kinase inhibition. More broadly, the strategy of using cryptic pockets outside the active site could be applied to other protein classes where selectivity is otherwise hard to achieve.

1.3 Project Aims

The project discussed in this thesis built on the α D pocket work previously reported by the Spring/Hyvönen groups (Section 1.2.6).^{265–267} The aim was to further investigate the druggability of the new α D-site and explore its utility as a binding pocket for small molecule inhibitors with negative allosteric modalities. It was believed that the development of inhibitors binding the poorly conserved α D pocket would provide far superior CK2 α selectivity than any published inhibitor to date.

The specific research objectives were two-fold: first, develop α D-site selective fragments with higher binding affinities than previously reported, and secondly, achieve CK2 α kinase inhibition by binding solely within the α D pocket. This would avoid growth into the ATP-binding site and the involvement of potentially promiscuous ATP-competitive warheads (*i.e.* CAM4066 **35**, Figure 24, **a**).²⁶⁵

As a starting point, the biaryl benzylamine scaffold of known α D-site binding fragment **34** would be exploited (Figure 24).²⁶⁵ It was envisioned that SBDD around the lower aryl ring (species **38 - 40**) would probe the flexibility of the α D pocket and lead efficiently to improved binding fragments.

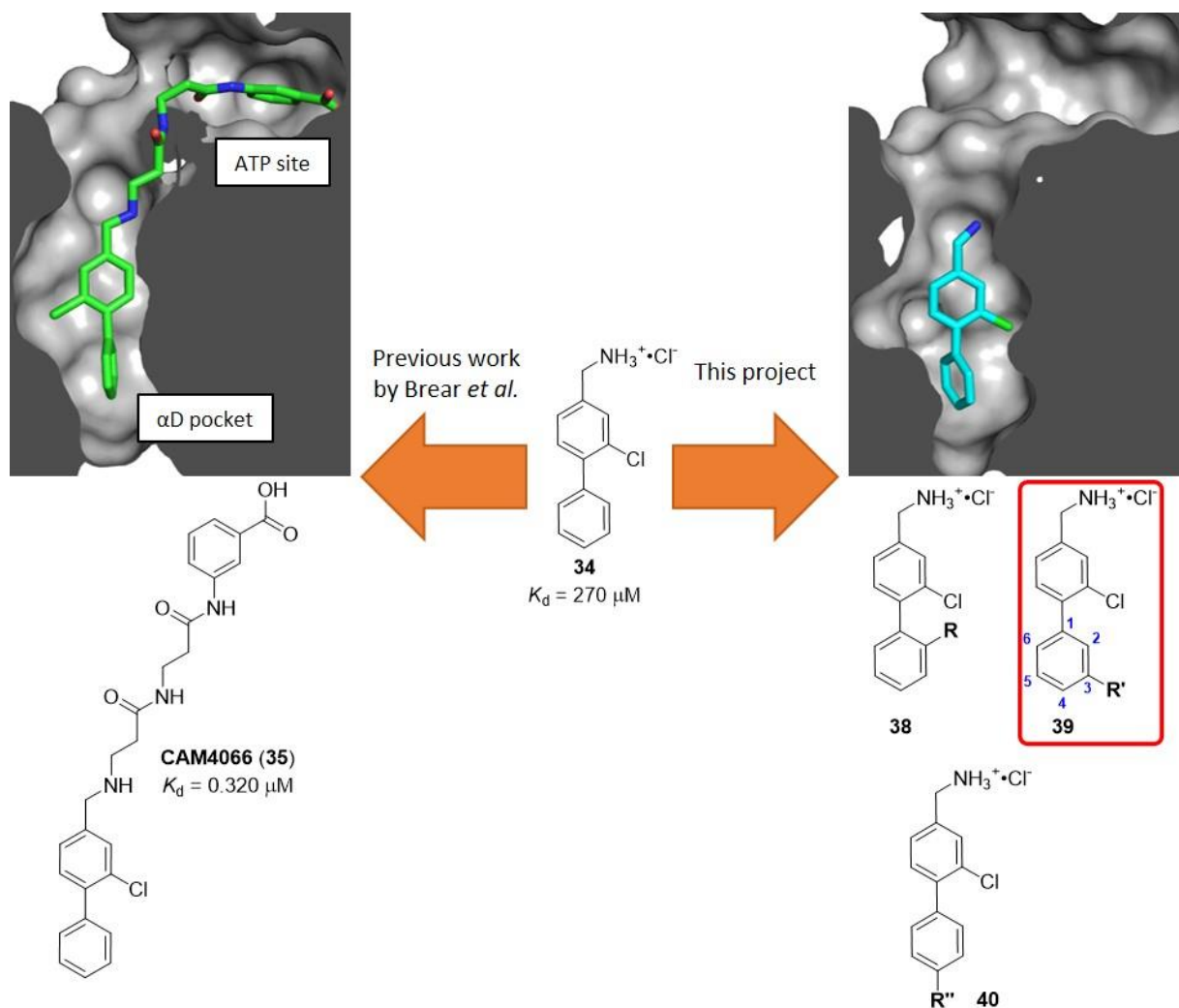


Figure 24: Illustration of the project aims. In the centre is shown α D-site binding fragment **34**, the starting point for SBDD in this project. Following the left arrow shows the X-ray crystal structure of CAM4066 **35** (green) (PDB: 5CU4) binding simultaneously in the α D pocket and ATP site. This work was previously reported by Brear *et al.*²⁶⁵ Following the right arrow shows the X-ray crystal structure of fragment **34** (blue) (PDB: 5CHS) in the α D pocket and scaffolds **38** - **40** investigated in this project. **R**, **R'** and **R''** represent substitution positions on fragment **34** for investigation. K_d values are given²⁶⁵ and the numbering system for the lower phenyl ring is shown in blue for later reference.

X-ray crystal structure analysis of fragment **34**, and the analogues leading to its development, revealed the extent of the α D loop flexibility, and thus the variability in volume of the α D pocket (Figure 25). In growing from initial hit **33** to lead fragment **34**, Brear *et al.* had also observed large rearrangements in the α D loop of up to 23.8 Å, for fragment **42**.²⁶⁶ This movement was significantly more fluid than in previous descriptions²⁶⁸ and suggested to us that it might be possible to accommodate fragments larger than biaryl **34** within the α D pocket. Based on this, we hypothesised that α D-site fragment growth to a critical size, and with optimal ligand-protein interactions, might cause sufficient conformational disruption of CK2 α so as to inhibit kinase activity. The impact of this work would be a first in class CK2 α allosteric inhibitor series with superior selectivity, instilled by exploiting the unique

α D binding site. This would validate the continued use of FBDD in kinase inhibitor programs and could lead to the development of novel anticancer therapies.

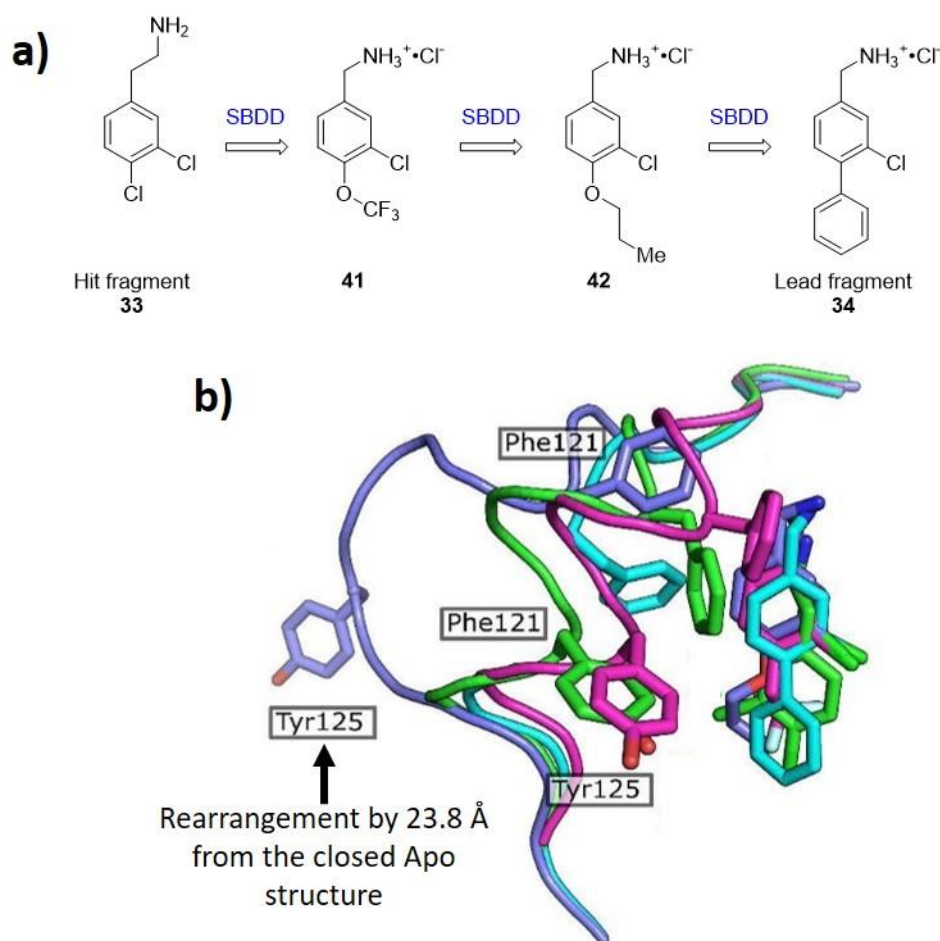


Figure 25: Investigating the flexibility of the α D loop. **a)** Chemical structures of key fragments in hit-to-lead generation from hit **33** to lead **34**. **b)** Superposition of X-ray crystal structures showing the relative position of the α D loop when fragments **33** (green) (PDB: 5CLP), **41** (magenta) (PDB: 5CVF), **42** (purple) (PDB: 5CS6) and **34** (blue) (PDB: 5CSH) are bound to CK2 α . Key residues Phe121 and Tyr125 are shown to highlight the flexibility of the α D loop upon binding a fragment. The largest rearrangement was observed for fragment **42** which moved 23.8 Å from its original position in the closed Apo structure (PDB: 3FWQ). Reprinted with permission from De Fusco et al.²⁶⁶ Copyright (2018) Elsevier.

Investigation into our hypothesis began by substituting positions around the lower aromatic ring of biaryl **34** to provide species of the form **38** - **40** (Figure 24). This portion of the fragment had not been optimised in previous publications so presented an unexplored starting point for fragment elaboration. Furthermore, it would effectively interrogate the flexibility of the bottom of the pocket. Three positions of substitution were considered (**38** - **40**) and the workload divided between three members of the Spring group. The focus in this thesis was substitution at the 3-position, highlighted by **R'** on scaffold **39** in Figure 24.

A suitable project approach was envisaged as follows:

1. Design a target-oriented fragment library utilising commercially available building blocks to ensure rapid and efficient later synthesis.
2. Screen the library *in silico* using the protein-bound X-ray crystal structure of lead fragment **34** and Schrödinger's Maestro package.
3. Perform chemical synthesis for library members with most promising docking results.
4. Submit synthesised compounds for X-ray crystallography by our Hyvönen group collaborator, Dr. Paul Brear, from the University of Cambridge Biochemistry Department.
5. Determine binding affinity (by ITC) and inhibitory activity (by CK2 α kinase assay) for fragments displaying α D-site selectivity. Also to be performed by Dr. Paul Brear.
6. Analyse combined structural and biochemical results to verify the binding position, compare with computational modelling predictions, identify false positives/negatives and establish fragments superior to current 'top leads' (*i.e.* benzylamine **34**).
7. Perform iterative cycles of structure-based optimisation, biochemical evaluation and combined analysis (steps 1-6) until lead-like compounds have been obtained.

In summary, we were searching for improved α D pocket binding fragments that could inhibit CK2 α kinase activity. Final candidates needed to exhibit good ligand efficiency ($LE > 0.38$)⁶⁰ and present physicochemical properties commensurate with the 'Rule of Three'.³⁰ This aim followed the typical SBDD sequence used in hit-to-lead generation during FBDD programs, as outlined in Section 1.1.4. It also represented the first complete application of fragment-based drug discovery to protein kinase CK2.

Chapter Two: Results and Discussion

2.1 Target-Oriented Fragment Library Design, Synthesis and Testing

2.1.1 Fragment Library Design

The fragment screening library required by this project had a different aim to the typical broad, commercial fragment libraries purchased for the start of FBDD programs. In this case, Brear *et al.* had already reported the identification of a hit fragment (**33**) and its subsequent development into an α D-site specific lead (**34**).²⁶⁵ Therefore, this project began at the SBDD stage of FBDD (introduced in Section 1.1.4) and utilised the X-ray crystal structure of current lead **34** for the rational design of a target-oriented fragment library.

Design of the structure-guided library began with analysis of the key protein-ligand binding elements for lead compound **34**. In order to best exploit the biaryl core, it was essential that the interactions between **34** and the α D pocket were understood and maintained. Analysis of the X-ray crystal structure of **34** in complex with CK2 α (PDB:3CSH) determined that the benzylamine moiety plays a crucial role in positioning the fragment within the α D pocket (Figure 26, a). The amine, protonated under crystallography conditions, makes HBD interactions to Pro159 and Val162 and participates in a water bridge with Asn118, Thr119 and two water molecules. It was also recognised that the α D pocket is lined by hydrophobic residues and the space is filled well by the biaryl core of **34** (Figure 26, b). Finally, the lower phenyl ring stacks against Met225 which locks the position of the ring within the lower part of the pocket (Figure 26, c). Furthermore, the ortho-substituted chlorine may force the biaryl into a pre-formed conformation that aids binding in the α D pocket. Based on this assumption, the chlorine substituent would be maintained.

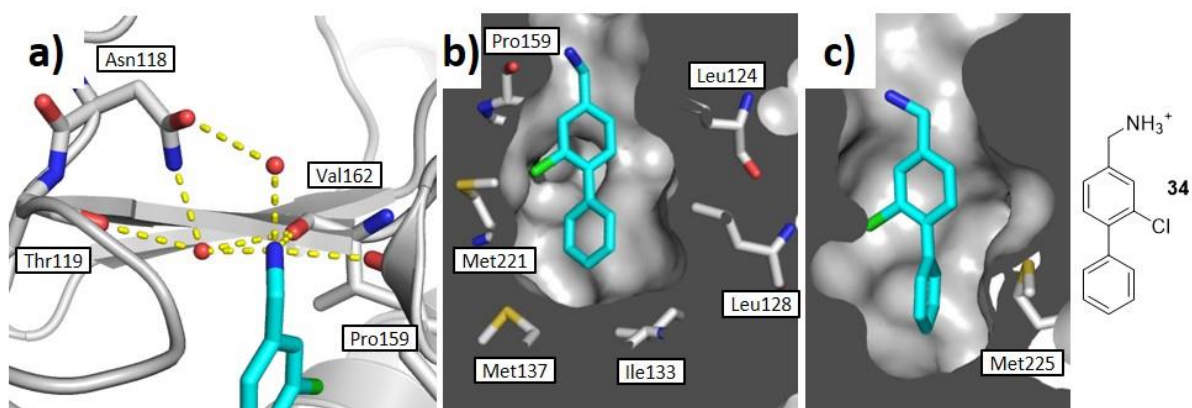


Figure 26: X-ray crystal structure views of lead fragment **34** (blue) in complex with CK2 α (grey) (PDB: 5CHS). **a)** Interaction of the amine of **34** with protein residues (white) and two water molecules. Polar contacts shown as dashed yellow lines. **b)** Lead fragment **34** bound in the α D site showing the molecule fills the hydrophobic cavity (white residues) efficiently. **c)** Lead fragment **34** bound in the α D site showing stacking interaction between lower phenyl ring and Met225 (white).

With these factors in mind, the lower portion of the α D pocket was investigated to determine whether substitution of the bottom phenyl ring at the 3-position (**43**) would provide fragments likely to bind (Figure 27, **a**). Visual inspection of biaryl **34** bound to CK2 α showed a vacant space in the pocket adjacent to the 3-position (Figure 27, **b**). This cavity is lined by hydrophobic residues (Met137, Ile140, Leu218, Leu222 and Met225) and appeared suitable to accommodate a substituent (Figure 27, **c**). Furthermore, given the reported flexibility of the α D helix, and observed scope for the α D pocket to deepen in the presence of larger fragments,²⁶⁶ substitution at the 3-position was deemed likely to be tolerated. Overall, available structural data for Brear *et al.*'s lead fragment **34** provided a strong precedent for the development of analogues of the form **43**.

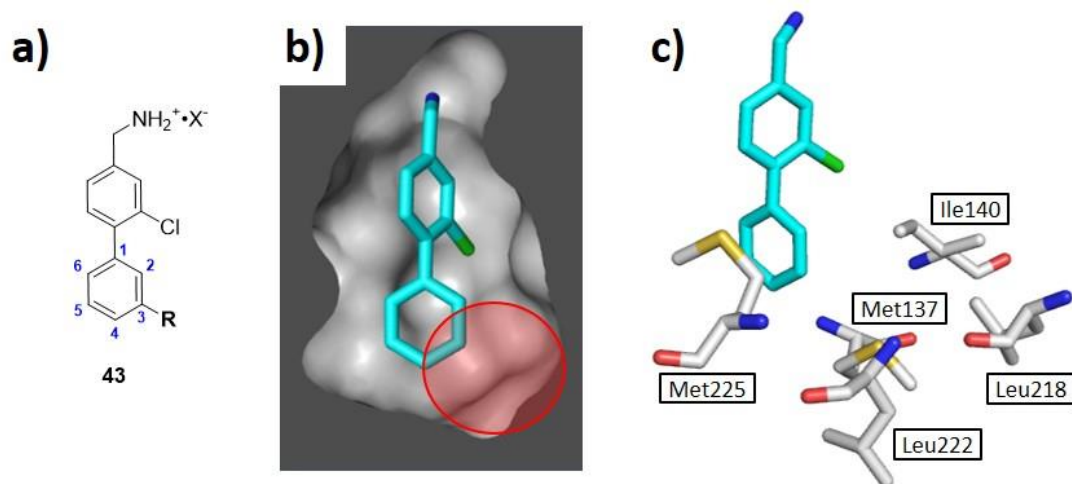


Figure 27: Investigation of a 3-position substituent on the lower phenyl ring. **a)** Chemical structure of biaryl, benzylamine scaffold **43** with 3-position highlighted by an **R** group. The blue numbers indicate the ring numbering system used throughout this chapter. **b)** X-ray crystal structure of **34** (blue) in complex with CK2 α (grey) (PDB: 5CHS) highlighting vacant space at the 3-position of the lower ring (red ring). **c)** X-ray crystal structure of **34** in complex with CK2 α (PDB: 5CHS) showing the hydrophobic residues (white) lining the cavity at the 3-position of the lower ring.

Following the above analysis, design of the target-oriented fragment library began. A diverse range of 3-position substituents were desired, but rapid and efficient chemical synthesis of each compound was also vital. As a result, only fragments derived from commercially available building blocks, bearing features suitable for Suzuki-Miyaura cross coupling, were considered. This provided an analogue library of 75 fragments that was screened *in silico* against CK2 α using Glide from the Schrödinger package, set to default parameters.^{269–272} Subsequent protein-ligand visualisation and image rendering was performed using Pymol from the Schrödinger package.²⁷³

The predicted binding modes for the top docking results were visually inspected and species maintaining the benzylamine H-bonding pattern, upper ring orientation and Met225 stacking interaction were prioritised. Within this refined collection, fragments predicted to efficiently occupy the 3-position hydrophobic cavity were further analysed. Fragments with polar groups, such as dibenzylamine **44**, were predicted to make HBD interactions with the backbone of Met221 (Figure 28, **a**). Fragments with non-polar groups, such as methyl **45** and vinyl **46**, were predicted to occupy the cavity without steric clash (Figure 28, **b** and **c** respectively). Overlay of the predicted structures in Figure 28 with a modelled structure of lead **34** and the reported structure of lead **34** (Figure 27, **b**) indicated precise alignment of the biaryl cores in all cases. This validated the use of computational modelling software to predict binding modes of close analogues.

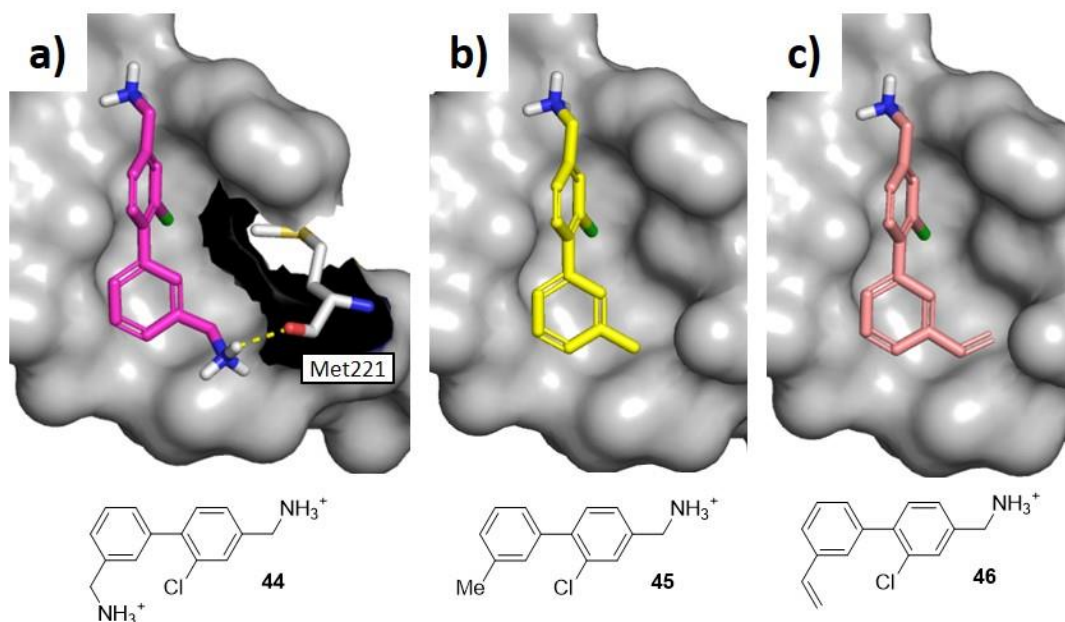
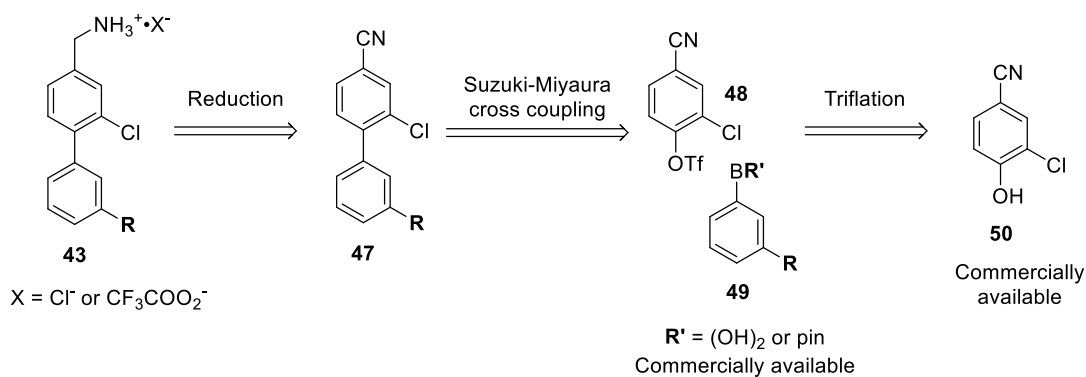


Figure 28: Computational modelling results for the target-oriented fragment library docked onto CK2 α (grey) (PDB: 5CHS). **a)** Dibenzylamine fragment **44** (magenta) and predicted HBD interaction to Met221 (white) shown by dashed yellow line. **b)** Methyl fragment **45** (yellow). **c)** Vinyl fragment **46** (pink).

The target-oriented fragment library was finally refined to 11 fragments which would efficiently interrogate the predicted interactions reported in Figure 28. This collection was considered accessible from readily available starting materials and would provide a variety of polar and non-polar substitution groups for X-ray crystallography and biochemical assessment.

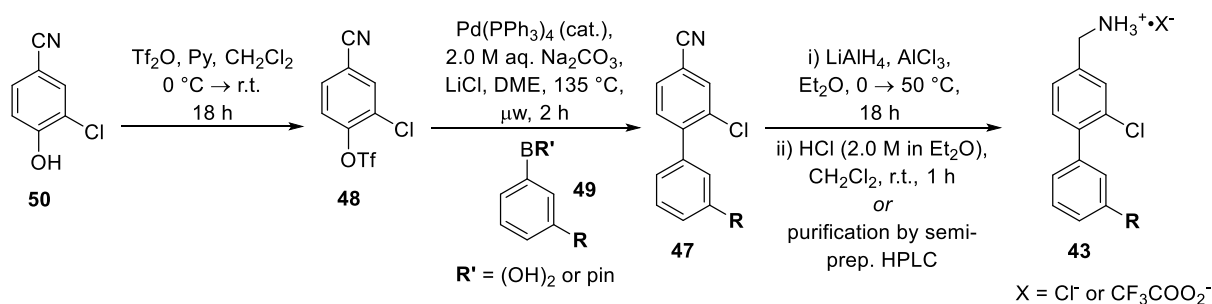
2.1.2 Fragment Library Synthesis

Following fragment library design, an efficient and modular approach for subsequent synthesis was desired. Ideally this would involve robust experimental conditions with broad substrate scope so that the fragment analogues could be made in as few synthetic steps as possible. Taking inspiration from Brear *et al.*,²⁶⁵ a retrosynthesis of benzylamine scaffold **43** was envisaged as follows (Scheme 1): first, the benzylamine moiety of **43** could be prepared by reduction of nitrile **47**. Biaryl scaffold **47** could come from Suzuki-Miyaura cross coupling between triflate species **48** and commercially available boronic acid/ester **49**. Triflate **48** could be prepared from commercially available alcohol **50**.



Scheme 1: Retrosynthetic analysis for benzylamine scaffold **43**. **R** represents the 3-position substituent, **BR'** represents either a boronic acid or ester and **X** represents the counter-ion of the benzylamine salt.

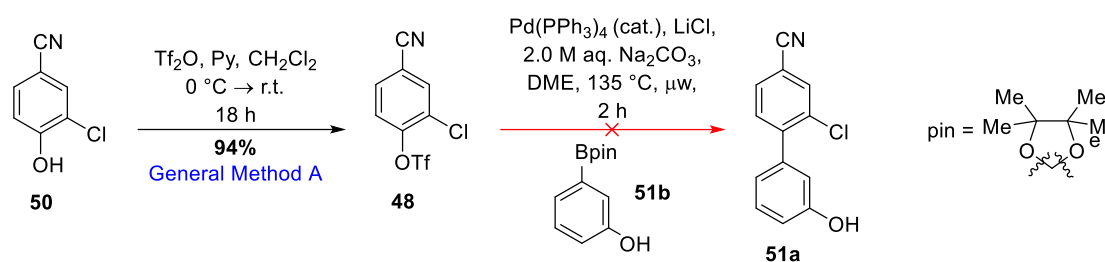
In the forward direction, experimental protocols from well-precedented literature (in particular those relating to lead **34**) were considered in order to provide the following conditions for testing (Scheme 2): application of a standard triflation protocol^{265,274} to alcohol **50** would provide cross coupling partner **48**, which would then be combined with boronic acid/ester **49** under typical Suzuki-Miyaura cross coupling conditions.^{265,274} This would give benzonitrile **47** which, upon reduction of the nitrile moiety using conditions developed by Brear *et al.*,^{265,266} would provide the crude free amine of final product **43**. Purification of **43** by manual flash column chromatography or semi-preparative HPLC would be decided following ¹H NMR, LCMS and TLC analysis of the crude reaction mixture. In the case of manual flash column chromatography, the free amine would then be converted to a benzylamine chloride salt.^{265,266} Semi-preparative HPLC would directly provide the trifluoroacetate salt. Salt formation would provide stability during storage and ease of later handling.



Scheme 2: Proposed forward synthesis for benzylamine scaffold **43**.^{265,266,274} **R** represents the 3-position substituent, **BR'** represents either a boronic acid or ester and **X** represents the counter-ion of the benzylamine salt.

Library fragment synthesis began as suggested in Scheme 2 with the triflation of commercially available alcohol **50** (Scheme 3).²⁷⁴ The reaction provided Suzuki-Miyaura cross coupling partner **48** in high yield, and these conditions are referred to as 'General Method A' hereafter (Section 4.2.1, Experimental General Methods). The proposed Suzuki-Miyaura protocol was attempted using boronic pinacol ester **51b** but failed to provide desired benzonitrile **51a**.^{265,274} Instead, ¹H NMR and LCMS

analysis of the crude reaction mixture indicated that the majority of triflate **48** had been hydrolysed to starting alcohol **50**. Traces of two other unidentified products were also observed, neither of which had ^1H NMR peaks or LCMS mass consistent with benzonitrile **51a**.



*Scheme 3: Attempted synthesis of first fragment **51a** using proposed literature conditions. The triflation conditions provided **48** from **50** in high yield and were repeated on later substrates under 'General Method A'.^{265,274} Suzuki-Miyaura cross coupling conditions failed to give benzonitrile **51a**.^{265,274}*

Following this, three alternative sets of Suzuki-Miyaura cross coupling conditions were attempted (Table 1). Entry 1 repeated the protocol from the proposed synthesis but with heating under reflux instead of microwave irradiation. Analysis of the crude reaction mixture gave the same results as Scheme 3, with majority triflate hydrolysis to alcohol **50**. The coupling partners used in Entry 2²⁷⁵ had the boron and pseudohalide moieties swapped such that benzonitrile building block **52** bore a boronic acid and phenolic partner **51c** had an iodine. However, these conditions resulted in a complex mixture of unidentified products when the crude reaction mixture was analysed by ^1H NMR and LCMS. Entry 2 was not investigated further. Returning to boronic pinacol ester **51b** and switching the pseudohalide for bromide **53**, in Entry 3,²⁷⁶ provided desired benzonitrile **51a** in good yield. Subsequent optimisation of reagent equivalents led to the conditions in Entry 4, where 1.1 eq. of bromide **53** and 1.0 eq. of boronic pinacol ester **51b** gave product **51a** in the highest yield of 93%. These optimal Suzuki-Miyaura cross coupling conditions, described by Entry 4, were used for the synthesis of all subsequent library fragments and are referred to as 'General Method B' (Section 4.2.2, Experimental General Methods).

Table 1: Screening of Suzuki-Miyaura cross coupling conditions for the synthesis of benzonitrile **51a**.^{265,275,276} Entry 4 describes the conditions referred to as General Method B hereafter.

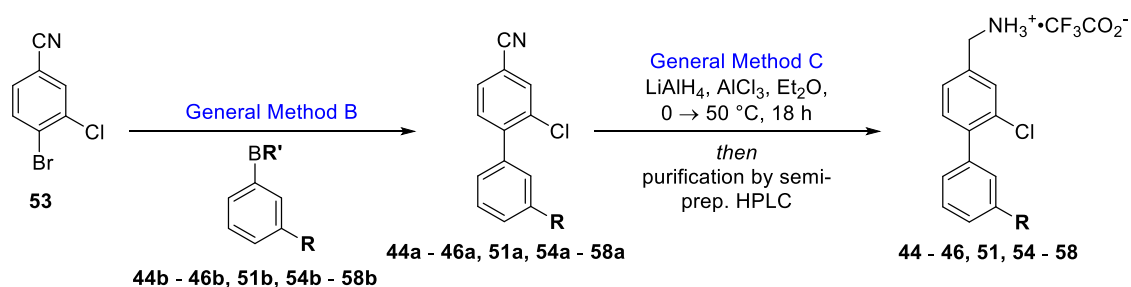
Entry	Conditions	Result
1	48 (1.5 eq.), 51b (1.0 eq.), Pd(PPh ₃) ₄ (cat.), LiCl, 2.0 M aq. Na ₂ CO ₃ , DME, reflux, 18 h	50 ^[a]
2	52 (2.0 eq.), 51c (1.0 eq.), Pd(PPh ₃) ₄ (cat.), Na ₂ CO ₃ , Toluene, EtOH, H ₂ O, 90 °C, 18 h	n/a ^[b]
3	53 (1.0 eq.), 51b (1.0 eq.), PdCl ₂ (dppf)•CH ₂ Cl ₂ (cat.), K ₃ PO ₄ , DME, EtOH, H ₂ O, 110 °C, μw, 1 h	81% ^[c]
4	53 (1.1 eq.), 51b (1.0 eq.), PdCl ₂ (dppf)•CH ₂ Cl ₂ (cat.) (0.05 eq.), K ₃ PO ₄ (1.20 eq.), DME, EtOH, H ₂ O, 110 °C, μw, 1 h	93% ^[c]

[a] Determined by ¹H NMR and LCMS analysis of the crude reaction mixture. [b] Complex mixture of unidentified products as determined by ¹H NMR and LCMS analysis of the crude reaction mixture. [c] Isolated yield of desired benzonitrile **51a**.

With benzonitrile fragment **51a** in hand, reduction of the nitrile moiety was performed as proposed in Scheme 2. Subsequent purification by semi-preparative HPLC provided final benzylamine fragment **51** in moderate yield (Table 2).^{265,266} This result ended the synthesis of the first benzylamine compound for the target-oriented fragment library. Following this success, the optimised Suzuki-Miyaura conditions (General Method B) and nitrile reduction protocol (General Method C) were applied in the synthesis of a further eight biphenyl, benzylamine fragments, as summarised in Table 2.

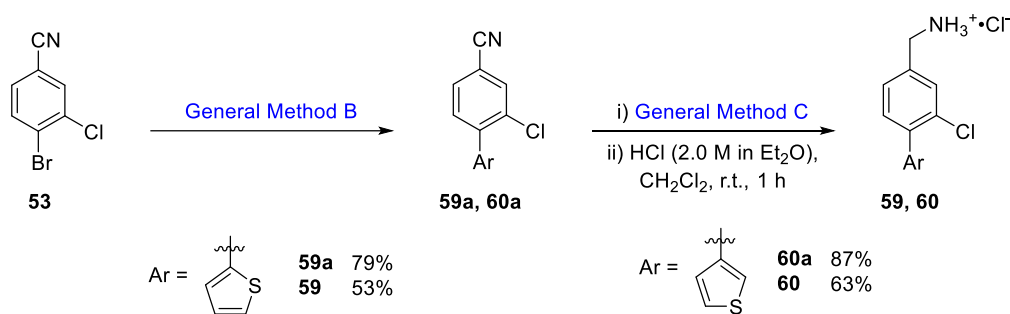
Suzuki-Miyaura cross coupling reactions between bromide **53** and a range of boronic acids and esters (Table 2) provided benzonitrile products **44a** – **46a** and **54a** – **58a**. The products were isolated in excellent yields of over 80% in all cases except one, nitrile derivative **44a**, which gave a good 75% yield. Subsequent reduction of the nitrile and purification by semi-preparative HPLC yielded the final library fragments as trifluoroacetate benzylamine salts **44** – **46** and **54** – **58**. Yields for this step ranged from poor, 6% for methylene alcohol **54** and 19% for alkyne **57**, to good, 71% for ethyl **55** and 77% for fluoro **56**. Methylene alcohol **54** was observed to co-elute with an unidentified side-product which led to poor recovery.

Table 2: Synthesis of target-oriented fragment library with biphenyl, benzylamine scaffolds. Isolated yield of the final fragment and benzonitrile precursor is provided, along with the identity of the boron species used in the Suzuki-Miyaura cross coupling.



Compound	R'	Compound	R	Yield (%)	Compound	R	Yield (%)
44b	(OH) ₂	44a	-CN	75	44	-CH ₂ NH ₃ ⁺ •CF ₃ CO ₂ ⁻	46
45b	(OH) ₂	45a	-Me	84	45	-Me	46
46b	(OH) ₂	46a	-CHCH ₂	85	46	-CHCH ₂	47
51b	pin	51a	-OH	93	51	-OH	45
54b	(OH) ₂	54a	-CH ₂ OH	87	54	-CH ₂ OH	6
55b	(OH) ₂	55a	-Et	81	55	-Et	71
56b	(OH) ₂	56a	-F	89	56	-F	77
57b	pin	57a	-CCH	85	57	-CCH	19
58b	(OH) ₂	58a	-CF ₃	95	58	-CF ₃	78

Two additional fragments, with an adjusted scaffold core, were also synthesised for the fragment library (Scheme 4). These fragments had thiophene moieties in place of the lower phenyl ring and looked promising in computational modelling. The sulfur lone pair on the lower ring was predicted to fill space within the bottom of the α D pocket in both cases. Synthesis of isomers **59** and **60** followed the same route as the biphenyl fragments, except final purification was performed by manual flash column chromatography and the benzylamine chloride salt was formed.



Scheme 4: Synthesis of two target-oriented fragment library compounds with thiophenyl, benzylamine scaffolds. Isolated yields for final fragments **59** and **60** are reported over two steps from benzonitrile precursors **59a** and **60a**.

Benzonitrile precursors **59a** and **60a** (Scheme 4) were prepared in comparable yields to the biphenyl fragments in Table 2. Reduction of the nitrile to provide benzylamines **59** and **60** proceeded without complication and in yields slightly higher than the average reported in Table 2. This may be owed to the relatively poor recovery rate often observed during semi-preparative HPLC purification.

In conclusion, a robust and modular synthetic approach for efficiently accessing biaryl benzylamine fragments was developed. The route was applied successfully in the synthesis of 11 target-oriented library fragments (Table 2 and Scheme 4), hosting a range of hydrophobic and polar moieties on the lower phenyl ring. Compounds were isolated in high yields following the Suzuki-Miyaura cross coupling step (General Method B) and good yields following nitrile reduction (General Method C) and salt formation.

2.1.3 Fragment Library Screening and Biochemical Assessment

The target-oriented fragment library, prepared in Table 2 and Scheme 4, Section 2.1.2, was submitted to our University of Cambridge Biochemistry collaborator, Dr. Paul Brear, for structural analysis and biochemical assessment.^a He co-crystallised the fragments with a K74A mutant of CK2 α before sending them for X-ray crystallography at the Diamond Light Source Synchrotron, Didcot. Samples exhibiting selective binding in the α D pocket, relative to the ATP- and CK2 α /CK2 β interface-sites, were then carried forward into biochemical testing *via* ITC to determine the binding constant (K_d). A CK2 α kinase assay was performed, using the ADP-Glo™ kinase assay kit (Promega), to determine whether the fragments could inhibit activity of the enzyme. For fragments capable of inhibition, a measurement of the % inhibition of kinase activity at a sample concentration of 100 μ M was recorded.

^a For this project, all raw X-ray crystal structure data was collected and refined by Dr. Paul Brear, Department of Biochemistry, University of Cambridge. He also performed all biochemical assays for the collection of K_d , % inhibition and IC₅₀ data. The analysis of this data, presented in this thesis, is my own work.

The results from X-ray crystallography and biochemical testing are presented in Table 3. Four fragments (methyl **45**, alcohol **51**, methylene alcohol **54** and thiophene **60**) were not observed to bind to CK2 α . They presented no electron density at any binding site on subunit α and were not considered further. The remaining seven fragments did bind to CK2 α and site-selectivity for the α D pocket was reported. Three of these fragments, derivatives ethyl **55**, fluoro **56** and 2-thiophene **59**, occupied the α D pocket with the same binding mode as lead fragment **34**, *i.e.* with the benzylamine moiety projecting towards the ATP-site and the lower phenyl ring stacked with Met225 (Figure 29, a). The binding positions also matched those predicted by the computational modelling, whereby the ethyl (**55**) and fluoro (**56**) groups and sulfur lone pair (**59**) fill the hydrophobic cavity at the 3-position (Figure 29, b, c and d respectively). Fluoro derivative **56** was observed to fill the α D pocket in two binding poses (Figure 29, c). This is potentially due to the small size of the fluoro substituent and flexibility of the pocket to accommodate a 180° rotation in the biaryl positioning.

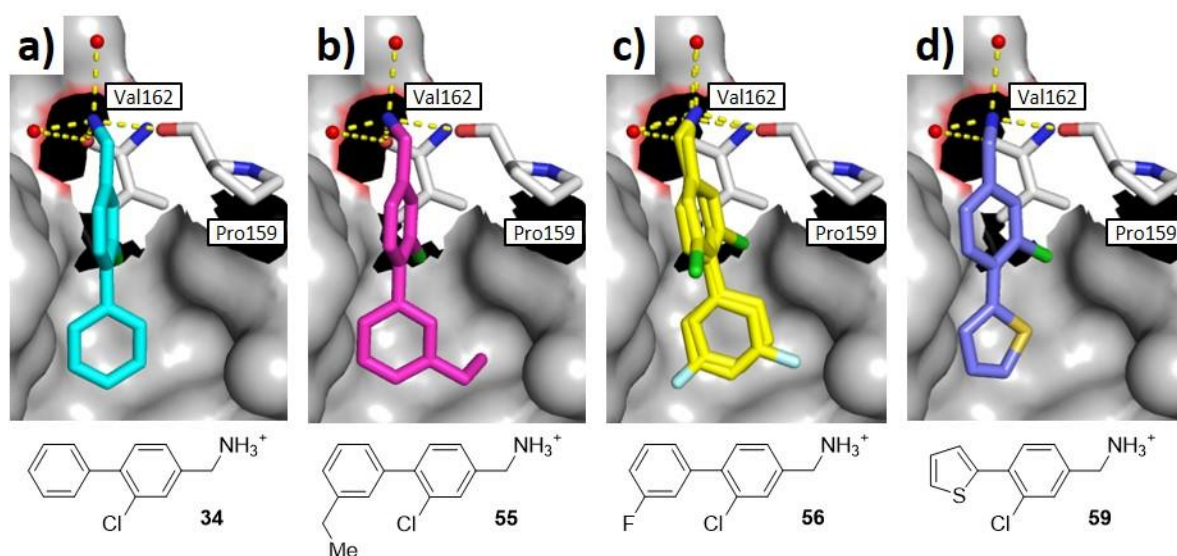


Figure 29: X-ray crystal structures of benzylamine fragments binding within the α D pocket (grey) and adopting the same binding mode as lead fragment **34**. **a)** Lead fragment **34** (blue). **b)** Ethyl derivative **55** (magenta). **c)** Fluoro derivative **56** (yellow) with two binding modes, both optimally utilising the α D pocket volume. **d)** 2-Thiophene derivative **59** (purple) with sulfur lone pair projecting into the vacant space. Polar interactions between the fragment, protein residues (white) and water molecules are highlighted by yellow dashed lines.

These three fragments were tested for binding affinities (K_d) but all measured over 750 μ M (Table 3). This was well above the K_d reported by Brear *et al.* for their original lead **34**, of 270 μ M.²⁶⁵ The fragments were also tested in a CK2 α kinase assay but none were reported to inhibit activity. Based on this, these fragments were deemed too weak to use in future SBDD and were not considered further.

Table 3: X-ray crystallography and biochemical testing results for target-oriented fragment library.

Compound	Ar	α D-site selective? ^[a]	α D-site binding mode ^[a]	K_d (μ M) ^{[b][c]}	% inhib. @ 100 μ M \pm SEM ^{[d][e]}
44		Y	Novel	>750	n.a.
45		n.d.	-	-	-
46		Y	Novel	>750	19 \pm 7
51		n.d.	-	-	-
54		n.d.	-	-	-
55		Y	Consistent with literature	>750	n.a.
56		Y	Consistent with literature	>750	n.a.
57		Y	Novel	>750	28 \pm 0.4
58		Y	Novel	750	32 \pm 5
59		Y	Consistent with literature	>750	n.a.
60		n.d.	-	-	-

[a] Determined from X-ray crystal structure data. [b] Measured by ITC. [c] Results are of one experiment. [d] Measured by CK2 α ADP-gloTM kinase assay. [e] Tests carried out in triplicate and reported as the mean. Y: yes. n.d.: no density observed on CK2 α . α D-site binding mode: novel or consistent with Brear *et al.* reported binding mode for lead **34**. n.a.: not active at concentration tested.

The remaining four fragments, dibenzylamine **44**, vinyl **46**, alkyne **57** and trifluoro **58**, were observed to bind in the α D pocket with binding modes that were previously unreported and unpredicted by computational modelling. The first of these modes was adopted by dibenzylamine derivative **44** (Table 3). Fragment **44** had originally been predicted to bind in the same manner as lead fragment **34** and interact with Met221 *via* a HBD (Figure 30, **a**). Instead, the 3-position benzylamine group displaced the original benzylamine moiety from its binding position (Figure 30, **b**). This forced the biaryl core to rotate 90° within the α D pocket. The rearrangement forced a new pocket opening and the benzylamine group on the chlorophenyl ring projected through it. This positioned the benzylamine moiety away from the protein and into solvent, where no polar interactions were reported. Overlay of lead fragment **34** with dibenzylamine species **44** highlights the fragment rotation within the α D pocket (Figure 30, **c**).

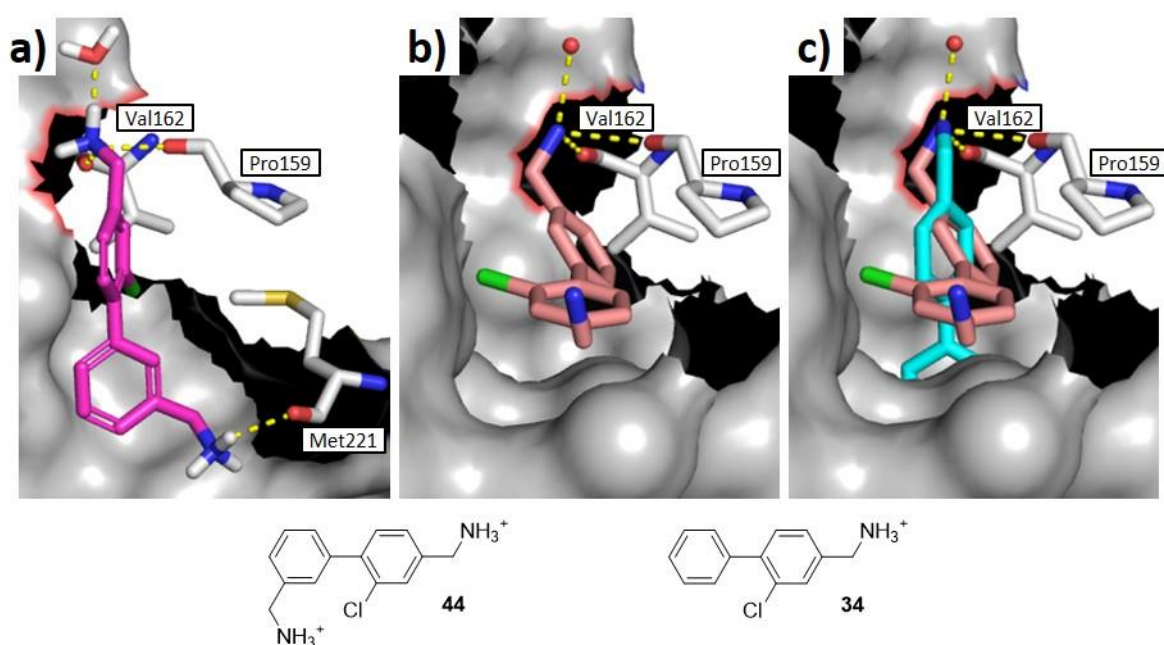


Figure 30: Binding mode comparison between predicted dibenzylamine **44**, recorded dibenzylamine **44** and lead fragment **34** in complex with CK2 α (grey). **a**) Dibenzylamine derivative **44** (magenta) from computational modelling, showing predicted HBD interaction to Met221 (white) as a dashed yellow line. **b**) Dibenzylamine derivative **44** (pink) from recorded X-ray crystal data, showing altered binding mode within the α D pocket. The HBD interactions with Pro159, Val162 (white) and water are shown by dashed yellow lines. **c**) Overlay of lead fragment **34** (blue) and dibenzylamine species **44** (pink) to demonstrate relative position of new binding mode.

When tested by ITC, the binding affinity for dibenzylamine derivative **44** was above 750 μ M and it failed in the kinase inhibition assay (Table 3). The interesting binding mode presented an opportunity for new SBDD, but the poor quality of the biochemical data halted further interest in this fragment scaffold.

The final three fragments, derivatives vinyl **46**, alkyne **57** and trifluoro **58**, also adopted a new α D-site binding mode (Figure 31). Relative to original lead **34** (Figure 31, a), these fragments were rotated clockwise by 90° and the benzylamine moiety induced an alternative pocket opening into the substrate-binding channel (Figure 31). In all cases, the amine group made HBD interactions with the sidechain of Glu230 and water molecules at the opening of the pocket. For vinyl **46**, an acetate molecule sat in the pocket opening and acted as a HBA for the benzylamine (Figure 31, b). The new binding mode is discussed further in Section 2.1.4, Analysis of the New Binding Mode.

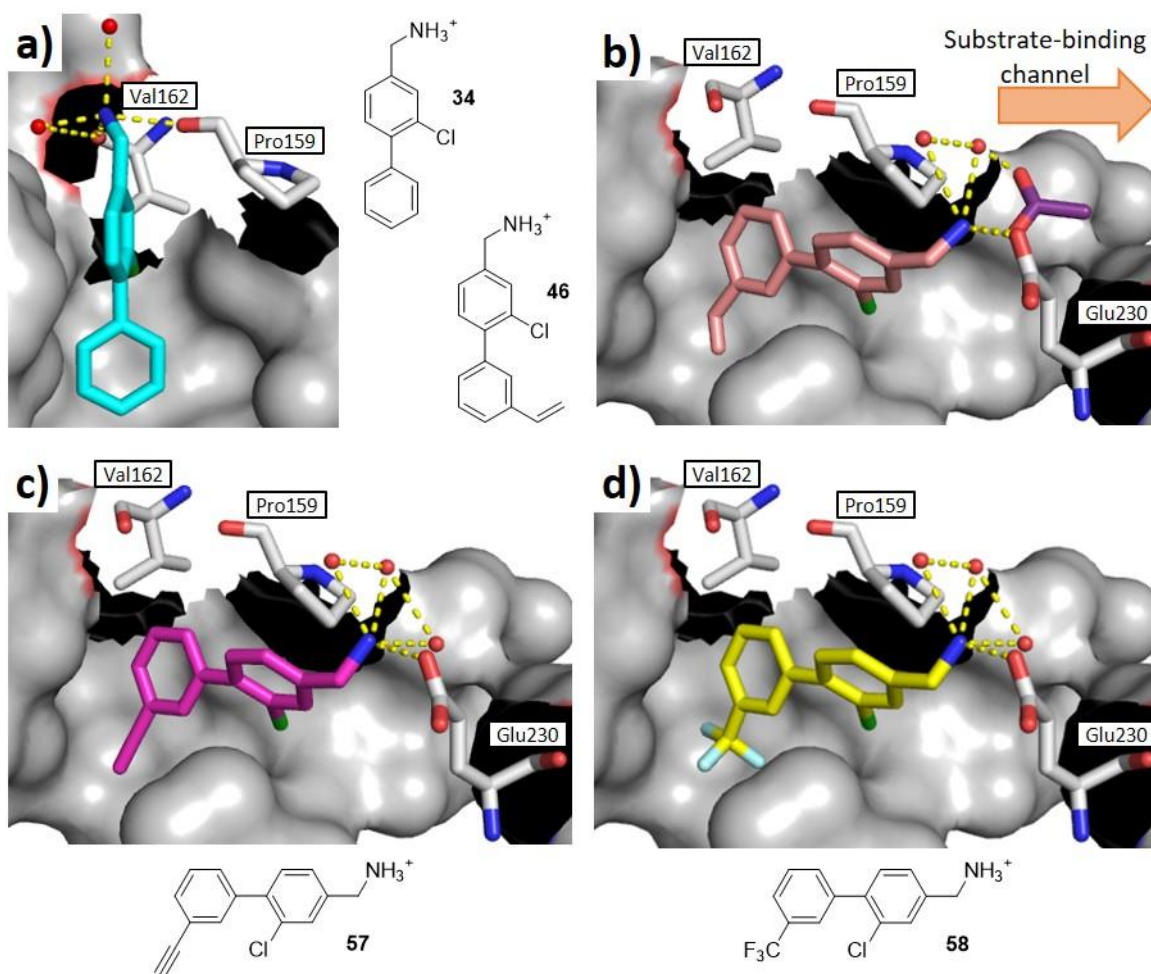


Figure 31: X-ray crystal structures comparing lead fragment **34** with the new binding mode towards the substrate-binding channel, indicated by orange arrow. **a)** Lead fragment **34** (blue). **b)** Vinyl derivative **46** (pink) with acetate (purple). **c)** Alkyne derivative **57** (magenta). **d)** Trifluoro derivative **58** (yellow). Pro159 and Val162 (white) have been highlighted in each image as reference to the binding position of lead fragment **34**. Polar interactions between the fragment, protein residues (white) and water molecules are highlighted by yellow dashed lines.

Biochemical assessment of fragments **46**, **57** and **58** returned binding affinities of >750, >750 and 750 μ M respectively (Table 3). Pleasingly, in the kinase assay all three fragments showed inhibition of CK2 α activity. Trifluoro derivative **58** performed the best, giving 32% activity inhibition, but the statistical

error of 5% overlaps with alkyne derivative **57**. To the best of our knowledge, this was the first observation of CK2 α inhibition by small molecules binding exclusively within the α D pocket. Furthermore, the novel binding mode adopted by these fragments had not been predicted by computational modelling and provided a new exit vector from the α D pocket.

In conclusion, a target-oriented fragment library consisting 11 members was screened against CK2 α by X-ray crystallography. Seven fragments were observed to bind selectively within the α D pocket, displaying both predicted and unpredicted binding modes. These fragments were subjected to ITC for binding affinity determination which showed very poor binding for four fragments (**44**, **55**, **56** and **59**) and weak binding for three fragments (**46**, **57** and **58**). Final assessment of the library fragments by CK2 α kinase inhibition assay revealed three derivatives capable of inhibiting protein activity: **46**, **57** and **58**. Interestingly, these successful candidates all bind in the α D pocket with an unexpected and novel binding mode (Figure 31).

The discovery of a new binding mode within the α D pocket highlights one of the major benefits of screening by X-ray crystallography rather than *in silico* or by biochemical assay. If structural biology had not featured so heavily in this project, then the novel binding pose may have gone undetected and the inhibitor series reported in Section 2.2 would not have been developed.

From this point forward, the new binding orientation adopted by vinyl **46**, alkyne **57** and trifluoro **58** derivatives became the focus of this project. To better understand the alternative binding mode, analysis of overlaid X-ray crystal structures was first performed. Based on this knowledge, development of an optimised inhibitor fragment series was then conducted followed by an investigation into the utility of the substrate-binding channel exit vector. The upcoming sections work through these aims in order.

2.1.4 Analysis of the New Binding Mode

As introduced in Section 2.1.3, fragments bearing vinyl (**46**), alkyne (**57**) or trifluoro (**58**) groups at the 3-position of the lower phenyl ring were observed to bind *via* a new mode within the α D pocket. Overlay of the X-ray crystal structures for these three fragments showed that the biaryl cores aligned precisely and that the 3-position substituent occupied a hydrophobic pocket (Figure 32, **a**). Superimposing lead fragment **34** onto this structure revealed the relative positioning of the old and new binding modes (Figure 32, **b**). The 3-position substituents sit where the lower phenyl ring of **34** sat, and the stacking interaction with Met225 is lost. By visual inspection of the overlaid X-ray crystal structures, all fragments reach the same depth within the α D pocket.

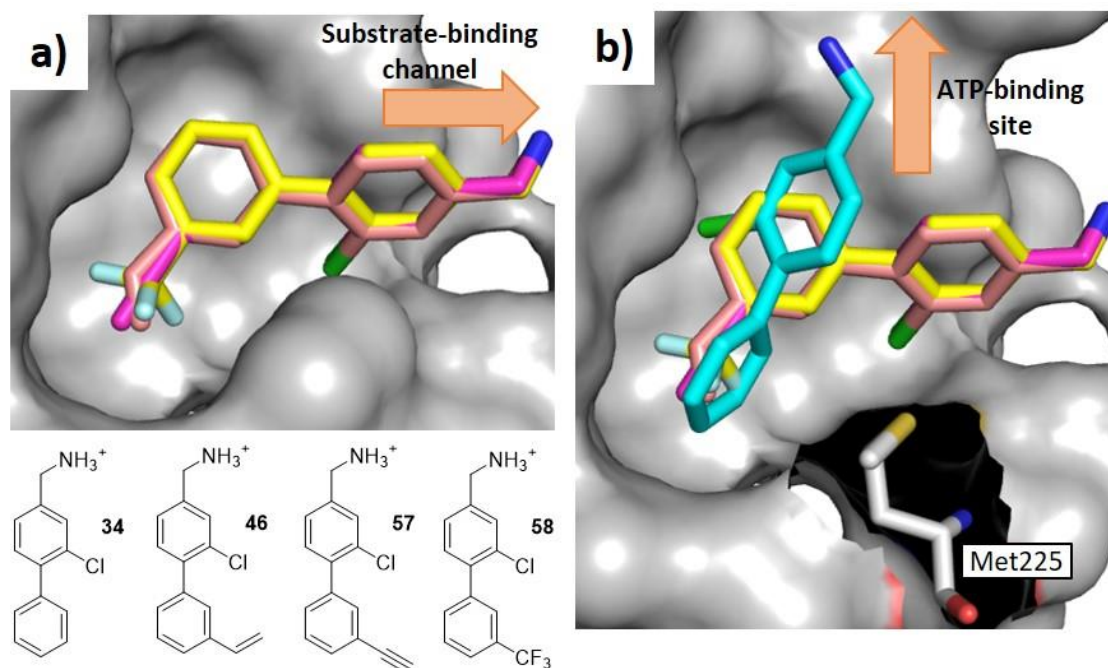


Figure 32: Overlaid X-ray crystal structures for the new binding mode with direction of substrate- and ATP-binding sites indicated by orange arrows. **a)** Vinyl derivative **46** (pink), alkyne derivative **57** (magenta) and trifluoro derivative **58** (yellow) binding modes overlay precisely within the α D pocket (grey). **b)** Original lead fragment **34** (blue) overlaid with the new binding mode to show overlap of lower phenyl ring and 3-position substituents of **46**, **57** and **58**. Stacking interaction between Met225 (white) and the fragment is lost in the new binding mode.

As the binding mode for all three derivatives (vinyl **46**, alkyne **57** and trifluoro **58**) was demonstrated to be consistent (Figure 32), the fragment providing the best resolution X-ray crystal structure and most promising biochemical data was used as the lead compound for further analysis. This was trifluoro benzylamine **58**, and the rest of this section focuses on comparing the structural data of **58** with that of Brear *et al.*'s lead fragment **34**.

Comparison of the α D pocket cavity for benzylamine **34** and trifluoro derivative **58** revealed the crucial rearrangement of three protein residues: Phe121, Tyr125 and Glu230 (Figure 33). The rest of the residues lining the pocket overlay well, with minimal movement observed.

1. Movement of Phe121

When fragment **34** (blue) is bound in the α D pocket, Phe121 lines the wall of the cavity in a position adjacent to the chlorophenyl ring (Figure 33, a). Upon binding trifluoro species **58** (yellow), Phe121 is displaced by the chlorophenyl ring and forced to rotate 90° anticlockwise. This movement creates an opening between the α D pocket and the substrate-binding channel, through which the benzylamine moiety of **58** protrudes. The sidechain of Phe121 displaces the two water molecules used by

benzylamine **34** for H-bonding and also blocks the ATP-site pocket opening, thus closing this exit vector.

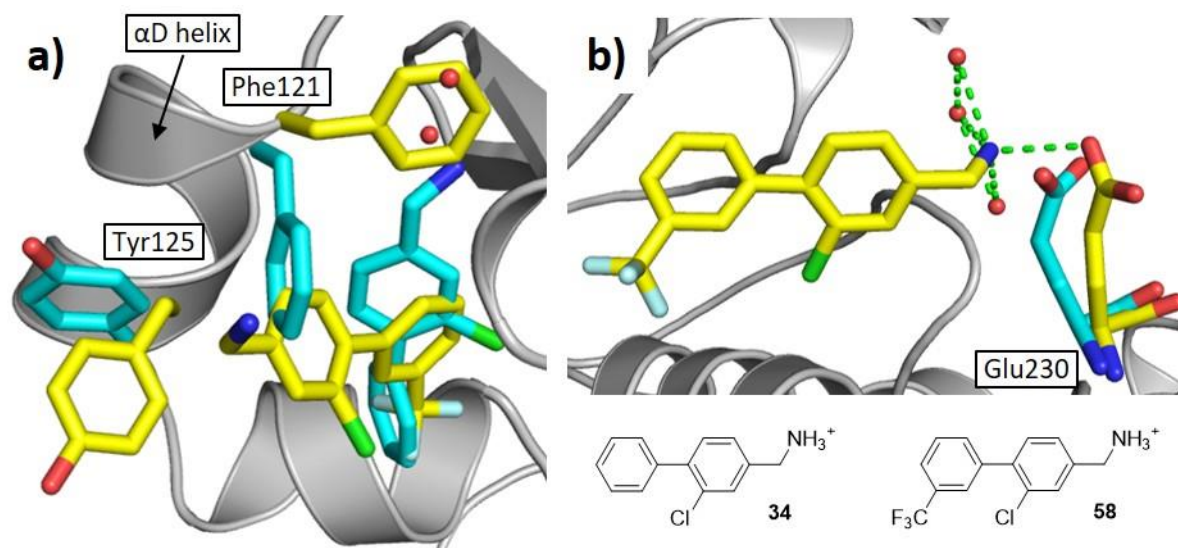


Figure 33: X-ray crystal structure comparison of original lead **34** (blue) and trifluoro fragment **58** (yellow). **a)** View of the α D pocket (grey) highlighting the relative movements of Phe121 and Tyr125 upon the binding of **58**. Water molecules from original lead **34** are shown and α D helix is labelled. **b)** View of the α D pocket (grey) highlighting the relative movement of Glu230 and entry of three water molecules. H-bonding network is shown by green dashed lines.

2. Movement of Tyr125

Tyr125 originally formed part of the pocket wall, however when trifluoro derivative **58** binds, this residue is forced to rotate down and away from the protein (Figure 33, **a**). This aids in opening the new gateway into the substrate-binding channel and widens the pocket opening to allow the benzylamine group to come through.

3. Movement of Glu230

Finally, Glu230 is pushed away from the protein core when trifluoro derivative **58** occupies the α D pocket (Figure 33, **b**). This movement helps widen the opening into the substrate-binding channel and allows for three water molecules to enter the pocket mouth. The three waters form a H-bonding network with benzylamine **58** and Glu230 which helps hold the fragment in the pocket.

Re-analysing the computational modelling results for trifluoro species **58** did not provide a clear reason for the new binding mode (Figure 34, **a**). The prediction software indicated sufficient space within the α D pocket for the accommodation of a trifluoro group, implying that an argument on the basis of sterics was not sufficient. Additionally, the biaryl ring conformation of fragment **58** predicted by the computational software (Figure 34, **a**) was not dissimilar to the conformation adopted in the X-

ray crystal structure (Figure 34, **b**). This implied that there was not a significant energy penalty arising from the biaryl ring conformation that would explain preference for one binding mode over the other.

Alternatively, hydrophobic interactions between the trifluoro of **58** and the residues lining the true binding mode (Leu128, Ile133, Tyr136, Met137, Ile140 and Met221) (Figure 34, **b**), may be more favourable than those in the predicted binding mode (Met137, Ile140, Leu218, Met221 and Met225) (Figure 34, **a**).

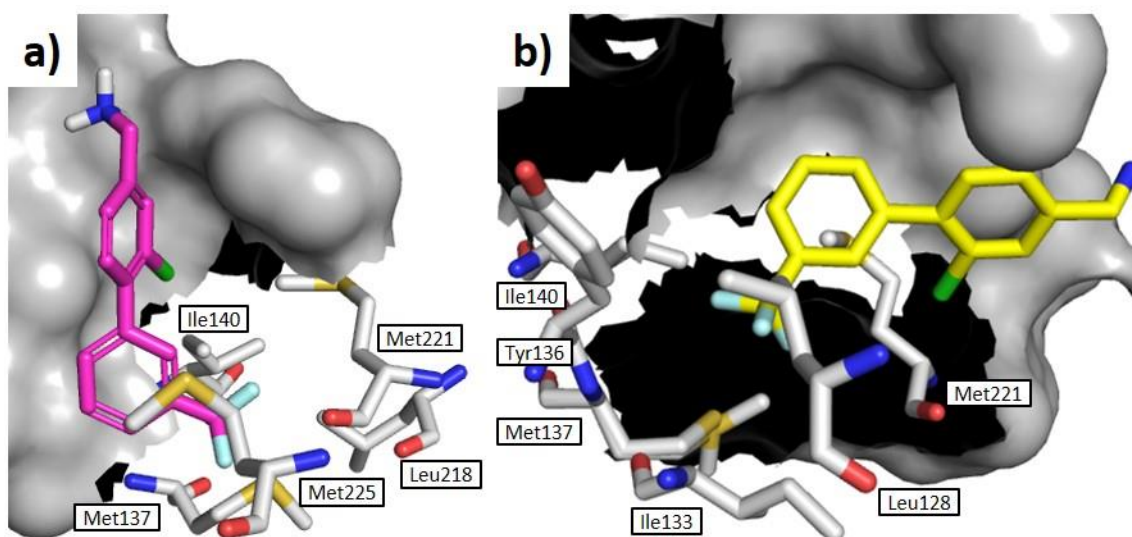


Figure 34: Comparison of trifluoro derivative **58** binding mode from computational modelling and X-ray crystallography. **a**) Computational modelling result for **58** (magenta) showing predicted binding mode consistent with lead fragment **34**. **b**) X-ray crystallography result for **58** (yellow) showing accommodation of the trifluoro group in an alternative hydrophobic pocket. Residues lining the hydrophobic pockets are shown in white.

With new hit species trifluoro **58** in hand, and binding mode analysis complete, the investigation was continued *via* traditional hit-to-lead generation (Section 1.1.4). Starting with the X-ray crystal structure of hit **58**, an SBDD approach was initiated with the aim of developing more potent CK2 α inhibitors (Section 2.2). Given sufficient data, the mode of action for this inhibitor series would then be considered (Section 2.2.5).

2.2 Structure-Based Optimisation of the New Binding Mode

2.2.1 Optimisation Strategy for Hit-to-Lead Generation

X-ray crystal structure analysis of trifluoro hit **58** showed three regions of the fragment that could be optimised: ring A, ring B and the head group (Figure 35). It was envisaged that:

1. The addition of a polar substituent to **ring A** may be able to replicate the HBD interaction that original lead **34** made with Pro159 and Val162, whilst maintaining the overall binding pose of **58**.
2. Alternative substitution pattern on **ring B** may more efficiently fill space within the middle portion of the α D pocket.
3. Changing the identity of the **head group** protruding into the substrate-binding channel may alter the position of the fragment within the α D pocket, potentially exploiting the depth of the pocket.



Figure 35: Graphic demonstrating the optimisation strategy for hit-to-lead generation from trifluoro fragment **58** hit.

A systematic optimisation at each position was performed, with the best fragment from each round being carried into the next. At each stage, fragments accessible from commercially available starting materials were screened *in silico*, before chemical synthesis of ligands with the best docking results was performed. If a fragment with biochemical data superior to that of the current lead was identified, then SBDD moved forward to the next optimisation site. In moving forward, the core scaffold of the improved fragment was maintained. This method efficiently provided the potent α D-selective inhibitor series reported herein (Sections 2.2.2 – 2.2.4).

2.2.2 SBDD on Ring A

An X-ray crystal structure overlay of hit **58** and original lead **34** suggested that the introduction of a HBD group at the 6-position of ring A might mimic the benzylamine of **34** (Figure 36, **b**). It was hypothesised that this polar group would be capable of replicating the HBD interactions with Pro159 and Val162 that were lost in discovery of the new binding mode. An alcohol substituent was added to fragment **58** at the 6-position (**61**) (Figure 36, **a**) and computational modelling was performed. The results looked promising, with the alcohol predicted to contact Pro159 and an α D pocket water (Figure 36, **c**). The predicted positions of the biaryl core and amine head group were consistent with hit **58**.

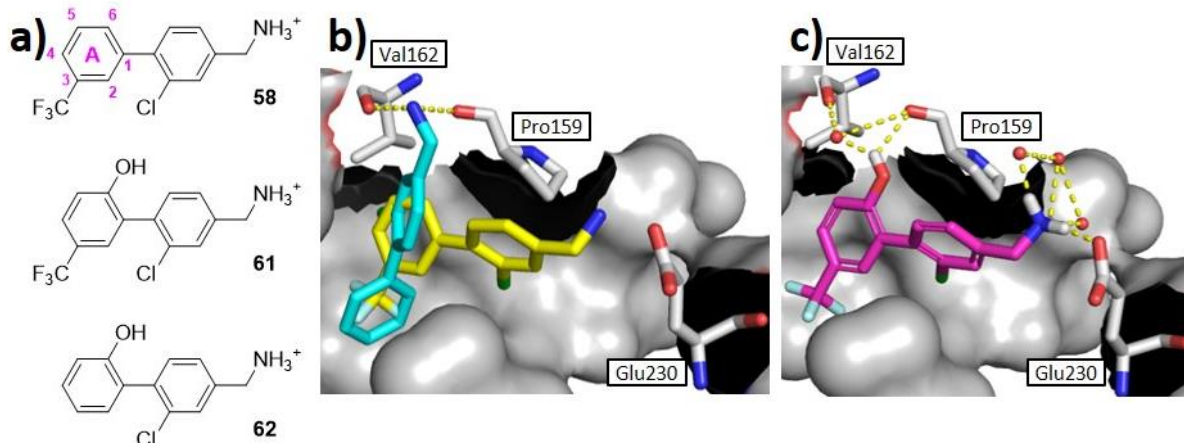
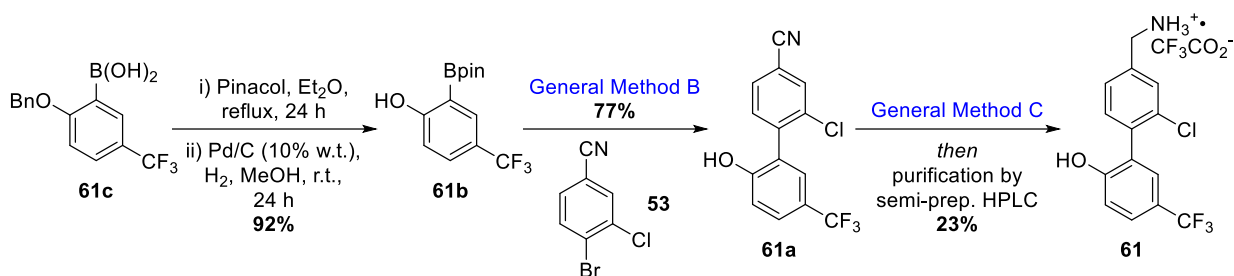


Figure 36: Preliminary work for SBDD on ring A. **a)** Chemical structures of hit fragment **58** with ring A and numbering scheme shown, proposed HBD fragment **61** and analogue **62** without ring A trifluoro group. **b)** X-ray crystal structure overlay of original lead **34** (blue) and hit **58** (yellow) in complex with CK2α (grey) to show overlap of the benzylamine moiety of **34** and the 6-position of ring A of **58**. **c)** Computational modelling results for **61** (magenta) showing predicted HBD interactions between 6-position alcohol, Pro159 (white) and water. H-bonding interactions are shown by yellow dashed lines.

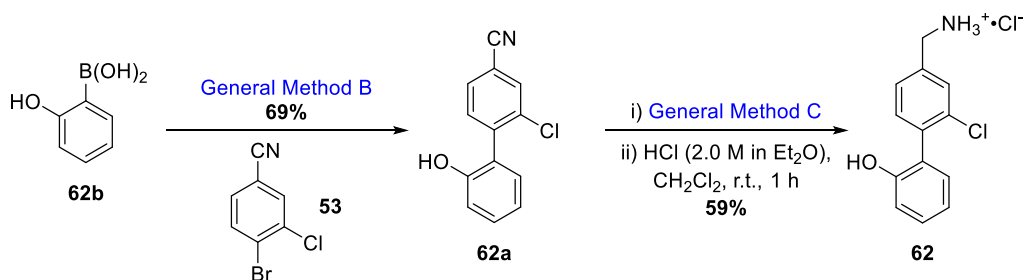
Computational modelling was followed by the synthesis of two molecules: HBD fragment **61** and analogue **62**, lacking the trifluoro group (Figure 36, a). Analogue **62** had been modelled *in silico* and was predicted to bind with the same interactions as **61** (Figure 36, c). We were interested to determine the importance of the trifluoro group towards promoting the observed binding mode and thus comparison of **61** and analogue **62** was deemed relevant.

Synthesis of HBD fragment **61** was performed under the general conditions developed in Section 2.1.2 (Scheme 5). Previous synthesis of alcohol fragments **51** and **54** (Table 2, Section 2.1.2) had shown that an alcohol protecting group was not necessary, so commercially available boronic acid **61c** was converted to a pinacol ester and the benzyl group removed.²⁷⁷ This gave Suzuki-Miyaura cross coupling partner **61b** in excellent yield over two steps. Deprotection of **61c** benzyl group was also attempted without initial boronic acid conversion to a pinacol ester, but recovery of the product boron species was very poor.²⁷⁸ With boronic ester **61b** in hand, General Method B was applied to **61b** and bromide **53** to provide benzonitrile **61a** in good yield. Finally, reducing conditions C and purification by semi-preparative HPLC gave desired product **61** in moderate yield.



Scheme 5: Synthesis of optimised ring A fragment **61** from commercially available **61c**. Following boronic ester formation and benzyl alcohol deprotection to give **61b**,²⁷⁷ General Methods B and C were applied to provide final product **61**. Isolated yield of **61b** is reported over two steps.

Synthesis of alcohol analogue **62** was performed under the same conditions as fragment **61**, but instead starting from commercially available boronic acid **62b**, which did not need protecting group removal (Scheme 6). General Method B provided Suzuki-Miyaura product **62a** in good yield and reduction of the nitrile by General Method C, followed by manual flash column chromatography and hydrochloride salt formation, gave final product **62** cleanly.



Scheme 6: Synthesis of fragment analogue **62** from commercially available boronic acid **62b** by General Methods B and C. Isolated yield of **62** is reported over two steps.

Optimised ring A fragments **61** and **62** were submitted for X-ray crystallography and biochemical assessment. Trifluoro fragment **61** was observed to bind the α D pocket selectively and as predicted by computational modelling (Figure 37, a). The 6-position alcohol formed a HBD interaction with Pro159 and a HBA interaction with an α D pocket water molecule. Interactions between the

benzylamine moiety and three substrate-binding channel water molecules were maintained but the contact with Glu230 was lost.

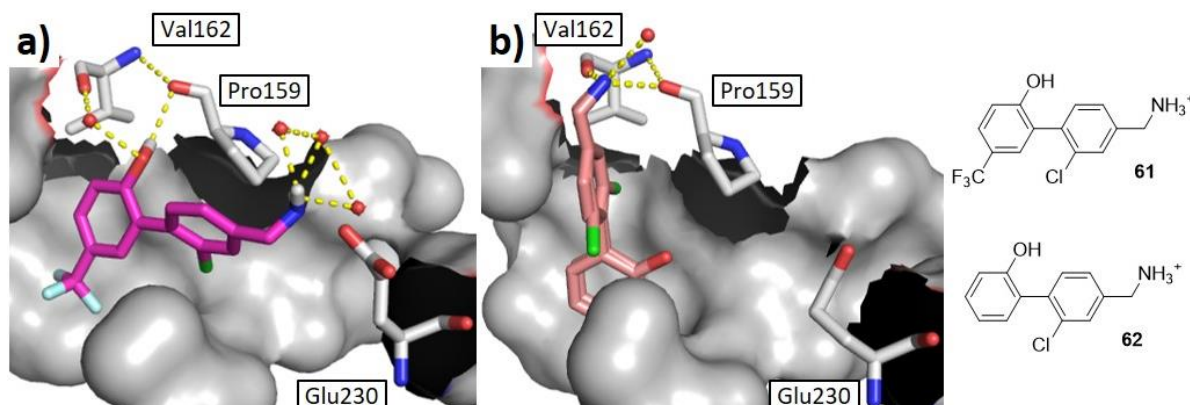


Figure 37: X-ray crystallography results for optimised fragments **61** and **62** in complex with CK2 α (grey). **a)** Optimised trifluoro species **61** (magenta) adopts the binding mode predicted by modelling. **b)** Analogue **62** (pink) reverts back to the original binding pose of lead **34**. Analogue **62** was observed to bind the α D pocket with two chlorophenyl ring orientations: chlorine pointing towards front or back of pocket. Polar interactions between the fragment, protein residues (white) and water molecules are highlighted by yellow dashed lines.

Fragment **62**, on the other hand, did not bind CK2 α as predicted and instead adopted the original fragment binding mode reported by Brear *et al.*²⁶⁵ (Figure 37, **b**). HBD interactions between the benzylamine and Pro159, Val162 and a water molecule were identified. The chlorophenyl ring was accommodated in the α D pocket *via* two binding modes, with the chlorine projecting either to the back of the pocket or to the front of the pocket.

Based on the X-ray crystallography data in Figure 37, it was decided that the 3-position trifluoro moiety of **58** and **61** was essential in promoting the new binding mode. Therefore, all future fragment analogues would bear this functional group. As alcohol **62** was not consistent with the binding mode under investigation, it was not considered further.

Benzylamine fragment **61**, bearing optimised ring A, was taken forward for biochemical assessment (Table 4). When tested in the CK2 α kinase inhibition assay, optimised benzylamine **61** performed better than previous lead **58**, reporting an improved 44% activity inhibition compared to an original 32%, although the statistical errors overlap by 1%. An IC₅₀ value of 100 μ M was also recorded for optimised **61**. The improved activity of ortho-alcohol substituted **61**, relative to fragment **58**, could partly be owed to the pre-formed conformation of the biaryl moiety. The chlorine and alcohol ortho-

substituted groups restrict free rotation of the two aryl rings and therefore reduce the entropic binding penalty associated with fragment **61** binding in the α D pocket.

Table 4: Biochemical testing results for optimised ring A fragment **61** in comparison to hit fragment **58**.

Compound	R	K_d (μ M) ^{[a][b]}	% inhib. @ 100 μ M \pm SEM ^{[c][d]}	IC ₅₀ \pm SEM (μ M) ^{[c][e]}
58	-H	750	32 \pm 5	n.d.
61	-OH	n.d.	44 \pm 8	100 \pm 18

[a] Measured by ITC. [b] Results are of one experiment. [c] Measured by CK2 α ADP-gloTM kinase assay. [d] Tests carried out in triplicate and reported as the mean. [e] Tests carried out in duplicate and reported as the mean. n.d.: no data

In conclusion, two ring A-optimised fragments (**61** and **62**) were designed, modelled and synthesised. Following X-ray crystallography, fragment **61** was observed to maintain the binding mode of hit **58**, but analogue **62** adopted Brear *et al.*'s published binding mode.²⁶⁵ The alcohol group added to fragment **61** successfully replicated the H-bonding network previously reported for the benzylamine moiety of Brear's lead fragment **34**.²⁶⁶ Biochemical assessment of optimised species **61** provided superior inhibition data relative to hit fragment **58**, and thus **61** became the new lead compound for future SBDD.

2.2.3 SBDD on the Amine Head Group

The benzylamine functional group at the head of biaryl scaffold **61** was considered next for optimisation. It was observed that the existing polar amine substituent was protonated and solvent exposed when bound in the α D pocket (Figure 37, **a**). Therefore, it was hypothesised that the energy penalty from fragment desolvation may not be balanced by the interactions made to the protein following binding. Based on this theory, we wanted to test alternative functional groups with reduced H-bonding ability.

An *in silico* screening library was constructed, guided by commercially available Suzuki-Miyaura cross coupling partners bearing a head group in the 1-position, a chlorine in the 3-position and a bromine in the 4-position. Results from computational modelling predicted that three species with alternative head groups would overlay well with the biaryl core of current lead **61**: nitrile **61a**, aldehyde **63** and methylene alcohol **64** (Figure 38). They were not predicted to make any interactions with Glu230 or

the three substrate-binding channel waters, but were expected to maintain the HBD/HBA interactions on optimised ring A.

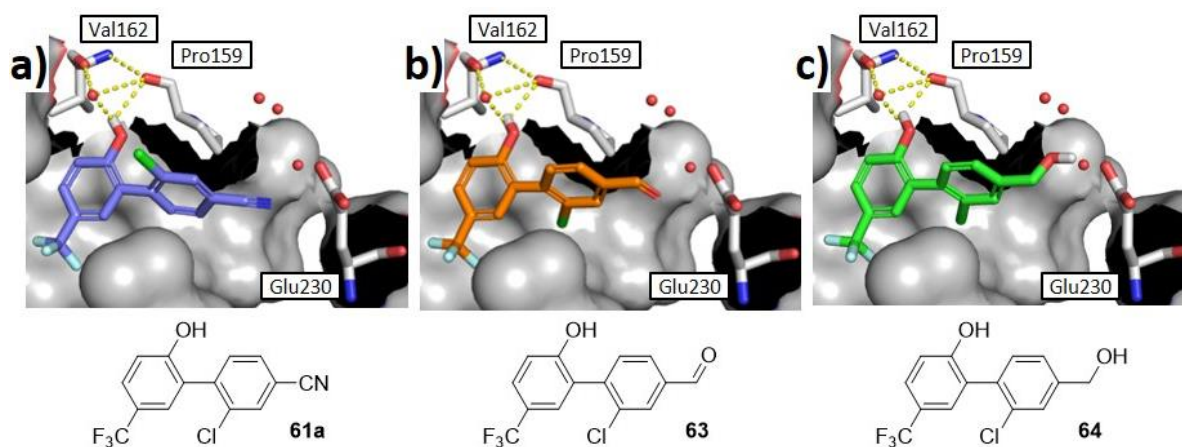
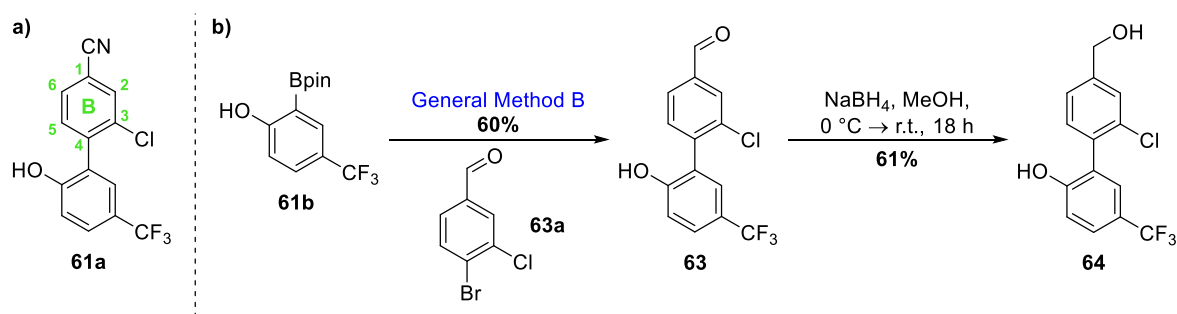


Figure 38: Computational modelling results for optimisation of the amine head group on lead fragment **61**. **a)** Nitrile **61a** (blue). **b)** Aldehyde **63** (orange). **c)** Methylene alcohol **64** (green). All three molecules were predicted to maintain the ring A interaction with Pro159 (white) and the α D pocket water, shown by dashed yellow lines. None of the molecules were predicted to interact with Glu230 (white) or the waters at the pocket opening.

Moving forward, synthesis of nitrile **61a** had already been performed *en route* to benzylamine **61** (Scheme 7, a). Aldehyde **63** was synthesised by Suzuki-Miyaura cross coupling between boronic ester **61b** and appropriate bromide **63a** (Scheme 7, b). This provided desired fragment **63** in good yield and subsequent aldehyde reduction under literature conditions²⁷⁹ delivered methylene alcohol **64** without complication.



Scheme 7: Synthesis of optimised head group fragments **61a**, **63** and **64**. **a)** Chemical structure of nitrile **61a** previously synthesised in Scheme 5. The numbering pattern used for ring B is shown in green. **b)** Synthesis of aldehyde **63** by General Method B and alcohol **64** by NaBH_4 reduction.²⁷⁹

The three fragments were submitted for structural analysis by X-ray crystallography, which revealed binding modes consistent with the computational modelling (Figure 39). Overlay of the biaryl core for nitrile **61a** with lead benzylamine **61** showed similar positioning of the fragments within the α D pocket,

and the interactions between ring A, Pro159 and the α D pocket water were maintained (Figure 39, a). Repeating this overlay for aldehyde **63** and alcohol **64** gave the same results as for nitrile **61a**.

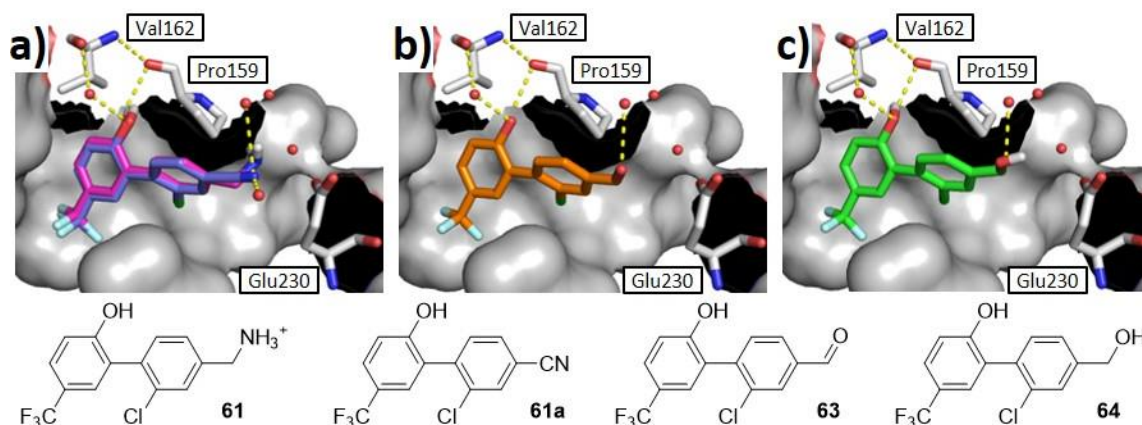


Figure 39: X-ray crystal structures following head group optimisation. **a)** Structure overlay of current lead **61** (magenta) and nitrile **61a** (blue) showing good overlap of the biaryl cores and maintenance of the optimised ring A interactions. **b)** Aldehyde **63** (orange). **c)** Alcohol **64** (green). Polar interactions between the fragment, protein residues (white) and water molecules are highlighted by yellow dashed lines.

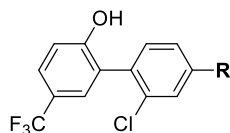
In further analysis, the nitrile group of **61a** was observed to make HBA interactions with two water molecules at the pocket mouth, and one of these waters had not been observed in prior structures (Figure 39, a). Aldehyde **63** and alcohol **64** both formed one HBA interaction with a substrate-binding channel water (Figure 39, b and c respectively). No interaction with Glu230 was observed for any fragment, which was probably due to repulsion between the carboxylate sidechain and head group lone pairs.

Biochemical assessment of the three fragments was conducted and the results compared to lead benzylamine **61** (Table 5). Exchanging the benzylamine for a nitrile (**61a**) gave superior kinase activity inhibition of 80% compared to 44%, and an improved IC_{50} of 51 relative to 100 μ M. Aldehyde **63** inhibited kinase activity to a poorer extent (34%) than lead **61** and was not investigated further. Alcohol **64** was a weaker binding fragment than nitrile **61a** (K_d of 68 compared to 22 μ M) and was also not investigated further. Overall, benzonitrile **61a** provided the best improvement on lead benzylamine **61** and was tested against HCT116 cancer cell lines to provide a GI_{50} of 69 μ M.^b The HCT116 cancer cell line was chosen in order to be continuous with previous publications on clinical candidate silmitasertib **20** and Brear *et al.*'s pro-CAM4066 **37**.²⁶⁵ However, the cell line does not explicitly overexpress CK2 α and no western blots were performed for this project, therefore effects

^b All GI_{50} data reported in this thesis was collected by Dr. Maxim Rossman, Department of Biochemistry, University of Cambridge. The analysis of this data, presented herein, is my own work.

may be due to off-target activity of the compounds. Further investigation, which is beyond the scope of this project, would be required to confirm activity against CK2 α in cells.

Table 5: Biochemical testing results for optimised head group fragments **61a**, **63** and **64** in comparison to lead fragment **61**.



Compound	R	K_d (μM) ^{[a][b]}	% inhib. @ 100 μM \pm SEM ^{[c][d]}	$\text{IC}_{50} \pm \text{SEM}$ (μM) ^{[c][e]}	$\text{GI}_{50} \pm \text{SEM}$ (μM) ^{[e][f]}
61	$-\text{CH}_2\text{NH}_3^+$	n.d.	44 \pm 8	100 \pm 18	n.d.
61a	$-\text{CN}$	22	80 \pm 8	51 \pm 10	69 \pm 9
63	$-\text{CHO}$	n.d.	34 \pm 2	n.d.	n.d.
64	$-\text{CH}_2\text{OH}$	68	n.d.	n.d.	n.d.

[a] Measured by ITC. [b] Results are of one experiment. [c] Measured by CK2 α ADP-gloTM kinase assay.
[d] Tests carried out in triplicate and reported as the mean. [e] Tests carried out in duplicate and reported as the mean.
[f] Inhibition of proliferation tested in HCT116 cell lines. n.d.: no data

In conclusion, optimisation of the amine head group was investigated and provided new lead benzonitrile **61a**. X-ray crystallography revealed an alternative H-bonding network at the αD pocket mouth for nitrile **61a** compared to benzylamine **61**. A new interaction to a water molecule was observed and no contact to Glu230 was reported. In biochemical testing, CK2 α inhibition data for nitrile **61a** was superior to starting fragment **61**.

2.2.4 SBDD on Ring B

The third step in our optimisation strategy was to investigate the substitution pattern of ring B (Figure 40). Inspection of the X-ray crystal structure for benzonitrile lead **61a** showed an opportunity to fill more space in the hydrophobic cavities around the 3-position chlorine and vacant 5-position. A polar interaction with the sidechain of Ser224 was also hypothesised if a HBD substituent were added at the 2-position.



Figure 40: Optimisation strategy for ring B. **a)** Chemical structure of **61a** highlighting three positions of interest for substitution: 2-, 3- and 5-positions of ring B. The numbering scheme for ring B is shown in green. **b)** X-ray crystal structure of **61a** (blue) in complex with CK2 α (grey) to show space around ring B (red circles) and Ser224 (white).

To test this hypothesis, a selection of commercially available benzonitrile building blocks with a 4-position bromine were identified. These were narrowed down to species bearing relevant 2-, 3- or 5-position substitution. The biaryl fragments accessible from these building blocks were then modelled against CK2 α *in silico*. Modelling results predicted reasonable overlay of the biaryl cores with lead **61a** for eight fragments. The optimised polar interactions for ring A were maintained in all cases, and water contacts with the nitrile were predicted for the majority of fragments. Hydrophobic ring substituents, such as 3-methyl species **65**, were predicted to occupy the chlorine binding pocket (Figure 41, **a**). Polar substituents, such as 2-amino derivative **66**, were expected to contact Ser224 and a water molecule in the α D pocket opening (Figure 41, **b**). Disubstituted fragments such as 3,5-dichloro biaryl **67** were predicted to occupy the original chlorine binding pocket and also the vacant space in the 5-position (Figure 41, **c**).

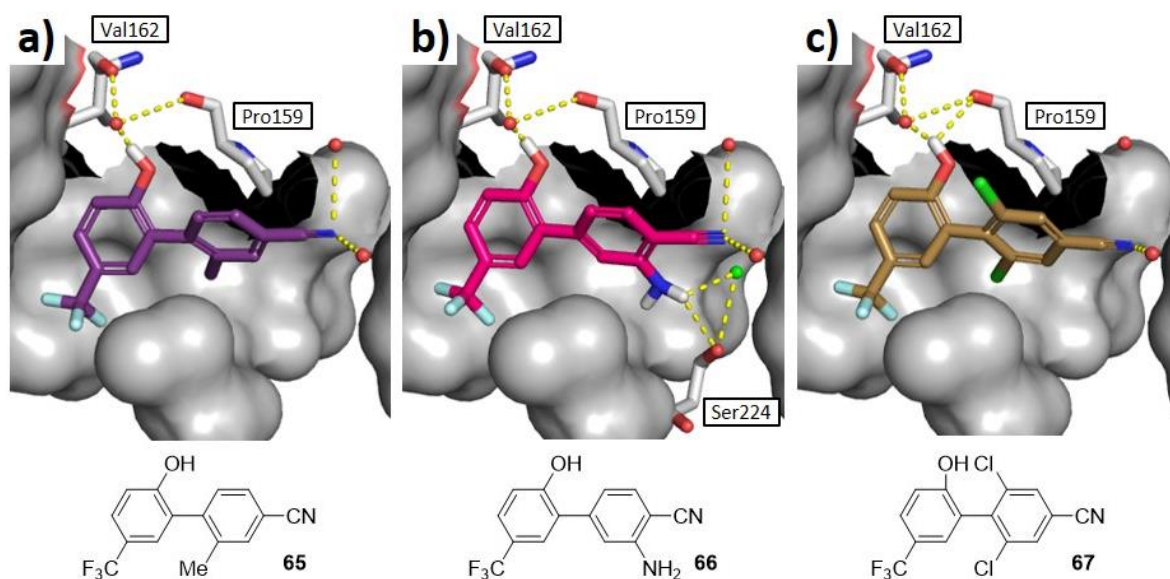
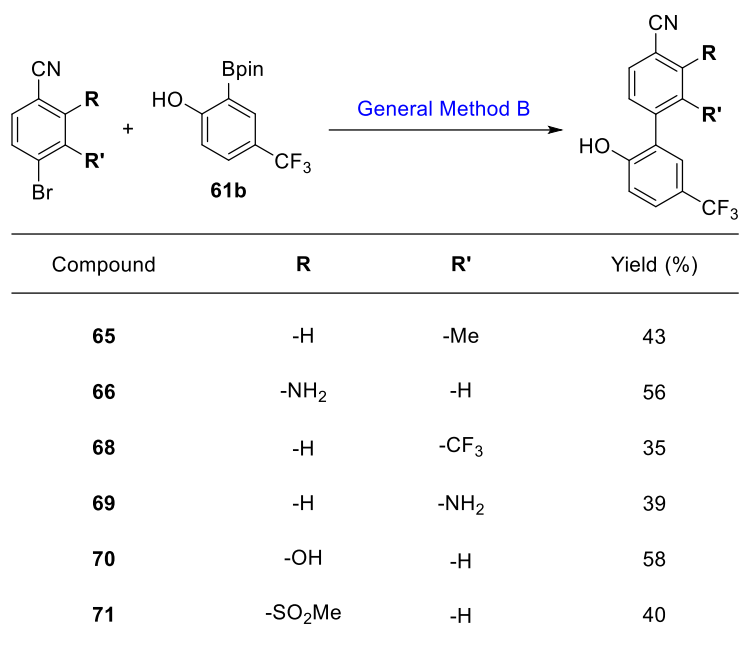


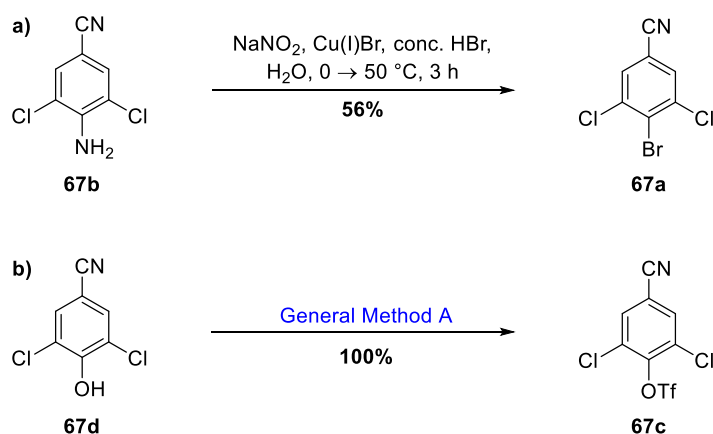
Figure 41: Computational modelling results for alternative substituents on ring B. **a)** 3-Methyl derivative **65** (purple). **b)** 2-Amino derivative **66** (pink) with additional HBD interactions with Ser224 (white) and water (green) shown. **c)** 3,5-Dichloro derivative **67** (brown). Predicted polar interactions between the fragment, protein residues (white) and water molecules are highlighted by yellow dashed lines.

Synthesis of six out of the eight benzonitrile fragments was performed by General Method B (Table 6). Suzuki-Miyaura cross coupling between bromides hosting a 3-position substituent and boronic ester **61b** provided 3-methyl **65**, 3-trifluoro **68** and 3-amino **69** derivatives in moderate yields. Under the same conditions, 2-position substituted benzonitrile products 2-amino **66**, 2-alcohol **70** and 2-methylsulfonyl **71** were also isolated and in slightly better yields. Co-elution of the bromide starting material and biaryl product during manual flash column chromatography was observed for 3-trifluoro **68**, 3-amino **69** and 2-methylsulfonyl **71** derivatives thus lowering the isolated yields.

Table 6: Synthesis of a benzonitrile fragment library to investigate alternative substituents at the 2- and 3-positions of ring B.



The final two fragments of interest in the structure-based optimisation of ring B were 3,5-dichloro and 3,5-dimethyl substituted benzonitriles **67** and **72**. Unfortunately the bromide cross coupling partner (**67a**) for 3,5-dichloro fragment **67** was not readily available. Instead, application of Sandmeyer conditions²⁸⁰ to commercially available amine **67b** yielded desired bromide **67a** in moderate yield, following a difficult work-up (Scheme 8, a). Commercially available dichloro alcohol **67d** was also converted quantitatively to triflate species **67c** following General Method A (Scheme 8, b). This provided an alternative Suzuki-Miyaura cross coupling partner for later investigation.

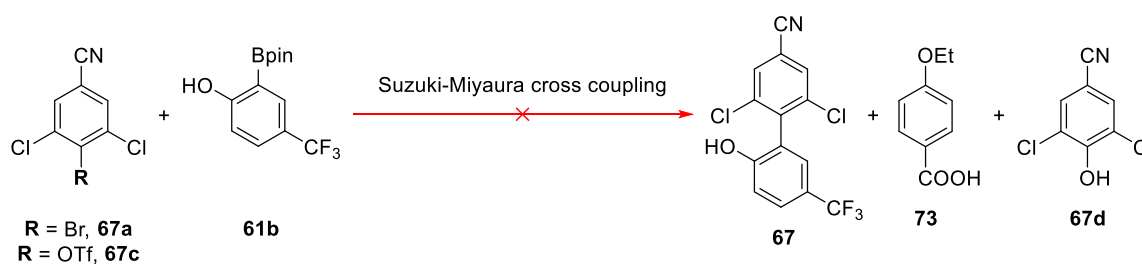


Scheme 8: Synthesis of Suzuki-Miyaura cross coupling partners for the later synthesis of 3,5-dichloro benzonitrile fragment **67**. a) Sandmeyer conditions to provide bromide **67a**.²⁸⁰ b) Application of General Method A to provide triflate **67c**.

With bromide **67a** and triflate **67c** in hand, studies towards the synthesis of 3,5-dichloro biaryl **67** began (Table 7). Application of General Method B, optimised for unhindered Suzuki-Miyaura cross

coupling, failed to provide desired benzonitrile **67** (Entry 1). Instead, by-product **73** was isolated in substantial yield and the structure identified as 4-ethoxybenzoic acid. Literature reading revealed that molecules bearing a trifluoro group *para* to a strong electron donating group are susceptible to hydrolysis when in base and at elevated temperatures.^{281,282} Therefore, it was hypothesised that by-product **73** could have arisen from the decomposition of boronic ester **61b** under Suzuki-Miyaura cross coupling conditions and in the presence of the EtOH/H₂O solvent system. Furthermore, steric hindrance around the bromide of cross coupling partner **67a** could reduce the rate of oxidative addition to palladium-(0).²⁸³⁻²⁸⁵ This would expose boronic ester **61b** to the palladium catalyst for an extended period of time and promote reductive elimination with a hydride, leading to by-product **73**. Interestingly, trifluoride hydrolysis was observed only twice more during the project (Section 2.3.3), despite the use of base and elevated temperature for multiple reactions.

Table 7: Suzuki-Miyaura cross coupling conditions tested in the synthesis of 3,5-dichloro benzonitrile **67**.



Entry	Conditions	Result		
		67	73 ^[a]	67d ^[b]
1	67a (1.0 eq.), 61b (1.2 eq.), General Method B	0%	54%	N
2	67c (1.0 eq.), 61b (1.2 eq.), General Method B	0%	0%	Y
3	67c (1.0 eq.), 61b (1.2 eq.), General Method B, reflux, 4 h	0%	20%	Y

[a] Isolated yield of by-product **73**, fully characterised to provide data consistent with CAS: 619-86-3.

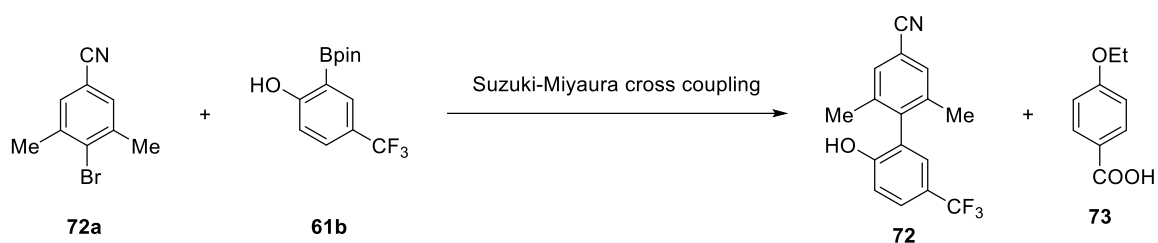
[b] Presence determined by ¹H NMR and LCMS analysis of the crude reaction mixture. Y: yes. N: no.

Following rationalisation of by-product **73**, attention turned to alternative Suzuki-Miyaura cross coupling partner, triflate **67c**. Literature suggested that the rate of oxidative addition of hindered aryl triflates to palladium-(0) is comparable to that of aryl bromides, and in some cases faster.²⁸⁶ To test this, triflate **67c** was subjected to General Method B (Entry 2). Analysis of the crude reaction mixture by ¹H NMR and LCMS did not show the presence of by-product **73**. However, instead it revealed hydrolysis of triflate **67c** back to starting alcohol **67d** – an observation reported for earlier triflate **48** as well (Table 1, Section 2.1.2). Entry 2 was repeated with heating under reflux instead of microwave irradiation to provide Entry 3. This time, both by-product **73** and hydrolysed species **67d** were observed. For all three entries, no trace species matching the predicted ¹H NMR peaks or LCMS mass

for desired product **67** were observed. General Method B was therefore determined unsuitable for the synthesis of 3,5-dichloro species **67**.

In parallel to this work, investigation into the synthesis of 3,5-dimethyl benzonitrile **72** was undertaken (Table 8). Application of General Method B (Entry 1) to commercially available bromide **72a** and boronic ester **61b** gave a complex mixture of unidentified products, as determined by ¹H NMR and LCMS analysis of the crude reaction mixture. Repeating these conditions with heating under reflux (Entry 2) resulted in the sole isolation of by-product **73** in moderate yield. Alternative Suzuki-Miyaura conditions adapted from Negoro *et al.*²⁸⁷ were attempted in Entry 3 and pleasingly provided desired 3,5-dimethyl product **72** in good yield.

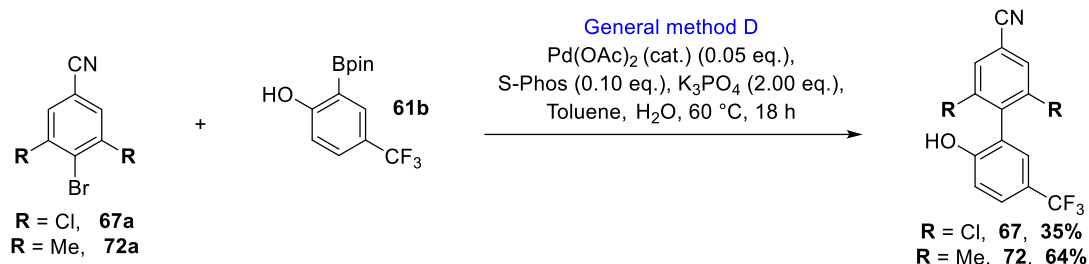
Table 8: Suzuki-Miyaura cross coupling conditions tested in the synthesis of benzonitrile **72** and the development of General Method D, described by the conditions in Entry 3.²⁸⁷



Entry	Conditions	Result	
		72 ^[a]	73 ^[b]
1	72a (1.0 eq.), 61b (1.2 eq.), General Method B	n/a ^[c]	n/a ^[c]
2	72a (1.0 eq.), 61b (1.2 eq.), General Method B, reflux, 4 h	0%	60%
3	72a (1.0 eq.), 61b (1.2 eq.), Pd(OAc) ₂ (cat.), S-Phos, K ₃ PO ₄ , Toluene, H ₂ O, 60 °C, 18 h	64%	0%

[a] Isolated yield of desired product **72**. [b] Isolated yield of by-product **73**, fully characterised to provide data consistent with CAS: 619-86-3. [c] Complex mixture of unidentified products as determined by ¹H NMR and LCMS analysis of the crude reaction mixture.

Following successful Suzuki-Miyaura cross coupling to provide 3,5-dimethyl fragment **72** (Table 8, Entry 3), the conditions were repeated using 3,5-dichloro bromide **67a** (Scheme 9). Gratifyingly, desired product **67** bearing chlorine substituents at the 3- and 5-positions of ring B was isolated without trace of by-product **73**. A lower yield of 35% compared to 64% (for 3,5-dimethyl species **72**) was isolated due to remaining bromide **67a** despite 18 hours heating under reflux. These Suzuki-Miyaura cross coupling conditions, suitable for hindered bromide cross coupling partners, form 'General Method D' (Section 4.2.4, Experimental General Methods).



Scheme 9: Synthesis of hindered 3,5-disubstituted benzonitrile fragments **67** and **72** by General Method D.

The eight fragments **65** – **72** hosting varying substitution patterns on ring B were submitted to Dr. Paul Brear for analysis by X-ray crystallography and biochemical assay. Inspection of the X-ray crystallography results found all eight fragments bound selectively in the α D pocket of CK2 α and adopted binding modes consistent with lead benzonitrile **61a**. A closer look at the binding pose of ring A revealed all fragments interacted with Pro159 *via* a HBD interaction and the α D pocket water *via* a HBA interaction. Additionally, all fragments except 3-trifluoro species **68** were reported to engage in an additional, new HBD interaction directly with Val162 (Figure 42, **b**).

It was observed that the position of ring B within the α D pocket was variable and depended on the ring substituent. Considering the 3-position substituents first, 3-methyl species **65** occupied the pocket with almost precise overlay of lead **61a** (Figure 42, **a**) and maintained the same HBA interactions between the nitrile and two substrate-binding channel water molecules (Figure 42, **b**). 3-Trifluoro derivative **68**, on the other hand, sat further forward in the α D pocket relative to lead **61a** (Figure 42, **a**). As a consequence, one HBA interaction with a water at the pocket mouth was lost (Figure 42, **c**). The electron density for ring B of 3-amino fragment **69** was particularly poor and could not be resolved accurately. As a result, this species was not considered further.

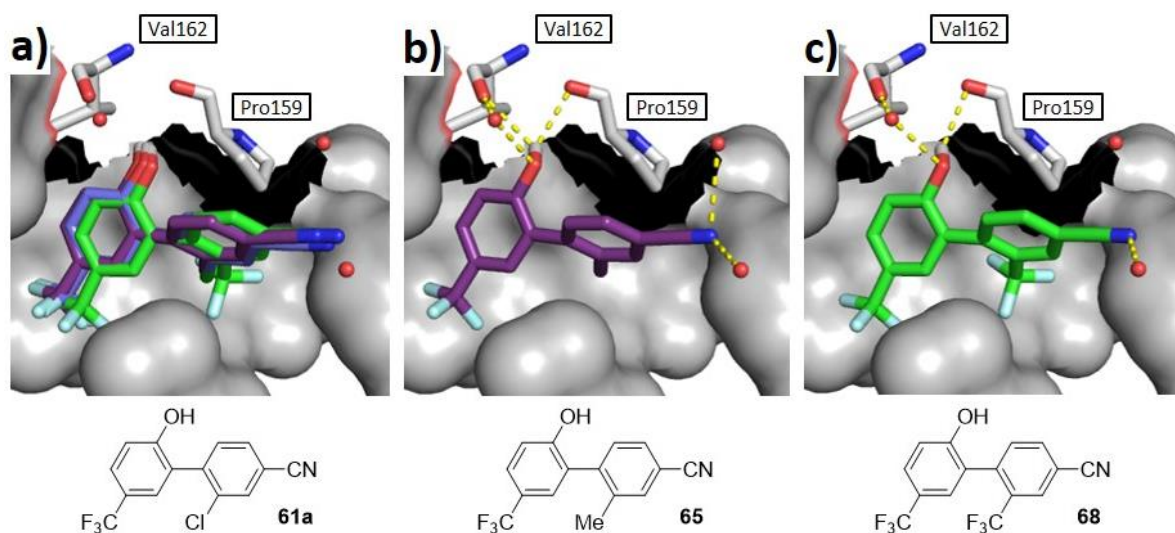


Figure 42: X-ray crystallography results for 3-position substituents on ring B in complex with CK2 α (grey). **a)** Overlay of lead **61a** (blue), 3-methyl derivative **65** (purple) and 3-trifluoro derivative **68** (green) to show relative positioning within the α D pocket. **b)** 3-Methyl derivative **65** (purple). **c)** 3-Trifluoro derivative **68** (green). Polar interactions between the fragment, protein residues (white) and water molecules are highlighted by yellow dashed lines.

Incorporation of a polar group at the 2-position of ring B successfully resulted in a H-bonding interaction with Ser224 (Figure 43). In further detail, ring B of 2-amino species **66** sat lower down in the α D pocket relative to lead **61a** (Figure 43, **a**). As a result both HBA interactions between the nitrile and substrate-binding channel water molecules were lost (Figure 43, **b**). Ring B of 2-alcohol derivative **70** was forced to sit higher in the α D pocket than lead **61a** (Figure 43, **a**). The HBA interactions at the pocket opening were maintained (Figure 43, **c**). Last, 2-methylsulfonyl fragment **71** overlaid exactly with 2-alcohol species **70** and contacted two substrate-binding channel waters, one *via* the nitrile moiety and one *via* the methylsulfonyl group (Figure 43, **d**).

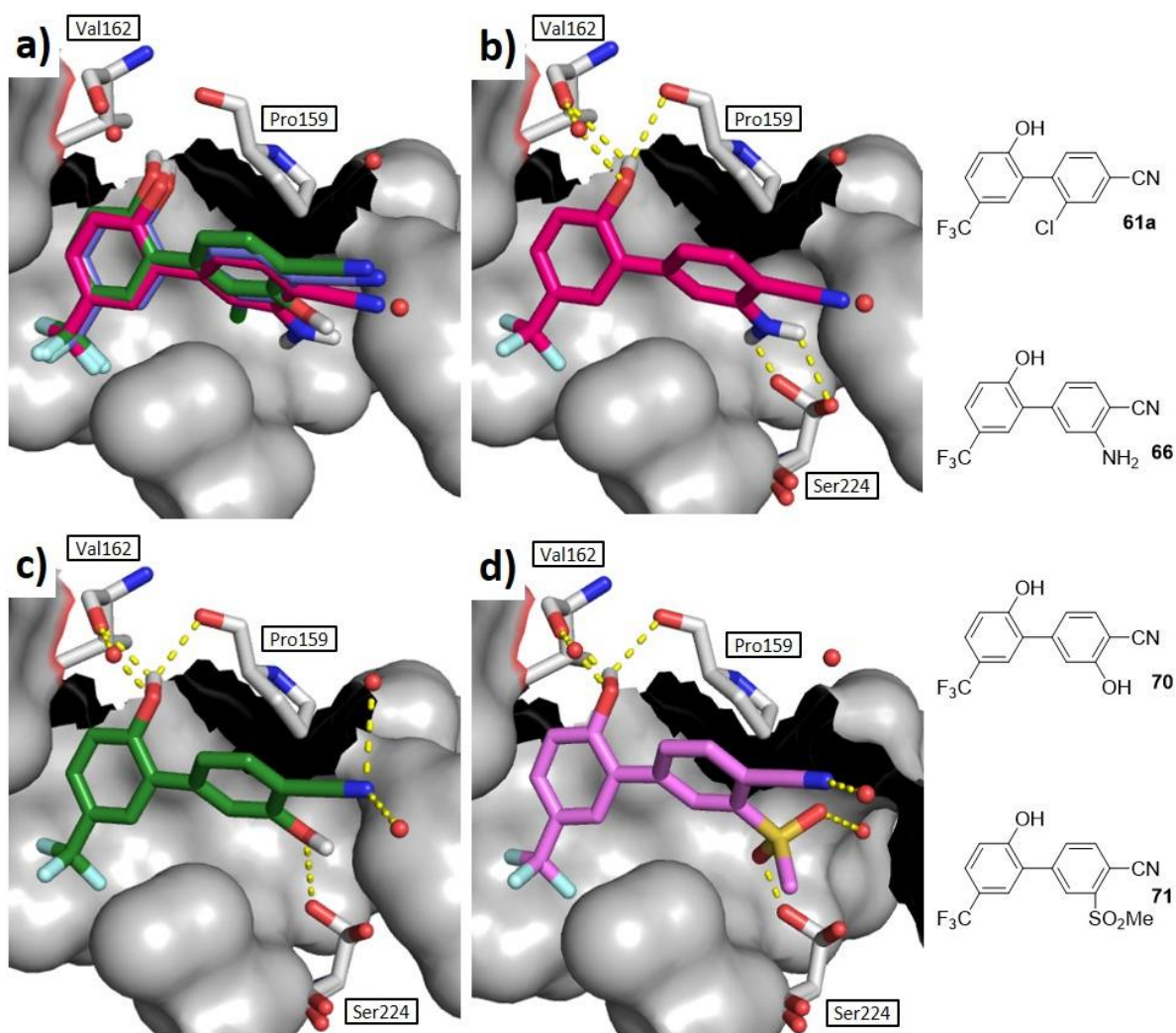


Figure 43: X-ray crystallography results for 2-position substituents on ring B in complex with CK2 α (grey). **a)** Overlay of lead **61a** (blue), 2-amino derivative **66** (pink) and 2-alcohol derivative **70** (green) to show relative positioning within the α D pocket. **b)** 2-Amino derivative **66** (pink). **c)** 2-Alcohol derivative **70** (green). **d)** 2-Methylsulfonyl derivative **71** (lilac). Polar interactions between the fragment, protein residues (white) and water molecules are highlighted by yellow dashed lines.

Finally, the X-ray crystal structures for disubstituted species **67** and **72** were analysed. Relative to current lead **61a**, ring B of both 3,5-dichloro **67** and 3,5-dimethyl **72** derivatives overlaid well (Figure 44, **a**). The 3-position chlorine of lead **61a** almost perfectly eclipsed the 3-position chlorine and methyl of **67** and **72** respectively. The 5-position substituent was observed to occupy a previously vacant hydrophobic cavity towards the front of the α D pocket, as computationally predicted (Figure 44, **b** and **c**). In both cases, the nitrile moiety maintained contact with the two water molecules in the mouth of the α D pocket.

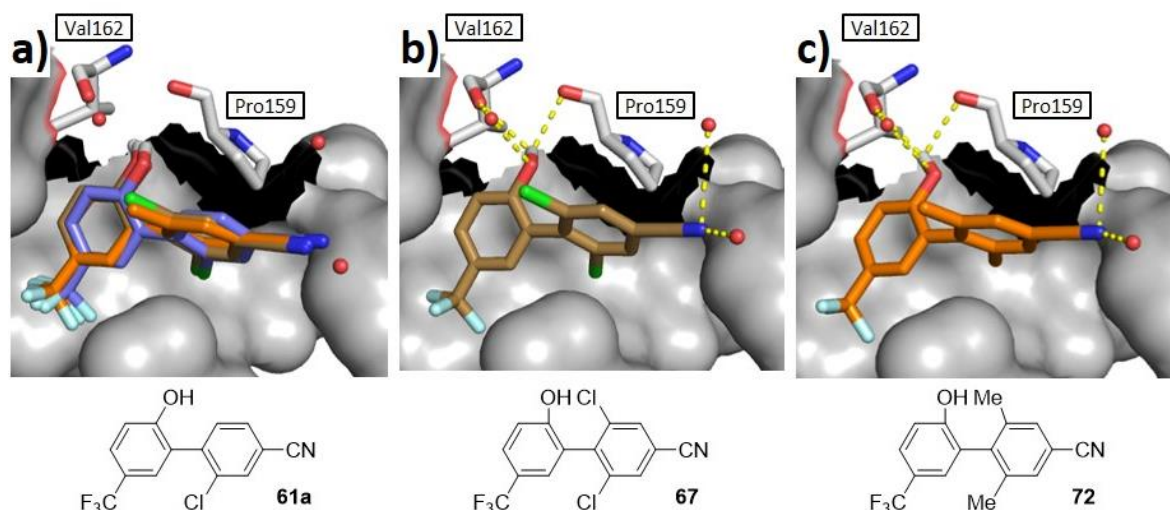


Figure 44: X-ray crystallography results for 3,5-position substituents on ring B in complex with CK2 α (grey). **a)** Overlay of lead **61a** (blue), 3,5-dichloro derivative **67** (brown) and 3,5-dimethyl derivative **72** (orange) to show relative positioning within the α D pocket. **b)** 3,5-Dichloro derivative **67** (brown). **c)** 3,5-Dimethyl derivative **72** (orange). Polar interactions between the fragment, protein residues (white) and water molecules are highlighted by yellow dashed lines.

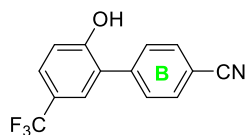
Following structural interrogation, the ring B substituted fragments (excluding 3-amino derivative **69**, due to poor structural data, discussed above) were tested for inhibition in a CK2 α kinase assay (Table 9). Pleasingly, all fragments **65** – **68** and **70** – **72** showed inhibition of CK2 α enzyme activity and the percentage inhibition was used as a relative measure to rank the compounds.

In comparison to current lead fragment **61a**, two species performed better: 3,5-dichloro **67** and 2-amino **66** with 95% and 91% kinase activity inhibition respectively (Table 9). The statistical errors for 3,5-dichloro **67** and 2-amino **66** were reported as 6% and 1% and therefore the data points for these two ligands overlap. As a result, 3,5-dichloro **67** and 2-amino **66** were considered to have comparable activity against CK2 α . 2-Methylsulfonyl derivative **71** reported inhibition of activity by 79%, which was comparable to the 80% reported for lead **61a**. There was then a distinct drop in inhibitory activity to 65% for fifth best fragment 3-methyl species **65** and another drop to 52% for sixth best candidate 3-trifluoro derivative **68**. The poorest performers of the fragment library – derivatives 2-alcohol **70** and 3,5-dimethyl **72** – presented substantially weaker CK2 α inhibition.

The IC₅₀ of fragment 3,5-dichloro **67** was determined as 9 μ M which was a significant improvement on current lead **61a**, of 51 μ M (Table 9). 3,5-Dichloro species **67** was then submitted for a cell-based assay. When tested against HCT116 cancer cell lines a GI₅₀ of 16 μ M was recorded. This was also a significant improvement on current lead **61a** (GI₅₀ of 69 μ M), and was comparable to Brear *et al.*'s best lead, pro-CAM4066 **37**, which recorded a GI₅₀ of 9 μ M.²⁶⁵ It is possible that addition of the second ortho-substituted chlorine on biaryl **67**, relative to fragment **61a**, locks the biaryl moiety such that the conformation required for binding in the α D pocket is pre-formed. This would minimise the energy

penalty due to loss of entropy upon binding and lead to a higher affinity fragment, as observed in Table 9.

Table 9: Biochemical testing results for substituted ring B fragment library in comparison to lead fragment **61a**. Compounds are reported according to relative rank order.



Relative rank	Compound	Ring B	% inhib. @ 100 $\mu\text{M} \pm \text{SEM}^{[a][b]}$	$\text{IC}_{50} \pm \text{SEM} (\mu\text{M})^{[a][c]}$	$\text{GI}_{50} \pm \text{SEM} (\mu\text{M})^{[c][d]}$
1	67		95 \pm 6	9 \pm 5	16 \pm 2
2	66		91 \pm 1	n.d.	n.d.
3	61a		80 \pm 8	51 \pm 10	69 \pm 69
4	71		79 \pm 0.02	n.d.	n.d.
5	65		65 \pm 0.01	n.d.	n.d.
6	68		52 \pm 0.03	n.d.	n.d.
7	70		34 \pm 4	n.d.	n.d.
8	72		22 \pm 2	n.d.	n.d.

[a] Measured by CK2 α ADP-gloTM kinase assay. [b] Tests carried out in triplicate and reported as the mean.

[c] Tests carried out in duplicate and reported as the mean. [d] Inhibition of proliferation tested in HCT116 cell lines.
n.d.: no data

In conclusion, a benzonitrile fragment library was synthesised in order to optimise the substituent on ring B. Three positions around the ring were investigated: the 2, 3, and 5-positions using hydrophobic and polar moieties. The approach towards 3,5-disubstituted fragments also led to the development of Suzuki-Miyaura cross coupling conditions for hindered substrates (General Method D). X-ray crystallography and biochemical assessment of the fragment library revealed two fragments superior to lead **61a**: 2-amino **66** and 3,5-dichloro **67**. Due to potential promiscuous reactivity of the amine

moiety of 2-amino derivative **66**, with respect to both future synthetic chemistry and protein binding, it was decided that 3,5-dichloro species **67** was the most suitable final lead compound from this series.

Overall, an optimised inhibitor fragment, 3,5-dichloro **67**, was developed by rational SBDD from initial benzylamine hit **58** (Table 10). Iterative rounds of fragment elaboration led to the introduction of a polar group to ring A (**61**), a nitrile group at the head of ring B (**61a**) and a second chlorine to ring B (**67**). Hit compound **58** provided a poor 32% inhibition of kinase activity, which was improved to 95% for 3,5-dichloro lead **67**. The IC₅₀ value was also greatly improved from 51 to 9 μM following the addition of a second chlorine to benzonitrile **61a**. Furthermore, a promising GI₅₀ of 16 μM was reported for final lead **67** when tested against HCT116 cancer cell lines. This activity level is comparable to Brear *et al.*'s best lead, pro-CAM4066 **37**, which recorded 9 μM.²⁶⁵

Table 10: Hit-to-lead generation of 3,5-dichloro benzonitrile **67** from benzylamine **58**.

	58 Hit fragment	61	61a	67 Lead fragment
K_d (μM)	750	n.d.	22	n.d.
% inhib. @ 100 μM	32	44	80	95
IC ₅₀ (μM)	n.d.	100	51	9
GI ₅₀ (μM)	n.d.	n.d.	69	16

n.d.: no data

2.2.5 Negative Allosteric Mode of Action

The final lead compound, 3,5-dichloro benzonitrile **67**, was observed to inhibit CK2α kinase activity by 95% when tested at a 100 μM assay concentration. Furthermore, studies in HCT116 cancer cell lines reported growth inhibition with a GI₅₀ value of 16 μM. Inspection of the X-ray crystal structure for fragment **67** revealed selective binding within the αD pocket and no ligand electron density at the ATP- or CK2β-binding sites. These observations implied a non-competitive mode of inhibition and thus a negative allosteric mode of action for the benzonitrile inhibitor series was considered.

Herein, three different potential mechanisms for the observed allosteric effects are proposed. These arguments are based on analysis of overlaid X-ray crystal structures and literature precedent.

Confirmation of these theories would require extended protein-ligand studies that are beyond the scope of this project, but a comparison to Brear *et al.*'s fragment **34** is provided as a starting point for further investigation.

2.2.5.1 Hypothesis One: Disruption of the ATP-Binding Site

In the active form of CK2 α , ATP can enter its binding site and form interactions with the hinge region (Gln114-Asn118). A phosphorylation event can then occur to leave ADP bound in the active site. Subsequent release of this molecule enables catalytic turnover of the kinase. When in the active form, the α D helix (Asp120-Thr127) adopts an open conformation, where it is released from the C-spine of the protein (Figure 45, **a**).

By comparing CK2 α in the open conformation (PDB: 5CVH) with the X-ray crystal structure of lead **67**, it was possible to gain insight regarding the effect of fragment **67** on the ATP-binding site. Overlay of the structures revealed that upon binding fragment **67**, the α D helix is pushed away from the protein core to a greater extent than in the open conformation (Figure 45, **a**). This movement causes a slight rearrangement of the hinge region, with effect most notable on residue Asn118.

To understand the importance of this observation, the open conformation was analysed further (Figure 45, **b**). Phe121, Tyr125 and Met225 occupy the α D pocket and Asn118 forms polar contacts with Thr119, Ile164 and a water molecule. The Asn118 H-bonding network holds the residue away from the mouth of the active site so that ATP can enter and ADP can leave.

When lead fragment **67** is bound to CK2 α , Phe121, Tyr125 and Met225 rotate out of the α D pocket so that a cavity forms for ligand binding (Figure 45, **c**). The movement of Phe121 has a pronounced knock-on effect at the hinge region. The upward rotation of the phenyl sidechain displaces Asn118 and the water molecule from their original positions. Asn118 is forced to rotate towards the mouth of the ATP-binding site and HBD interactions with Thr119 and Ile164 are lost. A new water molecule occupies the space adjacent to Phe121 and adopts polar interactions with Thr119 and Ile164. In its new position, Asn118 creates an electrostatic network involving ADP and three water molecules. The interactions bridge the mouth of the ATP-binding site and potentially inhibit catalytic turnover by blocking the release of ADP and entry of ATP. Additionally, the H-bonding contacts made to ADP might stabilise the molecule within the active site and hinder its release.

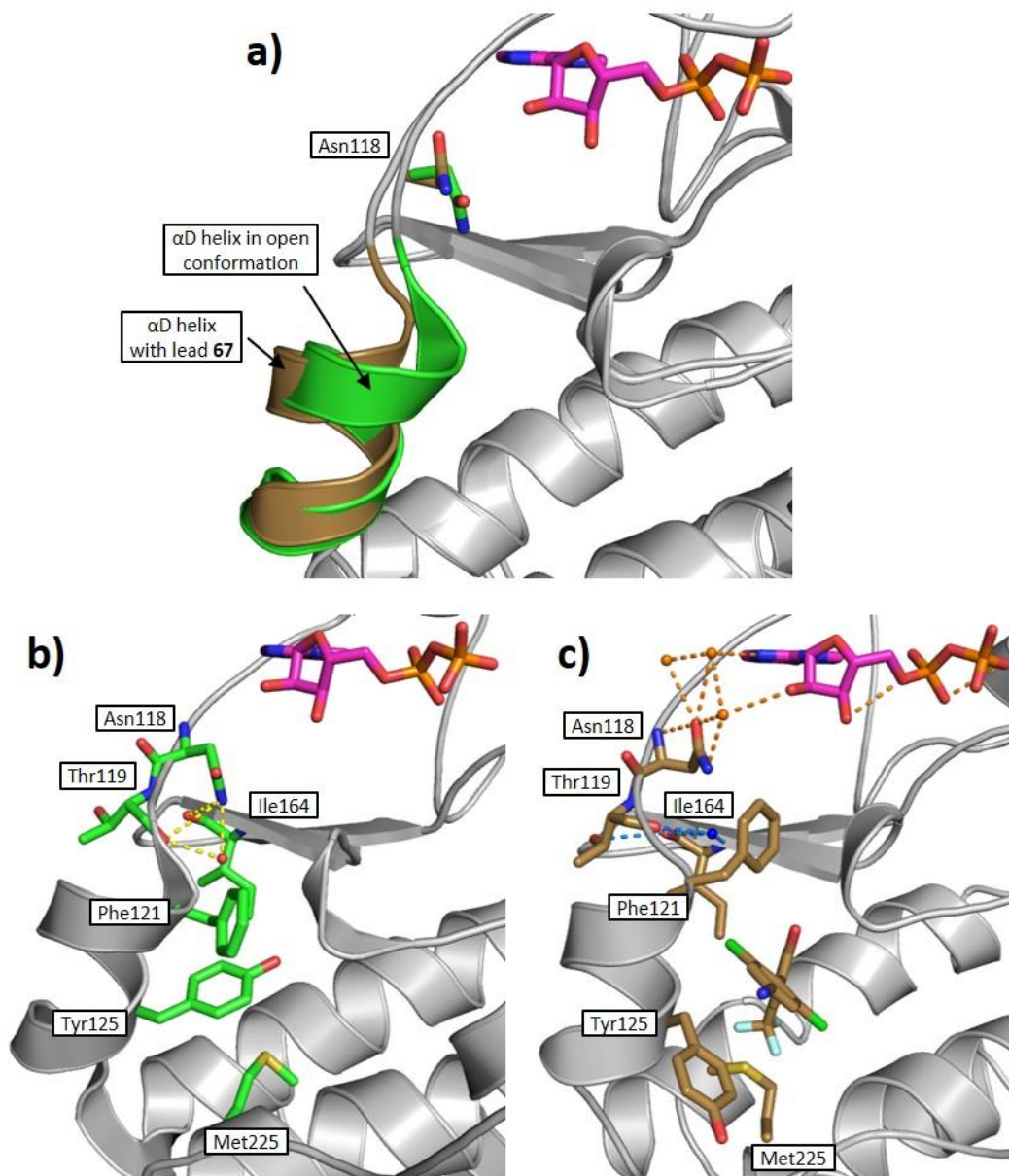


Figure 45: X-ray crystal structures showing disruption of the ATP-binding site following lead **67** binding. A molecule of ADP (magenta) is shown in the ATP-binding site. **a)** Overlay of CK2 α open conformation (green) (PDB: 3CVH) and CK2 α following lead **67** binding (brown) with relative positioning of α D helix and Asn118 highlighted. **b)** CK2 α open conformation (PDB: 3CVH) with key polar contacts (yellow) and residues (green) highlighted. **c)** Fragment **67** bound to CK2 α with key residues highlighted (brown). New water molecule (blue) adjacent to Phe121 and electrostatic network waters (orange) are shown. Polar interactions are included as dashed lines.

In summary, movement of residue Asn118 to its position across the mouth of the ATP-binding site was hypothesised as a mechanism for allosteric inhibition. In order to confirm this theory, protein residue mutation studies involving Asn118 and Phe121 would be necessary.^{264,288–290}

2.2.5.2 Hypothesis Two: Disruption of the Substrate-Binding Site

Molecular dynamics simulations predict that the substrate-binding channel terminates at the α D helix.¹²³ By comparing CK2 α in the active conformation (PDB: 5CVH) with the X-ray crystal structure of lead **67**, it was possible to gain insight regarding the effect of fragment **67** on the substrate-binding site. Overlay of the structures revealed that upon binding fragment **67**, the α D helix is pushed away from the protein core to a greater extent than in the open conformation (Figure 46, **a**). This movement may disrupt the terminal position of the substrate-binding channel such that substrate recognition, and thus enzyme activity, is lost.

Furthermore, upon binding fragment **67**, Tyr125 is forced to rotate away from the protein core (Figure 46, **a**). Tyr125 now sits within the original substrate-binding channel and potentially acts as a steric block towards substrate binding (Figure 46, **b**). The nitrile moiety of lead fragment **67** also protrudes from the α D pocket and sits within the substrate-binding channel, contributing to the steric blockade.

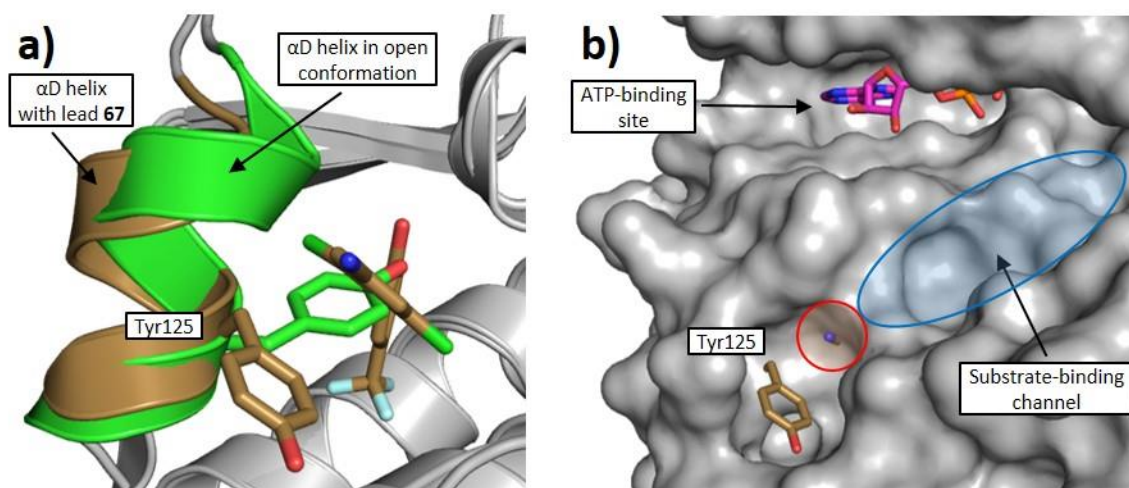


Figure 46: X-ray crystal structures showing disruption of the substrate-binding site following lead **67** binding. **a**) Overlay of CK2 α open conformation (green) (PDB: 3CVH) and CK2 α following lead **67** binding (brown) with relative positioning of α D helix and Tyr125 highlighted. **b**) Surface of CK2 α open conformation (PDB: 3CVH) (grey) with Tyr125 (brown) and fragment **67** (red circle) superimposed to show steric block towards substrate binding. A molecule of ADP (magenta) is shown in the ATP-binding site and the main section of the substrate-binding channel is highlighted (blue oval).

In conclusion, it was hypothesised that exaggerated movement of the α D helix might disrupt the terminal end of the substrate-binding channel such that substrates are no longer recognised. The observed rotation of Tyr125 and protrusion of benzonitrile **67** into the binding site helps further support this theory. A study into the ability of CK2 α to recognise different substrates would be necessary in order to confirm this mechanism of action. This could be possible by monitoring the substrate binding channel through protein-observed NMR when in the presence/absence of different

substrates and fragment **67**.²⁹¹ Protein mutation studies involving Tyr125 would also determine the role of this residue in the inhibition mechanism.^{264,288–290}

2.2.5.3 Hypothesis Three: Transition Between the Open and Closed Forms of CK2 α

During the catalytic cycle, the α D helix of CK2 adopts two common positions, referred to as open and closed. As mentioned above, in Section 2.2.5.1, the open conformation is the active form of the protein and is adopted in the presence of ATP/ADP. In this form, the α D helix is released from the protein core. The closed form is adopted following the release of ADP from the active site and has the α D helix pulled in tight to the C-spine. It is believed that the transition from the open to closed conformation aids catalytic turnover.¹³²

To better illustrate this, the closed form (PDB: 3FWQ) was overlaid with the open form of CK2 α arising from fragment **67** binding (Figure 47, **a**). When closed, residues Phe121 and Tyr125 occupy the α D pocket and the α D helix is seen buried in the core of the protein. Upon binding of fragment **67** the α D helix pulls away from the protein and takes the open conformation. While fragment **67** occupies the α D pocket, the α D helix is blocked from transitioning back to the closed conformation. As this transition is reported to aid catalytic turnover,¹³² inhibition of movement was considered a mechanism for allosteric inhibition.

Furthermore, it was observed that when lead inhibitor **67** is bound, Tyr125 occupies a new position parallel with Arg228 (Figure 47, **b**). It was proposed that these two residues may form a π -stacking interaction that rigidifies the α D helix in the open conformation. This could contribute towards hindering transition to the closed form.

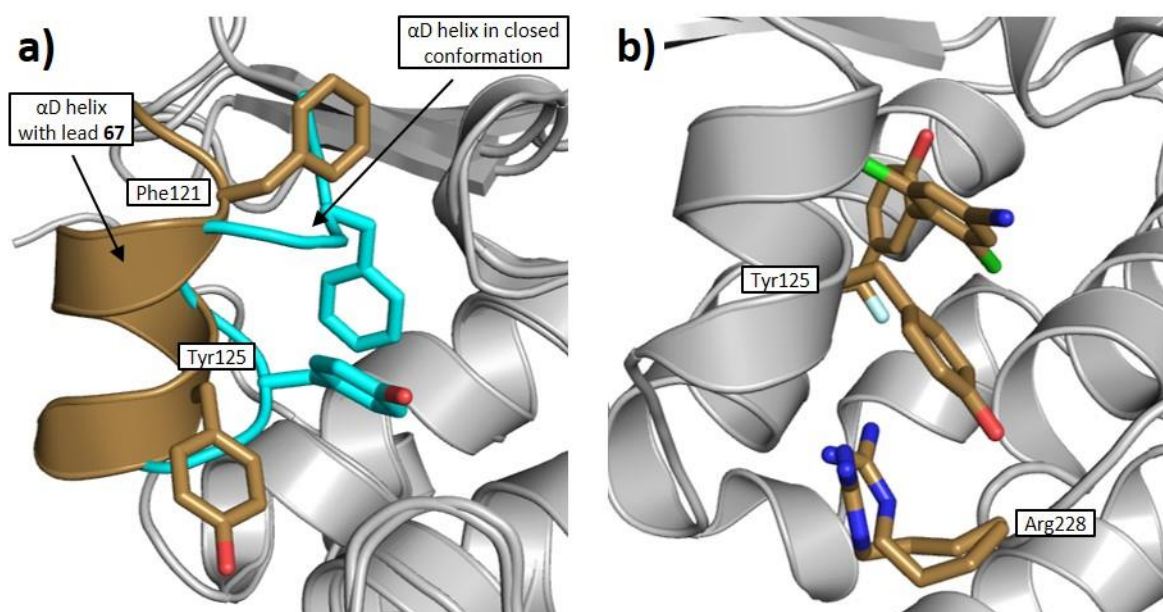


Figure 47: X-ray crystal structures demonstrating inhibition of the transition between open and closed forms of CK2α following lead **67** binding. **a)** Overlay of CK2α closed conformation (blue) (PDB: 3FWQ) and CK2α following lead **67** binding (brown) with relative positioning of αD helix, Phe121 and Tyr125 highlighted. **b)** Fragment **67** (brown) in complex with CK2α (grey). π -stacking between Tyr125 and Arg228 hypothesised by the parallel alignment of residues (brown).

In summary, it was hypothesised that binding lead fragment **67** inhibits transition of the αD helix between the open and closed conformations. Not only does the fragment physically block movement of the αD helix, but a potential π -stacking interaction between Tyr125 and Arg228 could also stabilise the protein in the open form. In order to confirm this theory, molecular dynamics simulations and NMR studies of labelled CK2α would be required.^{264,289} In these studies, the movement of the αD helix could be tracked and compared to the rate of ATP turnover. This would determine whether transition between the open and closed forms of CK2α is essential for catalysis.

2.2.5.4 Experimental Evidence

Following development of the three hypotheses presented above, X-ray crystal structure comparison with Brear *et al.*'s αD-site selective fragment **34** was proposed. Biaryl **34** was reported to bind the αD pocket with a K_d of 270 μ M but was inactive in the kinase assay.²⁶⁵ Therefore overlaying the X-ray crystal structure for fragment **34** in complex with CK2α (PDB: 5CSH) with the open form of CK2α (PDB: 5CVH), the closed form of CK2α (PDB: 3FWQ) and lead fragment **67** could validate/invalidate the three suggested mechanisms for allosteric inhibition.

By comparing CK2α in the open conformation (PDB: 5CVH) with the X-ray crystal structure of Brear *et al.*'s fragment **34** (PDB: 5CSH), it was possible to gain insight regarding the effect of biaryl **34** on the

ATP-binding site. Overlay of the X-ray crystal structures revealed that upon binding fragment **34**, the α D helix is not pushed away from the protein core to any greater extent than in the open conformation (Figure 48). As a result, there is no rearrangement of residue Asn118 and thus no disruption to the ATP-binding site. This suggests that the ATP-binding site mechanism, outlined in Section 2.2.5.1, could be responsible for the allosteric inhibition observed for lead fragment **67**.

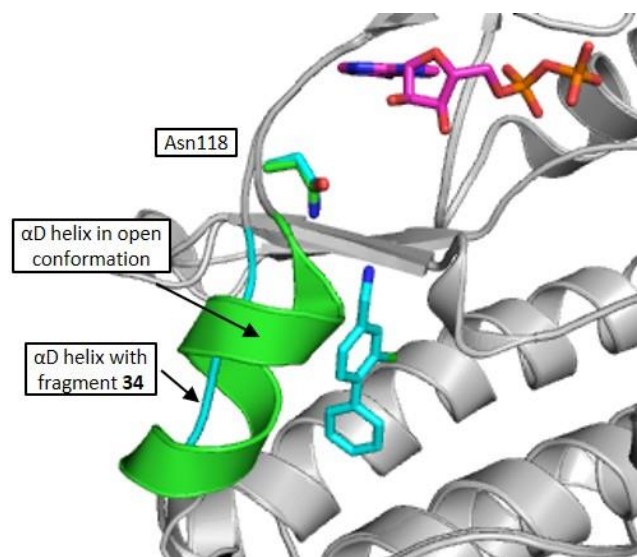


Figure 48: X-ray crystal structure overlay of CK2 α open conformation (green) (PDB: 3CVH) and CK2 α following fragment **34** binding (blue) (PDB: 5CSH) with relative positioning of α D helix and Asn118 highlighted. A molecule of ADP (magenta) is shown in the ATP-binding site.

Following this, a similar analysis was performed with respect to the substrate-binding channel. The X-ray crystal structures for Brear *et al.*'s fragment **34** (PDB: 5CSH) and lead fragment **67** were overlaid with the protein surface of CK2 α in the open confirmation (PDB: 5CVH) (Figure 49). This revealed that Tyr125 rotates into the substrate-binding channel following α D pocket binding of both fragments **34** and **67**. Upon closer inspection, Tyr125 blocks the terminal position of the substrate binding channel to a greater degree following the binding of fragment **67** than **34**, which could potentially explain the kinase activity inhibition observed for fragment **67** over **34**. Overall, this X-ray crystal structure overlay is not sufficient to fully validate allosteric inhibition by disruption of the substrate-binding channel, as presented in Section 2.2.5.2.

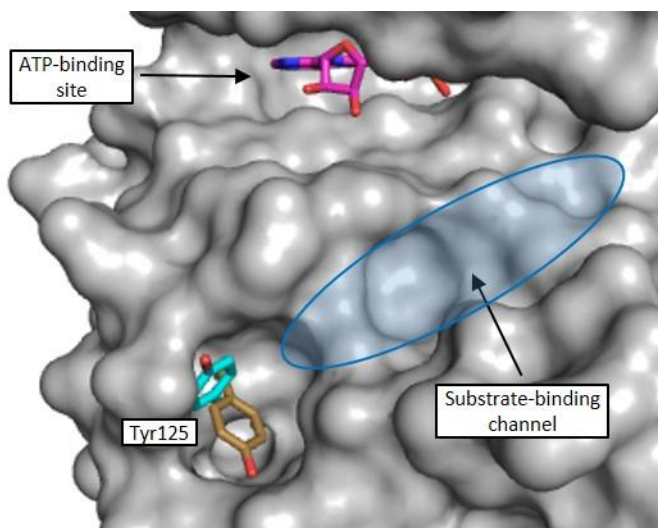


Figure 49: X-ray crystal structure overlay of Tyr125 following fragment **34** binding (blue) (PDB: 5CSH) and lead fragment **67** binding (brown) with CK2α open conformation protein surface (grey) (PDB: 3CVH). A molecule of ADP (magenta) is shown in the ATP-binding site and the main section of the substrate-binding channel is highlighted (blue oval).

Finally, analysis of the closed form of CK2α (PDB: 3FWQ) relative to the protein structure following binding of Brear *et al.*'s biaryl **34** was performed (PDB: 5CSH) (Figure 50). The X-ray crystal structure of lead fragment **67** was also overlaid to enable clearer comparison of the αD helix positions. From this it was clear that binding fragment **34** displaced the αD helix to a similar position as for lead fragment **67**. Furthermore, whilst fragment **34** occupies the αD pocket the transition between the open and closed forms of CK2α is inhibited. Brear *et al.*'s fragment **34** is not reported to inhibit CK2α kinase activity therefore this analysis discounts the allosteric inhibition mechanism put forward in Section 2.2.5.3.

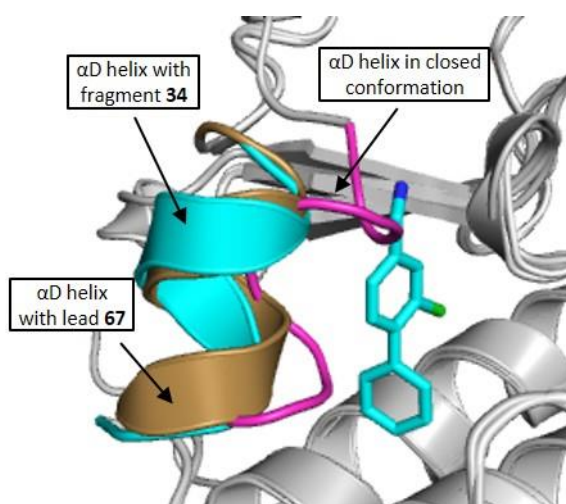


Figure 50: X-ray crystal structure overlay of CK2α closed conformation (magenta) (PDB: 3FWQ) with CK2α following fragment **34** binding (blue) (PDB: 5CSH) and fragment **67** binding (brown). The relative positions of the αD helix are highlighted and fragment **34** (blue) is shown blocking transition to the closed form.

To conclude, three mechanisms by which optimised benzonitrile inhibitor **67** could induce negative allosteric control over CK2 α have been presented. The third hypothesis, based on inhibition of the transition between the open and closed forms of CK2 α , was then discounted following X-ray crystal structure comparison to Brear *et al.*'s inactive fragment **34**.

To the best of our knowledge, fragment **67** represents a first-in-class allosteric inhibitor, binding selectively in the α D pocket. The arguments put forward in this thesis require further investigation but could form a basis for the future development of selective allosteric inhibitors. A recent publication by Jiang *et al.* goes some way towards supporting the allosteric mode of action hypothesised above.²³⁹ Jiang *et al.* utilised their Allosite algorithm to computationally identify potential allosteric sites on CK2 α . One of their results suggested a site composed of residues Phe121, Leu128 and Met225, which corresponds well with the α D pocket. No further work on this site has been published by them yet.

2.3 α D Pocket to Substrate-Binding Channel Linking Investigation

2.3.1 Background

To date, the substrate-binding channel of CK2 has not been investigated using small molecules, and limited success has been reported with peptides.^{251,292} One promising lead comes from Marin *et al.* as introduced in Section 1.2.1.1. Marin designed a pseudosubstrate (**19**) comprised of 12 amino acids and showed it to be selective for CK2, reporting a Michaelis constant, K_M , of 19 μ M.¹⁴⁶ Follow-up work by Sarno *et al.* used protein and peptide mutation studies to confirm that dodecapeptide **19** binds in the substrate channel.^{142,143} This work highlighted CK2 α residues that were vital for substrate recognition and mapped them to the relevant positions on dodecapeptide **19** (Figure 51, **a**). It was observed that His160 recognises the $n-2$ position, Arg191, Arg195 and Lys198 recognise the $n+1$ position, Lys49 recognises the $n+2$ position and Lys74-Lys77 recognise the $n+3$ position. Further work by Enkvist *et al.*²⁶² and Cozza *et al.*²⁵¹ corroborated these findings and also showed that substrate mutations from Asp to Ala at the $n+1$ and $n+3$ positions were the most detrimental to activity. As a result, these two positions are deemed the most important within the consensus sequence of CK2 substrates.²⁹³

Since the publication of Marin's pseudosubstrate (**19**) in 1994, no X-ray crystal structure of dodecapeptide **19**, or any other peptide, genuine substrate or bisubstrate inhibitor, in complex with CK2 α has been successfully resolved. Therefore, the exact binding pose adopted by these species has not been unambiguously confirmed. However, computational modelling by Cozza *et al.* utilised the mutation study data to propose a binding mode for dodecapeptide **19** (Figure 51, **b**).¹²³ Specific attention was given to the positioning of Ser and the $n+1$, $n+2$ and $n+3$ determinants. The *N*-terminal

portion was not modelled in detail as the arginyl tail (RRR) exists solely for the purpose of Marin's phosphocellulose assay,¹⁴⁶ and the neutral Ala residue at $n-3$ is known to be unnecessary for substrate recognition.²⁹⁴

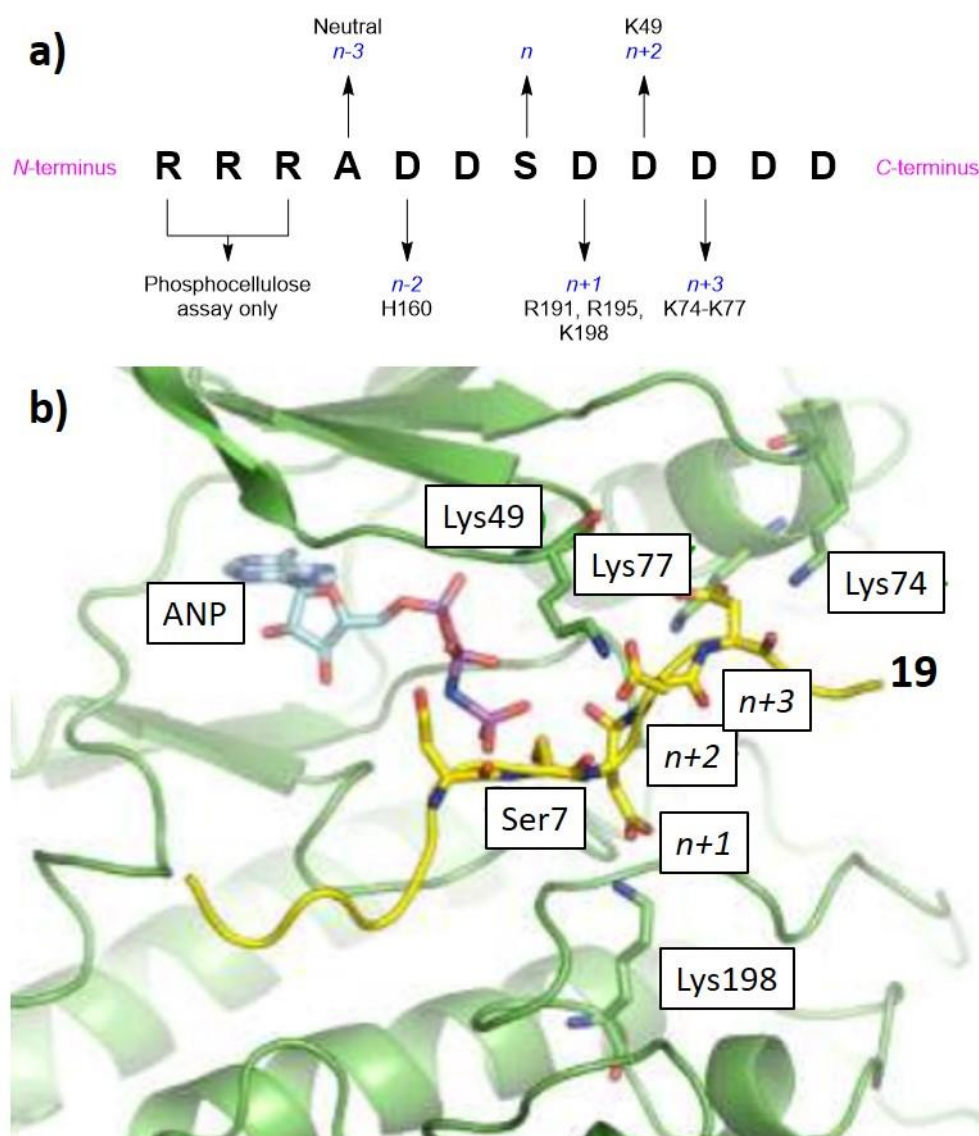


Figure 51: Analysis of Marin et al.'s dodecapeptide pseudosubstrate **19**.¹⁴⁶ **a)** Dodecapeptide **19** sequence with key determinants labelled.^{142,143} **b)** CK2 α substrate binding channel (green) with substrate mimic **19** (yellow) modelled. The most important protein residues are highlighted. Adapted from Cozza et al.,¹²³ Copyright (2018), with permission from John Wiley and Sons.

2.3.2 Project Aim and Preliminary Modelling

The work reported in this chapter aimed to develop a chemical probe for the substrate-binding channel. It was envisaged that this could be achieved by linking a high-affinity fragment, anchored in the α D pocket, to a CK2-specific peptide (Figure 52, a). We hoped to achieve an X-ray crystal structure

of this species in complex with CK2 α to unambiguously verify the binding position of the peptide within the substrate channel. This could also confirm which protein residues are key for recognition of the CK2 consensus sequence. If successful, this project would provide the first fully resolved X-ray crystal structure of CK2 with a peptide bound in the substrate channel – a PPI acknowledged as ‘highly challenging’.¹²²

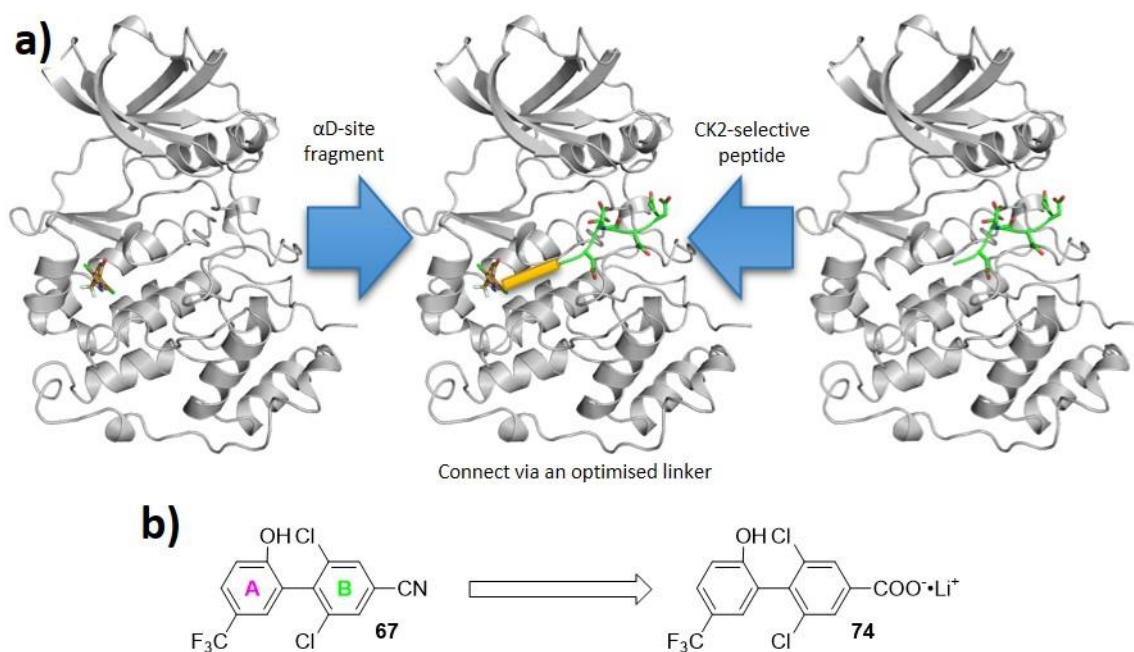


Figure 52: Figure to illustrate the project aim. **a)** αD pocket fragment **67** (brown) could be linked to a CK2-selective peptide (green) via a short, optimised linker (yellow). **b)** The optimised biaryl core of **67** would be maintained but nitrile head group would be more synthetically useful as a carboxylate (**74**).

To start, the αD-site fragment would bear optimised biaryl scaffold **67**, as determined in the SBDD program from Section 2.2 (Figure 52, **b**). The nitrile group on ring B of lead fragment **67** would be exchanged for a carboxylate group (**74**) to provide a more useful synthetic handle for the linking strategy. For the peptide, CK2-specific pseudosubstrate **19**, developed by Marin *et al.*, would be truncated to include only the ideal CK2 consensus sequence. Based on the literature reported in Section 2.3.1, this sequence should cover the $n-2$ to $n+3$ determinants, and thus hexamer DDSDDD **75** was identified as the target.²⁹⁵ Shortening the sequence to this crucial hexamer should also allow manageable molecular dynamics simulations and efficient synthesis.

To check the viability of the strategy, proposed hexamer **75** was modelled onto CK2 α (PDB: 2PVR) by Dr. Paul Brear using molecular dynamics (Figure 53). These results were compared to the literature reported protein-determinant interactions (Section 2.3.1) to ensure a reasonable binding position had been predicted.

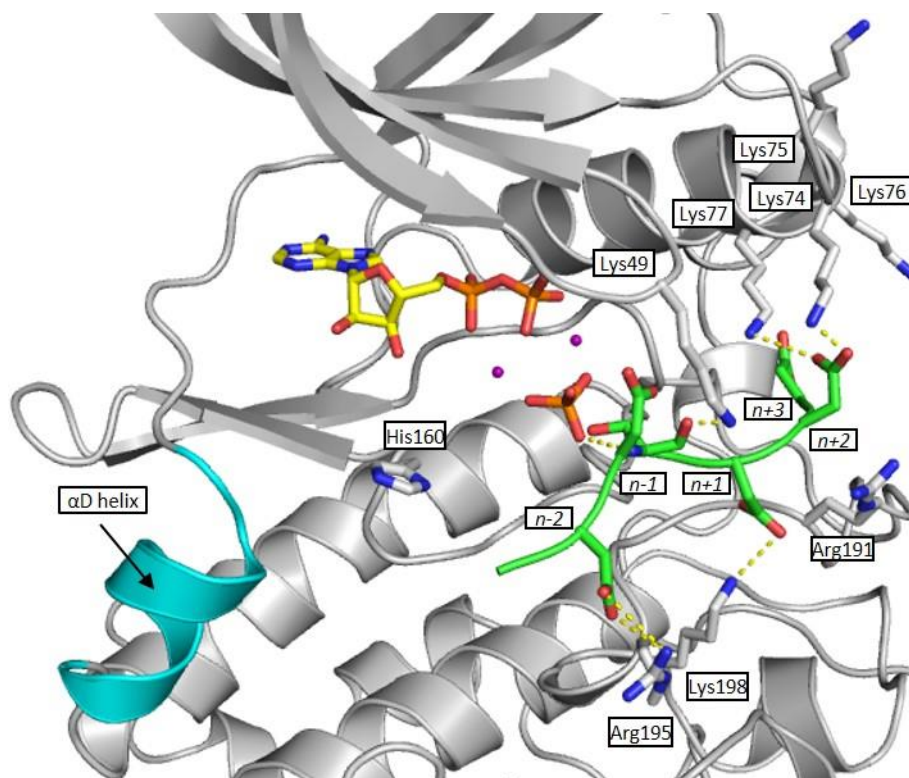


Figure 53: Results of molecular dynamics simulation performed by Dr. Paul Brear. Proposed hexamer **75** (green) was modelled onto CK2 α (PDB: 2PVR) (grey) with ADP (yellow), phosphate (orange) and Mg²⁺ (purple) in the ATP-site. CK2 α residues involved with substrate recognition are highlighted in white and predicted polar contacts are shown as dashed yellow lines. The α D helix is highlighted in blue to show relative positioning of α D pocket and substrate-binding channel.

Analysis of the molecular dynamics simulation showed that hexamer **75** was positioned as anticipated within the substrate-binding channel. The *N*-terminal tail of the hexamer projected towards His160, however the *n*-2 Asp did not make a HBA interaction with it. Instead the *n*-2 position was predicted to interact with Arg195. The Ser for phosphorylation was positioned adjacent to a phosphate, which was modelled to represent the terminal position of the ATP tail. The backbone of Ser contacted Lys49. The Asp at the *n*+1 position formed a HBA interaction with Lys198 as desired, but was not close enough to contact Arg191 or Arg195. At the *n*+2 position, the Asp residue was not predicted to interact with Lys49, but instead formed HBA contacts with Lys74 and Lys77. The final *n*+3 C-terminal Asp was not predicted to make any polar contacts. Overall, the majority of the key recognition residues were predicted to interact in some way with the hexamer, and this was deemed sufficient to proceed.

Next, modelled hexamer **75** was overlaid with the X-ray crystal structure of optimised lead fragment **67** (Figure 54). The relative position of the peptide and CK2 α residues were compared to see whether the conformation of the substrate-binding channel was altered following α D-fragment binding.

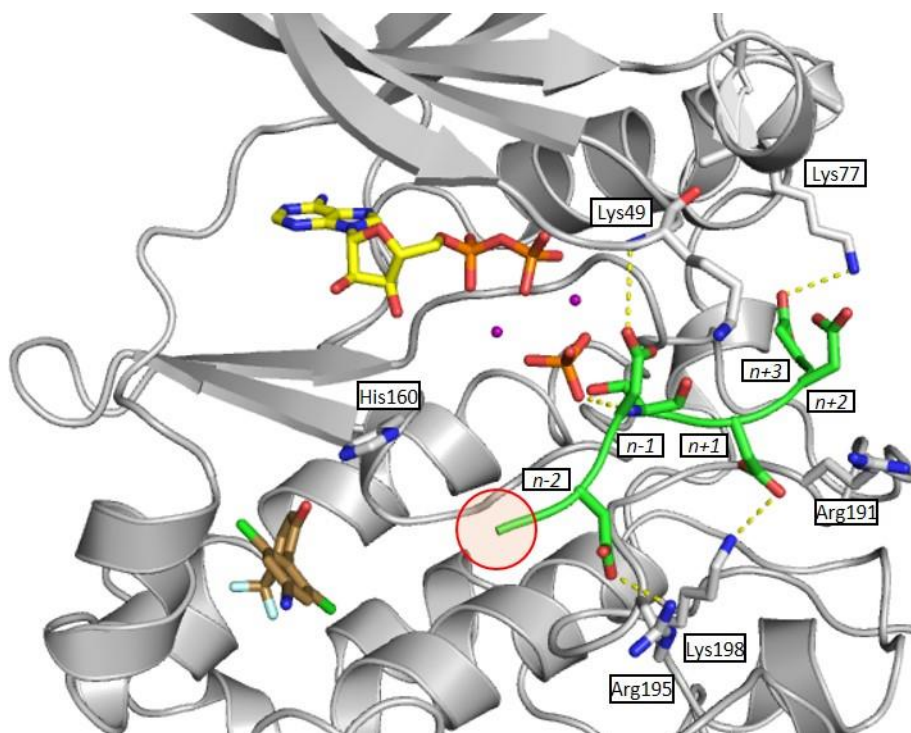


Figure 54: Overlay of modelled hexamer **75** (green) and lead fragment **67** protein crystal structure (grey) with ADP (yellow), phosphate (orange) and Mg^{2+} (purple) in the ATP-site. CK2 α residues involved with substrate recognition are highlighted in white and predicted polar contacts are shown as dashed yellow lines. This protein is a K74-K76 alanine mutant. The relative positioning of lead fragment **67** (brown) and N-terminal tail of hexamer **75** (red circle) implies linking the two species may be possible.

Pleasingly, results for the protein of fragment **67** were comparable to the Apo protein (Figure 54 vs. Figure 53). His160 was within range of the N-terminal tail and the $n-2$ Asp interacted with Arg195. The Asp at $n-1$ was now predicted to contact Lys49 and $n+1$ maintained the interaction with Lys198. Both interactions between the $n+2$ Asp and Lys74 and Lys77 were lost; however, this was due to the CK2 α Lys74-Lys76 Ala mutant used for crystallography. Rearrangement of the protein secondary structure in this region resulted in a HBA contact between the Asp at $n+3$ and Lys77, coincidentally matching that reported in the literature.¹⁴¹

It thus appeared that the binding of lead fragment **67** in the α D pocket did not have a significant effect on the shape of the substrate-binding channel. Therefore, it was considered reasonable to hypothesise that CK2 α could bind an α D-site fragment simultaneously to peptide hexamer **75**. Furthermore, the relative positioning of fragment **67** and modelled hexamer **75** implied linkage of the biaryl and N-terminal Asp *via* a short, optimised linker could be possible (Figure 54). As a result of the molecular dynamics reported above, the allosteric inhibition mechanism relating to disruption of the substrate-binding channel was discounted (outlined in Section 2.2.5.2). Figure 54 implies that

pseudosubstrate hexamer **75** can still bind CK2 α in the presence of inhibitor fragment **67** and thus contradicts this inhibition theory.

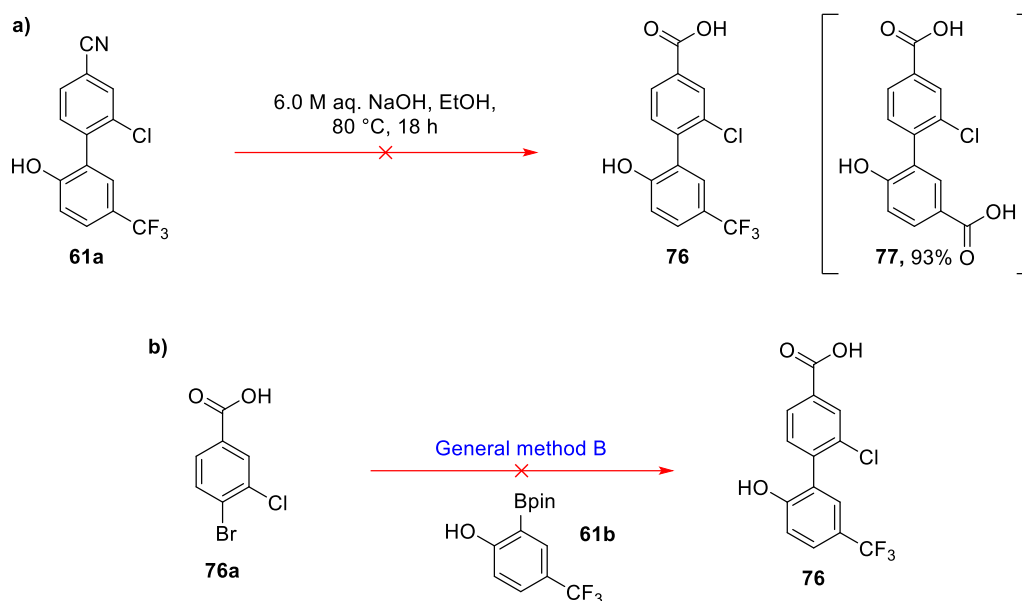
The work presented in the next sections report the studies towards this project aim. It starts with modification of optimised α D fragment **67** to introduce a carboxylate head group, then development of a suitable linker and finally the fragment-peptide linking step.

2.3.3 α D-Site Fragment Optimisation

In order to prepare α D-site fragment **67** for linker development, the nitrile head group needed to be exchanged for a functional group with greater synthetic tractability. It was envisaged that a carboxylic acid moiety would be most appropriate, as an amine or alcohol linker could be reliably coupled to the fragment under literature conditions.

Monochloride species **61a** and lead 3,5-dichloro **67** had been observed to give overlapping binding modes within the α D pocket (Figure 44, Section 2.2.4). With this in mind, synthetic accessibility of the two fragments was considered. Following Suzuki-Miyaura cross coupling, the former (**61a**) was synthesised in consistently higher yield (77%) than lead **67** (35%). Furthermore, bromide cross coupling partner **53**, for the preparation of monochloride **61a**, was commercially available, whereas equivalent bromide **67a**, for the preparation of 3,5-dichloro **67**, required chemical synthesis. It was thus decided that methodology development for the carboxylic acid head group was to be performed on cheaper and more readily accessible fragment **61a**.

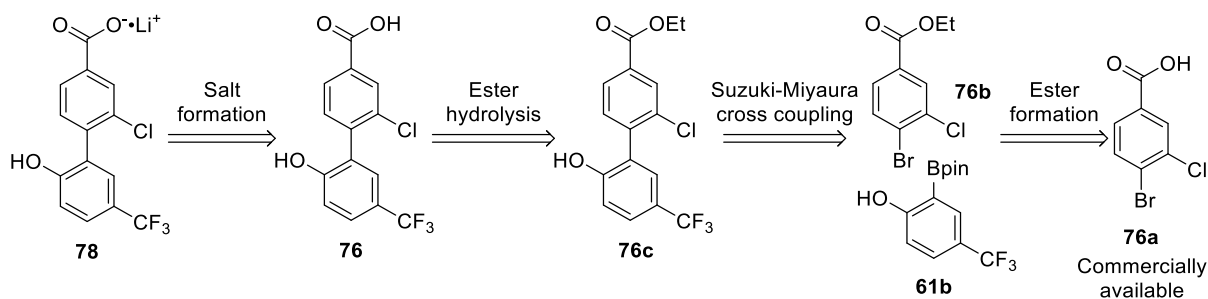
Initial studies attempted to hydrolyse nitrile **61a** directly to carboxylic acid **76** following literature conditions (Scheme 10, a).²⁹⁶ However, desired product **76** was not observed and instead by-product **77**, with a hydrolysed trifluoro group, was isolated in considerable yield. Literature reading revealed that molecules bearing a trifluoro group *para* to a strong electron donating group are susceptible to hydrolysis when in base and at elevated temperatures.^{281,282} This phenomenon was observed only twice more during the project (Table 7 and Scheme 12), despite the use of base and elevated temperature for multiple reactions.



Scheme 10: Initial studies towards the synthesis of carboxylic acid **76**. a) Direct hydrolysis of nitrile **61a**.²⁹⁶ b) Suzuki-Miyaura cross coupling using benzoic acid **76a** and General Method B.

Next, Suzuki-Miyaura cross coupling conditions from General Method B were applied to commercially available bromide **76a** and optimised boronic ester **61b** (Scheme 10, b). The presence of desired product **76** was detected by LCMS of the crude reaction mixture, but the species could not be isolated cleanly from acetic acid when purified by acid-doped flash column chromatography.

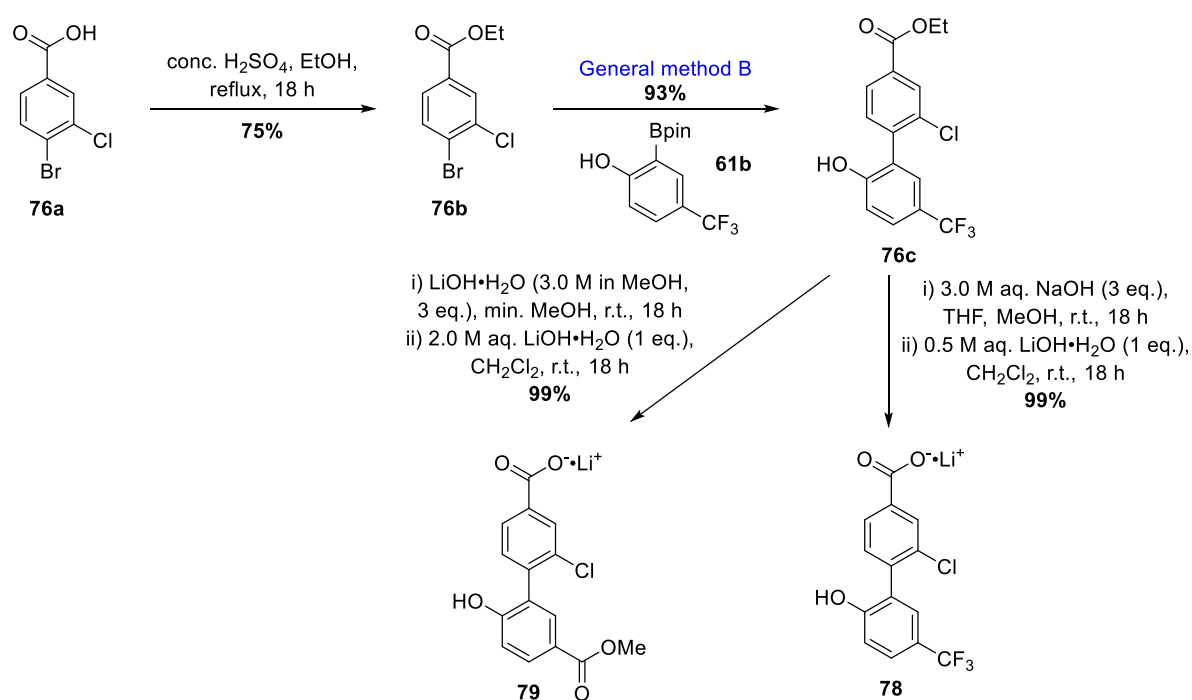
Following initial difficulties in obtaining hydrolysed fragment **76**, an alternative synthetic approach was sought. A retrosynthesis of desired lithium carboxylate **78** was envisaged as follows (Scheme 11): the carboxylate product **78** could be accessed from carboxylic acid **76**, which in turn could have come from hydrolysis of ethyl ester **76c**. The biaryl scaffold of **76c** could be provided by Suzuki-Miyaura cross coupling between ethyl ester bromide **76b** and boronic ester **61b**. Coupling partner **76b** was not readily available but could be produced in one step from commercially available benzoic acid **76a**.



Scheme 11: Retrosynthetic analysis for lithium carboxylate species **78** from commercially available benzoic acid **76a**.

In the forward direction, the formation of ethyl ester **76b** from benzoic acid **76a** proceeded without complication and in high yield (Scheme 12). Suzuki-Miyaura conditions from General Method B then

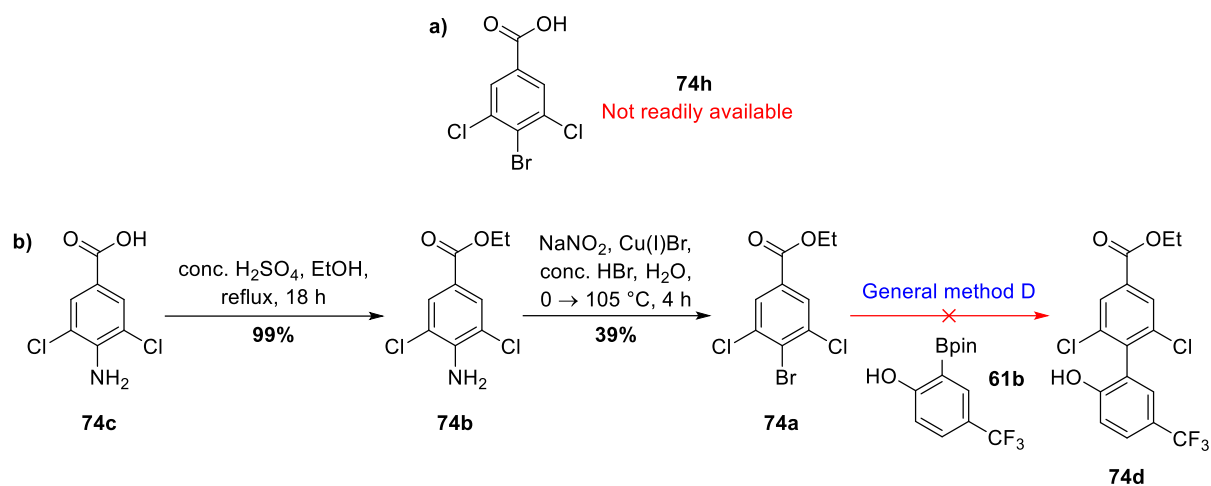
provided biaryl **76c** in excellent yield. Two sets of literature ester hydrolysis conditions were then attempted.²⁹⁷ Hydrolysis using LiOH·H₂O and minimal MeOH solvent failed to provide desired product **78** and instead gave quantitative yield of unexpected product **79**. A similar hydrolysis of the trifluoro group was reported in Scheme 10 and it is believed that methyl ester **79** formed under the same mechanism.^{281,282} Alternative ester hydrolysis by NaOH in dilute THF/MeOH, followed by lithium salt formation, gave desired product **78** in quantitative yield. Conversion from a carboxylic acid to lithium carboxylate salt simplified compound purification, provided ease of handling and offered stability during storage.



Scheme 12: Synthesis of lithium carboxylate species **78** from commercially available benzoic acid **76a** and isolation of unexpected product **79**.²⁹⁷

With a synthetic route to monochloride carboxylate **78** established, it was envisaged that the same conditions could now be applied to access 3,5-dichloro carboxylate **74**. General Method B would be substituted for General Method D, suitable for hindered Suzuki-Miyaura cross couplings.

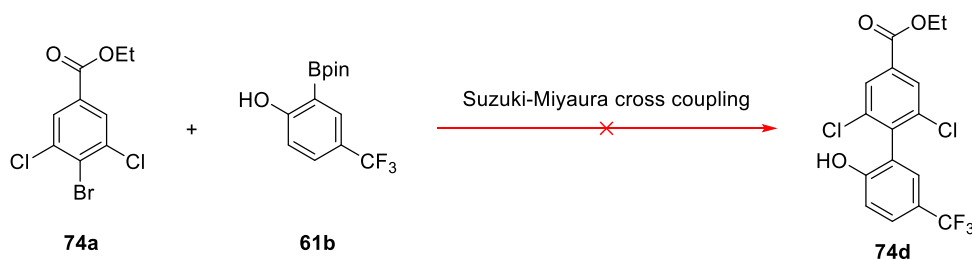
Unfortunately, 3,5-dichloro benzoic acid **74h** was not readily available as a starting material (Scheme 13, **a**). As a result, 3,5-dichloro ethyl ester **74a** was prepared from 3,5-dichloro amine **74c** instead (Scheme 13, **b**). This was performed in two steps: first, benzoic acid **74c** was converted to ethyl ester **74b** in quantitative yield, then Sandmeyer conditions²⁸⁰ gave bromide **74a** in moderate yield. Application of General Method D to fragments **74a** and **61b** failed to provide desired biaryl ester **74d**. Analysis of the crude reaction mixture revealed ¹H NMR peaks and an LCMS mass consistent with traces of product **74d**, but majority bromide **74a** was observed.



Scheme 13: a) Chemical structure of unavailable starting material **74h**. b) Alternative synthesis of bromide **74a** by esterification and Sandmeyer reaction.²⁸⁰ Followed by attempted Suzuki-Miyaura cross coupling towards biaryl **74d**.

Following this, six alternative Suzuki-Miyaura cross coupling protocols were attempted using bromide **74a** and boronic ester **61b** (Table 11). ¹H NMR and LCMS analysis of the crude reaction for Entry 1²⁹⁸ showed a complex mixture of unidentified products. No traces of desired product **74d** were detected and no bromide starting material **74a** could be recovered. Entries 2-5^{287,299-301} tested different palladium catalysts, bases and solvents but unfortunately only starting bromide **74a** could be recovered from each reaction. Entry 6³⁰² decomposed with heating.

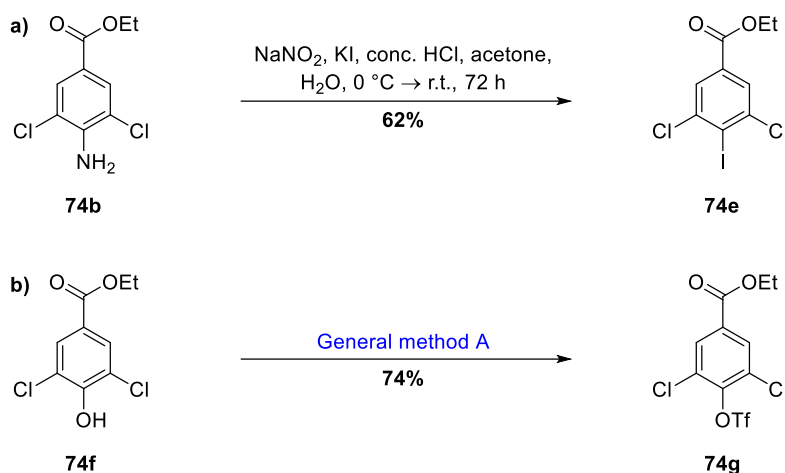
Table 11: Screening of Suzuki-Miyaura cross coupling conditions for the synthesis of 3,5-dichloro ester **74d**.^{287,298–302}



Entry	Conditions	Result	
		74d	74a ^[a]
1	Pd(PPh ₃) ₄ (cat.), K ₃ PO ₄ , 1,4-dioxane, 90 °C, 16 h	n/a ^[b]	n/a ^[b]
2	Pd(PPh ₃) ₄ (cat.), Na ₂ CO ₃ , DME, EtOH, H ₂ O, 80 °C, 16 h	0%	55%
3	PdCl ₂ (PPh ₃) ₂ (cat.), K ₃ PO ₄ , LiCl, 1,4-dioxane, 100 °C, 24 h	0%	61%
4	Pd(dppf)Cl ₂ ·CH ₂ Cl ₂ (cat.), KOAc, DMF, 90 °C, 16 h	0%	60%
5	Pd ₂ (dba) ₃ (cat.), Na ₂ CO ₃ , S-Phos, Toluene, H ₂ O, 100 °C, 24 h	0%	85%
6	Pd ₂ (dba) ₃ (cat.), Cs ₂ CO ₃ , PH(^t Bu) ₃ ⁺ ·BF ₄ ⁻ , 1,4-dioxane, 90 °C, 18 h	n/a ^[c]	n/a ^[c]

[a] Isolated yield of recovered bromide starting material **74a**. [b] Complex mixture of unidentified products.
[c] Reaction mixture decomposition.

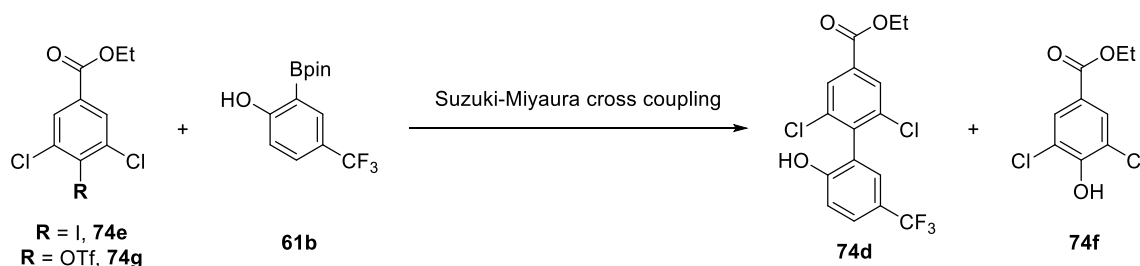
To continue the investigation towards biaryl **74d**, two alternative Suzuki-Miyaura cross coupling partners were prepared (Scheme 14). This was rationalised on the basis that oxidative addition of an aryl halide to palladium(0) is the first step in the Suzuki-Miyaura catalytic cycle, and that the relative reactivity of the halide governs the rate of this step.^{283,284,303} It is well established that the propensity of aryl halides towards oxidative addition increases in the order of ArCl < ArOTf ~ ArBr < ArI and thus iodo and triflate coupling partners **74e** and **74g** were considered.^{286,304} Iodo species **74e** was synthesised in good yield by a Sandmeyer reaction from amine **74b** (Scheme 14, a).³⁰⁵ General Method A then provided triflate fragment **74g** from commercially available alcohol **74f**, also in good yield (Scheme 14, b).



Scheme 14: Synthesis of alternative Suzuki-Miyaura cross coupling partners. a) Iodo species **74e**.³⁰⁵ b) Triflate species **74g**.

The new cross coupling partners iodo **74e** and triflate **74g** were tested in a variety of Suzuki-Miyaura cross coupling protocols (Table 12). Entry 1 used iodo species **74e** and General Method D, but failed to provide any trace of biaryl **74d** when examined by ¹H NMR and LCMS. This was also the case for iodo species **74e** and the conditions in Entry 2.²⁹⁸ The final attempt with iodo partner **74e** is described by Entry 3²⁸⁷ and only recovery of unreacted starting material was possible. Moving on to triflate cross coupling partner **74g**, the crude reaction mixture for Entry 4³⁰⁶ showed majority alcohol **74f**, arising from the hydrolysis of triflate **74g**. Pleasingly, entries 5 and 6 both gave desired biaryl product **74d** but in low yields of 15 and 22% respectively.²⁹⁹ During purification of biaryl **74d** by flash column chromatography, it was observed that hydrolysed triflate - alcohol **74f** - co-eluted with desired product **74d**, thus reducing the yield. Alternative elution systems were tested but no improvement was observed. At this point, Entry 6 was prioritised over Entry 5 as a superior yield of biaryl **74d** had been isolated.

Table 12: Screening of Suzuki-Miyaura cross coupling conditions for the synthesis of 3,5-dichloro ester **74d**.^{287,298,299,306}

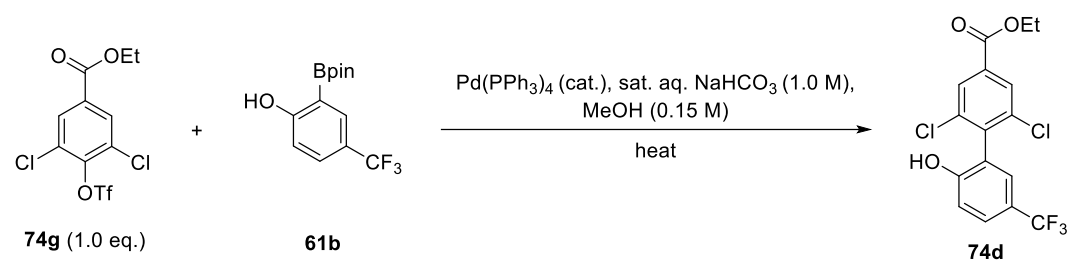


Entry	Conditions	Result		
		74d ^[a]	74e ^[b]	74f ^[c]
1	74e , General method D	n/a ^[d]	n/a ^[d]	n/a ^[d]
2	74e , Pd(PPh ₃) ₄ (cat.), K ₃ PO ₄ , 1,4-dioxane, 90 °C, 16 h	n/a ^[d]	n/a ^[d]	n/a ^[d]
3	74e , Pd(PPh ₃) ₄ (cat.), Na ₂ CO ₃ , DME, EtOH, H ₂ O, 80 °C, 16 h	0%	54%	n/a
4	74g , Pd ₂ (dba) ₃ (cat.), K ₃ PO ₄ , S-Phos, Toluene, 110 °C, 3 h	0%	n/a	Y
5	74g , PdCl ₂ (PPh ₃) ₂ (cat.), K ₃ PO ₄ , LiCl, 1,4-dioxane, 110 °C, 3 h	15%	n/a	Y
6	74g , Pd(PPh ₃) ₄ (cat.), sat. aq. NaHCO ₃ , MeOH, 110 °C, 3 h	22%	n/a	Y

[a] Isolated yield of desired product **74d**. [b] Isolated yield of recovered iodo starting material **74e**. [c] Presence determined by ¹H NMR and LCMS analysis of the crude reaction mixture. [d] Complex mixture of unidentified products.

Following the successful synthesis of 3,5-dichloro biaryl **74d**, a short optimisation study of the Suzuki-Miyaura cross coupling conditions in Entry 6, Table 12 was performed (Table 13). Entry 1 reports the original protocol used in the discovery of these conditions. Initial optimisation increased the palladium catalyst equivalents from 0.05 to 0.20 (Entry 2). Inspection of the crude reaction mixture by TLC and LCMS showed triflate **74g** remaining. The reaction time was then increased from 3 to 24 hours to give Entry 3. Pleasingly this pushed the reaction towards completion and minimal co-elution of alcohol **74f** was observed. A substantially improved isolated yield of 76% was obtained under these conditions. Entry 4 repeated Entry 3 except with a lower temperature of 80 instead of 110 °C, hoping to reduce the hydrolysis of triflate **74g**. Minimal co-elution of alcohol **74f** and biaryl **74d** was observed for this Entry, however reaction progress had been reduced and thus a lower yield of 54% was isolated. Returning to the conditions outlined in Entry 3 and lowering the equivalents of boronic ester **61b** from 2.5 to 1.2 provided the final test conditions in Entry 5. This was deemed relevant because boronic ester **61b** had to be synthesised over two steps from a limited availability starting material (Scheme 5, Section 2.2.2). Unfortunately, this modification saw a significant impact on the yield of biaryl **74d**: a drop from 76 to 45%, and was not investigated further.

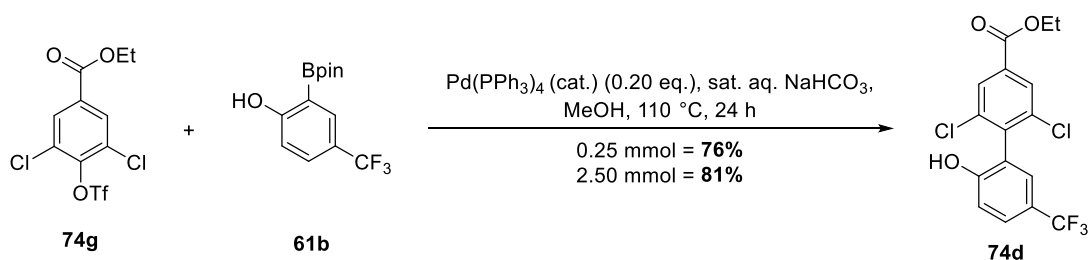
Table 13: Optimisation of Suzuki-Miyaura cross coupling conditions for the synthesis of 3,5-dichloro ester **74d**.



Entry	Conditions				Result ^{[a][b]}
	61b eq.	Pd eq.	Temp., °C	Time, h	
1	2.5	0.05	110	3	22%
2	2.5	0.20	110	3	74g remaining ^[c]
3	2.5	0.20	110	24	76%
4	2.5	0.20	80	24	54%
5	1.2	0.20	110	24	45%

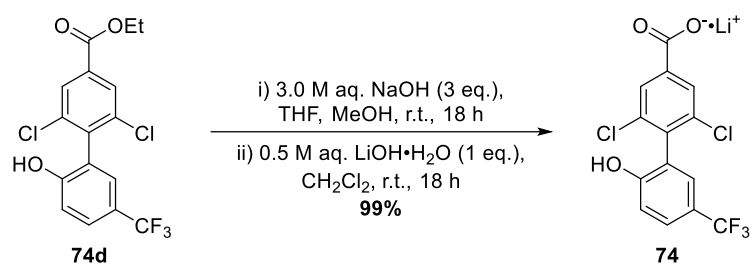
[a] Isolated yield of desired product **74d**. [b] Alcohol **74f** observed and co-eluted in early fractions of **74d** during flash column chromatography. [c] Determined by TLC and LCMS analysis of the crude reaction mixture.

With the optimised conditions from Entry 3 (Table 13) in hand, synthesis of biaryl **74d** was repeated on a 2.5 mmol scale – ten times the scale performed during optimisation (Scheme 15). Pleasingly, a high yield of 81% for biaryl **74d** was achieved and co-elution with alcohol **74f** was negligible.



Scheme 15: Optimised Suzuki-Miyaura cross coupling conditions for the synthesis of 3,5-dichloro ester **74d**.

With 3,5-dichloro ester **74d** in hand, hydrolysis of the ester moiety and subsequent lithium salt formation was performed (Scheme 16). Synthetic conditions developed for monochloride carboxylate **78** (Scheme 12) were used. This provided the desired 3,5-dichloro lithium carboxylate salt **74** in quantitative yield.



Scheme 16: Synthesis of final product 3,5-dichloro lithium carboxylate salt **74** from ester **74d**.

Following the successful synthesis of α D-site fragments **74** and **78**, X-ray crystallography was performed to verify the fragment binding modes (Figure 55). Comparison of the biaryl cores for 3,5-dichloro and monochloro carboxylates **74** and **78** with lead fragment benzonitrile **67** showed good structural overlay (Figure 55, a). Ring A, bearing the trifluoro and alcohol groups, remained deep within the α D pocket while ring B filled the middle portion of the pocket and protruded into the substrate-binding channel. It was observed that the carboxylate moieties of **74** and **78** sat higher in the α D pocket relative to the nitrile of **67**. In addition, residue Glu230 was pushed further away from the α D pocket opening (Figure 55, a). It was surmised that electrostatic repulsion between the carboxylate head group and Glu230 side chain was responsible for this rearrangement.

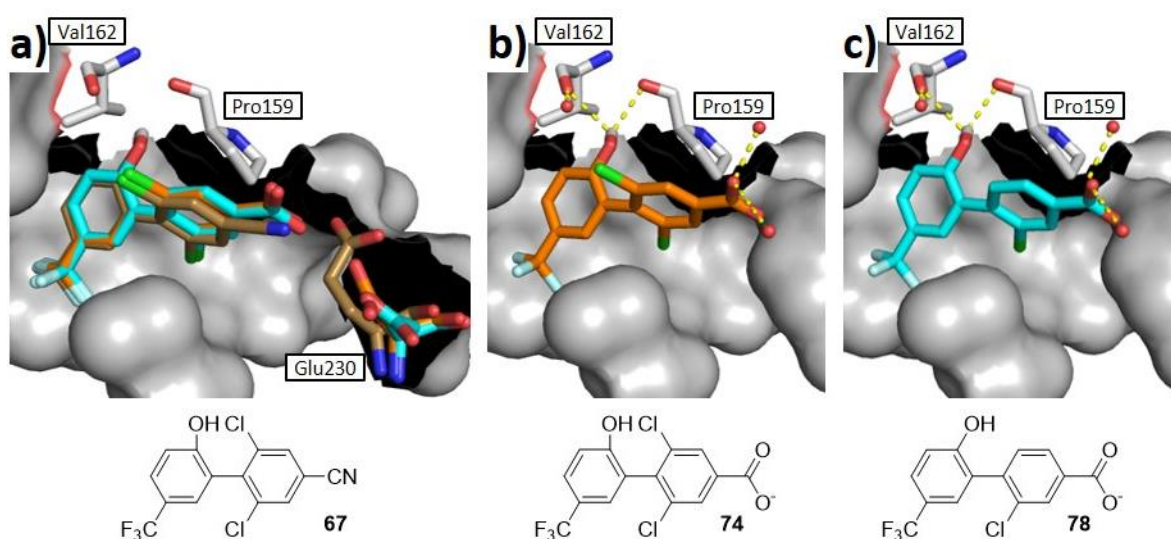


Figure 55: X-ray crystallography results for lithium carboxylate salts in complex with CK2 α (grey). **a)** Overlay of lead **67** (brown), 3,5-dichloro derivative **74** (orange) and monochloro derivative **78** (blue) to show relative positioning within the α D pocket. Residue Glu230 has been highlighted to show change in position. **b)** 3,5-Dichloro derivative **74** (orange). **c)** Monochloro derivative **78** (blue). Polar interactions between the fragment, protein residues (white) and water molecules are highlighted by yellow dashed lines.

3,5-Dichloro carboxylate **74** was observed to maintain interactions between the ring A alcohol, Pro159 and Val162, but contact to the α D pocket water molecule was lost (Figure 55, b). HBA interactions between the head group carboxylate and two water molecules in the substrate-binding channel were

also detected. Analysis of the X-ray crystal structure for monochloro carboxylate **78** revealed the same interactions as for dichloro analogue **74** (Figure 55, c).

Next, hexamer peptide **75** was superimposed onto the X-ray crystal structure for 3,5-dichloro carboxylate **74** (Figure 56). Hexamer **75** was observed to align well with the substrate-binding channel and thus protein residues relevant to substrate recognition were inspected. The relative positions of the residues matched what was expected from earlier studies (Section 2.3.2) but only one interaction was within range for detection: a HBA interaction between the $n+1$ Asp and Lys198.

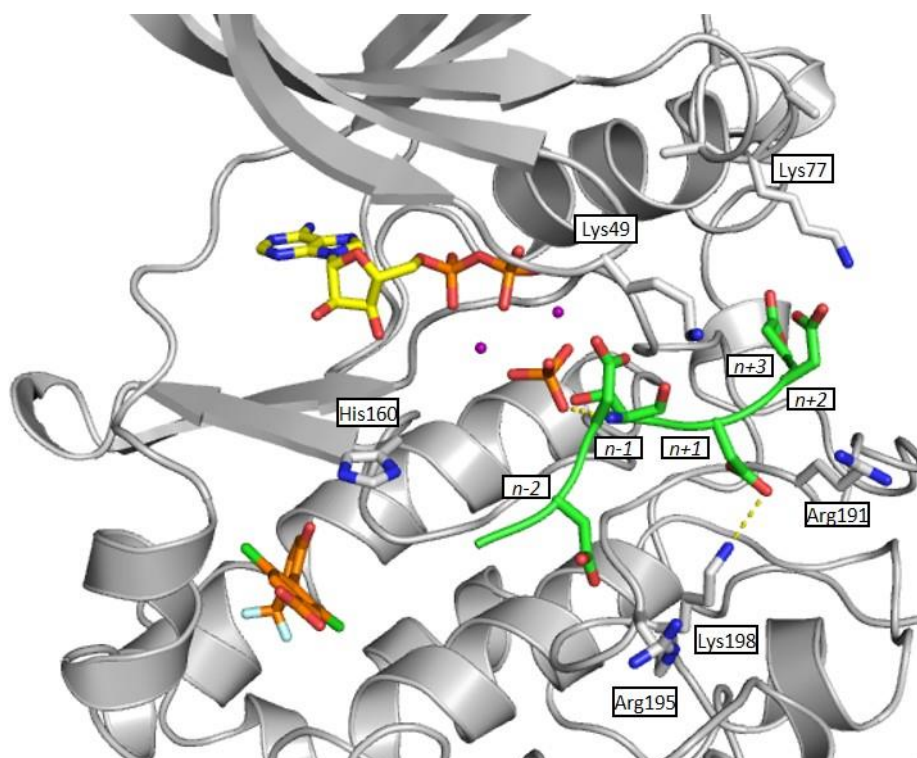


Figure 56: Overlay of modelled hexamer **75** (green) and 3,5-dichloro carboxylate **74** (orange) protein crystal structure (grey) with ADP (yellow), phosphate (orange) and Mg^{2+} (purple) in the ATP-site. CK2 α residues involved with substrate recognition are highlighted (white) and predicted polar contacts are shown as dashed yellow lines. This protein is a K74-K76 alanine mutant.

This analysis was repeated for monochloro carboxylate **78** (Figure 57). Superimposing hexamer **75** showed good alignment with the substrate-binding channel, and residues responsible for substrate recognition were positioned within appropriate distance. Two HBA interactions were observed involving the Asp at $n+1$, Lys198 and Arg191, which match those reported in the literature.

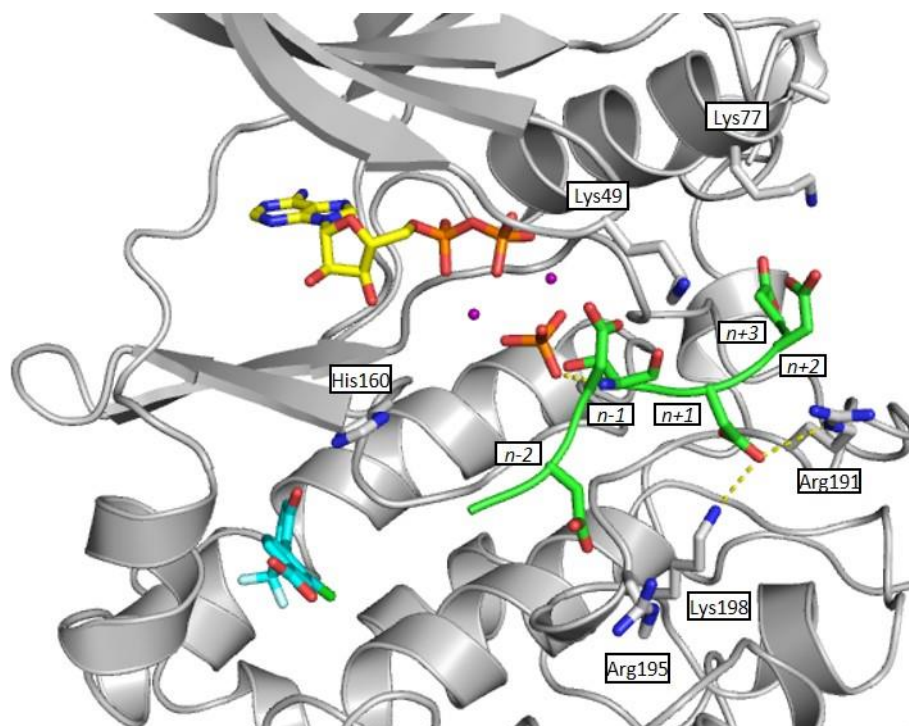


Figure 57: Overlay of modelled hexamer **75** (green) and monochloro carboxylate **78** (blue) protein crystal structure (grey) with ADP (yellow), phosphate (orange) and Mg^{2+} (purple) in the ATP-site. CK2 α residues involved with substrate recognition are highlighted (white) and predicted polar contacts are shown as dashed yellow lines. This protein is a K74-K76 alanine mutant.

In conclusion, two lithium carboxylate salt analogues were synthesised: 3,5-dichloro carboxylate **74** and monochloro carboxylate **78**. The carboxylate moiety was deemed a suitable head group for use in later linker development. X-ray crystallography showed carboxylate fragments **74** and **78** bound selectively in the α D pocket, and the residues lining the substrate-binding channel remained consistent for hexamer **75** binding. Following these promising results, the project progressed into linker development.

Before moving forward, a note on the synthetic accessibility of 3,5-dichloro carboxylate **74** must be mentioned. At the time of linker development, studies towards the Suzuki-Miyaura protocol for 3,5-dichloro ester **74d** were ongoing. Therefore 3,5-dichloro carboxylate **74** was not available for use at this stage. Instead, monochloro carboxylate **78** was used in the linker optimisation phase and then substituted for 3,5-dichloro carboxylate **74** at the point of final fragment linking.

2.3.4 Linker Optimisation

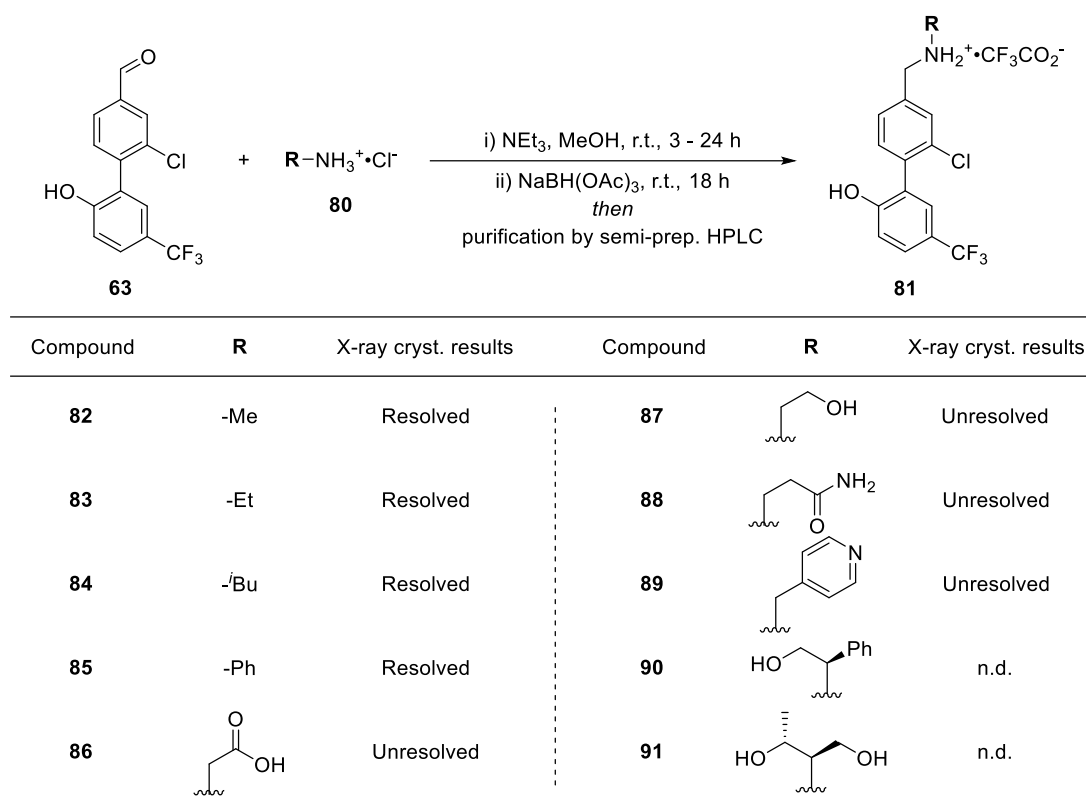
2.3.4.1 Optimisation Strategy and Previous Work

Fragment linking is considered the more challenging route of fragment optimisation.^{15,307} Introduction of a linker that does not interfere with the binding mode of the original fragments is difficult and was explained in greater detail in Section 1.1.4, Hit-to-Lead Generation.

In order to maintain the optimised α D fragment binding pose, we envisaged developing a linker *via* iterative growth of carboxylate fragment **78** towards the substrate-binding channel. Each cycle would involve rational structure-based design of multiple linkers and screening *in silico*. The most promising candidates would then be synthesised and submitted for structural determination by X-ray crystallography. The best result from each set would serve as the starting point for SBDD in the next round, and thus development of an efficient linker should be possible.

Before proceeding, prior work by Part III masters student, Antanas Radzevičius, was reviewed. This work derivatized aldehyde **63** by reductive amination using commercially available primary amines **80** (Table 14). His aim was to investigate the opening of the α D pocket and utility of this exit vector for binding small molecules in the substrate-binding channel. Radzevičius designed and screened a library of secondary amines bearing scaffold **81** and then synthesised the top hits and submitted them to Dr. Paul Brear for X-ray crystallography (Table 14).

Table 14: Reductive amination fragment library **82 – 91** synthesised by Antanas Radzevičius and X-ray crystallography results.



Resolved: electron density for the ligand could be accurately defined. Unresolved: electron density for the ligand could not be accurately defined. n.d.: no density observed on CK2 α .

Of the ten fragments submitted for X-ray crystallography, eight fragments (**82 – 89**) were observed to bind CK2 α . Electron density for chiral fragments **90** and **91** was not detected at any binding site on the α subunit. Fragments **82 – 89** were selective for the α D pocket and the biaryl core was well defined in each case. Small, aliphatic amines **82 – 84** showed good electron density at the opening of the α D pocket, but larger aliphatic or aromatic moieties **85 – 89** had weak or unresolved electron density for the amine portion.

Based on these unpromising results, it was decided that an alternative peptide-based approach to the linker would be taken in this project. It was hypothesised that a linker resembling the natural peptide substrates might interact with the binding channel more successfully. Literature studies showed that the substrate-binding channel of CK2 α is highly basic and therefore complementary Asp and Glu residues would be the focus for linker design.²⁹⁵

2.3.4.2 Development of a Peptide Linker

2.3.4.2.1 Initial Peptide Linker Test Set

The peptide linker strategy began with computational modelling of α D-site fragments bearing up to a tetramer peptide chain. Carboxylate fragment **78** was extended by one amino acid at a time, starting with the addition of a single Ala residue, **92** (Figure 58, **a**). For each additional amino acid, the predicted polar contacts between the peptide and protein were examined and only fragments predicted to enhance ligand binding were considered further. All modelled fragments overlaid well with parent carboxylate **78** and were predicted to maintain the polar interactions at ring A. The most promising results from the *in silico* screen are shown in Figure 58.

Addition of a single Ala residue (**92**) was predicted to form a HBA interaction between the terminal acid group and His160 in the α D pocket opening (Figure 58, **a**). A HBA contact between the amide carbonyl of fragment **92** and a substrate-binding channel water was also predicted. Extension by a second Ala (**93**) maintained the interaction to the water molecule and the new terminal acid group was predicted to contact both His160 and Lys121 (Figure 58, **b**). Adding an Asp residue gave tripeptide **94** which was predicted to lie along the substrate-binding channel (Figure 58, **c**). The Asp sidechain was anchored in place by a HBA interaction with Ser194 and the terminal acid group was within contact distance of the His160 backbone. The interaction to a water at the mouth of the pocket was maintained. The final round of fragment growth added a second Asp residue and both terminal acid (**95**) and amide (**96**) were modelled (Figure 58, **d** and **e** respectively). The tetramer was expected to project along the substrate-binding channel with a similar predicted binding mode for both molecules. In both cases, the HBA interaction to water was maintained and His160 was predicted to contact the peptide backbone and first Asp residue. The terminal Asp was shown to contact Ser194 and the backbone of Arg195, and the terminal acid/amide groups were predicted to interact with Lys158 as HBAs.

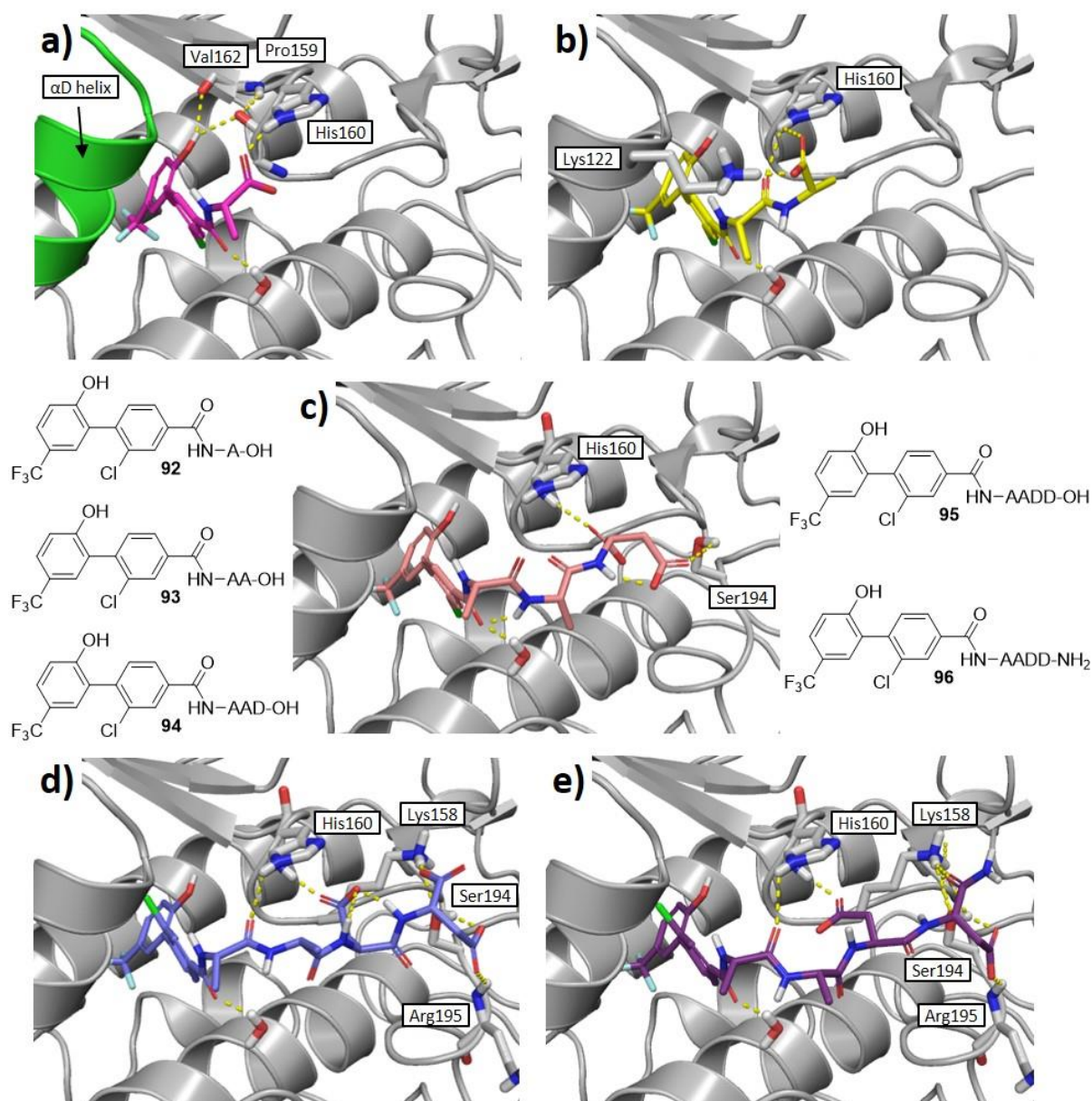


Figure 58: Computational modelling results for initial peptide linkers docked onto monochloro carboxylate **78** protein structure (grey). **a)** Ala derivative **92** (magenta) with Pro159 and Val162 highlighted (white) to show ring A interactions maintained (omitted from other images for simplicity). The α D helix is highlighted in green. **b)** AA derivative **93** (yellow). **c)** AAD derivative **94** (pink). **d)** AADD with terminal acid **95** (blue). **e)** AADD with terminal amide **96** (purple). Predicted polar interactions between the fragment, protein residues (white) and water molecules are highlighted by yellow dashed lines.

Following analysis of the modelling data, fragment-peptides **92** and **93** were synthesised by traditional manual Fmoc-Solid-Phase Peptide Synthesis (Fmoc-SPPS). Tripeptide **94** and tetramers **95** and **96** were synthesised by microwave Fmoc-SPPS (Table 15).³⁰⁸ While the peptides were still resin-bound, the *N*-terminal amino acid was Fmoc-deprotected and coupled with monochloro carboxylate **78**. The fragment-capped peptide was then fully deprotected, cleaved from the resin and purified by semi-

preparative HPLC to provide the desired product. Fragments **92** – **96** were all isolated in low yields ranging from 19% for Ala derivative **92** down to 6% for di-Ala species **93**.

Table 15: Fmoc-SPPS of initial peptide linker species **92** – **96** and X-ray crystallography results for the peptide chain.

Compound	Sequence	Fmoc-SPPS method	Yield (%)	Peptide chain resolved?
92	78-A-OH	Manual	19	Y
93	78-AA-OH	Manual	6	N
94	78-AAD-OH	Microwave	17	Y
95	78-AADD-OH	Microwave	7	N
96	78-AADD-NH₂	Microwave	12	N

Y: yes, electron density of peptide chain strong enough to resolve accurately.
 N: no, electron density of peptide chain too weak to resolve accurately.

Next, test linker species **92** – **96** were submitted to Dr. Paul Brear for structural determination by X-ray crystallography. In all cases, electron density for the α D-site biaryl moiety was strong and showed selective binding within the α D pocket. Overlay of the test species biaryl cores with parent carboxylate **78** also showed a consistent positioning within the α D pocket, and ring A interactions were maintained (Figure 59, **a**). Unfortunately, the peptide chain could only be resolved for two structures: Ala derivative **92** and tripeptide **94** (Figure 59).

Upon closer inspection of Ala derivative **92**, it was observed that the ligand bound to the protein *via* two modes (Figure 59, **b**). Ring B of the biaryl core was accommodated with the 3-position chlorine pointing to the back of the pocket, but also towards the front of the pocket. The Ala residue projected out of the α D pocket opening and either towards the substrate-binding channel or towards the α D helix. In both binding modes, Glu230 is involved in a HBA interaction with the fragment amide. Tripeptide **94** was reported to bind CK2 α with strong electron density for an unexpected binding mode (Figure 59, **c** and **d**). The tripeptide chain was not shown to lie within the substrate-binding channel, but instead project away from the protein surface and towards the α D helix. Contacts between the Asp residue and Lys122 were detected, as well as multiple H-bonding interactions between the peptide backbone and water molecules. The C-terminal end of the ligand was highly solvent exposed in this binding mode.

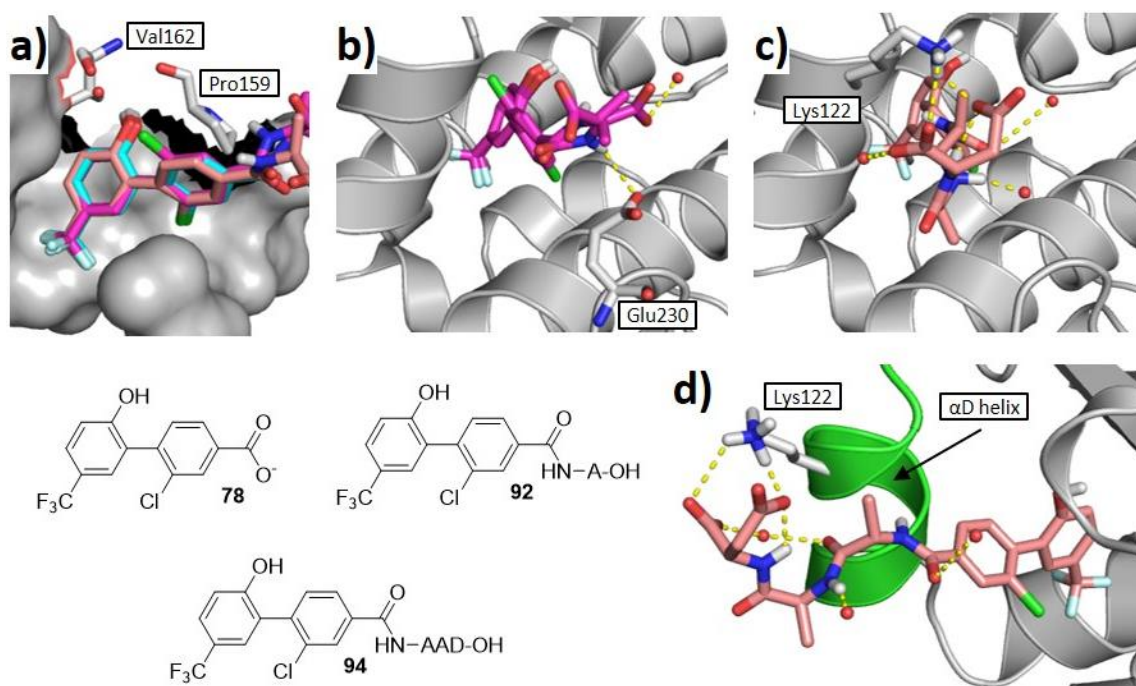


Figure 59: X-ray crystallography results for test linker species **92** and **94** in complex with CK2 α (grey). **a)** Overlay of carboxylate **78** (blue), Ala derivative **92** (magenta) and tripeptide **94** (pink) to show relative positioning within the α D pocket. **b)** Ala derivative **92** (magenta). **c)** Tripeptide **94** (pink) viewed from the same angle as Ala derivative **92**. **d)** Tripeptide **94** (pink) viewed from the core of the protein to demonstrate peptide chain angled towards solvent. The α D helix is highlighted in green. Polar interactions between the fragment, protein residues (white) and water molecules are highlighted by yellow dashed lines.

In summary, five linker test species **92** – **96** were designed, synthesised and tested by X-ray crystallography. While only two species (**92** and **94**) could be fully resolved, electron density was observed in the α D pocket for all five ligands. This validated the use of α D-binding fragment **78** as a molecular ‘anchor’ for the development of the linker.

2.3.4.2.2 Polyanionic Tripeptide Linkers

To move forward with linker development, it was decided that tripeptides would be investigated further. Test fragment **94**, bearing the sequence AAD, provided the X-ray crystal structure with best electron density in the previous round. In contrast, dimer **93** and tetramers **95** and **96** were unresolved. Unfortunately, tripeptide **94** did not present the binding mode desired, but with rational structure-guided design it was believed that influence over the binding pose may be possible. To this end, a library of polyanionic tripeptide ligands was constructed and screened *in silico*. The results were analysed to determine the impact of different residues at each position of the peptide chain. The most promising amino acids are reported below.

Ligands bearing an Asp residue adjacent to the α D-site fragment were consistently predicted to bind in one of two modes. The first suggested a HBA interaction between the Asp residue and His160, while the second showed a HBA contact to Lys122 (Figure 60, **a** and **b** respectively). Both binding modes were predicted to secure the ligand at the mouth of the α D pocket and position the peptide chain towards the substrate-binding channel. Of all residues examined, an Asp at this position was best.

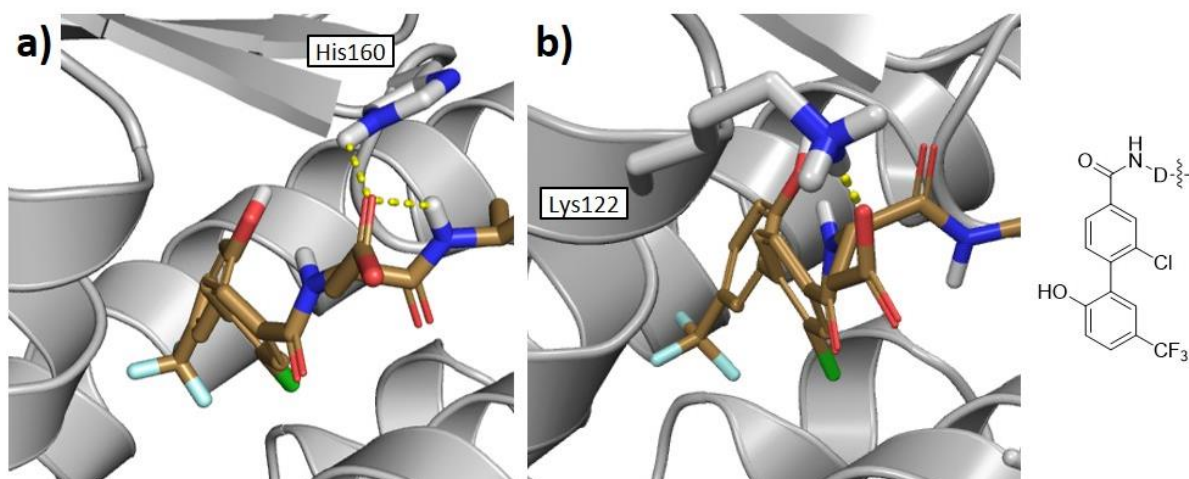


Figure 60: Computational modelling results for Asp residue adjacent to α D-site fragment. **a)** Asp predicted to make HBA interaction with His160. **b)** Asp predicted to make HBA with Lys122. Predicted polar interactions between the fragment (brown), protein residues (white) and water molecules are highlighted by yellow dashed lines.

Next, the central position of the tripeptide chain was considered. An Ala residue at this position was observed to efficiently fill space along the substrate channel, but was not predicted to make any polar contacts to the protein. Substituting for a Lys showed a potential HBD interaction to Glu230, while Gln might contact Lys122 as a HBA (Figure 61, **a** and **b** respectively). Finally, a Trp residue in the middle of the chain was predicted to occupy a shallow pocket within the substrate-binding channel, but no polar or π -stacking interactions could be identified (Figure 61, **c**).

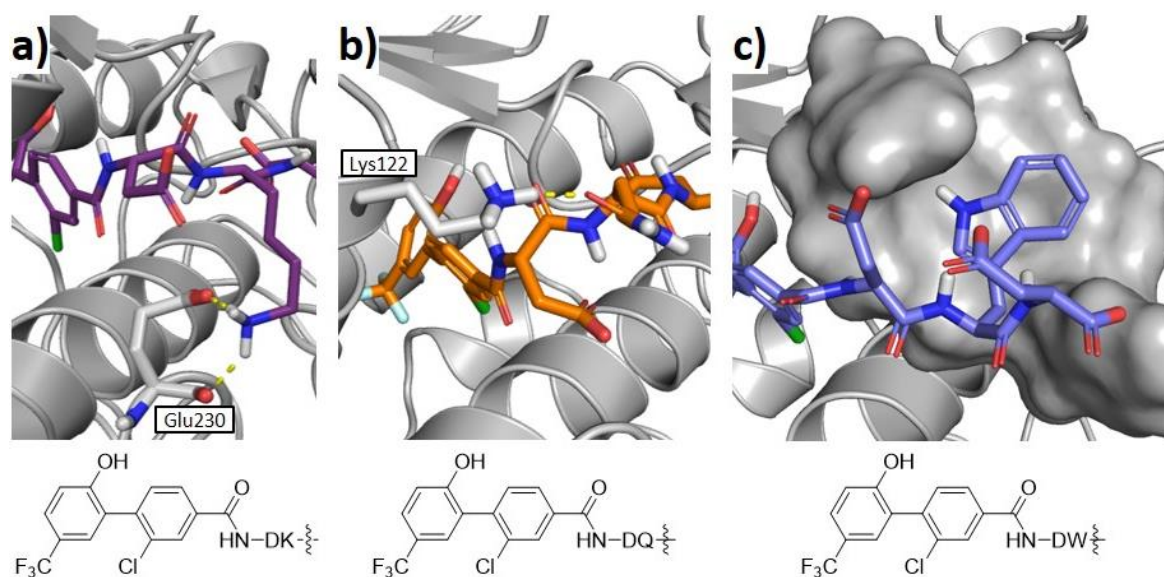


Figure 61: Computational modelling results for residue in the middle position of the tripeptide chain. **a)** Lys (purple) predicted to make HBD interaction with Glu230. **b)** Gln (orange) predicted to make HBA interaction with Lys122. **c)** Trp (blue) predicted to fill shallow pocket (grey) in substrate-binding channel. Predicted polar interactions between the fragment, protein residues (white) and water molecules are highlighted by yellow dashed lines.

The C-terminal position of the tripeptide was interrogated using amino acids bearing carboxylate and amide sidechains. The two best results were Asp and Glu residues, which were predicted to contact Lys158/Ser194 and Lys158/His160 respectively (Figure 62, **a** and **b** respectively). Substituting Glu for Asn maintained the two contacts to Lys158 and His160 (Figure 62, **c**). It was hypothesised that the electrostatic interactions between the terminal amino acid and substrate-binding site would anchor the peptide within the channel.

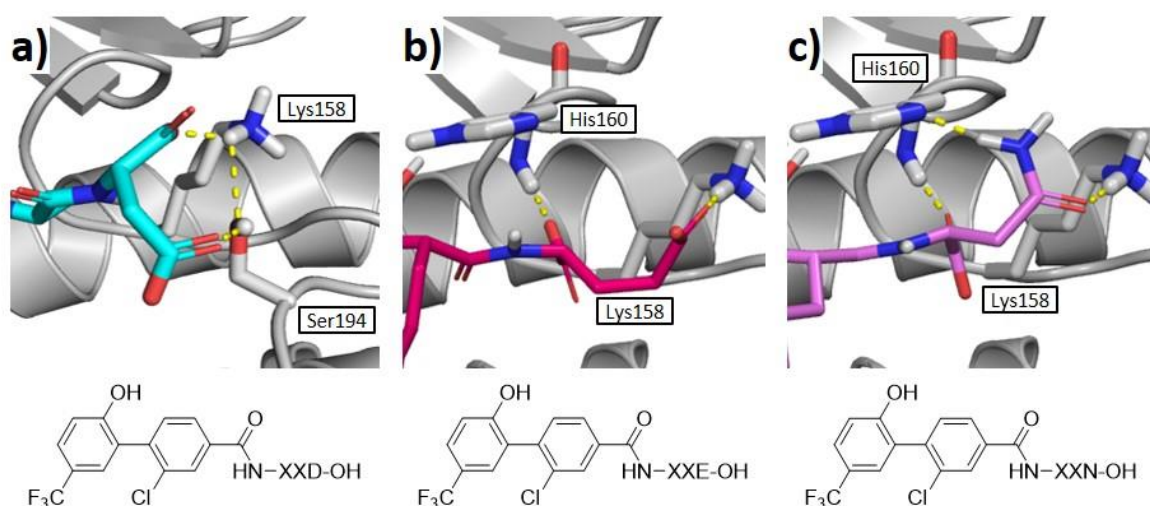


Figure 62: Computational modelling results for C-terminal residue. **a)** Asp (blue) predicted to make HBA interaction with Lys158 and Ser194. **b)** Glu (pink) predicted to make HBA interaction with Lys158 and His160. **c)** Asn (lilac) predicted to make HBA interaction with Lys158 and HBA/HBD interactions with His160. Predicted polar interactions between the fragment, protein residues (white) and water molecules are highlighted by yellow dashed lines.

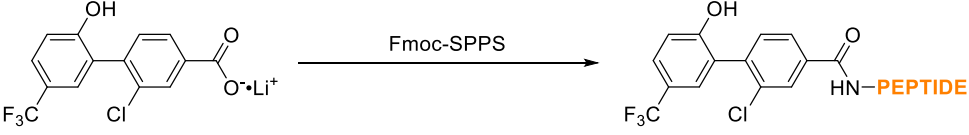
In summary, from the computational modelling it was learnt that:

1. An Asp residue directly adjacent to the α D-site fragment looked most promising for orienting the peptide chain towards the substrate-channel.
2. An Ala, Lys, Gln or Trp residue at the middle position of the tripeptide could be beneficial for binding.
3. An Asp, Glu or Asn residue at the C-terminus might hold the chain within the channel by polar interactions.

Based on these guidelines, six tripeptides (**97** – **102**) hosting combinations of the above residues were synthesised (Table 16). The first two species, DAD **97** and DKD **98**, were prepared by microwave Fmoc-SPPS without complication and in moderate yields. Ligands DKE **99** and DQD **100** were also prepared using microwave irradiation but a substantial by-product was observed in both cases (**99a** and **100a** respectively). Isolation and characterisation of the by-product revealed fragment scaffold **103**. This species was believed to form during the TFA peptide deprotection and resin cleavage step, performed under microwave irradiation for 30 minutes. To prevent future by-product formation, the microwave reactor was no longer used for this step and instead the cleavage cocktail was left to shake at room temperature. Pleasingly, scaffold **103** was not observed in any of the following reactions. Fifth tripeptide DKN **101** was synthesised in better yield but alternative by-product **101a** was isolated. Characterisation of this minor species provided a structure consistent with fragment scaffold **104** which could form during the overnight coupling of carboxylate fragment **78**. Future synthesis reduced fragment **78** coupling time to 3.5 minutes and removed DIPEA from the reaction mixture. Following

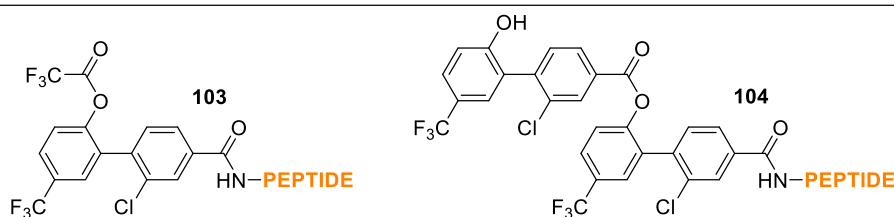
these changes, scaffold **104** was not detected again. Final ligand DWD **102** was synthesised by manual Fmoc-SPPS. Analysis of the crude reaction mixture by analytical HPLC showed a much cleaner trace than for earlier tripeptides **97** – **101**. Furthermore, the desired product was isolated in good yield. At this point, it was decided that all future short peptides would be prepared by manual Fmoc-SPPS.

Table 16: Fmoc-SPPS of tripeptide library **97** – **102** and isolation of by-product species **99a**, **100a** and **101a**.



78

Compound	Sequence	Fmoc-SPPS method	Yield (%)	By-product	Yield (%)
97	78 -DAD-OH	Microwave	15	n/a	n/a
98	78 -DKD-NH ₂	Microwave	30	n/a	n/a
99	78 -DKE-OH	Microwave	16	103 -DKE-OH (99a)	8
100	78 -DQD-OH	Microwave	12	103 -DQD-OH (100a)	10
101	78 -DKN-OH	Microwave	39	104 -DKN-OH (101a)	4
102	78 -DWD-OH	Manual	21	n/a	n/a



The six tripeptides **97** – **102** were submitted to Dr. Paul Brear for X-ray crystallography. Two fragments, DKE **99** and DQD **100**, did not bind to CK2 α , but the remaining four fragments were observed to bind selectively in the α D pocket. The fragments overlaid well with carboxylate fragment **78** and the ring A interactions with Pro159, Val162 and the α D pocket water were maintained (Figure 63, **a**). In all four cases, **97**, **98**, **101** and **102**, the Asp residue adjacent to the α D-site fragment was well resolved and showed consistent positioning (Figure 63, **b**). A HBA interaction with His160 and a water molecule was detected. However, the orientation of the Asp residue differed to the computational modelling (Figure 60). As a result, the tripeptide chains of fragments **97**, **98**, **101** and **102** projected away from the substrate-binding channel and towards the α D helix, as observed for earlier AAD tripeptide **94** (Figure 59, **d**).

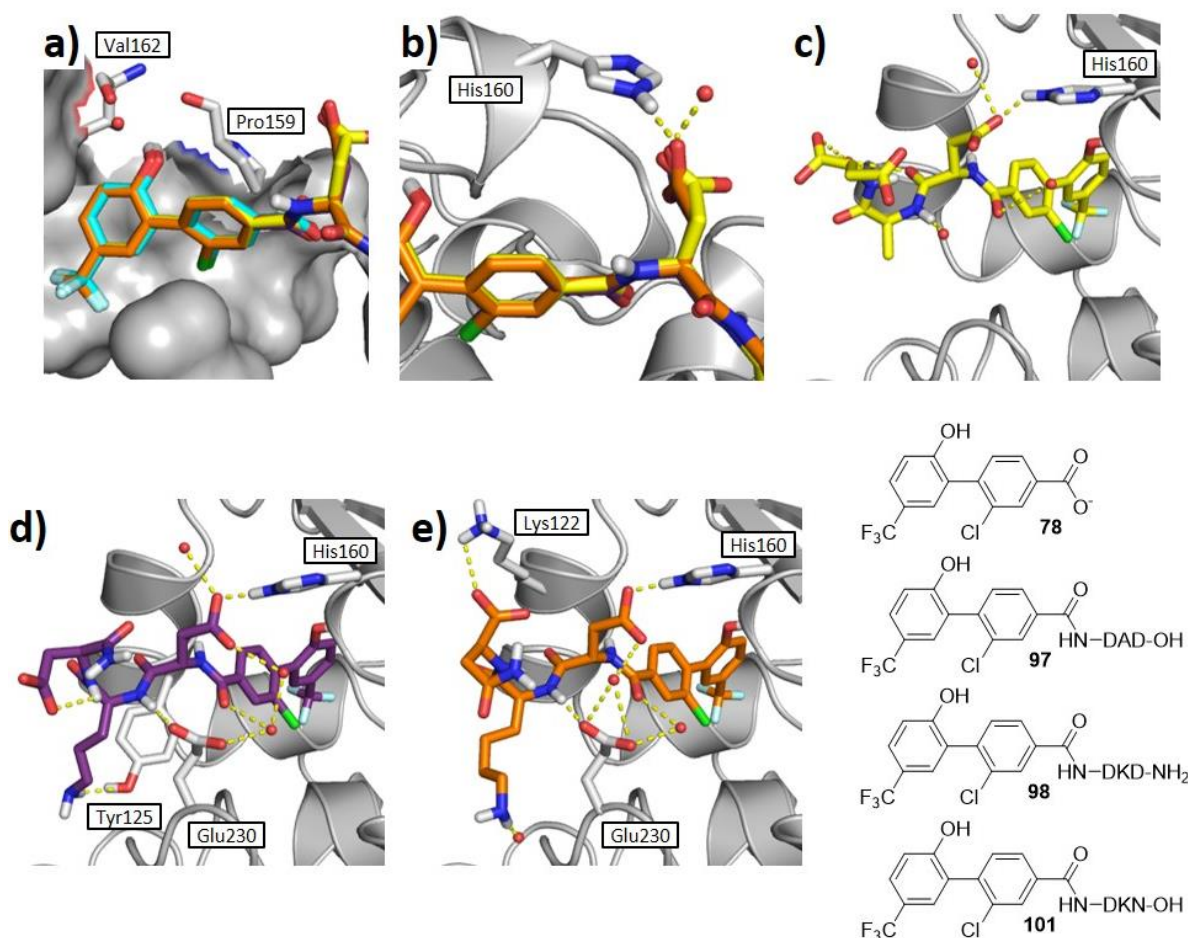


Figure 63: X-ray crystallography results for tripeptide linker species in complex with CK2 α (grey). **a)** Overlay of carboxylate **78** (blue), DAD derivative **97** (yellow), DKD derivative **98** (purple) and DKN derivative **101** (orange) to show relative positioning within the α D pocket. **b)** Overlay of first Asp residue for DAD derivative **97** (yellow), DKD derivative **98** (purple) and DKN derivative **101** (orange) to show consistent position at the mouth of the α D pocket. **c)** DAD derivative **97** (yellow). **d)** DKD derivative **98** (purple). **e)** DKN derivative **101** (orange). Polar interactions between the fragment, protein residues (white) and water molecules are highlighted by yellow dashed lines.

For DAD fragment **97**, the Ala sidechain was observed to fill space at the protein surface and the backbone contacted a water molecule (Figure 63, **c**). The terminal Asp made a HBA interaction with water but no contacts to the protein were detected. DKD derivative **98** showed greater interaction with the protein (Figure 63, **d**). The Lys sidechain contacted Tyr125 as a HBD and the backbone contacted Glu230. The C-terminus was not observed to interact with the protein or solvent. Fragment DKN **101** lost the Lys-Tyr125 interaction but instead the C-terminal acid group formed a HBA interaction with Lys122 (Figure 63, **e**). Final fragment DWD **102** could not be resolved past the first Asp residue.

Overall, tripeptide library **97** – **102** did not bind to CK2 α as predicted. Rational structure-based peptide design was not sufficient to influence the binding mode towards the substrate-binding channel as

hoped. Analysis of the X-ray crystal structures for **97**, **98** and **101** showed that H-bonding to His160 held the linker in the wrong orientation for substrate channel binding. HBA interactions with Lys122 on the α D helix may have also prevented the peptide chain from adopting the desired binding position.

2.3.4.2.3 Alternative Peptide Linkers

In an effort to achieve the goal of directing the peptide linker towards the substrate-binding channel, it was hypothesised that disrupting the aforementioned Asp-His160 interaction, at the mouth of the α D pocket, could be sufficient to change the binding mode. From this, three new strategies were considered:

1. Substitution of the first Asp residue by a moiety with greater structural rigidity and no H-bonding ability.
2. Introduction of greater ligand flexibility within the mouth of the α D pocket.
3. Maintain the current Asp-His160 interaction but change the chirality of the Asp residue.

In each case, the theory was tested by design and *in silico* screening of relevant peptides. Promising candidates were synthesised by manual Fmoc-SPPS and submitted for X-ray crystallography. The results from each investigation are reported herein.

Investigation 1: Rigidifying the peptide chain

It was surmised that rigidifying the peptide chain at the opening of the α D pocket might lock the linker in a conformation towards the substrate-binding channel. The residue directly adjacent to α D fragment **78** was in the most appropriate position to achieve this aim, and thus Asp was substituted for Pro. Two tetrapeptides, **78**-PGGD (**105**) and **78**-PGGN (**106**), were designed and modelled using the Schrödinger package. The software predicted both species to lie within the substrate-binding channel and maintain the optimised α D pocket binding pose (Figure 64).

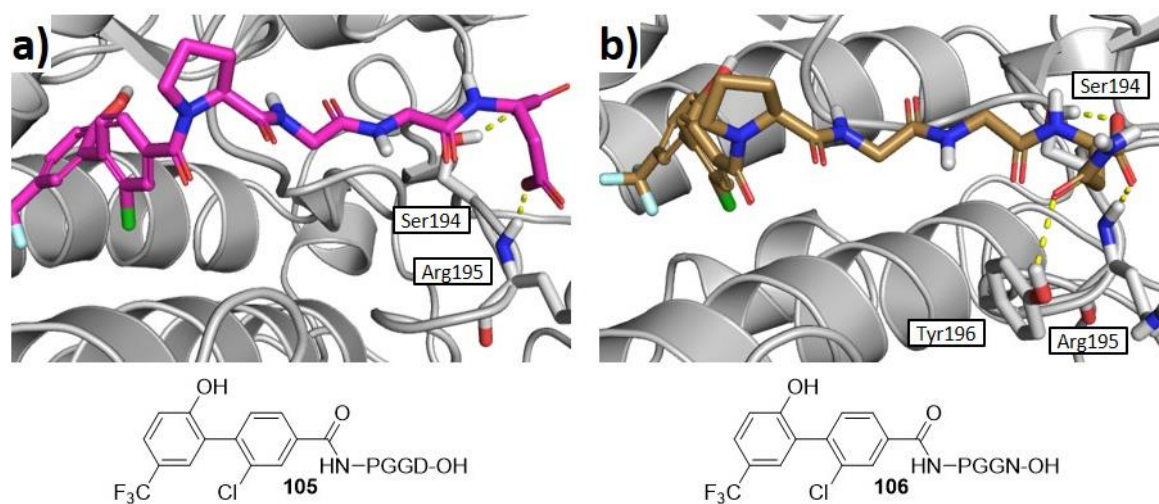


Figure 64: Computational modelling results for investigation into rigidifying the peptide chain. **a)** PGGD derivative **105** (magenta). **b)** PGN derivative **106** (brown). Predicted polar interactions between the fragment, protein residues (white) and water molecules are highlighted by yellow dashed lines.

The Pro residue at the α D pocket opening was predicted to direct the peptide chain down the substrate channel (Figure 64). H-bonding interactions involving the C-terminal Asp/Asn then anchored the linker to the protein surface. The Asp of PGGD derivative **105** was predicted to make HBA contacts with Ser194 and the backbone of Arg195 (Figure 64, **a**). The Asn of PGN species **106** was shown to interact with Ser194, Tyr196 and the backbone of Arg195 (Figure 64, **b**).

Following modelling, tetramers **105** and **106** were synthesised by manual Fmoc-SPPS (Table 17). No by-products were observed by LCMS or HPLC analysis of the crude reaction mixtures and both products were isolated in moderate yields.

Table 17: Manual Fmoc-SPPS and X-ray crystallography results for tetramers **105** and **106** to investigate rigidifying the peptide chain.



Compound	Sequence	Yield (%)	X-ray cryst. results
105	78 -PGGD-OH	30	d.b.
106	78 -PGGN-OH	18	d.b.

d.b.: did not bind to CK2 α

X-ray crystallography for tetramer species **105** and **106** in complex with CK2 α was conducted, but unfortunately no electron density for either ligand was observed. From this it was concluded that Pro residue substitution may not be the solution and was not considered further.

Investigation 2: Increasing the flexibility of the peptide chain

Structural data for the tripeptides suggested that the amide bond linking α D-site fragment **78** to the tripeptide chain locked the angle at which the chain exited the α D pocket. Amide bonds are known to reduce free rotation and thus it was hypothesised that the optimal binding mode may be prevented due to lack of freedom. To test this, we envisaged linking a tripeptide sequence to aldehyde fragment **63** *via* reductive amination. The resulting ligand would then have a flexible benzylamine moiety at the opening of the α D pocket.

To this end, species **107** bearing the optimised α D-site biaryl core and a DAD tripeptide sequence, was designed and docked onto CK2 α (Figure 65). Computational modelling predicted the peptide would lie in the substrate-binding channel and ring A interactions would be maintained. The first Asp was expected to contact His160, as previously observed, and the C-terminal Asp was predicted to interact with Lys158 and Ser194.

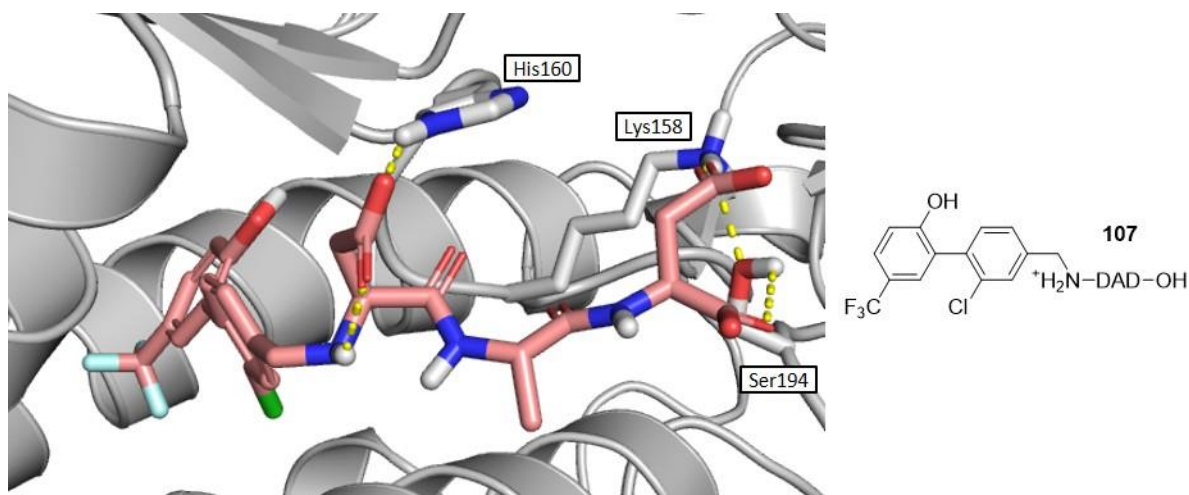
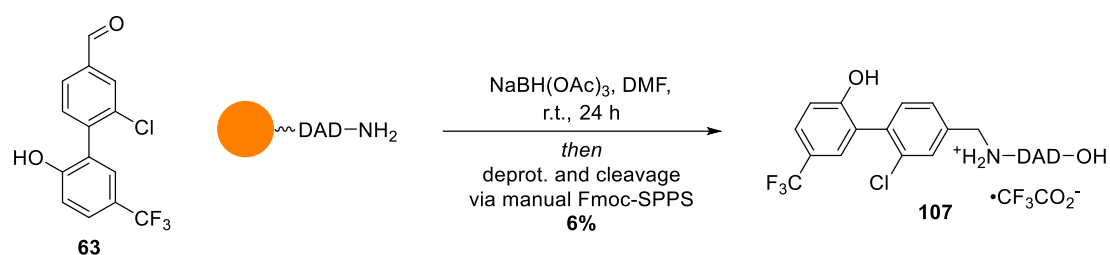


Figure 65: Computational modelling result for investigation into increasing flexibility of the peptide chain. Reductive amination product **107** (pink) is shown on CK2 α (grey). Predicted polar interactions between the fragment, protein residues (white) and water molecules are highlighted by yellow dashed lines.

Synthesis of species **107** by literature Fmoc-SPPS reductive amination provided the desired test species in poor yield, but sufficient quantity for X-ray crystallography (Scheme 17).³⁰⁹ Inspection of the crystallography data showed clear electron density for the α D-site portion of derivative **107**, but the peptide chain could not be resolved. This investigation was terminated here.



Scheme 17: Synthesis of reductive amination product **107** to investigate peptide chain flexibility.³⁰⁹ The orange circle represents the resin-bound peptide.

Investigation 3: Changing the chirality of the peptide chain

The final strategy was to change the chirality of the first peptide residue from an *L*-Asp to a *D*-Asp. It was envisaged that this would maintain the Asp-His160 interaction but the peptide chain would be forced to change direction. In order to test this theory, tripeptides bearing a *D*-Asp adjacent to the α D-site fragment were modelled onto CK2 α . Two peptides, dAD **108** and dKD **109**, provided the best predicted results (Figure 66).

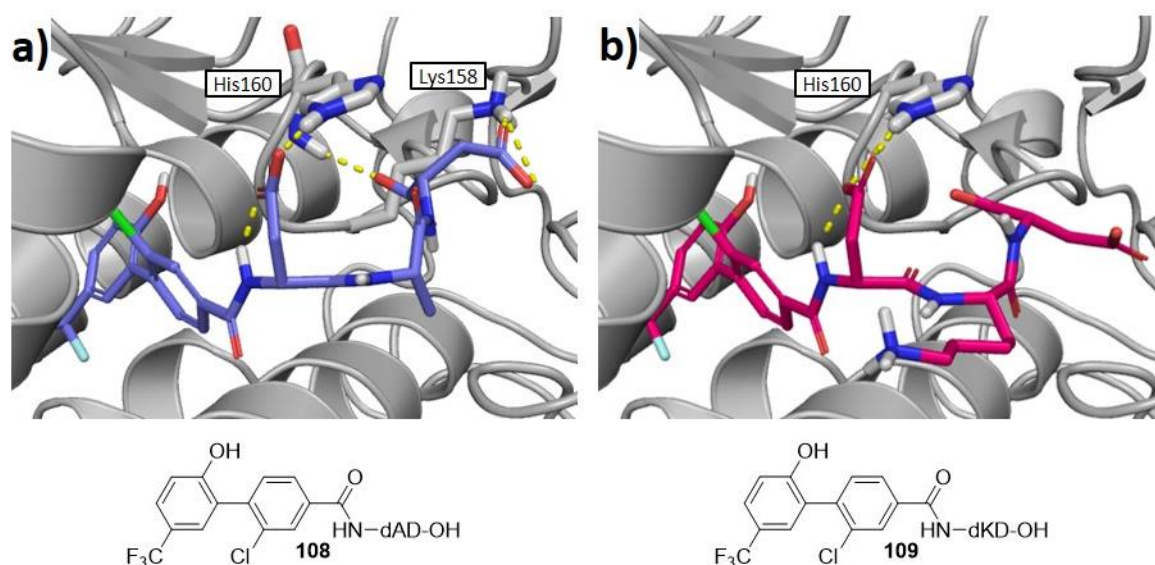


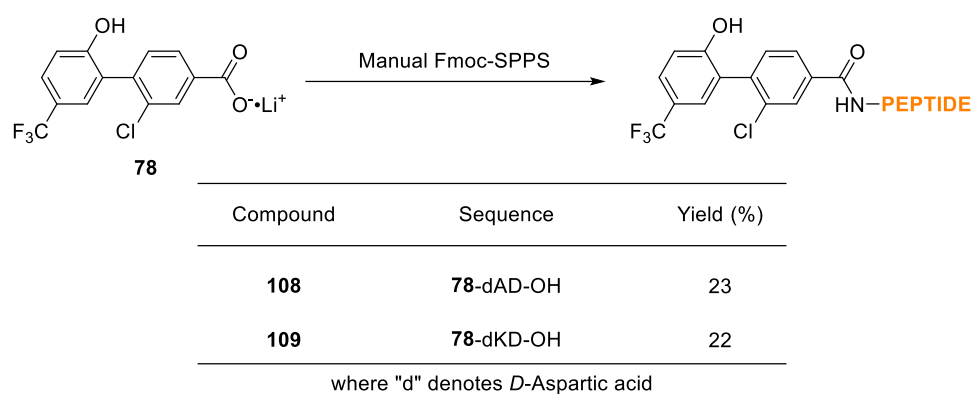
Figure 66: Computational modelling results for investigation into changing the chirality of the peptide chain. **a)** dAD derivative **108** (blue). **b)** dKD derivative **109** (magenta). Predicted polar interactions between the fragment, protein residues (white) and water molecules are highlighted by yellow dashed lines.

In both cases, the ring A and Asp-His160 H-bonding interactions were maintained (Figure 66). The remaining two residues of the tripeptide chain were also predicted to bind along the substrate channel. For dAD species **108**, the Ala residue filled space and the C-terminal Asp made two HBA interactions with Lys158 and the backbone of His160 (Figure 66, **a**). dKD derivative **109** was not

predicted to make any electrostatic interactions other than Asp-His160, but the peptide chain was accommodated neatly within the substrate channel, thus this ligand was considered for synthesis (Figure 66, **b**).

Manual Fmoc-SPPS of *D*-Asp fragments **108** and **109** proceeded without complication to provide the desired linkers in moderate yields (Table 18). The samples were then submitted for structural determination by X-ray crystallography.

Table 18: Manual Fmoc-SPPS of linkers **108** and **109** to investigate changing amino acid chirality.



To our delight, X-ray crystallography for both tripeptides **108** and **109** gave binding modes within the substrate-binding channel (Figure 67). Both ligands were observed to bind selectively within the α D pocket and the ring A position was maintained. In further detail, dAD species **108** was seen to bind in two modes, both of which projected along the substrate-binding channel (Figure 67, **a**). In one mode, the *D*-Asp interaction with His160 was maintained, but in the second it was lost. In both modes, the Ala residue filled space and the *C*-terminal Asp contacted Lys158 and the backbones of His160 and Tyr196. The tripeptide backbone was observed to interact with two water molecules and Glu230. The second ligand, dKD **109**, was found to bind CK2 α with one binding mode (Figure 67, **b**). The *D*-Asp was not reported to interact with His160. The Lys residue in the middle of the tripeptide chain was not shown to contact the protein either, but the *C*-terminal Asp interacted with Ser194 and the backbone of His160. Two water molecules and Glu230 were reported to contact the tripeptide backbone in a similar manner to dAD species **108**.

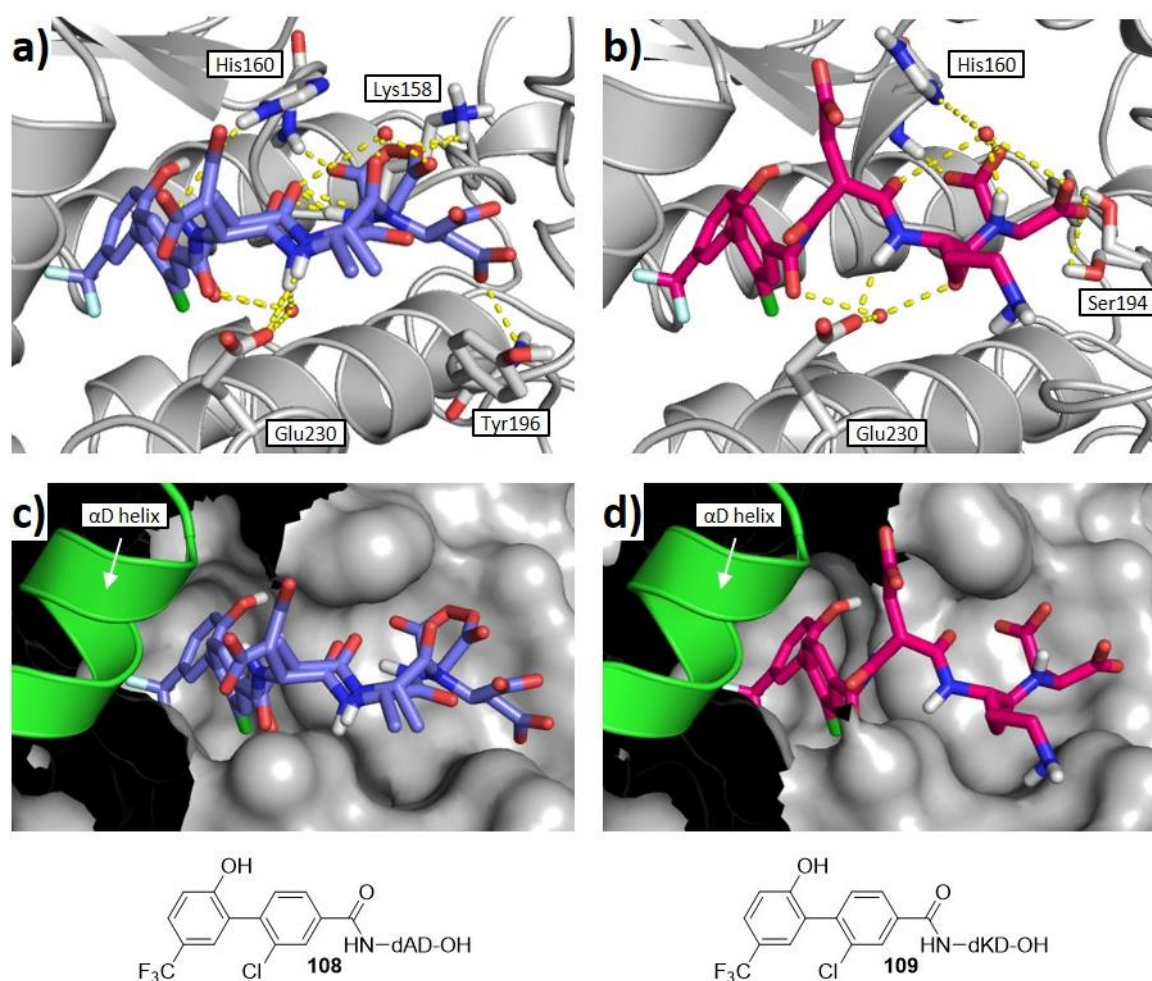


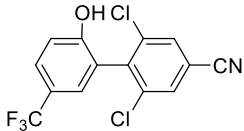
Figure 67: X-ray crystallography results for investigation into D-Asp linkers. **a)** dAD derivative **108** (blue). **b)** dKD derivative **109** (magenta). **c)** dAD derivative **108** (blue) with CK2 α protein surface (grey) and α D helix (green). **d)** dKD derivative **109** (magenta) with CK2 α protein surface (grey) and α D helix (green). Polar interactions between the fragment, protein residues (white) and water molecules are highlighted by yellow dashed lines.

In order to show ligands **108** and **109** protruding from the α D pocket, and projecting towards the substrate-binding channel, the protein surface was laid over the X-ray crystal structures (Figure 67, **c** and **d** respectively). The α D helix is shown as a cartoon so that the pocket opening is better revealed. In both cases, the tripeptide chain lies on the surface of the protein and within the narrow groove at the terminus of the substrate-binding channel.

Following the successful X-ray crystallography, D-Asp fragments **108** and **109** were submitted for biochemical assessment by kinase inhibition assay (Table 19). Pleasingly, dAD linker **108** performed well, reporting 96% kinase activity inhibition. Within statistical error, this was comparable to α D-site lead fragment **67** which inhibited activity by 95%. Additionally, an IC₅₀ value of 23 μ M was recorded for linker species **108**, which is weaker, but still comparable, to lead **67** (9 μ M IC₅₀). Unfortunately, dKD

109 performed poorly in the assay with only 9% activity inhibition, and as a result this linker was not considered further.

Table 19: Biochemical assessment of *D*-Asp linkers **108** and **109** and comparison to lead benzonitrile fragment **67**.

Compound	Structure	% inhib. @ 100 (μ M) \pm SEM ^{[a][b]}	IC ₅₀ \pm SEM (μ M) ^{[a][c]}
67		95 \pm 6	9 \pm 5
108	78-dAD-OH	96 \pm 1	23 \pm 15
109	78-dKD-OH	9 \pm 6	n.d.

[a] Measured by CK2 α ADP-gloTM kinase assay. [b] Tests carried out in triplicate and reported as the mean. [c] Tests carried out in duplicate and reported as the mean. n.d.: no data

In summary, three alternative strategies for linker development were investigated. The first two strategies focussed on linker rigidity and linker flexibility respectively. However, despite promising computational data no X-ray crystal structures could be resolved for these species. The third strategy substituted an *L*-Asp for a *D*-Asp within the tripeptide linker. Two ligands, dAD **108** and dKD **109**, were synthesised and showed the desired binding mode in X-ray crystallography. To the best of our knowledge, this is the first example of a fully resolved X-ray crystal structure of CK2 α with a small molecule co-crystallised in the substrate-binding channel. Subsequent biochemical assessment of the *D*-Asp species showed dAD derivative **108** as far superior to dKD **109**, and comparable to previous lead fragment, benzonitrile **67**.

To conclude, an α D-site anchored tripeptide was successfully designed, synthesised and tested. Ligand **108**, bearing the sequence dAD, displayed strongest electron density along the substrate-binding channel and performed best in the CK2 α inhibition assay. Following this result, the project moved on to the final step: fragment linking to hexamer peptide **75**.

2.3.5 Fragment Linking

With dAD tripeptide **108** in hand, project focus turned towards joining this fragment to hexamer **75**. To assess the feasibility of this aim, modelled hexamer **75** was overlaid with the X-ray crystal structure of tripeptide **108** (Figure 68). CK2 α residues that are crucial for substrate recognition were inspected and pleasingly multiple electrostatic contacts between the protein and peptide **75** were predicted. This confirmed that the binding of ligand **108** to CK2 α did not significantly disrupt the conformation of the substrate-binding channel.

In detail, the $n-2$ Asp was expected to contact Arg195 and the $n-1$ Asp was expected to interact with the backbone of Lys49. The Asp at $n+1$ was within range to contact Arg191 and Lys198, which matched reports in the literature.^{142,143} The two C-terminal Asp residues were not predicted to contact the protein, but this is due to the Lys74-Lys76 Ala mutant used for crystallography.

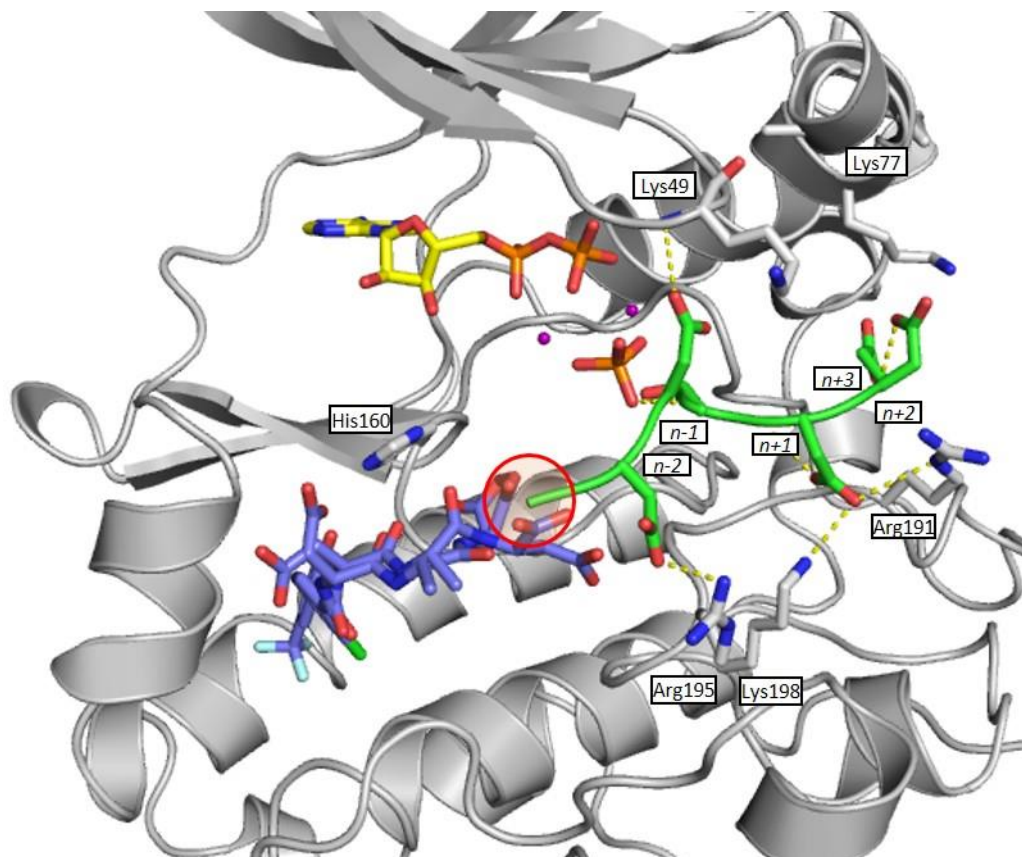
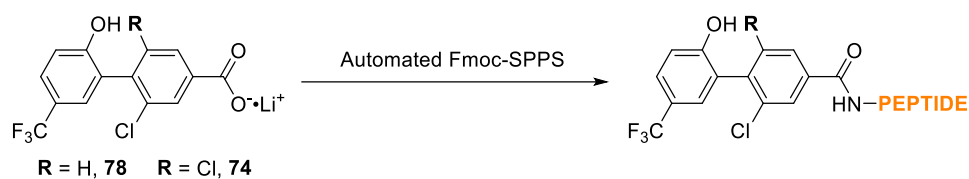


Figure 68: Overlay of modelled hexamer **75** (green) and dAD linker **108** (blue) protein crystal structure (grey) with ADP (yellow), phosphate (orange) and Mg^{2+} (purple) in the ATP-site. CK2 α residues involved with substrate recognition are highlighted (white) and predicted polar contacts are shown as dashed yellow lines. This protein is a K74-K76 alanine mutant. The relative positioning of dAD linker **108** and the N-terminal tail of hexamer **75** (red circle) implied that directly linking the two species may be possible.

Visual inspection of the C-terminal Asp of tripeptide **108** relative to the N-terminal Asp of hexamer **75**, showed significant overlap of these two moieties (Figure 68). This suggested that direct linkage of these two species *via* an amide bond may provide the chemical probe desired in the project aim (Section 2.3.2). This proposed ligand would be nine amino acids long with an α D anchoring fragment at the N-terminus. The peptide sequence would be: dADDDSDDD.

To this end, automated Fmoc-SPPS using a Liberty Blue Peptide Synthesiser was performed to provide proposed chemical probe **110** in moderate yield (Table 20). 3,5-Dichloro carboxylate **74** was also available, so synthesis was repeated using this α D-site fragment to give second probe **111** also in moderate yield.

Table 20: Automated Fmoc-SPPS and X-ray crystallography results for chemical probes **110** and **111**.



Compound	Sequence	Yield (%)	α D fragment resolved?	Peptide chain resolved?
110	78 -dADDDSDDD-OH	13	Y	N
111	74 -dADDDSDDD-OH	15	n.d.	n.d.

d: *D*-Aspartic acid. Y: yes, electron density strong enough to resolve accurately.
 N: no, electron density too weak to resolve accurately. n.d.: no density observed

Following synthesis of probes **110** and **111**, X-ray crystallography was performed to determine the binding modes. Monochloro derivative **110** was observed to bind selectively within the α D pocket with good electron density, but the peptide chain could not be resolved (Table 20). Unfortunately, no electron density was detected at any site on CK2 α for 3,5-dichloro derivative **111**.

In conclusion, a tripeptide linker with α D-site anchor (**108**) was successfully designed and synthesised. Overlay of this structure with hexamer peptide **75**, derived from molecular dynamics, showed potential for the two species to be directly linked *via* an amide bond. Synthesis of two chemical probes, **110** and **111**, was performed without complication, however X-ray crystallography failed to accurately reveal the binding modes for the two species. Further work is currently ongoing in the Spring/Hyvönen groups to investigate this issue.

Chapter Three: Conclusions and Future Work

3.1 Conclusions

The project reported in this thesis was a continuation of the work published by Brear *et al.* on the α D pocket of protein kinase CK2.^{265–267} It was based on the elaboration of Brear *et al.*'s lead fragment **34** at the 3-position of ring A, in order to investigate the flexibility of the α D pocket.

A compound library of biaryl, benzylamine fragments was designed and screened *in silico* against CK2 α , using the X-ray crystal structure for lead species **34** (Figure 69, **a**). Docking results were analysed, and fragments predicted to maintain the binding pose of lead **34**, while efficiently occupying the pocket space adjacent to the 3-position of ring A, were considered for synthesis. A robust and modular synthetic route to access the benzylamine scaffold was determined, and a target-oriented fragment library consisting 11 members was synthesised. X-ray crystallography revealed seven fragments bound selectively in the α D pocket, and of these, three fragments (**55**, **56** and **59**) were observed to maintain the binding mode of lead benzylamine **34**. Biochemical assessment reported poor binding affinities for these fragments ($K_d > 750 \mu\text{M}$) and no activity inhibition in the CK2 α kinase assay. The remaining four fragments bound in the α D pocket *via* two unpredicted, and previously unreported, binding modes. Dibenzylamine derivative **44** created a new, solvent-exposed α D pocket opening, but had poor binding affinity ($K_d > 750 \mu\text{M}$) and was not observed to inhibit kinase activity. The final three fragments (**46**, **57** and **58**) adopted a binding mode perpendicular to Brear *et al.*'s lead **34**, and forced a pocket opening into the substrate-binding channel (Figure 69, **b**). Derivatives **46**, **57** and **58** were reported to inhibit CK2 α kinase activity (19, 28 and 32% respectively) despite the weak binding affinities (>750, >750 and 750 μM respectively). Analysis of the new binding mode revealed crucial rearrangement of three protein residues (Phe121, Tyr125 and Glu230) relative to Brear *et al.*'s published binding pose.

Trifluoro derivative **58** was the most potent of the fragments adopting the new binding mode, and thus provided a hit species for elaboration into more effective CK2 α inhibitors. Subsequent work modified ring A at the 6-position to introduce a H-bonding group (Figure 69, **c**). X-ray crystallography of alcohol derivative **61** revealed interactions between the alcohol moiety, Pro159 and an α D pocket water molecule. Improved CK2 α inhibition relative to hit **58** was reported (44% compared to 32%) and an IC_{50} value of 100 μM was recorded. Next, the amine head group was substituted for less polar moieties, which led to the development of benzonitrile **61a** (Figure 69, **c**). Structural analysis by X-ray crystallography showed ring A interactions were maintained and that polar contacts involving the

nitrile of **61a** were reduced relative to the amine of **61**. Following biochemical assessment, benzonitrile **61a** was observed to inhibit kinase activity by 80% and provided an IC₅₀ value of 51 μM – an improvement on prior benzylamine **61** in both cases. A GI₅₀ value of 69 μM was also determined. Finally, the substitution pattern of ring B was optimised in order to better fill this portion of the binding pocket. A library of eight fragments was synthesised and 3,5-dichloro derivative **67** performed best in the kinase assay (95% relative to 80% for benzonitrile **61a**) (Figure 69, c). Analysis of the X-ray crystal structure for 3,5-dichloro fragment **67** revealed that the ring A and nitrile binding positions were maintained and that the additional chlorine occupied a previously vacant space towards the front of the pocket (Figure 69, d). Relative to benzonitrile **61a**, superior IC₅₀ and GI₅₀ values of 9 and 16 μM were recorded for 3,5-dichloro species **67**. Furthermore, this GI₅₀ activity level was comparable to that of Brear *et al.*'s best lead, pro-CAM4066 **37**, which was reported as 9 μM.²⁶⁵ The SBDD programme thus resulted in the discovery of lead fragment 3,5-dichloro benzonitrile **67**.

Following development of optimised lead benzonitrile inhibitor **67**, three mechanisms by which it could induce negative allosteric control over CK2α were presented. These included disruption of the ATP- and substrate-binding sites and inhibition of the transition between the open and closed forms of CK2α. Analysis of overlaid X-ray crystal structures and literature precedent provided grounding for each hypothesis, but confirmation of these theories was beyond the scope of this project.

To the best of our knowledge, lead fragment 3,5-dichloro **67** represented a first-in-class allosteric inhibitor, binding selectively in the αD pocket of CK2. Furthermore, this was the first observation of fragments binding in the αD pocket and adopting this binding mode. An αD pocket opening towards the substrate-binding channel had not previously been reported in the literature, and presented an exploitable exit vector for investigation of the substrate-binding site. To this end, a linker strategy was envisaged, in which optimised αD-site fragment **67** could be linked to CK2-selective pseudosubstrate **75**. It was postulated that the αD-site portion of the molecule would anchor the species to the protein and enable X-ray crystallography of the pseudosubstrate in complex with the substrate-binding channel.

To begin linker development, the nitrile head groups of lead fragment **67** and earlier derivative **61a** were exchanged for lithium carboxylate groups. A variety of tri- and tetra-peptide linkers with αD-site fragment **61a** anchors were then designed, synthesised and tested by X-ray crystallography. Analysis of the structural data revealed that the peptidic portions of these molecules did not lie within the substrate-binding channel as hoped. Instead, they formed H-bonding interactions with Lys122 on the αD helix, or were disordered within the solvent and thus unresolved. Introduction of an *L*-Asp residue to the peptide chain led to the development of tripeptide linker species dAD **108** which crystallised in

the α D pocket and substrate-binding channel as desired (Figure 69, e). Biochemical data comparable to lead benzonitrile fragment **67** was collected for dAD derivative **108**, with 96% kinase inhibition and an IC_{50} of 23 μ M. Amide bond fragment linking between anchored dAD linker **108** and hexamer **75** was performed to provide final chemical probe **110**. This species was observed to bind the α D pocket of CK2 α , however the peptide chain was disordered and could not be resolved.

In conclusion, this project validated the use of FBDD against protein kinase CK2 in the search for a novel binding pocket and allosteric mode of action. A first in class negative allosteric inhibitor, fragment **67**, binding in the α D pocket of protein kinase CK2 α was developed. Lead fragment **67** was then elaborated into anchored tripeptide **108** which provided the first fully resolved X-ray crystal structure of CK2 α with a small molecule accommodated in the substrate-binding site. This work could be used towards the future development of α D-site selective inhibitor fragments, and provides a starting point for further investigation of the substrate-binding channel.

3.2 Future Work

The future work for this project can be divided into four areas: the binding mode, the negative allosteric mode of action, further development of the α D-site fragment and the substrate-binding channel probe.

With respect to the novel binding mode, the future work would be to better understand the factors promoting this fragment pose over that reported by Brear *et al.*²⁶⁵ Since numerous X-ray crystal structures for both binding modes are available, molecular dynamics simulations could be performed in order to determine the contribution of the trifluoro group towards binding.

The negative allosteric mode of action for lead fragment **67** is yet to be fully investigated. Three mechanisms for the proposed allosteric inhibition were presented, but the hypotheses were not experimentally verified. This work would require CK2 α residue mutation studies to ascertain the impact of lead fragment **67** on the ATP- and substrate-binding sites.^{264,288–290} A study into the ability of CK2 α to recognise different substrates would also be necessary in order to analyse the predicted disruption to the substrate-binding channel.²⁹¹ The effect of fragment **67** on the transition between the open and closed forms of CK2 α would require molecular dynamics simulations and NMR studies of labelled CK2 α .^{264,289} An improved understanding of the mechanism of action would aid future development of α D-site inhibitors.

When considering lead benzonitrile **67**, an additional round of optimisation could be performed. This would focus on interrogating the flexibility of the α D pocket around the trifluoro group by substitution

with bulkier moieties (Figure 70). As reported previously, the α D helix has been observed to move by as much as 23.8 Å from its position in the closed Apo protein,²⁶⁶ and thus fragments larger than lead **67** might be accommodated. If fragments are able to bind deeper within the α D pocket, then they may display enhanced potency. The X-ray crystal structure of lead benzonitrile **67** in complex with CK2 α could be used as a starting point for the design of new fragments.

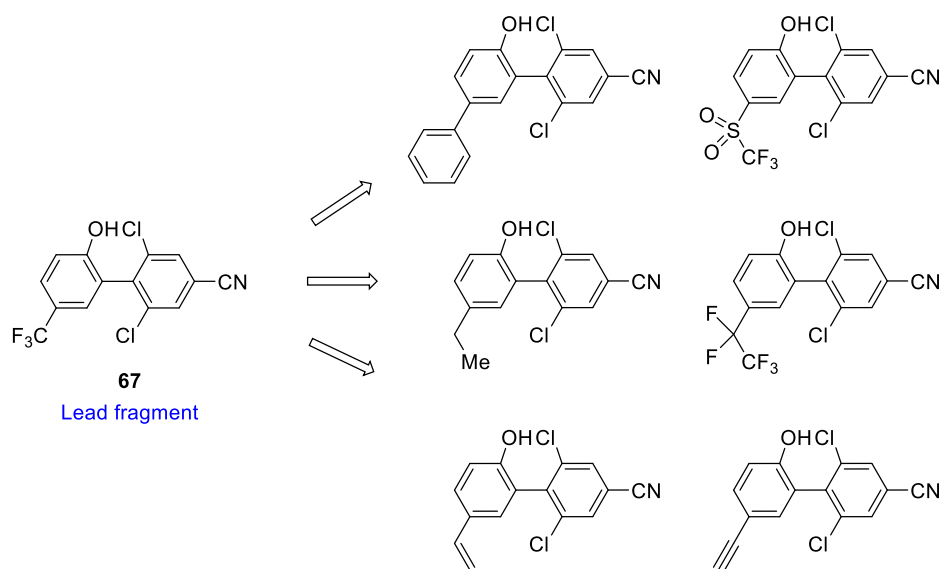


Figure 70: Future work to investigate the flexibility of the α D pocket around the trifluoro group of lead fragment **67**. Analysis of the X-ray crystal structure of fragment **67** in complex with CK2 α showed the pocket is lined by hydrophobic residues, thus non-polar substituents would be appropriate for testing.

Finally, the linking strategy adopted to investigate the substrate-binding channel did not return an effective chemical probe. Molecular dynamics simulations could be performed using α D-site anchored tripeptide **108** and pseudosubstrate **75** in order to better understand the relative binding positions of these two species. From this, a more informative decision towards linking the two molecules could be made.

Chapter Four: Experimental

4.1 General Experimental

Toluene, hexane, diethyl ether, ethyl acetate, methanol, THF and dichloromethane were dried and distilled using standard methods.²⁹³ All reagents and other solvents were purchased at the highest commercial quality and used without further purification. Reactions were carried out under an atmosphere of nitrogen and in oven-dried glassware unless otherwise stated. All reactions were monitored by TLC, LCMS and ¹H NMR spectra taken from the reaction.

Room temperature (r.t.) refers to ambient temperature. All temperatures below 0 °C are that of the external bath. Temperatures of 0 °C were maintained using an ice-water bath.

Microwave irradiation was performed in a Biotage® microwave reactor.

Analytical thin layer chromatography (TLC) was performed using pre-coated Merck glass backed silica gel plates (Silicagel 60 F254). Flash column chromatography was undertaken on Fluka or Material Harvest silica gel (230–400 mesh) under a positive pressure of nitrogen unless otherwise stated. Visualization was achieved using ultraviolet light (254 nm) and chemical staining with basic potassium permanganate solution or ninhydrin as appropriate. Retention factors (R_f) are quoted to 0.01.

Liquid chromatography-mass spectra (LCMS) were measured on a Waters ACQUITY H-Class UPLC with an ESCi Multi-Mode ionization Waters SQ Detector 2 spectrometer (LC system: solvent A: 2mM ammonium acetate in water/acetonitrile (95:5); solvent B: 100% acetonitrile; column: AQUITY UPLC CSH C18, 2.1 x 50 mm, 1.7 μ m, 130 Å; gradient: 5-95% B over 3 min with constant 0.1% formic acid). Retention times (t_r) are quoted to 0.01 min.

Analytical high pressure liquid chromatography (HPLC) was performed on an Agilent 1260 Infinity system fitted with a Supelcosil ABZ+Plus column (150 mm x 4.6 mm, 3 μ m) using linear gradient systems (solvent A: 0.05% (v/v) TFA in water, solvent B: 0.05% (v/v) TFA in acetonitrile) over 15 min at a flow rate of 1 mL min⁻¹ and UV detection (λ_{max} = 220 nm and 254 nm). Retention times (t_r) are quoted to 0.01 min.

Semi-preparative HPLC purification was performed on an Agilent 1260 Infinity system fitted with a Supelcosil ABZ+Plus column (250 mm x 21.2 mm, 5 μm) using linear gradient systems (solvent A: 0.1% (v/v) TFA in water, solvent B: 0.05% (v/v) TFA in acetonitrile) over 20 min at a flow rate of 20 mL min^{-1} and UV detection ($\lambda_{\text{max}} = 220 \text{ nm}$ and 254 nm).

Melting points were obtained on a Buchi B-545 melting point apparatus and are uncorrected.

Infrared (IR) spectra were recorded on a Perkin Elmer Spectrum One FT-IR Spectrometer fitted with an ATR sampling accessory as either solids or neat films, either through direct application or deposited in CDCl_3 . Selected absorptions are reported in wavenumbers (cm^{-1}) with the following abbreviations: w, weak; m, medium; s, strong; br, broad.

Magnetic resonance spectra were processed using MestReNova v. 6.0.2-5475 or TopSpin v. 3.5 (Bruker). An aryl, quaternary, or two or more possible assignments were given when signals could not be distinguished by any means. Measured coupling constants are reported uncorrected or as a multiplet when coupling constant cannot be determined.

Proton magnetic resonance spectra were recorded using an internal deuterium lock (at 298 K unless stated otherwise) on Bruker DPX (400 MHz; ^1H - ^{13}C DUL probe), Bruker Avance III HD (400 MHz; Smart probe), Bruker Avance III HD (500 MHz; Smart probe) and Bruker Avance III HD (500 MHz; DCH Cryoprobe) spectrometers. Proton assignments are supported by ^1H - ^1H COSY, ^1H - ^{13}C HSQC or ^1H - ^{13}C HMBC spectra, or by analogy. Chemical shifts (δ) are quoted in ppm to the nearest 0.01 ppm and are referenced to the residual non-deuterated solvent peak. Discernible coupling constants for mutually coupled protons are reported as measured values in Hertz, rounded to the nearest 0.1 Hz. Data are reported as: chemical shift, number of nuclei, multiplicity (br, broad; s, singlet; d, doublet; t, triplet; q, quartet; m, multiplet; or a combination thereof), coupling constants and assignment. Diastereotopic protons are assigned as X and X', where X' designates the lower-field proton.

Carbon magnetic resonance spectra were recorded using an internal deuterium lock (at 298 K unless stated otherwise) on Bruker DPX (101 MHz), Bruker Avance III HD (101 MHz) and Bruker Avance III HD (126 MHz) spectrometers with broadband proton decoupling. Carbon spectra assignments are supported by DEPT editing, ^1H - ^{13}C HSQC or ^1H - ^{13}C HMBC spectra, or by analogy. Chemical shifts (δ) are quoted in ppm to the nearest 0.1 ppm and are referenced to the deuterated solvent peak. Data are reported as: chemical shift, number of nuclei (if not one), multiplicity (if not a singlet), coupling constants and assignment.

For F-containing compounds, the presence of F substituent(s) was confirmed from splitting patterns in ^{13}C NMR spectra.

The numbering of molecules used for ^{13}C and ^1H NMR assignments does not conform to IUPAC standards.

High-resolution mass spectra (HRMS) were measured on a Micromass Q-TOF or a Waters LCT Premier Mass Spectrometer using electrospray ionisation [ESI]. Masses are quoted within the 5ppm error limit.

4.2 General Methods

4.2.1 General Method A: Phenol triflation

To a solution of phenol (1.0 eq.) in anhydrous CH_2Cl_2 (~0.3 M) was added pyridine (3.0 eq.) or NEt_3 (2.25 eq.). The solution was cooled to 0 °C and trifluoromethanesulfonic anhydride (1.1 – 1.4 eq.) was added dropwise over 30 minutes. The reaction was allowed to warm to room temperature and stirred overnight. The volatiles were removed under reduced pressure and the residue was diluted with H_2O and extracted with EtOAc three times. The organic layer was washed with 10% aqueous HCl, 5% aqueous Na_2CO_3 , a saturated aqueous solution of NaCl and H_2O , then dried over MgSO_4 , filtered and concentrated *in vacuo*. The crude product was then purified by flash column chromatography to yield the desired product.

Conditions adapted from literature protocol.²⁵⁹

4.2.2 General Method B: Suzuki coupling of unhindered substrates

The aryl bromide (1.10 eq.), appropriate boronic acid (1.00 eq.), $\text{PdCl}_2(\text{dppf})\cdot\text{CH}_2\text{Cl}_2$ (0.05 eq.) and K_3PO_4 (1.20 eq.) were weighed into a microwave tube and solvated with DME (0.3 – 0.5 M), EtOH (1.3 – 1.5 M) and H_2O (2.1 – 2.3 M). The reaction mixture was degassed by bubbling nitrogen through the solution for 5 minutes and then heated to 110 °C under microwave irradiation for 1-2 hours, until completion by TLC monitoring. The reaction was allowed to cool to room temperature, filtered through celite washing with Et_2O and the solvent removed under reduced pressure. The residue was dissolved in $\text{Et}_2\text{O}/\text{H}_2\text{O}$ and extracted three times with Et_2O . The combined organic extracts were washed with a saturated aqueous solution of NaCl, dried over MgSO_4 , filtered and concentrated *in vacuo*. The crude product was then purified by flash column chromatography to yield the desired product.

Conditions adapted from literature protocol.²⁶¹

4.2.3 General Method C: Benzonitrile reduction

To a stirred suspension of LiAlH₄ (2.0 – 4.0 eq.) in Et₂O (~0.25 M) was added AlCl₃ (2.0 – 4.0 eq.) and the reaction mixture cooled to 0 °C for 10 minutes. The reaction was allowed to warm to room temperature and the nitrile (1.0 eq.) was added portionwise. The reaction was stirred at room temperature for 30 minutes and then heated at 50 °C overnight. After cooling to room temperature, a saturated aqueous solution of potassium sodium tartrate tetrahydrate and Et₂O were added and the mixture stirred for 1 hour. The reaction mixture was diluted with 2.0 M aqueous NaCO₃ and extracted three times with Et₂O. The combined organic extracts were washed with a saturated aqueous solution of NaCl, dried over MgSO₄, filtered and concentrated *in vacuo*. The crude product was then purified by flash column chromatography or semi-preparative HPLC, as determined necessary by ¹H NMR and LCMS analysis of the crude reaction mixture, to yield the desired product.

Conditions adapted from literature protocol.^{250,251}

4.2.4 General Method D: Suzuki coupling of hindered substrates

The aryl bromide (1.0 eq.), appropriate boronic acid (1.2 eq.), Pd(OAc)₂ (0.05 eq.), S-Phos (0.10 eq.) and K₃PO₄ (2.00 eq.) were weighed into an oven-dried RBF and solvated with toluene (0.5 M) and H₂O (3.5 M). The reaction mixture was degassed and back-filled with nitrogen before heating at 60 °C for 18 hours. The reaction was allowed to cool to room temperature, filtered through celite washing with Et₂O and the solvent removed under reduced pressure. The residue was dissolved in Et₂O/H₂O and extracted three times with Et₂O. The combined organic extracts were washed with a saturated aqueous solution of NaCl, dried over MgSO₄, filtered and concentrated *in vacuo*. The crude product was then purified by flash column chromatography to yield the desired product.

Conditions adapted from literature protocol.²⁷²

4.2.5 Manual Fmoc Solid-Phase Peptide Synthesis (Fmoc-SPPS)

Peptides were synthesised using Rink amide MBHA resin (loading: 0.40 mmol/g), pre-loaded Asp Wang resin (loading: 0.70 mmol/g), pre-loaded Glu Wang resin (loading: 0.65 mmol/g) or pre-loaded Asn Wang resin (loading: 0.58 mmol/g) and *N*-terminal capping was performed with lithium carboxylate **78**. The side-chain protecting groups used for the different amino acids were as follows: ^tBu for

aspartic acid, glutamic acid and serine; Boc for lysine and tryptophan; and Trt for asparagine and glutamine.

Reactions were conducted in disposable 12 mL syringes with 20 μm frits on a Vac-Man Laboratory Vacuum Manifold.

Resin swelling was carried out with DMF (10 mL) for 30 minutes and the resin was then drained and rinsed with DMF (3 x 6 mL), MeOH (3 x 6 mL) and CH_2Cl_2 (3 x 6 mL).

Fmoc deprotections were performed with a solution of 6% (w/w) piperazine in DMF with 0.1 M HOBT additive (6 mL, 2 x 1 minute) with vigorous shaking and washing with DMF (3 x 6 mL), MeOH (3 x 6 mL) and CH_2Cl_2 (3 x 6 mL) after the second deprotection step.

Fmoc-protected amino acid couplings were performed by first pre-activating the fmoc amino acid (2 eq.) with HATU (2 eq.) in DMF (3 mL) for 5 minutes. This solution was added to the resin and shaken vigorously for 30 seconds before the addition of DIPEA (4 eq.) and vigorous shaking for 3 minutes. The resin was drained and rinsed with DMF (3 x 6 mL), MeOH (3 x 6 mL) and CH_2Cl_2 (3 x 6 mL).

Deprotection and coupling completion was monitored by the Chloranil test. A saturated solution of chloranil in toluene (50 μL) was mixed with acetaldehyde (200 μL) in a clean vial and a small portion of dry resin added. The vial was capped and shaken vigorously for 30 seconds. No discolouration of the beads indicated a completed coupling step whereas a blue discolouration of the beads indicated incomplete coupling. In the case of incomplete coupling the resin was subjected to a second round of coupling conditions.

N-terminal capping with lithium carboxylate **78** was performed following the same procedure as for fmoc-protected amino acid coupling except without the addition of DIPEA.

Peptide-resin cleavage and side-chain deprotection was carried out by treatment with a TFA/ H_2O /TIPS 95:2.5:2.5 cleavage cocktail (10 mL) for 30 minutes. The mixture was filtered, the resin washed with MeCN and the solvent removed under a stream of nitrogen. The crude peptide residue was then triturated with ice-cold Et_2O before LCMS analysis and semi-preparative HPLC purification.

4.2.6 Microwave Fmoc Solid-Phase Peptide Synthesis (Fmoc-SPPS)

Peptides were synthesised using Rink amide MBHA resin (loading: 0.40 mmol/g), pre-loaded Asp Wang resin (loading: 0.70 mmol/g), pre-loaded Glu Wang resin (loading: 0.65 mmol/g) or pre-loaded Asn Wang resin (loading: 0.58 mmol/g) and *N*-terminal capping was performed with lithium carboxylate **78**. The side-chain protecting groups used for the different amino acids were as follows: $t\text{Bu}$ for

aspartic acid, glutamic acid and serine; Boc for lysine and tryptophan; and Trt for asparagine and glutamine.

Reactions were conducted in 25 mL glass microwave vials using a Biotage® microwave reactor. The resin was transferred into disposable 12 mL syringes with 20 µm frits on a Vac-Man Laboratory Vacuum Manifold for drainage and washing steps.

Resin swelling was carried out with DMF (10 mL) for 30 minutes and the resin was then drained and rinsed with DMF (3 x 6 mL), MeOH (3 x 6 mL) and CH₂Cl₂ (3 x 6 mL).

Fmoc deprotections were performed with a solution of 6% (w/w) piperazine in DMF with 0.1 M HOBt additive (10 mL) for 3 minutes at 70 °C and 35 W followed by drainage and washing with DMF (3 x 6 mL), MeOH (3 x 6 mL) and CH₂Cl₂ (3 x 6 mL).

Fmoc-protected amino acid couplings were performed by first pre-activating the fmoc amino acid (4 eq.) with HATU (4 eq.) in DMF (6 mL) for 5 minutes. This solution was added to the resin along with DIPEA (12 eq.) and the microwave vial sealed rapidly. The microwave coupling reaction was performed for 5 minutes at 72 °C and 25 W. The resin was drained and rinsed with DMF (3 x 6 mL), MeOH (3 x 6 mL) and CH₂Cl₂ (3 x 6 mL).

Deprotection and coupling completion was monitored by the Chloranil test. A saturated solution of chloranil in toluene (50 µL) was mixed with acetaldehyde (200 µL) in a clean vial and a small portion of dry resin added. The vial was capped and shaken vigorously for 30 seconds. No discolouration of the beads indicated a completed coupling step whereas a blue discolouration of the beads indicated incomplete coupling. In the case of incomplete coupling the resin was subjected to a second round of coupling conditions.

N-terminal capping with lithium carboxylate **78** was not performed using the microwave reactor. Instead lithium carboxylate **78** (2 eq.) was pre-activated with HATU (2 eq.) in DMF (6 mL) for 5 minutes. This solution was added to the resin followed by DIPEA (4 eq.) and the reaction put on the shaker for 18 hours. The resin was drained and rinsed with DMF (3 x 6 mL), MeOH (3 x 6 mL) and CH₂Cl₂ (3 x 6 mL).

Peptide-resin cleavage and side-chain deprotection was carried out by treatment with a TFA/H₂O/TIPS 95:2.5:2.5 cleavage cocktail (10 mL) for 30 minutes at 40 °C and 15 W. The mixture was filtered, the resin washed with MeCN and the solvent removed under a stream of nitrogen. The crude peptide residue was then triturated with ice-cold Et₂O before LCMS analysis and semi-preparative HPLC purification.

Conditions adapted from literature protocol.²⁹¹

4.2.7 Automated Fmoc Solid-Phase Peptide Synthesis (Fmoc-SPPS)

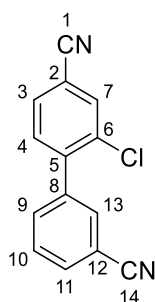
Automated peptide synthesis was carried out on a CEM Liberty Blue Automated Microwave Peptide Synthesiser fitted with a HT-12 resin loader using Rink amide MBHA resin (loading: 0.40 mmol/g) or pre-loaded Asp Wang resin (loading: 0.70 mmol/g). All peptides were synthesised using Fmoc-protected amino acids in DMF (5 eq.), DIC in DMF (1.0 M, 5 eq.) and activator Oxyma Pure in DMF (1.0 M, 10 eq.). Amino acids were coupled for 2 min with microwave irradiation using 30 W power at 90 °C. Fmoc-deprotection was achieved by microwave heating with 20 W power at 90 °C with 6% (w/w) piperazine in DMF with 0.1 M HOBt additive for 1 min.

The side-chain protecting groups used for the different amino acids were as follows: ^tBu for aspartic acid, glutamic acid and serine.

N-terminal capping with lithium carboxylate **74** or **78** was performed manually, as described in Section 4.2.5, except with shaking for 24 hours. The final deprotection and cleavage was performed manually, as described in Section 4.2.5. The crude peptide residue was then triturated with ice-cold Et₂O before LCMS analysis and semi-preparative HPLC purification.

4.3 Experimental Details for Target-Oriented Fragment Library

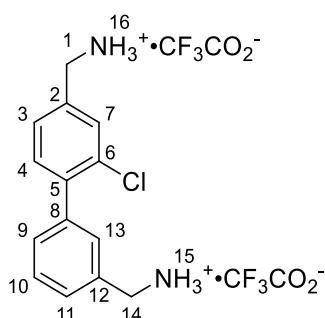
2'-Chloro-[1,1'-biphenyl]-3,4'-dicarbonitrile (**44a**)



Prepared by General Method **B** using 3-chloro-4-bromobenzonitrile (150 mg, 0.69 mmol), 3-cyanophenylboronic acid (93 mg, 0.63 mmol), PdCl₂(dppf).CH₂Cl₂ (26 mg, 0.032 mmol), K₃PO₄ (161 mg, 0.76 mmol), DME (2.0 mL), EtOH (0.5 mL) and H₂O (0.3 mL). The crude product was purified by flash column chromatography (silica gel, gradient elution: 20:80 Et₂O:Hexane to 30:70 Et₂O:Hexane) to provide the title compound **44a** as a white solid (113 mg, 0.47 mmol, 75%):

R_f 0.19 (2:3 Et₂O:Hexane); **m.p.** 153-154 °C; **IR** ν_{\max} 3064 (w, C-H), 2971 (w, C-H), 2232 (s, C≡N), 1579 (w, C=C), 1539 (w, C=C), 1493 (w, C=C); **¹H NMR** (500 MHz, CDCl₃) δ 7.83 (1H, d, *J* = 2.5 Hz, H7), 7.77 – 7.73 (2H, m, H11/H13), 7.70 – 7.76 (2H, m, H3/H9), 7.61 (1H, td, *J* = 7.5, 1.0 Hz, H10), 7.45 (1H, d, *J* = 8.0 Hz, H4); **¹³C NMR** (125 MHz, CDCl₃) δ 142.8 (C5), 138.7 (C8), 133.6 (C7/C9), 133.54 (C6), 133.49 (C7/C9), 132.6 (C13), 132.2 (C11), 131.8 (C4), 130.7 (C3), 129.4 (C10), 118.2 (C14), 117.0 (C1), 113.7 (C2), 112.9 (C12); **HRMS** (ESI) calcd for [C₁₄H₇N₂³⁵Cl + H]⁺: 239.0376, found: 239.0381.

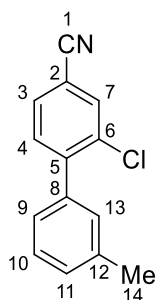
(2'-Chloro-[1,1'-biphenyl]-3,4'-diyl)dimethanamine TFA salt (44)



Prepared by General Method **C** using LiAlH₄ (55 mg, 1.44 mmol), Et₂O (4.0 mL), AlCl₃ (59 mg, 1.44 mmol) and **44a** (85 mg, 0.36 mmol). The crude amine was purified by semi-preparative HPLC (5-35% B) to provide title compound **44** as a yellow oil (78 mg, 0.16 mmol, 46%):

HPLC *t_r* = 6.65 mins (5-35% B); **IR** ν_{\max} 2988 (br s, NH₃⁺), 1667 (s, C=C), 1526 (m, C=C), 1345 (w, C=C); **¹H NMR** (500 MHz, d₆-DMSO) δ 8.44 – 8.24 (6H, m, H15/H16), 7.73 (1H, d, *J* = 1.5 Hz, H7), 7.55 – 7.50 (4H, m, H3/H10/H11/H13), 7.48 – 7.44 (2H, m, H4/H9), 4.15 – 4.07 (4H, m, H1/H14); **¹³C NMR** (125 MHz, d₆-DMSO) δ 139.3 (C5), 138.4 (C8), 135.7 (C2), 134.6 (C12), 131.6 (C4), 131.3 (C6), 130.4 (C7), 129.7 (C10), 129.4 (C9), 128.6 (C11/C13), 128.5 (C11/C13), 128.2 (C3), 42.2 (C14), 41.4 (C1); **HRMS** (ESI) calcd for [C₁₄H₁₅N₂³⁵Cl + H]⁺: 247.1002, found: 247.1000.

2-Chloro-3'-methyl-[1,1'-biphenyl]-4-carbonitrile (45a)

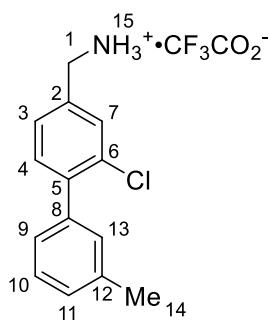


Prepared by General Method **B** using 3-chloro-4-bromobenzonitrile (150 mg, 0.69 mmol), 3-methylphenylboronic acid (86 mg, 0.63 mmol), PdCl₂(dppf).CH₂Cl₂ (26 mg, 0.032 mmol), K₃PO₄ (161

mg, 0.76 mmol), DME (2.0 mL), EtOH (0.5 mL) and H₂O (0.3 mL). The crude product was purified by flash column chromatography (silica gel, elution: 5:95 Et₂O:Hexane) to provide the title compound **45a** as a white solid (120 mg, 0.53 mmol, 84%):

R_f 0.25 (1:19 Et₂O:Hexane); **m.p.** 72–73 °C; **IR** ν_{\max} 3073 (w, C-H), 2971 (w, C-H), 2230 (m, C≡N), 1589 (w, C=C), 1539 (w, C=C), 1475 (m, C=C); **¹H NMR** (500 MHz, CDCl₃) δ 7.78 (1H, d, *J* = 1.0 Hz, H7), 7.61 (1H, dd, *J* = 10.0, 1.0 Hz, H3), 7.45 (1H, d, *J* = 10.0 Hz, H4), 7.37 (1H, t, *J* = 8.0 Hz, H10), 7.28 - 7.25 (1H, m, H11), 7.25 - 7.25 (2H, m, H9/H13), 2.43 (3H, s, H14); **¹³C NMR** (125 MHz, CDCl₃) δ 145.5 (C5), 138.1 (C12), 137.6 (C8), 133.5 (C6), 133.3 (C7), 132.0 (C4), 130.3 (C3), 129.7 (C13), 129.4 (C11), 128.2 (C10), 126.1 (C9), 117.5 (C1), 112.3 (C2), 21.4 (C14); **HRMS** (ESI) calcd for [C₁₄H₁₀N³⁵Cl + H]⁺: 228.0580, found: 228.0577.

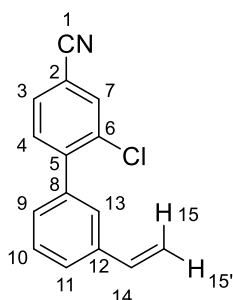
(2-Chloro-3'-methyl-[1,1'-biphenyl]-4-yl)methanamine TFA salt (**45**)



Prepared by General Method **C** using LiAlH₄ (33 mg, 0.88 mmol), Et₂O (2.0 mL), AlCl₃ (116 mg, 0.88 mmol) and **45a** (100 mg, 0.44 mmol). The crude amine was purified by semi-preparative HPLC (20-70% B) to provide title compound **45** as a white solid (70 mg, 0.20 mmol, 46%):

HPLC *t_r* = 7.73 mins (20-70% B); **m.p.** 143–144 °C; **IR** ν_{\max} 2988 (br s, NH₃⁺), 1673 (s, C=C), 1596 (m, C=C), 1530 (m, C=C), 1482 (m, C=C); **¹H NMR** (500 MHz, d₆-DMSO) δ 8.33 (3H, br s, H15), 7.70 (1H, d, *J* = 1.5 Hz, H7), 7.49 (1H, dd, *J* = 8.0, 1.5 Hz, H3), 7.45 (1H, d, *J* = 8.0 Hz, H4), 7.36 (1H, t, *J* = 7.5 Hz, H10), 7.26 - 7.19 (3H, m, H9/H11/H13), 4.11 (2H, s, H1), 2.37 (3H, s, H14); **¹³C NMR** (125 MHz, d₆-DMSO) δ 140.0 (C5), 138.2 (C8), 137.6 (C12), 135.3 (C2), 131.7 (C4), 131.4 (C6), 130.3 (C7), 129.7 (C13), 128.6 (C11), 128.3 (C10), 128.1 (C3), 126.3 (C9), 41.4 (C1), 21.1 (C14); **HRMS** (ESI) calcd for [C₁₄H₁₄N³⁵Cl + H]⁺: 232.0893, found: 232.0897.

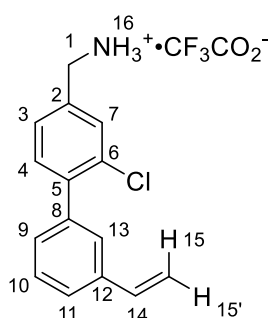
2-Chloro-3'-vinyl-[1,1'-biphenyl]-4-carbonitrile (**46a**)



Prepared by General Method **B** using 3-chloro-4-bromobenzonitrile (150 mg, 0.69 mmol), 3-vinylphenylboronic acid (93 mg, 0.63 mmol), PdCl₂(dppf).CH₂Cl₂ (26 mg, 0.032 mmol), K₃PO₄ (161 mg, 0.76 mmol), DME (2.0 mL), EtOH (0.5 mL) and H₂O (0.3 mL). The crude product was purified by flash column chromatography (silica gel, elution: 10:90 Et₂O:Hexane) to provide the title compound **46a** as a white solid (128 mg, 0.53 mmol, 85%):

R_f 0.27 (1:19 Et₂O:Hexane); **m.p.** 93-94 °C; **IR** ν_{\max} 3066 (w, C-H), 2232 (m, C≡N), 1597 (m, C=C), 1489 (s, C=C), 1380 (s, C=C); **¹H NMR** (400 MHz, CDCl₃) δ 7.79 (1H, d, *J* = 1.6 Hz, H7), 7.63 (1H, dd, *J* = 8.0, 1.6 Hz, H3), 7.52 - 7.41 (4H, m, H4/H10/H11/H13), 7.32 (1H, dt, *J* = 7.6, 1.6 Hz, H9), 6.77 (1H, dd, *J* = 17.6, 10.8 Hz, H14), 5.81 (1H, dd, *J* = 17.6, 0.4 Hz, H15), 5.33 (1H, dd, *J* = 10.8, 0.4 Hz, H15'); **¹³C NMR** (100 MHz, CDCl₃) δ 145.2 (C5), 137.9 (C8/C12), 137.8 (C8/C12), 136.2 (C14), 133.6 (C6), 133.4 (C7), 132.0 (C4), 130.4 (C3), 128.6 (C10), 128.4 (C9), 126.9 (C13), 126.4 (C11), 117.5 (C1), 114.9 (C15), 112.5 (C2); **HRMS** (ESI) calcd for [C₁₅H₁₀N³⁵Cl + H]⁺: 240.0580, found: 240.0583.

(2-Chloro-3'-vinyl-[1,1'-biphenyl]-4-yl)methanamine TFA salt (**46**)



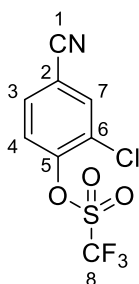
Prepared by General Method **C** using LiAlH₄ (32 mg, 0.84 mmol), Et₂O (2.0 mL), AlCl₃ (112 mg, 0.84 mmol) and **46a** (100 mg, 0.42 mmol). The crude amine was purified by semi-preparative HPLC (20-70% B) to provide title compound **46** as a yellow solid (72 mg, 0.20 mmol, 47%):

HPLC *t_r* = 7.92 mins (20-70% B); **m.p.** 122-123 °C; **IR** ν_{\max} 2922 (br s, NH₃⁺), 1599 (w, C=C), 1476 (m, C=C); **¹H NMR** (500 MHz, d₆-DMSO) δ 7.54 (1H, d, *J* = 0.5 Hz, H7), 7.51 (1H, dt, *J* = 7.5, 1.5 Hz, H11), 7.48 (1H, t, *J* = 1.5 Hz, H13), 7.43 (1H, t, *J* = 7.5 Hz, H10), 7.37 - 7.33 (2H, m, H3/H4), 7.31 (1H, dt, *J* =

7.5, 1.5 Hz, H9), 6.79 (1H, dd, $J = 17.5, 11.0$ Hz, H14), 5.89 (1H, dd, $J = 17.5, 1.0$ Hz, H15), 5.30 (1H, dd, $J = 11.0, 1.0$ Hz, H15'), 3.75 (2H, s, H1); ^{13}C NMR (125 MHz, d_6 -DMSO) δ 146.1 (C2), 139.2 (C8), 137.4 (C5), 137.2 (C12), 136.5 (C14), 131.2 (C4), 131.1 (C6), 128.9 (C9), 128.5 (C10), 128.2 (C7), 127.1 (C13), 126.2 (C3), 125.3 (C11), 114.9 (C15), 44.9 (C1); HRMS (ESI) calcd for $[\text{C}_{15}\text{H}_{14}\text{N}^{35}\text{Cl} + \text{H}]^+$: 244.0893, found: 244.0895.

NH_3 peak (H16) too broad to be observed in ^1H NMR.

2-Chloro-4-cyanophenyl trifluoromethanesulfonate (48)

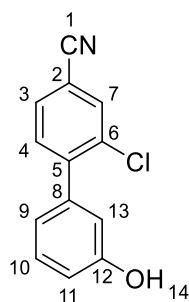


Prepared by General Method **A** using 3-chloro-4-hydroxybenzonitrile (3.00 g, 19.54 mmol), anhydrous CH_2Cl_2 (60 mL), anhydrous pyridine (4.78 mL, 58.62 mmol) and trifluoromethanesulfonic anhydride (3.61 mL, 21.45 mmol). The crude residue was purified by flash column chromatography (silica gel, gradient elution: 5:95 Et_2O :Hexane to 15:85 Et_2O :Hexane) to provide the title compound **48** as a white solid (5.24 g, 18.35 mmol, 94%):

R_f 0.31 (1:4 Et_2O :Hexane); IR ν_{max} 3076 (w, C-H), 2245 (w, $\text{C}\equiv\text{N}$), 1575 (w, C=C), 1478 (w, C=C); ^1H NMR (400 MHz, CDCl_3) δ 7.87 (1H, d, $J = 2.0$ Hz, H7), 7.69 (1H, dd, $J = 8.8, 2.0$ Hz, H3), 7.52 (1H, d, $J = 8.8$ Hz, H4); ^{13}C NMR (100 MHz, CDCl_3) δ 148.5 (C5), 134.9 (C7), 132.2 (C3), 128.9 (C6), 124.2 (C4), 118.5 (1C, q, $J = 318.8$ Hz, C8), 116.0 (C1), 113.7 (C2); HRMS (ESI) calcd for $[\text{C}_8\text{H}_3\text{NO}_3\text{S}^{35}\text{ClF}_3 + \text{H}]^+$: 285.9553, found: 285.9555.

Spectroscopic data consistent with that reported in the literature.^{250,251}

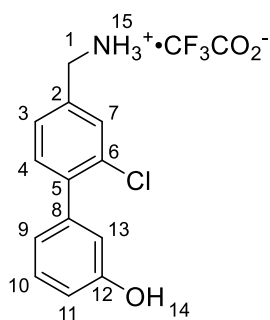
2-Chloro-3'-hydroxy-[1,1'-biphenyl]-4-carbonitrile (51a)



Prepared by General Method **B** using 3-chloro-4-bromobenzonitrile (2.16 g, 10.00 mmol), 3-hydroxyphenylboronic acid pinacol ester (2.00 g, 9.08 mmol), PdCl₂(dppf).CH₂Cl₂ (371 mg, 0.45 mmol), K₃PO₄ (2.30 g, 10.84 mmol), DME (20 mL), EtOH (6 mL) and H₂O (4 mL). The crude product was purified by flash column chromatography (silica gel, gradient elution: 5:95 Et₂O:Hexane to 40:60 Et₂O:Hexane) to provide the title compound **51a** as a white solid (1.93 g, 8.40 mmol, 93%):

R_f 0.19 (2:3 Et₂O:Hexane); **m.p.** 141-142 °C; **IR** ν_{\max} 3355 (br, O-H), 2988 (w, C-H), 2246 (m, C≡N), 1616 (w, C=C), 1582 (s, C=C), 1469 (s, C=C); **¹H NMR** (400 MHz, d₆-DMSO) δ 9.69 (1H, s, H14), 8.15 (1H, d, *J* = 1.6 Hz, H7), 7.88 (1H, dd, *J* = 8.0, 1.6 Hz, H3), 7.57 (1H, d, *J* = 8.0 Hz, H4), 7.29 (1H, t, *J* = 8.0 Hz, H10), 6.87 – 6.80 (3H, m, H9/H11/H13); **¹³C NMR** (100 MHz, d₆-DMSO) δ 157.3 (C12), 144.8 (C5), 138.6 (C8), 133.4 (C7), 132.3 (C4), 132.3 (C6), 131.3 (C3), 129.7 (C10), 119.7 (C9), 117.6 (C1), 115.9 (C11), 115.6 (C13), 111.8 (C2); **HRMS** (ESI) calcd for [C₁₃H₈NO³⁵Cl + H]⁺: 229.0289, found: 229.0286.

4'-(Aminomethyl)-2'-chloro-[1,1'-biphenyl]-3-ol TFA salt (**51**)

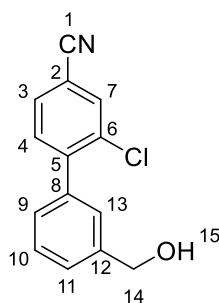


Prepared by General Method **C** using LiAlH₄ (83 mg, 2.18 mmol), Et₂O (10 mL), AlCl₃ (291 mg, 2.18 mmol) and **51a** (90 mg, 0.39 mmol). The crude amine was purified by semi-preparative HPLC (20-70% B) to provide title compound **51** as a white solid (63 mg, 0.18 mmol, 45%):

HPLC *t_r* = 6.87 mins (5-95% B); **m.p.** 119–120 °C; **IR** ν_{\max} 3344 (m, NH₂), 2923 (br, O-H), 1574 (s, C=C), 1471 (s, C=C); **¹H NMR** (400 MHz, d₆-DMSO) δ 9.55 (1H, br s, H14), 7.51 (1H, d, *J* = 0.8 Hz, H7), 7.35 – 7.21 (3H, m, H3/H4/H10), 6.81 – 6.76 (3H, m, H9/H11/H13), 3.74 (2H, s, H1); **¹³C NMR** (100 MHz, d₆-DMSO) δ 157.1 (C12), 145.8 (C2), 140.1 (C8), 137.7 (C5), 131.03 (C4), 130.97 (C6), 129.3 (C10), 128.3 (C7), 126.1 (C3), 120.0 (C9), 116.2 (C11), 114.6 (C13), 44.8 (C1); **HRMS** (ESI) calcd for [C₁₃H₁₂NO³⁵Cl + H]⁺: 234.0686, found: 234.0693.

NH₃ peak (H15) too broad to be observed in ¹H NMR.

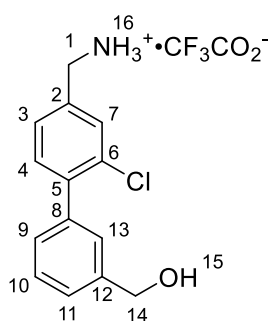
2-Chloro-3'-(hydroxymethyl)-[1,1'-biphenyl]-4-carbonitrile (**54a**)



Prepared by General Method **B** using 3-chloro-4-bromobenzonitrile (150 mg, 0.69 mmol), 3-(hydroxymethyl)phenylboronic acid (96 mg, 0.63 mmol), PdCl₂(dppf).CH₂Cl₂ (26 mg, 0.032 mmol), K₃PO₄ (161 mg, 0.76 mmol), DME (2.0 mL), EtOH (0.5 mL) and H₂O (0.3 mL). The crude product was purified by flash column chromatography (silica gel, gradient elution: 30:70 Et₂O:Hexane to 50:50 Et₂O:Hexane) to provide the title compound **54a** as a brown oil (133 mg, 0.55 mmol, 87%):

R_f 0.16 (3:2 Et₂O:Hexane); IR ν_{\max} 3216 (br, O-H), 2231 (s, C≡N), 1479 (m, C=C), 1429 (m, C=C); ¹H NMR (500 MHz, d₆-DMSO) δ 8.18 (1H, d, *J* = 1.5 Hz, H7), 7.91 (1H, dd, *J* = 8.0, 1.5 Hz, H3), 7.60 (1H, d, *J* = 8.0 Hz, H4), 7.46 (1H, t, *J* = 8.0 Hz, H10), 7.43 – 7.38 (2H, m, H11/H13), 7.33 (1H, dt, *J* = 7.5, 1.5 Hz, H9), 5.28 (1H, t, *J* = 5.5 Hz, H15), 4.57 (2H, d, *J* = 5.5 Hz, H14); ¹³C NMR (125 MHz, d₆-DMSO) δ 144.9 (C5), 143.0 (C12), 137.1 (C8), 133.4 (C7), 132.4 (C4), 132.3 (C6), 131.4 (C3), 128.3 (C10), 127.4 (C9), 127.0 (C13), 126.7 (C11), 117.6 (C1), 111.9 (C2), 62.7 (C14); HRMS (ESI) calcd for [C₁₄H₁₀NO³⁵Cl + H]⁺: 244.0529, found: 244.0539.

(4'-(Aminomethyl)-2'-chloro-[1,1'-biphenyl]-3-yl)methanol TFA salt (**54**)

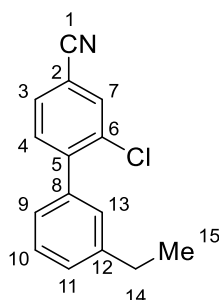


Prepared by General Method **C** using LiAlH₄ (62 mg, 1.64 mmol), Et₂O (2.5 mL), AlCl₃ (219 mg, 1.64 mmol) and **54a** (100 mg, 0.41 mmol). The crude amine was purified by semi-preparative HPLC (5-95% B) to provide title compound **54** as a clear oil (9 mg, 0.02 mmol, 6%):

HPLC *t_r* = 9.12 mins (5-95% B); IR ν_{\max} 2988 (br s, O-H/NH₃⁺), 1674 (s, C=C), 1644 (m, C=C), 1622 (m, C=C), 1509 (w, C=C), 1483 (w, C=C); ¹H NMR (500 MHz, d₆-DMSO) δ 8.28 (3H, br s, H16), 7.70 (1H, s, H7), 7.52 – 7.41 (3H, m, H3/H4/H10), 7.39 – 7.34 (2H, m, H11/H13), 7.30 – 7.26 (1H, m, H9), 5.27 (1H,

t, $J = 5.0$ Hz, H15), 5.56 (2H, d, $J = 5.0$ Hz, H14), 4.11 (2H, br s, H1); ^{13}C NMR (125 MHz, d_6 -DMSO) δ 142.8 (C12), 140.1 (C5), 138.0 (C8), 135.8 (C2), 131.7 (C3), 131.4 (C6), 130.3 (C7), 128.1 (2C, C4/C10), 127.6 (C9), 127.1 (C13), 126.1 (C11), 62.8 (C14), 41.5 (C1); HRMS (ESI) calcd for $[\text{C}_{14}\text{H}_{14}\text{N}^{35}\text{Cl} + \text{H}]^+$: 248.0842, found: 248.0843.

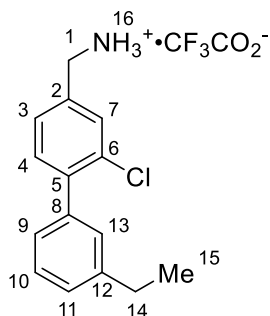
2-Chloro-3'-ethyl-[1,1'-biphenyl]-4-carbonitrile (55a)



Prepared by General Method **B** using 3-chloro-4-bromobenzonitrile (150 mg, 0.69 mmol), 3-ethylphenylboronic acid (95 mg, 0.63 mmol), $\text{PdCl}_2(\text{dppf})\cdot\text{CH}_2\text{Cl}_2$ (26 mg, 0.032 mmol), K_3PO_4 (161 mg, 0.76 mmol), DME (2.0 mL), EtOH (0.5 mL) and H_2O (0.3 mL). The crude product was purified by flash column chromatography (silica gel, elution: 5:95 Et_2O :Hexane) to provide the title compound **55a** as a yellow oil (123 mg, 0.51 mmol, 81%):

R_f 0.54 (1:4 Et_2O :Hexane); IR ν_{max} 2970 (s, C-H), 2901 (m, C-H), 2232 (s, $\text{C}\equiv\text{N}$), 1597 (w, $\text{C}=\text{C}$), 1538 (w, $\text{C}=\text{C}$), 1473 (m, $\text{C}=\text{C}$); ^1H NMR (500 MHz, CDCl_3) δ 7.78 (1H, d, $J = 2.0$ Hz, H7), 7.61 (1H, dd, $J = 7.0, 2.0$ Hz, H3), 7.47 (1H, d, $J = 8.0$ Hz, H4), 7.39 (1H, td, $J = 7.5, 1.0$ Hz, H10), 7.31 - 7.27 (1H, m, H9/H11), 7.27 - 7.24 (2H, m, H9/H11/H13), 2.73 (2H, q, $J = 7.5$ Hz, H14), 1.29 (3H, t, $J = 7.5$ Hz, H15); ^{13}C NMR (125 MHz, CDCl_3) δ 144.6 (C5), 144.4 (C12), 137.6 (C8), 133.6 (C6), 133.3 (C7), 132.1 (C4), 130.3 (C3), 128.6 (C13), 128.3 (C10), 128.2 (C11), 126.4 (C9), 117.6 (C1), 112.3 (C2), 28.8 (C14), 15.5 (C15); HRMS (ESI) calcd for $[\text{C}_{15}\text{H}_{12}\text{N}^{35}\text{Cl} + \text{H}]^+$: 242.0731, found: 242.0770.

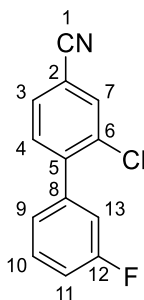
(2-Chloro-3'-ethyl-[1,1'-biphenyl]-4-yl)methanamine TFA salt (55)



Prepared by General Method **C** using LiAlH₄ (25 mg, 0.66 mmol), Et₂O (1.5 mL), AlCl₃ (88 mg, 0.66 mmol) and **55a** (80 mg, 0.33 mmol). The crude amine was purified by semi-preparative HPLC (20-70% B) to provide title compound **55** as a white solid (84 mg, 0.23 mmol, 71%):

HPLC t_r = 8.37 mins (20-70% B); **m.p.** 121–122 °C; **IR** ν_{\max} 2963 (br s, NH₃⁺), 1675 (s, C=C), 1595 (m, C=C), 1524 (w, C=C), 1476 (w, C=C); **¹H NMR** (400 MHz, d₆-DMSO) δ 8.32 (3H, br s, H16), 7.70 (1H, d, J = 1.2 Hz, H7), 7.51 – 7.45 (2H, m, H3/H4), 7.39 (1H, t, J = 7.6 Hz, H10), 7.29 – 7.20 (3H, m, H9/H11/H13), 4.11 (2H, s, H1), 2.67 (2H, q, J = 8.0 Hz, H14), 1.21 (3H, t, J = 8.0 Hz, H15); **¹³C NMR** (100 MHz, d₆-DMSO) δ 143.9 (C12), 140.1 (C5), 138.2 (C8), 135.3 (C2), 131.7 (C4), 131.4 (C6), 130.3 (C7), 128.6 (C13), 128.3 (C10), 128.1 (C3), 127.5 (C11), 126.6 (C9), 41.5 (C1), 28.2 (C14), 15.7 (C15); **HRMS** (ESI) calcd for [C₁₅H₁₆N³⁵Cl + H]⁺: 246.1044, found: 246.1047.

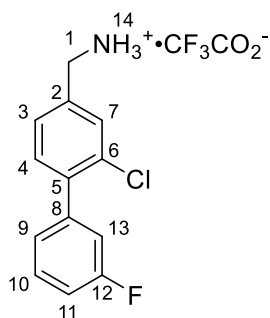
2-Chloro-3'-fluoro-[1,1'-biphenyl]-4-carbonitrile (**56a**)



Prepared by General Method **B** using 3-chloro-4-bromobenzonitrile (150 mg, 0.69 mmol), 3-fluorophenylboronic acid (88 mg, 0.63 mmol), PdCl₂(dppf).CH₂Cl₂ (26 mg, 0.032 mmol), K₃PO₄ (161 mg, 0.76 mmol), DME (2.0 mL), EtOH (0.5 mL) and H₂O (0.3 mL). The crude product was purified by flash column chromatography (silica gel, gradient elution: 1:99 Et₂O:Hexane to 2:98 Et₂O:Hexane) to provide the title compound **56a** as a white solid (130 mg, 0.56 mmol, 89%):

R_f 0.37 (1:4 Et₂O:Hexane); **m.p.** 73-74 °C; **IR** ν_{\max} 3072 (w, C-H), 2971 (w, C-H), 2232 (m, C≡N), 1616 (w, C=C), 1583 (s, C=C), 1541 (w, C=C), 1500 (w, C=C); **¹H NMR** (400 MHz, CDCl₃) δ 7.80 (1H, d, J = 1.2 Hz, H7), 7.63 (1H, dd, J = 8.0, 1.2 Hz, H3), 7.49 – 7.42 (2H, m, H4/H10), 7.21 (1H, dt, J = 8.0, 1.2 Hz, H9), 7.19 - 7.13 (2H, m, H11/H13); **¹³C NMR** (100 MHz, CDCl₃) δ 162.5 (1C, d, J = 240 Hz, C12), 144.0 (1C, d, J = 2.4 Hz, C5), 140.0 (1C, d, J = 8.3 Hz, C8), 133.54 (C6), 133.46 (C7), 131.9 (C4), 130.5 (C3), 130.1 (1C, d, J = 8.3 Hz, C10), 124.9 (1C, d, J = 3.0 Hz, C9), 117.3 (C1), 116.3 (1C, d, J = 22.5 Hz, C11/C13), 115.7 (1C, d, J = 20.8 Hz, C11/C13), 113.0 (C2); **HRMS** (ESI) calcd for [C₁₃H₇N³⁵Cl¹⁹F + H]⁺: 232.0329, found: 232.0340.

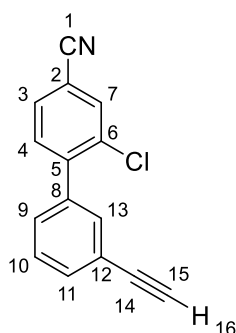
(2-Chloro-3'-fluoro-[1,1'-biphenyl]-4-yl)methanamine TFA salt (**56**)



Prepared by General Method **C** using LiAlH₄ (33 mg, 0.87 mmol), Et₂O (2.0 mL), AlCl₃ (116 mg, 0.87 mmol) and **56a** (100 mg, 0.43 mmol). The crude amine was purified by semi-preparative HPLC (5-55% B) to provide title compound **56** as a white solid (116 mg, 0.33 mmol, 77%):

HPLC *t_r* = 11.61 mins (5-55% B); **m.p.** 152–153 °C; **IR** *u*_{max} 2988 (br s, NH₃⁺), 1675 (s, C=C), 1589 (s, C=C), 1527 (m, C=C), 1474 (m, C=C); **¹H NMR** (500 MHz, d₆-DMSO) δ 8.26 (3H, br s, H₁₄), 7.73 (1H, br s, H₇), 7.56–7.50 (3H, m, H₃/H₄/H₁₀), 7.31–7.25 (3H, m, H₉/H₁₁/H₁₃), 4.11 (2H, s, H₁); **¹³C NMR** (125 MHz, d₆-DMSO) δ 161.9 (1C, d, *J* = 242.6 Hz, C₁₂), 140.4 (1C, d, *J* = 8.0 Hz, C₈), 138.5 (C₅), 135.9 (C₂), 131.7 (C₄), 131.3 (C₆), 130.4 (1C, d, *J* = 8.5 Hz, C₁₀), 130.5 (C₇), 128.2 (C₃), 125.6 (C₉), 116.1 (1C, d, *J* = 21.9 Hz, C₁₁/C₁₃), 114.9 (1C, d, *J* = 20.7 Hz, C₁₁/C₁₃), 41.4 (C₁); **HRMS** (ESI) calcd for [C₁₃H₁₁N³⁵Cl¹⁹F + H]⁺: 236.0642, found: 236.0645.

2-Chloro-3'-ethynyl-[1,1'-biphenyl]-4-carbonitrile (**57a**)

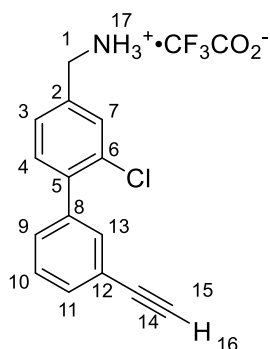


Prepared by General Method **B** using 3-chloro-4-bromobenzonitrile (150 mg, 0.69 mmol), 3-ethynylphenylboronic acid pinacol ester (144 mg, 0.63 mmol), PdCl₂(dppf).CH₂Cl₂ (26 mg, 0.032 mmol), K₃PO₄ (161 mg, 0.76 mmol), DME (2.0 mL), EtOH (0.5 mL) and H₂O (0.3 mL). The crude product was purified by flash column chromatography (silica gel, gradient elution: 5:95 Et₂O:Hexane to 30:70 Et₂O:Hexane) to provide the title compound **57a** as a brown solid (131 mg, 0.55 mmol, 88%):

R_f 0.34 (1:4 Et₂O:Hexane); **m.p.** 96–97 °C; **IR** *u*_{max} 3277 (m, C≡C-H), 2231 (m, C≡N), 1578 (w, C=C), 1472 (s, C=C); **¹H NMR** (400 MHz, CDCl₃) δ 7.79 (1H, d, *J* = 1.6 Hz, H₇), 7.63 (1H, dd, *J* = 8.0, 1.6 Hz, H₃), 7.59

- 7.54 (2H, m, H11/H13), 7.47 - 7.40 (3H, m, H4/H9/H10), 3.14 (1H, s, H16); ^{13}C NMR (100 MHz, CDCl_3) δ 144.3 (C5), 137.8 (C8), 133.6 (C6), 133.4 (C7), 132.6 (C11/C13), 132.3 (C11/C13), 131.9 (C4), 130.5 (C3), 129.5 (C9), 128.5 (C10), 122.5 (C12), 117.4 (C1), 112.9 (C2), 82.9 (C14), 77.2 (C15); HRMS (ESI) calcd for $[\text{C}_{15}\text{H}_8\text{N}^{35}\text{Cl} + \text{H}]^+$: 238.0424, found: 238.0419.

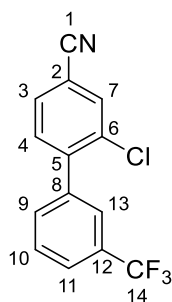
(2-Chloro-3'-ethynyl-[1,1'-biphenyl]-4-yl)methanamine TFA salt (57)



Prepared by General Method C using LiAlH_4 (16 mg, 0.42 mmol), Et_2O (0.84 mL), AlCl_3 (56 mg, 0.42 mmol) and **57a** (50 mg, 0.21 mmol). The crude amine was purified by semi-preparative HPLC (25-40% B) to provide title compound **57** as a yellow oil (13 mg, 0.04 mmol, 19%):

HPLC t_r = 13.10 mins (20-35% B); IR ν_{max} 3299 (w, $\text{C}\equiv\text{C-H}$), 2907 (br, NH_3^+), 1666 (s, $\text{C}=\text{C}$), 1629 (m, $\text{C}=\text{C}$), 1532 (m, $\text{C}=\text{C}$), 1473 (w, $\text{C}=\text{C}$); ^1H NMR (500 MHz, d_6 -DMSO) δ 8.27 (3H, br s, H17), 7.72 (1H, br s, H7), 7.55 (1H, dt, J = 8.0, 1.5 Hz, H11), 7.53 - 7.49 (4H, m, H3/H4/H10/H13), 7.46 (1H, dt, J = 7.5, 1.5 Hz, H9), 4.27 (1H, s, H16), 4.12 (2H, br s, H1); ^{13}C NMR (125 MHz, d_6 -DMSO) δ 138.8 (C5), 138.6 (C8), 135.8 (C2), 132.2 (C13), 131.7 (C4), 131.35 (C11), 131.32 (C6), 130.3 (C7), 130.0 (C9), 128.9 (C10), 128.2 (C3), 121.9 (C12), 83.1 (C14), 81.5 (C15), 41.4 (C1); HRMS (ESI) calcd for $[\text{C}_{15}\text{H}_{12}\text{N}^{35}\text{Cl} + \text{H}]^+$: 242.0737, found: 242.0737.

2-Chloro-3'-(trifluoromethyl)-[1,1'-biphenyl]-4-carbonitrile (58a)

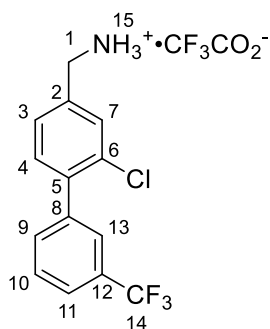


Prepared by General Method B using 3-chloro-4-bromobenzonitrile (150 mg, 0.69 mmol), 3-(trifluoromethyl)phenylboronic acid (120 mg, 0.63 mmol), $\text{PdCl}_2(\text{dppf})\cdot\text{CH}_2\text{Cl}_2$ (26 mg, 0.032 mmol), K_3PO_4 (161 mg, 0.76 mmol), DME (2.0 mL), EtOH (0.5 mL) and H_2O (0.3 mL). The crude product was

purified by flash column chromatography (silica gel, gradient elution: 2:98 Et₂O:Hexane to 4:96 Et₂O:Hexane) to provide the title compound **58a** as a white solid (169 mg, 0.60 mmol, 95%):

R_f 0.32 (1:4 Et₂O:Hexane); **m.p.** 76–77 °C; **IR** ν_{\max} 3077 (w, C-H), 2236 (m, C≡N), 1539 (w, C=C), 1483 (m, C=C), 1432 (m, C=C); **¹H NMR** (500 MHz, CDCl₃) δ 7.82 (1H, d, *J* = 1.0 Hz, H7), 7.74 – 7.71 (1H, m, H11), 7.71 – 7.69 (1H, m, H13), 7.66 (1H, dd, *J* = 8.0, 1.0 Hz, H3), 7.64 - 7.60 (2H, m, H9/H10), 7.48 (1H, d, *J* = 8.0 Hz, H4); **¹³C NMR** (125 MHz, CDCl₃) δ 143.7 (C5), 138.2 (C8), 133.6 (C6), 133.5 (C7), 132.5 (C9), 131.9 (C4), 131.0 (1C, q, *J* = 32.9 Hz, C12), 130.6 (C3), 129.0 (C10), 125.9 (1C, q, *J* = 3.5 Hz, C13), 125.5 (1C, q, *J* = 3.4 Hz, C11), 121.7 (1C, q, *J* = 268.1 Hz, C14), 117.2 (C1), 113.3 (C2); **HRMS** (ESI) calcd for [C₁₄H₇N³⁵Cl¹⁹F₃ + H]⁺: 282.0297, found: 282.0306.

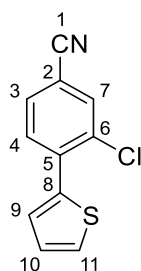
(2-Chloro-3'-(trifluoromethyl)-[1,1'-biphenyl]-4-yl)methanamine TFA salt (**58**)



Prepared by General Method **C** using LiAlH₄ (27 mg, 0.70 mmol), Et₂O (1.75 mL), AlCl₃ (93 mg, 0.70 mmol) and **58a** (100 mg, 0.35 mmol). The crude amine was purified by semi-preparative HPLC (20-60% B) to provide title compound **58** as a white solid (109 mg, 0.27 mmol, 78%):

HPLC *t_r* = 9.55 mins (20-60% B); **m.p.** 154–155 °C; **IR** ν_{\max} 2902 (br s, NH₃⁺), 1670 (s, C=C), 1632 (w, C=C), 1480 (w, C=C); **¹H NMR** (500 MHz, d₆-DMSO) δ 8.37 (3H, br s, H15), 7.83 – 7.80 (1H, m, H7), 7.77 – 7.71 (4H, m, H7/H9/H10/H13), 7.58 – 7.53 (2H, m, H3/H4), 4.13 (2H, s, H1); **¹³C NMR** (125 MHz, d₆-DMSO) δ 139.1 (C8), 138.2 (C5), 136.2 (C2), 133.5 (C9), 131.8 (C4), 131.3 (C6), 130.4 (C7), 129.6 (C10), 129.2 (1C, q, *J* = 31.9 Hz, C12), 128.3 (C3), 125.7 (1C, q, *J* = 4.3 Hz, C13), 124.8 (1C, q, *J* = 4.3 Hz, C11), 124.1 (1C, q, *J* = 272.1 Hz, C14), 41.3 (C1); **HRMS** (ESI) calcd for [C₁₄H₁₁N³⁵Cl¹⁹F₃ + H]⁺: 286.0605, found: 286.0595.

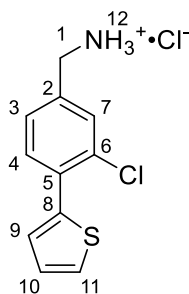
3-Chloro-4-(thiophen-2-yl)benzonitrile (59a)



Prepared by General Method **B** using 3-chloro-4-bromobenzonitrile (150 mg, 0.69 mmol), 2-thienylboronic acid (81 mg, 0.63 mmol), PdCl₂(dppf).CH₂Cl₂ (26 mg, 0.032 mmol), K₃PO₄ (161 mg, 0.76 mmol), DME (2.0 mL), EtOH (0.5 mL) and H₂O (0.3 mL) with microwave irradiation for 4 hours at 110 °C. The crude product was purified by flash column chromatography (silica gel, elution: 6:94 Et₂O:Hexane) to provide the title compound **59a** as a white solid (120 mg, 0.55 mmol, 79%):

R_f 0.34 (1:4 Et₂O:Hexane); **m.p.** 174-175 °C; **IR** ν_{\max} 3098 (m, C-H), 2233 (m, C≡N), 1595 (m, C=C), 1538 (w, C=C), 1477 (m, C=C); **¹H NMR** (500 MHz, CDCl₃) δ 7.78 (1H, d, *J* = 2.0 Hz, H7), 7.67 (1H, d, *J* = 7.5 Hz, H4), 7.58 (1H, dd, *J* = 7.5, 2.0 Hz, H3), 7.53 – 7.50 (2H, m, H9/H11), 7.17 (1H, dd, *J* = 5.0, 3.5 Hz, H10); **¹³C NMR** (125 MHz, CDCl₃) δ 138.1 (C8), 137.8 (C5), 134.0 (C7), 132.8 (C6), 131.6 (C4), 130.3 (C3), 128.1 (C9/C11), 128.1 (C9/C11), 127.6 (C10), 117.4 (C1), 111.9 (C2); **HRMS** (ESI) calcd for [C₁₁H₆N³⁵ClS + H]⁺: 219.9988, found: 219.9986.

(3-Chloro-4-(thiophen-2-yl)phenyl)methanamine HCl salt (59)

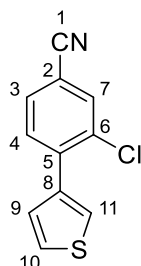


Prepared by General Method **C** using LiAlH₄ (35 mg, 0.92 mmol), Et₂O (2.0 mL), AlCl₃ (123 mg, 0.92 mmol) and **59a** (100 mg, 0.46 mmol). The crude amine was dissolved in CH₂Cl₂ (0.5 mL) and HCl (2M in Et₂O) (2.3 mL, 4.6 mmol) added dropwise. The reaction was stirred for 1 hour before the precipitate was filtered, washed with cold Et₂O and dried to provide the title compound **59** as a yellow solid (64 mg, 0.25 mmol, 53%):

HPLC *t_r* = 7.54 mins (5-95% B); **m.p.** 246-247 °C; **IR** ν_{\max} 2923 (br s, NH₃⁺), 1526 (m, C=C), 1415 (m, C=C); **¹H NMR** (400 MHz, d₆-DMSO) δ 8.60 (3H, br s, H12), 7.78 (1H, d, *J* = 1.6 Hz, H7), 7.72 (1H, dd, *J* = 5.2, 0.8 Hz, H11), 7.69 (1H, d, *J* = 8.4 Hz, H4), 7.54 (1H, dd, *J* = 78.4, 1.6 Hz, H3), 7.48 (1H, dd, *J* = 3.6, 0.8 Hz,

H9), 7.19 (1H, dd, $J = 5.2, 3.5$ Hz, H10), 4.06 (2H, s, H1); $^{13}\text{C NMR}$ (100 MHz, d_6 -DMSO) δ 138.6 (C8), 135.6 (C2), 132.3 (C5), 131.3 (C4), 131.0 (C7), 130.7 (C6), 128.4 (C3), 128.4 (C9), 127.8 (C11), 127.6 (C10), 41.2 (C1); **HRMS** (ESI) calcd for $[\text{C}_{11}\text{H}_{10}\text{N}^{35}\text{ClS} + \text{H}]^+$: 224.0301, found: 224.0293.

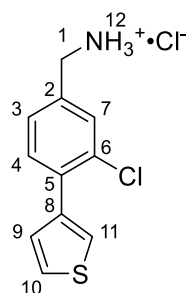
3-Chloro-4-(thiophen-3-yl)benzonitrile (60a)



Prepared by General Method **B** using 3-chloro-4-bromobenzonitrile (150 mg, 0.69 mmol), 3-thienylboronic acid (81 mg, 0.63 mmol), $\text{PdCl}_2(\text{dppf}) \cdot \text{CH}_2\text{Cl}_2$ (26 mg, 0.032 mmol), K_3PO_4 (161 mg, 0.76 mmol), DME (2.0 mL), EtOH (0.5 mL) and H_2O (0.3 mL). The crude product was purified by flash column chromatography (silica gel, elution: 5:95 Et_2O :Hexane) to provide the title compound **60a** as a white solid (120 mg, 0.55 mmol, 87%):

R_f 0.34 (1:4 Et_2O :Hexane); **m.p.** 178-179 °C; **IR** ν_{max} 3118 (w, C-H), 2232 (m, $\text{C}\equiv\text{N}$), 1596 (m, C=C), 1521 (w, C=C), 1478 (m, C=C); $^1\text{H NMR}$ (400 MHz, CDCl_3) δ 7.77 (1H, dd, $J = 1.6, 0.4$ Hz, H7), 7.61 – 7.57 (2H, m, H3/H11), 7.55 (1H, dd, $J = 8.0, 0.4$ Hz, H4), 7.44 (1H, dd, $J = 5.2, 3.2$ Hz, H9), 7.34 (1H, dd, $J = 5.2, 1.3$ Hz, H10); $^{13}\text{C NMR}$ (100 MHz, CDCl_3) δ 140.0 (C5), 137.6 (C8), 133.6 (C7), 133.2 (C6), 131.6 (C4), 130.4 (C3), 128.3 (C10), 125.8 (C9/C11), 125.7 (C9/C11), 117.5 (C1), 112.0 (C2); **HRMS** (ESI) calcd for $[\text{C}_{11}\text{H}_6\text{N}^{35}\text{ClS} + \text{H}]^+$: 219.9988, found: 219.9987.

(3-Chloro-4-(thiophen-3-yl)phenyl)methanamine HCl salt (60)

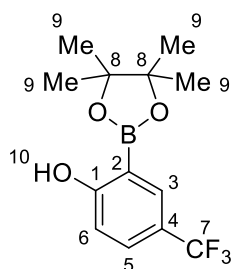


Prepared by General Method **C** using LiAlH_4 (35 mg, 0.92 mmol), Et_2O (2.0 mL), AlCl_3 (123 mg, 0.92 mmol) and **60a** (100 mg, 0.46 mmol). The crude amine was dissolved in CH_2Cl_2 (0.5 mL) and HCl (2M in Et_2O) (2.3 mL, 4.6 mmol) added dropwise. The reaction was stirred for 1 hour before the precipitate was filtered, washed with cold Et_2O and dried to provide the title compound **60** as a yellow solid (73 mg, 0.29 mmol, 63%):

HPLC t_r = 7.53 mins (5-95% B); **m.p.** 235-236 °C; **IR** ν_{\max} 2913 (br s, NH_3^+), 1605 (m, C=C), 1523 (m, C=C), 1493 (m, C=C); **$^1\text{H NMR}$** (500 MHz, $\text{d}_6\text{-DMSO}$) δ 8.59 (3H, br s, H12), 7.77 – 7.74 (2H, m, H7/H11), 7.67 (1H, dd, J = 4.5, 3.0 Hz, H9), 7.57 (1H, d, J = 7.5 Hz, H4), 7.53 (1H, dd, J = 7.5, 1.5 Hz, H3), 7.36 (1H, dd, J = 4.5, 1.0 Hz, H10), 4.06 (2H, s, H1); **$^{13}\text{C NMR}$** (125 MHz, $\text{d}_6\text{-DMSO}$) δ 138.5 (C8), 135.6 (C2), 135.0 (C5), 131.8 (C4), 131.5 (C6), 131.0 (C7), 129.0 (C10), 128.6 (C3), 126.6 (C9), 125.6 (C11), 41.6 (C1); **HRMS** (ESI) calcd for $[\text{C}_{11}\text{H}_{10}\text{N}^{35}\text{ClS} + \text{H}]^+$: 224.0301, found: 224.0309.

4.4 Experimental Details for Structure-Based Optimisation of the New Binding Mode

2-(4,4,5,5-Tetramethyl-1,3,2-dioxaborolan-2-yl)-4-(trifluoromethyl)phenol (**61b**)



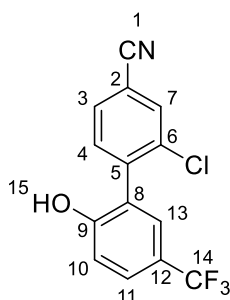
To a flask charged with 2-benzyloxy-5-(trifluoromethyl)phenylboronic acid (1.00 g, 3.38 mmol) and pinacol (600 mg, 5.07 mmol) was added dry Et_2O (17 mL) before refluxing overnight. Following cooling to room temperature, the solvent was removed under reduced pressure and the residue dissolved in dry MeOH (24 mL). To the solution was added palladium (10% w.t. on charcoal) (180 mg, 0.17 mmol) at room temperature. The reaction was stirred under a H_2 atmosphere overnight and then filtered through Celite and the solvent evaporated to provide the title compound **61b** as a white solid in sufficient purity (895 mg, 3.11 mmol, 92%):

R_f 0.12 (1:1 EtOAc:Hexane); **m.p.** 79-80 °C; **IR** ν_{\max} 3422 (br s, O-H), 2984 (m, C-H), 1631 (s, C=C), 1595 (m, C=C), 1496 (m, C=C); **$^1\text{H NMR}$** (400 MHz, DMSO-d_6) δ 10.00 (1H, s, H10), 7.71 (1H, d, J = 2.2 Hz, H3), 7.62 (1H, dd, J = 8.6, 2.4 Hz, H5), 6.98 (1H, d, J = 8.6 Hz, H6), 1.29 (12H, s, H9); **$^{13}\text{C NMR}$** (101 MHz, DMSO-d_6) δ 165.6 (C1), 133.2 (1C, q, J = 3.8 Hz, C3), 129.8 (1C, q, J = 3.4 Hz, C5), 124.8 (1C, q, J = 270.8 Hz, C7), 119.2 (1C, q, J = 31.9 Hz, C4), 116.0 (C6), 83.6 (2C, C8), 24.6 (4C, C9); **HRMS** (ESI) calcd for $[\text{C}_{13}\text{H}_{16}\text{O}_3\text{F}_3^{11}\text{B} + \text{H}]^+$: 289.1223, found: 289.1226.

C2 signal lost in the baseline.

Conditions adapted from literature protocol.²⁶²

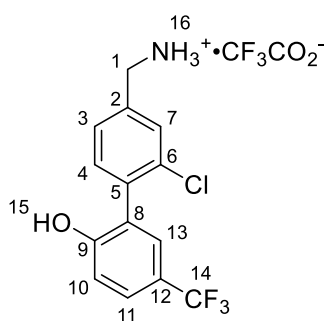
2-Chloro-2'-hydroxy-5'-(trifluoromethyl)-[1,1'-biphenyl]-4-carbonitrile (**61a**)



Prepared by General Method **B** using 3-chloro-4-bromobenzonitrile (165 mg, 0.76 mmol), boronic ester **61b** (199 mg, 0.69 mmol), PdCl₂(dppf).CH₂Cl₂ (29 mg, 0.035 mmol), K₃PO₄ (177 mg, 0.83 mmol), DME (2.2 mL), EtOH (0.5 mL) and H₂O (0.3 mL). The crude product was purified by flash column chromatography (silica gel, gradient elution: 5:95 Et₂O:Hexane to 20:80 Et₂O:Hexane) to provide the title compound **61a** as a white solid (160 mg, 0.54 mmol, 77%):

R_f 0.28 (1:1 Et₂O:Hexane); **m.p.** 93-94 °C; **IR** ν_{\max} 3340 (s, O-H), 2245 (m, C≡N), 1614 (m, C=C), 1592 (m, C=C), 1479 (s, C=C); **¹H NMR** (500 MHz, DMSO-d₆) δ 10.70 (1H, s, H15), 8.15 (1H, d, *J* = 1.5 Hz, H7), 7.88 (1H, dd, *J* = 7.9, 1.6 Hz, H3), 7.64 (1H, dd, *J* = 8.6, 2.0 Hz, H11), 7.59 (1H, d, *J* = 7.9 Hz, H4), 7.48 (1H, d, *J* = 1.9 Hz, H13), 7.13 (1H, d, *J* = 8.6 Hz, H10); **¹³C NMR** (126 MHz, DMSO-d₆) δ 157.8 (C9), 141.5 (C5), 133.9 (C6), 133.0 (C4), 132.7 (C7), 130.9 (C3), 127.5 (1C, q, *J* = 3.1 Hz, C13), 127.4 (1C, q, *J* = 2.9 Hz, C11), 125.2 (C8), 124.5 (1C, q, *J* = 271.0 Hz, C14), 119.5 (1C, q, *J* = 32.2 Hz, C12), 117.5 (C1), 116.2 (C10), 112.1 (C2); **HRMS** (ESI) calcd for [C₁₄H₇NO³⁵ClF₃ + H]⁺: 298.0247, found: 298.0242.

4'-(Aminomethyl)-2'-chloro-5'-(trifluoromethyl)-[1,1'-biphenyl]-2-ol TFA salt (**61**)

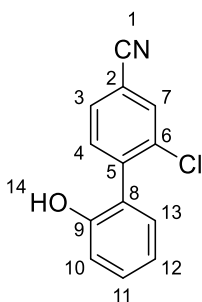


Prepared by General Method **C** using LiAlH₄ (33 mg, 0.88 mmol), Et₂O (1.1 mL) and **61a** (67 mg, 0.22 mmol) and stirred at 0 °C for 30 minutes before allowed to warm to room temperature for 1h and quenched. The crude amine was purified by semi-preparative HPLC (5-95% B) to provide title compound **61** as a white solid (21 mg, 0.05 mmol, 23%):

HPLC *t_r* = 9.58 mins (5-95% B); **m.p.** 172-173 °C; **IR** ν_{\max} 3176 (br s, O-H/NH₃⁺), 2989 (m, C-H), 1669 (m, C=C), 1625 (m, C=C), 1511 (w, C=C); **¹H NMR** (400 MHz, DMSO-d₆) δ 10.65 (1H, s, H15), 8.30 (3H, s br,

H16), 7.68 (1H, d, $J = 1.4$ Hz, H7), 7.61 (1H, dd, $J = 8.6, 2.0$ Hz, H11), 7.47 (1H, dd, $J = 7.9, 1.6$ Hz, H3), 7.43 (1H, d, $J = 7.8$ Hz, H4), 7.37 (1H, d, $J = 2.1$ Hz, H13), 7.12 (1H, d, $J = 8.5$ Hz, H10), 4.11 (2H, s, H1); $^{13}\text{C NMR}$ (101 MHz, DMSO- d_6) δ 158.2 (C9), 136.4 (C5), 135.5 (C6), 132.9 (C2), 132.1 (C4), 129.6 (C7), 127.8 – 127.4 (1C, m, C13), 127.6 (C3), 127.0 – 126.7 (1C, m, C11), 126.1 (C8), 124.6 (1C, q, $J = 271.0$ Hz, C14), 119.3 (1C, q, $J = 32.1$ Hz, C12) 116.1 (C10), 41.5 (C1); **HRMS** (ESI) calcd for $[\text{C}_{14}\text{H}_{11}\text{NO}^{35}\text{ClF}_3 + \text{H}]^+$: 302.0554, found: 302.0551.

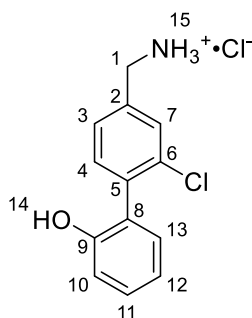
2-Chloro-2'-hydroxy-[1,1'-biphenyl]-4-carbonitrile (**62a**)



Prepared by General Method **B** using 3-chloro-4-bromobenzonitrile (150 mg, 0.69 mmol), 2-hydroxyphenylboronic acid (87 mg, 0.63 mmol), $\text{PdCl}_2(\text{dppf})\cdot\text{CH}_2\text{Cl}_2$ (26 mg, 0.032 mmol), K_3PO_4 (161 mg, 0.76 mmol), DME (2.0 mL), EtOH (0.5 mL) and H_2O (0.3 mL). The crude product was purified by flash column chromatography (silica gel, gradient elution: 5:95 Et_2O :Hexane to 20:80 Et_2O :Hexane) to provide the title compound **62a** as a white solid (100 mg, 0.44 mmol, 69%):

R_f 0.33 (1:1 Et_2O :Hexane); **m.p.** 141–142 °C; **IR** ν_{max} 3340 (s, O-H), 2245 (m, $\text{C}\equiv\text{N}$), 1614 (m, $\text{C}=\text{C}$), 1592 (m, $\text{C}=\text{C}$); $^1\text{H NMR}$ (500 MHz, DMSO- d_6) δ 9.72 (1H, s, H14), 8.10 (1H, d, $J = 1.6$ Hz, H7), 7.83 (1H, dd, $J = 7.9, 1.7$ Hz, H3), 7.52 (1H, d, $J = 7.9$ Hz, H4), 7.26 (1H, td, $J = 8.2, 1.7$ Hz, H11), 7.10 (1H, dd, $J = 7.6, 1.6$ Hz, H13), 6.95 (1H, dd, $J = 8.2, 0.7$ Hz, H10), 6.89 (1H, td, $J = 7.5, 1.0$ Hz, H12); $^{13}\text{C NMR}$ (126 MHz, DMSO- d_6) δ 154.3 (C9), 143.2 (C5), 133.9 (C6), 133.0 (C4), 132.6 (C7), 130.6 (C3), 130.2 (C13), 130.0 (C11), 124.7 (C8), 118.9 (C12), 117.7 (C1), 115.7 (C10), 111.5 (C2); **HRMS** (ESI) calcd for $[\text{C}_{13}\text{H}_8\text{NO}^{35}\text{Cl} + \text{H}]^+$: 230.0373, found: 230.0373.

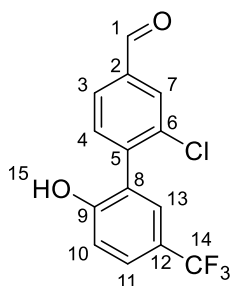
4'-(Aminomethyl)-2'-chloro-[1,1'-biphenyl]-2-ol HCl salt (**62**)



Prepared by General Method **C** using LiAlH₄ (33 mg, 0.88 mmol), Et₂O (1.1 mL), AlCl₃ (117 mg, 0.88 mmol) and **62a** (50 mg, 0.22 mmol). The crude amine was dissolved in CH₂Cl₂ (0.5 mL) and HCl (2M in Et₂O) (1.1 mL, 2.2 mmol) added dropwise. The reaction was stirred for 1 hour before the precipitate was filtered, washed with cold Et₂O and dried to provide the title compound **62** as a brown solid (35 mg, 0.13 mmol, 59%):

HPLC *t_r* = 7.63 mins (5-95% B); **m.p.** 314-315 °C; **IR** ν_{max} 3204 (br s, O-H/NH₃⁺), 2919 (m, C-H), 1606 (s, C=C), 1485 (m, C=C); **¹H NMR** (400 MHz, DMSO-*d*₆) δ 9.61 (1H, s, H14), 8.52 (3H, s br, H15), 7.68 (1H, d, *J* = 1.5 Hz, H7), 7.47 (1H, dd, *J* = 7.9, 1.6 Hz, H3), 7.34 (1H, d, *J* = 7.8 Hz, H4), 7.21 (1H, ddd, *J* = 8.1, 7.5, 1.7 Hz, H11), 7.05 (1H, dd, *J* = 7.5, 1.7 Hz, H13), 6.95 (1H, dd, *J* = 8.1, 0.8 Hz, H10), 6.85 (1H, td, *J* = 7.4, 1.0 Hz, H12), 4.06 (2H, s, H1); **¹³C NMR** (101 MHz, DMSO-*d*₆) δ 154.6 (C9), 137.9 (C5), 134.9 (C2), 132.9 (C6), 132.1 (C4), 130.6 (C13), 129.6 (C7), 129.3 (C11), 127.4 (C3), 125.6 (C8), 118.7 (C12), 115.6 (C10), 41.4 (C1); **HRMS** (ESI) calcd for [C₁₃H₁₂NO³⁵Cl + H]⁺: 234.0680, found: 234.0671.

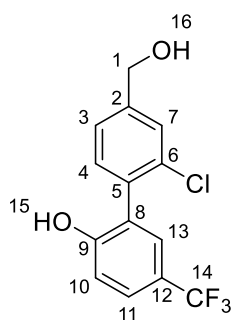
2-Chloro-2'-hydroxy-5'-(trifluoromethyl)-[1,1'-biphenyl]-4-carbaldehyde (**63**)



Prepared by General Method **B** using 3-chloro-4-bromobenzaldehyde (150 mg, 0.69 mmol), boronic ester **61b** (181 mg, 0.63 mmol), PdCl₂(dppf).CH₂Cl₂ (29 mg, 0.035 mmol), K₃PO₄ (177 mg, 0.83 mmol), DME (2.0 mL), EtOH (0.5 mL) and H₂O (0.3 mL). The crude product was purified by flash column chromatography (silica gel, gradient elution: 15:85 Et₂O:Hexane to 35:65 Et₂O:Hexane) to provide the title compound **63** as a white solid (124 mg, 0.41 mmol, 60%):

HPLC t_r = 13.25 mins (5-95% B); **m.p.** 159-160 °C; **IR** ν_{\max} 3258 (s, O-H), 2988 (m, C-H), 1683 (s, C=O), 1618 (w, C=C), 1599 (m, C=C), 1554 (s, C=C), 1520 (m, C=C); **$^1\text{H NMR}$** (400 MHz, DMSO- d_6) δ 10.71 (1H, s br, H15), 10.04 (1H, s, H1), 8.05 (1H, d, J = 1.3 Hz, H7), 7.91 (1H, dd, J = 7.8, 1.4 Hz, H3), 7.67 – 7.57 (2H, m, H4/H11), 7.47 (1H, d, J = 2.1 Hz, H13), 7.13 (1H, d, J = 8.6 Hz, H10); **$^{13}\text{C NMR}$** (101 MHz, DMSO- d_6) δ 192.0 (C1), 158.0 (C9), 142.1 (C5), 136.9 (C2), 133.9 (C6), 132.9 (C4), 130.1 (C7), 127.5 (C3), 127.5 (1C, q, J = 6.4 Hz, C13), 127.2 (1C, q, J = 3.7 Hz, C11), 125.7 (C8), 124.6 (1C, q, J = 271.0 Hz, C14), 119.4 (1C, q, J = 32.2 Hz, C12), 116.2 (C10); **HRMS** (ESI) calcd for $[\text{C}_{14}\text{H}_8\text{O}_2^{35}\text{ClF}_3 + \text{H}]^+$: 301.0243, found: 301.0239.

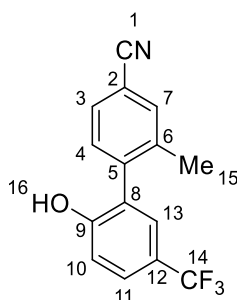
2'-Chloro-4'-(hydroxymethyl)-5-(trifluoromethyl)-[1,1'-biphenyl]-2-ol (**64**)



To a stirred solution of aldehyde **63** (50 mg, 0.16 mmol) in dry MeOH (3.2 mL) at 0 °C was added NaBH₄ (19 mg, 0.50 mmol) as a single portion. The mixture was allowed to warm to room temperature with stirring overnight before removal of the solvent *in vacuo*. The residue was dissolved in Et₂O/H₂O and extracted three times with Et₂O. The combined organic extracts were washed with a saturated aqueous solution of NaCl, dried over MgSO₄, filtered and concentrated *in vacuo*. The crude alcohol was then purified by semi-preparative HPLC (5-95% B) to provide title compound **64** as a white solid (31 mg, 0.10 mmol, 61%):

HPLC t_r = 12.23 mins (5-95% B); **m.p.** 150-151 °C; **IR** ν_{\max} 3451 (br s, O-H), 3078 (s, O-H), 1675 (m, C=C), 1608 (m, C=C), 1533 (m, C=C); **$^1\text{H NMR}$** (400 MHz, DMSO- d_6) δ 10.26 (1H, s br, H15), 7.58 (1H, dd, J = 8.6, 2.0 Hz, H11), 7.46 (1H, s, H7), 7.37 (1H, d, J = 2.2 Hz, H13), 7.34 – 7.28 (2H, m, H3/H4), 7.09 (1H, d, J = 8.5 Hz, H10), 5.36 (1H, s br, H16), 4.54 (2H, d, J = 3.5 Hz, H1); **$^{13}\text{C NMR}$** (101 MHz, DMSO- d_6) δ 158.2 (C9), 144.3 (C2), 134.4 (C5), 132.5 (C6), 131.6 (C4), 127.8 (1C, q, J = 3.7 Hz, C13), 126.8 (C7), 126.6 (C8), 126.5 (1C, q, J = 3.8 Hz, C11), 124.9 (C3), 124.7 (1C, q, J = 270.9 Hz, C14), 119.3 (1C, q, J = 32.1 Hz, C12), 116.0 (C10), 62.0 (C1); **HRMS** (ESI) calcd for $[\text{C}_{14}\text{H}_{10}\text{O}_2^{35}\text{ClF}_3]$: 302.0321, found: 302.0319. Conditions adapted from literature protocol.²⁶⁴

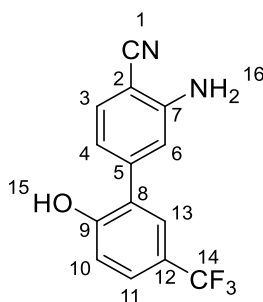
2'-Hydroxy-2-methyl-5'-(trifluoromethyl)-[1,1'-biphenyl]-4-carbonitrile (**65**)



Prepared by General Method **B** using 3-methyl-4-bromobenzonitrile (56 mg, 0.28 mmol), boronic ester **61b** (75 mg, 0.26 mmol), PdCl₂(dppf).CH₂Cl₂ (11 mg, 0.013 mmol), K₃PO₄ (66 mg, 0.31 mmol), DME (0.85 mL), EtOH (0.25 mL) and H₂O (0.15 mL). The crude product was purified by flash column chromatography (silica gel, gradient elution: 10:90 EtOAc:Hexane to 25:75 EtOAc:Hexane) to provide the title compound **65** as a white solid (31 mg, 0.11 mmol, 43%):

R_f 0.22 (3:7 EtOAc:Hexane); **m.p.** 125-126 °C; **IR** ν_{\max} 3364 (s, O-H), 2235 (m, C≡N), 1618 (s, C=C), 1605 (m, C=C), 1518 (w, C=C); **¹H NMR** (500 MHz, DMSO-d₆) δ 10.57 (1H, s, H16), 7.77 (1H, s br, H7), 7.69 (1H, d, *J* = 7.8 Hz, H3), 7.61 (1H, d, *J* = 8.5 Hz, H11), 7.46 – 7.30 (2H, m, H4/H13), 7.12 (1H, d, *J* = 8.5 Hz, H10), 2.15 (3H, s, H15); **¹³C NMR** (126 MHz, DMSO-d₆) δ 157.6 (C9), 142.5 (C5), 138.3 (C8), 133.0 (C7), 131.1 (C4), 129.4 (C3), 127.3 (2C, br s, C6/C13), 126.7 (1C, q, *J* = 3.1 Hz, C11), 124.6 (1C, q, *J* = 270.9 Hz, C14), 119.7 (1C, q, *J* = 32.1 Hz, C12), 118.9 (C1), 116.1 (C10), 110.4 (C2), 19.2 (C15); **HRMS** (ESI) calcd for [C₁₅H₁₀NOF₃ + H]⁺: 278.0793, found: 278.0800.

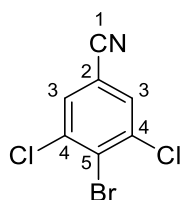
3-Amino-2'-hydroxy-5'-(trifluoromethyl)-[1,1'-biphenyl]-4-carbonitrile (**66**)



Prepared by General Method **B** using 2-amino-4-bromobenzonitrile (56 mg, 0.28 mmol), boronic ester **61b** (75 mg, 0.26 mmol), PdCl₂(dppf).CH₂Cl₂ (11 mg, 0.013 mmol), K₃PO₄ (66 mg, 0.31 mmol), DME (0.85 mL), EtOH (0.25 mL) and H₂O (0.15 mL). The crude product was purified by flash column chromatography (silica gel, gradient elution: 10:90 EtOAc:Hexane to 30:70 EtOAc:Hexane) to provide the title compound **66** as a white solid (40 mg, 0.14 mmol, 56%):

R_f 0.37 (1:1 EtOAc:Hexane); **m.p.** 210-211 °C; **IR** ν_{\max} 3363 (s, N-H), 3302 (s, N-H), 2988 (m, C-H), 2221 (m, C≡N), 1613 (m, C=C), 1562 (s, C=C), 1454 (m, C=C); **¹H NMR** (500 MHz, DMSO-d₆) δ 10.61 (1H, s, H15), 7.55 (1H, d br, *J* = 8.5 Hz, H11), 7.48 (1H, s br, H13), 7.41 (1H, d, *J* = 8.1 Hz, H3), 7.11 (1H, d, *J* = 8.5 Hz, H10), 6.99 (1H, s br, H6), 6.79 (1H, d br, *J* = 8.1 Hz, H4), 6.06 (2H, s, H16); **¹³C NMR** (126 MHz, DMSO-d₆) δ 157.8 (C9), 151.4 (C1), 142.6 (C5), 132.1 (C3), 127.4 (C8), 126.9 (1C, *q*, *J* = 3.0 Hz, C13), 126.4 (1C, *q*, *J* = 2.9 Hz, C11), 124.6 (1C, *q*, *J* = 271.0 Hz, C14), 119.9 (1C, *q*, *J* = 32.1 Hz, C12), 118.2 (C7), 117.2 (C4), 116.6 (C10), 115.7 (C6), 92.3 (C2); **HRMS** (ESI) calcd for [C₁₄H₉N₂OF₃ - H]⁻: 277.0589 found: 277.0589.

4-Bromo-3,5-dichlorobenzonitrile (**67a**)

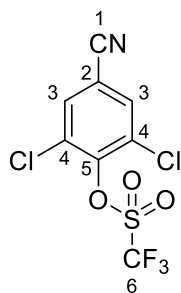


To a stirred solution of 4-amino-3,5-dichlorobenzonitrile (1.38 g, 7.38 mmol) in conc. HBr (14 mL) at 0 °C was added sodium nitrite (560 mg, 8.11 mmol) in H₂O (2.5 mL) followed by copper (I) bromide (2.12 g, 14.76 mmol) in conc. HBr (2.5 mL) and H₂O (13.3 mL). The mixture was allowed to warm to room temperature before heating at 50 °C for 3 hours. After cooling to room temperature the reaction mixture was stirred for a further 18 hours before the residue was dissolved in CH₂Cl₂/H₂O and extracted three times with CH₂Cl₂. The combined organic extracts were washed with a saturated aqueous solution of NaCl, dried over MgSO₄, filtered and concentrated *in vacuo*. The crude product was purified by flash column chromatography (silica gel, gradient elution: 2.5:97.5 EtOAc:Hexane to 10:90 EtOAc:Hexane) to provide the title compound **67a** as a white solid (1.04 g, 4.16 mmol, 56%):

R_f 0.64 (1:1 EtOAc:Hexane); **m.p.** 137-138 °C; **IR** ν_{\max} 3061 (w, C-H), 2235 (m, C≡N), 1533 (m, C=C), 1411 (w, C=C); **¹H NMR** (400 MHz, CDCl₃) δ 7.65 (2H, s, H3); **¹³C NMR** (101 MHz, CDCl₃) δ 138.0 (2C, C4), 131.3 (2C, C3), 130.1 (C5), 116.0 (C1), 113.0 (C2); **HRMS** (ESI) calcd for [C₇H₂NCl₂Br]: 248.8748, found: 248.8746.

Conditions adapted from literature protocol.²⁶⁵ Spectroscopic data consistent with that reported for commercially available 4-bromo-3,5-dichlorobenzonitrile (CAS: 1160574-40-2).

2,6-Dichloro-4-cyanophenyl trifluoromethanesulfonate (**67c**)

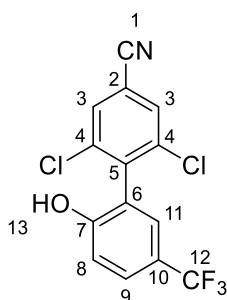


Prepared by General Method **A** using 3,5-dichloro-4-hydroxybenzonitrile (966 mg, 5.14 mmol), anhydrous CH_2Cl_2 (16 mL), anhydrous pyridine (1.29 mL, 15.96 mmol) and trifluoromethanesulfonic anhydride (0.96 mL, 5.85 mmol). The crude residue was used without further purification. Title compound **67c** was a white solid (1.68 g, 5.14 mmol, 100%):

R_f 0.46 (1:4 EtOAc:Hexane); **m.p.** = 95-96 °C; **IR** ν_{max} : 2238 (m, C≡N), 1204 (w, C=C); **$^1\text{H NMR}$** (400 MHz, CDCl_3): δ 7.76 (2H, s, H3); **$^{13}\text{C NMR}$** (101 MHz, CDCl_3) δ 145.9 (C5), 133.1 (2C, C3), 131.1 (2C, C4), 118.5 (1C, q, J = 321.4 Hz, C6), 115.2 (C1), 114.0 (C2); **LCMS** t_r = 4.07 min, calcd for $[\text{C}_8\text{H}_2\text{Cl}_2\text{F}_3\text{NO}_3\text{S} + \text{K}]^+$: 359.16, found: 358.21.

Spectroscopic data consistent with that reported in the literature.²⁵²

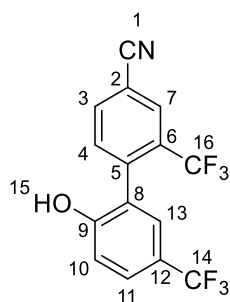
2,6-Dichloro-2'-hydroxy-5'-(trifluoromethyl)-[1,1'-biphenyl]-4-carbonitrile (**67**)



Prepared by General Method **D** using bromide **67a** (103 mg, 0.41 mmol), boronic ester **61b** (142 mg, 0.49 mmol), $\text{Pd}(\text{OAc})_2$ (5 mg, 0.02 mmol), S-Phos (16 mg, 0.04 mmol), K_3PO_4 (174 mg, 0.82 mmol), toluene (0.82 mL) and H_2O (0.12 mL). The crude product was purified by flash column chromatography (silica gel, gradient elution: 10:90 EtOAc:Hexane to 30:70 EtOAc:Hexane) to provide the title compound **67** as a white solid (47 mg, 0.14 mmol, 35%):

R_f 0.49 (1:1 EtOAc:Hexane); **m.p.** 198-199 °C; **IR** ν_{max} 3295 (s, O-H), 2988 (m, C-H), 2253 (m, C≡N), 1618 (w, C=C), 1536 (s, C=C), 1518 (m, C=C); **¹H NMR** (400 MHz, DMSO-*d*₆) δ 10.73 (1H, s, H13), 8.21 (2H, s, H3), 7.66 (1H, dd, *J* = 8.6, 2.0 Hz, H9), 7.49 (1H, d, *J* = 2.1 Hz, H11), 7.14 (1H, d, *J* = 8.6 Hz, H8); **¹³C NMR** (101 MHz, DMSO-*d*₆) δ 157.7 (C7), 140.5 (C5), 135.7 (2C, C4), 131.6 (2C, C3), 127.8 (1C, q, *J* = 3.6 Hz, C9), 127.4 (1C, q, *J* = 3.8 Hz, C11), 124.5 (1C, q, *J* = 271.0 Hz, C12), 123.0 (C6), 119.7 (1C, q, *J* = 32.3 Hz, C10), 116.5 (C2), 116.4 (C8), 113.2 (C1); **HRMS** (ESI) calcd for [C₁₄H₆NOCl₂F₃ + H]⁺: 331.9857 found: 331.9853.

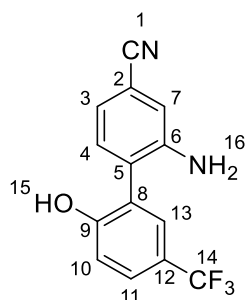
2'-Hydroxy-2,5'-bis(trifluoromethyl)-[1,1'-biphenyl]-4-carbonitrile (**68**)



Prepared by General Method **B** using 3-trifluoromethyl-4-bromobenzonitrile (95 mg, 0.38 mmol), boronic ester **61b** (100 mg, 0.34 mmol), PdCl₂(dppf).CH₂Cl₂ (14 mg, 0.017 mmol), K₃PO₄ (87 mg, 0.41 mmol), DME (1.12 mL), EtOH (0.3 mL) and H₂O (0.2 mL) with 1 hour microwave irradiation. The crude product was purified by flash column chromatography (silica gel, gradient elution: 5:95 EtOAc:Hexane to 12.5:87.5 EtOAc:Hexane) to provide the title compound **68** as a white solid (39 mg, 0.12 mmol, 35%):

R_f 0.56 (1:1 EtOAc:Hexane); **m.p.** 195-196 °C; **IR** ν_{max} 3288 (s, O-H), 2988 (m, C-H), 2255 (m, C≡N), 1622 (s, C=C), 1522 (m, C=C), 1499 (s, C=C); **¹H NMR** (500 MHz, DMSO-*d*₆) δ 10.64 (1H, s br, H15), 8.39 (1H, d, *J* = 1.1 Hz, H7), 8.19 (1H, dd, *J* = 8.0, 1.3 Hz, H3), 7.66 – 7.60 (2H, m, H4/H11), 7.42 (1H, d, *J* = 1.3 Hz, H13), 7.10 (1H, d, *J* = 8.6 Hz, H10); **¹³C NMR** (126 MHz, DMSO-*d*₆) δ 157.9 (C9), 141.0 (C5), 135.8 (C3), 133.9 (C4), 130.3 (1C, q, *J* = 4.9 Hz, C7), 129.2 (1C, q, *J* = 30.6 Hz, C6), 127.4 (1C, q, *J* = 3.0 Hz, C11), 127.1 (1C, q, *J* = 3.1 Hz, C13), 125.1 (C8), 124.5 (1C, q, *J* = 270.9 Hz, C14), 123.0 (1C, q, *J* = 274.5 Hz, C16), 119.0 (1C, q, *J* = 32.3 Hz, C12), 117.6 (C1), 115.8 (C10), 111.6 (C2); **HRMS** (ESI) calcd for [C₁₅H₇NOF₆]: 331.0432, found: 331.0431.

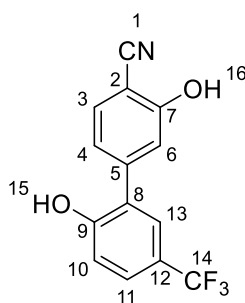
2-Amino-2'-hydroxy-5'-(trifluoromethyl)-[1,1'-biphenyl]-4-carbonitrile (**69**)



Prepared by General Method **B** using 3-amino-4-bromobenzonitrile (75 mg, 0.38 mmol), boronic ester **61b** (100 mg, 0.34 mmol), PdCl₂(dppf).CH₂Cl₂ (14 mg, 0.017 mmol), K₃PO₄ (87 mg, 0.41 mmol), DME (1.12 mL), EtOH (0.3 mL) and H₂O (0.2 mL). The crude product was purified by flash column chromatography (silica gel, gradient elution: 10:90 EtOAc:Hexane to 25:75 EtOAc:Hexane) to provide the title compound **69** as a beige solid (37 mg, 0.13 mmol, 39%):

R_f 0.31 (1:1 EtOAc:Hexane); **m.p.** 212-213 °C; **IR** ν_{\max} 3660 (s, N-H), 3358 (s, N-H/O-H), 2987 (m, C-H), 2228 (m, C≡N), 1618 (s, C=C), 1561 (w, C=C), 1503 (m, C=C); **¹H NMR** (500 MHz, DMSO-d₆) δ 10.56 (1H, s br, H15), 7.58 (1H, dd, *J* = 8.6, 2.0 Hz, H11), 7.39 (1H, d, *J* = 2.1 Hz, H13), 7.14 – 7.09 (2H, m, H4/H10), 7.07 (1H, d, *J* = 1.6 Hz, H7), 6.98 (1H, dd, *J* = 7.7, 1.7 Hz, H3), 5.14 (2H, s br, H16); **¹³C NMR** (126 MHz, DMSO-d₆) δ 158.0 (C9), 146.9 (C6), 131.9 (C4), 128.0 (1C, q, *J* = 3.2 Hz, C13), 127.0 (C5), 126.5 (1C, q, *J* = 3.1 Hz, C11), 125.4 (C8), 123.6 (1C, q, *J* = 270.9 Hz, C14), 119.9 (1C, q, *J* = 32.0 Hz, C12), 119.4 (C1), 119.0 (C3), 117.3 (C7), 116.5 (C10), 110.8 (C2); **HRMS** (ESI) calcd for [C₁₄H₉N₂OF₃]: 278.0667, found: 278.0665.

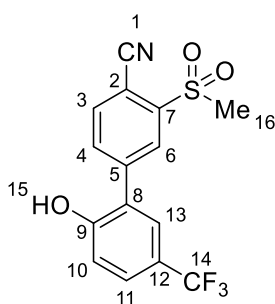
2',3-Dihydroxy-5'-(trifluoromethyl)-[1,1'-biphenyl]-4-carbonitrile (**70**)



Prepared by General Method **B** using 2-hydroxyl-4-bromobenzonitrile (56 mg, 0.28 mmol), boronic ester **61b** (75 mg, 0.26 mmol), PdCl₂(dppf).CH₂Cl₂ (11 mg, 0.013 mmol), K₃PO₄ (66 mg, 0.31 mmol), DME (0.85 mL), EtOH (0.25 mL) and H₂O (0.15 mL). The crude product was purified by flash column chromatography (silica gel, gradient elution: 10:90 EtOAc:Hexane to 30:70 EtOAc:Hexane) to provide the title compound **70** as a white solid (42 mg, 0.15 mmol, 58%):

R_f 0.25 (1:1 EtOAc:Hexane); **m.p.** 201-202 °C; **IR** ν_{max} 3355 (s, O-H), 3122 (s, O-H), 2987 (m, C-H), 2243 (m, C≡N), 1615 (s, C=C), 1579 (m, C=C), 1450 (m, C=C); **¹H NMR** (400 MHz, DMSO-*d*₆) δ 11.09 (1H, s br, H15/H16), 10.76 (1H, s br, H15/H16), 7.64 (1H, d, *J* = 8.1 Hz, H3), 7.58 (1H, dd, *J* = 8.6, 2.1 Hz, H11), 7.55 (1H, d, *J* = 2.0 Hz, H13), 7.24 (1H, d, *J* = 1.3 Hz, H6), 7.17 – 7.09 (2H, m, H4/H10); **¹³C NMR** (101 MHz, DMSO-*d*₆) δ 159.8 (C7), 157.8 (C9), 143.2 (C5), 132.9 (C3), 127.1 (1C, q, *J* = 3.6 Hz, C13), 126.8 (1C, q, *J* = 3.6 Hz, C11), 126.6 (C8), 124.6 (1C, q, *J* = 271.0 Hz, C14), 120.5 (2C, s br, C2/C10), 120.1 (1C, q, *J* = 32.1 Hz, C12), 117.1 (C1), 116.8 (1C, C4/C6), 116.7 (1C, C4/C6); **HRMS** (ESI) calcd for [C₁₄H₈NO₂F₃ - H]⁻: 278.0429, found: 278.0468.

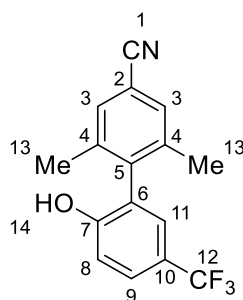
2'-Hydroxy-3-(methylsulfonyl)-5'-(trifluoromethyl)-[1,1'-biphenyl]-4-carbonitrile (71)



Prepared by General Method **B** using 2-methylsulfonyl-4-bromobenzonitrile (74 mg, 0.28 mmol), boronic ester **61b** (75 mg, 0.26 mmol), PdCl₂(dppf).CH₂Cl₂ (11 mg, 0.013 mmol), K₃PO₄ (66 mg, 0.31 mmol), DME (0.85 mL), EtOH (0.25 mL) and H₂O (0.15 mL). The crude product was purified by flash column chromatography (silica gel, gradient elution: 10:90 EtOAc:Hexane to 30:70 EtOAc:Hexane) to provide the title compound **71** as a clear oil (35 mg, 0.10 mmol, 40%):

R_f 0.23 (1:1 EtOAc:Hexane); **IR** ν_{max} 2988 (s, O-H), 2933 (m, C-H), 2233 (m, C≡N), 1619 (s, C=C), 1598 (m, C=C); **¹H NMR** (500 MHz, DMSO-*d*₆) δ 11.07 (1H, s, H15), 8.34 (1H, d, *J* = 1.6 Hz, H6), 8.23 (1H, d, *J* = 8.0 Hz, H3), 8.16 (1H, dd, *J* = 8.0, 1.7 Hz, H4), 7.78 (1H, d, *J* = 2.0 Hz, H13), 7.66 (1H, dd, *J* = 8.6, 2.1 Hz, H11), 7.18 (1H, d, *J* = 8.6 Hz, H10), 3.43 (3H, s, H16); **¹³C NMR** (126 MHz, DMSO-*d*₆) δ 158.0 (C9), 142.3 (C5), 141.9 (C7), 135.8 (C3), 134.4 (C4), 129.9 (C6), 127.8 (1C, q, *J* = 3.1 Hz, C11), 127.7 (1C, q, *J* = 3.1 Hz, C13), 124.8 (C8), 124.5 (1C, q, *J* = 271.2 Hz, C14), 120.4 (1C, q, *J* = 32.4 Hz, C12), 117.0 (C10), 115.9 (C1), 108.0 (C2), 43.1 (C15); **HRMS** (ESI) calcd for [C₁₅H₁₀NO₃SF₃ - H]⁻: 240.0255, found: 240.0263.

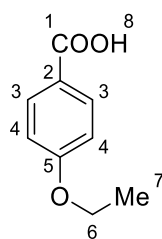
2'-Hydroxy-2,6-dimethyl-5'-(trifluoromethyl)-[1,1'-biphenyl]-4-carbonitrile (**72**)



Prepared by General Method **D** using 4-bromo-3,5-dimethylbenzonitrile (86 mg, 0.41 mmol), boronic ester **61b** (142 mg, 0.49 mmol), Pd(OAc)₂ (5 mg, 0.02 mmol), S-Phos (16 mg, 0.04 mmol), K₃PO₄ (174 mg, 0.82 mmol), toluene (0.82 mL) and H₂O (0.12 mL). The crude product was purified by flash column chromatography (silica gel, gradient elution: 10:90 EtOAc:Hexane to 20:80 EtOAc:Hexane) to provide the title compound **72** as a yellow solid (76 mg, 0.26 mmol, 64%):

R_f 0.59 (1:1 EtOAc:Hexane); **m.p.** 128-129 °C; **IR** ν_{\max} 3372 (s, O-H), 2987 (m, C-H), 2244 (m, C≡N), 1624 (s, C=C), 1589 (m, C=C), 1508 (s, C=C); **¹H NMR** (400 MHz, DMSO-d₆) δ 10.43 (1H, s, H14), 7.64 – 7.56 (3H, m, H3/H9), 7.30 (1H, d, *J* = 2.1 Hz, H11), 7.13 (1H, d, *J* = 8.5 Hz, H8), 1.99 (6H, s, H13); **¹³C NMR** (101 MHz, DMSO-d₆) δ 157.4 (C7), 142.5 (C5), 138.1 (2C, C4), 130.5 (2C, C3), 126.9 (1C, q, *J* = 3.7 Hz, C11), 126.6 (1C, q, *J* = 3.7 Hz, C9), 125.9 (C6), 124.7 (1C, q, *J* = 270.9 Hz, C12), 120.0 (1C, q, *J* = 32.1 Hz, C10), 119.0 (C1), 116.3 (C8), 110.1 (C2), 19.8 (2C, C13); **HRMS** (ESI) calcd for [C₁₆H₁₂NOF₃ - H]⁻: 290.0793 found: 290.0798.

4-Ethoxybenzoic acid (**73**)



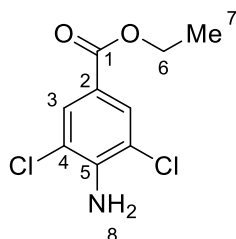
Isolated as a by-product (**73**) and characterised:

R_f 0.43 (1:1 EtOAc:Hexane); **¹H NMR** (500 MHz, DMSO-d₆) δ 10.30 (1H, s, H8), 7.81 (2H, d, *J* = 8.7 Hz, H3), 6.84 (2H, d, *J* = 8.7 Hz, H4), 4.24 (2H, q, *J* = 7.1 Hz, H6), 1.29 (3H, t, *J* = 7.1 Hz, H7); **¹³C NMR** (126 MHz, DMSO-d₆) δ 165.6 (C5), 161.9 (C1), 131.4 (2C, C3), 120.5 (C2), 115.3 (2C, C4), 60.1 (C6), 14.3 (C7); **HRMS** (ESI) calcd for [C₉H₁₀O₃]: 166.0630 found: 166.0630.

Spectroscopic data consistent with that reported for commercially available 4-ethoxybenzoic acid (CAS: 619-86-3).

4.5 Experimental Details for α D Pocket to Substrate-Binding Channel Linker Investigation

Ethyl 4-amino-3,5-dichlorobenzoate (**74b**)

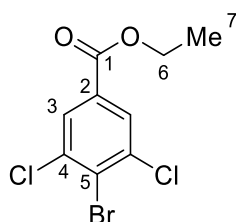


To a stirred suspension of 4-amino-3,5-dichlorobenzoic acid (1.00 g, 4.85 mmol) in EtOH (20 mL) was added conc. H_2SO_4 (1 mL) dropwise before refluxing for 18 hours. The mixture was allowed to cool to room temperature before neutralising with a saturated aqueous solution of NaHCO_3 and extracting with EtOAc three times. The combined organic extracts were washed with a saturated aqueous solution of NaHCO_3 and a saturated aqueous solution of NaCl before drying over MgSO_4 , filtering and concentration *in vacuo*. The crude product was then purified by flash column chromatography using a short (~5 cm) silica gel plug with 10:90 EtOAc:Hexane to provide the title compound **74b** as a cream solid (1.13 g, 4.82 mmol, 99%):

R_f 0.60 (1:20:80 NEt_3 :EtOAc:Cyclohexane); **m.p.** 85–86 °C; **IR** ν_{max} 3481 (s, N-H), 3375 (s, C-H), 1699 (s, C=O), 1610 (m, C=C), 1554 (s, C=C), 1495 (m, C=C); **¹H NMR** (500 MHz, $\text{DMSO-}d_6$) δ 7.72 (2H, s, H3), 6.39 (2H, s, H8), 4.24 (2H, q, $J = 7.1$ Hz, H6), 1.28 (3H, t, $J = 7.1$ Hz, H7); **¹³C NMR** (126 MHz, $\text{DMSO-}d_6$) δ 164.1 (C1), 145.5 (C2), 129.1 (2C, C3), 117.5 (C5), 117.2 (2C, C4), 60.7 (C6), 14.3 (C7); **HRMS** (ESI) calcd for $[\text{C}_9\text{H}_9\text{NO}_2^{35}\text{Cl}_2 + \text{H}]^+$: 234.0089, found: 234.0083.

Spectroscopic data consistent with that reported for commercially available ethyl 4-amino-3,5-dichlorobenzoate (CAS: 74878-31-2).

Ethyl 4-bromo-3,5-dichlorobenzoate (**74a**)

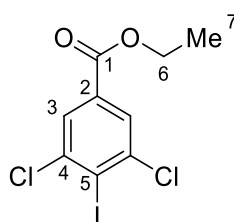


To a stirred suspension of **74b** (1.07 g, 4.55 mmol) in conc. HBr (4.55 mL) at 0 °C was added sodium nitrite (409 mg, 5.92 mmol) in H₂O (2.96 mL). Following warming to room temperature, a solution of copper (I) bromide (1.31 g, 9.10 mmol) in conc. HBr (4.55 mL) was added and the reaction heated at 105 °C for 4 hours. After cooling to 0 °C the reaction was quenched with ice cold H₂O and extracted into EtOAc three times. The combined organic extracts were washed with a saturated aqueous solution of NaCl, dried over MgSO₄, filtered and concentrated *in vacuo*. The crude product was purified by flash column chromatography (silica gel, gradient elution: 0:100 EtOAc:Cylcohexane to 1.5:98.5 EtOAc:Cylcohexane) to provide the title compound **74a** as a white solid (526 mg, 1.77 mmol, 39%):

R_f 0.34 (5:95 EtOAc:Cylcohexane); **m.p.** 113-114 °C; **IR** ν_{\max} 1713 (s, C=O), 1548 (m, C=C), 1368 (s, C=C); **¹H NMR** (500 MHz, DMSO-*d*₆) δ 8.02 (2H, s, H3), 4.34 (2H, q, *J* = 7.1 Hz, H6), 1.33 (3H, t, *J* = 7.1 Hz, H7); **¹³C NMR** (126 MHz, DMSO-*d*₆) δ 163.3 (C1), 136.0 (2C, C4), 131.2 (C2), 128.9 (2C, C3), 128.2 (C5), 62.0 (C6), 14.1 (C7); **HRMS** (ESI) calcd for [C₉H₇O₂³⁵Cl₂⁸¹Br + H]⁺: 296.9085, found: 296.9079.

Conditions adapted from literature protocol and compound referenced but no spectroscopic data reported.²⁶⁵

Ethyl 4-iodo-3,5-dichlorobenzoate (**74e**)

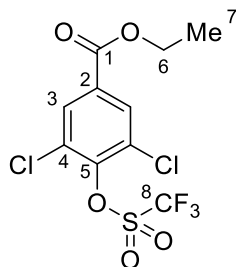


To a stirred solution of **74b** (500 mg, 2.14 mmol) in acetone (2.68 mL) and conc. HCl (21.40 mL) at 0 °C was added sodium nitrite (193 mg, 1.40 mmol) in H₂O (2.5 mL) dropwise. The solution was stirred at 0 °C for 2 hours before a solution of potassium iodide (1.07 g, 6.42 mmol) in H₂O (3.21 mL) was added. The mixture was allowed to warm to room temperature and stirred for a further 72 hours before extraction into EtOAc three times. The combined organic extracts were washed with a saturated aqueous solution of NaCl, dried over MgSO₄, filtered and concentrated *in vacuo*. The crude product was purified by flash column chromatography (silica gel, gradient elution: 0:100 EtOAc:Cyclohexane to 5:95 EtOAc:Cyclohexane) to provide the title compound **74e** as a white solid (455 mg, 1.32 mmol, 62%):

R_f 0.73 (1:9 EtOAc:Cylcohexane); **m.p.** 114-115 °C; **IR** ν_{\max} 1707 (s, C=O), 1541 (m, C=C), 1365 (s, C=C); **¹H NMR** (500 MHz, DMSO-*d*₆) δ 7.90 (2H, s, H3), 4.32 (2H, q, *J* = 7.1 Hz, H6), 1.32 (3H, t, *J* = 7.1 Hz, H7); **¹³C NMR** (126 MHz, DMSO-*d*₆) δ 163.5 (C1), 140.5 (2C, C4), 132.1 (C2), 127.3, (2C, C3), 111.8, (C5), 61.9, (C6), 14.1 (C7); **HRMS** (ESI) calcd for [C₉H₇O₂³⁵Cl₂¹²⁷I + H]⁺: 344.8946, found: 344.8942.

Conditions adapted from literature protocol and spectroscopic data consistent with that reported.²⁸⁸

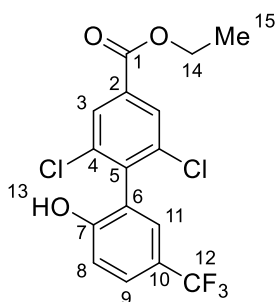
Ethyl 3,5-dichloro-4-(((trifluoromethyl)sulfonyl)oxy)benzoate (**74g**)



Prepared by General Method **A** using ethyl 3,5-dichloro-4-hydroxybenzoate (2.00 g, 8.51 mmol), anhydrous CH_2Cl_2 (28.0 mL), anhydrous NEt_3 (2.65 mL, 19.2 mmol) and trifluoromethanesulfonic anhydride (2.00 mL, 11.9 mmol). The crude residue was purified by flash column chromatography (silica gel, gradient elution: 0:100 EtOAc:cyclohexane to 5:95 EtOAc:Cyclohexane) to provide the title compound **74g** as a white solid (2.31 g, 6.29 mmol, 74%):

R_f 0.35 (2:98 EtOAc:Cyclohexane); **m.p.** 89-90 °C; **IR** ν_{max} 1717 (s, C=O), 1569 (m, C=C), 1541 (s, C=C), 1431 (w, C=C); **¹H NMR** (400 MHz, $\text{DMSO}-d_6$) δ 8.18 (2H, s, H3), 4.34 (2H, q, $J = 7.1$ Hz, H6), 1.32 (3H, t, $J = 7.1$ Hz, H7); **¹³C NMR** (126 MHz, $\text{DMSO}-d_6$) δ 162.9 (C1), 144.6 (C5), 132.3 (C2), 130.8 (2C, C3), 128.8 (2C, C4), 118.1 (1C, q, $J = 321.2$ Hz, C8), 62.5 (C6), 14.2 (C7); **HRMS** (ESI) calcd for $[\text{C}_{10}\text{H}_7\text{O}_5\text{S}^{35}\text{Cl}_2\text{F}_3 + \text{H}]^+$: 366.9422, found: 366.9416.

Ethyl 2,6-dichloro-2'-hydroxy-5'-(trifluoromethyl)-[1,1'-biphenyl]-4-carboxylate (**74d**)

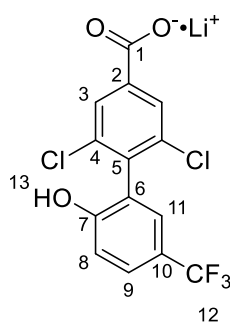


A solution of triflate **74g** (920 mg, 2.50 mmol), boronic ester **61b** (1.80 g, 6.25 mmol) and $\text{Pd}(\text{PPh}_3)_4$ (580 mg, 0.50 mmol) in MeOH (16.7 mL) and saturated aqueous NaHCO_3 (2.50 mL) was degassed by bubbling argon through the stirred mixture for 10 minutes before heating at 110 °C for 20 hours. The reaction was allowed to cool to room temperature, filtered through celite washing with EtOAc and the solvent removed under reduced pressure. The residue was dissolved in EtOAc/ H_2O and extracted with EtOAc three times. The combined organic extracts were washed with a saturated aqueous solution of

NaCl, dried over MgSO₄, filtered and concentrated *in vacuo*. The crude product was purified by flash column chromatography (silica gel, gradient elution: 0:100 EtOAc:Cyclohexane to 10:90 EtOAc:Cylcohexane) to provide the title compound **74d** as a white solid (772 mg, 2.04 mmol, 81%):

R_f 0.24 (1:4 EtOAc:Cylcohexane); **m.p.** 153-154 °C; **IR** ν_{\max} 3217 (br s, O-H), 1685 (s, C=O), 1615 (m, C=C), 1546 (m, C=C), 1517 (w, C=C), 1475 (w, C=C); **¹H NMR** (500 MHz, DMSO-*d*₆) δ 10.70 (1H, s, H13), 8.01 (2H, s, H3), 7.66 (1H, dd, *J* = 8.7, 2.3 Hz, H9), 7.46 (1H, d, *J* = 2.3 Hz, H11), 7.14 (1H, d, *J* = 8.5 Hz, H8), 4.37 (2H, q, *J* = 7.1 Hz, H14), 1.34 (3H, t, *J* = 7.1 Hz, H15); **¹³C NMR** (126 MHz, DMSO-*d*₆) δ 163.6 (C1), 157.8 (C7), 139.8 (C5), 135.4 (2C, C4), 131.9 (C2), 128.3 (2C, C3), 127.8 (1C, q, *J* = 3.7 Hz, C11), 127.6 (1C, q, *J* = 4.0 Hz, C9), 124.6 (1C, q, *J* = 271.0 Hz, C12), 123.5 (C6), 119.73 (1C, q, *J* = 32.2 Hz, C10), 116.4 (C8), 61.8 (C14), 14.1 (C15); **HRMS** (ESI) calcd for [C₁₆H₁₁O₃³⁵Cl₂F₃ + H]⁺: 379.0116, found: 379.0106.

Lithium 2,6-dichloro-2'-hydroxy-5'-(trifluoromethyl)-[1,1'-biphenyl]-4-carboxylate (**74**)



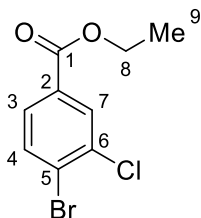
To a stirred solution of ester **74d** (607 mg, 1.60 mmol) in THF (3.55 mL) and MeOH (1.78 mL) was added a 3.0 M aqueous solution of NaOH (1.60 mL, 4.80 mmol) dropwise. After stirring for 18 hours the reaction mixture was quenched with 2.0 M aqueous HCl and extracted into EtOAc three times. The combined organic extracts were washed with a saturated aqueous solution of NaCl, dried over Na₂SO₄ for 10 minutes, filtered and concentrated *in vacuo* to provide the crude carboxylic acid of **74** (694 mg). The crude material was dissolved in minimal CH₂Cl₂ with stirring and a 0.5 M aqueous solution of LiOH·H₂O (3.20 mL, 1.60 mmol) added dropwise. After 18 hours the excess CH₂Cl₂ and H₂O was blown off and the lithium salt was freeze dried to provide the title compound **74** as a white solid in sufficient purity for the next step (566 mg, 1.59 mmol, 99%):

R_f 0.51 (1:50:50 AcOH:EtOAc:Cylcohexane); **m.p.** 222-223 °C; **IR** ν_{\max} 3377 (br s, O-H), 1620 (s, C=O), 1572 (m, C=C), 1529 (s, C=C), 1436 (w, C=C); **¹H NMR** (500 MHz, DMSO-*d*₆) δ 7.89 (2H, s, H3), 7.56 (1H, dd, *J* = 8.7, 2.4 Hz, H9), 7.33 (1H, d, *J* = 2.3 Hz, H11), 7.14 (1H, d, *J* = 8.6 Hz, H8); **¹³C NMR** (126 MHz, DMSO-*d*₆) δ 166.1 (C1), 159.1 (C7), 142.7 (C2), 135.6 (C5), 133.8 (2C, C4), 128.4 (2C, C3), 127.8 (1C, q,

$J = 3.8$ Hz, C11), 127.2 (1C, q, $J = 3.9$ Hz, C9), 124.9 (1C, q, $J = 270.7$ Hz, C12), 124.6 (C6), 118.8 (1C, d, $J = 30.5$ Hz, C10), 116.5 (C8); **HRMS** (ESI) calcd for $[C_{14}H_6O_3^{35}Cl_2F_3 + H]$: 349.9724, found: 349.9720.

H13 is a very broad singlet and lost in the baseline upon spectra processing.

Ethyl 4-bromo-3-chlorobenzoate (**76b**)

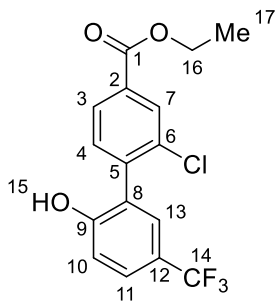


To a stirred suspension of 4-bromo-3-chlorobenzoic acid (1.00 g, 4.25 mmol) in EtOH (10 mL) was added conc. H_2SO_4 (1 mL) dropwise before refluxing for 18 hours. The mixture was allowed to cool to room temperature before neutralising with a saturated aqueous solution of $NaHCO_3$ and extracting with EtOAc three times. The combined organic extracts were then washed with a saturated aqueous solution of $NaHCO_3$ and a saturated aqueous solution of NaCl before drying over $MgSO_4$, filtering and concentration *in vacuo*. The crude product was then purified by flash column chromatography using a short (~5 cm) silica gel plug with 10:90 EtOAc:Hexane to provide the title compound **76b** as a white solid (838 mg, 3.18 mmol, 75%):

R_f 0.49 (1:4 EtOAc:Hexane); **m.p.** 40-41 °C; **IR** ν_{max} 1719 (s, C=O), 1586 (m, C=C), 1458 (m, C=C); **¹H NMR** (400 MHz, $CDCl_3$) δ 8.11 (1H, d, $J = 1.9$ Hz, H7), 7.77 (1H, dd, $J = 8.3, 2.0$ Hz, H3), 7.70 (1H, d, $J = 8.3$ Hz, H4), 4.38 (2H, q, $J = 7.1$ Hz, H8), 1.40 (3H, t, $J = 7.1$ Hz, H9); **¹³C NMR** (101 MHz, $CDCl_3$) δ 165.0 (C1), 135.0 (C6), 134.0 (C4), 131.4 (C7), 131.2 (C2), 128.8 (C3), 128.0 (C5), 61.8 (C8), 14.4 (C9); **HRMS** (ESI) calcd for $[C_9H_8O_2^{35}Cl^{79}Br + H]^+$: 262.9474, found: 262.9474.

Spectroscopic data consistent with that reported for commercially available ethyl 4-bromo-3-chlorobenzoate (CAS: 120077-67-0).

Ethyl 2-chloro-2'-hydroxy-5'-(trifluoromethyl)-[1,1'-biphenyl]-4-carboxylate (**76c**)

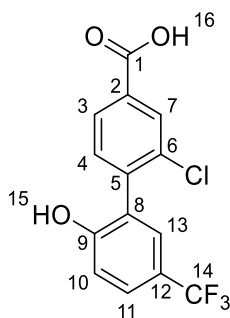


Prepared by General Method **B** with refluxing for 4 hours using ester **76b** (1.14 g, 4.34 mmol), boronic ester **61b** (1.50 g, 5.21 mmol), $PdCl_2(dppf) \cdot CH_2Cl_2$ (177 mg, 0.22 mmol), K_3PO_4 (1.11 g, 5.21 mmol),

DME (14.5 mL), EtOH (4.30 mL) and H₂O (2.20 mL). The crude product was purified by flash column chromatography (silica gel, gradient elution: 5:95 EtOAc:Hexane to 25:75 EtOAc:Hexane) to provide the title compound **76c** as a white solid (1.40 g, 4.05 mmol, 93%):

R_f 0.48 (1:1 EtOAc:Hexane); **m.p.** 128-129 °C; **IR** ν_{\max} 3264 (br s, O-H), 1686 (s, C=O), 1617 (m, C=C); **¹H NMR** (500 MHz, DMSO-d₆) δ 10.63 (1H, s, H15), 8.02 (1H, d, *J* = 1.6 Hz, H7), 7.94 (1H, dd, *J* = 8.0, 1.7 Hz, H3), 7.63 (1H, dd, *J* = 8.8, 2.2 Hz, H11), 7.54 (1H, d, *J* = 7.9 Hz, H4), 7.46 (1H, d, *J* = 2.1 Hz, H13), 7.12 (1H, d, *J* = 8.5 Hz, H10), 4.36 (2H, q, *J* = 7.1 Hz, H16), 1.34 (3H, t, *J* = 7.1 Hz, H17); **¹³C NMR** (126 MHz, DMSO-d₆) δ 164.5 (C1), 157.9 (C9), 141.0 (C5), 133.3 (C6), 132.5 (C4), 130.9 (C2), 129.4 (C7), 127.8 – 127.4 (1C, m, C13), 127.6 (C3), 127.3 – 126.9 (1C, m, C11), 125.7 (C8), 124.6 (1C, q, *J* = 273.2 Hz, C14), 119.4 (1C, q, *J* = 32.2 Hz, C12), 116.2 (C10), 61.3 (C16), 14.1 (C17); **HRMS** (ESI) calcd for [C₁₆H₁₂O₃³⁵ClF₃ + H]⁺: 345.0505, found: 345.0514.

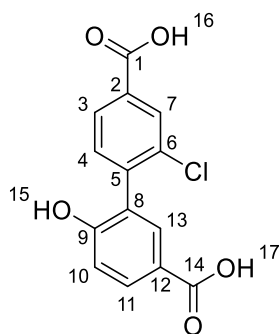
2-Chloro-2'-hydroxy-5'-(trifluoromethyl)-[1,1'-biphenyl]-4-carboxylic acid (**76**)



Prepared by General Method **B** using 4-bromo-3-chlorobenzoic acid (162 mg, 0.69 mmol), boronic ester **61b** (240 mg, 0.83 mmol), PdCl₂(dppf)·CH₂Cl₂ (28 mg, 0.035 mmol), K₃PO₄ (177 mg, 0.83 mmol), DME (2.30 mL), EtOH (0.69 mL) and H₂O (0.35 mL). The crude product was purified by flash column chromatography (silica gel, 1:2:98 AcOH:MeOH:CH₂Cl₂) to provide the title compound **76** as a yellow oil (146 mg, 0.46 mmol, 67%):

R_f 0.37 (1:10:90 AcOH:MeOH:CH₂Cl₂); **IR** ν_{\max} 2923 (br s, O-H), 1680 (s, C=O), 1581 (m, C=C), 1536 (m, C=C); **¹H NMR** (400 MHz, DMSO-d₆) δ 12.68 (1H, s br, H16), 10.64 (1H, s br, H15), 8.00 (1H, s, H7), 7.92 (1H, d, *J* = 7.8 Hz, H3), 7.62 (1H, d, *J* = 7.2 Hz, H11), 7.51 (1H, d, *J* = 7.9 Hz, H4), 7.45 (1H, d, *J* = 1.4 Hz, H13), 7.12 (1H, d, *J* = 8.4 Hz, H10); **¹³C NMR** (101 MHz, DMSO-d₆) δ 166.1 (C1), 157.9 (C9), 140.6 (C5), 133.2 (C2/C6), 132.3 (C4), 132.0 (C2/C6), 129.7 (C7), 127.7 (C3), 127.6 (1C, q, *J* = 3.3 Hz, C13), 127.1 (1C, q, *J* = 4.3 Hz, C11), 125.8 (C8), 124.6 (1C, q, *J* = 271.0 Hz, C14), 119.4 (1C, q, *J* = 32.1 Hz, C12), 116.1 (C10); **HRMS** (ESI) calcd for [C₁₄H₈O₃³⁵ClF₃]: 316.0114, found: 316.0099.

2'-Chloro-6-hydroxy-[1,1'-biphenyl]-3,4'-dicarboxylic acid (**77**)

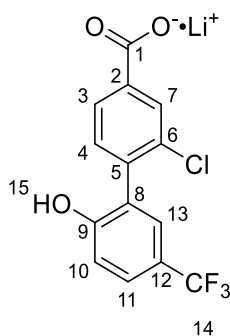


To a stirred solution of nitrile **61a** (155 mg, 0.52 mmol) in EtOH (2.1 mL) was added a 6.0 M aqueous solution of NaOH (2.10 mL, 12.6 mmol) and the reaction heated at 80 °C for 18 hours. Following cooling to room temperature and then to 0 °C, the reaction was quenched with a 2.0 M aqueous solution of HCl and extracted into EtOAc three times. The combined organic extracts were then washed with a saturated aqueous solution of NaCl, dried over MgSO₄, filtered and concentration *in vacuo*. The residual oil was then freeze dried to provide the title compound **77** as a beige solid in sufficient purity for analysis (142 mg, 0.49 mmol, 93%):

LCMS t_r 1.22 min, calcd for [C₁₄H₉O₅³⁵Cl - H]⁻ 291.0, [M-H]⁻ 291.2; **m.p.** decomp. above 350 °C; **IR** ν_{max} 2927 (br s, O-H), 1677 (s, C=O), 1606 (m, C=C), 1552 (m, C=C); **¹H NMR** (500 MHz, DMSO-d₆) δ 10.54 (1H, s, H15), 8.00 (1H, d, J = 1.6 Hz, H7), 7.92 (1H, dd, J = 7.9, 1.7 Hz, H3), 7.85 (1H, d, J = 2.2 Hz, H11), 7.68 (1H, d, J = 2.2 Hz, H13), 7.49 (1H, d, J = 7.9 Hz, H4), 7.02 (1H, d, J = 8.6 Hz, H10), 3.51 (2H, s br, H16/H17); **¹³C NMR** (126 MHz, DMSO-d₆) δ 166.9 (C14), 166.1 (C1), 158.7 (C9), 141.3 (C5), 133.0 (C2), 132.3 (C4), 132.1 (C13), 131.7 (C6), 131.5 (C11), 129.7 (C7), 127.7 (C3), 125.2 (C8), 121.3 (C12), 115.6 (C10); **HRMS** (ESI) calcd for [C₁₄H₉O₅³⁵Cl - H]⁻: 291.0060, found: 291.0062.

Conditions adapted from literature protocol.²⁸¹

Lithium 2-chloro-2'-hydroxy-5'-(trifluoromethyl)-[1,1'-biphenyl]-4-carboxylate (**78**)

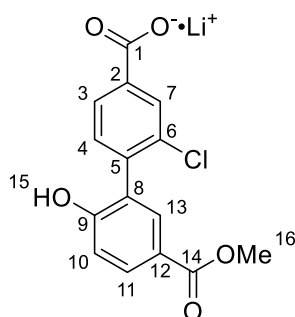


To a stirred solution of ester **76c** (694 mg, 2.01 mmol) in THF (4.78 mL) and MeOH (2.39 mL) was added a 3.0 M aqueous solution of NaOH (2.01 mL, 6.03 mmol) dropwise. After stirring for 18 hours the reaction mixture was quenched with 2.0 M aqueous HCl and extracted into EtOAc three times. The combined organic extracts were washed with a saturated aqueous solution of NaCl, dried over Na₂SO₄ for 10 minutes, filtered and concentrated *in vacuo* to provide the crude carboxylic acid of **78**. The crude material was dissolved in minimal CH₂Cl₂ with stirring and a 0.5 M aqueous solution of LiOH·H₂O (4.02 mL, 2.01 mmol) added dropwise. After 18 hours the excess CH₂Cl₂ and H₂O was blown off and the lithium salt was freeze dried to provide the title compound **78** as a beige solid in sufficient purity for the next step (645 mg, 2.00 mmol, 99%):

LCMS *t*_r 1.46 min, calcd for [C₁₄H₈O₃³⁵ClF₃ - H]⁻ 315.0, [M-H]⁻ 315.2; **m.p.** 210-211 °C; **IR** *ν*_{max} 2923 (m, C-H), 1692 (m, C=O), 1581 (s, C=C), 1536 (s, C=C), 1404 (m, C=C); **¹H NMR** (500 MHz, DMSO-d₆) δ 11.80 (1H, s, H15), 7.97 (1H, d, *J* = 1.3 Hz, H7), 7.85 (1H, dd, *J* = 7.8, 1.4 Hz, H3), 7.54 (1H, dd, *J* = 8.6, 2.2 Hz, H11), 7.37 (1H, d, *J* = 2.1 Hz, H13), 7.29 (1H, d, *J* = 7.8 Hz, H4), 7.23 (1H, d, *J* = 8.6 Hz, H10); **¹³C NMR** (126 MHz, DMSO-d₆) δ 167.4 (C1), 159.0 (C9), 141.0 (C2), 137.0 (C5), 131.9 (C6), 131.0 (C4), 129.7 (C7), 127.6 (1C, q, *J* = 2.5 Hz, C13), 127.4 (C3), 126.7 (C8), 126.4 (1C, q, *J* = 1.4 Hz, C11), 124.8 (1C, q, *J* = 270.8 Hz, C14), 118.5 (1C, q, *J* = 31.9 Hz, C12), 116.3 (C10); **HRMS** (ESI) calcd for [C₁₄H₇O₃³⁵ClF₃ + H]: 316.0114, found: 316.0099.

Conditions adapted from literature protocol.²⁸²

Lithium 2-chloro-2'-hydroxy-5'-(methoxycarbonyl)-[1,1'-biphenyl]-4-carboxylate (**79**)



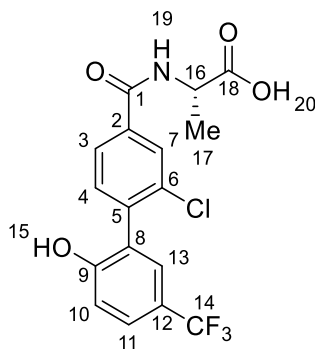
To a stirred solution of ester **76c** (4.72 g, 13.7 mmol) in minimal MeOH was added LiOH·H₂O (3.0 M in MeOH, 13.7 mL, 41.1 mmol) and the reaction stirred at room temperature for 18 hours. After quenching with 2.0 M aqueous HCl the reaction mixture was extracted into EtOAc three times. The combined organic extracts were dried over MgSO₄, filtered and reduced *in vacuo* to provide the crude carboxylic acid of **79**. The crude material was dissolved in minimal CH₂Cl₂ with stirring and a 2.0 M aqueous solution of LiOH·H₂O (6.84 mL, 13.7 mmol) added dropwise. After 18 hours the excess CH₂Cl₂ and H₂O was blown off and the lithium salt was freeze dried to provide the title compound **79** as a white solid in sufficient purity for analysis (4.24 g, 13.6 mmol, 99%):

LCMS t_r 1.30 min, calcd for $[C_{15}H_{11}O_5^{35}Cl - H]^-$ 305.0, $[M-H]^-$ 305.2; **m.p.** 305-306 °C; **IR** ν_{max} 3257 (br s, O-H), 1692 (s, C=O), 1591 (m, C=C), 1538 (m, C=C); **1H NMR** (500 MHz, DMSO- d_6) δ 7.96 (1H, d, J = 1.3 Hz, H7), 7.86 – 7.78 (2H, m, H3/H11), 7.67 (1H, d, J = 2.3 Hz, H13), 7.28 (1H, d, J = 7.8 Hz, H4), 7.11 (1H, d, J = 8.6 Hz, H10), 3.78 (3H, s, H16); **^{13}C NMR** (126 MHz, DMSO- d_6) δ 167.1 (C1), 166.0 (C14), 159.9 (C9), 140.5 (C2/C6), 137.4 (C5), 132.2 (C13), 132.0 (C2/C6), 131.0 (C4), 130.8 (C3/C11), 129.6 (C7), 127.4 (C3/C11), 126.3 (C8), 119.5 (C12), 115.9 (C10), 51.7 (C16); **HRMS** (ESI) calcd for $[C_{15}H_{10}O_5^{35}Cl + H]$: 306.0295, found: 306.0298.

H15 is a very broad singlet and lost in the baseline upon spectra processing.

Conditions adapted from literature protocol.²⁸²

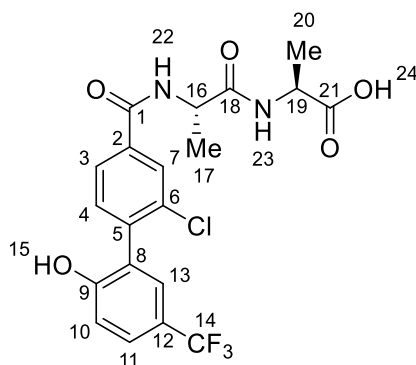
(2-Chloro-2'-hydroxy-5'-(trifluoromethyl)-[1,1'-biphenyl]-4-carbonyl)-L-alanine (**92**)



Prepared by manual Fmoc-SPPS to provide the title compound **92** as a white solid (5 mg, 0.01 mmol, 19%):

HPLC t_r = 11.22 mins (5-95% B); **m.p.** 157-158 °C; **IR** ν_{max} 3292 (br s, O-H), 1710 (s, C=O), 1662 (s, C=O), 1606 (m, C=C), 1532 (m, C=C); **1H NMR** (500 MHz, DMSO- d_6) δ 12.60 (1H, s br, H20), 10.60 (1H, s, H15), 8.84 (1H, d, J = 7.2 Hz, H19), 8.04 (1H, d, J = 1.7 Hz, H7), 7.89 (1H, dd, J = 8.0, 1.7 Hz, H3), 7.62 (1H, dd, J = 8.6, 2.0 Hz, H11), 7.49 (1H, d, J = 8.0 Hz, H4), 7.44 (1H, d, J = 2.1 Hz, H13), 7.12 (1H, d, J = 8.5 Hz, H10), 4.51 – 4.34 (1H, m, H16), 1.41 (3H, d, J = 7.3 Hz, H17); **^{13}C NMR** (126 MHz, DMSO- d_6) δ 174.1 (C18), 164.6 (C1), 158.0 (C9), 139.1 (C5), 134.9 (C2/C6), 132.9 (C2/C6), 132.0 (C4), 128.0 (C7), 127.6 (1C, q, J = 3.1 Hz, C13), 127.0 (1C, q, J = 1.8 Hz, C11), 126.1 (C3), 125.9 (C8), 124.6 (1C, q, J = 270.8 Hz, C14), 119.4 (1C, q, J = 32.3 Hz, C12), 116.1 (C10), 48.3 (C16), 16.9 (C17); **HRMS** (ESI) calcd for $[C_{17}H_{13}NO_4^{35}ClF_3 + H]^+$: 388.0563, found: 388.0565.

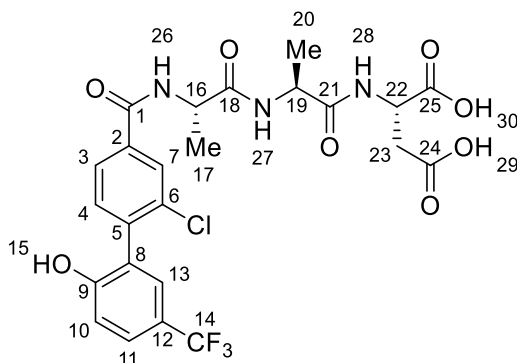
(2-Chloro-2'-hydroxy-5'-(trifluoromethyl)-[1,1'-biphenyl]-4-carbonyl)-L-alanyl-L-alanine (93)



Prepared by manual Fmoc-SPPS to provide the title compound **93** as a white solid (4 mg, 0.01 mmol, 6%):

HPLC t_r = 10.60 mins (5-95% B); **m.p.** 164-165 °C; **IR** ν_{\max} 3334 (br s, O-H), 1721 (s, C=O), 1637 (s, C=O), 1618 (m, C=C), 1538 (m, C=C), 1455 (s, C=C); **$^1\text{H NMR}$** (500 MHz, DMSO- d_6) δ 12.51 (1H, s br, H24), 10.58 (1H, s, H15), 8.69 (1H, d, J = 7.6 Hz, H22), 8.23 (1H, d, J = 7.3 Hz, H23), 8.06 (1H, d, J = 1.7 Hz, H7), 7.89 (1H, dd, J = 8.0, 1.8 Hz, H3), 7.62 (1H, dd, J = 8.6, 1.9 Hz, H11), 7.47 (1H, d, J = 8.0 Hz, H4), 7.44 (1H, d, J = 2.2 Hz, H13), 7.11 (1H, d, J = 8.5 Hz, H10), 4.59 – 4.46 (1H, m, H16), 4.23 (1H, quint, J = 7.3 Hz, H19), 1.36 (3H, d, J = 7.2 Hz, H17), 1.30 (3H, d, J = 7.3 Hz, H20); **$^{13}\text{C NMR}$** (126 MHz, DMSO- d_6) δ 174.1 (C21), 172.0 (C18), 164.5 (C1), 158.0 (C9), 139.0 (C5), 135.1 (C2/C6), 132.8 (C2/C6), 131.9 (C4), 128.1 (C7), 127.6 (1C, q, J = 2.5 Hz, C13), 127.1 – 126.8 (1C, m, C11), 126.1 (C3), 126.0 (C8), 124.6 (1C, q, J = 271.0 Hz, C14), 119.4 (1C, q, J = 32.0 Hz, C12) 116.1, (C10), 48.7 (C16), 47.5 (C19), 17.8 (C17), 17.1 (C20); **HRMS** (ESI) calcd for $[\text{C}_{20}\text{H}_{18}\text{N}_2\text{O}_5^{35}\text{ClF}_3 + \text{H}]^+$: 459.0950, found: 459.0935.

(2-Chloro-2'-hydroxy-5'-(trifluoromethyl)-[1,1'-biphenyl]-4-carbonyl)-L-alanyl-L-alanyl-L-aspartic acid (94)

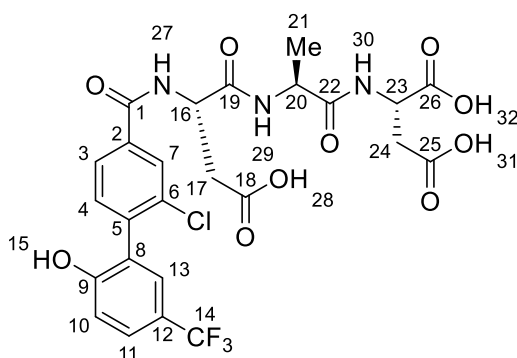


Prepared by microwave Fmoc-SPPS to provide the title compound **94** as a white solid (20 mg, 0.04 mmol, 17%):

HPLC t_r = 9.78 mins (5-95% B); **m.p.** decomp. above 350 °C; **IR** ν_{\max} 3308 (br s, O-H), 1731 (s, C=O), 1663 (s, C=O), 1624 (m, C=C), 1598 (s, C=C), 1536 (m, C=C); **$^1\text{H NMR}$** (500 MHz, DMSO- d_6) δ 12.50 (2H,

s br, H29/H30), 10.58 (1H, s, H15), 8.72 (1H, d, $J = 7.3$ Hz, H26), 8.14 – 8.01 (3H, m, H7/H27/H28), 7.89 (1H, dd, $J = 8.0, 1.7$ Hz, H3), 7.62 (1H, dd, $J = 8.6, 2.0$ Hz, H11), 7.47 (1H, d, $J = 8.0$ Hz, H4), 7.44 (1H, d, $J = 2.2$ Hz, H13), 7.11 (1H, d, $J = 8.5$ Hz, H10), 4.57 – 4.44 (2H, m, H16/H22), 4.32 (1H, quint, $J = 7.1$ Hz, H19), 2.68 (1H, dd, $J = 16.7, 5.9$ Hz, H23), 2.60 (1H, dd, $J = 16.7, 6.6$ Hz, H23'), 1.35 (3H, d, $J = 7.2$ Hz, H17), 1.23 (3H, d, $J = 7.1$ Hz, H20); $^{13}\text{C NMR}$ (126 MHz, DMSO- d_6) δ 172.2 (1C, C24/C25), 172.0 (C21), 171.8 (C18), 171.7 (1C, C24/C25), 164.6 (C1), 158.0 (C9), 139.0 (C5), 135.0 (C6), 132.9 (C2), 131.9 (C4), 128.1 (C7), 127.6 (1C, q, $J = 2.8$ Hz, C13), 127.0 (1C, q, $J = 2.5$ Hz, C11), 126.1 (C3), 126.0 (C8), 124.6 (1C, q, $J = 271.0$ Hz, C14), 119.4 (1C, q, $J = 32.1$ Hz, C12), 116.1 (C10), 49.0 (C16), 48.5 (C22), 47.9 (C19), 36.0 (C23), 18.2 (C20), 17.8 (C17); **HRMS** (ESI) calcd for $[\text{C}_{24}\text{H}_{23}\text{N}_3\text{O}_8^{35}\text{ClF}_3 + \text{H}]^+$: 574.1204, found: 574.1204.

(2-Chloro-2'-hydroxy-5'-(trifluoromethyl)-[1,1'-biphenyl]-4-carbonyl)-L-aspartyl-L-alanyl-L-aspartic acid (97)

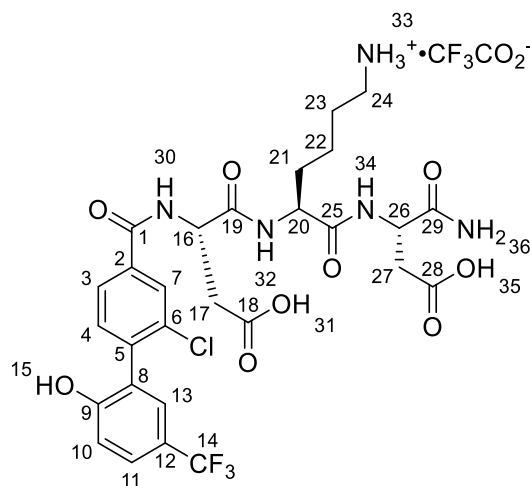


Prepared by microwave Fmoc-SPPS to provide the title compound **97** as a white solid (20 mg, 0.03 mmol, 15%):

HPLC $t_r = 9.51$ mins (5-95% B); **m.p.** decomp. above 350 °C; **IR** ν_{max} 3309 (br s, O-H), 2923 (m, C-H), 1705 (s, C=O), 1663 (s, C=O), 1628 (w, C=C), 1597 (m, C=C), 1536 (m, C=C); $^1\text{H NMR}$ (500 MHz, DMSO- d_6) δ 12.56 (3H, s br, H28/H31/H32), 10.58 (1H, s, H15), 8.84 (1H, d, $J = 7.6$ Hz, H27), 8.13 (1H, d, $J = 7.7$ Hz, H30), 8.09 (1H, d, $J = 7.5$ Hz, H29), 8.03 (1H, d, $J = 1.7$ Hz, H7), 7.87 (1H, dd, $J = 8.0, 1.7$ Hz, H3), 7.62 (1H, dd, $J = 8.6, 2.0$ Hz, H11), 7.49 (1H, d, $J = 8.0$ Hz, H4), 7.45 (1H, d, $J = 2.2$ Hz, H13), 7.11 (1H, d, $J = 8.5$ Hz, H10), 4.80 (1H, ddd, $J = 9.5, 7.7, 4.6$ Hz, H16), 4.49 (1H, dd, $J = 13.6, 6.4$ Hz, H23), 4.30 (1H, quint, $J = 7.1$ Hz, H20), 2.83 (1H, dd, $J = 16.7, 4.5$ Hz, H17), 2.76 – 2.62 (2H, m, H17'/H24), 2.57 (1H, dd, $J = 16.6, 6.4$ Hz, H24'), 1.22 (3H, d, $J = 7.1$ Hz, H21); $^{13}\text{C NMR}$ (126 MHz, DMSO- d_6) δ 172.3 (1C, C25/C26), 171.9 (2C, C18/C22), 171.7 (1C, C25/C26), 170.2 (C19), 164.8 (C1), 158.0 (C9), 139.1 (C5), 134.9 (C6), 132.9 (C2), 132.0 (C4), 128.0 (C7), 127.6 (1C, q, $J = 2.8$ Hz, C13), 127.2 – 126.6 (1C, m, C11), 126.1 (C3), 126.0 (C8), 124.6 (1C, q, $J = 270.9$ Hz, C14), 119.4 (1C, q, $J = 32.2$ Hz, C12), 116.1 (C10), 50.3 (C16), 48.5

(C23), 48.1 (C20), 36.2 (C24), 35.9 (C17), 18.1 (C21); **HRMS** (ESI) calcd for $[C_{25}H_{23}N_3O_{10}^{35}ClF_3 + H]^+$: 618.1102, found: 618.1131.

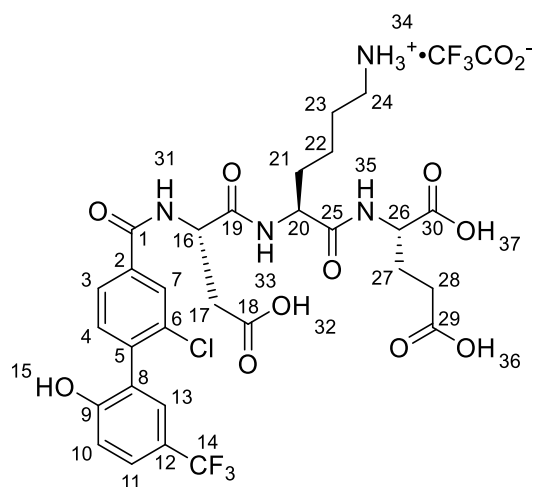
(S)-4-Amino-3-((S)-6-amino-2-((S)-3-carboxy-2-(2-chloro-2'-hydroxy-5'-(trifluoromethyl)-[1,1'-biphenyl]-4-carboxamido)propanamido)hexanamido)-4-oxobutanoic acid TFA salt (98)



Prepared by microwave Fmoc-SPPS to provide the title compound **98** as a white solid (57 mg, 0.07 mmol, 30%):

HPLC t_r = 8.37 mins (5-95% B); **m.p.** decomp. above 350 °C; **IR** ν_{max} 2974 (br s, O-H/ NH_3^+), 1645 (s, C=O), 1583 (m, C=C), 1532 (m, C=C); **1H NMR** (500 MHz, DMSO- d_6) δ 12.40 (2H, s br, H36), 10.64 (1H, s, H15), 8.90 (1H, d, J = 7.2 Hz, H30), 8.19 (1H, d, J = 7.5 Hz, H32), 8.09 – 7.98 (2H, m, H7/H34), 7.87 (1H, dd, J = 8.0, 1.8 Hz, H3), 7.67 (3H, s br, H33), 7.62 (1H, dd, J = 8.6, 2.0 Hz, H11), 7.49 (1H, d, J = 8.0 Hz, H4), 7.44 (1H, d, J = 1.9 Hz, H13), 7.16 – 7.08 (1H, m, H10), 4.83 – 4.72 (1H, m, H16), 4.50 – 4.39 (1H, m, H26), 4.22 – 4.08 (1H, m, H20), 2.90 – 2.51 (6H, m, H17/H24/H27), 1.76 – 1.63 (1H, m, H21), 1.62 – 1.43 (3H, m, H21'/H23), 1.40 – 1.26 (2H, m, H22); **^{13}C NMR** (126 MHz, DMSO- d_6) δ 172.4 (1C, C18/C28/C29), 172.0 (1C, C18/C28/C29), 171.9 (1C, C18/C28/C29), 171.2 (C25), 171.0 (C19), 165.0 (C1), 158.0 (C9), 139.2 (C5), 134.8 (C6), 132.9 (C2), 132.0 (C4), 128.1 (C7), 127.6 – 127.4 (1C, m, C13), 127.0 (1C, q, J = 3.3 Hz, C11), 126.2 (C3), 125.9 (C8), 124.6 (1C, q, J = 270.9 Hz, C14), 119.4 (1C, q, J = 32.1 Hz, C12), 116.1 (C10), 52.8 (C20), 50.6 (C16), 49.4 (C26), 38.7 (C24), 36.0 (C27), 35.7 (C17), 30.8 (C21), 26.5 (C23), 22.0 (C22); **HRMS** (ESI) calcd for $[C_{28}H_{31}N_5O_9^{35}ClF_3 + H]^+$: 674.1841, found: 674.1870.

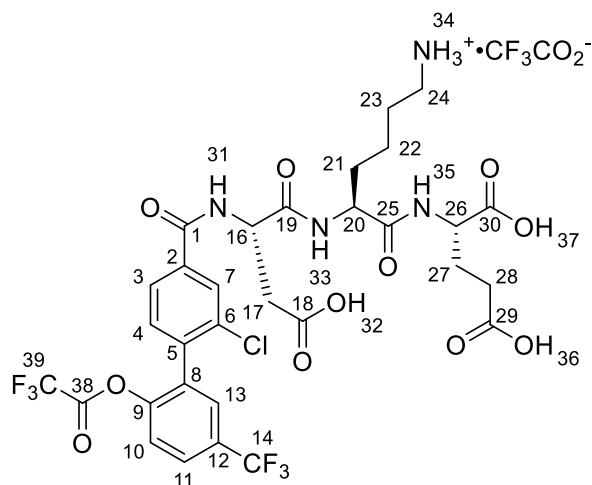
(2-Chloro-2'-hydroxy-5'-(trifluoromethyl)-[1,1'-biphenyl]-4-carbonyl)-L-aspartyl-L-lysyl-L-glutamic acid TFA salt (99**)**



Prepared by microwave Fmoc-SPPS to provide the title compound **99** as a white solid (29 mg, 0.04 mmol, 16%):

HPLC t_r = 8.54 mins (5-95% B); **m.p.** decomp. above 350 °C; **IR** ν_{\max} 3127 (br s, O-H/NH₃⁺), 1710 (s, C=O), 1650 (s, C=O), 1528 (m, C=C), 1453 (w, C=C); **¹H NMR** (500 MHz, DMSO-*d*₆) δ 12.37 (3H, s br, H32/H36/H37), 10.63 (1H, s, H15), 8.87 (1H, d, J = 7.3 Hz, H31), 8.09 (1H, d, J = 2.9 Hz, H33), 8.07 (1H, d, J = 2.4 Hz, H35), 8.03 (1H, d, J = 1.7 Hz, H7), 7.86 (1H, dd, J = 8.0, 1.7 Hz, H3), 7.67 (3H, s br, H34), 7.62 (1H, dd, J = 8.6, 1.5 Hz, H11), 7.49 (1H, d, J = 8.0 Hz, H4), 7.44 (1H, d, J = 2.2 Hz, H13), 7.12 (1H, d, J = 8.5 Hz, H10), 4.80 – 4.71 (1H, m, H16), 4.28 (1H, td, J = 8.6, 5.0 Hz, H20), 4.23 – 4.15 (1H, m, H26), 2.90 – 2.67 (4H, m, H17/H24), 2.32 – 2.23 (2H, m, H28), 2.03 – 1.92 (1H, m, H27), 1.86 – 1.75 (1H, m, H27'), 1.75 – 1.64 (1H, m, H21), 1.62 – 1.44 (3H, m, H21'/H23), 1.35 – 1.32 (2H, m, H22); **¹³C NMR** (126 MHz, DMSO-*d*₆) δ 173.7 (C29), 173.1 (C30), 171.9 (C18), 171.5 (C25), 170.6 (C16), 164.9 (C1), 158.0 (C9), 139.2 (C5), 134.8 (C6), 132.9 (C2), 132.0 (C4), 128.0 (C7), 127.6 (1C, q, J = 3.2 Hz, C13), 127.1 – 126.8 (1C, m, C11), 126.1 (C3), 125.9 (C8), 124.6 (1C, q, J = 270.9 Hz, C14), 119.4 (1C, q, J = 32.0 Hz, C12), 116.1 (C10), 52.1 (C20), 51.2 (C26), 50.6 (C16), 38.8 (C24), 35.8 (C17), 31.1 (C21), 30.0 (C28), 26.6 (C23), 26.2 (C27), 22.0 (C22); **HRMS** (ESI) calcd for [C₂₉H₃₂N₄O₁₀³⁵ClF₃]: 688.1759, found: 688.1744.

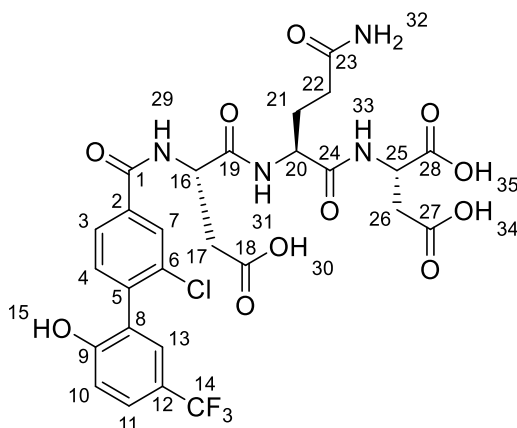
(2-Chloro-2'-(2,2,2-trifluoroacetoxy)-5'-(trifluoromethyl)-[1,1'-biphenyl]-4-carbonyl)-L-aspartyl-L-lysyl-L-glutamic acid TFA salt (99a)



Prepared by microwave Fmoc-SPPS to provide the title compound **99a** as a white solid (17 mg, 0.02 mmol, 8%):

HPLC t_r = 7.35 mins (5-95% B); **m.p.** decomp. above 350 °C; **IR** ν_{\max} 2951 (br s, O-H/NH₃⁺), 1660 (s, C=O), 1526 (m, C=C), 1420 (m, C=C); **¹H NMR** (500 MHz, DMSO-*d*₆) δ 12.32 (3H, s br, H32/H36/H37), 8.91 (1H, d, J = 7.3 Hz, H31), 8.15 (1H, d, J = 1.3 Hz, H7), 8.10 (1H, d, J = 7.7 Hz, H35), 8.08 (1H, d, J = 8.0 Hz, H33), 8.05 (1H, dd, J = 9.0, 2.1 Hz, H11), 7.97 (1H, dd, J = 8.0, 1.7 Hz, H3), 7.94 (1H, d, J = 2.1 Hz, H13), 7.74 – 7.67 (4H, m, H4/H34), 7.63 (1H, d, J = 8.6 Hz, H10), 4.83 – 4.72 (1H, m, H16), 4.31 – 4.22 (1H, m, H20), 4.22 – 4.13 (1H, m, H26), 2.86 – 2.67 (4H, m, H17/H24), 2.31 – 2.23 (2H, m, H28), 2.03 – 1.93 (1H, m, H27), 1.84 – 1.65 (2H, m, H21/H27'), 1.60 – 1.47 (3H, m, H21'/H23), 1.42 – 1.28 (2H, m, H22); **¹³C NMR** (126 MHz, DMSO-*d*₆) δ 173.7 (C29), 173.1 (C30), 171.8 (C18), 171.5 (C25), 170.5 (C16), 164.4 (C1), 157.9 (1C, q, J = 31.8 Hz, C38), 152.0 (C9), 136.2 (C5), 136.0 (C6), 132.8 (C2), 131.8 (C4), 129.2 (1C, s br, C13), 129.1 (C8), 128.5 (1C, s br, C11), 128.3 (C7), 126.7 (C3), 126.7 (1C, q, J = 33.1 Hz, C12), 123.6 (1C, q, J = 272.3 Hz, C14), 117.2 (C10), 116.7 (1C, q, J = 335.6 Hz, C39), 52.2 (C20), 51.2 (C26), 50.7 (C16), 38.7 (C24), 35.9 (C17), 31.2 (C21), 30.0 (C28) 26.6 (C23), 26.2 (C27), 22.0 (C22); **LCMS** t_r 0.98 min, calcd for [C₃₁H₃₁N₄O₁₁³⁵ClF₆ - H]⁻ 785.0, [M-H]⁻ 785.8.

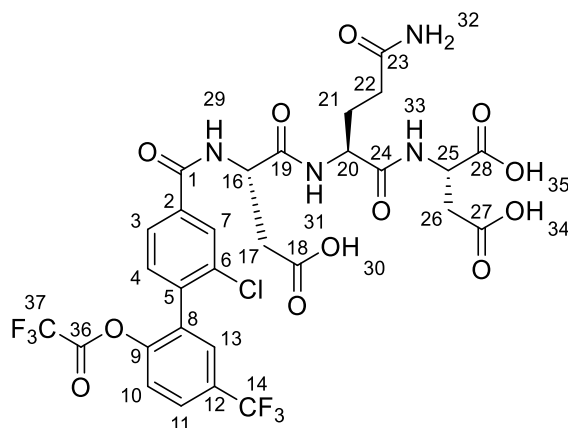
(2-Chloro-2'-hydroxy-5'-(trifluoromethyl)-[1,1'-biphenyl]-4-carbonyl)-L-aspartyl-L-glutaminyl-L-aspartic acid (100)



Prepared by microwave Fmoc-SPPS to provide the title compound **100** as a white solid (17 mg, 0.03 mmol, 12%):

HPLC t_r = 9.00 mins (5-95% B); **m.p.** decomp. above 350 °C; **IR** ν_{\max} 3333 (br s, O-H/NH₃⁺), 1716 (s, C=O), 1643 (s, C=O), 1530 (m, C=C), 1410 (w, C=C); **¹H NMR** (500 MHz, DMSO-*d*₆) δ 12.42 (3H, s br, H30/H34/H35), 10.58 (1H, s, H15), 8.86 (1H, d, J = 7.5 Hz, H29), 8.21 (1H, d, J = 8.0 Hz, H33), 8.08 (1H, d, J = 8.0 Hz, H31), 8.03 (1H, d, J = 1.7 Hz, H7), 7.87 (1H, dd, J = 8.0, 1.7 Hz, H3), 7.62 (1H, dd, J = 8.6, 1.9 Hz, H11), 7.49 (1H, d, J = 8.0 Hz, H4), 7.45 (1H, d, J = 2.1 Hz, H13), 7.19 (1H, s br, H32), 7.12 (1H, d, J = 8.5 Hz, H10), 6.74 (1H, s br, H32'), 4.79 (1H, ddd, J = 9.6, 7.5, 4.5 Hz, H16), 4.53 (1H, dd, J = 14.2, 6.4 Hz, H25), 4.27 (1H, td, J = 8.5, 5.0 Hz, H20), 2.83 (1H, dd, J = 16.7, 4.4 Hz, H17), 2.75 – 2.65 (2H, m, H17'/H26), 2.59 (1H, dd, J = 16.7, 6.7 Hz, H26'), 2.21 – 2.07 (2H, m, H22), 1.96 – 1.87 (1H, m, H21), 1.82 – 1.68 (1H, m, H21'); **¹³C NMR** (126 MHz, DMSO-*d*₆) δ 173.8 (C23), 172.2 (C18/C27), 171.9 (C28), 171.6 (C18/C27), 171.0 (C24), 170.5 (C19), 165.0 (C1), 158.0 (C9), 139.1 (C8), 134.9 (C6), 132.9 (C2), 131.9 (C4), 128.1 (C7), 127.8 – 127.3 (1C, m, C13), 127.2 – 126.7 (1C, m, C11), 126.2 (C3), 126.0 (C8), 124.6 (1C, q, J = 270.8 Hz, C14), 119.4 (1C, q, J = 32.1 Hz, C12), 116.1 (C10), 52.1 (C20), 50.5 (C16), 48.5 (C25), 35.9 (2C, C17/C26), 31.3 (C22), 28.0 (C21); **HRMS** (ESI) calcd for [C₂₇H₂₆N₄O₁₁³⁵ClF₃ + H]⁺: 675.1302, found: 675.1300.

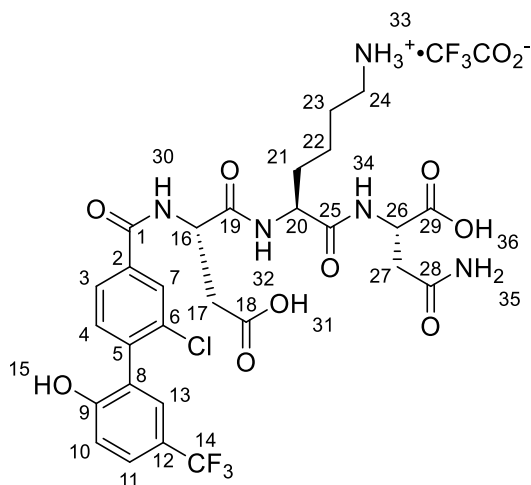
(2-Chloro-2'-(2,2,2-trifluoroacetoxy)-5'-(trifluoromethyl)-[1,1'-biphenyl]-4-carbonyl)-L-aspartyl-L-glutaminyl-L-aspartic acid (100a)



Prepared by microwave Fmoc-SPPS to provide the title compound **100a** as a white solid (17 mg, 0.02 mmol, 10%):

HPLC t_r = 7.67 mins (5-95% B); **m.p.** decomp. above 350 °C; **IR** ν_{\max} 3315 (br s, O-H), 1650 (s, C=O), 1527 (m, C=C), 1411 (m, C=C); **¹H NMR** (500 MHz, DMSO- d_6) δ 12.49 (3H, s br, H30/H34/H35), 8.92 (1H, d, J = 7.4 Hz, H29), 8.25 (1H, d, J = 8.0 Hz, H33), 8.15 (1H, d, J = 1.4 Hz, H7), 8.08 – 8.00 (2H, m, H11/H31), 8.00 – 7.92 (2H, m, H3/H13), 7.72 (1H, d, J = 8.0 Hz, H4), 7.63 (1H, d, J = 8.7 Hz, H10), 7.21 (1H, s br, H32), 6.75 (1H, s br, H32'), 4.84 – 4.75 (1H, m, H16), 4.52 (1H, dd, J = 14.1, 6.5 Hz, H25), 4.32 – 4.22 (1H, m, H20), 2.84 (1H, dd, J = 16.7, 4.1 Hz, H17), 2.77 – 2.64 (2H, m, H17'/H26), 2.59 (1H, dd, J = 16.7, 6.7 Hz, H26'), 2.18 – 2.05 (2H, m, H22), 1.98 – 1.87 (1H, m, H21), 1.77 – 1.70 (1H, m, H2); **¹³C NMR** (126 MHz, DMSO- d_6) δ 173.8 (C23), 172.2 (C28), 171.8 (C18), 171.6 (C27), 171.0 (C24), 170.4 (C19), 164.5 (C1), 158.0 (1C, q, J = 32.8 Hz, C36), 152.0 (C9), 136.2 (C5), 136.0 (C6), 132.8 (C2), 131.8 (C4), 129.5 – 129.2 (1C, m, C13), 129.1 (C8), 128.7 – 128.4 (1C, m, C11), 128.3 (C7), 126.7 (C3), 126.7 (1C, q, J = 32.6 Hz, C12), 123.6 (1C, q, J = 272.5 Hz, C14), 117.3 (C10), 116.8 (1C, q, J = 294.3 Hz, C37), 52.0 (C20), 50.6 (C16), 48.5 (C25), 35.9 (2C, C17/C26), 31.3 (C22), 28.1 (C21); **HRMS** (ESI) calcd for $[C_{29}H_{27}N_4O_{12}^{35}ClF_6]$: 770.1062, found: 770.1038.

(2-Chloro-2'-hydroxy-5'-(trifluoromethyl)-[1,1'-biphenyl]-4-carbonyl)-L-aspartyl-L-lysyl-L-asparagine TFA salt (101)

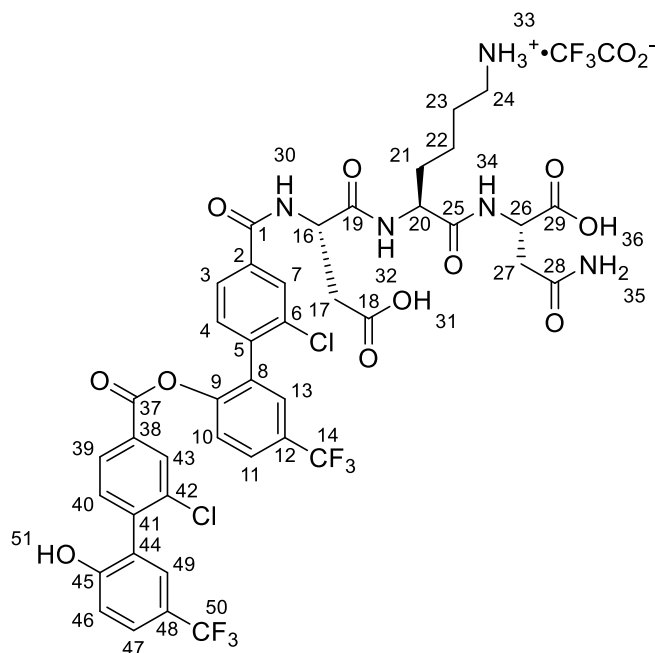


Prepared by microwave Fmoc-SPPS to provide the title compound **101** as a white solid (50 mg, 0.06 mmol, 39%):

HPLC t_r = 8.29 mins (5-95% B); **m.p.** decomp. above 350 °C; **IR** ν_{\max} 3065 (br s, O-H/NH₃⁺), 1651 (s, C=O), 1519 (m, C=C), 1429 (w, C=C); **¹H NMR** (500 MHz, DMSO-*d*₆) δ 12.41 (2H, s br, H31/H36), 10.64 (1H, s, H15), 8.87 (1H, d, J = 7.4 Hz, H30), 8.12 (1H, d, J = 7.9 Hz, H34), 8.07 (1H, d, J = 8.1 Hz, H32), 8.03 (1H, d, J = 1.7 Hz, H7), 7.86 (1H, dd, J = 8.0, 1.7 Hz, H3), 7.77 – 7.56 (4H, m, H11/H33), 7.49 (1H, d, J = 8.0 Hz, H4), 7.44 (1H, d, J = 2.2 Hz, H13), 7.40 (1H, s br, H35), 7.12 (1H, d, J = 8.5 Hz, H10), 6.92 (1H, s br, H35'), 4.78 (1H, ddd, J = 9.7, 7.4, 4.5 Hz, H16), 4.50 (1H, dd, J = 13.9, 6.3 Hz, H26), 4.28 (1H, td, J = 8.6, 4.9 Hz, H20), 2.84 (1H, dd, J = 16.8, 4.4 Hz, H17), 2.78 – 2.70 (3H, m, H17'/H24), 2.56 (1H, dd, J = 15.7, 5.7 Hz, H27), 1.76 – 1.63 (1H, m, H21), 1.60 – 1.45 (3H, m, H20'/H23), 1.41 – 1.27 (2H, m, H22); **¹³C NMR** (126 MHz, DMSO-*d*₆) δ 172.6 (C29), 171.9 (C18), 171.2 (C25/C28), 171.1 (C25/C28), 170.5 (C19), 164.9 (C1), 158.0 (C9), 139.2 (C5), 134.9 (C6), 132.9 (C2), 132.0 (C4), 128.0 (C7), 127.6 (1C, s br, C13), 127.0 (1C, s br, C11), 126.1 (C3), 125.9 (C8), 124.6 (1C, q, J = 270.9 Hz, C14), 119.38 (1C, q, J = 32.3 Hz, C12), 116.1 (C10), 52.0 (C20), 50.6 (C16), 48.7 (C26), 38.8 (C24), 36.5 (C27), 35.8 (C17), 31.3 (C21), 26.6 (C23), 21.9 (C22); **HRMS** (ESI) calcd for [C₂₈H₃₁N₅O₉³⁵ClF₃]: 673.1762, found: 673.1735.

H27' is hidden under the DMSO solvent peak, confirmed by 2D NMR analysis

(2-Chloro-2'-((2-chloro-2'-hydroxy-5'-(trifluoromethyl)-[1,1'-biphenyl]-4-carbonyl)oxy)-5'-(trifluoromethyl)-[1,1'-biphenyl]-4-carbonyl)-L-aspartyl-L-lysyl-L-asparagine TFA salt (101a**)**

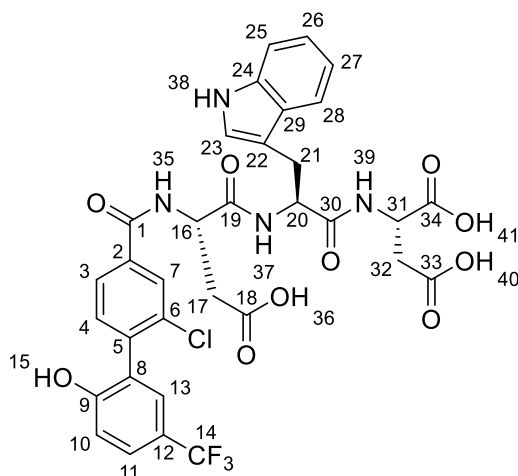


Prepared by microwave Fmoc-SPPS to provide the title compound **101a** as a white solid (7 mg, 0.01 mmol, 4%):

HPLC t_r = 11.24 mins (5-95% B); **m.p.** decomp. above 350 °C; **IR** ν_{\max} 3082 (br s, O-H/NH₃⁺), 1718 (s, C=O), 1662 (br s, C=O), 1535 (m, C=C), 1422 (w, C=C); **¹H NMR** (500 MHz, DMSO-*d*₆) δ 12.33 (2H, s br, H31/H36), 10.71 (1H, s, H51), 8.87 (1H, d, J = 7.2 Hz, H30), 8.12 (1H, d, J = 7.7 Hz, H32), 8.09 – 8.04 (2H, m, H7/H34), 8.02 (1H, dd, J = 8.8, 2.0 Hz, H11), 7.95 (1H, d, J = 1.7 Hz, H43), 7.93 – 7.84 (3H, m, H3/H13/H39), 7.82 (1H, d, J = 8.5 Hz, H10), 7.71 – 7.58 (5H, m, H4/H47/H47), 7.55 (1H, d, J = 8.0 Hz, H40), 7.49 (1H, d, J = 2.0 Hz, H49), 7.39 (1H, s br, H35), 7.12 (1H, d, J = 8.5 Hz, H46), 6.91 (1H, s br, H35'), 4.74 (1H, ddd, J = 9.8, 7.3, 4.4 Hz, H16), 4.48 (1H, dd, J = 13.9, 6.2 Hz, H26), 4.31 – 4.18 (1H, m, H20), 2.80 (1H, dd, J = 16.8, 4.2 Hz, H17), 2.77 – 2.64 (3H, m, H17'/H24), 2.55 (1H, dd, J = 15.8, 5.7 Hz, H27), 1.74 – 1.63 (1H, m, H21), 1.57 – 1.43 (3H, m, H21'/H23), 1.38 – 1.27 (2H, m, H22); **¹³C NMR** (126 MHz, DMSO-*d*₆) δ 172.6 (C29), 171.8 (C18), 171.2 (C25/C28), 171.2 (C25/C28), 170.5 (C19), 164.5 (C1), 162.3 (C37), 157.8 (C45), 150.6 (C9), 142.2 (C41), 137.0 (C5), 135.6 (C2/C6), 133.7 (C38/C42), 132.9 (C40), 132.4 (C2/C4), 132.3 (C8), 131.9 (C4), 129.9 (C43), 129.0 (C38/C42), 128.3 (C7), 128.3 (1C, s br, C13), 128.0 (C43), 127.6 (1C, s br, C49), 127.4 – 127.2 (2C, m, C11/C47), 126.8 (1C, q, J = 61.8 Hz, C12), 126.5 (C3), 125.4 (C44), 124.6 (1C, q, J = 271.1 Hz, C50), 124.3 (C10), 123.8 (1C, q, J = 272.5 Hz, C14), 119.5 (1C, q, J = 32.2 Hz, C48), 116.2 (C46), 52.1 (C20), 50.5 (C16), 48.7 (C26), 38.8 (C24), 36.5 (C27), 35.8 (C17), 31.2 (C21), 26.6 (C23), 21.9 (C22); **HRMS** (ESI) calcd for [C₄₂H₃₇N₅O₁₁³⁵Cl₂F₆]: 971.1771, found: 971.1687.

(H27' is hidden under the DMSO solvent peak, confirmed by 2D NMR analysis)

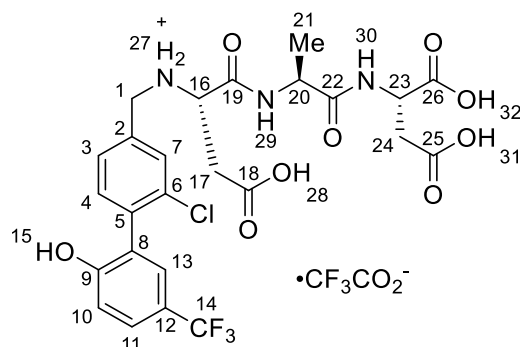
(2-Chloro-2'-hydroxy-5'-(trifluoromethyl)-[1,1'-biphenyl]-4-carbonyl)-L-aspartyl-L-tryptophyl-L-aspartic acid (102)



Prepared by manual Fmoc-SPPS to provide the title compound **102** as a white solid (32 mg, 0.04 mmol, 21%):

HPLC t_r = 6.57 mins (40-60% B); **m.p.** decomp. above 350 °C; **IR** U_{max} 3305 (br s, O-H), 1716 (s, C=O), 1641 (s, C=O), 1521 (s, C=C), 1423, (m, C=C); **1H NMR** (500 MHz, DMSO- d_6) δ 12.47 (3H, s br, H36/H40/H41), 10.78 (1H, d, J = 1.9 Hz, H38), 10.59 (1H, s, H15), 8.78 (1H, d, J = 7.6 Hz, H35), 8.30 (1H, d, J = 7.8 Hz, H39), 8.00 (1H, d, J = 8.0 Hz, H37), 7.97 (1H, d, J = 1.7 Hz, H7), 7.81 (1H, dd, J = 8.0, 1.7 Hz, H3), 7.62 (1H, dd, J = 8.6, 2.0 Hz, H11), 7.57 (1H, d, J = 7.9 Hz, H28), 7.47 (1H, d, J = 8.0 Hz, H4), 7.45 (1H, d, J = 2.1 Hz, H13), 7.29 (1H, d, J = 8.1 Hz, H25), 7.15 (1H, d, J = 2.3 Hz, H23), 7.12 (1H, d, J = 8.5 Hz, H10), 7.05 – 6.98 (1H, m, H26), 6.95 – 6.89 (1H, m, H27), 4.78 (1H, ddd, J = 9.6, 7.7, 4.5 Hz, H16), 4.60 – 4.50 (2H, m, H20/H31), 3.15 (1H, dd, J = 14.8, 4.3 Hz, H21), 2.98 (1H, dd, J = 14.9, 8.7 Hz, H21'), 2.78 (1H, dd, J = 16.7, 4.4 Hz, H17), 2.72 – 2.60 (2H, m, H17'/H32), 2.59 – 2.52 (1H, m, H32'); **^{13}C NMR** (126 MHz, DMSO- d_6) δ 172.3 (C33/C34), 171.9 (C18), 171.7 (C33/C34), 171.2 (C13), 170.4 (C19), 164.9 (C1), 158.0 (C9), 139.1 (C5), 136.0 (C24), 134.8 (C6), 132.9 (C2), 131.9 (C4), 128.1 (C7), 127.6 (1C, s br, C13), 127.4 (C29), 127.0 (1C, s br, C11), 126.1 (C3), 126.0 (C8), 124.6 (1C, q, J = 270.9 Hz, C14), 123.7 (C23), 120.8 (C26), 119.4 (1C, q, J = 32.2 Hz, C12), 118.3 (C28), 118.2 (C27), 116.1 (C10), 111.2 (C25), 109.8 (C22), 53.4 (C20), 50.4 (C16), 48.7 (C31), 36.1 (C17/C32), 35.8 (C17/C32), 27.5 (C21); **HRMS** (ESI) calcd for $[C_{33}H_{28}N_4O_{10}^{35}ClF_3 - H]^-$: 731.1373, found: 731.1363.

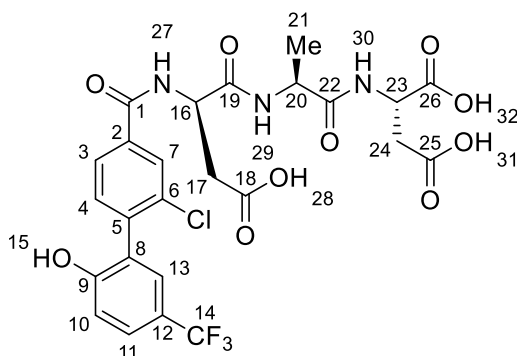
((2-Chloro-2'-hydroxy-5'-(trifluoromethyl)-[1,1'-biphenyl]-4-yl)methyl)-L-aspartyl-L-alanyl-L-aspartic acid TFA salt (107)



Prepared by manual Fmoc-SPPS except following deprotection of the final Asp residue a solution of aldehyde **63** (60 mg, 0.2 mmol) in DMF (1.67 mL) was added and the mixture shaken for 5 minutes. NaBH(OAc)₃ (212 mg, 1.0 mmol) was added as one portion and the reaction left to shake for 24 hours before the resin was drained and rinsed with DMF (3 x 6 mL), MeOH (3 x 6 mL) and CH₂Cl₂ (3 x 6 mL). Final peptide deprotection and resin cleavage was performed as described in the manual Fmoc-SPPS general procedure to provide the title compound **107** as a white solid (4 mg, 0.01 mmol, 6%):

HPLC *t_r* = 8.90 mins (5-95% B); **m.p.** decomp. above 350 °C; **¹H NMR** (500 MHz, DMSO-*d*₆) δ 10.49 (1H, s, H15), 8.37 (1H, s br, H29), 8.22 (1H, d, *J* = 7.9 Hz, H30), 7.58 (1H, dd, *J* = 8.6, 2.0 Hz, H11), 7.55 (1H, s br, H7), 7.40 – 7.34 (2H, m, H3/H13), 7.32 (1H, d, *J* = 7.8 Hz, H4), 7.10 (1H, d, *J* = 8.5 Hz, H10), 4.52 (1H, dd, *J* = 14.2, 6.5 Hz, H23), 4.36 (1H, dt, *J* = 14.5, 7.1 Hz, H20), 3.91 – 3.58 (3H, m, H1/H16), 2.73 – 2.55 (4H, m, H17/H24), 1.23 (3H, d, *J* = 7.0 Hz, H21); **¹³C NMR** (126 MHz, DMSO-*d*₆) δ 172.3 (C25/C26), 171.8 (C22), 171.6 (C25/C26), 158.1 (C9), 135.0 (C5), 132.6 (C6), 131.7 (C4), 129.0 (C7), 127.8 (1C, s br, C13), 127.0 (C3), 126.6 (1C, s br, C11), 126.4 (C8), 124.7 (1C, q, *J* = 271.0 Hz, C14), 119.3 (1C, dd, *J* = 64.0, 31.9 Hz, C12), 116.0 (C10), 57.3 (C16), 49.5 (C1), 48.6 (C23), 47.9 (C20), 36.8 (C17), 36.0 (C24), 18.4 (C21); **LCMS** *t_r* 1.19 min, calcd for [C₂₅H₂₅N₃O₉³⁵ClF₃ - H]⁻ 602.1, [M-H]⁻ 602.5; **HRMS** (ESI) calcd for [C₂₅H₂₅N₃O₉³⁵ClF₃]: 603.1231, found: 603.1210.

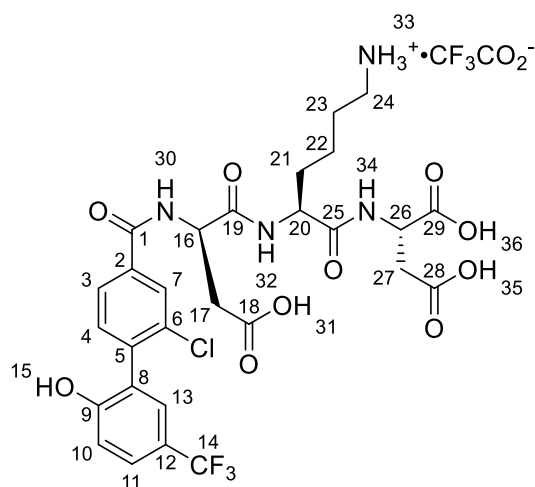
(2-Chloro-2'-hydroxy-5'-(trifluoromethyl)-[1,1'-biphenyl]-4-carbonyl)-D-aspartyl-L-alanyl-L-aspartic acid (108)



Prepared by manual Fmoc-SPPS to provide the title compound **108** as a white solid (15 mg, 0.02 mmol, 23%):

HPLC t_r = 9.77 mins (5-95% B); **m.p.** decomp. above 350 °C; **IR** ν_{\max} 3307 (br s, O-H), 1716 (s, C=O), 1641 (s, C=O), 1530 (m, C=C); **$^1\text{H NMR}$** (500 MHz, DMSO- d_6) δ 12.42 (3H, s br, H28/H31/H32), 10.58 (1H, s, H15), 8.88 (1H, d, J = 7.4 Hz, H27), 8.20 (1H, d, J = 8.1 Hz, H30), 8.09 (1H, d, J = 7.8 Hz, H29), 8.04 (1H, d, J = 1.7 Hz, H7), 7.87 (1H, dd, J = 8.0, 1.7 Hz, H3), 7.62 (1H, dd, J = 8.6, 2.0 Hz, H11), 7.49 (1H, d, J = 8.0 Hz, H4), 7.45 (1H, d, J = 2.1 Hz, H13), 7.12 (1H, d, J = 8.5 Hz, H10), 4.77 (1H, ddd, J = 8.8, 7.5, 5.3 Hz, H16), 4.54 (1H, dd, J = 14.3, 6.8 Hz, H23), 4.41 – 4.27 (1H, m, H20), 2.79 (1H, dd, J = 16.5, 5.2 Hz, H17), 2.75 – 2.65 (2H, m, H17'/H24), 2.59 (1H, dd, J = 16.6, 7.0 Hz, H24'), 1.21 (3H, d, J = 7.1 Hz, H21); **$^{13}\text{C NMR}$** (126 MHz, DMSO- d_6) δ 172.2 (1C, C25/C26), 171.8 (2C, C18/C22), 171.6 (1C, C25/C26), 170.0 (C19), 165.0 (C1), 158.0 (C9), 139.2 (C5), 134.8 (C6), 132.9 (C2), 131.9 (C4), 128.1 (C7), 127.6 (1C, s br, C13), 127.0 (1C, s br, C11), 126.2 (C3), 126.0 (C8), 124.6 (1C, q, J = 270.9 Hz, C14), 119.4 (1C, q, J = 32.4 Hz, C12), 116.1 (C10), 50.6 (C16), 48.6 (C23), 47.9 (C20), 35.9 (C24), 35.9 (C17), 18.3 (C21); **HRMS** (ESI) calcd for $[\text{C}_{25}\text{H}_{23}\text{N}_3\text{O}_{10}^{35}\text{ClF}_3 + \text{H}]^+$: 618.1102, found: 618.1091.

(2-Chloro-2'-hydroxy-5'-(trifluoromethyl)-[1,1'-biphenyl]-4-carbonyl)-D-aspartyl-L-lysyl-L-aspartic acid TFA salt (109)



Prepared by manual Fmoc-SPPS to provide the title compound **109** as a white solid (18 mg, 0.02 mmol, 22%):

HPLC t_r = 8.85 mins (5-95% B); **m.p.** decomp. above 350 °C; **IR** ν_{\max} 3072 (br s, O-H/NH₃⁺), 1715 (s, C=O), 1636 (s, C=O), 1520 (m, C=C), 1428 (w, C=C); **¹H NMR** (500 MHz, DMSO-*d*₆) δ 12.46 (3H, s br, H31/H35/H36), 10.63 (1H, s, H15), 8.90 (1H, d, J = 7.2 Hz, H30), 8.24 (1H, d, J = 8.0 Hz, H32), 8.08 (1H, d, J = 8.0 Hz, H34), 8.04 (1H, d, J = 1.7 Hz, H7), 7.87 (1H, dd, J = 8.0, 1.7 Hz, H3), 7.78 – 7.56 (4H, m, H11/H33), 7.49 (1H, d, J = 8.0 Hz, H4), 7.44 (1H, d, J = 2.2 Hz, H13), 7.12 (1H, d, J = 8.5 Hz, H10), 4.78 (1H, ddd, J = 8.8, 7.2, 5.4 Hz, H16), 4.54 (1H, dd, J = 14.0, 7.0 Hz, H26), 4.31 (1H, td, J = 8.7, 4.7 Hz, H20), 2.83 – 2.65 (5H, m, H17/H24/H27), 2.60 (1H, dd, J = 16.6, 7.1 Hz, H27'), 1.77 – 1.65 (1H, m, H21), 1.59 – 1.42 (3H, m, H21'/H23), 1.34 – 1.23 (2H, m, H22); **¹³C NMR** (126 MHz, DMSO-*d*₆) δ 172.2 (1C, C28/C29), 171.8 (C18), 171.6 (1C, C28/C29), 171.1 (C25), 170.4 (C19), 165.1 (C1), 158.0 (C9), 139.2 (C5), 134.8 (C6), 132.9 (C2), 132.0 (C4), 128.1 (C7), 127.6 (1C, s br, C13), 127.0 (1C, s br, C11), 126.2 (C3), 125.9 (C8), 124.6 (1C, q, J = 270.9 Hz, C14), 119.4 (1C, q, J = 32.1 Hz, C12), 116.1 (C10), 51.8 (C20), 50.8 (C16), 48.6 (C26), 38.7 (C24), 35.90 (1C, C17/C27), 35.85 (1C, C17/C27), 30.7 (C21), 26.6 (C23), 21.9 (C22); **HRMS** (ESI) calcd for [C₂₈H₃₀N₄O₁₀³⁵ClF₃ + H]⁺: 675.1681, found: 675.1697.

Characterisation data for peptides of 4 amino acids or longer:

Number	Sequence	Yield (%)	HPLC t _r (min) (5-95% B)	HPLC t _r (min) (20-60% B)	Calculated MW [M+H] ⁺ (Da)	Found MW [M+H] ⁺ (Da)	Fmoc-SPPS method
95	78-AADD-OH	7	9.45	6.57 ¹	689.1468	689.1452	Microwave
96	78-AADD-NH ₂	12	9.22	5.56 ¹	688.1633	688.1635	Microwave
105	78-PGGD-OH	30	9.56	9.40	643.1413	643.1400	Manual
106	78-PGGN-OH	18	9.07	8.92	642.1573	642.1557	Manual
110	78-dADDDSDDD-OH	13	8.70	8.49	1280.2764	1280.2712	Automated
111	74-dADDDSDDD-OH	15	9.01	8.89	1312.2229 ²	1312.2288 ³	Automated

All peptides were purified by semi-preparative HPLC with a gradient of 30-50% over 20 min and reported HPLC t_r refers to the retention time reported on the analytical HPLC.

¹ HPLC t_r (min) (30-80% B)

² Calculated MW [M-H]⁻ (Da)

³ Found MW [M-H]⁻ (Da)

4.6 Computational Docking Procedure

All the docking studies reported herein were performed using Glide from the Schrödinger package, set to default parameters.^{254–257}

The protein structures were prepared from the PDB files of the X-ray crystal structures generated by Dr. Paul Brear (Hyvönen Group, Department of Biochemistry, University of Cambridge). The protein structure was prepared for docking using the Protein Preparation Wizard application. Bond orders were assigned, hydrogen atoms added and water molecules beyond 5 Å from hetero groups were deleted. The structure was refined by sampling of hydrogen bonds and water molecule orientations at pH 7 ± 2. To keep the conformation of the protein as close as possible to the X-ray crystal structures, no modifications such as ‘cap termini’, ‘filling loops’ or ‘side chain’ were performed. The energy of the structure was then minimised.

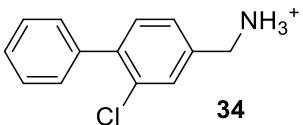
The parent ligands of the X-ray crystal structures were used as the templates for Glide grid generation. No positional constraints were given and all parameters were left as default. An OPLS_2005 force field was used.

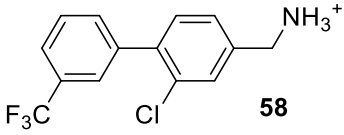
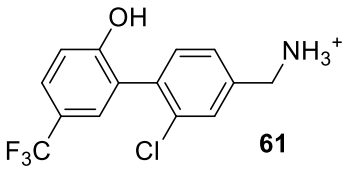
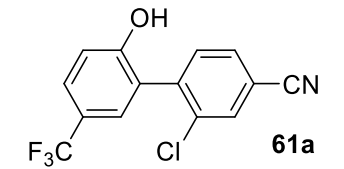
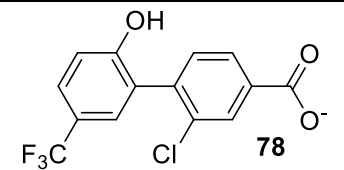
Chemical structures were imported from SDF files. Ligands were then prepared with the Ligand Preparation wizard, using OPLS_2005 as the force field. All other parameters were left as default. Conformations of the output structures were generated by the Conformation Generation wizard using fast mode, default setting and OPLS_2005 force field.

Virtual screening mode was then used to rigidly dock molecules into the receptor grid. The docking score consisted of Van Der Waals, lipophilic, hydrogen bonding and metal interaction components, along with non-hydrogen bonding polar interactions in hydrophobic sites.

Subsequent protein-ligand visualisation and image rendering was performed using Pymol from the Schrödinger package.²⁵⁸

The following X-ray crystal structure PDB files were used for computational docking. The chemical structures of the original αD pocket ligands are provided and the figure numbers reporting the results:

PDB File	Ligand Chemical Structure	Docking Results
5CHS	 34	Figure 28

58		Figure 36
61		Figure 38
61a		Figure 41
78		Figure 55, 57, 58, 59, 61, 62 and 63

4.7 Crystallisation and Screening Conditions

Crystallisation and screening experiments were conducted by Dr. Paul Brear, Department of Biochemistry, University of Cambridge. Cell-based assays were conducted by Dr Maxim Rossman, Department of Biochemistry, University of Cambridge.

Protein Expression and Purification

Two constructs of CK2 α were used in this project. For ITC and kinase activity assays CK2 α _WT was used (residues 2-329). For crystallization purposes CK2 α _KA was used. CK2 α _KA (residues 2-329) contained four mutations designed to aid crystallization by reducing the overall charge of the protein; R21S, K74A, K75A and K76A. CK2 α _KA was cloned into pHAT2 vector to give constructs with cleavable His6-tags. Recombinant plasmids containing one of the two constructs (CK2 α _WT/CK2 α _KA) were introduced into *Escherichia coli* BL21(DE3) for protein production. Single colonies of the cells were grown in 6x1L of 2xTY with 100 μ g/mL ampicillin at 37°C. Isopropylthio- β -D-galactopyranoside (IPTG) was added to a final concentration of 0.4 mM to induce expression when the optical density at 600 nm reached 0.6. The cells were incubated overnight at 25°C then harvested by centrifugation at 4,000 g for 20 minutes. The same extraction and purification procedure was used for both constructs, with the exception that CK2 α _KA used 350 mM NaCl in the buffer, whereas, CK2 α _WT required 500 mM NaCl. The cell pellets were suspended in 20 mM Tris, 350/500 mM NaCl, pH 8.0 and lysed using a high pressure homogenizer. Protease inhibitor cocktail tablets (one tablet per 50 mL extract; Roche Diagnostics) and DNase I were then added. The crude cell extract was then centrifuged at 10,000 g for 45 minutes, the supernatant was filtered with a 0.22 μ m filter. The soluble supernatant was applied on a Ni Sepharose Fast Flow 6 column at pH 8.0, washed and eluted in 20 mM Tris pH 8.0, 350/500 mM NaCl, 200 mM imidazole. After overnight dialysis into 20 mM Tris, pH 8.0, 350/500 mM NaCl the N-terminal His6-Tag was cleaved overnight by TEV protease and passed through a second metal affinity column to remove uncleaved protein and the protease. The cleaved protein was further purified on a Sepharose Q HP anion-exchange column and the main peak fraction from this column was further purified by gel filtration on a Superdex 75 16/60 HiPrep column equilibrated with Tris 20 mM, pH 8.0, 350/500 mM NaCl. Pure protein was concentrated to 15 mg/mL and flash frozen in liquid nitrogen.

X-ray Crystallography

CK2 α _KA at 5 mg/mL in 20 mM Tris, pH 8.0, 350 mM NaCl, 1 mM DTT, and 25 mM ATP was crystallised with 112.5 mM MES pH 6.5, 35% glycerol ethoxylate and 180 mM ammonium acetate in a 1:1 ratio with a total volume of 2 μ L by the hanging drop vapour-diffusion method. The fragments were soaked as singletons at 2-100 mM into these crystals for 15–20 h in 107 mM MES pH 6.5, 35% glycerol ethoxylate and 1.04 M ammonium acetate after which the crystals were cryo-cooled in liquid nitrogen for data collection. 12 X-ray diffraction data was collected at the Diamond synchrotron radiation source, then processed using the pipedream package by Global Phasing Ltd. Structures were solved by using programs from the CCP4 package. Models were iteratively refined and rebuilt by using AutoBuster and Coot programs. Ligand coordinates and restraints were generated from their SMILES strings using the Grade software package. All crystal structures reported in this thesis are of the resolution 1.4 – 2.5 Å.

Isothermal Titration Calorimetry (ITC)

All ITC experiments were performed at 25 °C using a MicroCal itc200 instrument (GE Healthcare). CK2 α _WT (20 mg/mL, 20 mM Tris pH 8.0, 500 mM NaCl) was diluted in Tris buffer (200 mM Tris, 300 mM NaCl, 10% DMSO) and concentrated to 20-50 μ M. Compounds in 100x stock solutions were diluted into the buffer ensuring that the DMSO concentrations were carefully matched. In a typical experiment CK2 α _WT (40 μ M) was loaded into the sample cell and 0.4-2.0 mM of the ligand was titrated in nineteen 2 μ L injections of 2 s duration at 150 s intervals, with injector speed of 750 rpm. Heats of dilution were determined in identical experiments, but without protein in the cell. The data fitting was performed with a single site binding model using the Origin software package. Experiments were performed only once.

Kinase Assays

The kinase assays were performed using the ADP-Glo™ kinase assay kit (Promega). 50 nM CK2 α _WT was incubated in the kinase reaction buffer (40 mM Tris pH7.5, 200 mM NaCl, 20 mM MgCl₂, 0.1 mg/mL BSA, 25 μ M ATP, 50 μ M substrate peptide (RRRADDSDDDD, Enzo Life Sciences Inc.), 5% (v/v) DMSO) in the presence of different concentrations of the inhibitor at 25 °C for 40 min. 5 μ L aliquots of the kinase reaction were quenched with 5 μ L of ADP-glo™ solution. After another 40 min the kinase detection reagent was added and maintained at 25 °C for 30 minutes. The luminescence was recorded using a PHERAstar FS plate reader (BMG LABTECH) with an integration time of 1 s. Percentage

inhibition was calculated relative to a DMSO control and a baseline measurement without ATP. The IC₅₀ curves were fitted using Sigma plot 11.0. Percentage inhibition experiments were carried out in triplicate and IC₅₀ experiments were carried out in duplicate.

Cell Culture

All cell lines used were obtained from ATCC and were supplied as mycoplasma free. HCT116 colon carcinoma cells were maintained in McCoy's 5A (1x) + Glutamax-I growth medium (Gibco, 36600-021) supplemented with fetal bovine serum (FBS, Gibco Life Technologies, 10270-106) at a final concentration of 10%. All cells were grown at 37°C / 5% CO₂ in a humidified environment and all the assays were performed using these culturing conditions.

Growth Inhibition Assays

Adherent cell lines (HCT116) were seeded into flat-bottomed tissue culture 96-well plates in a volume of 150 µL of growth medium. HCT116 cells were seeded at 750 cells per well. After 24 hours, compounds dissolved in DMSO were diluted in growth medium and were added to cells such that the final DMSO concentration was 1% (v/v) and the final volume in the well was 200 µL. Cells were then incubated in the presence compound for 72 hours before fixation. Without removing supernatant 100 µL of cold 10% (v/v) trichloroacetic acid was added to each well and the plates were incubated for 30 minutes at 4 °C. After that the plates were washed three times in tap water and left to dry at room temperature. The fixed cells were stained in a 0.057% sulforhodamine B/1% acetic acid solution (w/v) and incubated at room temperature with agitation for 30 minutes after which the dye was removed and the plates washed in 1% (v/v) acetic acid and left to dry. The dye was then solubilised in 200 µL 10 mM Tris solution (pH 10.5) and incubated for 30 minutes under agitation. The 510 nm absorbance was then measured using a PHERAstar plus plate reader (BMG Labtech). Percentage of growth inhibition was calculated relative to DMSO controls and GI₅₀ values were calculated using Graphpad Prism. All experiments were carried out in duplicate.

References

- 1 C. N. Johnson, D. A. Erlanson, C. W. Murray and D. C. Rees, *J. Med. Chem.*, 2017, **60**, 89–99.
- 2 G. Bollag, J. Tsai, J. Zhang, C. Zhang, P. Ibrahim, K. Nolop and P. Hirth, *Nat. Rev. Drug Discov.*, 2012, **11**, 873–886.
- 3 FDA labelling information - Zelboraf (vemurafenib), http://www.accessdata.fda.gov/drugsatfda_docs/label/2011/202429s000lbl.pdf, (accessed 13 March 2018).
- 4 A. J. Souers, J. D. Levenson, E. R. Boghaert, S. L. Ackler, N. D. Catron, J. Chen, B. D. Dayton, H. Ding, S. H. Enschede, W. J. Fairbrother, D. C. S. Huang, S. G. Hymowitz, S. Jin, S. L. Khaw, P. J. Kovar, L. T. Lam, J. Lee, H. L. Maecker, K. C. Marsh, K. D. Mason, M. J. Mitten, P. M. Nimmer, A. Oleksijew, C. H. Park, C. M. Park, D. C. Phillips, A. W. Roberts, D. Sampath, J. F. Seymour, M. L. Smith, G. M. Sullivan, S. K. Tahir, C. Tse, M. D. Wendt, Y. Xiao, J. C. Xue, H. Zhang, R. A. Humerickhouse, S. H. Rosenberg and S. W. Elmore, *Nat. Med.*, 2013, **19**, 202–208.
- 5 Fragments in the clinic: 2016 edition, <http://practicalfragments.blogspot.co.uk/2016/07/fragments-in-clinic-2016-edition.html>, (accessed 26 January 2018).
- 6 D. A. Erlanson, S. W. Fesik, R. E. Hubbard, W. Jahnke and H. Jhoti, *Nat. Rev. Drug Discov.*, 2016, **15**, 605–619.
- 7 P. G. Wyatt, A. J. Woodhead, V. Berdini, J. A. Boulstridge, M. G. Carr, D. M. Cross, D. J. Davis, L. A. Devine, T. R. Early, R. E. Feltell, E. J. Lewis, R. L. McMenamin, E. F. Navarro, M. A. O'Brien, M. O'Reilly, M. Reule, G. Saxty, L. C. A. Seavers, D.-M. Smith, M. S. Squires, G. Trewartha, M. T. Walker and A. J.-A. Woolford, *J. Med. Chem.*, 2008, **51**, 4986–4999.
- 8 M. E. Kennedy, A. W. Stamford, X. Chen, K. Cox, J. N. Cumming, M. F. Dockendorf, M. Egan, L. Ereshefsky, R. A. Hodgson, L. A. Hyde, S. Jhee, H. J. Kleijn, R. Kuvelkar, W. Li, B. A. Mattson, H. Mei, J. Palcza, J. D. Scott, M. Tanen, M. D. Troyer, J. L. Tseng, J. A. Stone, E. M. Parker and M. S. Forman, *Sci. Transl. Med.*, 2016, **8**, 1–13.
- 9 D. R. Artis, J. J. Lin, C. Zhang, W. Wang, U. Mehra, M. Perreault, D. Erbe, H. I. Krupka, B. P. England, J. Arnold, A. N. Plotnikov, A. Marimuthu, H. Nguyen, S. Will, M. Signaevsky, J. Kral, J. Cantwell, C. Settachatgull, D. S. Yan, D. Fong, A. Oh, S. Shi, P. Womack, B. Powell, G. Habets, B. L. West, K. Y. J. Zhang, M. V. Milburn, G. P. Vlasuk, K. P. Hirth, K. Nolop, G. Bollag, P. N. Ibrahim and J. F. Tobin, *Proc. Natl. Acad. Sci.*, 2009, **106**, 262–267.

- 10 C. W. Murray and D. C. Rees, *Nat. Chem.*, 2009, **1**, 187–192.
- 11 M. Baker, *Nat. Rev. Drug Discov.*, 2013, **12**, 5–7.
- 12 B. J. Davis and S. D. Roughley, *Annu. Rep. Med. Chem.*, 2017, **50**, 371–439.
- 13 B. Lamoree and R. E. Hubbard, *Essays Biochem.*, 2017, **61**, 453–464.
- 14 R. A. E. Carr, M. Congreve, C. W. Murray and D. C. Rees, *Drug Discov. Today*, 2005, **10**, 987–992.
- 15 A. Ciulli and C. Abell, *Curr. Opin. Biotechnol.*, 2007, **18**, 489–496.
- 16 C. W. Murray and T. L. Blundell, *Curr. Opin. Struct. Biol.*, 2010, **20**, 497–507.
- 17 G. G. Ferenczy and G. M. Keseru, *J. Med. Chem.*, 2013, **56**, 2478–2486.
- 18 M. J. Waring, J. Arrowsmith, A. R. Leach, P. D. Leeson, S. Mandrell, R. M. Owen, G. Pairaudeau, W. D. Pennie, S. D. Pickett, J. Wang, O. Wallace and A. Weir, *Nat. Rev. Drug Discov.*, 2015, **14**, 475–486.
- 19 R. Macarron, M. N. Banks, D. Bojanic, D. J. Burns, D. A. Cirovic, T. Garyantes, D. V. S. Green, R. P. Hertzberg, W. P. Janzen, J. W. Paslay and U. Schopfer, *Nature*, 2011, **10**, 188–195.
- 20 A. Barker, J. G. Kettle, T. Nowak and J. E. Pease, *Drug Discov. Today*, 2013, **18**, 298–304.
- 21 S. L. McGovern, E. Caselli, N. Grigorieff and B. K. Shoichet, *J. Med. Chem.*, 2002, **45**, 1712–1722.
- 22 C. M. Park, M. Bruncko, J. Adickes, J. Bauch, H. Ding, A. Kunzer, K. C. Marsh, P. Nimmer, A. R. Shoemaker, X. Song, S. K. Tahir, C. Tse, X. Wang, M. D. Wendt, X. Yang, H. Zhang, S. W. Fesik, S. H. Rosenberg and S. W. Elmore, *J. Med. Chem.*, 2008, **51**, 6902–6915.
- 23 J. P. Burke, Z. Bian, S. Shaw, B. Zhao, C. M. Goodwin, J. Belmar, C. F. Browning, D. Vigil, A. Friberg, D. M. V. Camper, O. W. Rossanese, T. Lee, E. T. Olejniczak and S. W. Fesik, *J. Med. Chem.*, 2015, **58**, 3794–3805.
- 24 D. E. Scott, A. G. Coyne, A. Venkitaraman, T. L. Blundell, C. Abell and M. Hyvönen, *ChemMedChem*, 2015, **10**, 296–303.
- 25 D. E. Scott, A. G. Coyne, S. A. Hudson and C. Abell, *Biochemistry*, 2012, **51**, 4990–5003.
- 26 G. M. Keseru, D. A. Erlanson, G. G. Ferenczy, M. M. Hann, C. W. Murray and S. D. Pickett, *J. Med. Chem.*, 2016, **59**, 8189–8206.
- 27 R. J. Hall, P. N. Mortenson and C. W. Murray, *Prog. Biophys. Mol. Biol.*, 2014, **116**, 82–91.

- 28 W. F. Lau, J. M. Withka, D. Hepworth, T. V. Magee, Y. J. Du, G. A. Bakken, M. D. Miller, Z. S. Hendsch, V. Thanabal, S. A. Kolodziej, L. Xing, Q. Hu, L. S. Narasimhan, R. Love, M. E. Charlton, S. Hughes, W. P. Van Hoorn and J. E. Mills, *J. Comput. Aided. Mol. Des.*, 2011, **25**, 621–636.
- 29 M. M. Hann, A. R. Leach and G. Harper, *J. Chem. Inf. Comput. Sci.*, 2001, **41**, 856–864.
- 30 M. Congreve, R. Carr, C. Murray and H. Jhoti, *Drug Discov. Ther.*, 2003, **8**, 876–877.
- 31 C. W. Murray and D. C. Rees, *Angew. Chemie - Int. Ed.*, 2016, **55**, 488–492.
- 32 N. Baurin, F. Aboul-Ela, X. Barril, B. Davis, M. Drysdale, B. Dymock, H. Finch, C. Fromont, C. Richardson, H. Simmonite and R. E. Hubbard, *J. Chem. Inf. Comput. Sci.*, 2004, **44**, 2157–2166.
- 33 J. Baell and M. A. Walters, *Nature*, 2014, **513**, 481–483.
- 34 A. D. Gossert and W. Jahnke, *Prog. Nucl. Magn. Reson. Spectrosc.*, 2016, **97**, 82–125.
- 35 J. J. Bowling, W. R. Shadrack, E. C. Griffith, R. E. Lee, E. C. Griffith and R. E. Lee, in *Special Topics in Drug Discovery*, ed. D. T. Chen, InTech, London, 2016, pp. 25–51.
- 36 A. D. Morley, A. Pugliese, K. Birchall, J. Bower, P. Brennan, N. Brown, T. Chapman, M. Drysdale, I. H. Gilbert, S. Hoelder, A. Jordan, S. V. Ley, A. Merritt, D. Miller, M. E. Swarbrick and P. G. Wyatt, *Drug Discov. Today*, 2013, **18**, 1221–1227.
- 37 C. C. Genick, D. Barlier, D. Monna, R. Brunner, C. Bé, C. Scheufler and J. Ottl, *J. Biomol. Screen.*, 2014, **19**, 707–714.
- 38 Poll results: affiliation, fragment-finding methods, and library size, www.practicalfragments.blogspot.hu/2014/01/poll-results-affiliation-fragment.html, (accessed 20 January 2018).
- 39 C. Swain, Fragment-Based Screening: What can we learn from published hits?, www.optibrium.com/downloads/Swain_Fragments.pdf, (accessed 20 January 2016).
- 40 M. Mayer and B. Meyer, *Angew. Chemie Int. Ed.*, 1999, **38**, 1784–1788.
- 41 C. Dalvit, G. Fogliatto, A. Stewart, M. Veronesi and B. Stockman, *J. Biomol. NMR*, 2001, **21**, 349–359.
- 42 I. R. Kleckner and M. P. Foster, *Biochim Biophys Acta .*, 2011, **1814**, 942–968.
- 43 T. L. Blundell, H. Jhoti and C. Abell, *Nat. Rev. Drug Discov.*, 2002, **1**, 45–54.
- 44 A. M. Giannetti, in *Methods in Enzymology*, ed. L. C. Kuo, Elsevier, Amsterdam, 1st edn., 2011,

- pp. 169–218.
- 45 E. A. Lewis and K. P. Murphy, in *Protein-Ligand Interactions: Methods and Applications*, ed. G. Ulrich Nienhaus, Humana Press, Totowa, NJ, 2005, pp. 1–15.
- 46 E. Freire, O. L. Mayorga and M. Straume, *Anal. Chem.*, 1990, **62**, 950–959.
- 47 M. M. Lopez and G. I. Makhatadze, in *Calcium-Binding Protein Protocols: Volume 2: Methods and Techniques*, ed. H. J. Vogel, Springer New York, Totowa, NJ, 2002, pp. 121–126.
- 48 A. Velazquez-Campoy, H. Ohtaka, A. Nezami, S. Muzammil and E. Freire, *Curr. Protoc. Cell Biol.*, 2004, 1–24.
- 49 F. E. Torres, M. I. Recht, J. E. Coyle, R. H. Bruce and G. Williams, *Curr. Opin. Struct. Biol.*, 2010, **20**, 598–605.
- 50 A. Ciulli, G. Williams, A. G. Smith, T. L. Blundell and C. Abell, *J. Med. Chem.*, 2006, **49**, 4992–5000.
- 51 S. B. Shuker, P. J. Hajduk, R. P. Meadows and S. W. Fesik, *Science*, 1996, **274**, 1531–1534.
- 52 E. H. Mashalidis, P. Śledå, S. Lang and C. Abell, *Nat. Protoc.*, 2013, **8**, 2309–2324.
- 53 D. Kozakov, L. E. Grove, D. R. Hall, T. Bohnuud, S. E. Mottarella, L. Luo, B. Xia, D. Beglov and S. Vajda, *Nat. Protoc.*, 2015, **10**, 733–755.
- 54 D. Alvarez-Garcia and X. Barril, *J. Med. Chem.*, 2014, **57**, 8530–8539.
- 55 V. Vivat-Hannah, C. Atmanene, D. Zeyer, A. Van Dorsselaer and S. Sanglier-Cianfèrani, *Future Med. Chem.*, 2009, **2**, 35–50.
- 56 X. Chen, S. Qin, S. Chen, J. Li, L. Li, Z. Wang, Q. Wang, J. Lin, C. Yang and W. Shui, *Sci. Rep.*, 2015, **5**, 1–8.
- 57 A. L. Hopkins, G. M. Keserü, P. D. Leeson, D. C. Rees and C. H. Reynolds, *Nat. Rev. Drug Discov.*, 2014, **13**, 105–121.
- 58 A. L. Hopkins, C. R. Groom and A. Alex, *Drug Discov. Today*, 2004, **9**, 430–431.
- 59 P. D. Leeson and B. Springthorpe, *Nat. Rev. Drug Discov.*, 2007, **6**, 881–890.
- 60 S. Schultes, C. De Graaf, E. E. J. Haaksma, I. J. P. De Esch, R. Leurs and O. Krämer, *Drug Discov. Today Technol.*, 2010, **7**, 157–162.
- 61 W. P. Jencks, *Proc. Natl. Acad. Sci.*, 1981, **78**, 4046–4050.

- 62 M. Nazaré, H. Matter, D. W. Will, M. Wagner, M. Urmann, J. Czech, H. Schreuder, A. Bauer, K. Ritter and V. Wehner, *Angew. Chemie - Int. Ed.*, 2012, **51**, 905–911.
- 63 G. Chessari and A. J. Woodhead, *Drug Discov. Today*, 2009, **14**, 668–675.
- 64 J. M. Adams and S. Cory, *Genetics*, 2007, **26**, 1324–1337.
- 65 T. Oltersdorf, S. W. Elmore, A. R. Shoemaker, R. C. Armstrong, D. J. Augeri, B. A. Belli, M. Bruncko, T. L. Deckwerth, J. Dinges, P. J. Hajduk, M. K. Joseph, S. Kitada, S. J. Korsmeyer, A. R. Kunzer, A. Letai, C. Li, M. J. Mitten, D. G. Nettesheim, S. C. Ng, P. M. Nimmer, J. M. O'Connor, A. Oleksijew, A. M. Petros, J. C. Reed, W. Shen, S. K. Tahir, C. B. Thompson, K. J. Tomaselli, B. Wang, M. D. Wendt, H. Zhang, S. W. Fesik and S. H. Rosenberg, *Nature*, 2005, **435**, 677–681.
- 66 L. H. Boise, M. González-García, C. E. Postema, L. Ding, T. Lindsten, L. A. Turka, X. Mao, G. Nuñez and C. B. Thompson, *Cell*, 1993, **74**, 597–608.
- 67 FDA labelling information - Venclexta (venetoclax), https://www.accessdata.fda.gov/drugsatfda_docs/label/2016/208573s000lbl.pdf, (accessed 13 March 2018).
- 68 B. C. Doak, R. S. Norton and M. J. Scanlon, *Pharmacol. Ther.*, 2016, **167**, 28–37.
- 69 P. M. Pollock and P. S. Meltzer, *Cancer Cell*, 2002, **2**, 5–7.
- 70 R. E. Hubbard, *J. Synchrotron Radiat.*, 2008, **15**, 227–230.
- 71 G. G. Ferenczy and G. M. Keseru, *J. Chem. Inf. Model.*, 2012, **52**, 1039–1045.
- 72 C. W. Murray and M. L. Verdonk, *J. Comput. Aided. Mol. Des.*, 2002, **16**, 741–753.
- 73 S. M. Saalau-Bethell, A. J. Woodhead, G. Chessari, M. G. Carr, J. Coyle, B. Graham, S. D. Hiscock, C. W. Murray, P. Pathuri, S. J. Rich, C. J. Richardson, P. A. Williams and H. Jhoti, *Nat. Chem. Biol.*, 2012, **8**, 920–925.
- 74 J. Torres, T. J. Stevens and M. Samsó, *Trends Biochem. Sci.*, 2003, **28**, 137–144.
- 75 J. J. Lacapère, E. Pebay-Peyroula, J. M. Neumann and C. Etchebest, *Trends Biochem. Sci.*, 2007, **32**, 259–270.
- 76 E. P. Carpenter, K. Beis, A. D. Cameron and S. Iwata, *Curr. Opin. Struct. Biol.*, 2008, **18**, 581–586.
- 77 E. Valkov, T. Sharpe, M. Marsh, S. Greive and M. Hyvönen, in *Fragment-Based Drug Discovery and X-Ray Crystallography*, eds. T. G. Davies and M. Hyvönen, Springer, Berlin, 2011, pp. 145–179.

- 78 P. Bamborough, C. W. Chung, R. C. Furze, P. Grandi, A. M. Michon, R. J. Sheppard, H. Barnett, H. Diallo, D. P. Dixon, C. Douault, E. J. Jones, B. Karamshi, D. J. Mitchell, R. K. Prinjha, C. Rau, R. J. Watson, T. Werner and E. H. Demont, *J. Med. Chem.*, 2015, **58**, 6151–6178.
- 79 E. H. Demont, C. W. Chung, R. C. Furze, P. Grandi, A. M. Michon, C. Wellaway, N. Barrett, A. M. Bridges, P. D. Craggs, H. Diallo, D. P. Dixon, C. Douault, A. J. Emmons, E. J. Jones, B. V. Karamshi, K. Locke, D. J. Mitchell, B. H. Mouzon, R. K. Prinjha, A. D. Roberts, R. J. Sheppard, R. J. Watson and P. Bamborough, *J. Med. Chem.*, 2015, **58**, 5649–5673.
- 80 A. G. Waterson, J. P. Kennedy, J. D. Patrone, N. F. Pelz, M. D. Feldkamp, A. O. Frank, B. Vangamudi, E. M. Souza-Fagundes, O. W. Rossanese, W. J. Chazin and S. W. Fesik, *ACS Med. Chem. Lett.*, 2015, **6**, 140–145.
- 81 G. Chessari, I. M. Buck, J. E. H. Day, P. J. Day, A. Iqbal, C. N. Johnson, E. J. Lewis, V. Martins, D. Miller, M. Reader, D. C. Rees, S. J. Rich, E. Tamanini, M. Vitorino, G. A. Ward, P. A. Williams, G. Williams, N. E. Wilsher and A. J. A. Woolford, *J. Med. Chem.*, 2015, **58**, 6574–6588.
- 82 J. A. Christopher, S. J. Aves, K. A. Bennett, A. S. Doré, J. C. Errey, A. Jazayeri, F. H. Marshall, K. Okrasa, M. J. Serrano-Vega, B. G. Tehan, G. R. Wiggin and M. Congreve, *J. Med. Chem.*, 2015, **58**, 6653–6664.
- 83 S. Nakanishi, *Science*, 1992, **258**, 597–603.
- 84 D. Berg, J. Godau, C. Trenkwalder, K. Eggert, I. Csoti, A. Storch, H. Huber, M. Morelli-Canelo, M. Stamelou, V. Ries, M. Wolz, C. Schneider, T. Di Paolo, F. Gasparini, S. Hariry, M. Vandemeulebroecke, W. Abi-Saab, K. Cooke, D. Johns and B. Gomez-Mancilla, *Mov. Disord.*, 2011, **26**, 1243–1250.
- 85 J. Kalliomaki, K. Huizar, M. Kagedal, B. Hagglof and M. Schmelz, *Eur. J. pain*, 2013, **17**, 1465–1471.
- 86 J. C. Pecknold, D. J. McClure, L. Appeltauer, L. Wrzesinski and T. Allan, *J. Clin. Psychopharmacol.*, 1982, **2**, 129–133.
- 87 J. A. Quiroz, P. Tamburri, D. Deptula, L. Banken, U. Beyer, M. Rabbia, N. Parkar, P. Fontoura and L. Santarelli, *JAMA psychiatry*, 2016, **73**, 675–684.
- 88 J. Barker, T. Hesterkamp and M. Whittaker, *Drug Discov. World*, 2008, **9**, 69–75.
- 89 C. Avendaño and J. C. Menéndez, in *Medicinal Chemistry of Anticancer Drugs*, Elsevier, Amsterdam, 2008, pp. 251–305.

- 90 J. Zhang, P. L. Yang and N. S. Gray, *Nat Rev Cancer*, 2009, **9**, 28–39.
- 91 P. Cohen, *Nat. Rev. Drug Discov.*, 2002, **1**, 309–315.
- 92 G. Manning, D. B. Whyte, R. Martinez, T. Hunter and S. Sudarsanam, *Science*, 2002, **298**, 1912–1934.
- 93 T. Irie and M. Sawa, *Chem. Pharm. Bull.*, 2018, **66**, 29–36.
- 94 Kinase-Disease Associations, <https://www.cellsignal.com/contents/resources-reference-tables/kinase-disease-associations/science-tables-kinase-disease>, (accessed 29 January 2018).
- 95 P. N. Mortenson, V. Berdini and M. O’Reilly, *Methods Enzymol.*, 2014, **548**, 69–92.
- 96 P. Traxler and P. Furet, *Pharmacol. Ther.*, 1999, **82**, 195–206.
- 97 Y. Liu and N. S. Gray, *Nat. Chem. Biol.*, 2006, **2**, 358–364.
- 98 C. Lipinski, F. Lombardo, B. W. Dominy and P. J. Feeney, *Adv. Drug Deliv. Rev.*, 1997, **23**, 3–25.
- 99 I. Akritopoulou-Zanze and P. J. Hajduk, *Drug Discov. Today*, 2009, **14**, 291–297.
- 100 L. A. Smyth and I. Collins, *J. Chem. Biol.*, 2009, **2**, 131–151.
- 101 Z. A. Knight and K. M. Shokat, *Chem. Biol.*, 2005, **12**, 621–637.
- 102 C. Yung-Chi and W. H. Prusoff, *Biochem. Pharmacol.*, 1973, **22**, 3099–3108.
- 103 T. W. Traut, *Mol. Cell. Biochem.*, 1994, **140**, 1–22.
- 104 S. J. Pollack, K. S. Beyer, C. Lock, I. Müller, D. Sheppard, M. Lipkin, D. Hardick, P. Blurton, P. M. Leonard, P. A. Hubbard, D. Todd, C. M. Richardson, T. Ahrens, M. Baader, D. O. Hafenbradl, K. Hilyard and R. W. Bürli, *J. Comput. Aided. Mol. Des.*, 2011, **25**, 677–687.
- 105 S. Betzi, R. Alam, M. Martin, D. J. Lubbers, H. Han, S. R. Jakkraj, G. I. Georg and E. Schönbrunn, *ACS Chem. Biol.*, 2011, **6**, 492–501.
- 106 D. W. Litchfield, *Biochem. J.*, 2003, **369**, 1–15.
- 107 G. Burnett and E. P. Kennedy, *J. Biol. Chem.*, 1954, **211**, 969–980.
- 108 C. Franchin, C. Borgo, S. Zaramella, L. Cesaro, G. Arrigoni, M. Salvi and L. A. Pinna, *Pharmaceuticals*, 2017, **10**, 1–8.
- 109 L. Pinna and F. Meggio, *Prog Cell Cycle Res*, 1997, **3**, 77–97.
- 110 K. A. Ahmad, G. Wang, G. Unger, J. Slaton and K. Ahmed, *Adv. Enzym. Regul.*, 2008, **48**, 179–

- 187.
- 111 D. A. Canton and D. W. Litchfield, *Cell. Signal.*, 2006, **18**, 267–275.
- 112 E. Seldin, DC Landesman-Bollag, M. Farago, N. Currier, D. Lou and I. Dominguez, *Mol. Cell. Biochem.*, 2005, **404**, 63–67.
- 113 J. S. Duncan and D. W. Litchfield, *Biochim. Biophys. Acta*, 2008, **1784**, 33–47.
- 114 A. A. Kramerov, M. Saghizadeh, S. Caballero, L. C. Shaw, S. Li Calzi, M. Bretner, M. Montenarh, L. A. Pinna, M. B. Grant and A. V. Ljubimov, *Mol. Cell.*, 2008, **316**, 177–86.
- 115 M. Ruzzene and L. A. Pinna, *Biochim. Biophys. Acta*, 2010, **1804**, 499–504.
- 116 I. Dominguez, G. Sonenshein and D. Seldin, *Cell Mol Life Sci.*, 2009, **66**, 1850–1857.
- 117 R. Allada and R. Meissner, *Mol. Cell. Biochem.*, 2005, **274**, 141–149.
- 118 L. Hauck, C. Harms, J. An, J. Rohne, K. Gertz, R. Dietz, M. Endres, R. Von Harsdorf, C. A. Jones, N. R. London, H. Chen, K. W. Park, D. Sauvaget, R. A. Stockton and J. D. Wythe, *Nat. Med.*, 2008, **14**, 315–324.
- 119 R. C. Axtell, L. Xu, S. R. Barnum and C. Raman, *J. Immunol.*, 2006, **177**, 8542–8549.
- 120 N. N. Singh and D. P. Ramji, *J. Mol. Med.*, 2008, **86**, 887–897.
- 121 J. H. Trembley, Z. Chen, G. Unger, J. Slaton, B. T. Kren, C. Van Waes and K. Ahmed, *BioFactors*, 2010, **36**, 187–195.
- 122 J. Jose, M. Le-Borgne, L. A. Pinna and M. Montenarh, *Pharmaceuticals*, 2017, **10**, 8–11.
- 123 G. Cozza, A. Bortolato and S. Moro, *Med. Res. Rev.*, 2010, **30**, 419–462.
- 124 K. Niefind, *EMBO J.*, 1998, **17**, 2451–2462.
- 125 O. Filhol, J.-L. Martiel and C. Cochet, *EMBO Rep.*, 2004, **5**, 351–355.
- 126 K. Niefind, B. Guerra, I. Ermakowa and O. G. Issinger, *EMBO J.*, 2001, **20**, 5320–5331.
- 127 W. Zhou, X. Qin, X. Yan, X. Xie, L. Li, S. Fang, J. Long, J. Adelman, W.-J. Tang and Y. Shen, *Chinese Sci. Bull.*, 2009, **54**, 220–226.
- 128 T. Kinoshita, T. Nakaniwa, Y. Sekiguchi, Y. Sogabe, A. Sakurai, S. Nakamura and I. Nakanishi, *J. Synchrotron Radiat.*, 2013, **20**, 974–979.
- 129 J. C. Reed, *J. Biol. Chem.*, 1995, 270, 10395–10404.

- 130 J. Reed, A. Bidwai and C. Glover, *J. Biol. Chem.*, 1994, **269**, 18192–18200.
- 131 P. Salinas, D. Fuentes, E. Vidal, X. Jordana, M. Echeverria and L. Holuigue, *Plant Cell Physiol.*, 2006, **47**, 1295–1308.
- 132 K. Niefind and O. G. Issinger, *Biochim. Biophys. Acta*, 2010, **1804**, 484–492.
- 133 X. Xu, E. S. Rich and D. C. Seldin, *Genomics*, 1998, **48**, 79–86.
- 134 X. Xu, P. A. Toselli, L. D. Russell and D. C. Seldin, *Nat. Genet.*, 1999, **23**, 118–121.
- 135 X. Xu, E. Landesman-Bollag, P. Channavajhala and D. Seldin, *Mol. Cell. Biochem.*, 1999, **191**, 65–74.
- 136 D. W. Litchfield, D. Bosc, D. Canton, R. Saulnier, G. Vilc and C. Zhang, *Mol. Cell. Biochem.*, 2001, 21–29.
- 137 K. Klopffleisch, O. G. Issinger and K. Niefind, *Acta Crystallogr.*, 2012, **68**, 883–892.
- 138 E. D. Scheeff and P. E. Bourne, *PLoS Comput. Biol.*, 2005, **1**, 359–381.
- 139 M. Varjosalo, S. Keskitalo, A. VanDrogen, H. Nurkkala, A. Vichalkovski, R. Aebbersold and M. Gstaiger, *Cell Rep.*, 2013, **3**, 1306–1320.
- 140 P. Vaglio, S. Sarno, O. Marina, F. Meggio, O. G. Issinger and L. A. Pinna, *FEBS Lett.*, 1996, **380**, 25–28.
- 141 S. Sarno, P. Vaglio, O. Marin, F. Meggio, O. G. Issinger and L. A. Pinna, *Eur. J. Biochem.*, 1997, **248**, 290–295.
- 142 S. Sarno, P. Vaglio, F. Meggio, O. G. Issinger and L. A. Pinna, *J. Biol. Chem.*, 1996, **271**, 10595–10601.
- 143 S. Sarno, P. Vaglio, O. Marin, O. G. Issinger, K. Ruffato and L. A. Pinna, *Biochemistry*, 1997, **36**, 11717–11724.
- 144 L. N. Johnson, M. E. M. Noble and D. J. Owen, *Cell*, 1996, **85**, 149–158.
- 145 K. Niefind, J. Raaf and O. G. Issinger, *Cell. Mol. Life Sci.*, 2009, **66**, 1800–1816.
- 146 O. Marin, F. Meggio and L. A. Pinna, *Biochem. Biophys. Res. Commun.*, 1994, **198**, 898–905.
- 147 S. Sarno, P. Ghisellini and L. A. Pinna, *J. Biol. Chem.*, 2002, **277**, 22509–22514.
- 148 A. C. Bibby and D. W. Litchfield, *Int. J. Biol. Sci.*, 2005, **1**, 67–79.

- 149 M. Chen and J. A. Cooper, *Proc. Natl. Acad. Sci.*, 1997, **94**, 9136–9140.
- 150 B. Guerra, O.-G. Issinger and J. Y. J. Wang, *Oncogene*, 2003, **22**, 4933–4942.
- 151 K. J. Livak, *Genetics*, 1990, **124**, 303–316.
- 152 J. Raaf, E. Brunstein, O. G. Issinger and K. Niefind, *Protein Sci.*, 2008, **17**, 2180–2186.
- 153 F. Meggio, B. Boldyreff, O. Issinger and L. Piña, *Biochemistry*, 1994, **33**, 4336–4342.
- 154 F. Meggio, B. Boldyreff, O. Marin, L. Pinna and O. Issinger, *Eur. J. Biochem.*, 1992, **204**, 293–279.
- 155 M. Antonelli, J. L. Daniotti, D. Rojo, C. C. Allende and J. E. Allende, *Eur. J. Biochem.*, 1996, **241**, 272–279.
- 156 M. A. Pagano, S. Sarno, G. Poletto, G. Cozza, L. A. Pinna and F. Meggio, *Mol. Cell. Biochem.*, 2005, **274**, 23–29.
- 157 C. V. C. Glover, *J. Biol. Chem.*, 1986, **261**, 14349–14354.
- 158 E. Valero, S. De Bonis, O. Filhol, R. H. Wade, J. Langowski, E. M. Chambaz and C. Cochet, *J. Biol. Chem.*, 1995, **270**, 8345–8352.
- 159 B. Guerra and O. G. Issinger, *Curr. Med. Chem.*, 2008, **15**, 1870–1886.
- 160 S. Tawfic, S. Yu, H. Wang, R. Faust, A. Davis and K. Ahmed, *Histol. Histopathol.*, 2001, **16**, 573–582.
- 161 J. H. Trembley, G. Wang, G. Unger, J. Slaton and K. Ahmed, *Cell. Mol. Life Sci.*, 2009, **66**, 1858–1867.
- 162 S. Sarno and L. A. Pinna, *Mol. Biosyst.*, 2008, **4**, 889–894.
- 163 G. M. Unger, A. T. Davis, J. W. Slaton and K. Ahmed, *Curr. Cancer Drug Targets*, 2004, **4**, 77–84.
- 164 M. Daya-Makin, J. S. Sanghera, T. L. Mogentale, M. Lipp, J. Parchomchuk, J. C. Hogg and P. S.L., *Cancer Res.*, 1994, **54**, 2262–2268.
- 165 L. Tornatore, A. Sandomenico, D. Raimondo, C. Low, A. Rocci, C. Tralau-Stewart, D. Capece, D. D’Andrea, M. Bua, E. Boyle, M. vanDuin, P. Zoppoli, A. Jaxa-Chamiec, A. K. Thotakura, J. Dyson, B. A. Walker, A. Leonardi, A. Chambery, C. Driessen, P. Sonneveld, G. Morgan, A. Palumbo, A. Tramontano, A. Rahemtulla, M. Ruvo and G. Franzoso, *Cancer Cell*, 2014, **26**, 495–508.
- 166 E. Landesman-Bollag, R. Romieu-Mourez, D. H. Song, G. E. Sonenshein, R. D. Cardiff and D. C.

- Seldin, *Oncogene*, 2001, **20**, 3247–3257.
- 167 Y. Hao, C. Wang, B. Cao, B. M. Hirsch, J. Song, S. D. Markowitz, R. M. Ewing, D. Sedwick, L. Liu, W. Zheng and Z. Wang, *Cancer Cell*, 2013, **23**, 583–593.
- 168 F. Qaiser, J. H. Trembley, B. T. Kren, J. J. Wu, A. K. Naveed and K. Ahmed, *J. Cell. Biochem.*, 2014, **115**, 2103–2115.
- 169 C. E. Ortega, Y. Seidner and I. Dominguez, *PLoS One*, 2014, **9**, 1–25.
- 170 M. Gapany, R. A. Faust, S. Tawfic, A. Davis, G. L. Adams and K. Ahmed, *Mol. Med.*, 1995, **1**, 659–666.
- 171 M. Chua, C. Ortega, A. Sheikh, M. Lee, H. Abdul-Rassoul, K. Hartshorn and I. Dominguez, *Pharmaceuticals*, 2017, **10**, 1–30.
- 172 A. V Ljubimov, S. Caballero, A. M. Aoki, L. A. Pinna, M. B. Grant and R. Castellon, *Invest. Ophthalmol. Vis. Sci.*, 2004, **45**, 4583–4591.
- 173 D. Hanahan and R. A. Weinberg, *Cell*, 2000, **100**, 57–70.
- 174 H. Zhang, S. Jiang, X. Zhang, Z. Zhou, Q. Pan, C. Chen, J. Zhao, Y. Tang, J. Xia and D. Weng, *Oncotarget*, 2015, **6**, 34800–34817.
- 175 P. Channavajhala and D. C. Seldin, *Oncogene*, 2002, **21**, 5280–5288.
- 176 E. Landesman-Bollag, D. H. Song, R. Romieu-Mourez, D. J. Sussman, R. D. Cardiff, G. E. Sonenshein and D. C. Seldin, *Mol. Cell. Biochem.*, 2001, **227**, 153–165.
- 177 M. A. Kelliher, D. C. Seldin and P. Leder, *EMBO J.*, 1996, **15**, 5160–5166.
- 178 E. Landesman-Bollag, P. L. Channavajhala, R. D. Cardiff and D. C. Seldin, *Oncogene*, 1998, **16**, 2965–2974.
- 179 G. Di Maira, F. Brustolon, J. Bertacchini, K. Tosoni, S. Marmiroli, L. A. Pinna and M. Ruzzene, *Oncogene*, 2007, **26**, 6915–6926.
- 180 S. Mishra, A. Reichert, J. Cunnick, D. Senadheera, B. Hemmeryckx, N. Heisterkamp and J. Groffen, *Oncogene*, 2003, **22**, 8255–8262.
- 181 S. Mishra, V. Pertz, B. Zhang, P. Kaur, H. Shimada, J. Groffen, Z. Kazimierczuk, L. A. Pinna and N. Heisterkamp, *Leukemia*, 2007, **21**, 178–180.
- 182 F. A. Piazza, M. Ruzzene, C. Gurrieri, B. Montini, L. Bonanni, G. Chioetto, G. Di Maira, F. Barbon,

- A. Cabrelle, R. Zambello, F. Adami, L. Trentin, L. A. Pinna and G. Semenzato, *Blood*, 2006, **108**, 1698–1708.
- 183 I. Weinstein, *Science*, 2002, **297**, 64–65.
- 184 N. L. Solimini, J. Luo and S. J. Elledge, *Cell*, 2007, **130**, 986–988.
- 185 R. Nagel, E. A. Semenova and A. Berns, *EMBO Rep.*, 2016, **17**, 1516–1531.
- 186 J. S. Kim, J. I. Eom, J.-W. Cheong, A. J. Choi, J. K. Lee, W. I. Yang and Y. H. Min, *Clin. Cancer Res.*, 2007, **13**, 1019–1028.
- 187 A. Silva, J. A. Yunes, B. A. Cardoso, L. R. Martins, P. Y. Jotta, M. Abecasis, A. E. Nowill, N. R. Leslie, A. A. Cardoso and J. T. Barata, *J. Clin. Invest.*, 2008, **118**, 3762–3774.
- 188 J. H. Park, J. J. Kim and Y. S. Bae, *Biochem. Biophys. Res. Commun.*, 2013, **433**, 420–425.
- 189 H. Jia, Y. Liu, R. Xia, C. Tong, T. Yue, J. Jiang and J. Jia, *J. Biol. Chem.*, 2010, **285**, 37218–37226.
- 190 Y. Zheng, H. Qin, S. J. Frank, L. Deng, D. W. Litchfield, A. Tefferi, A. Pardanani, F. T. Lin, J. Li, B. Sha and E. N. Benveniste, *Blood*, 2011, **118**, 156–166.
- 191 L. Macias Alvarez, J. Revuelta-Cervantes and I. Dominguez, in *Biochemistry and Molecular Biology: Protein Kinase CK2*, ed. L. A. Pinna, Wiley, New York, 2013, pp. 105–149.
- 192 S. F. Eddy, S. Guo, E. G. Demicco and G. E. Sonenshein, *Cancer Res.*, 2005, **65**, 11375–11383.
- 193 Z. L. Chu, T. A. McKinsey, L. Liu, X. Qi and D. W. Ballard, *Mol. Cell. Biol.*, 1996, **16**, 5974–5984.
- 194 J. A. McElhinny, S. A. Trushin, G. D. Bren, N. Chester and C. V. Paya, *Mol. Cell. Biol.*, 1996, **16**, 899–906.
- 195 D. Wang, S. D. Westerheide, J. L. Hanson and J. Baldwin A.S., *J. Biol. Chem.*, 2000, **275**, 32592–32597.
- 196 A. Chantôme, A. Pance, N. Gauthier, D. Vandroux, J. Chenu, E. Solary, J. F. Jeannin and S. Reveneau, *J. Biol. Chem.*, 2004, **279**, 23953–23960.
- 197 C. Van Waes, *Clin. Cancer Res.*, 2007, **13**, 1076–1082.
- 198 M. Brown, J. Cohen, P. Arun, Z. Chen and C. Van Waes, *Expert Opin. Ther. Targets*, 2008, **12**, 1109–1122.
- 199 M. S. Brown, O. T. Diallo, M. Hu, R. Ehsanian, X. Yang, P. Arun, H. Lu, V. Korman, G. Unger, K. Ahmed, C. Van Waes and Z. Chen, *Clin. Cancer Res.*, 2010, **16**, 2295–2307.

- 200 D. H. Song, D. J. Sussman and D. C. Seldin, *J. Biol. Chem.*, 2000, **275**, 23790–23797.
- 201 D. H. Song, I. Dominguez, J. Mizuno, M. Kaut, S. C. Mohr and D. C. Seldin, *J. Biol. Chem.*, 2003, **278**, 24018–24025.
- 202 E. M. Sale and G. J. Sale, *Cell. Mol. Life Sci.*, 2008, **65**, 113–127.
- 203 J. Torres and R. Pulido, *J. Biol. Chem.*, 2001, **276**, 993–998.
- 204 M.-A. Arevalo and A. Rodriguez-Tebar, *Mol. Biol. Cell*, 2006, **17**, 3369–3377.
- 205 G. Di Maira, M. Salvi, G. Arrigoni, O. Marin, S. Sarno, F. Brustolon, L. A. Pinna and M. Ruzzene, *Cell Death Differ.*, 2005, **12**, 668–677.
- 206 S. Sato, N. Fujita and T. Tsuruo, *Proc. Natl. Acad. Sci.*, 2000, **97**, 10832–10837.
- 207 D. R. McIlwain, T. Berger and T. W. Mak, *Cold Spring Harb. Perspect. Biol.*, 2013, **5**, 1–29.
- 208 F. Meggio and L. A. Pinna, *FASEB J.*, 2003, **17**, 349–368.
- 209 S. Desagher, A. Osen-Sand, S. Montessuit, E. Magnenat, F. Vilbois, A. Hochmann, L. Journot, B. Antonsson and J. C. Martinou, *Mol. Cell*, 2001, **8**, 601–611.
- 210 A. Krippner-Heidenreich, R. V. Talanian, R. Sekul, R. Kraft, H. Thole, H. Ottleben and B. Lüscher, *Biochem. J.*, 2001, **358**, 705–715.
- 211 M. Ruzzene, D. Penzo and L. A. Pinna, *Biochem. J.*, 2002, **364**, 41–47.
- 212 J. Walter, A. Schindzielorz, J. Grünberg and C. Haass, *Proc. Natl. Acad. Sci.*, 1999, **96**, 1391–1396.
- 213 X. Yin, S. Gu and J. X. Jiang, *Cell Commun. Adhes.*, 2001, **8**, 373–376.
- 214 J. Torres, J. Rodriguez, M. P. Myers, M. Valiente, J. D. Graves, N. K. Tonks and R. Pulido, *J. Biol. Chem.*, 2003, **278**, 30652–30660.
- 215 G. Wang, K. A. Ahmad, G. Unger, J. W. Slaton and K. Ahmed, *J. Cell. Biochem.*, 2006, **99**, 382–391.
- 216 M. E. Gleave and B. P. Monia, *Nat. Rev. Cancer*, 2005, **5**, 468–479.
- 217 D. Y. Lou, I. Dominguez, P. Toselli, E. Landesman-Bollag, C. O'Brien and D. C. Seldin, *Mol. Cell. Biol.*, 2008, **28**, 131–139.
- 218 R. Padmanabha, J. L. Chen-Wu, D. E. Hanna and C. V Glover, *Mol. Cell. Biol.*, 1990, **10**, 4089–

- 4099.
- 219 T. Buchou, M. Vernet, O. Blond, H. H. Jensen, H. Pointu, B. B. Olsen, C. Cochet, O. Issinger and B. Boldyreff, *Mol. Cell. Biol.*, 2003, **23**, 908–915.
- 220 J. W. Slaton, G. M. Unger, D. T. Sloper, A. T. Davis and K. Ahmed, *Mol. Cancer Res.*, 2004, **2**, 712–721.
- 221 K. A. Ahmad, G. Wang, J. Slaton, G. Unger and K. Ahmed, *Anticancer. Drugs*, 2005, **16**, 1037–1043.
- 222 G. Wang, G. Unger, K. a Ahmad, J. W. Slaton and K. Ahmed, *Mol. Cell. Biochem.*, 2005, **274**, 77–84.
- 223 H. Wang, A. Davis, S. Yu and K. Ahmed, *Mol. Cell. Biochem.*, 2001, **227**, 167–174.
- 224 V. Giroux, *FASEB J.*, 2006, **20**, 1982–1991.
- 225 G. Cozza and L. A. Pinna, *Expert Opin. Ther. Targets*, 2016, **20**, 319–340.
- 226 FDA Orphan Drug Status - Sildenafil, <https://www.accessdata.fda.gov/scripts/opdlisting/oopd/detailedIndex.cfm?cfgridkey=548516>, (accessed 24 April 2018).
- 227 NCT02128282: Study of CX-4945 in Combination With Gemcitabine and Cisplatin for Frontline Treatment of Cholangiocarcinoma, <https://clinicaltrials.gov/show/NCT02128282>, (accessed 1 March 2018).
- 228 R. Battistutta, *Cell. Mol. Life Sci.*, 2009, **66**, 1868–1889.
- 229 H. M. Berman, T. Battistuz, T. N. Bhat, W. F. Bluhm, P. E. Bourne, K. Burkhardt, Z. Feng, G. L. Gilliland, L. Iype, S. Jain, P. Fagan, J. Marvin, D. Padilla, V. Ravichandran, B. Schneider, N. Thanki, H. Weissig, J. D. Westbrook and C. Zardecki, *Acta Crystallogr.*, 2002, **58**, 899–907.
- 230 E. Vangrevelinghe, K. Zimmermann, J. Schoepfer, R. Portmann, D. Fabbro and P. Furet, *J. Med. Chem.*, 2003, **46**, 2656–2662.
- 231 D. B. Kitchen, H. Decornez, J. R. Furr and J. Bajorath, *Nat. Rev. Drug Discov.*, 2004, **3**, 935–949.
- 232 R. Battistutta, E. De Moliner, S. Sarno, G. Zanotti and L. A. Pinna, *Protein Sci.*, 2001, **10**, 2200–2206.
- 233 A. Siddiqui-Jain, D. Drygin, N. Streiner, P. Chua, F. Pierre, S. E. O'Brien, J. Bliesath, M. Omori, N. Huser, C. Ho, C. Proffitt, M. K. Schwaebel, D. M. Ryckman, W. G. Rice and K. Anderes, *Cancer*

- Res.*, 2010, **70**, 10288–10298.
- 234 L. R. Martins, P. Lúcio, A. Melão, I. Antunes, B. A. Cardoso, R. Stansfield, M. T. S. Bertilaccio, P. Ghia, D. Drygin, M. G. Silva and J. T. Barata, *Leukemia*, 2014, **28**, 179–182.
- 235 F. Pierre, P. C. Chua, S. E. O’Brien, A. Siddiqui-Jain, P. Bourbon, M. Haddach, J. Michaux, J. Nagasawa, M. K. Schwaebe, E. Stefan, A. Vialettes, J. P. Whitten, T. K. Chen, L. Darjania, R. Stansfield, K. Anderes, J. Bliesath, D. Drygin, C. Ho, M. Omori, C. Proffitt, N. Streiner, K. Trent, W. G. Rice and D. M. Ryckman, *J. Med. Chem.*, 2011, **54**, 635–654.
- 236 H. Kim, K. Choi, H. Kang, S. Y. Lee, S. W. Chi, M. S. Lee, J. Song, D. Im, Y. Choi and S. Cho, *PLoS One*, 2014, **9**, 1–8.
- 237 J. E. Dowling, M. Alimzhanov, L. Bao, C. Chuaqui, C. R. Denz, E. Jenkins, N. A. Larsen, P. D. Lyne, T. Pontz, Q. Ye, G. A. Holdgate, L. Snow, N. O’Connell and A. D. Ferguson, *ACS Med. Chem. Lett.*, 2016, **7**, 300–305.
- 238 R. Prudent, C. F. Sautel and C. Cochet, *Biochim. Biophys. Acta - Proteins Proteomics*, 2010, **1804**, 493–498.
- 239 H. M. Jiang, J. K. Dong, K. Song, T. D. Wang, W. K. Huang, J. M. Zhang, X. Y. Yang, Y. Shen and J. Zhang, *Acta Pharmacol. Sin.*, 2017, **38**, 1691–1698.
- 240 S. Lu, S. Li and J. Zhang, *Med. Res. Rev.*, 2014, **34**, 1242–1285.
- 241 R. Prudent and C. Cochet, *Chem. Biol.*, 2009, **16**, 112–120.
- 242 K. Gunasekaran, B. Ma and R. Nussinov, *Proteins Struct. Funct. Genet.*, 2004, **57**, 433–443.
- 243 H. N. Motlagh, J. O. Wrabl, J. Li and V. J. Hilser, *Nature*, 2014, **508**, 331–339.
- 244 Q. Shen, F. Cheng, H. Song, W. Lu, J. Zhao, X. An, M. Liu, G. Chen, Z. Zhao and J. Zhang, *Am. J. Hum. Genet.*, 2017, **100**, 5–20.
- 245 Q. Shen, G. Wang, S. Li, X. Liu, S. Lu, Z. Chen, K. Song, J. Yan, L. Geng, Z. Huang, W. Huang, G. Chen and J. Zhang, *Nucleic Acids Res.*, 2016, **44**, 527–535.
- 246 W. Huang, S. Lu, Z. Huang, X. Liu, L. Mou, Y. Luo, Y. Zhao, Y. Liu, Z. Chen, T. Hou and J. Zhang, *Bioinformatics*, 2013, **29**, 2357–2359.
- 247 J. Raaf, E. Brunstein, O. G. Issinger and K. Niefind, *Chem. Biol.*, 2008, **15**, 111–117.
- 248 F. Benavent Acero, C. S. Capobianco, J. Garona, S. M. Cirigliano, Y. Perera, A. J. Urtreger, S. E. Perea, D. F. Alonso and H. G. Farina, *Lung Cancer*, 2017, **107**, 14–21.

- 249 J. W. Scott, S. Galic, K. L. Graham, R. Foitzik, N. X. Y. Ling, T. A. Dite, S. M. A. Issa, C. G. Langendorf, Q. P. Weng, H. E. Thomas, T. W. Kay, N. C. Birnberg, G. R. Steinberg, B. E. Kemp and J. S. Oakhill, *Chem. Biol.*, 2015, **22**, 705–711.
- 250 Y. Perera, H. G. Farina, I. Hernández, O. Mendoza, J. M. Serrano, O. Reyes, D. E. Gómez, R. E. Gómez, B. E. Acevedo, D. F. Alonso and S. E. Perea, *Int. J. Cancer*, 2008, **122**, 57–62.
- 251 G. Cozza, S. Zanin, S. Sarno, E. Costa, C. Girardi, G. Ribaud, M. Salvi, G. Zagotto, M. Ruzzene and L. A. Pinna, *Biochem J*, 2015, **471**, 415–430.
- 252 H. Rahnel, K. Viht, D. Lavogina, O. Mazina, T. Haljasorg, E. Enkvist and A. Uri, *ChemMedChem*, 2017, **12**, 1723–1736.
- 253 F. Meggio, D. Shugar and L. A. Pinna, *Eur. J. Biochem.*, 1990, **187**, 89–94.
- 254 B. Laudet, C. Barette, V. Dulery, O. Renaudet, P. Dumy, A. Metz, R. Prudent, A. Deshiere, O. Dideberg, O. Filhol and C. Cochet, *Biochem. J.*, 2007, **408**, 363–373.
- 255 B. Laudet, V. Moucadet, R. Prudent, O. Filhol, Y. S. Wong, D. Royer and C. Cochet, *Mol. Cell. Biochem.*, 2008, **316**, 63–69.
- 256 B. Bestgen, Z. Belaid-Choucair, T. Lomberget, M. Le Borgne, O. Filhol and C. Cochet, *Pharmaceuticals*, 2017, **10**, 1–15.
- 257 R. Prudent, V. Moucadet, B. Laudet, C. Barette, L. Lafanechère, B. Hasenknopf, J. Li, S. Bareyt, E. Lacôte, S. Thorimbert, M. Malacria, P. Gouzerh and C. Cochet, *Chem. Biol.*, 2008, **15**, 683–692.
- 258 V. Lamba and I. Ghosh, *Curr. Pharm. Des.*, 2012, **18**, 2936–2945.
- 259 D. Lavogina, E. Enkvist and A. Uri, *ChemMedChem*, 2010, **5**, 23–34.
- 260 D. Lavogina, M. Lust, I. Viil, N. König, G. Raidaru, J. Rogozina, E. Enkvist, A. Uri and D. Bossemeyer, *J. Med. Chem.*, 2009, **52**, 308–321.
- 261 A. Pflug, J. Rogozina, D. Lavogina, E. Enkvist, A. Uri, R. A. Engh and D. Bossemeyer, *J. Mol. Biol.*, 2010, **403**, 66–77.
- 262 E. Enkvist, K. Viht, N. Bischoff, J. Vahter, S. Saaver, G. Raidaru, O. G. Issinger, K. Niefind and A. Uri, *Org. Biomol. Chem.*, 2012, **10**, 8645–8653.
- 263 Z. Hou, I. Nakanishi, T. Kinoshita, Y. Takeji, M. Yasue, R. Misu, Y. Suzuki, S. Nakamura, T. Kure, H. Ohno, K. Murata, K. Kitaura, A. Hirasawa, G. Tsujimoto, S. Oishi and N. Fujii, *J. Med. Chem.*,

- 2012, **55**, 2899–2903.
- 264 L. R. Masterson, A. Mascioni, N. J. Traaseth, S. S. Taylor and G. Veglia, *Proc. Natl. Acad. Sci. U. S. A.*, 2008, **105**, 506–511.
- 265 P. Brear, C. De Fusco, K. Hadje Georgiou, N. J. Francis-Newton, C. J. Stubbs, H. F. Sore, A. R. Venkitaraman, C. Abell, D. R. Spring and M. Hyvönen, *Chem. Sci.*, 2016, **7**, 6839–6845.
- 266 C. De Fusco, P. Brear, J. Iegre, K. H. Georgiou, H. F. Sore, M. Hyvönen and D. R. Spring, *Bioorganic Med. Chem.*, 2017, **25**, 3471–3482.
- 267 J. Iegre, P. Brear, C. De Fusco, M. Yoshida, S. L. Mitchell, M. Rossmann, L. Carro, H. F. Sore, M. Hyvönen and D. R. Spring, *Chem. Sci.*, 2018, **9**, 3041–3049.
- 268 A. Gouron, A. Milet and H. Jamet, *Biophys. J.*, 2014, **106**, 1134–1141.
- 269 Schrödinger, Glide, New York, 2018.
- 270 R. A. Friesner, R. B. Murphy, M. P. Repasky, L. L. Frye, J. R. Greenwood, T. A. Halgren, P. C. Sanschagrin and D. T. Mainz, *J. Med. Chem.*, 2006, **49**, 6177–6196.
- 271 R. A. Friesner, J. L. Banks, R. B. Murphy, T. A. Halgren, J. J. Klicic, D. T. Mainz, M. P. Repasky, E. H. Knoll, M. Shelley, J. K. Perry, D. E. Shaw, P. Francis and P. S. Shenkin, *J. Med. Chem.*, 2004, **47**, 1739–1749.
- 272 T. A. Halgren, R. B. Murphy, R. A. Friesner, H. S. Beard, L. L. Frye, W. T. Pollard and J. L. Banks, *J. Med. Chem.*, 2004, **47**, 1750–1759.
- 273 Schrödinger, The PyMOL Molecular Graphics System, Version 2.0.
- 274 M. I. Dawson, Z. Xia, G. Liu, J. A. Fontana, L. Farhana, B. B. Patel, S. Arumugarajah, M. Bhuiyan, X. K. Zhang, Y. H. Han, W. B. Stallcup, J. I. Fukushi, T. Mustelin, L. Tautz, Y. Su, D. L. Harris, N. Waleh, P. D. Hobbs, L. Jong, W. R. Chao, L. J. Schiff and B. P. Sani, *J. Med. Chem.*, 2007, **50**, 2622–2639.
- 275 Y. Q. Fang, J. Yuen and M. Lautens, *J. Org. Chem.*, 2007, **72**, 5152–5160.
- 276 A. M. Birch, S. Groombridge, R. Law, A. G. Leach, C. D. Mee and C. Schramm, *J. Med. Chem.*, 2012, **55**, 3923–3933.
- 277 US Pat., US2007249686 (A1), 2007.
- 278 EP Pat., EP1799658, 2007.

- 279 US Pat., WO2004056315 (A2), 2004.
- 280 US Pat., US19910729847, 1993.
- 281 J. Bornstein, S. A. Leone, W. F. Sullivan and O. F. Bennett, *J. Am. Chem. Soc.*, 1957, **79**, 1745–1748.
- 282 R. G. Jones, *J. Am. Chem. Soc.*, 1947, **69**, 2346–2350.
- 283 N. Miyaura and A. Suzuki, *Chem. Rev.*, 1995, **95**, 2457–2483.
- 284 A. Suzuki, *J. Organomet. Chem.*, 1999, **576**, 147–168.
- 285 S. P. Stanforth, *Tetrahedron*, 1998, **54**, 263–303.
- 286 A. Jutand and A. Mosleh, *Organometallics*, 1995, **14**, 1810–1817.
- 287 US Pat., US7968552 (B2), 2011.
- 288 G. M. Carlson and A. W. Fenton, *Biophys. J.*, 2016, **110**, 1912–1923.
- 289 S. Lu, R. Deng, H. Jiang, H. Song, S. Li, Q. Shen, W. Huang, R. Nussinov, J. Yu and J. Zhang, *Structure*, 2015, **23**, 1725–1734.
- 290 L. G. Ahuja, A. P. Kornev, C. L. McClendon, G. Veglia and S. S. Taylor, *Proc. Natl. Acad. Sci.*, 2017, **114**, 931–940.
- 291 C. Nienberg, C. Garmann, A. Gratz, A. Bollacke, C. Götz and J. Jose, *Pharmaceuticals*, 2017, **10**, 1–26.
- 292 W. Lee, S. Hyeon, B. Jin, J. Na, S. Kim and K. Kim, *Proc. Natl. Acad. Sci. U. S. A.*, 2013, **110**, 19360–19365.
- 293 O. Marin, F. Meggio, F. Marchiori, G. Borin and L. A. Pinna, *Eur. J. Biochem.*, 1986, **160**, 239–244.
- 294 J. W. Perich, E. C. Reynolds, F. Meggio, O. Marin and L. A. Pinna, *Biochemistry*, 1992, **31**, 5893–5897.
- 295 F. Meggio, O. Marin and L. A. Pinna, *Cell. Mol. Biol. Res.*, 1994, **40**, 401–409.
- 296 L. Ma, J. M. Falkowski, C. Abney and W. Lin, *Nat. Chem.*, 2010, **2**, 838–846.
- 297 US Pat., WO/2012/162409, 2010.
- 298 CN Pat., CN105237337 A, 2016.

- 299 US Pat., US2007/0032488 A1, 2007.
- 300 JP Pat., JP2016/222632A, 2016.
- 301 US Pat., WO2014142363A1, 2014.
- 302 US Pat., WO2009131090 A1, 2009.
- 303 K. Vikse, T. Naka, J. S. McIndoe, M. Besora and F. Maseras, *ChemCatChem*, 2013, **5**, 3604–3609.
- 304 P. Fitton and E. A. Rick, *J. Organomet. Chem.*, 1971, **28**, 287–291.
- 305 A. Ghosh, J. Luo, C. Liu, G. Weltrowska, C. Lemieux, N. N. Chung, Y. Lu and P. W. Schiller, *J. Med. Chem.*, 2008, **51**, 5866–5870.
- 306 US Pat., US20140249151A1, 2014.
- 307 P. J. Hajduk and J. Greer, *Nat. Rev. Drug Discov.*, 2007, **6**, 211–219.
- 308 J. M. Collins, in *Microwaves in Organic Synthesis*, eds. A. Hoz and A. Loupy, Wiley, Hoboken, 3rd edn., 2013, pp. 897–959.
- 309 K. Pels and T. Kodadek, *ACS Comb. Sci.*, 2015, **17**, 152–155.

Appendix

Appendix 1: A Fragment-Based Drug Discovery Approach for the Development of Selective Inhibitors of Protein Kinase CK2 α

Appendix 1A: ^1H and ^{13}C NMR Spectra

Appendix 1B: Analytical HPLC Traces for Selected Peptides

Appendix 1C: Mass Spectra for Selected Peptides

Appendix 2: Publications

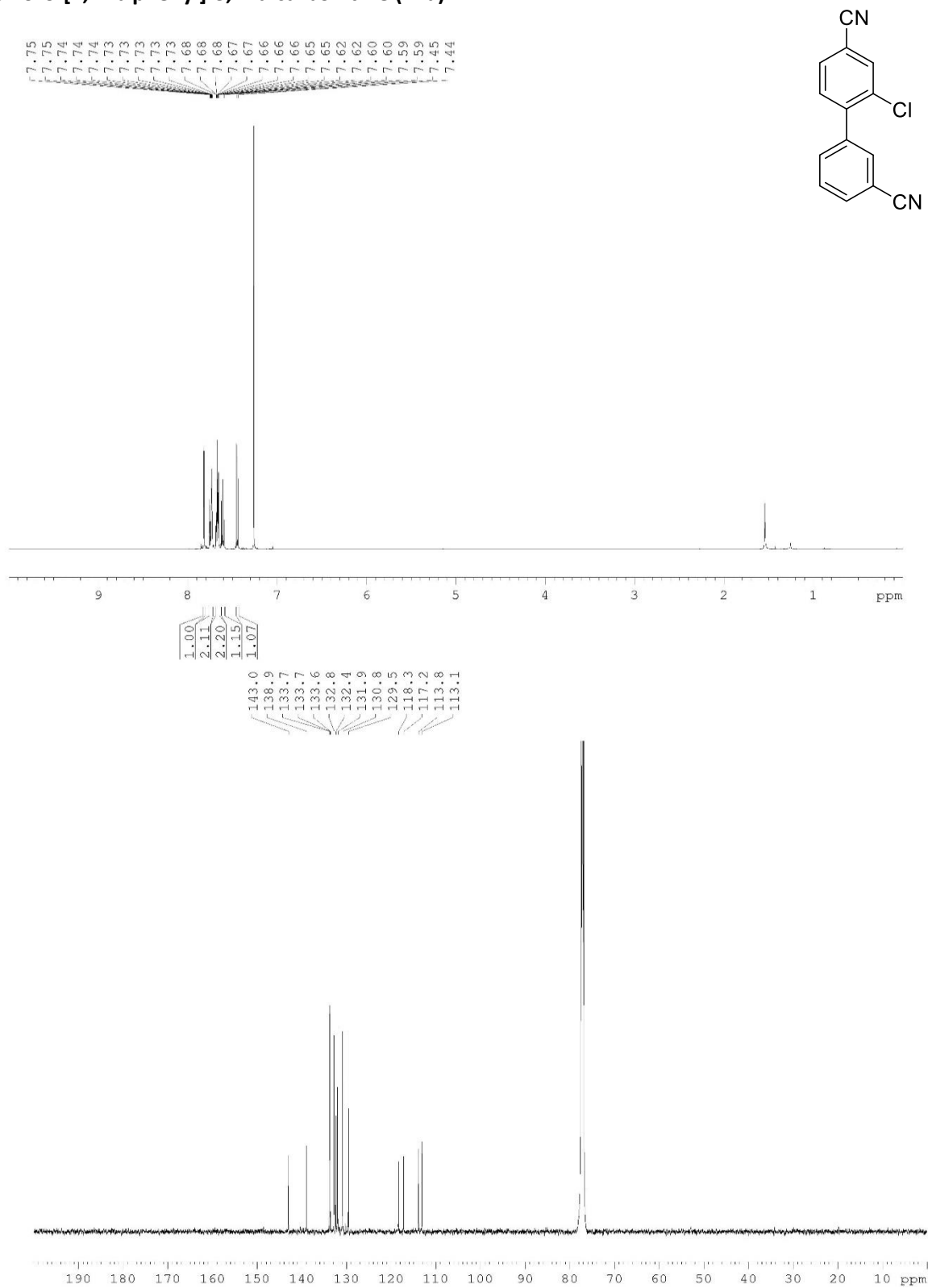
Appendix 2A: Second-Generation CK2 α Inhibitors Targeting the αD Pocket

Appendix 2B: Partially Saturated Bicyclic Heteroaromatics as an sp^3 -Enriched Fragment Collection

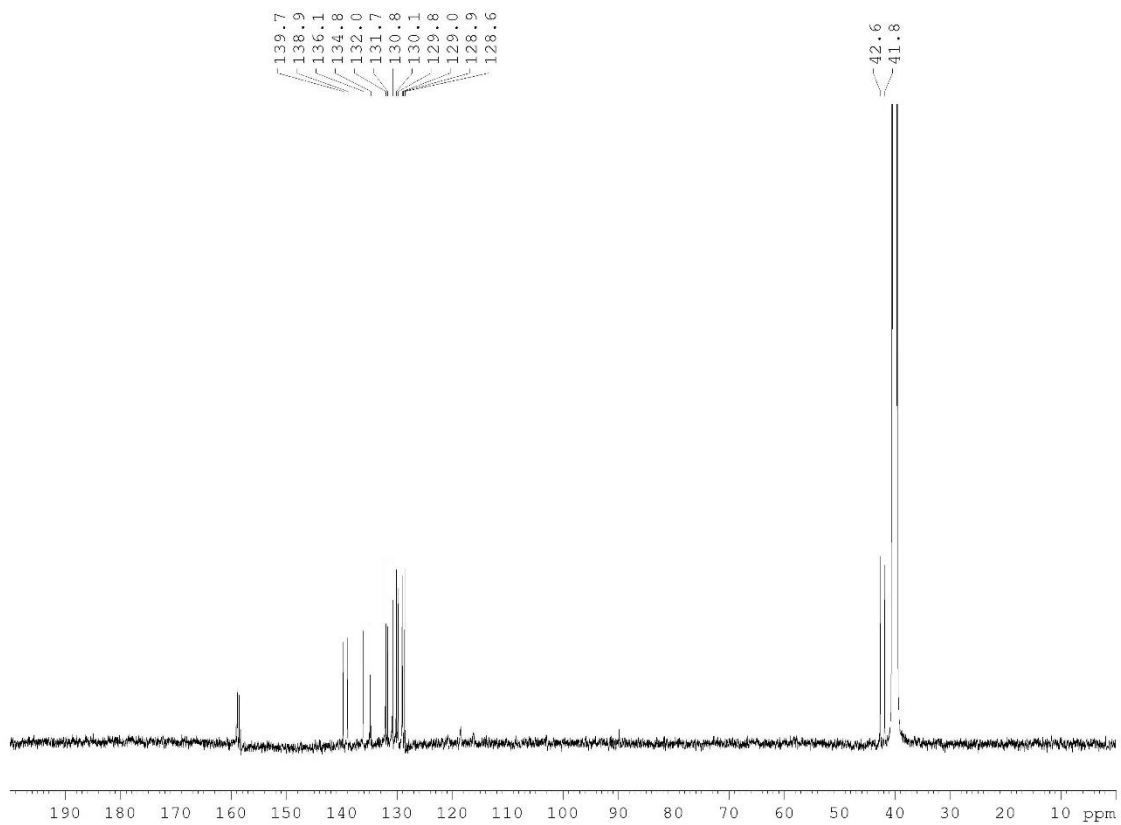
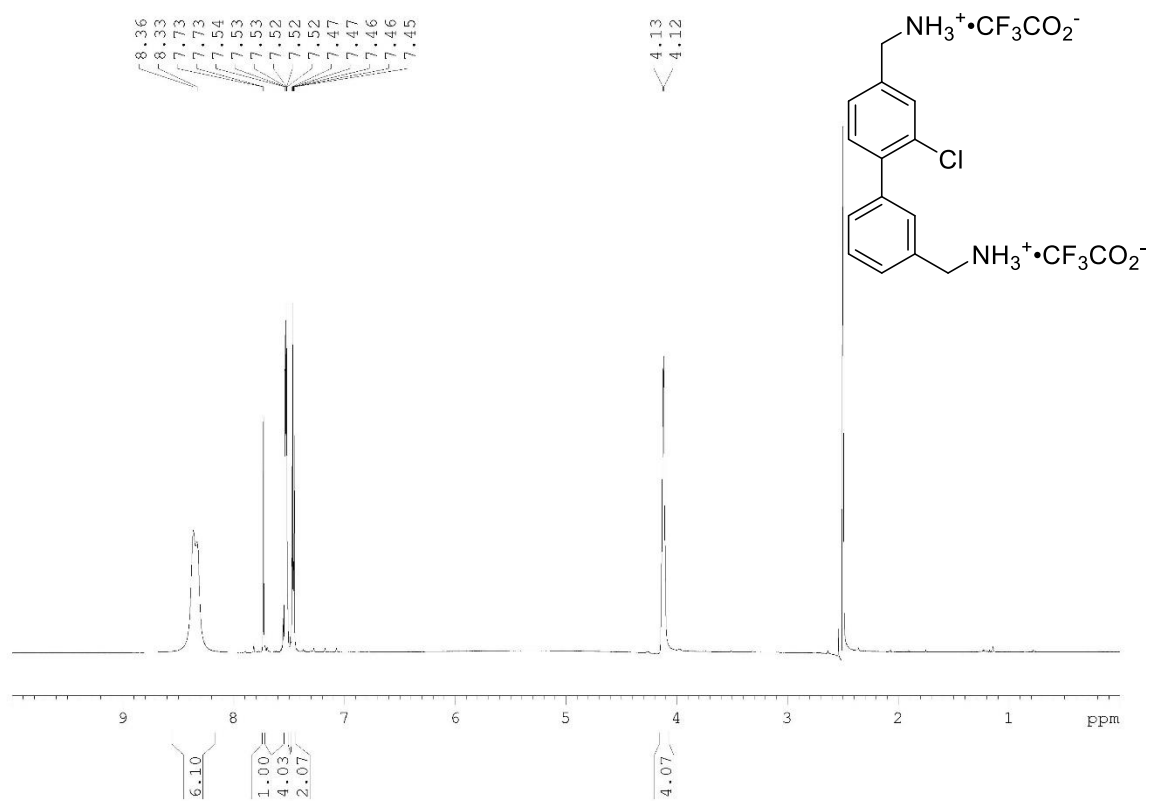
Appendix 1: A Fragment-Based Drug Discovery Approach for the Development of Selective Inhibitors of Protein Kinase CK2 α

Appendix 1A: ^1H and ^{13}C NMR Spectra

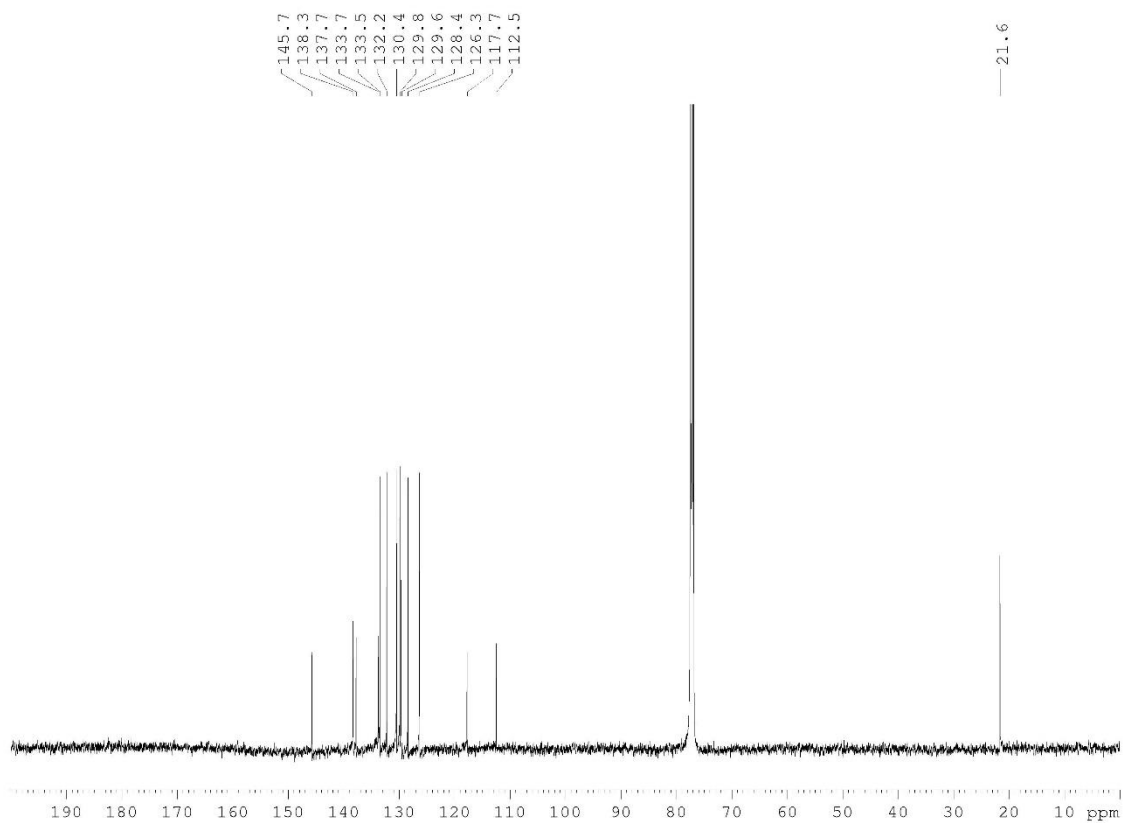
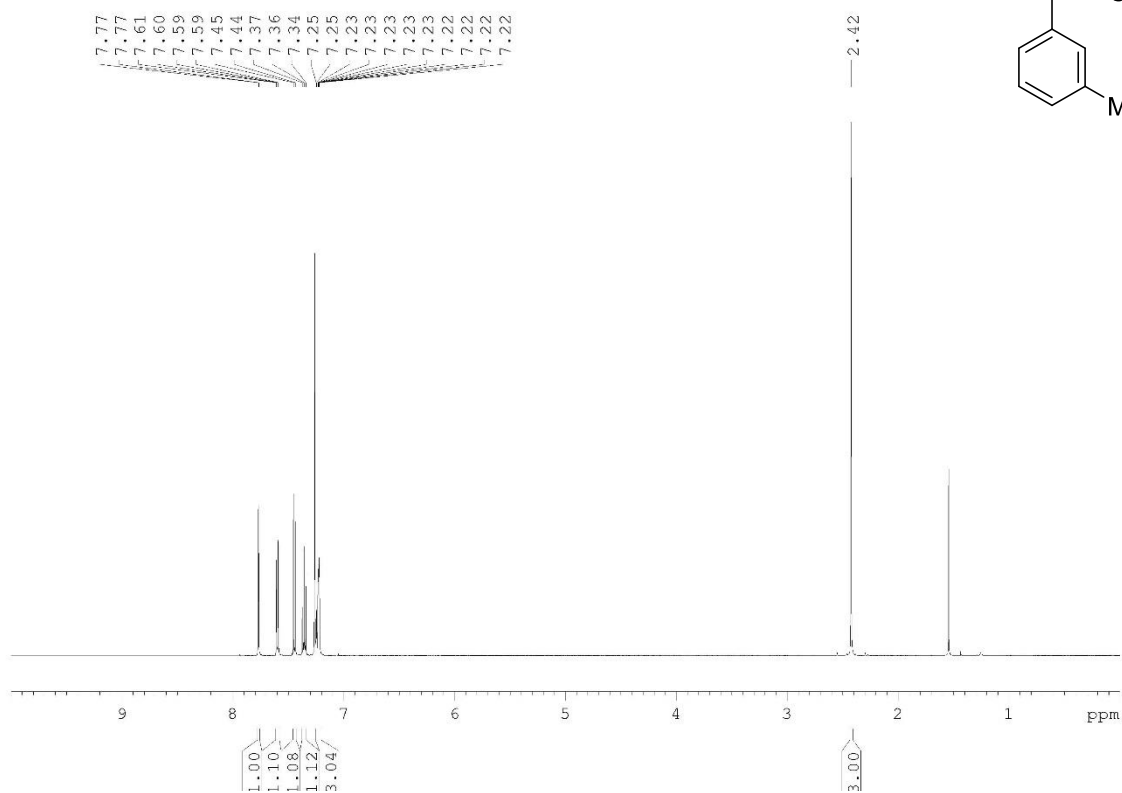
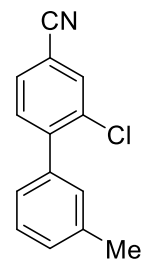
2'-Chloro-[1,1'-biphenyl]-3,4'-dicarbonitrile (44a)



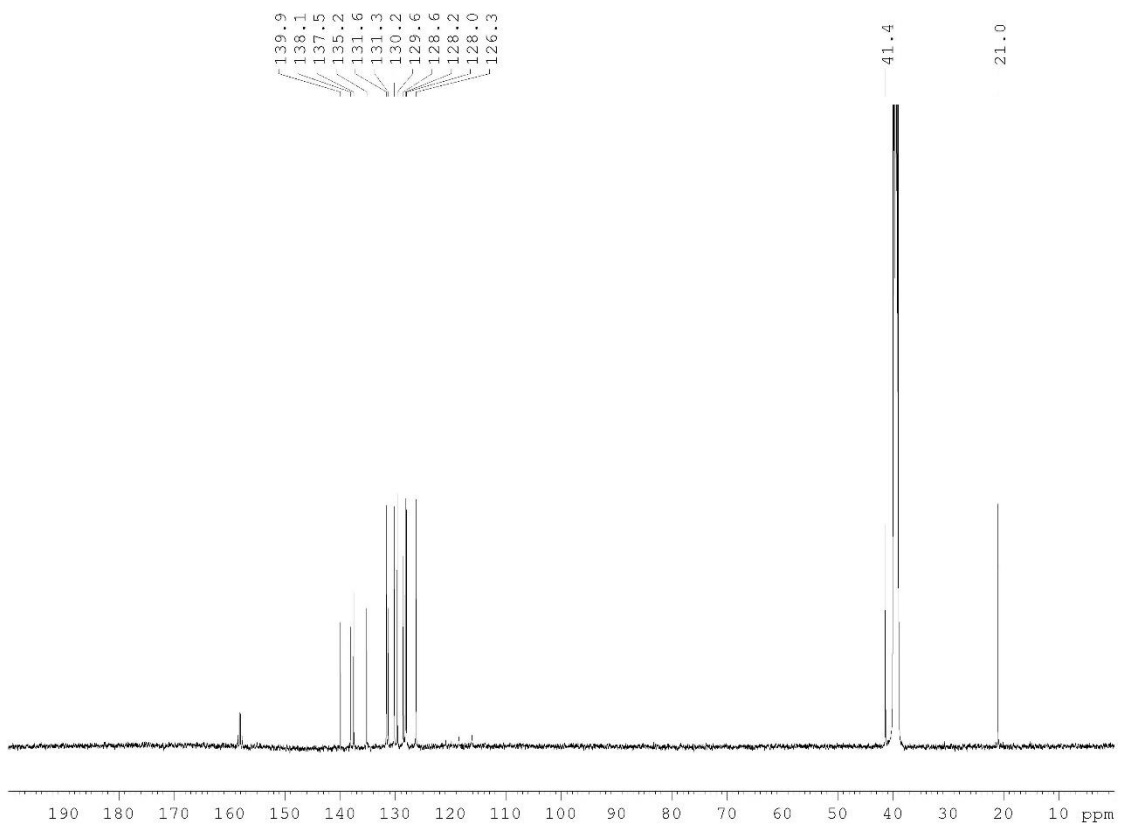
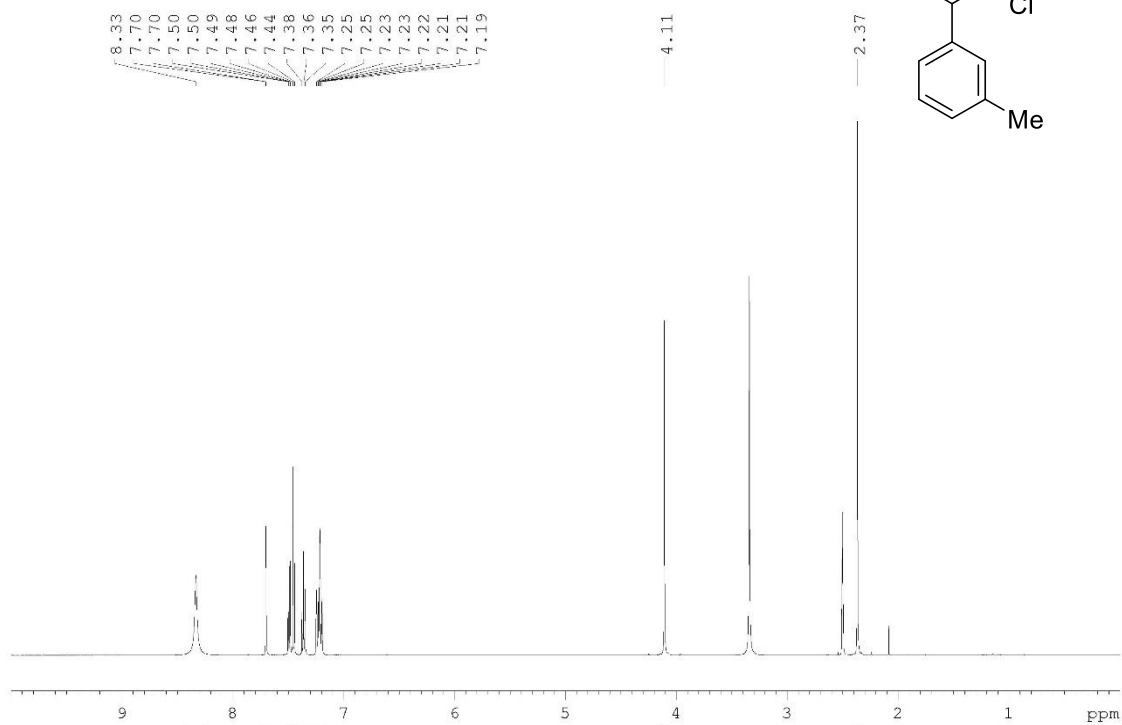
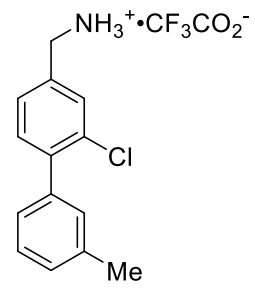
(2'-Chloro-[1,1'-biphenyl]-3,4'-diyl)dimethanamine TFA salt (44)



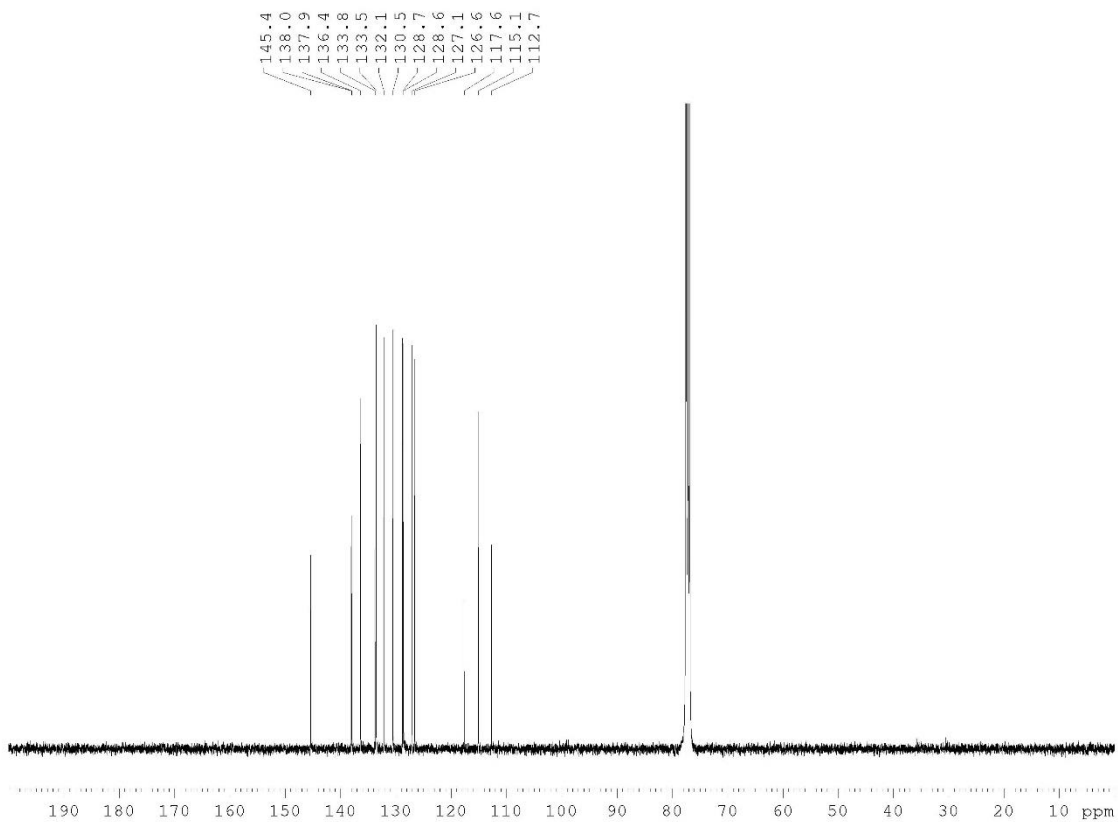
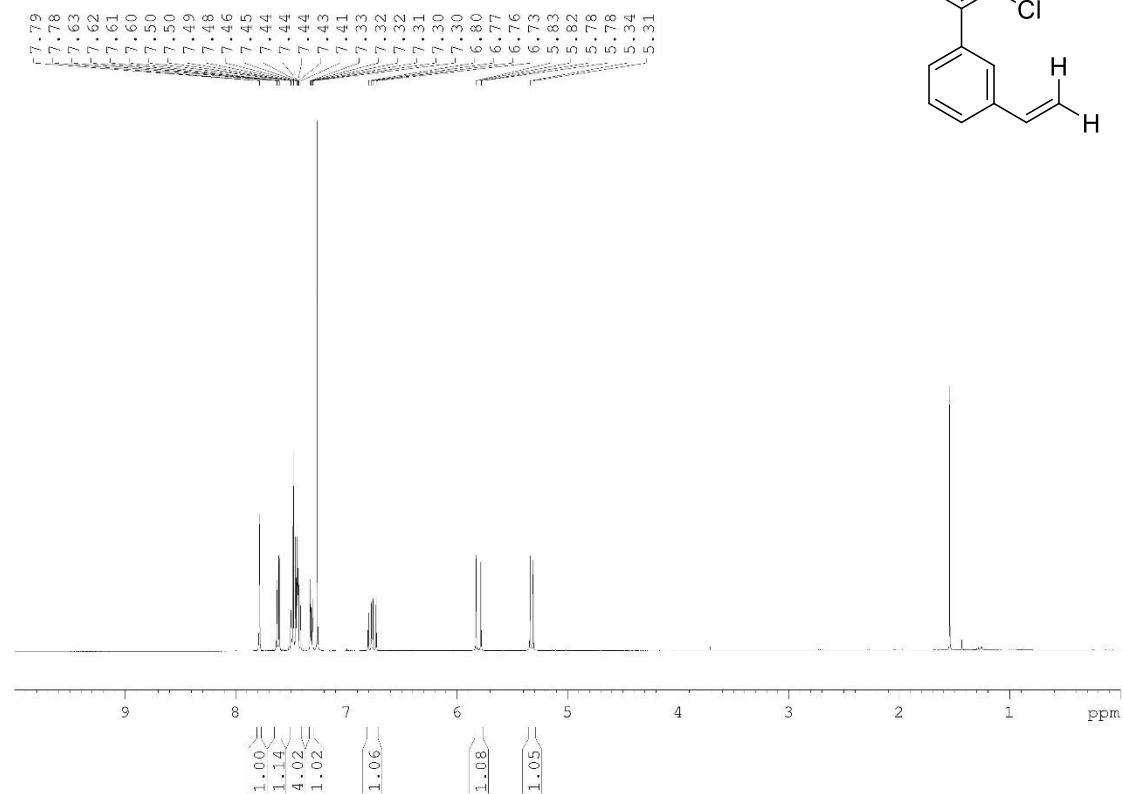
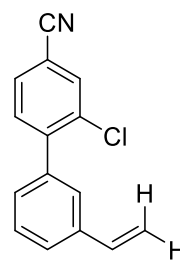
2-Chloro-3'-methyl-[1,1'-biphenyl]-4-carbonitrile (45a)



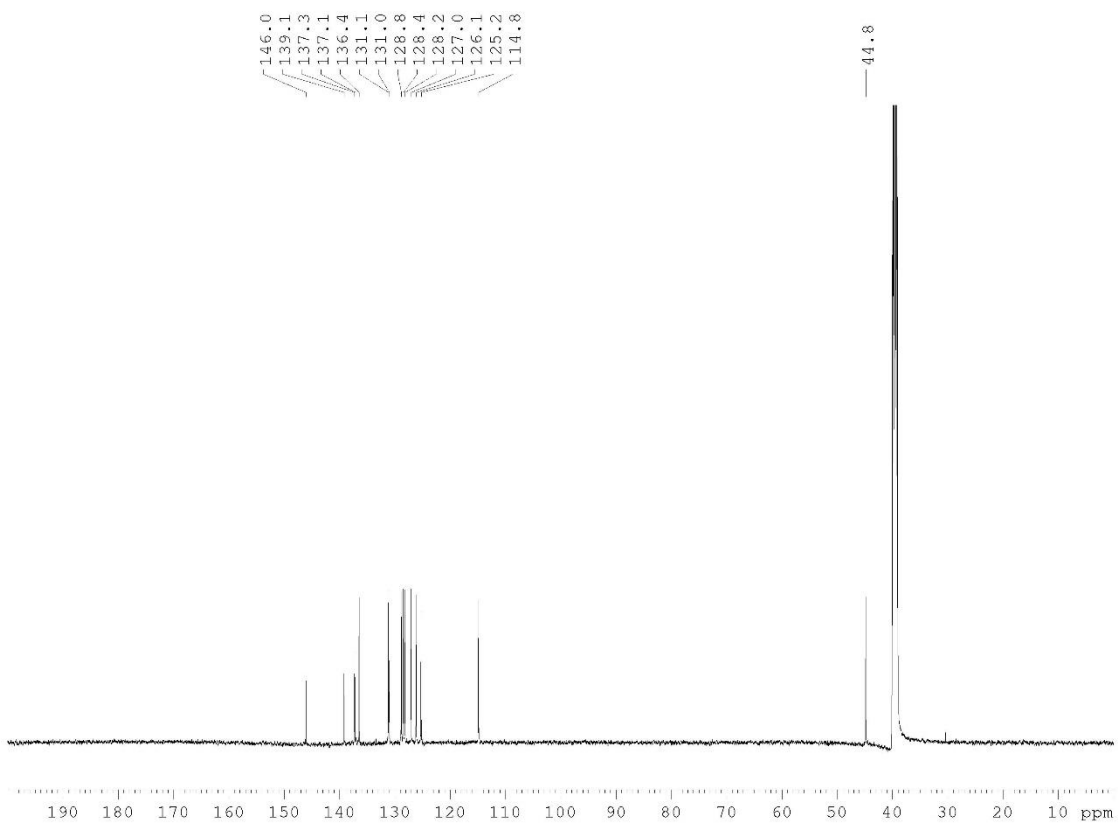
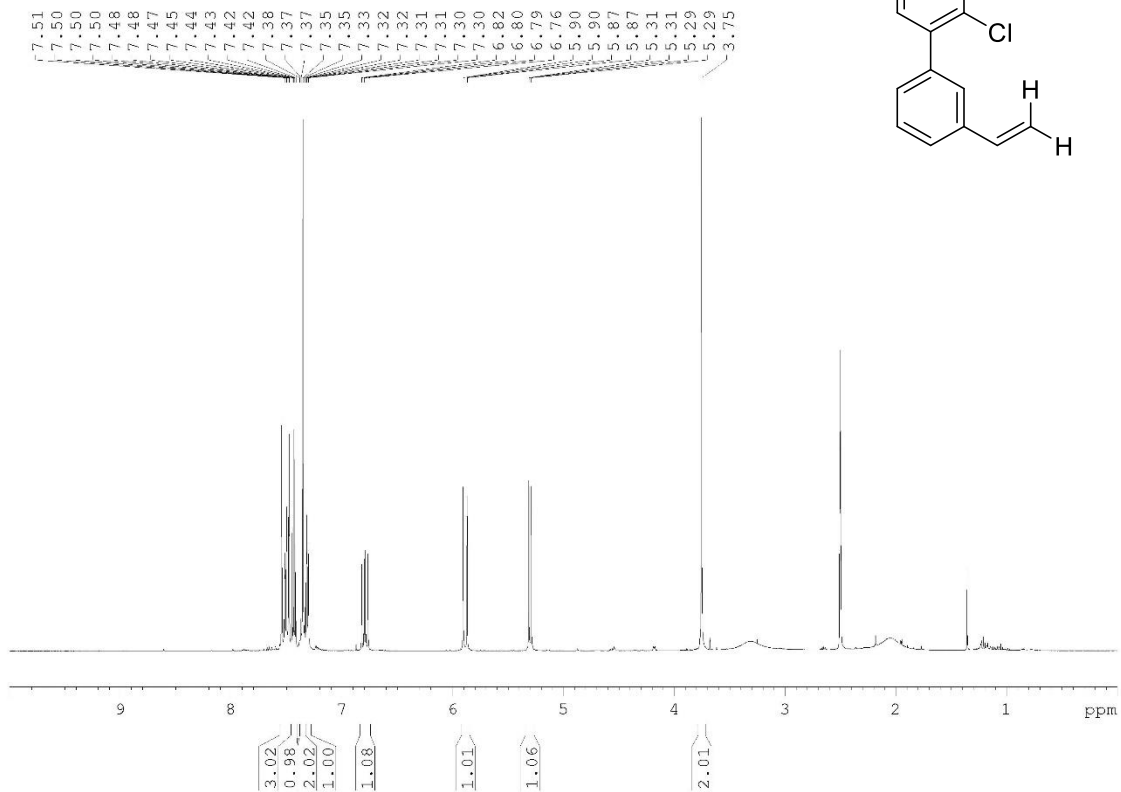
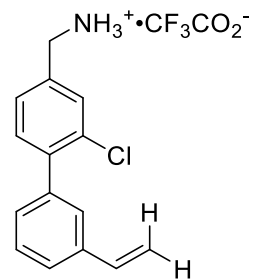
(2-Chloro-3'-methyl-[1,1'-biphenyl]-4-yl)methanamine TFA salt (45)



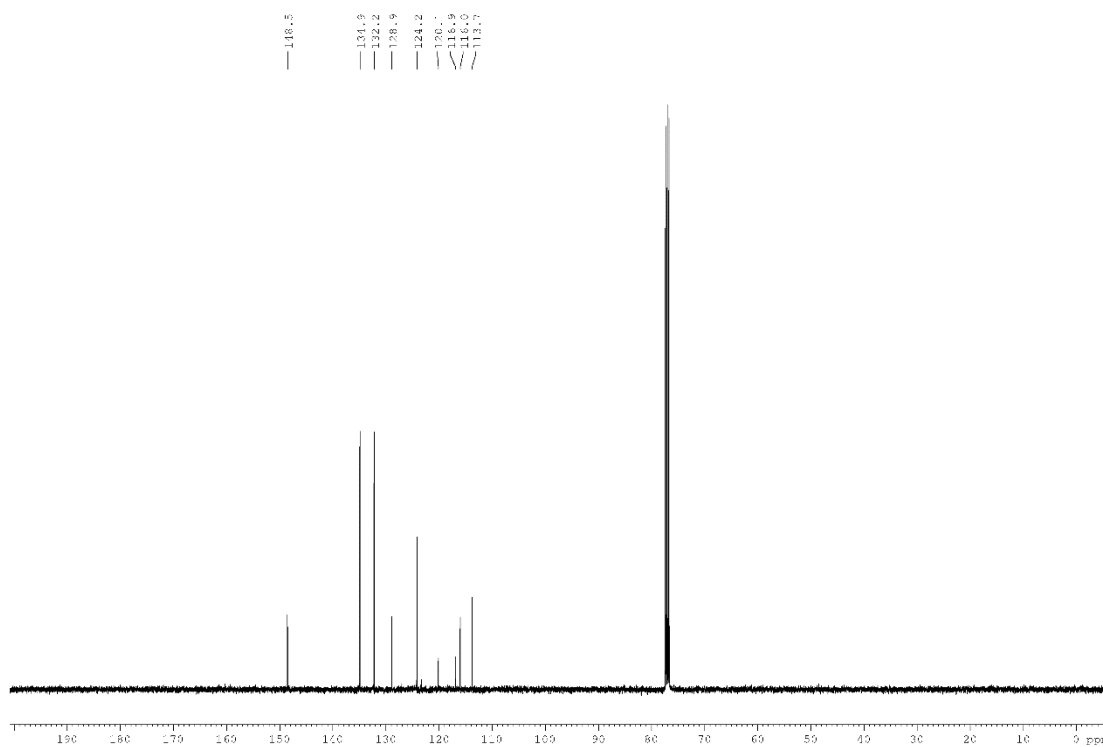
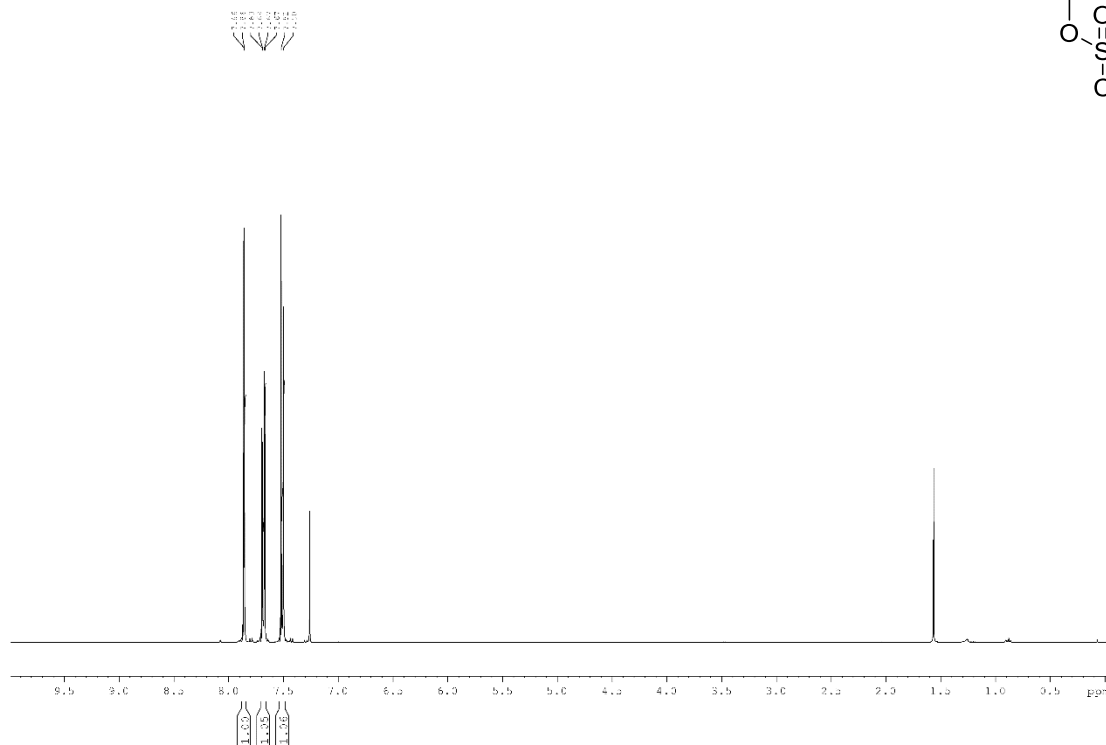
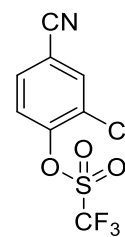
2-Chloro-3'-vinyl-[1,1'-biphenyl]-4-carbonitrile (46a)



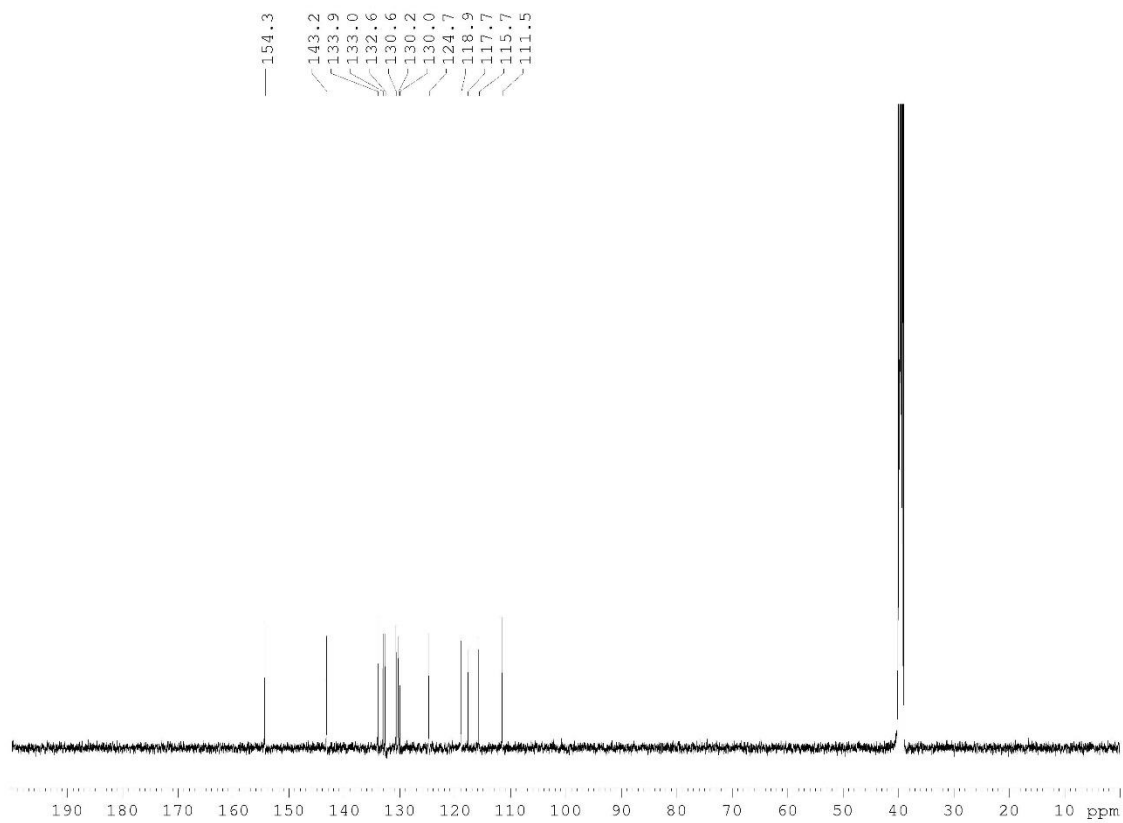
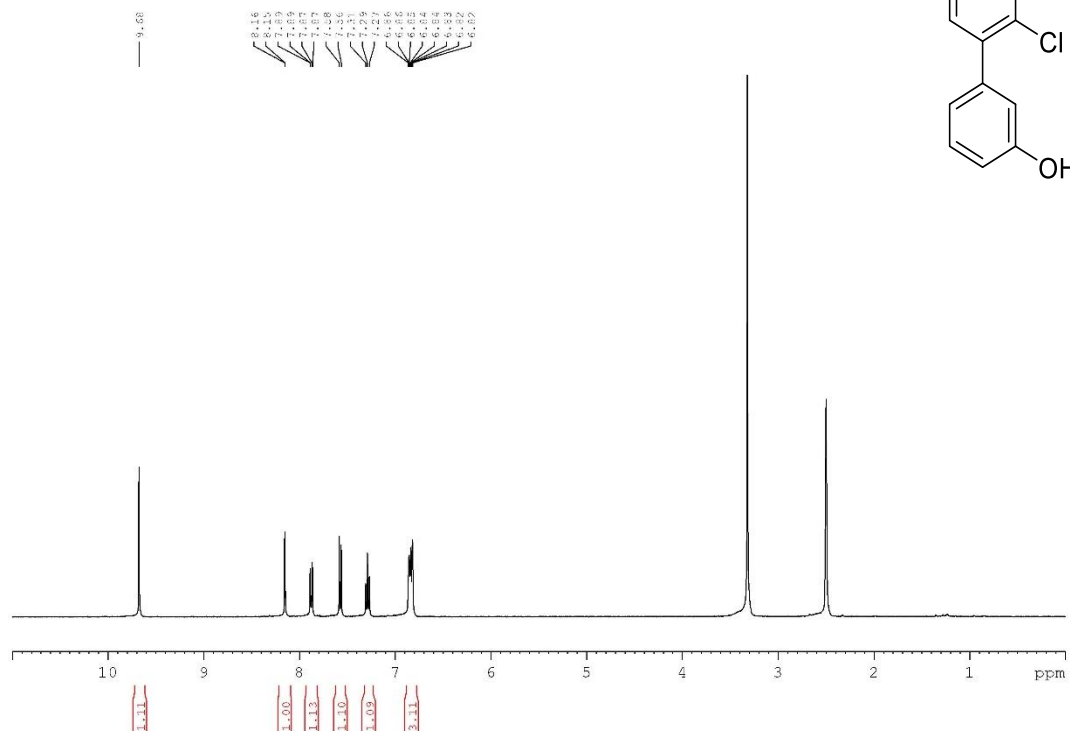
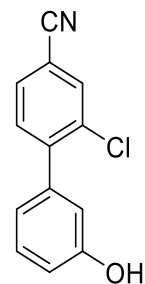
(2-Chloro-3'-vinyl-[1,1'-biphenyl]-4-yl)methanamine TFA salt (46)



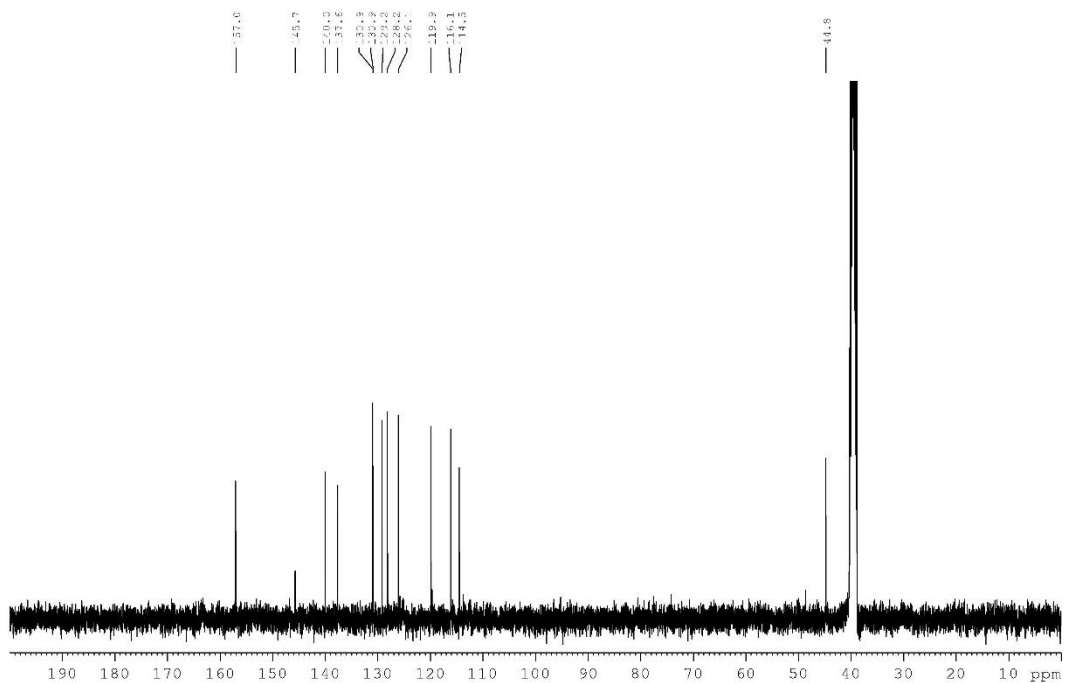
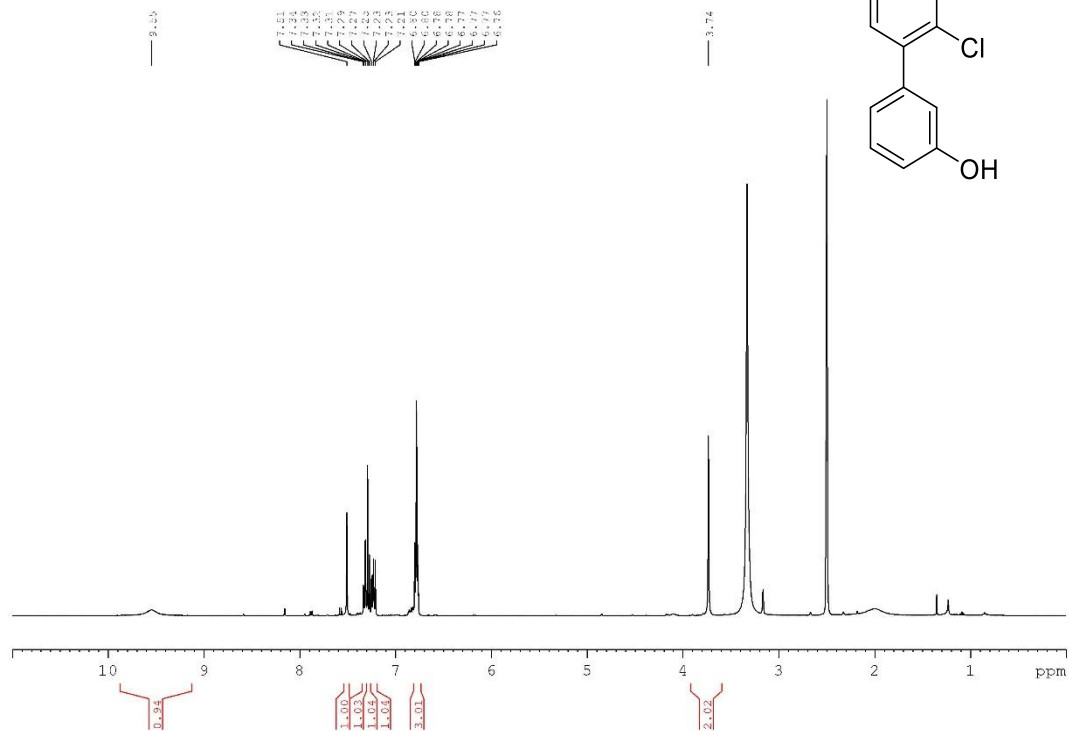
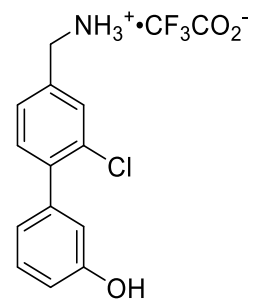
2-Chloro-4-cyanophenyl trifluoromethanesulfonate (48)



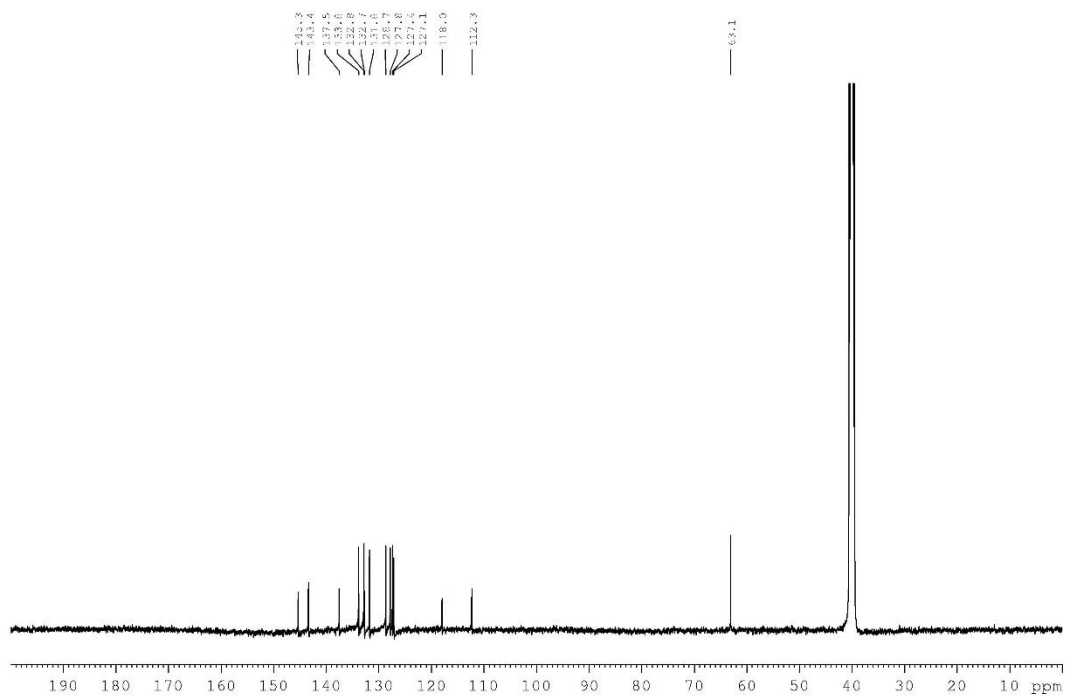
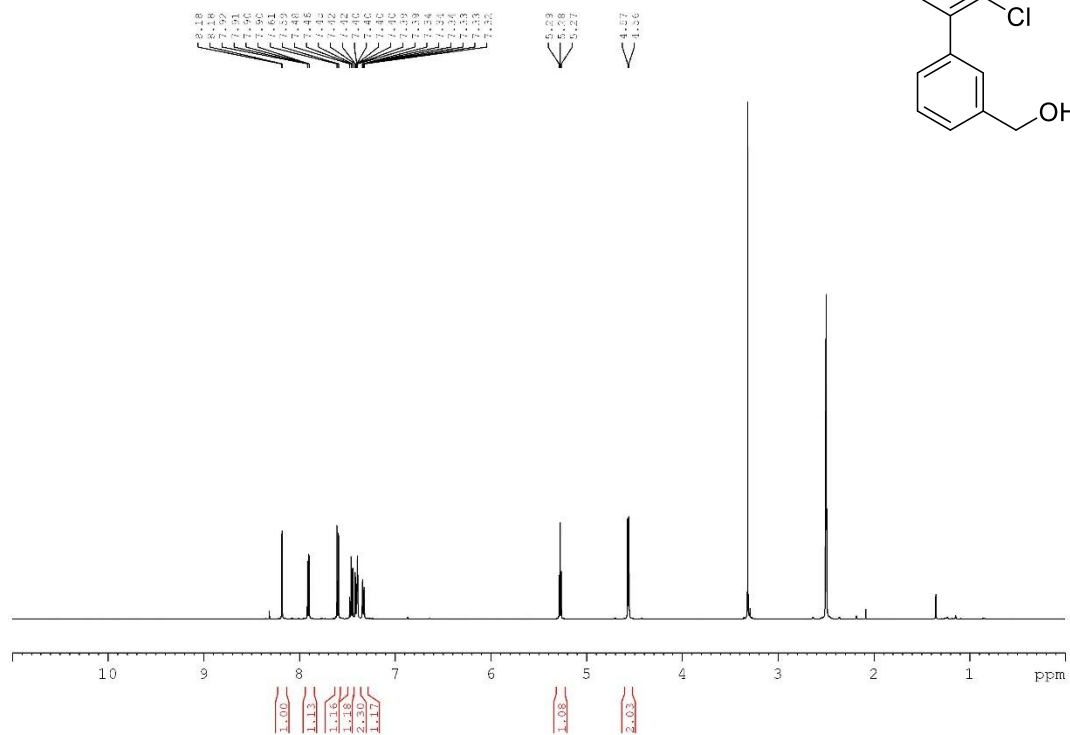
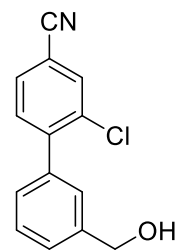
2-Chloro-3'-hydroxy-[1,1'-biphenyl]-4-carbonitrile (51a)



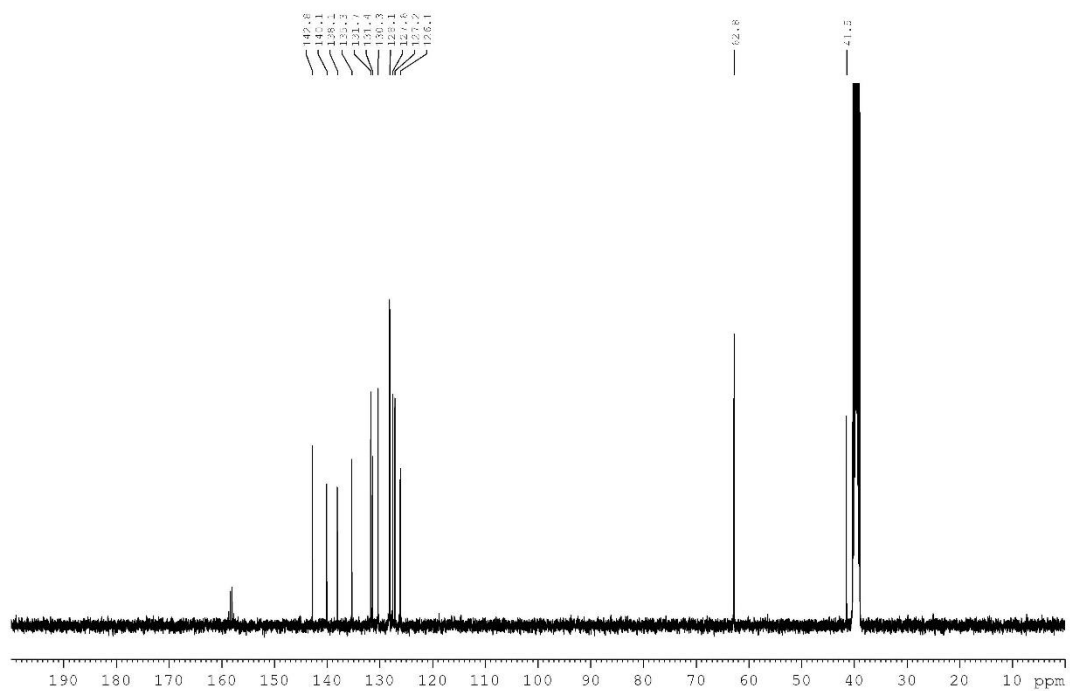
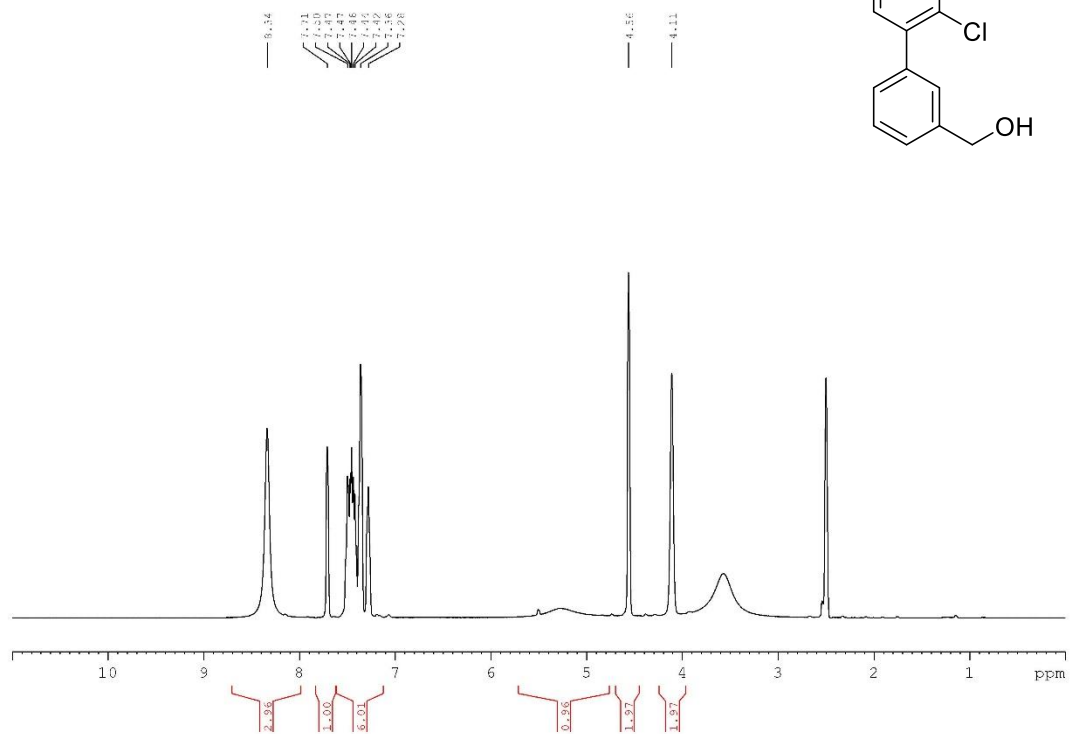
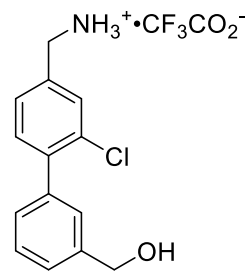
4'-(Aminomethyl)-2'-chloro-[1,1'-biphenyl]-3-ol TFA salt (51)



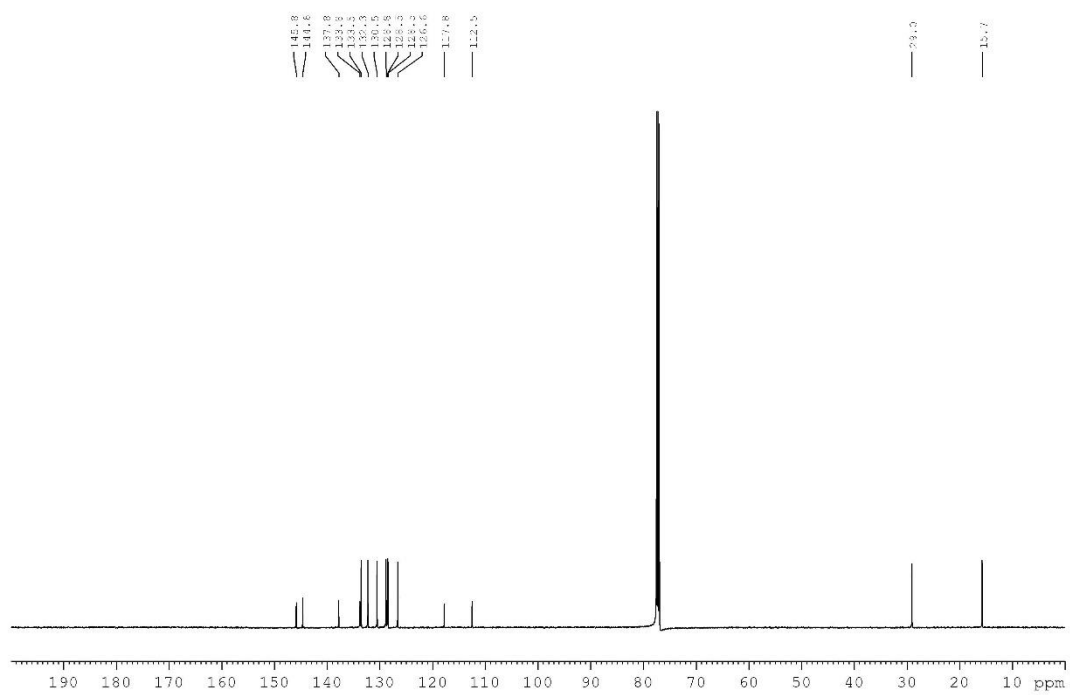
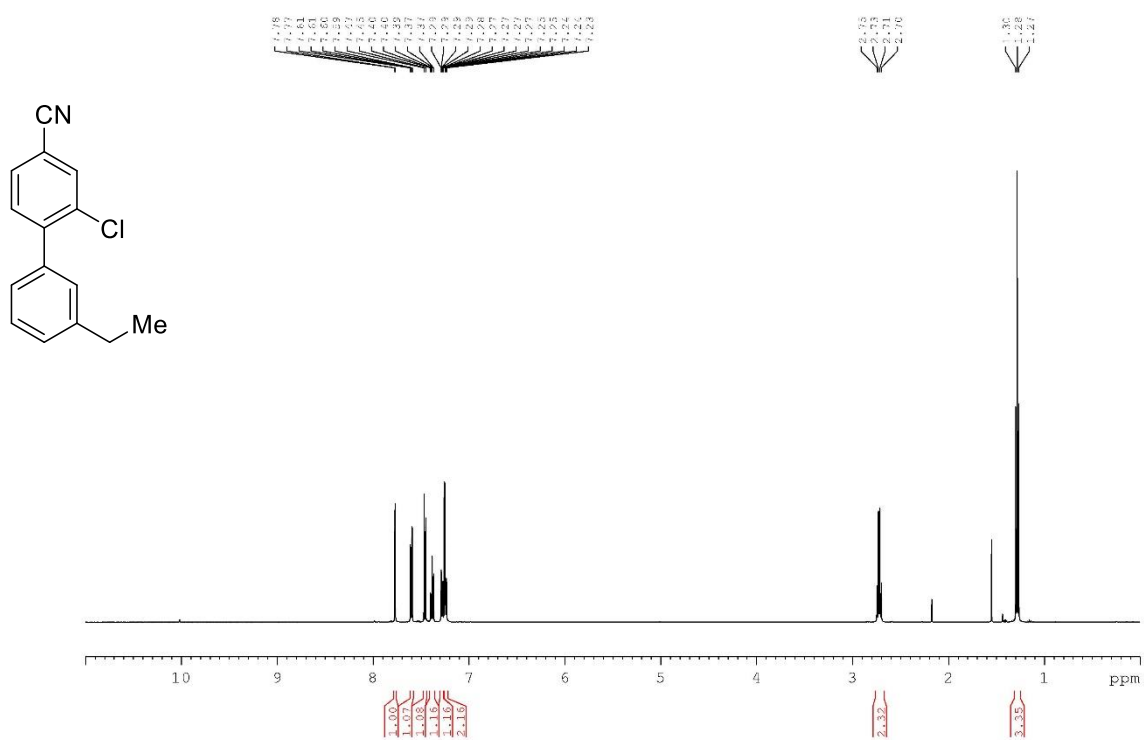
2-Chloro-3'-(hydroxymethyl)-[1,1'-biphenyl]-4-carbonitrile (54a)



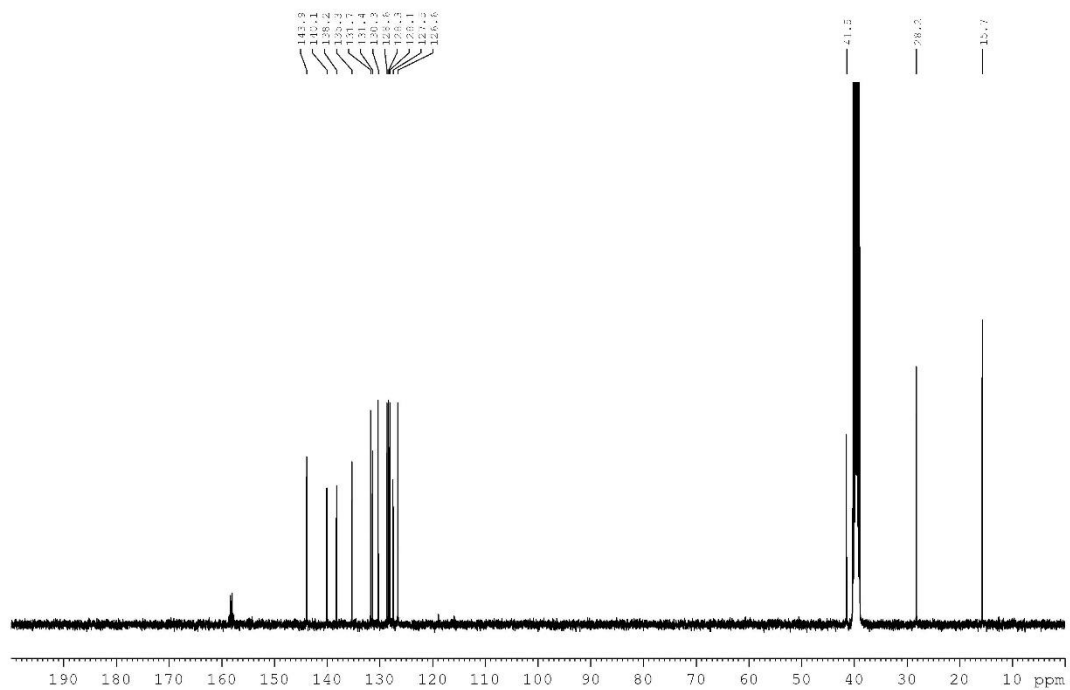
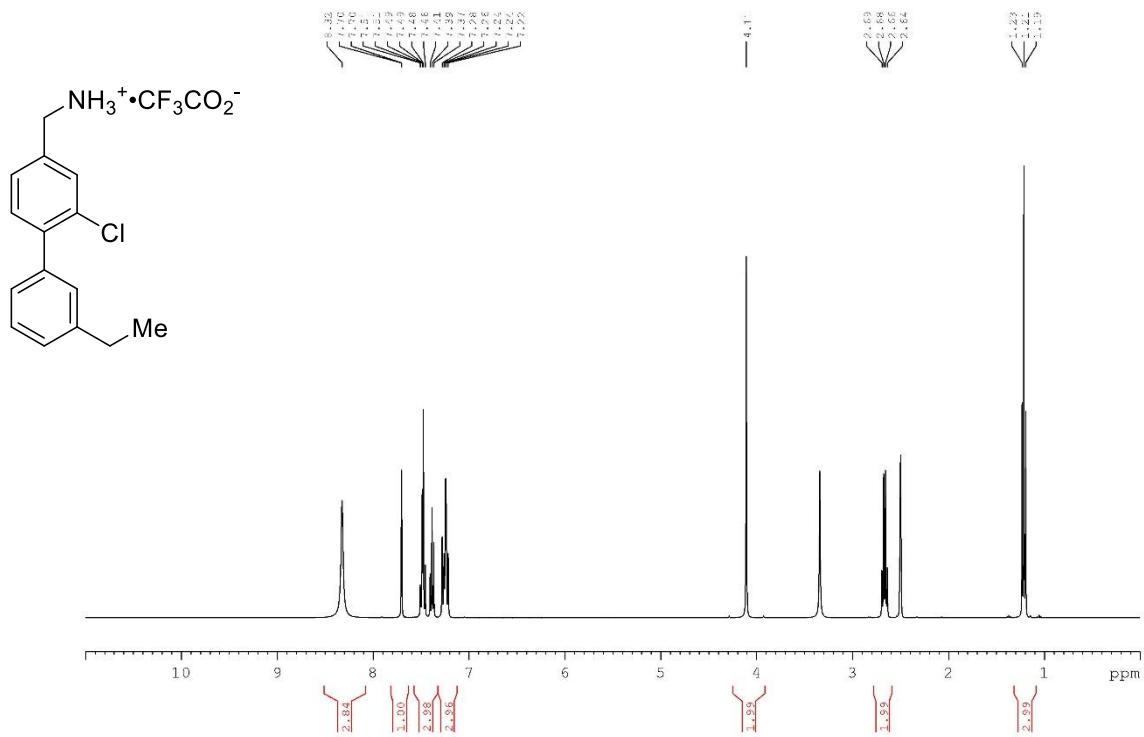
(4'-(Aminomethyl)-2'-chloro-[1,1'-biphenyl]-3-yl)methanol TFA salt (54)



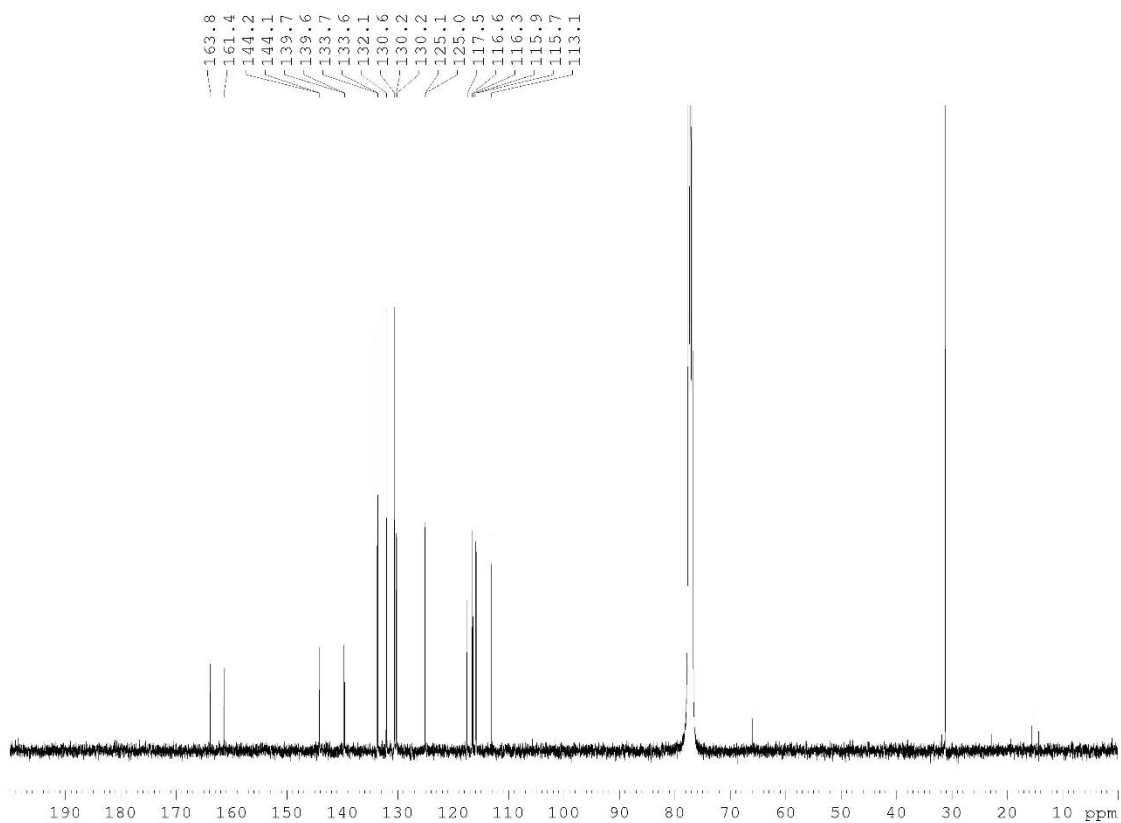
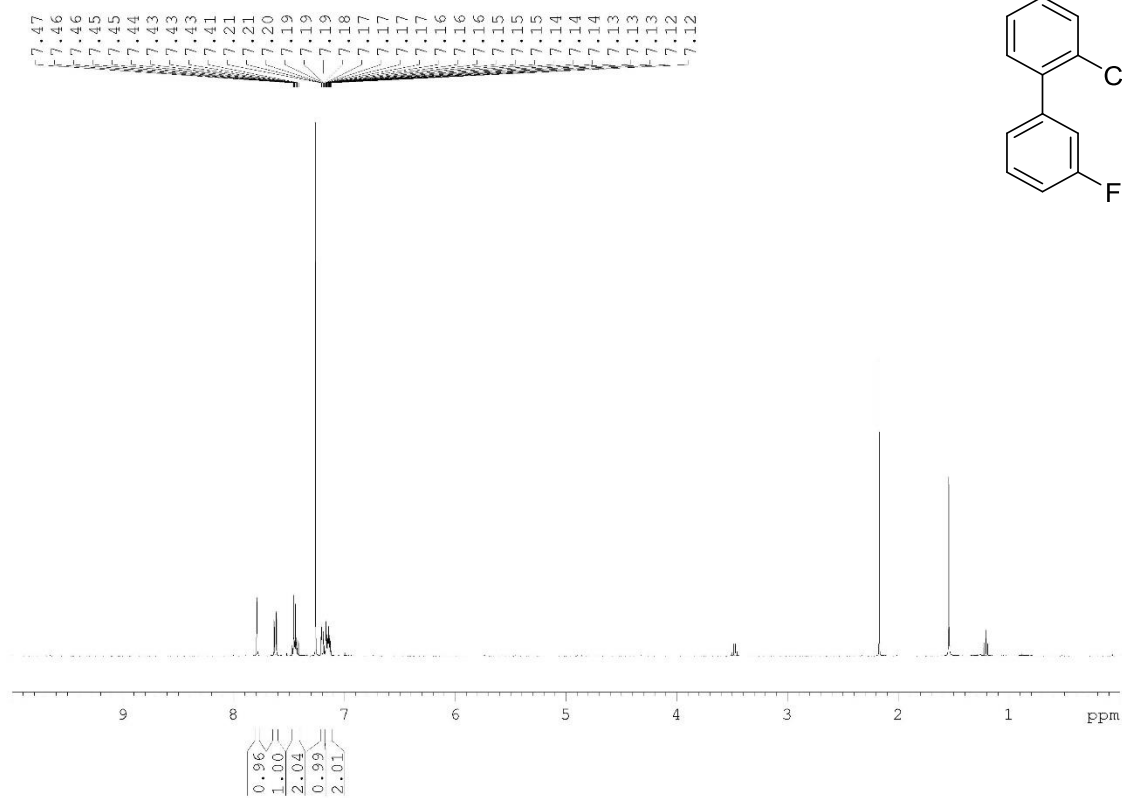
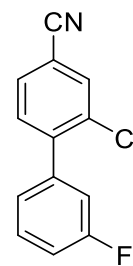
2-Chloro-3'-ethyl-[1,1'-biphenyl]-4-carbonitrile (55a)



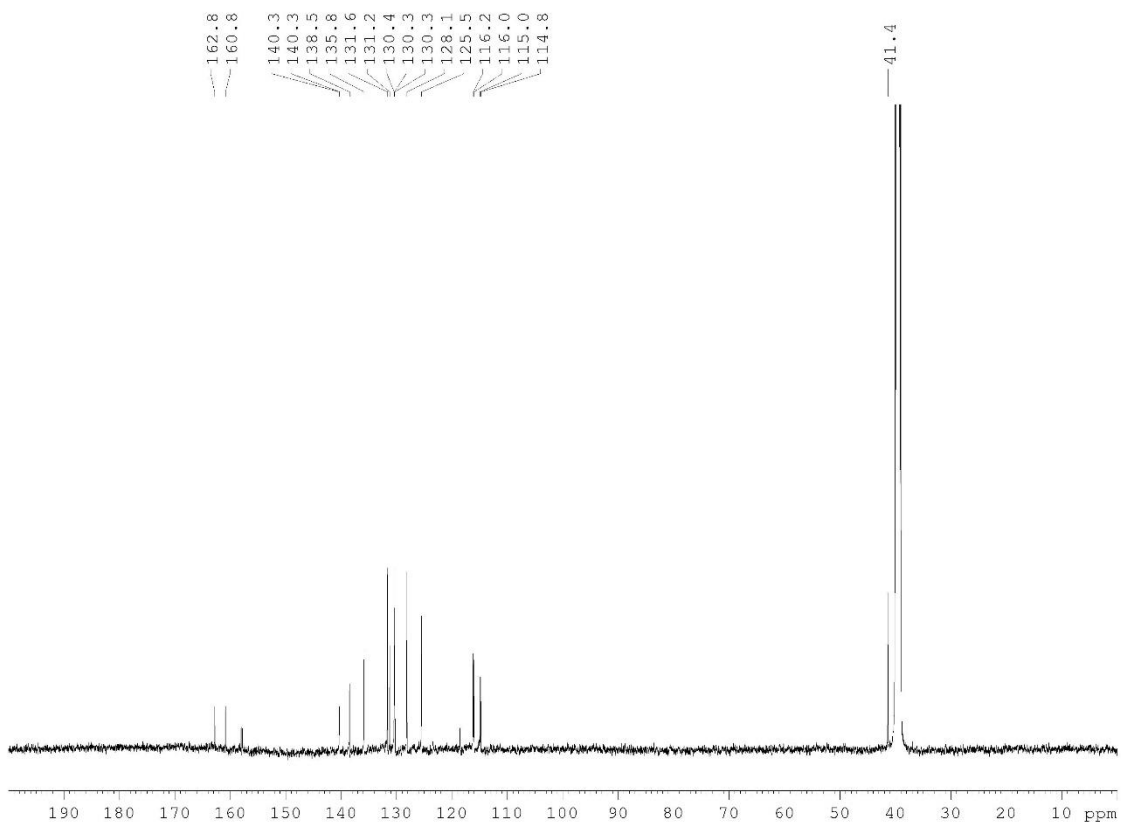
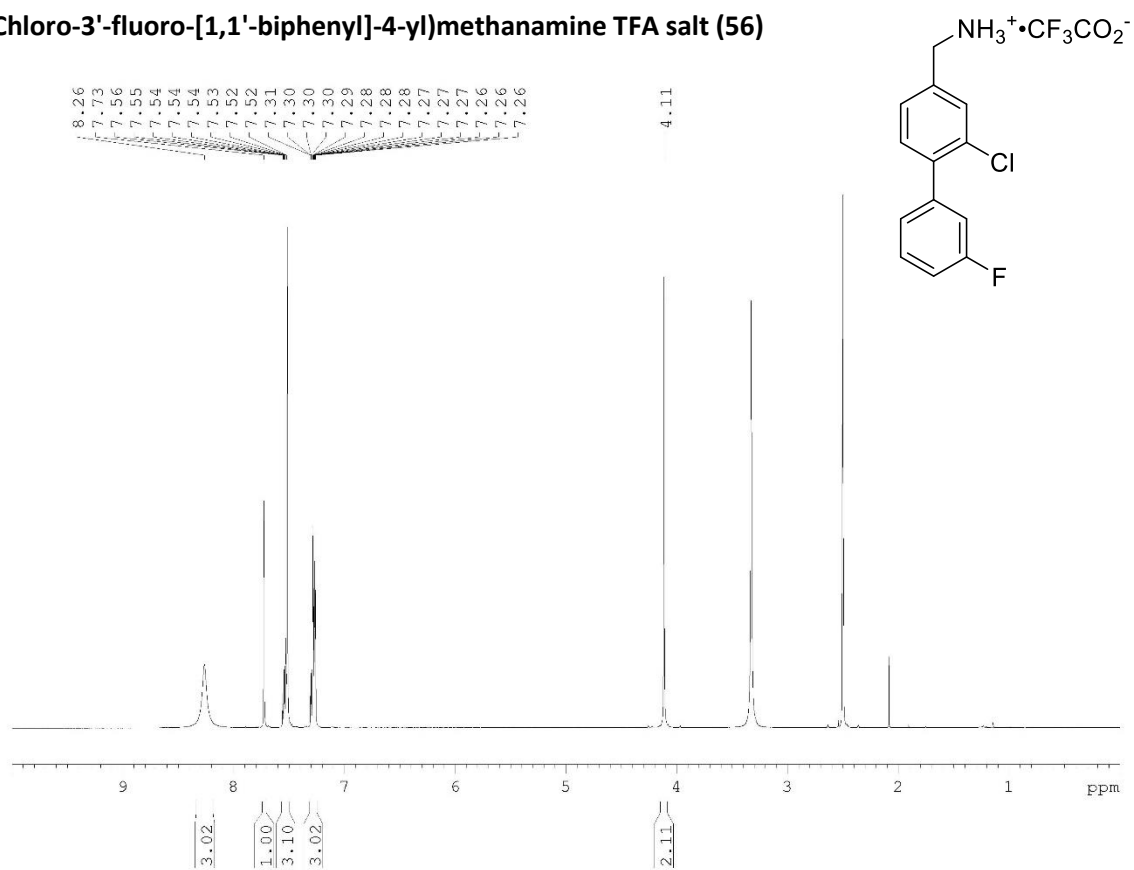
(2-Chloro-3'-ethyl-[1,1'-biphenyl]-4-yl)methanamine TFA salt (55)



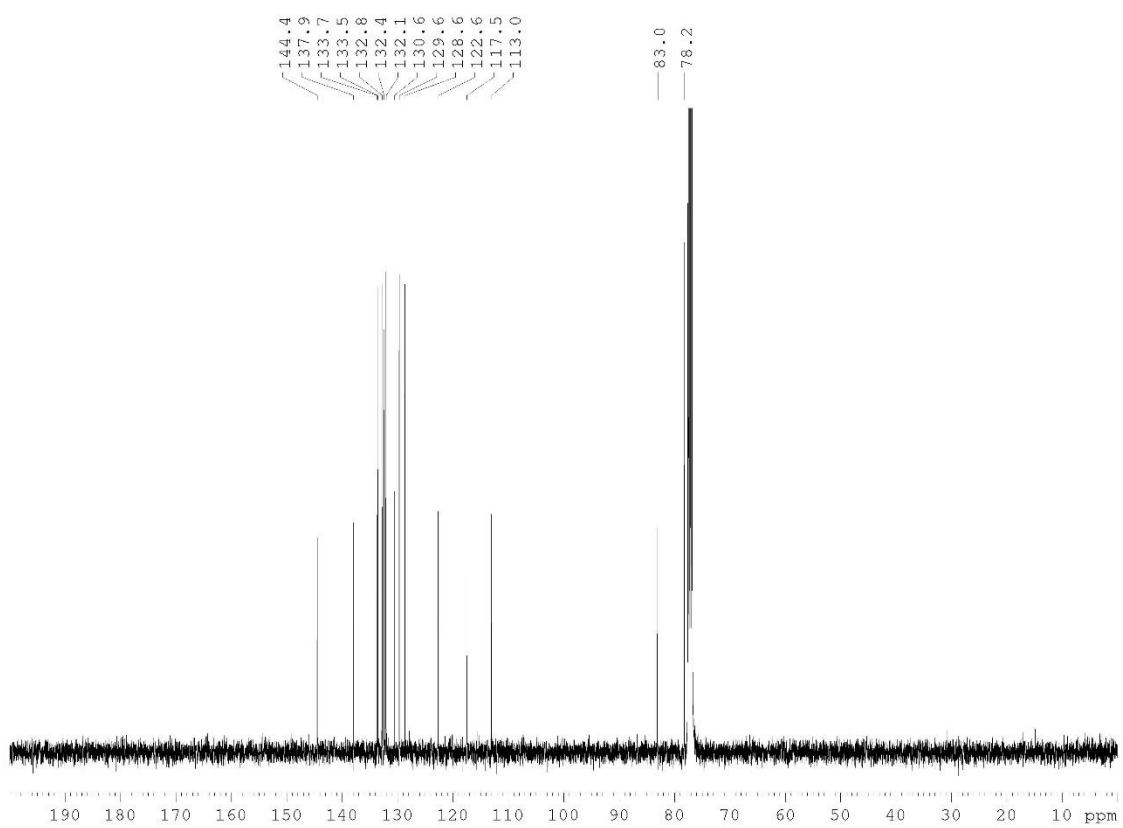
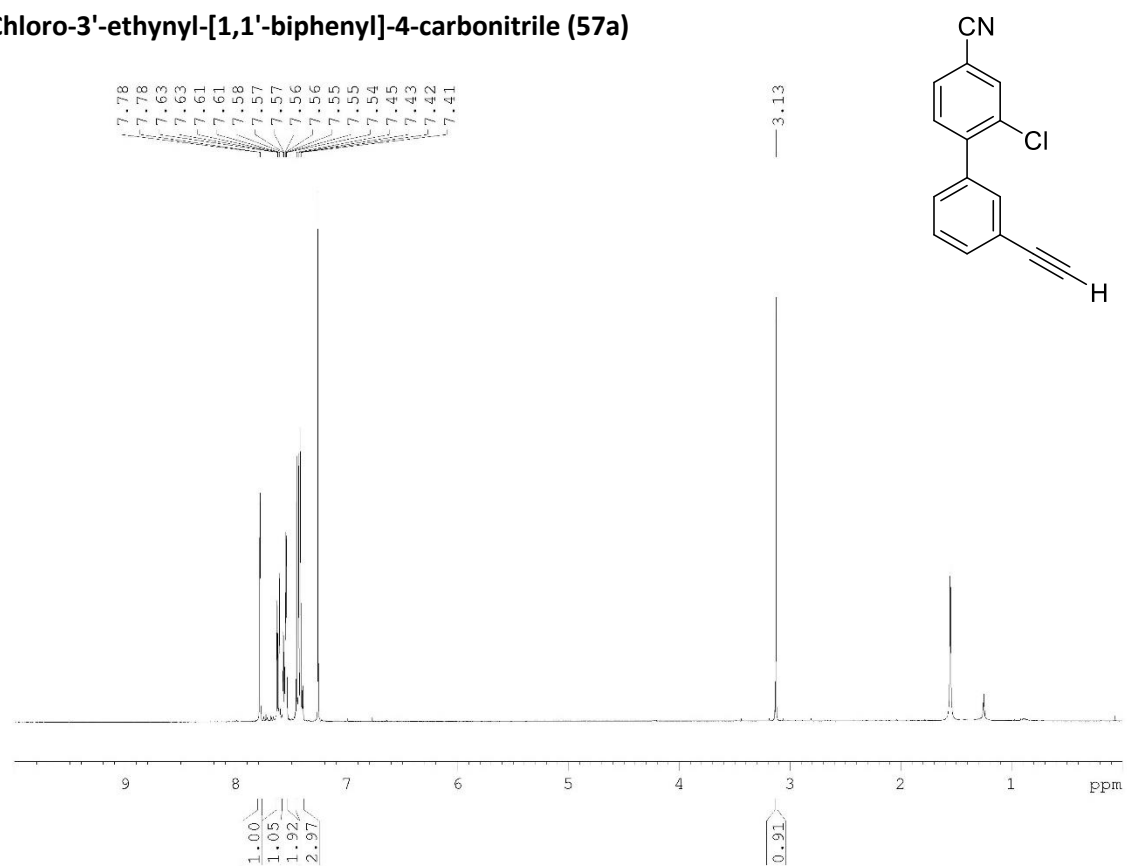
2-Chloro-3'-fluoro-[1,1'-biphenyl]-4-carbonitrile (56a)



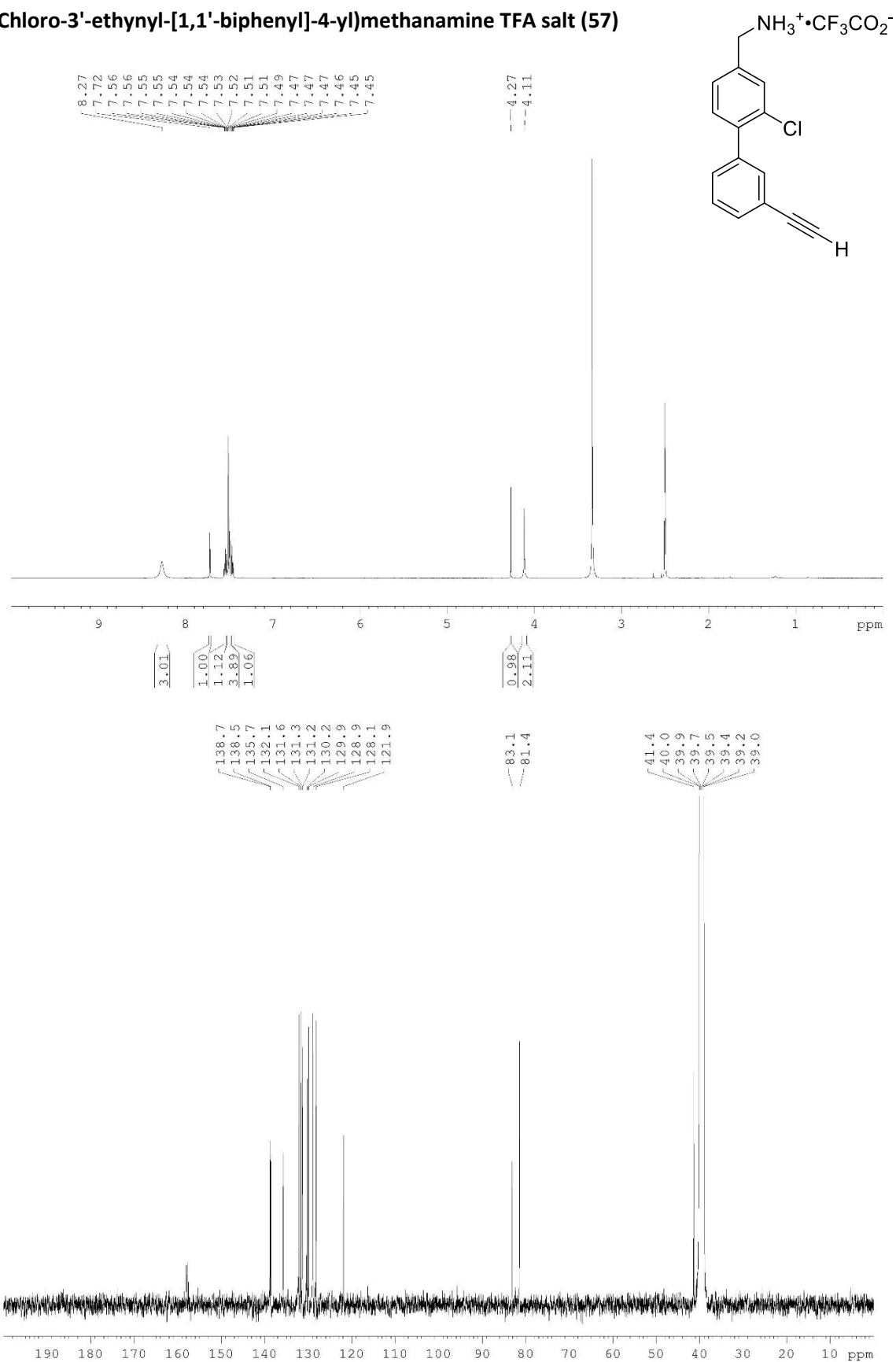
(2-Chloro-3'-fluoro-[1,1'-biphenyl]-4-yl)methanamine TFA salt (56)



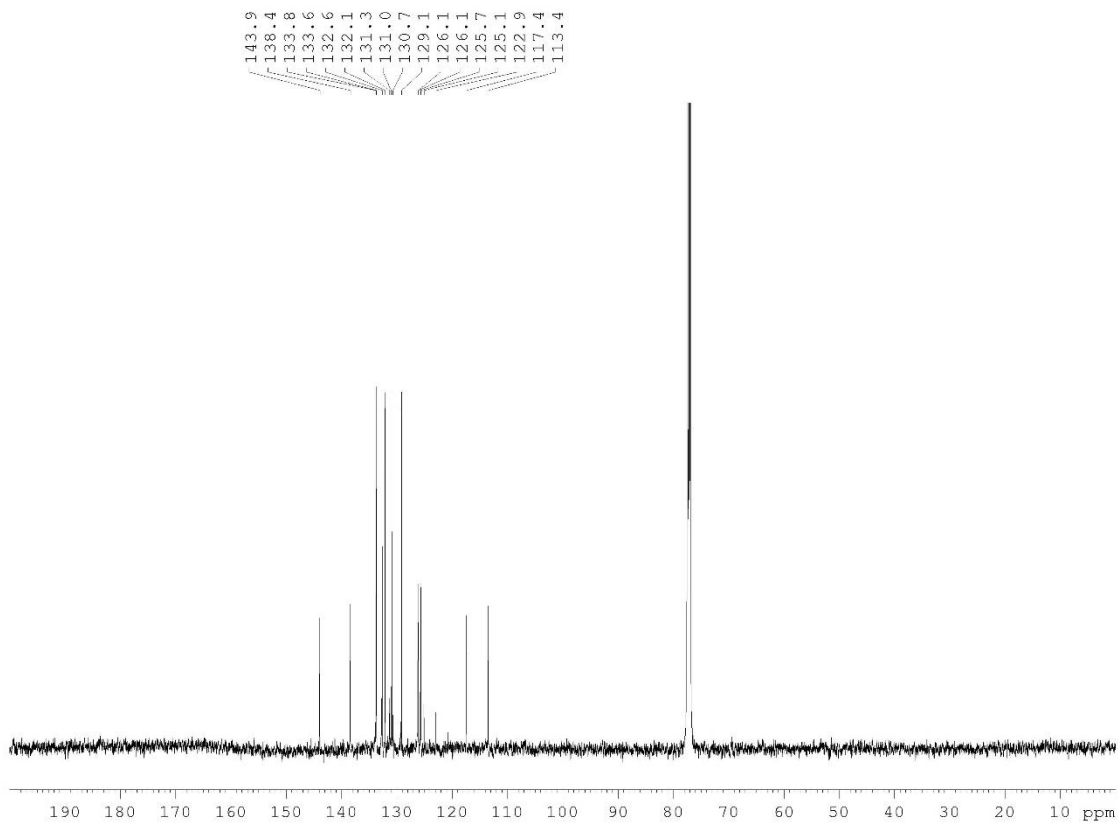
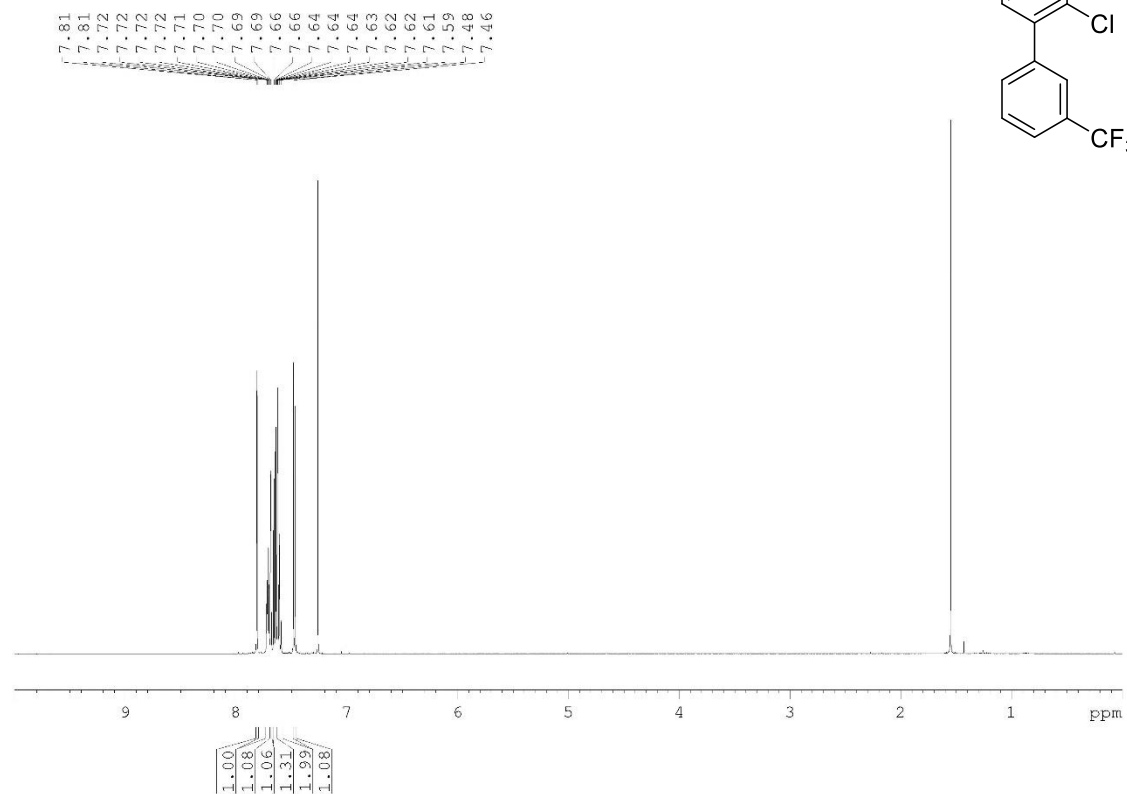
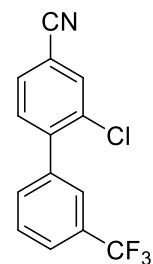
2-Chloro-3'-ethynyl-[1,1'-biphenyl]-4-carbonitrile (57a)



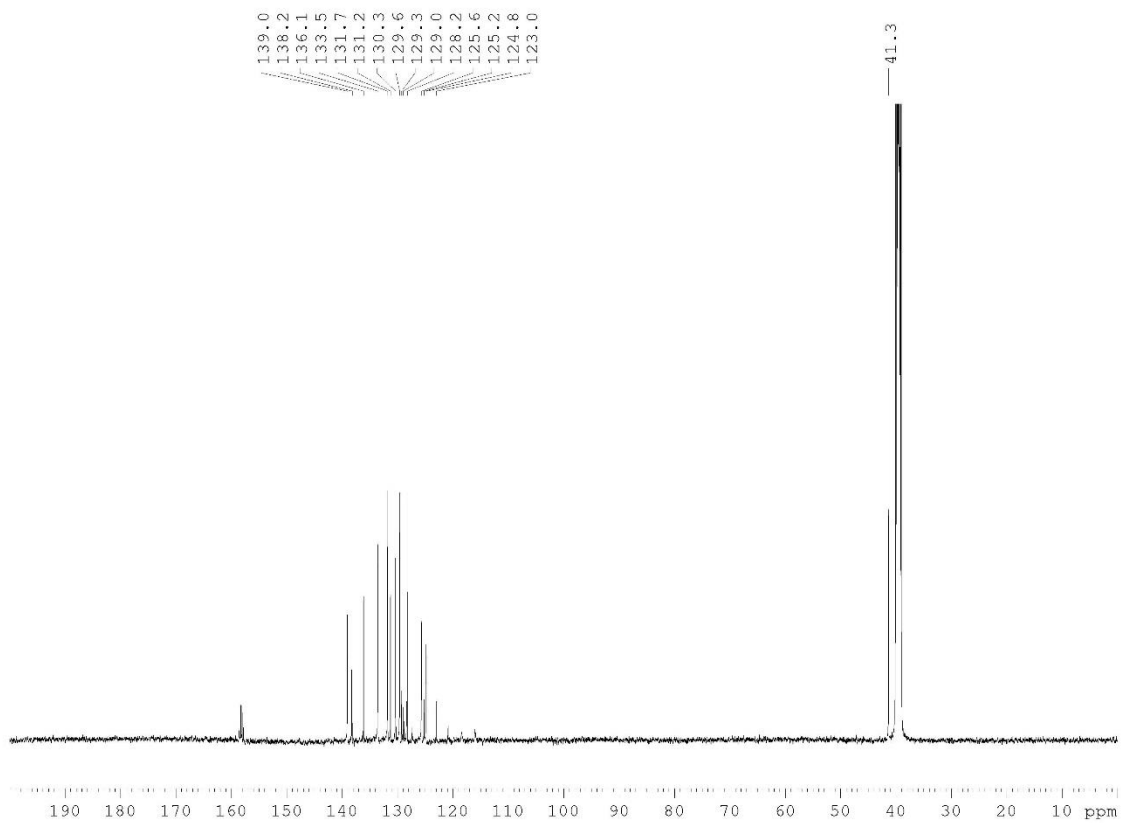
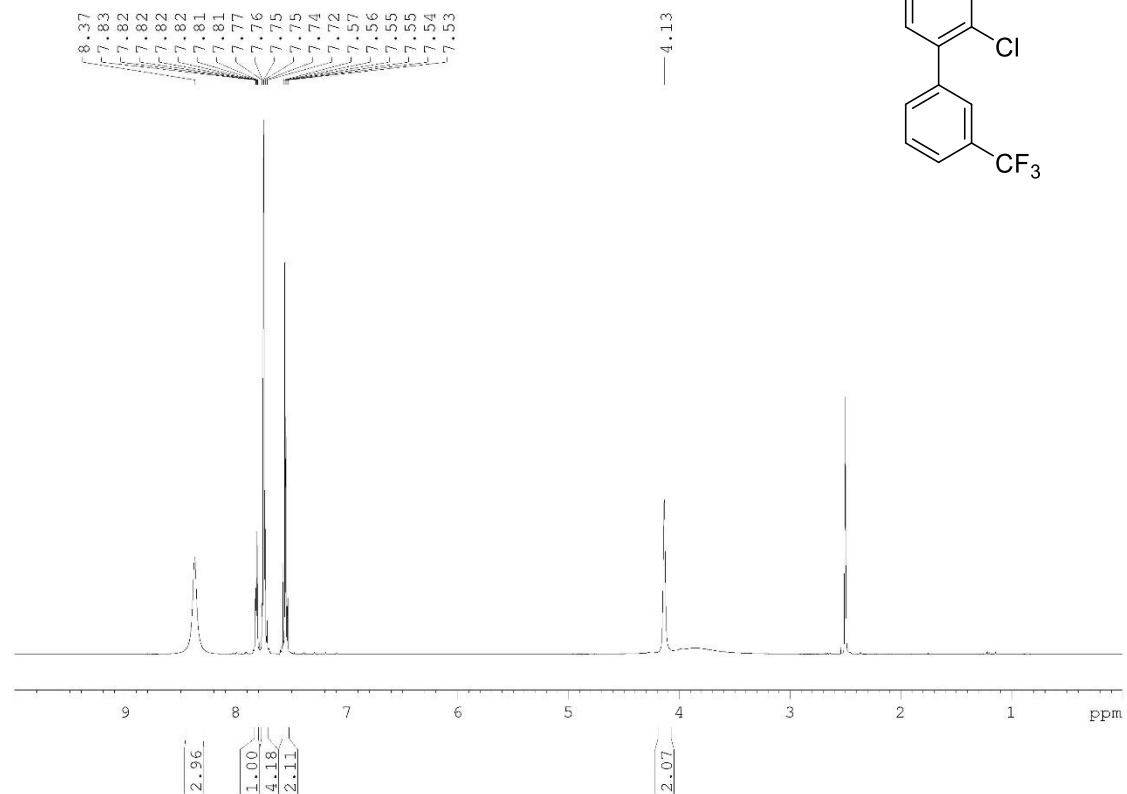
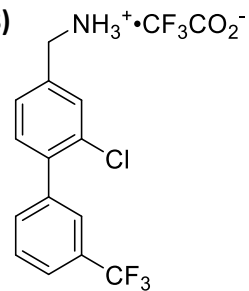
(2-Chloro-3'-ethynyl-[1,1'-biphenyl]-4-yl)methanamine TFA salt (57)



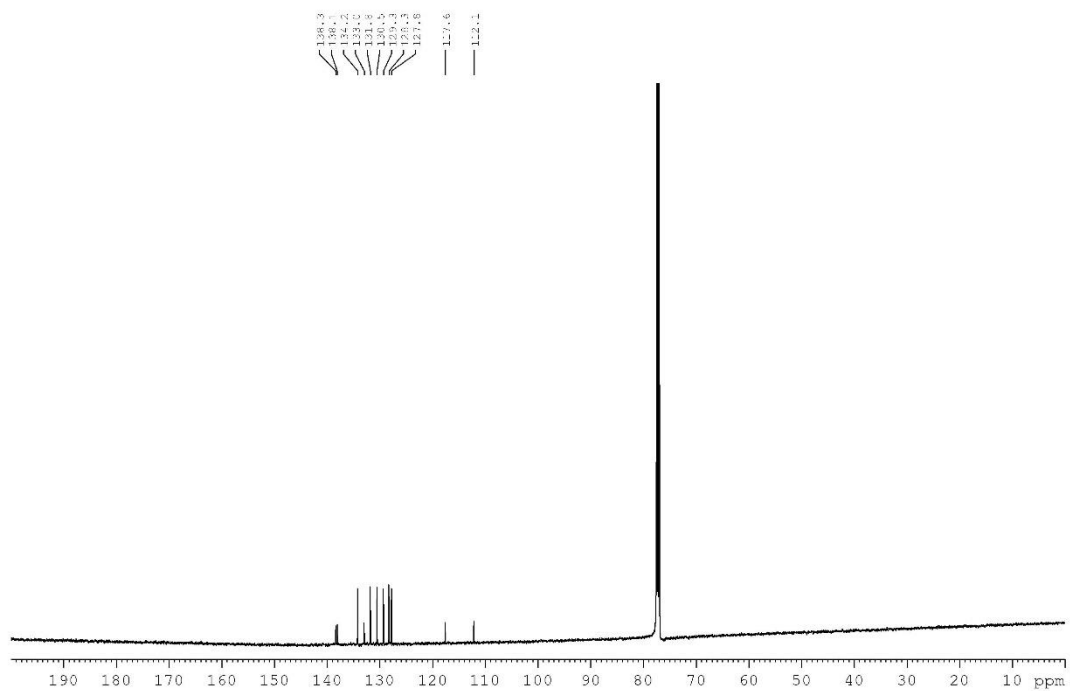
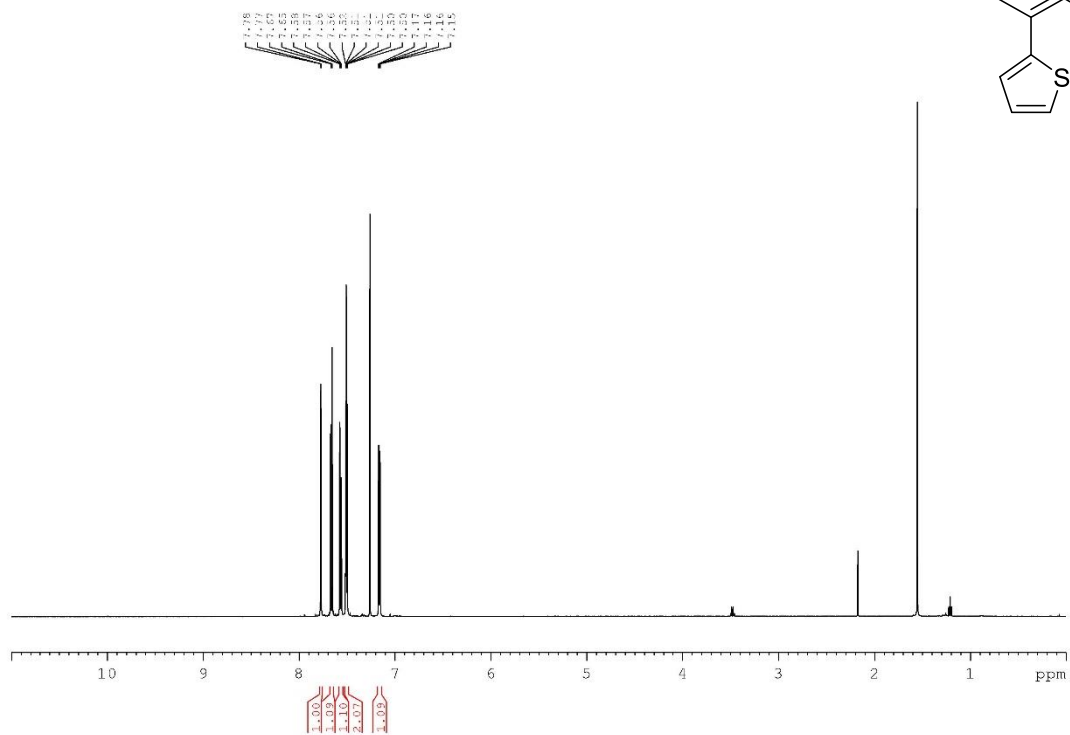
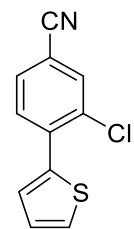
2-Chloro-3'-(trifluoromethyl)-[1,1'-biphenyl]-4-carbonitrile (58a)



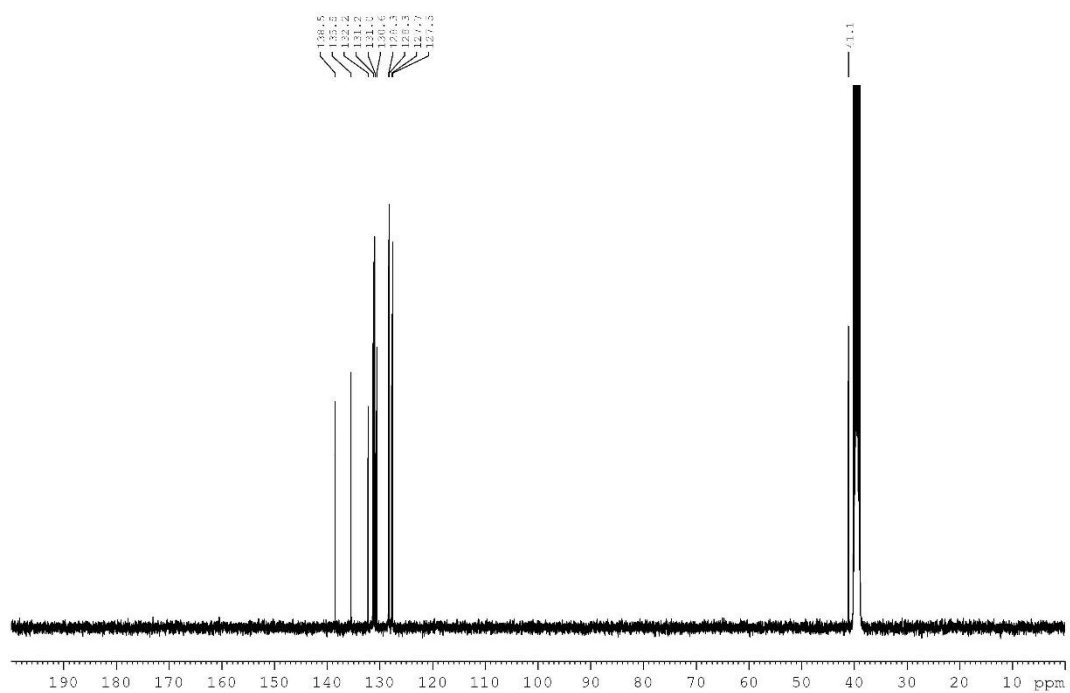
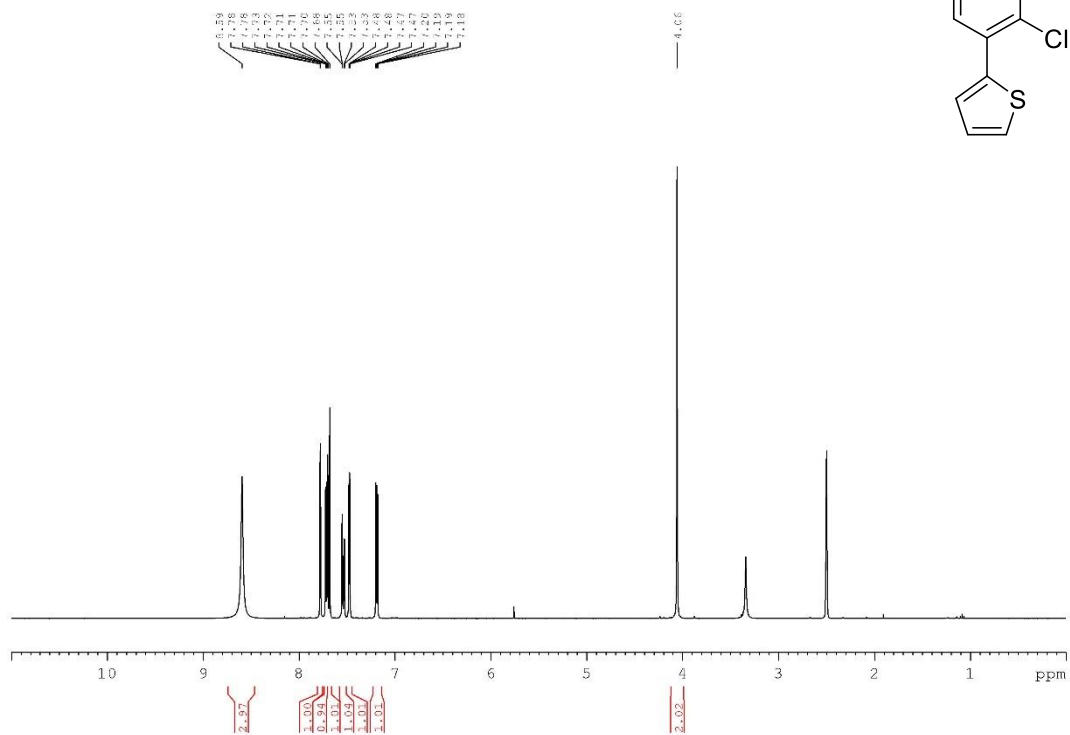
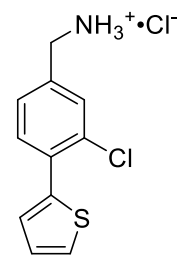
(2-Chloro-3'-(trifluoromethyl)-[1,1'-biphenyl]-4-yl)methanamine TFA salt (58)



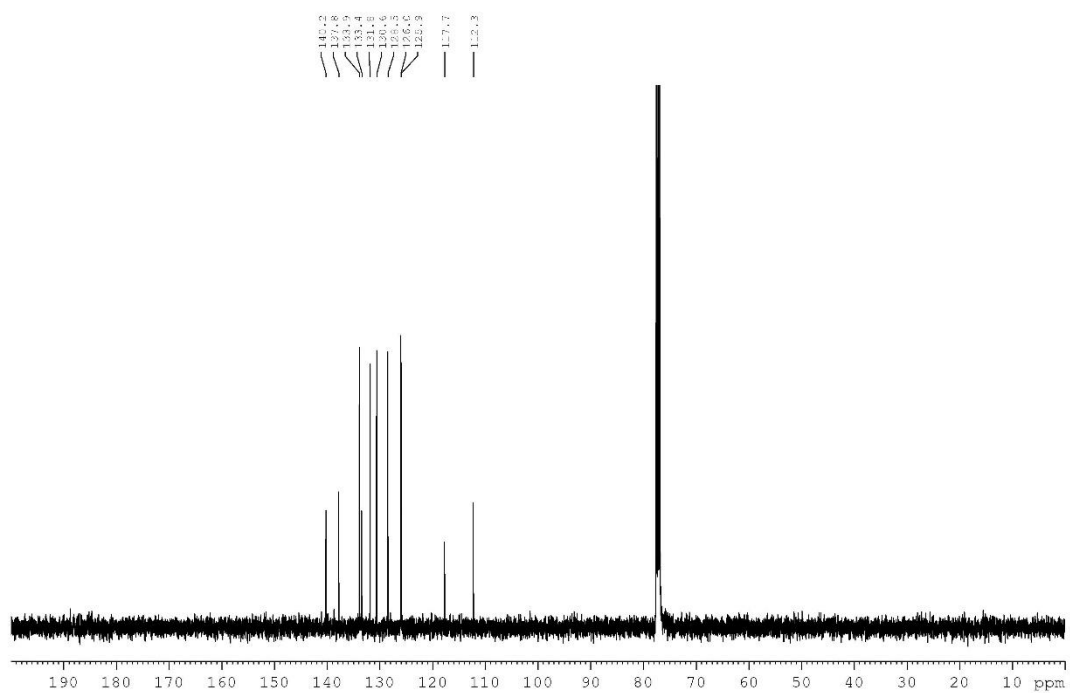
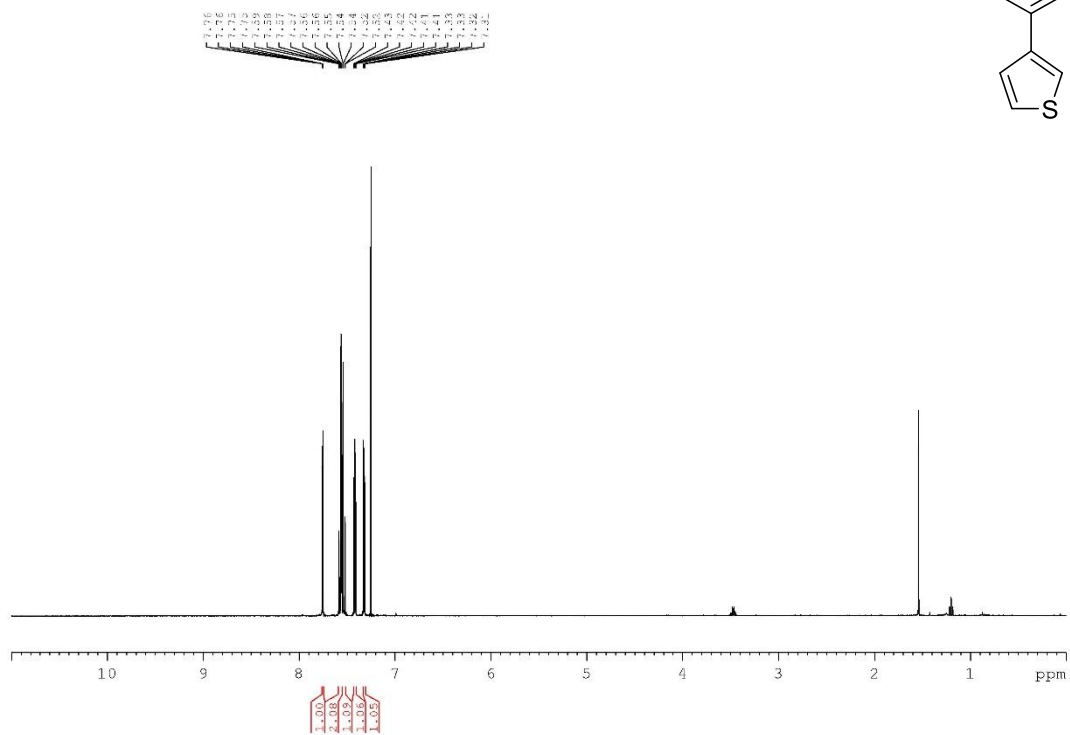
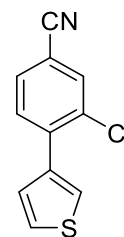
3-Chloro-4-(thiophen-2-yl)benzonitrile (59a)



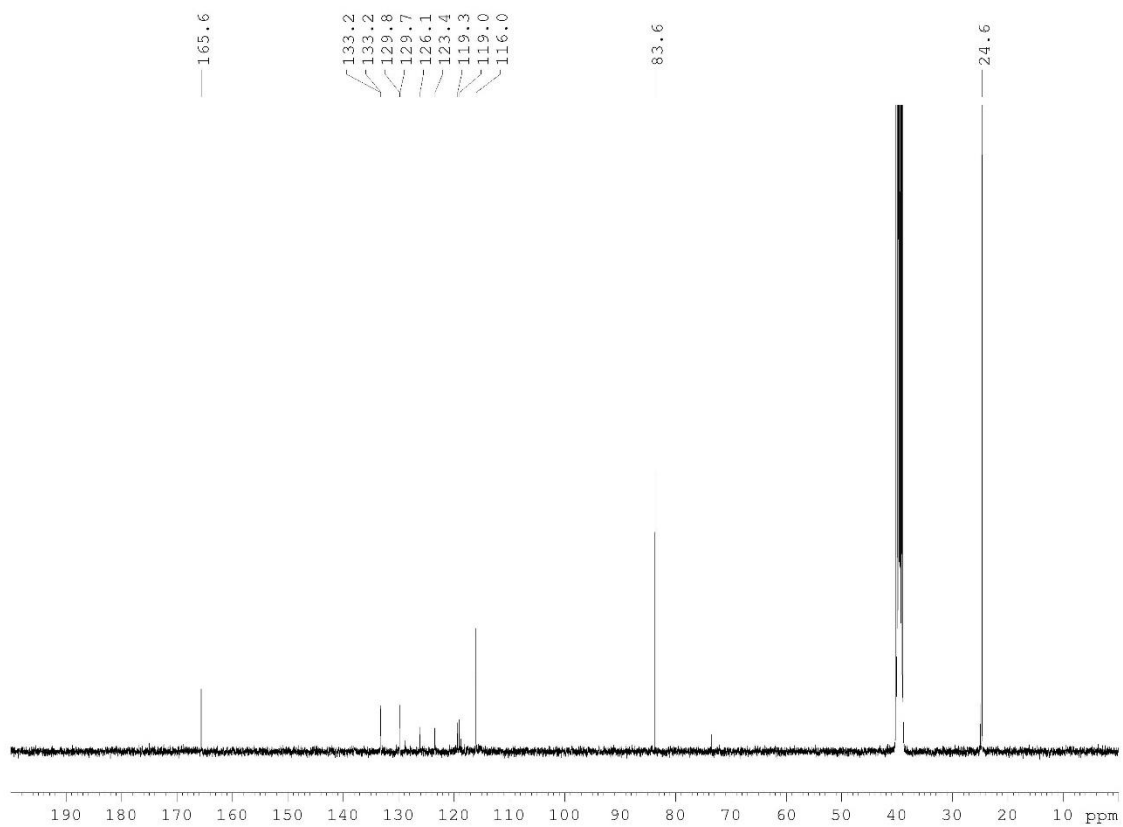
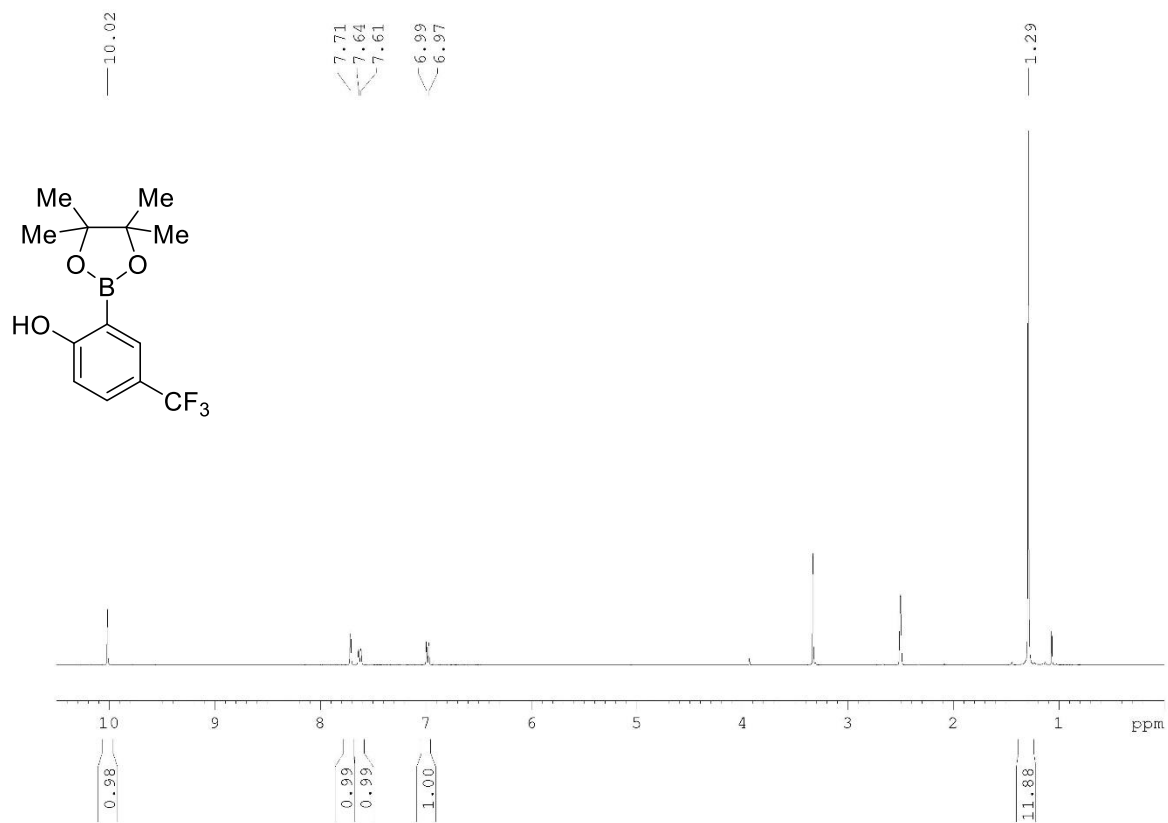
(3-Chloro-4-(thiophen-2-yl)phenyl)methanamine HCl salt (59)



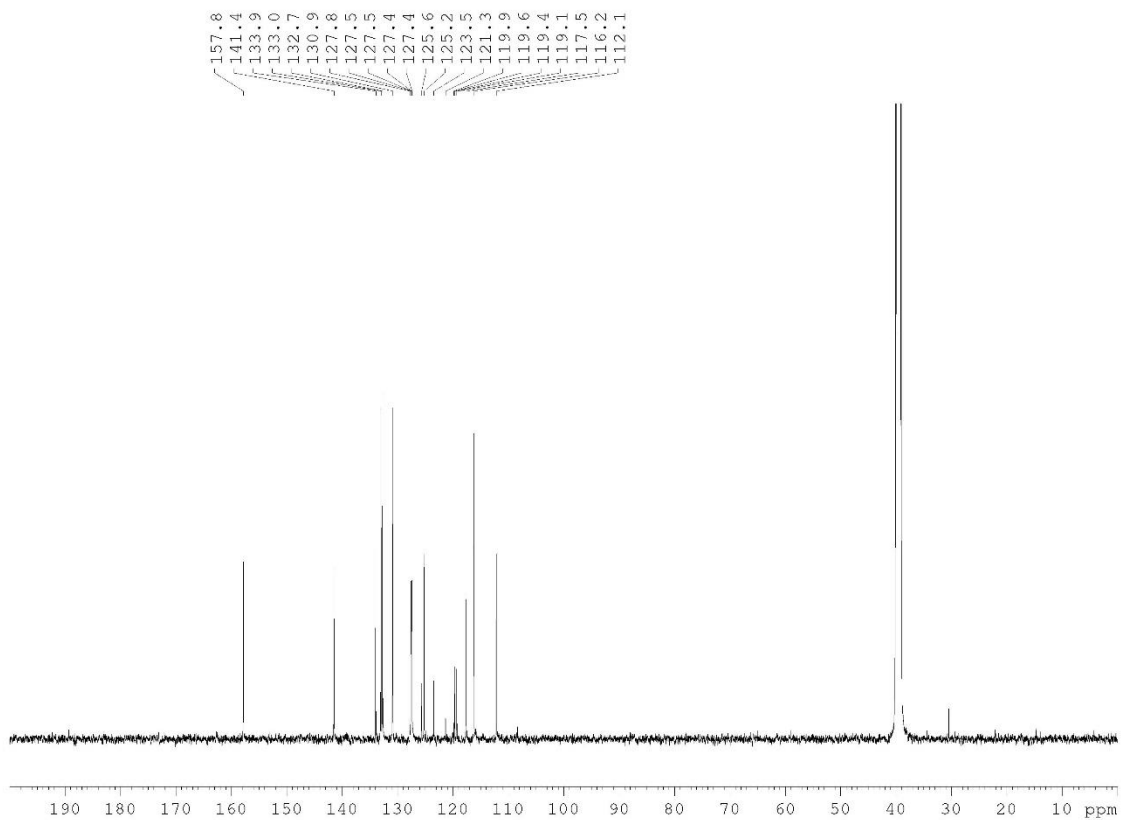
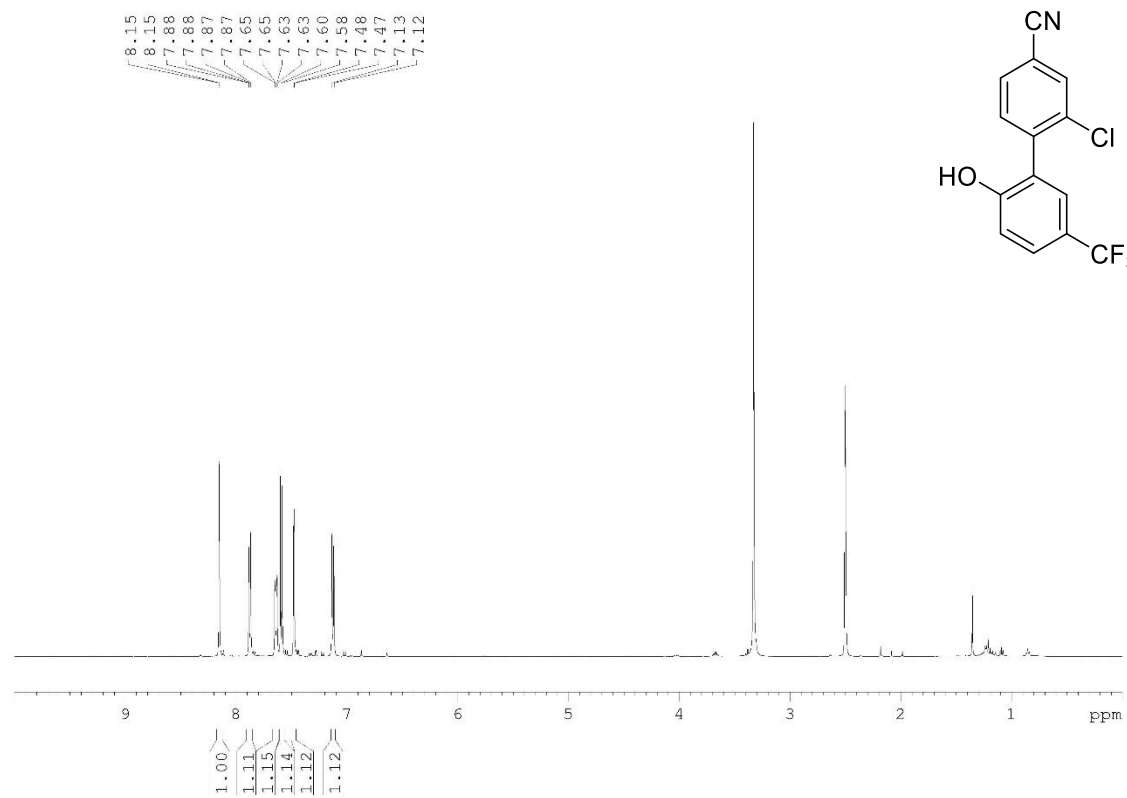
3-Chloro-4-(thiophen-3-yl)benzonitrile (60a)



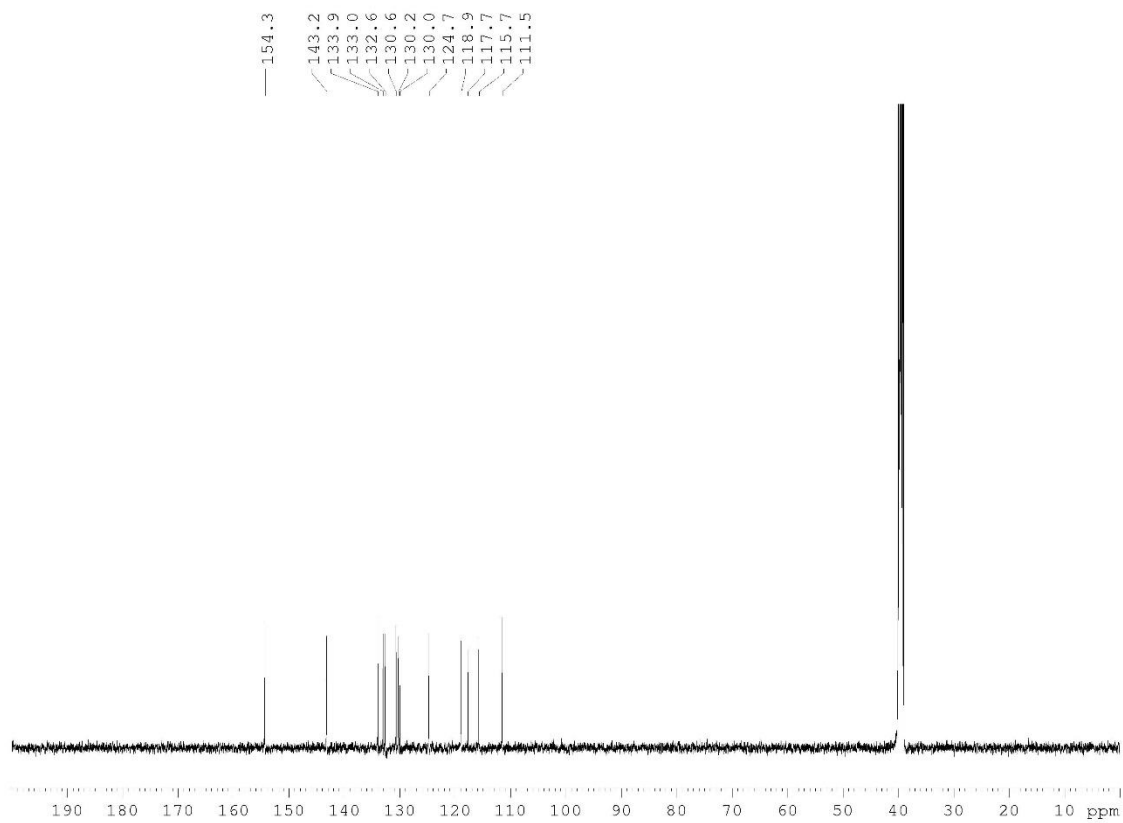
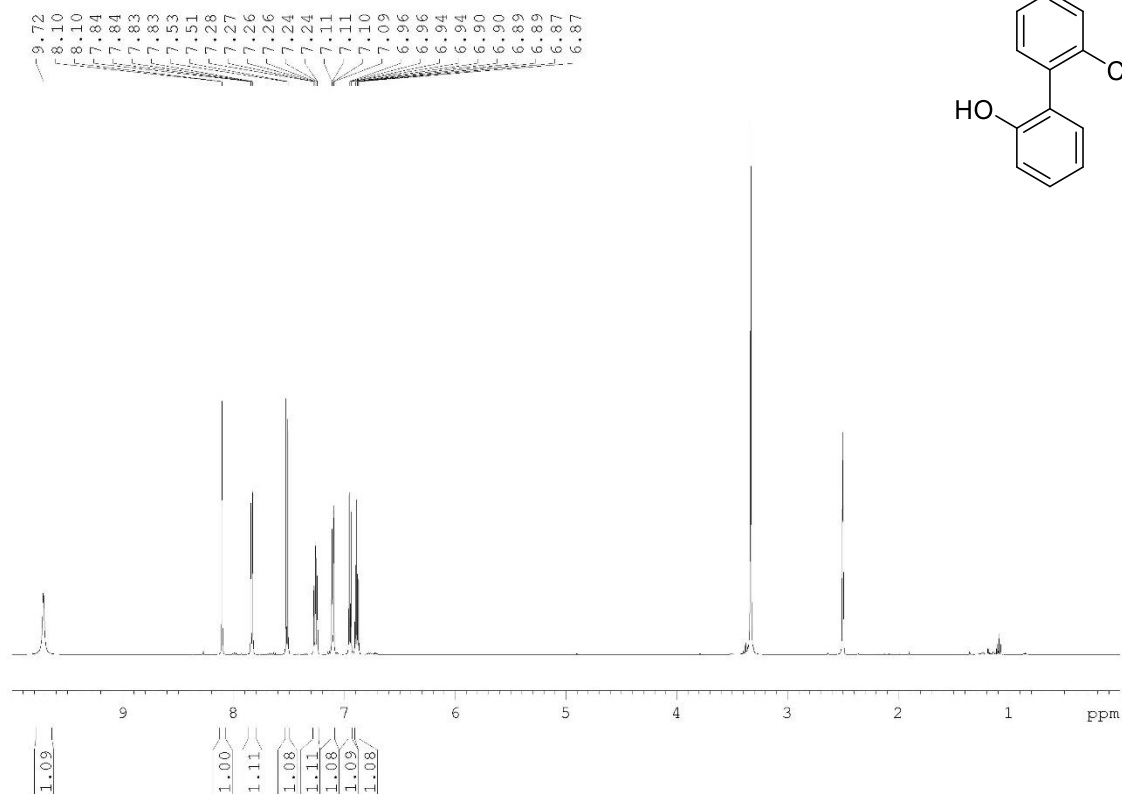
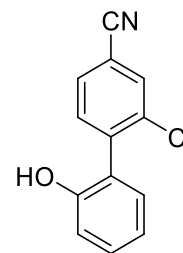
2-(4,4,5,5-Tetramethyl-1,3,2-dioxaborolan-2-yl)-4-(trifluoromethyl)phenol (61b)



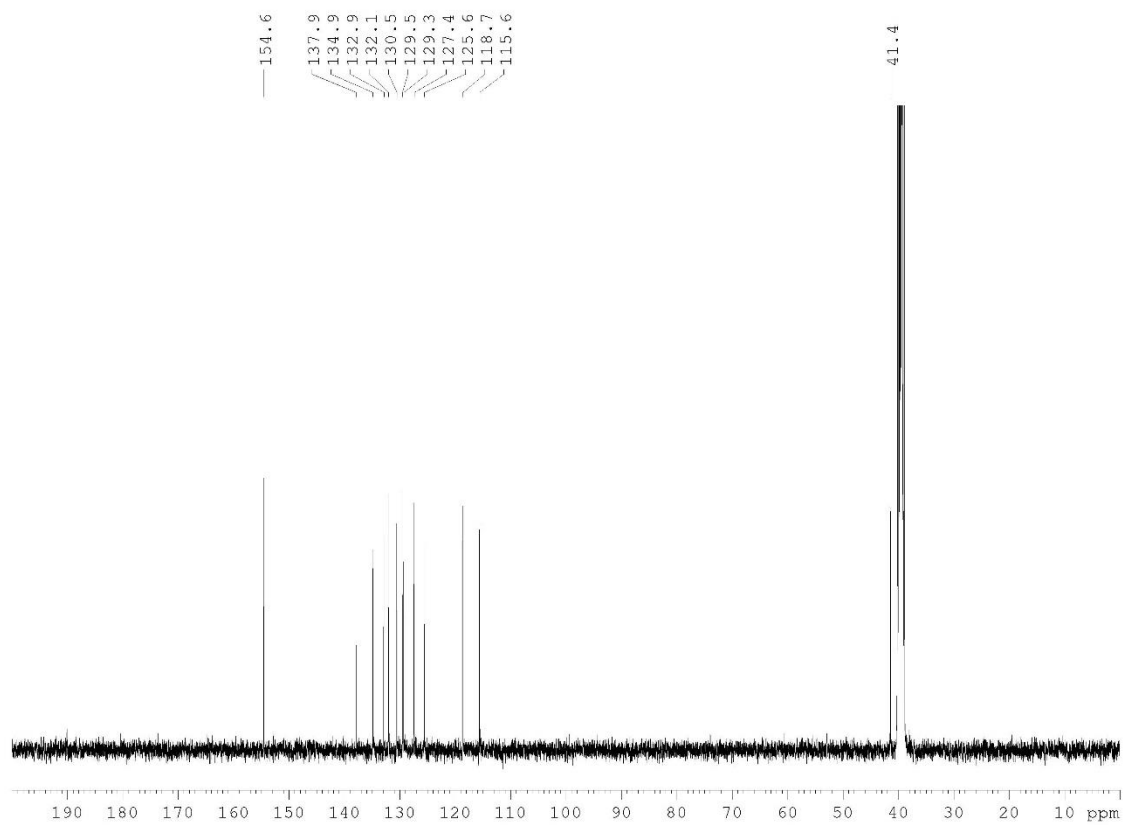
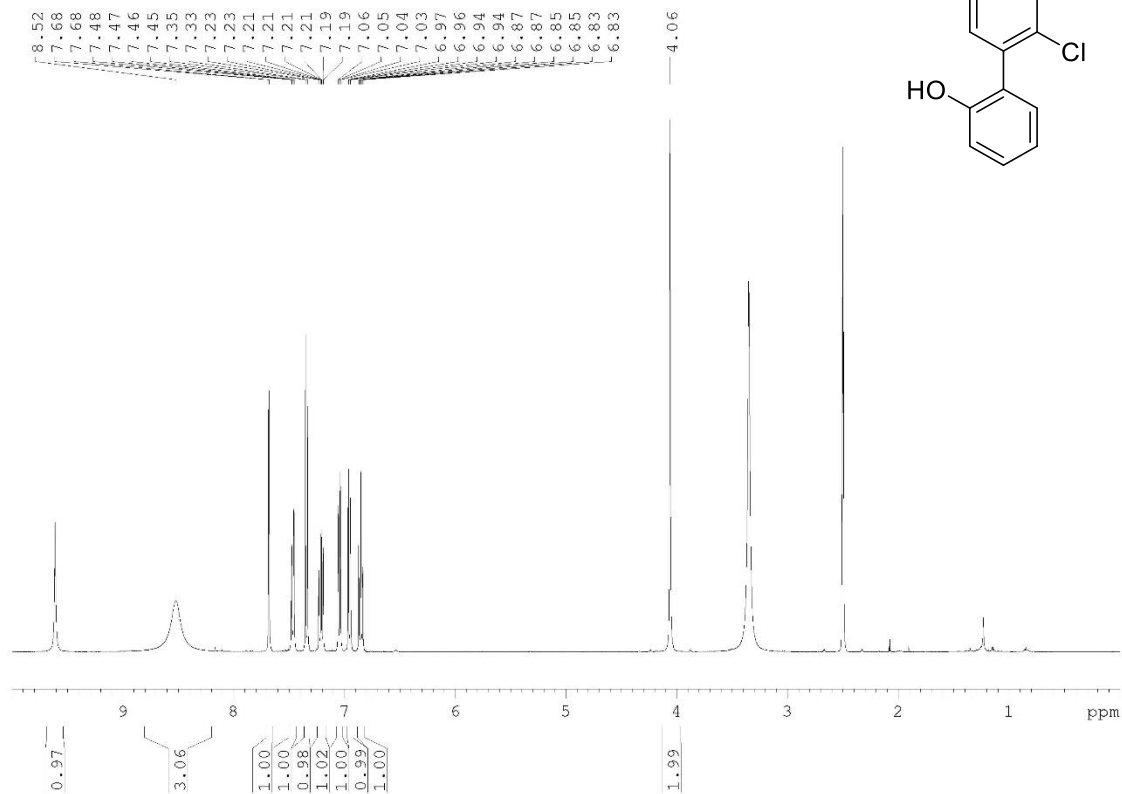
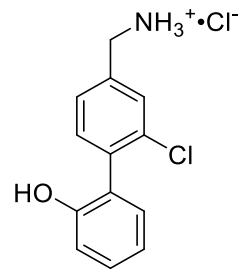
2-Chloro-2'-hydroxy-5'-(trifluoromethyl)-[1,1'-biphenyl]-4-carbonitrile (61a)



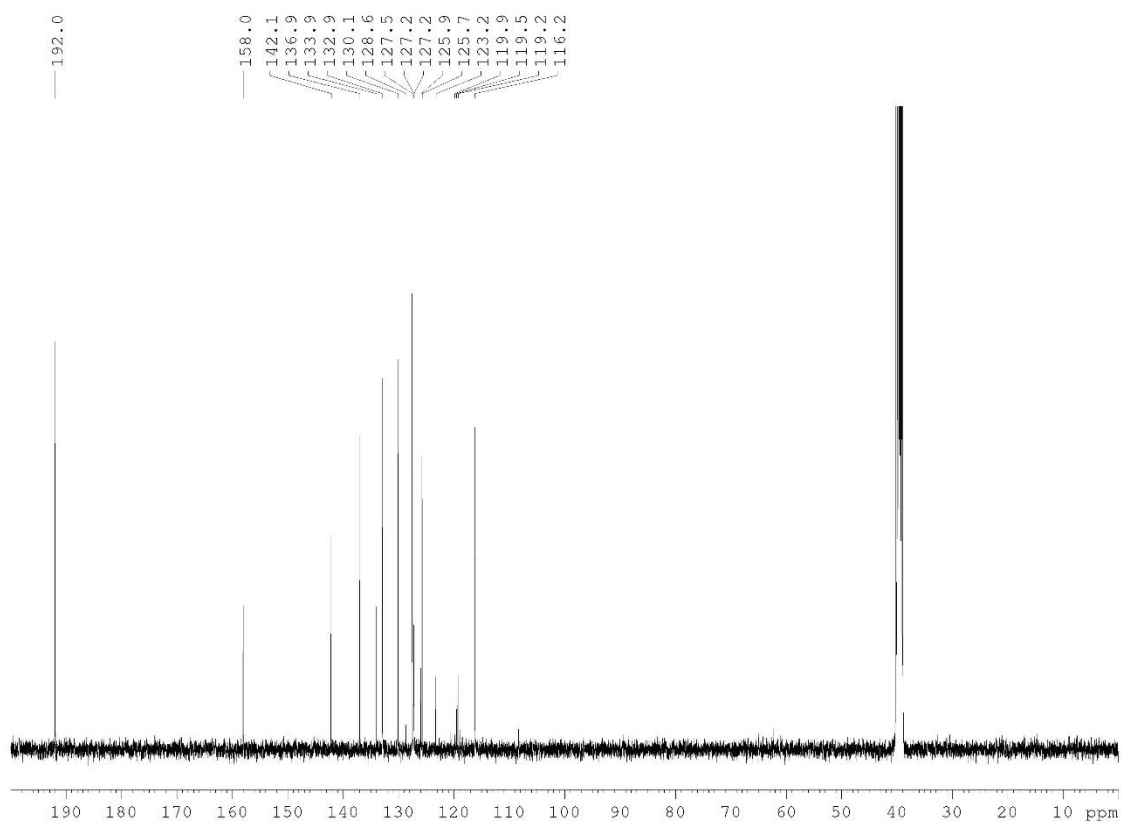
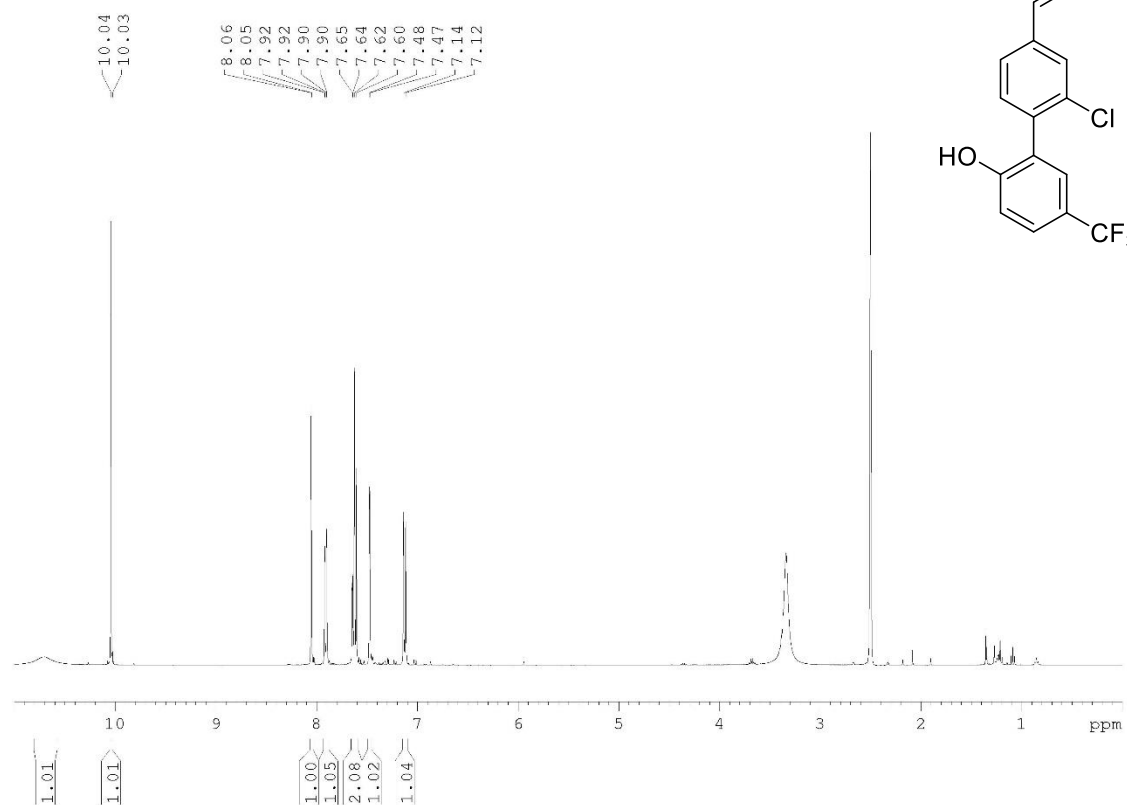
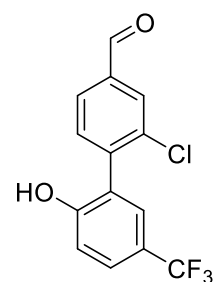
2-Chloro-2'-hydroxy-[1,1'-biphenyl]-4-carbonitrile (62a)



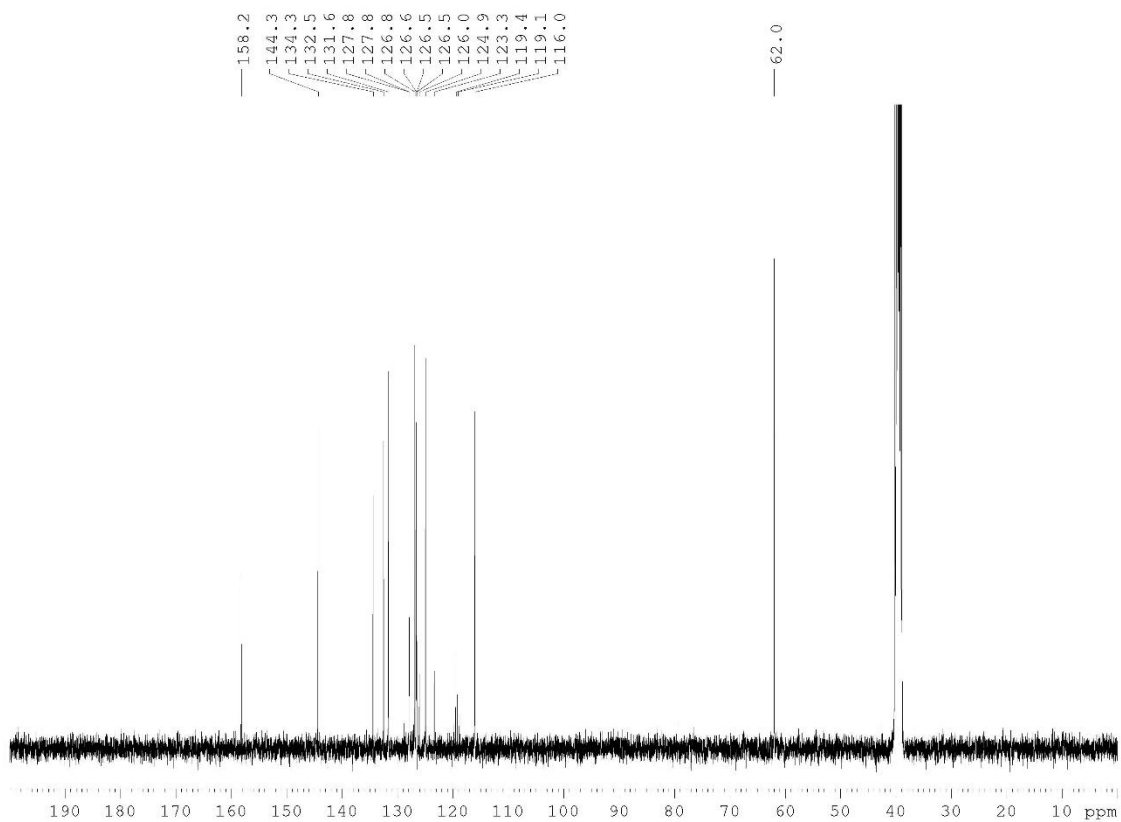
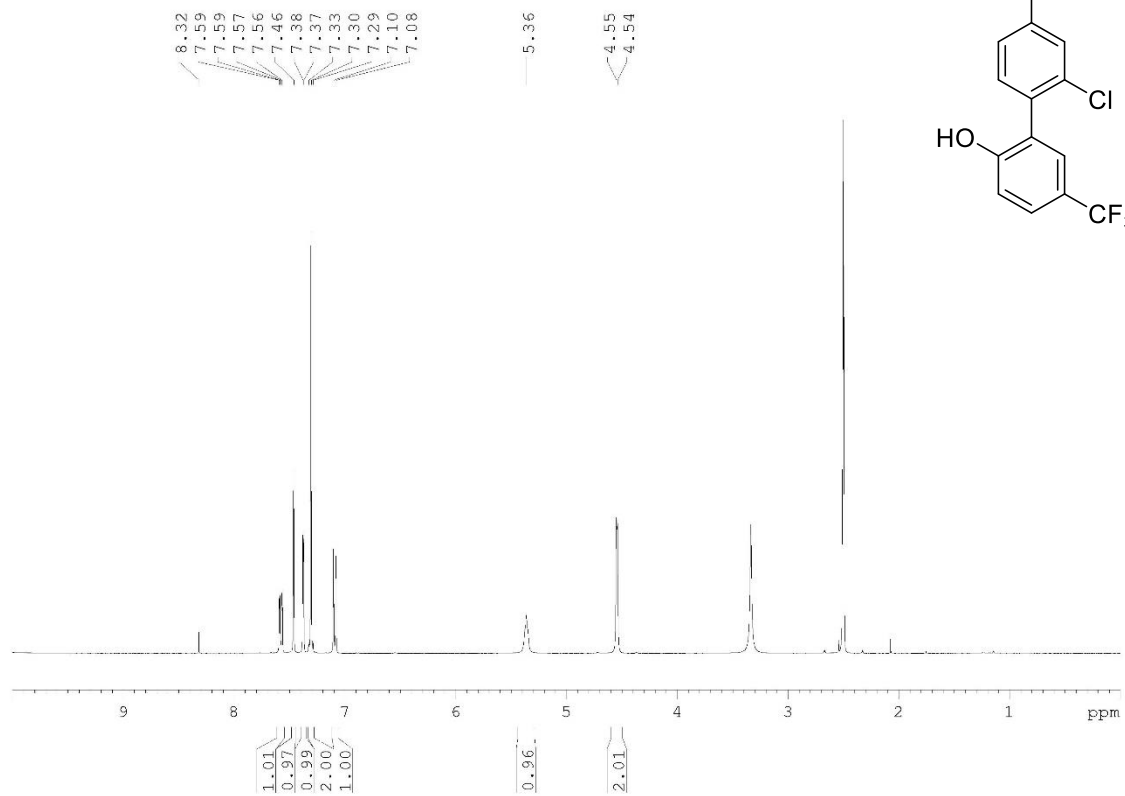
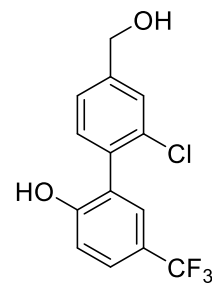
4'-(aminomethyl)-2'-chloro-[1,1'-biphenyl]-2-ol HCl salt (66)



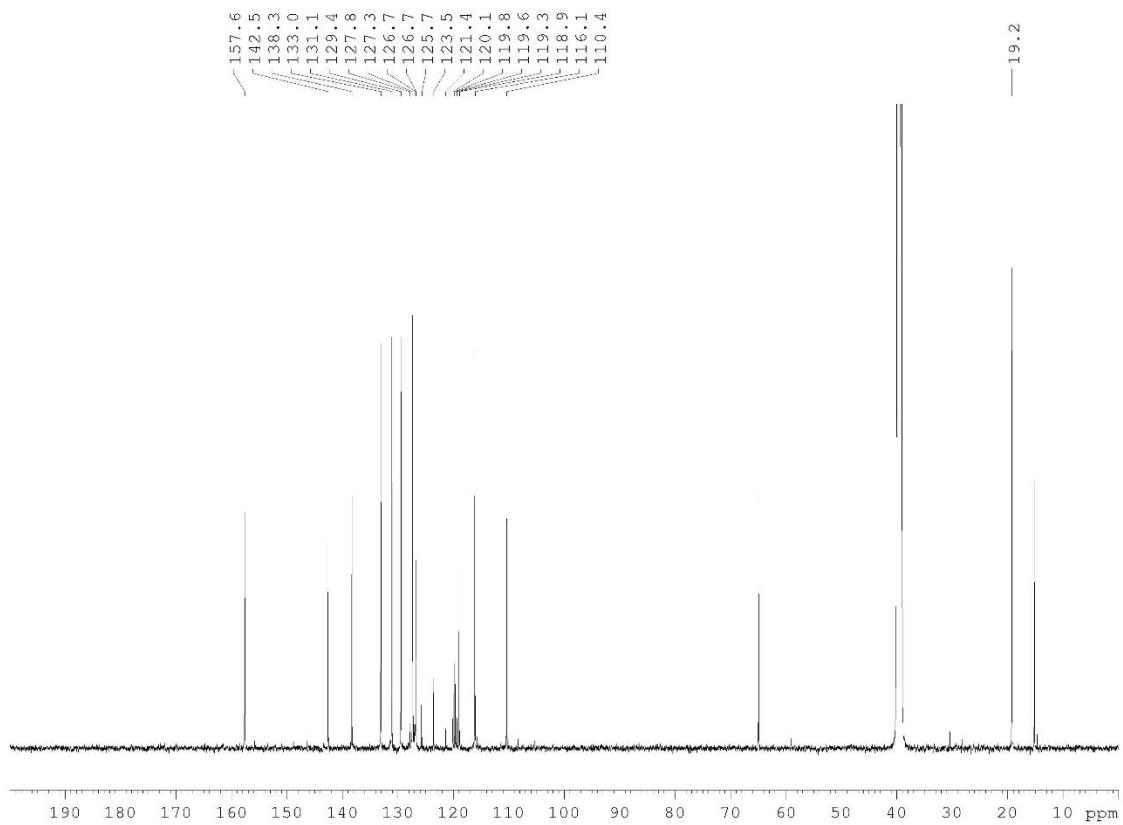
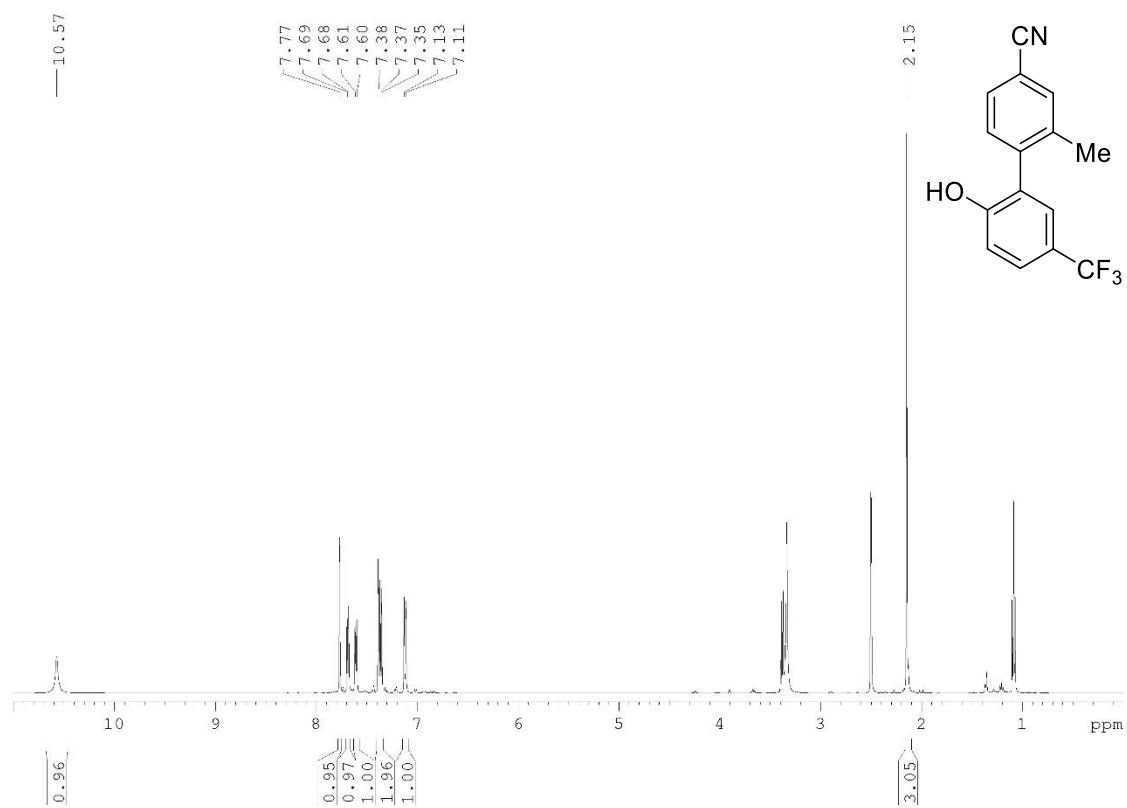
2-chloro-2'-hydroxy-5'-(trifluoromethyl)-[1,1'-biphenyl]-4-carbaldehyde (63)



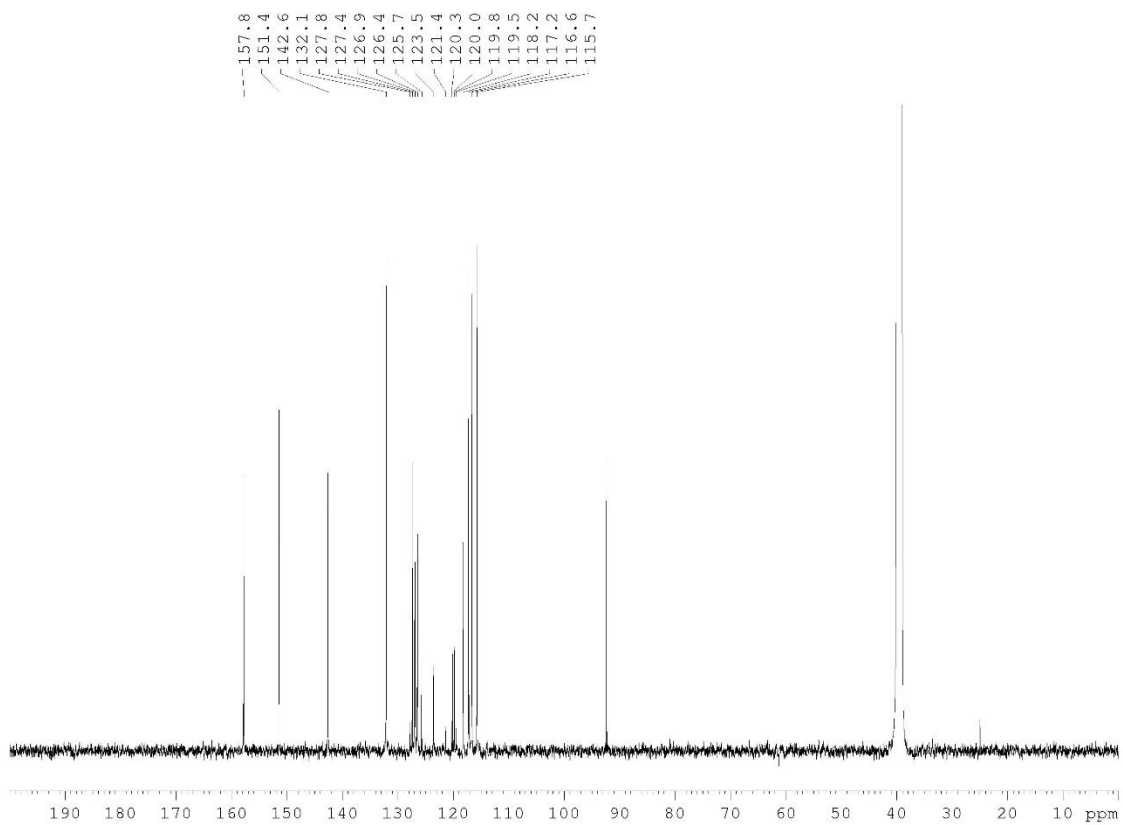
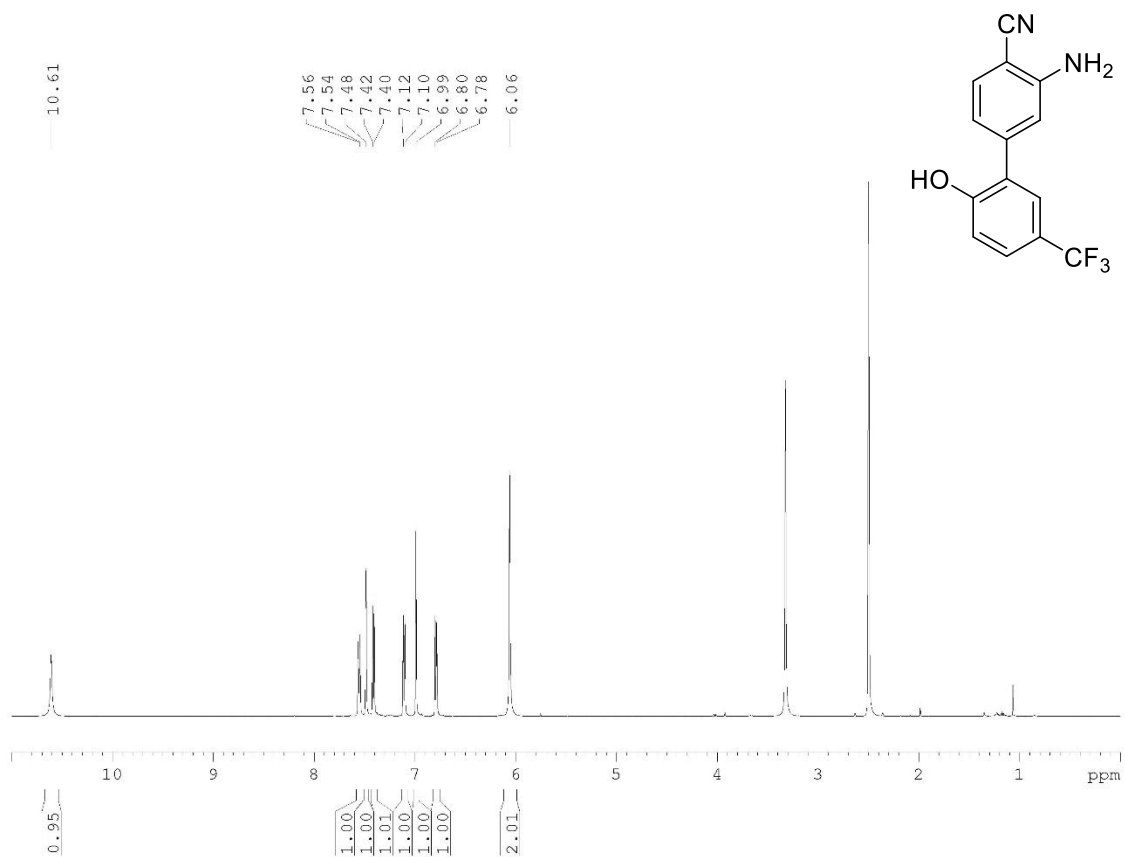
2'-chloro-4'-(hydroxymethyl)-5-(trifluoromethyl)-[1,1'-biphenyl]-2-ol (64)



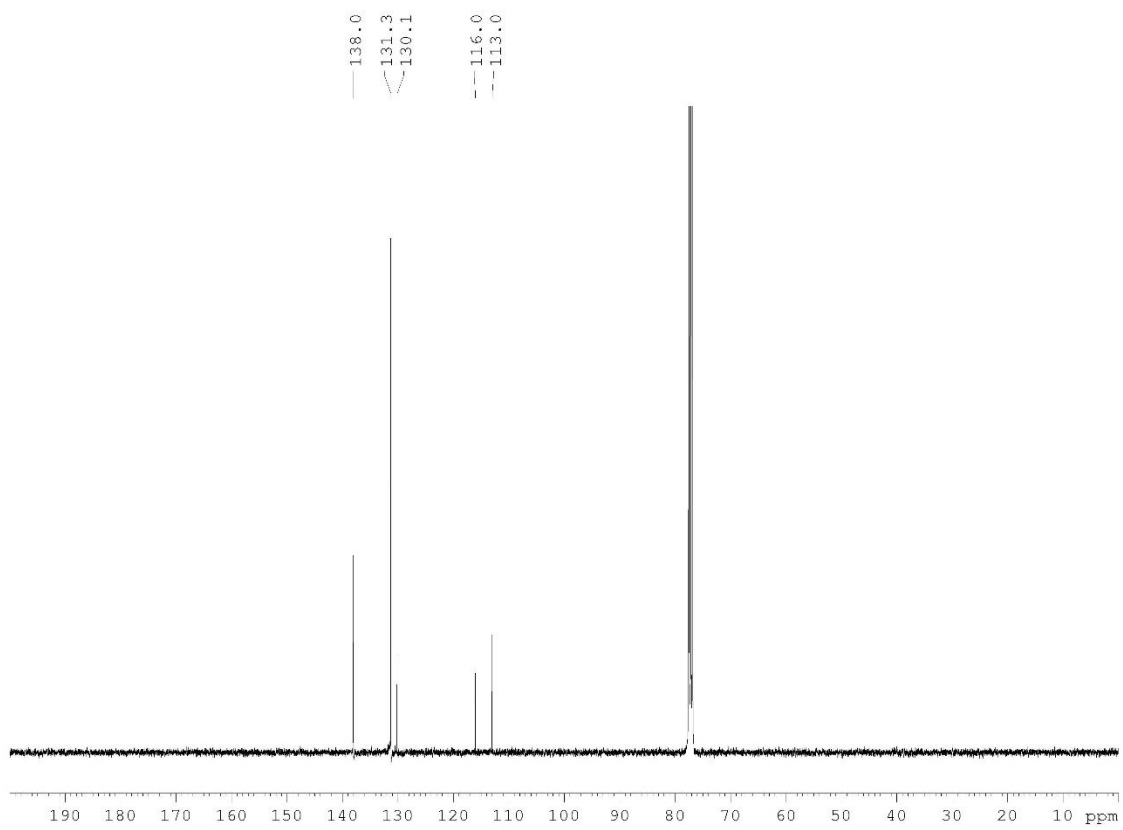
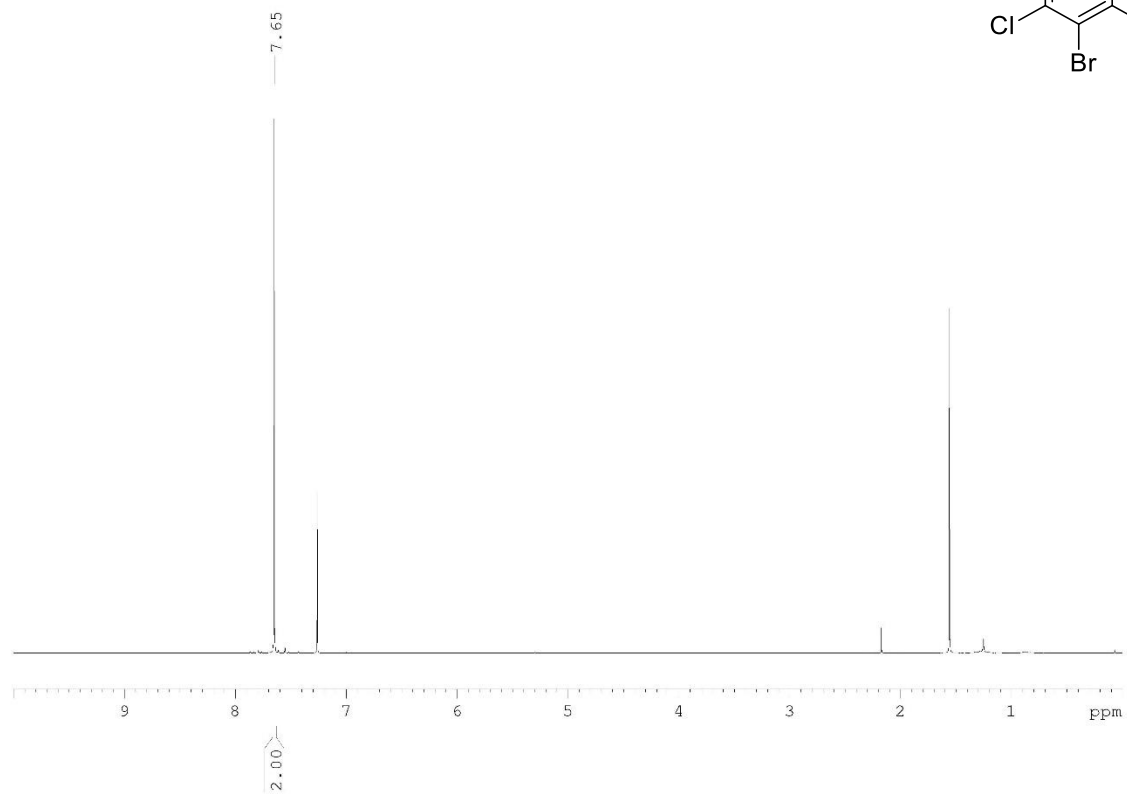
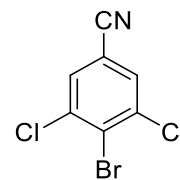
2'-hydroxy-2-methyl-5'-(trifluoromethyl)-[1,1'-biphenyl]-4-carbonitrile (65)



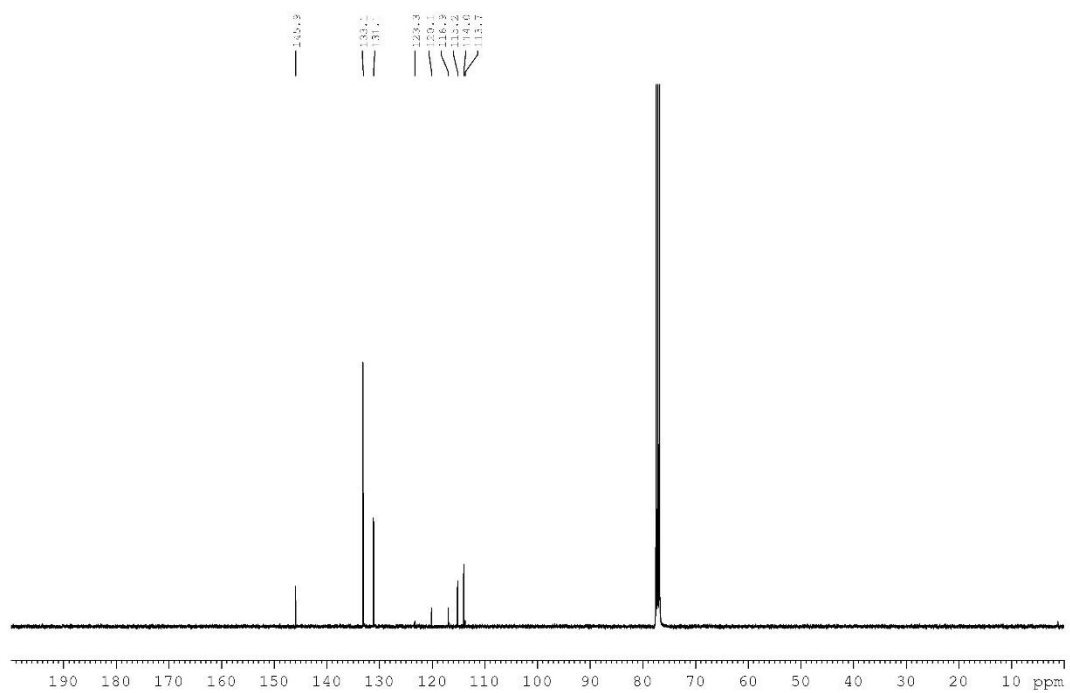
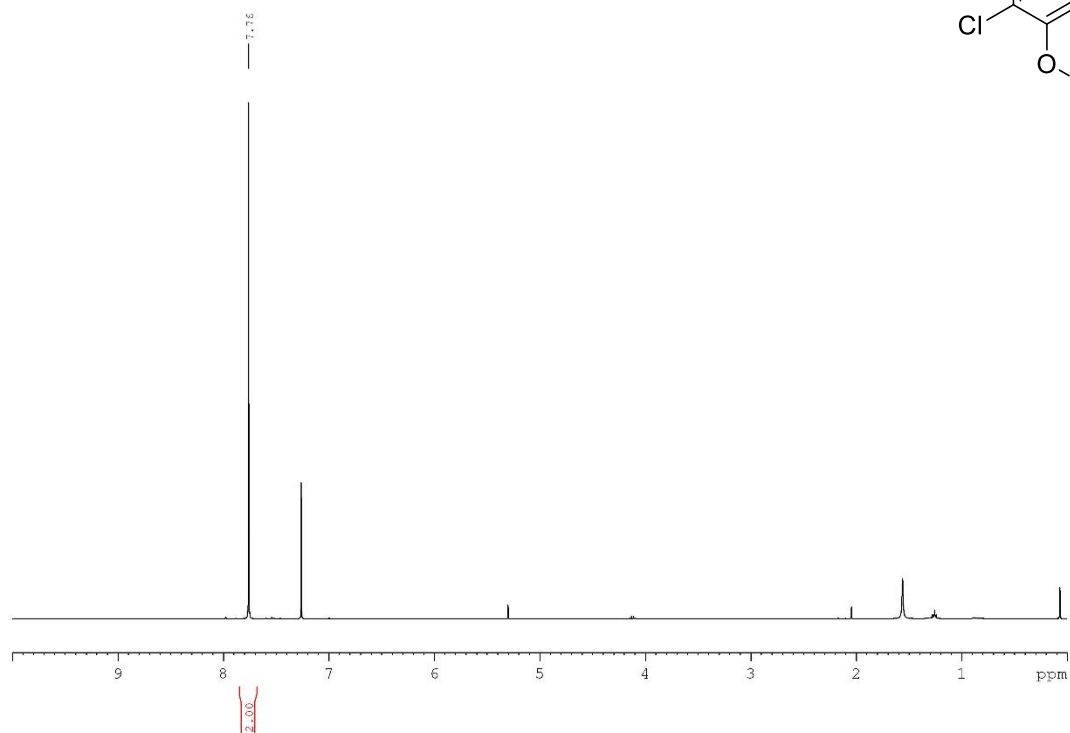
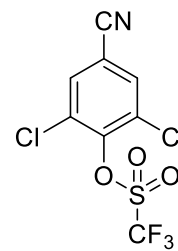
3-amino-2'-hydroxy-5'-(trifluoromethyl)-[1,1'-biphenyl]-4-carbonitrile (66)



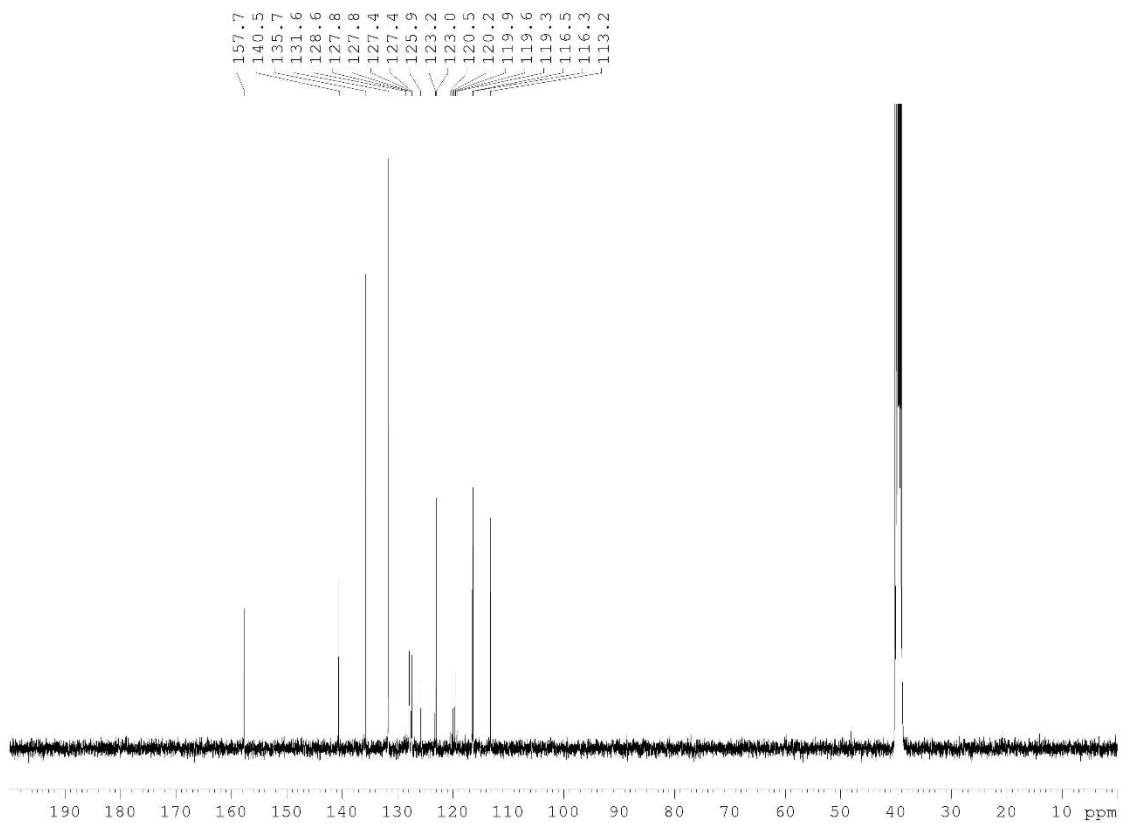
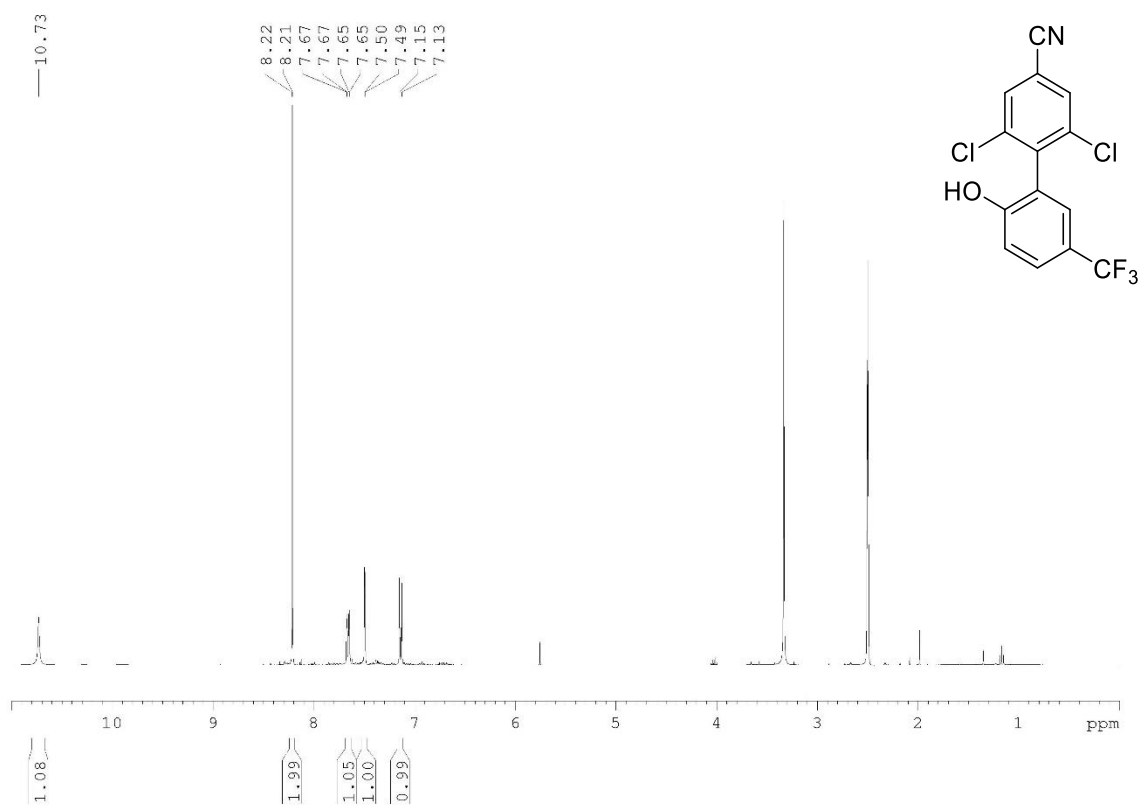
4-bromo-3,5-dichlorobenzonitrile (67a)



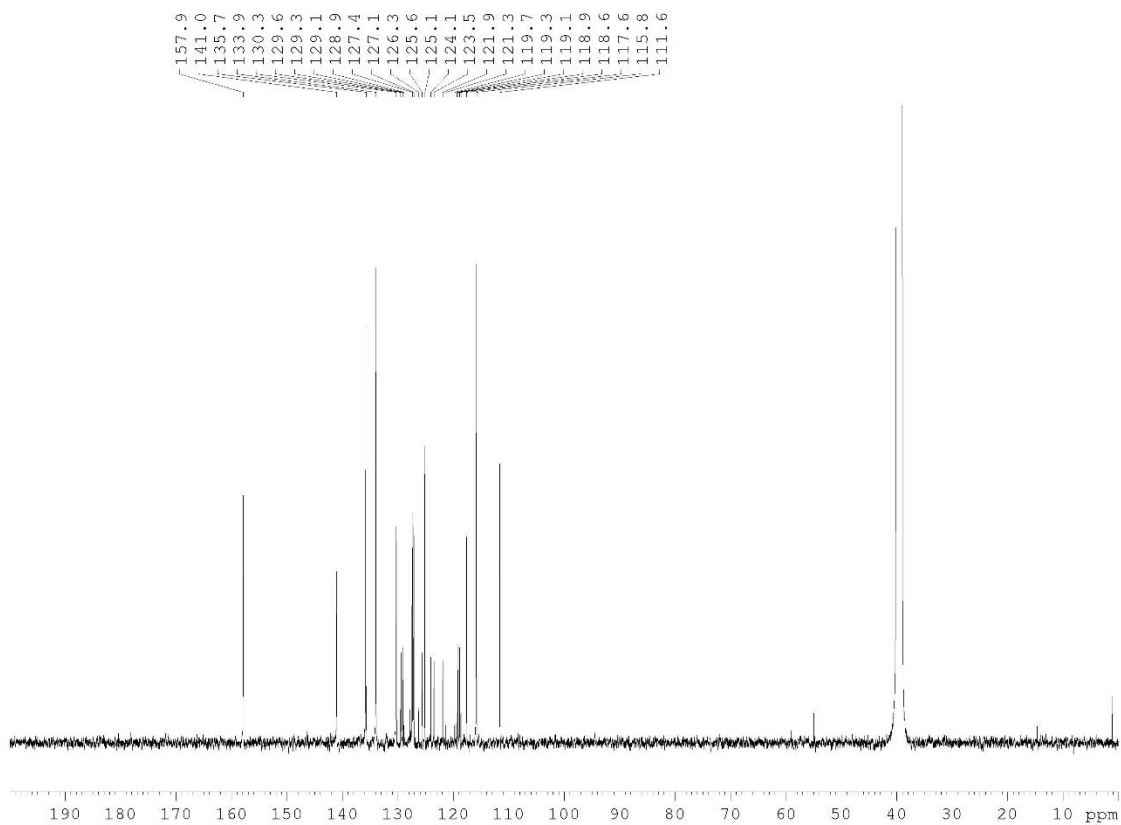
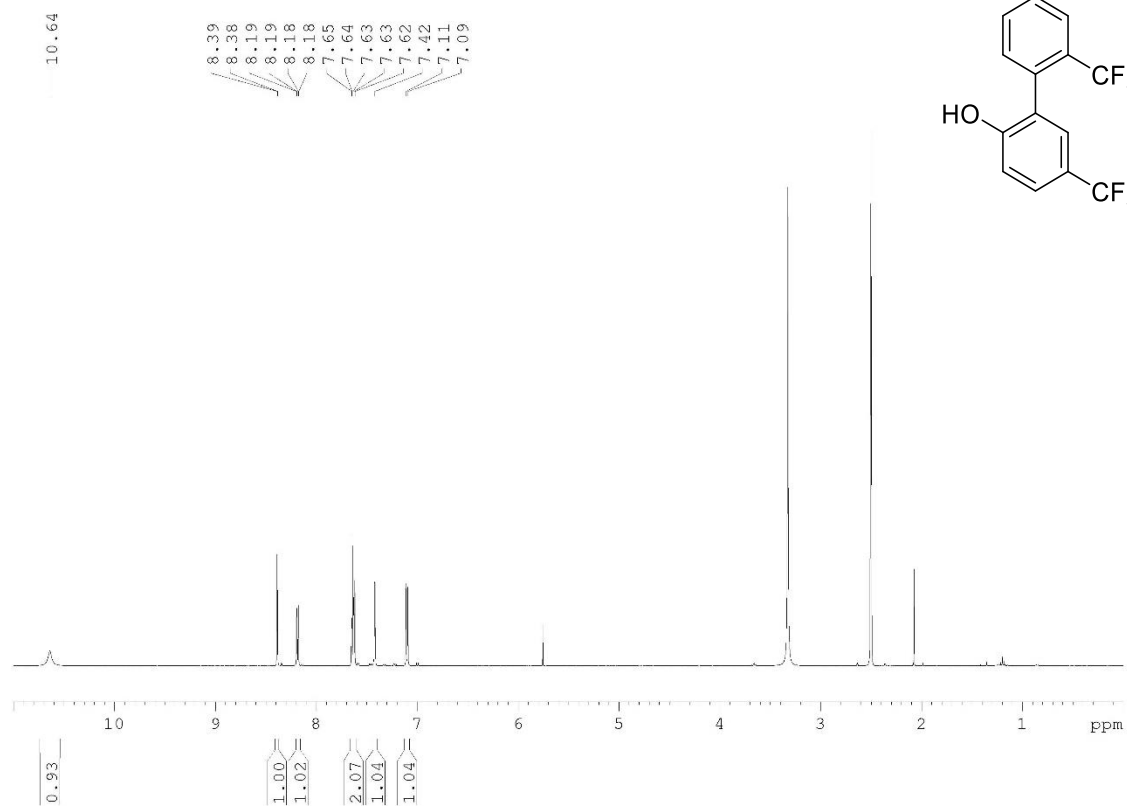
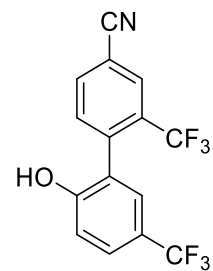
2,6-Dichloro-4-cyanophenyl trifluoromethanesulfonate (67c)



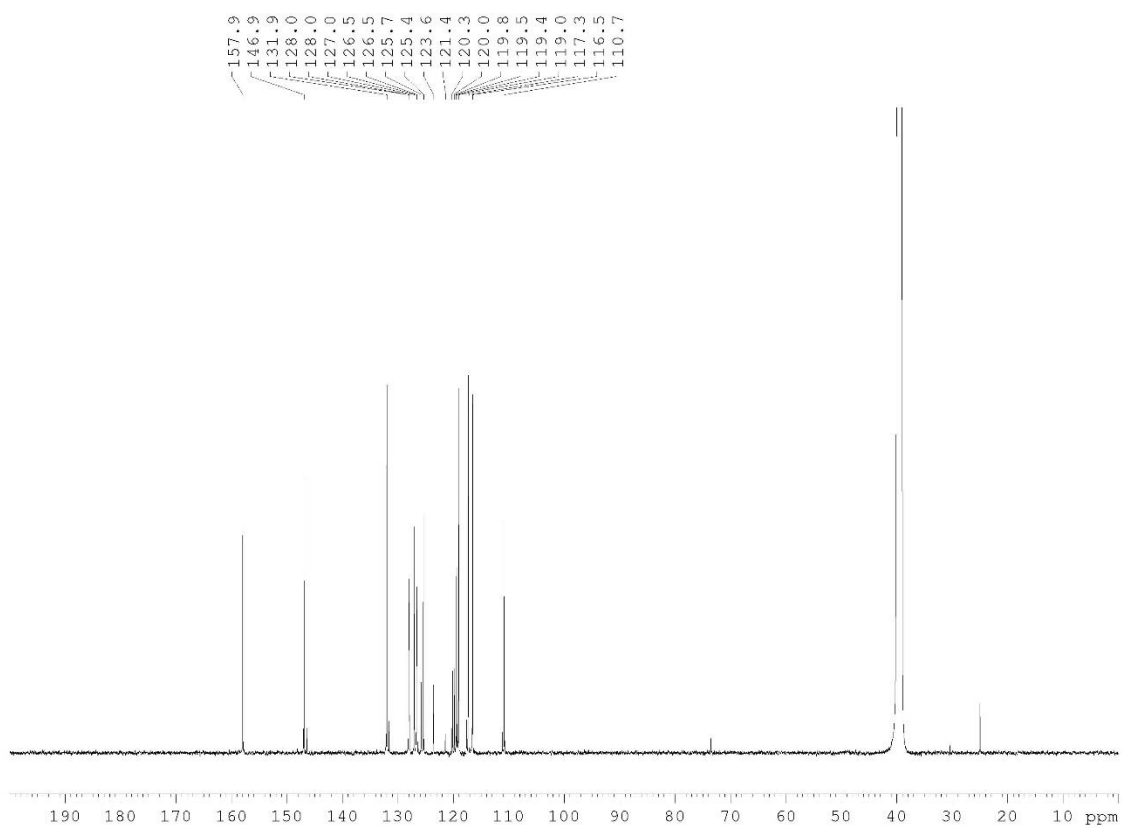
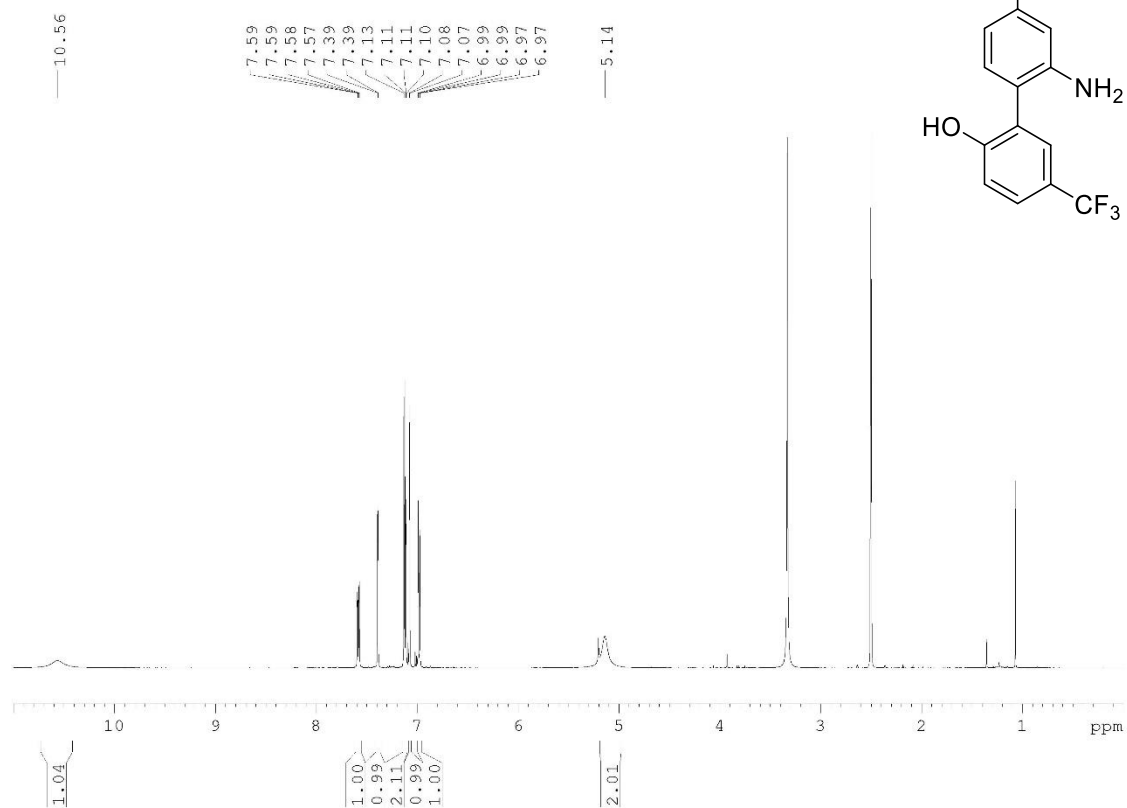
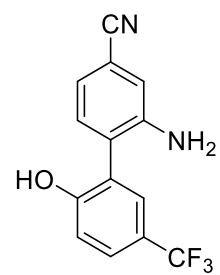
2,6-dichloro-2'-hydroxy-5'-(trifluoromethyl)-[1,1'-biphenyl]-4-carbonitrile (67)



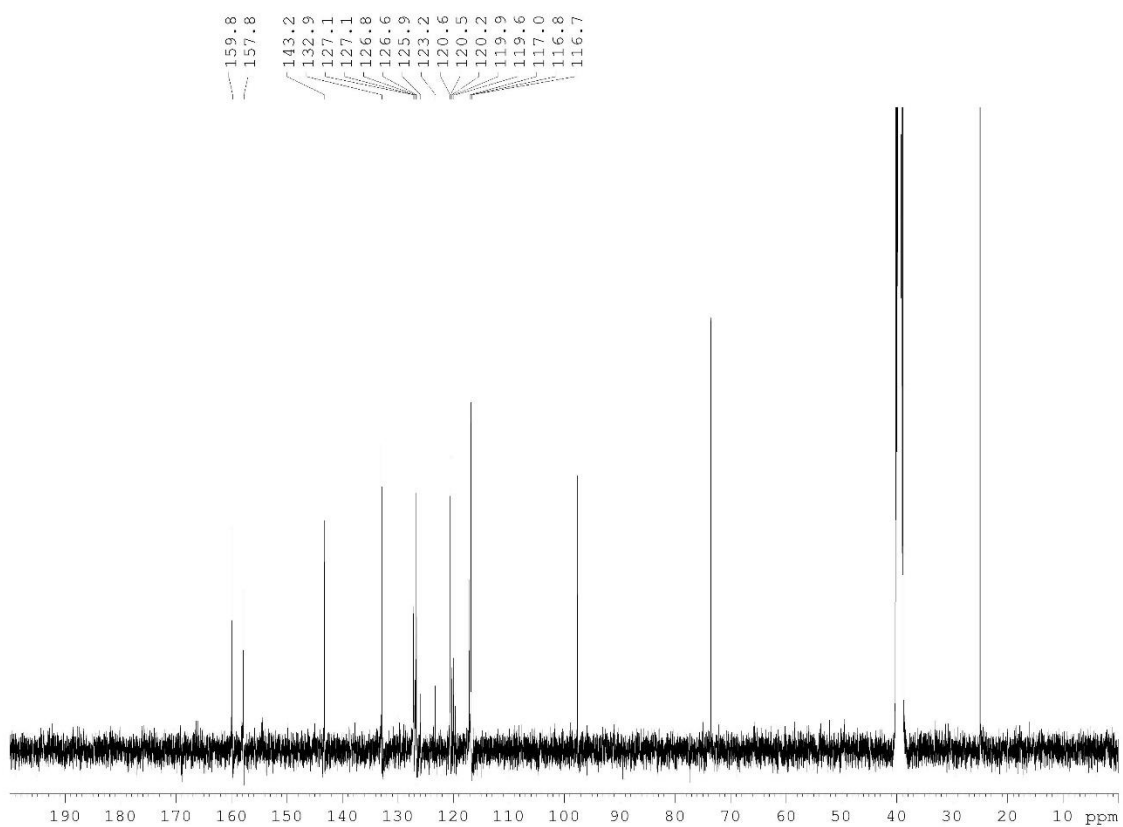
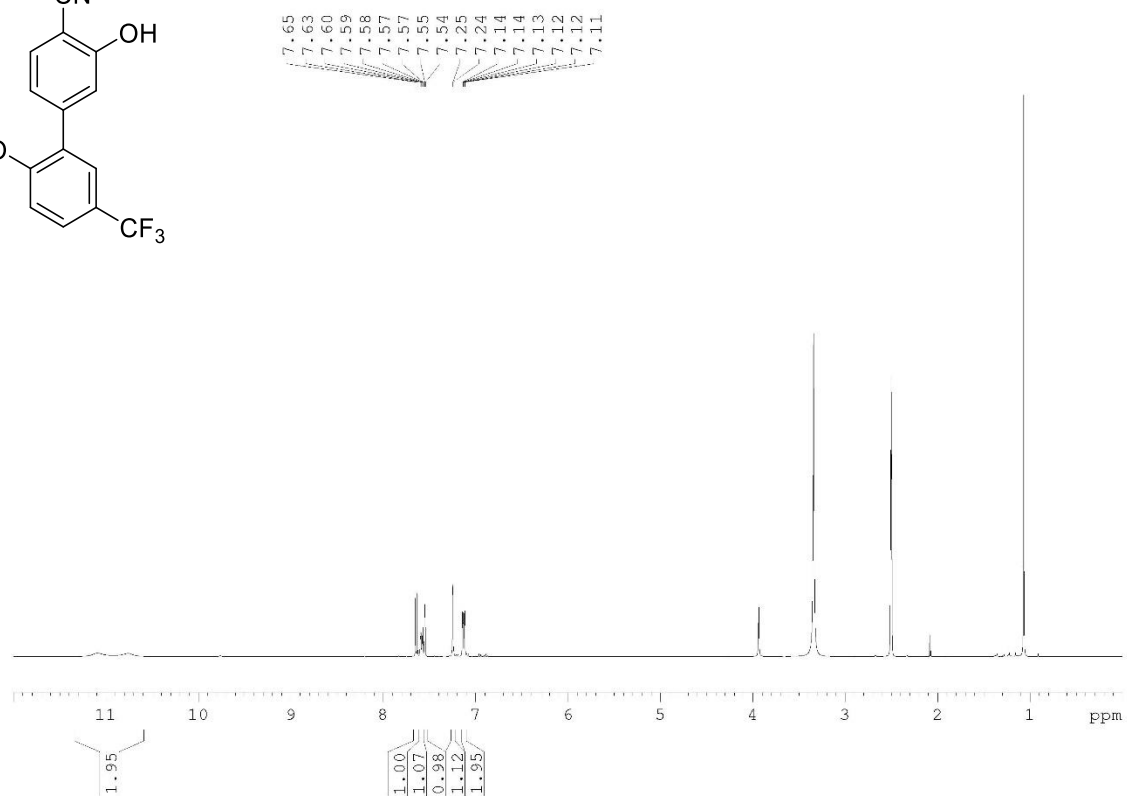
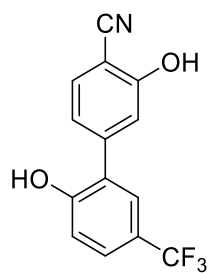
2'-hydroxy-2,5'-bis(trifluoromethyl)-[1,1'-biphenyl]-4-carbonitrile (68)



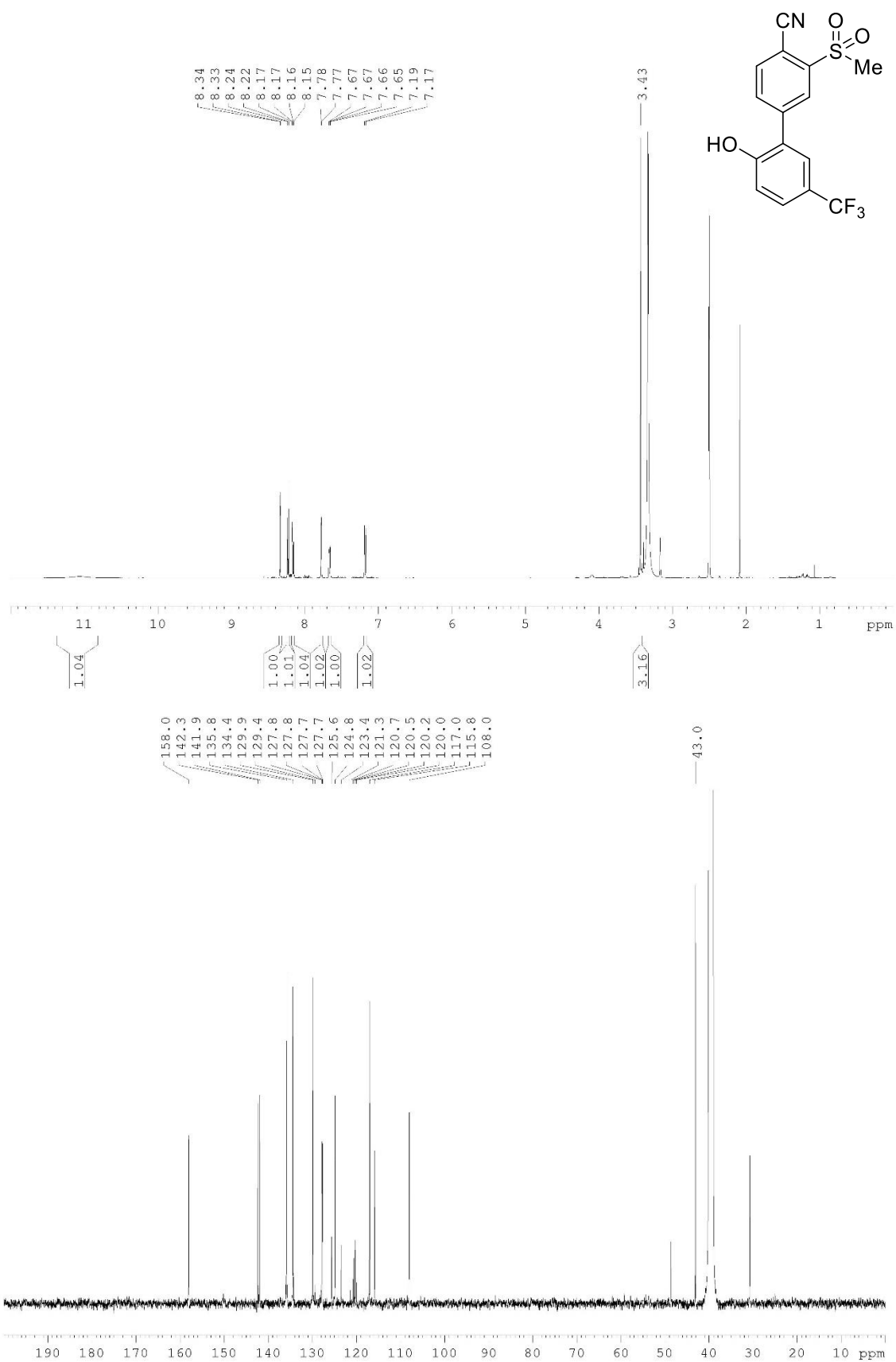
2-amino-2'-hydroxy-5'-(trifluoromethyl)-[1,1'-biphenyl]-4-carbonitrile (69)



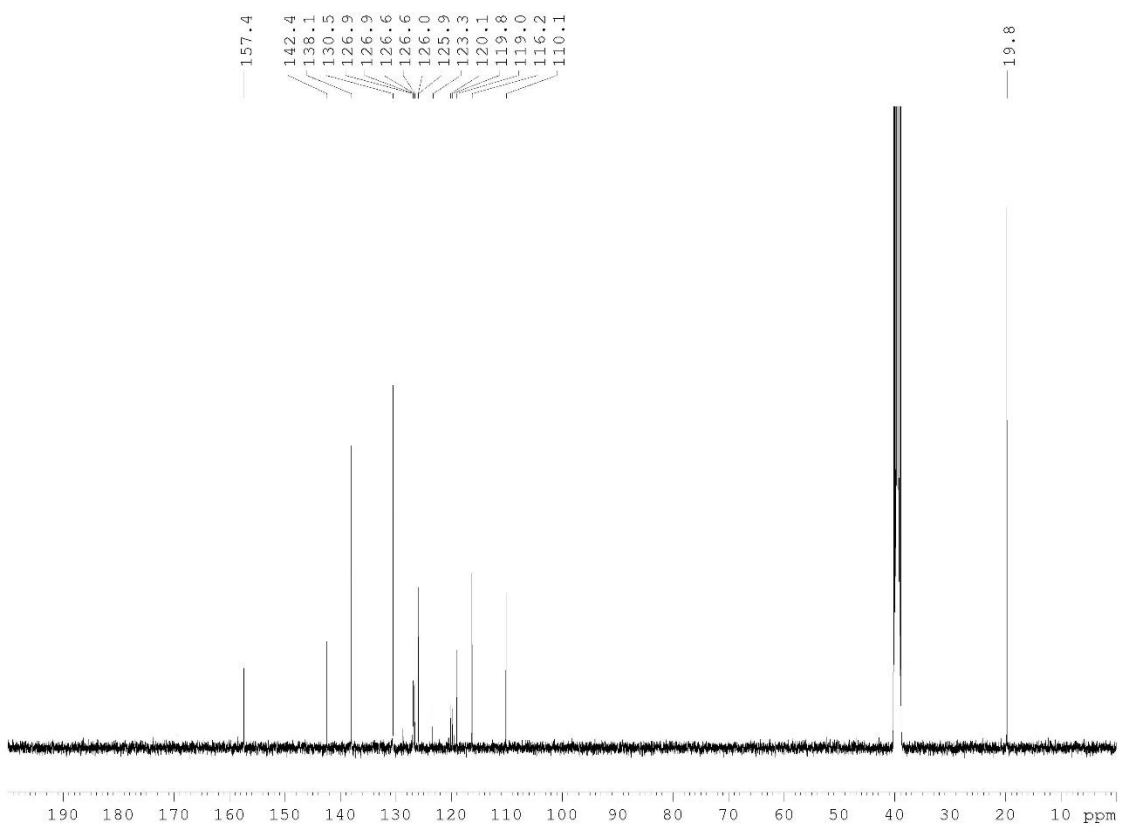
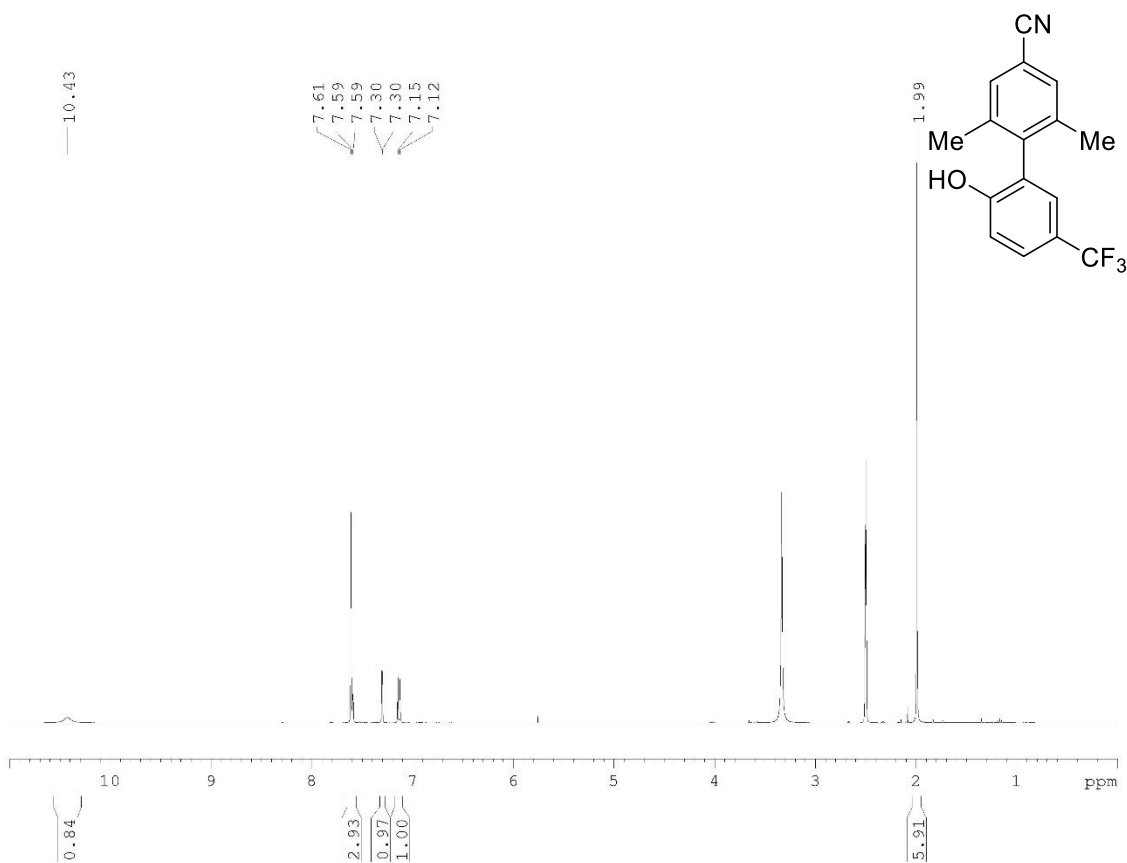
2',3-dihydroxy-5'-(trifluoromethyl)-[1,1'-biphenyl]-4-carbonitrile (70)



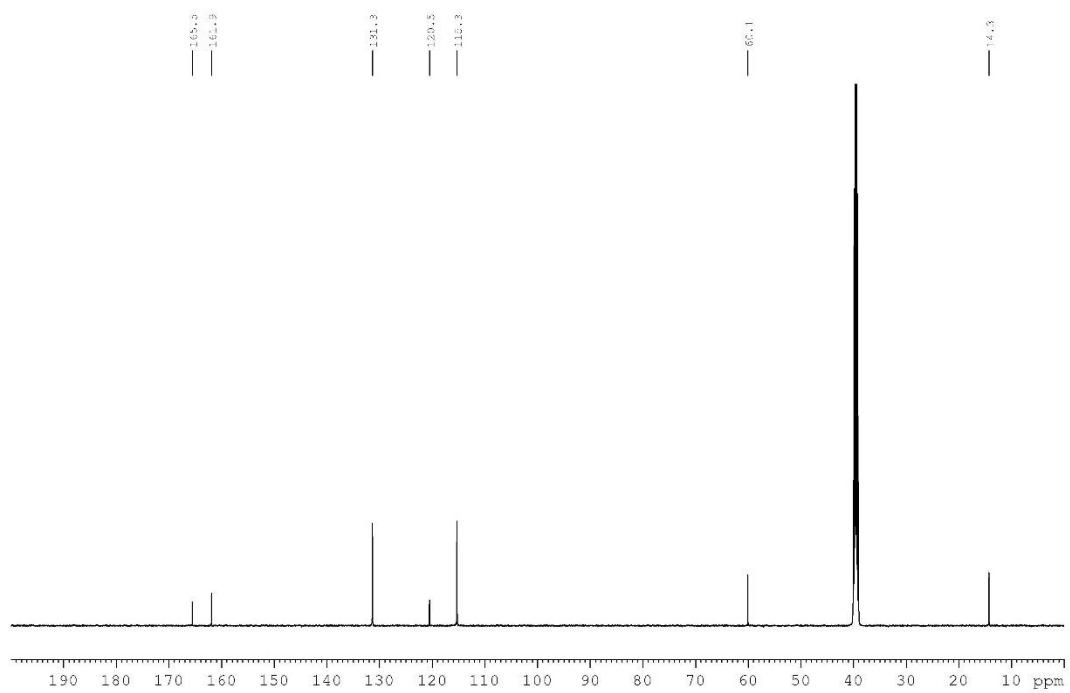
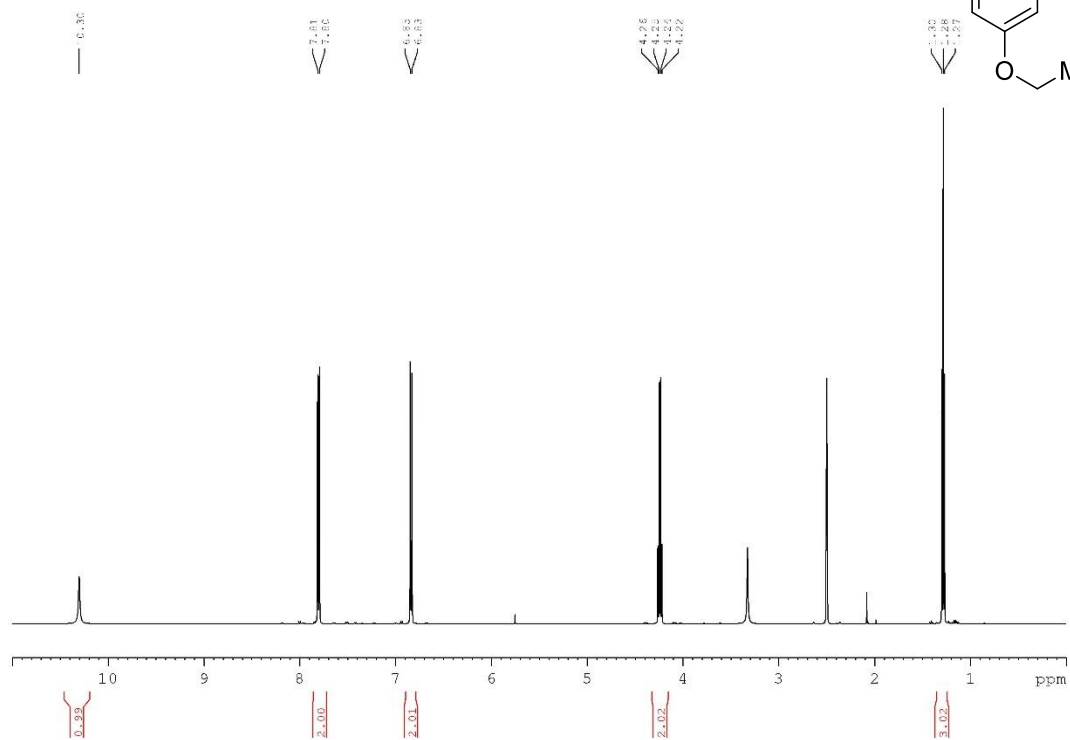
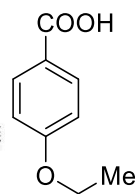
2'-hydroxy-3-(methylsulfonyl)-5'-(trifluoromethyl)-[1,1'-biphenyl]-4-carbonitrile (71)



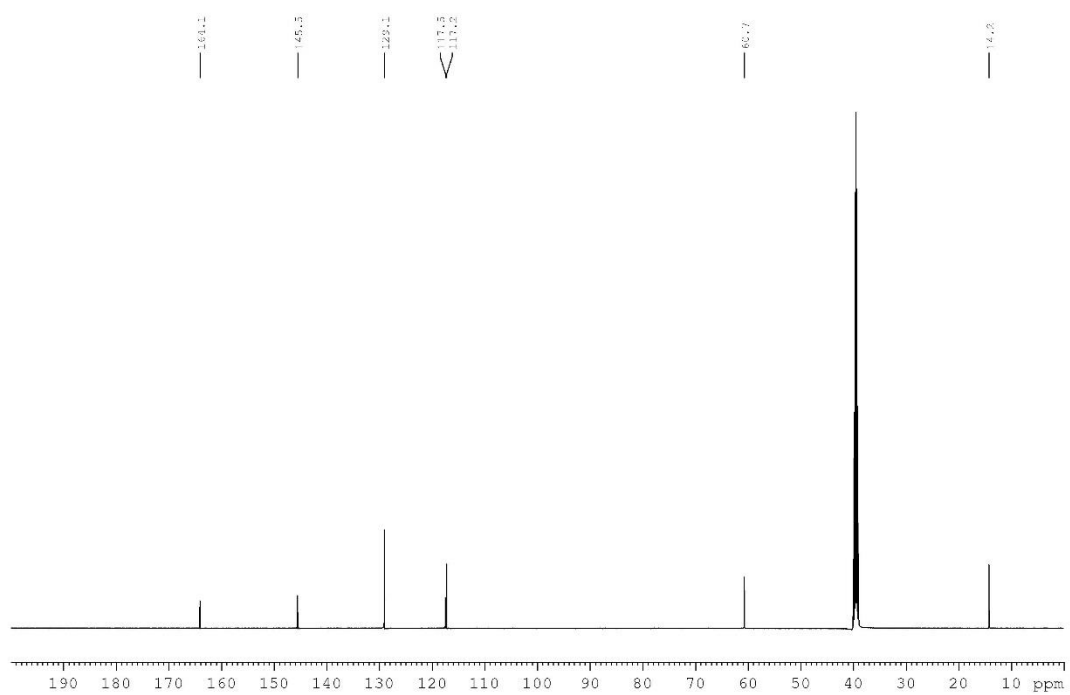
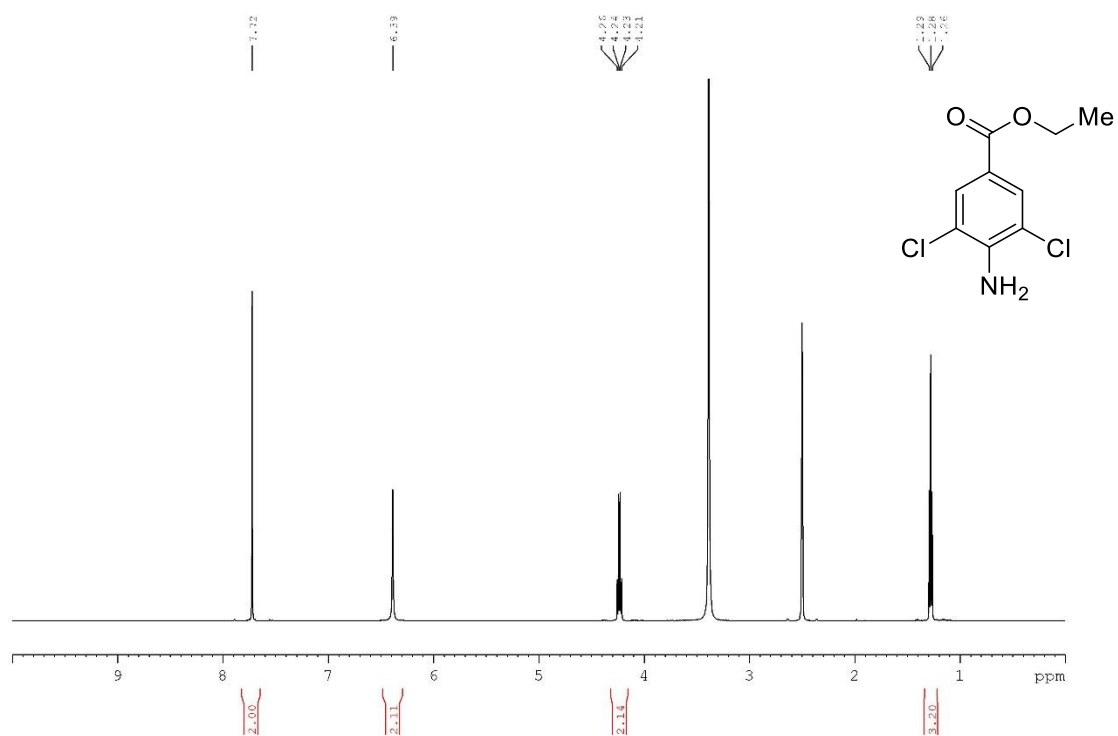
2'-hydroxy-2,6-dimethyl-5'-(trifluoromethyl)-[1,1'-biphenyl]-4-carbonitrile (72)



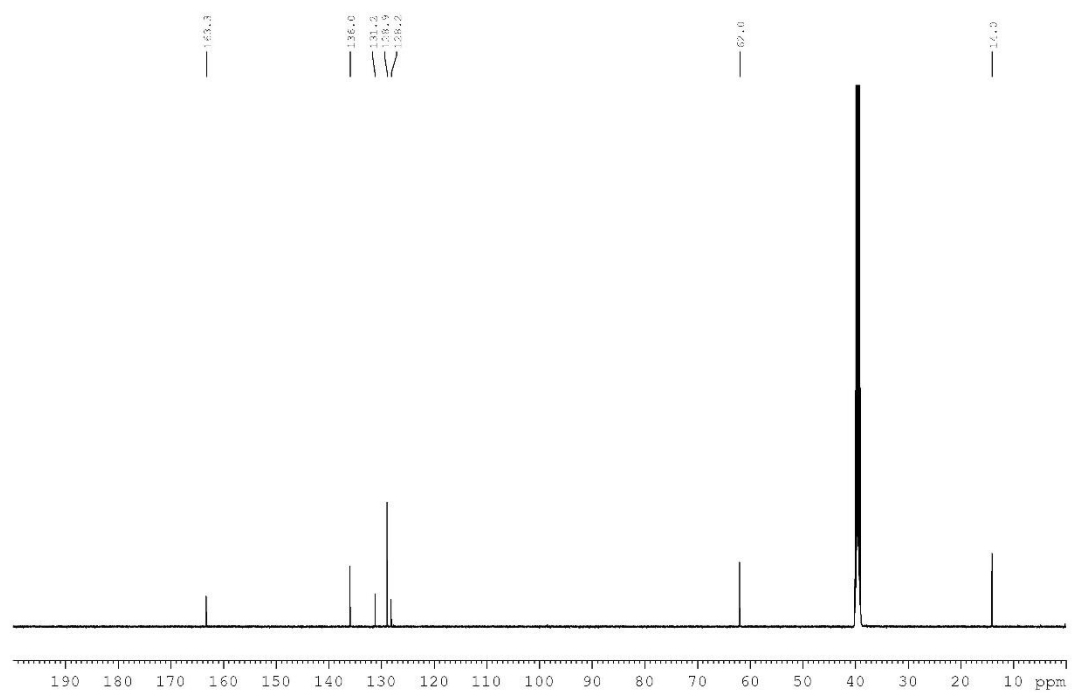
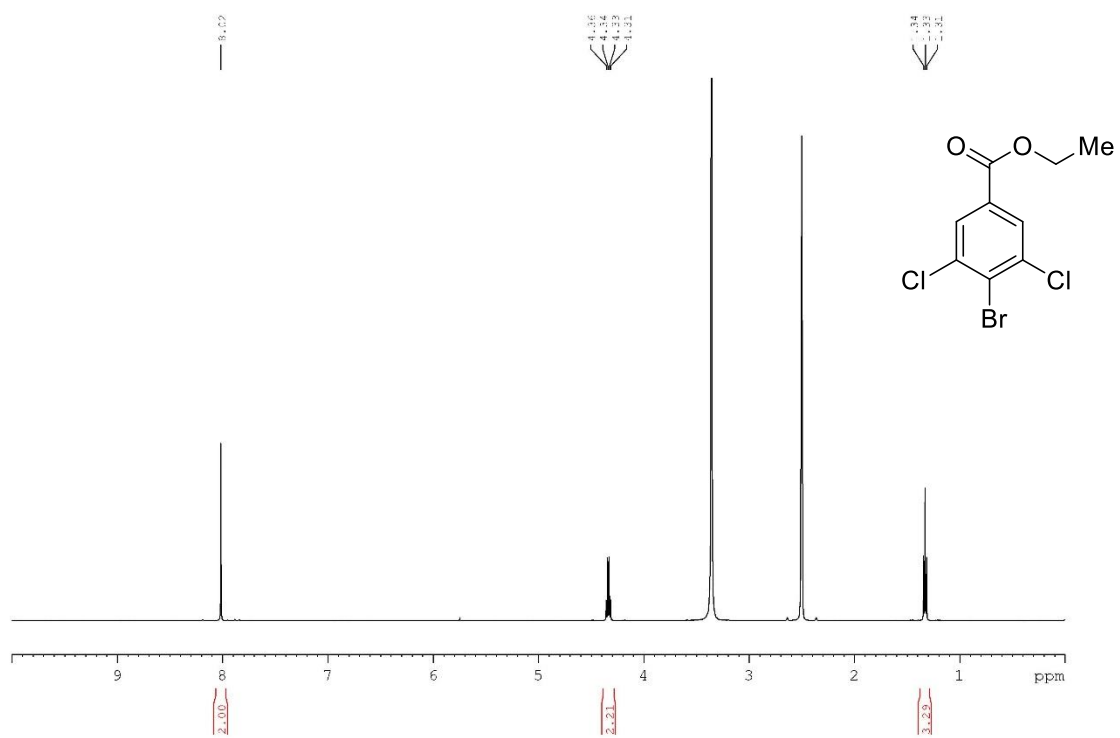
4-ethoxybenzoic acid (73)



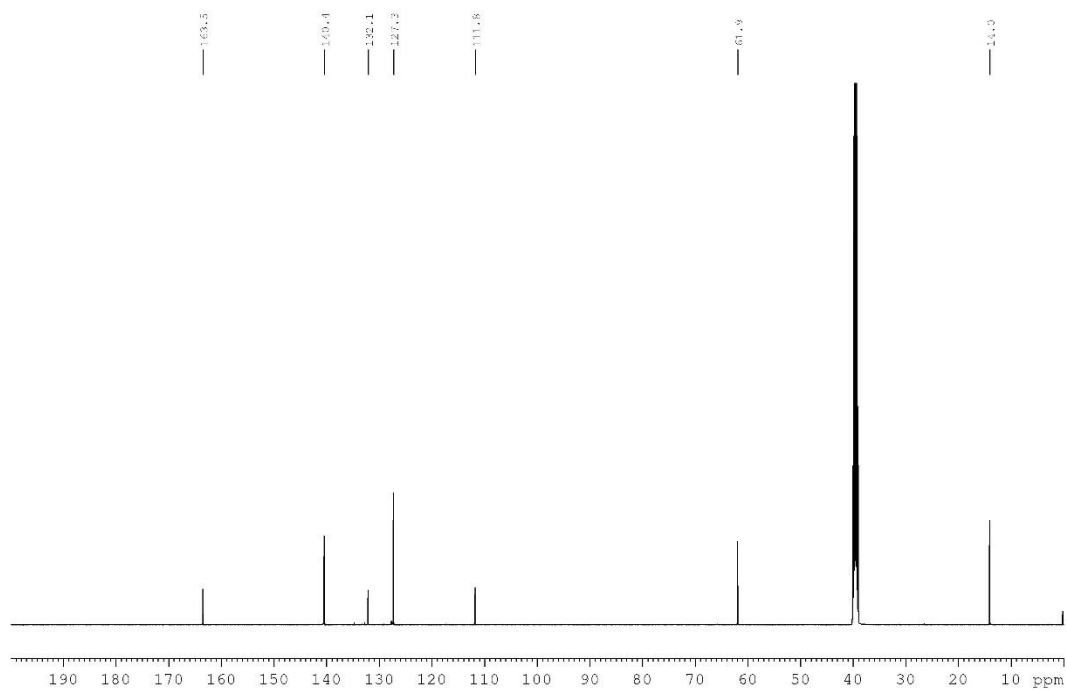
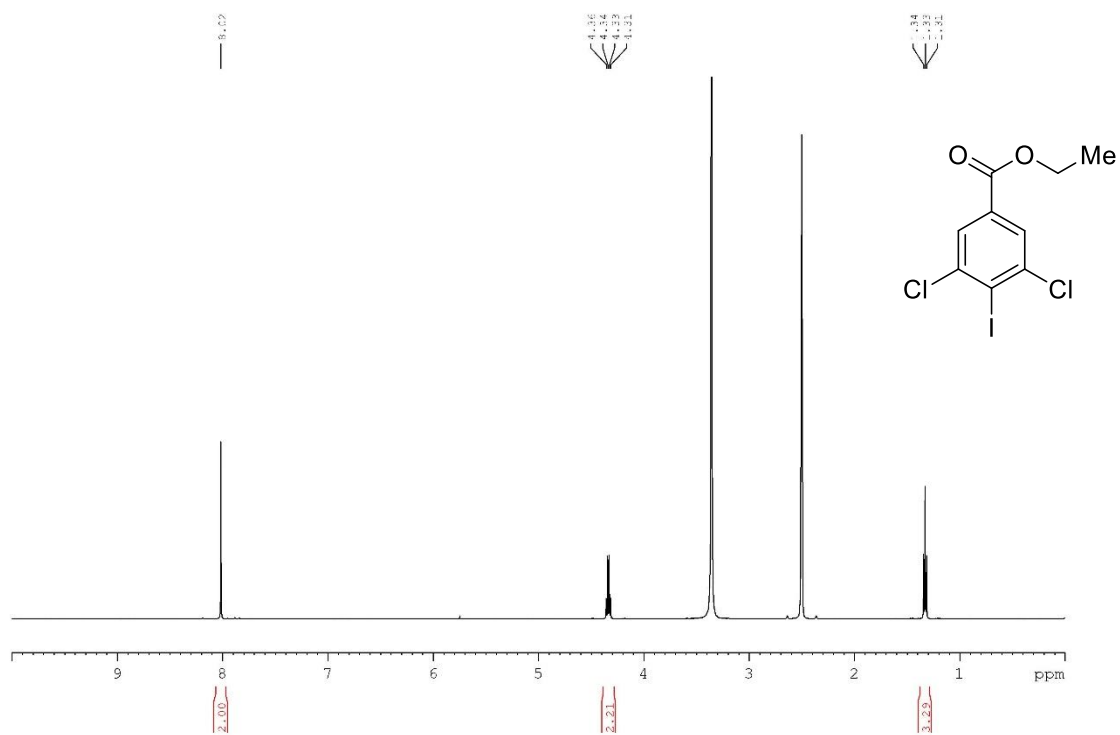
Ethyl 4-amino-3,5-dichlorobenzoate (74b)



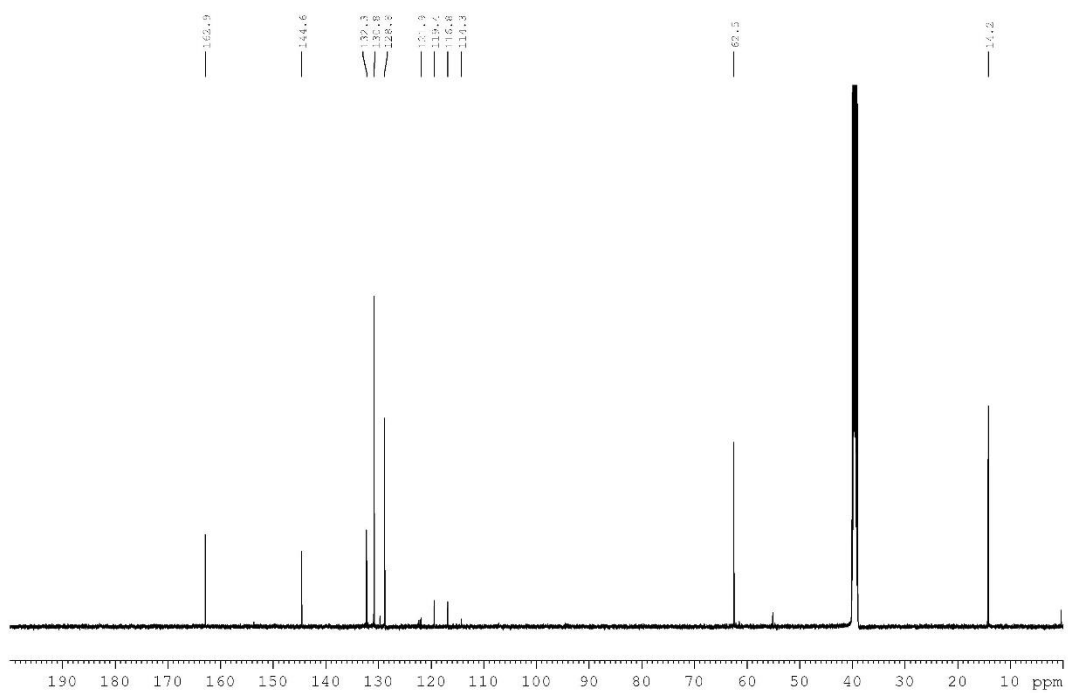
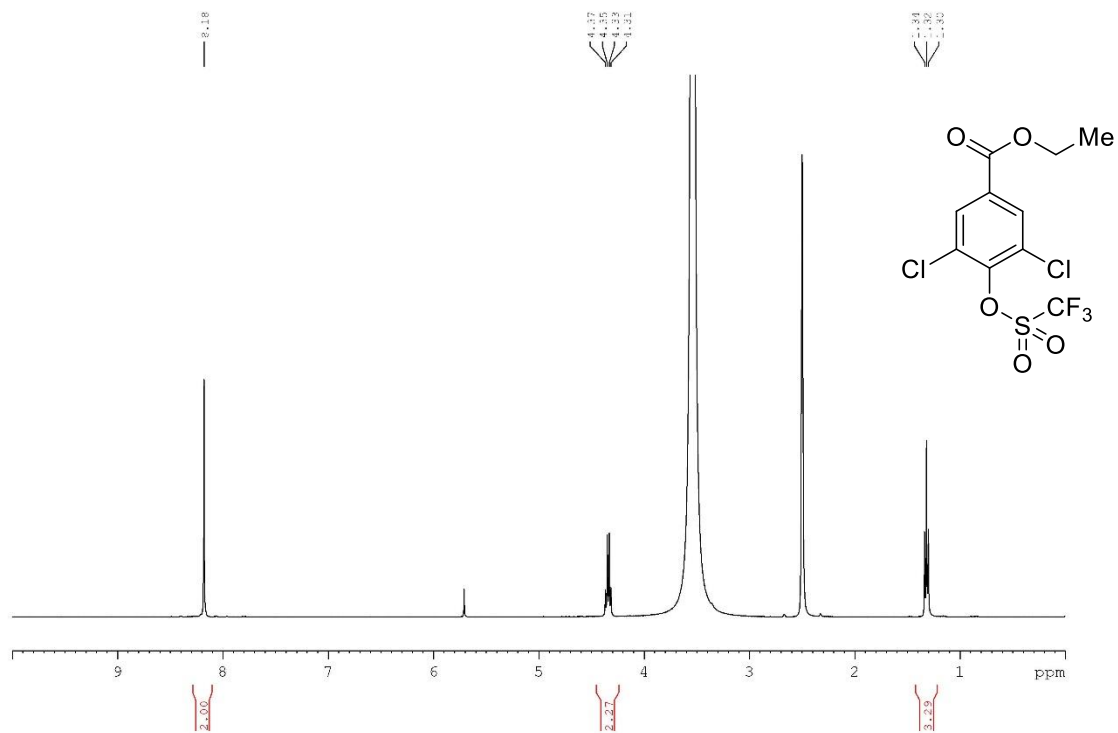
Ethyl 4-bromo-3,5-dichlorobenzoate (74a)



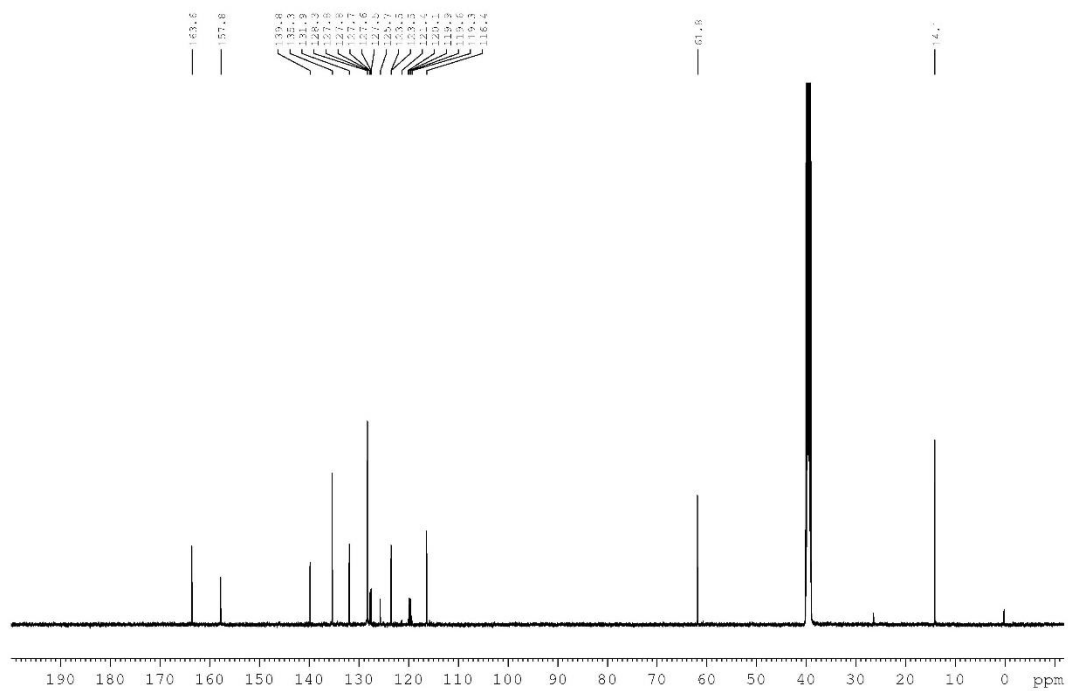
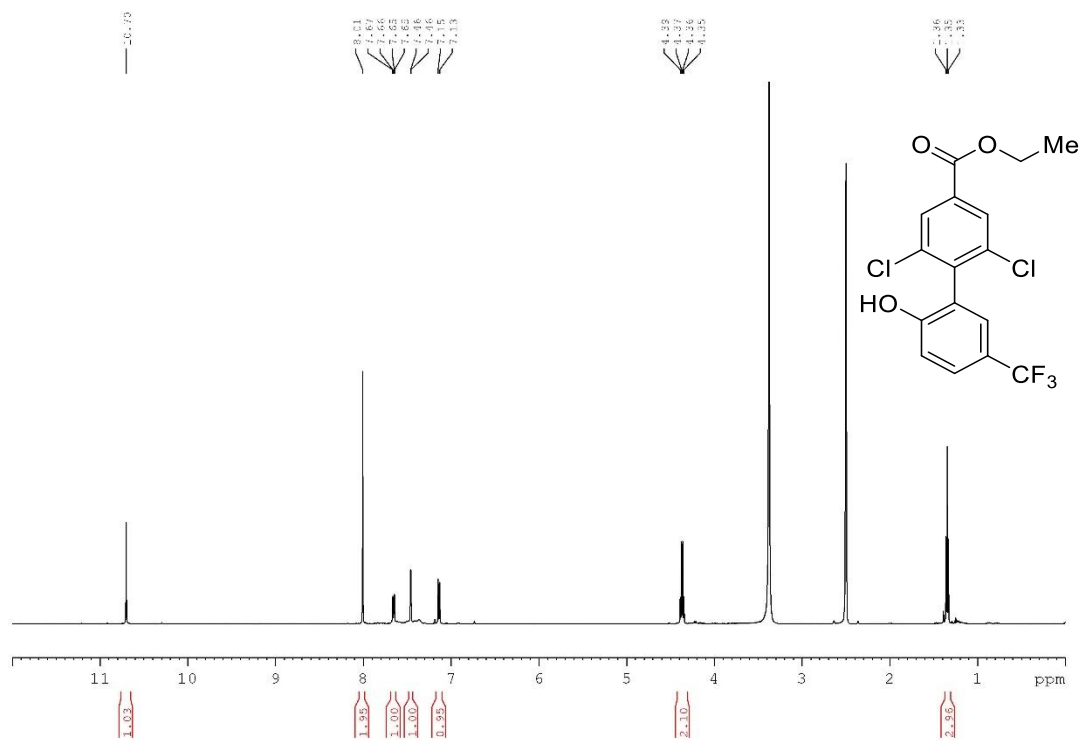
Ethyl 4-iodo-3,5-dichlorobenzoate (74e)



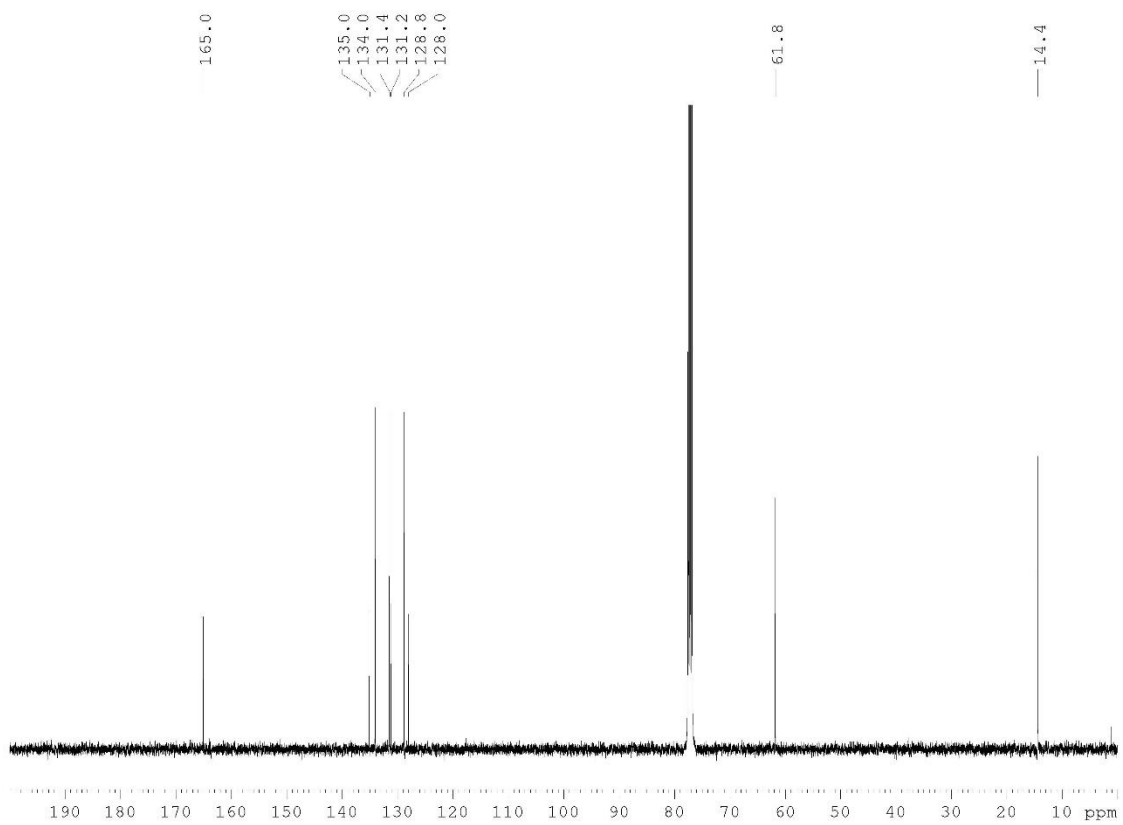
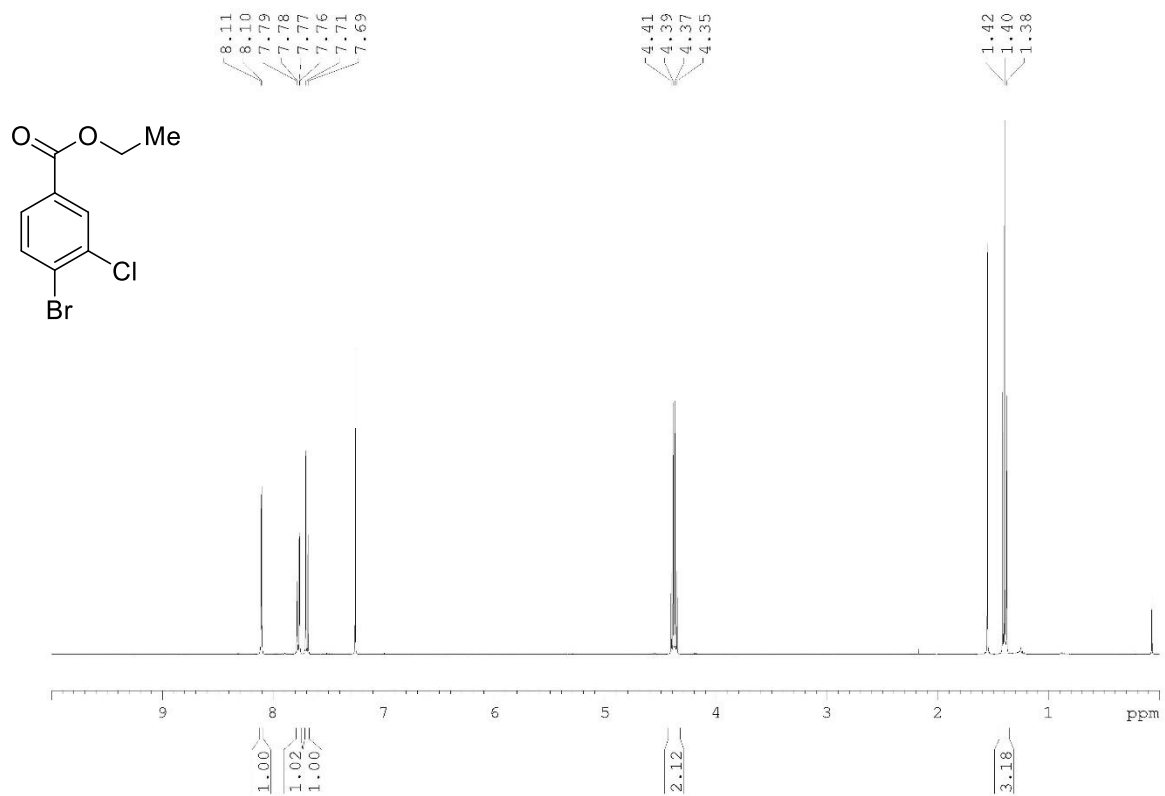
Ethyl 3,5-dichloro-4-(((trifluoromethyl)sulfonyl)oxy)benzoate (74g)



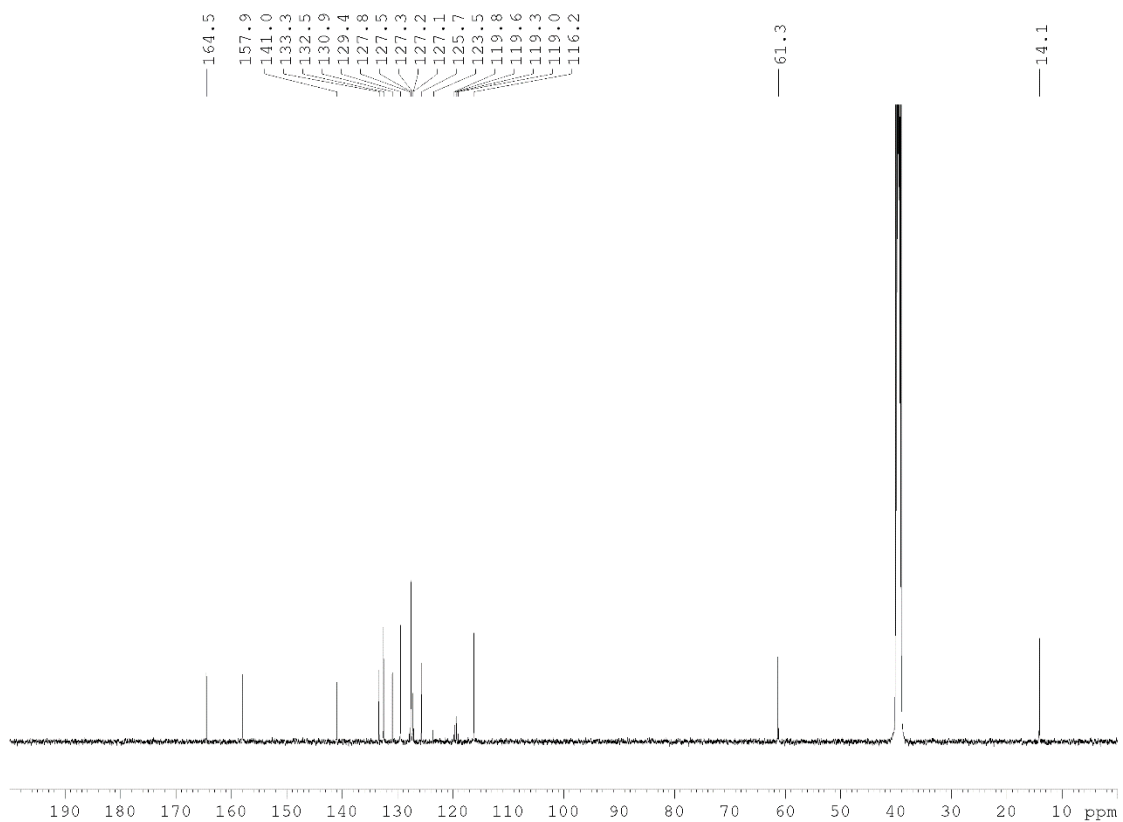
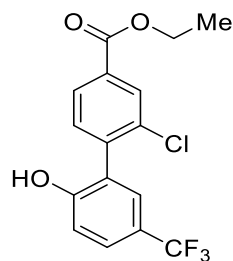
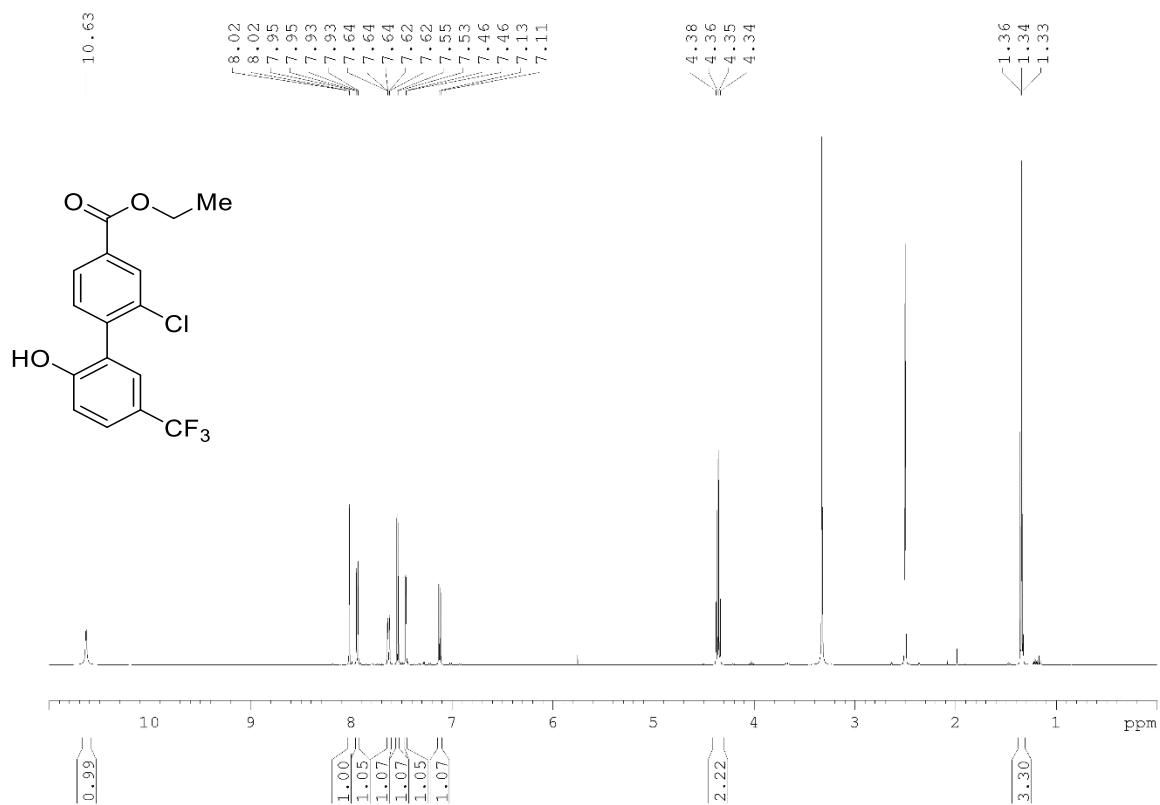
Ethyl 2,6-dichloro-2'-hydroxy-5'-(trifluoromethyl)-[1,1'-biphenyl]-4-carboxylate (74d)



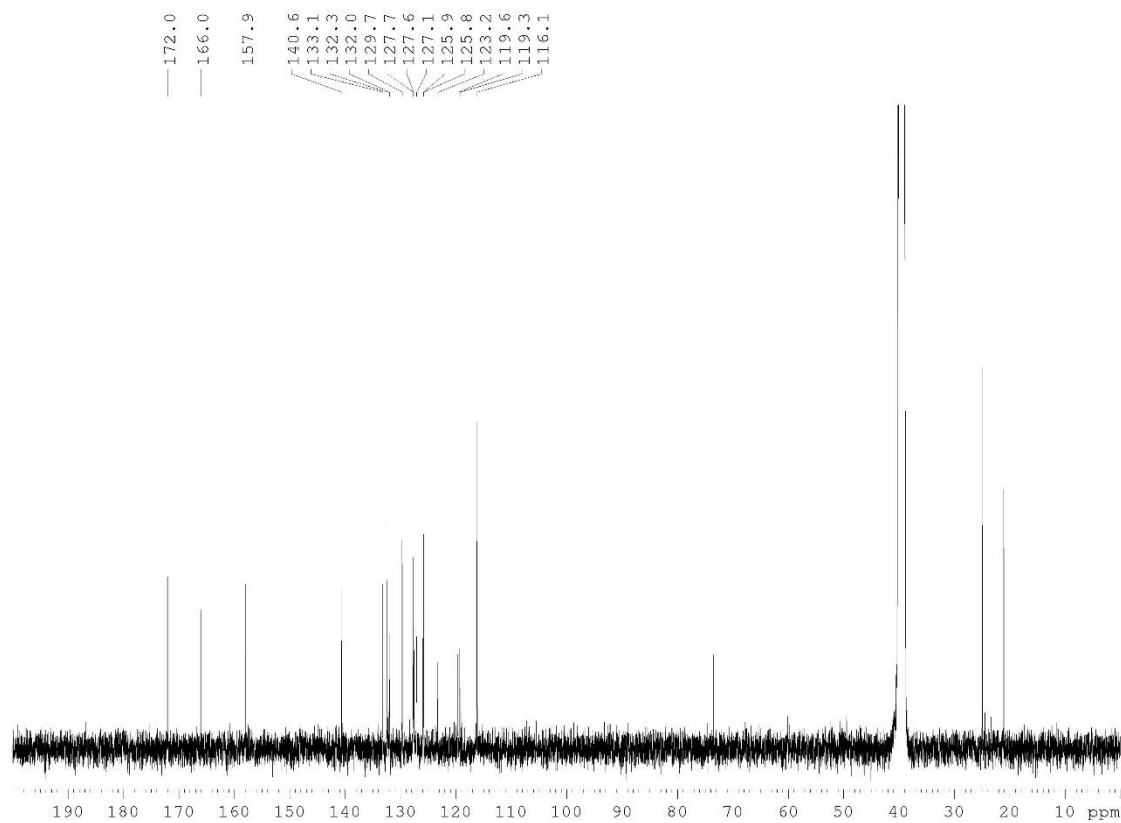
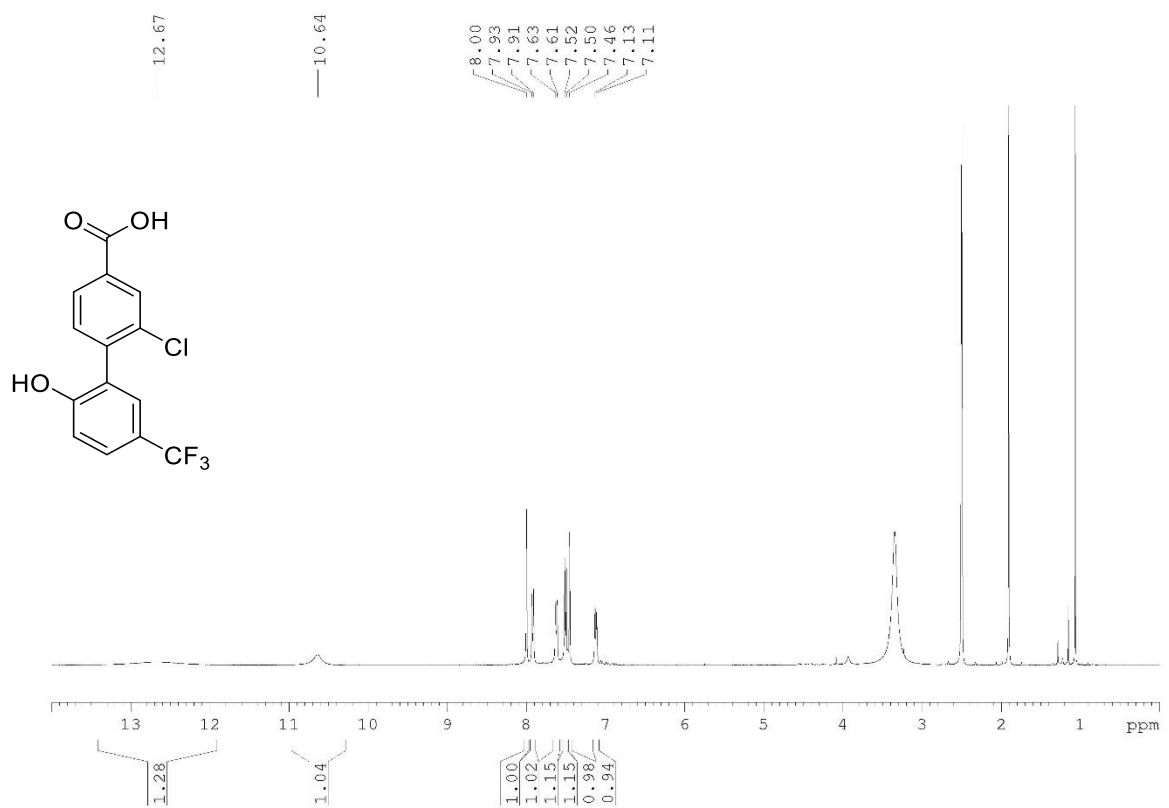
Ethyl 4-bromo-3-chlorobenzoate (76b)



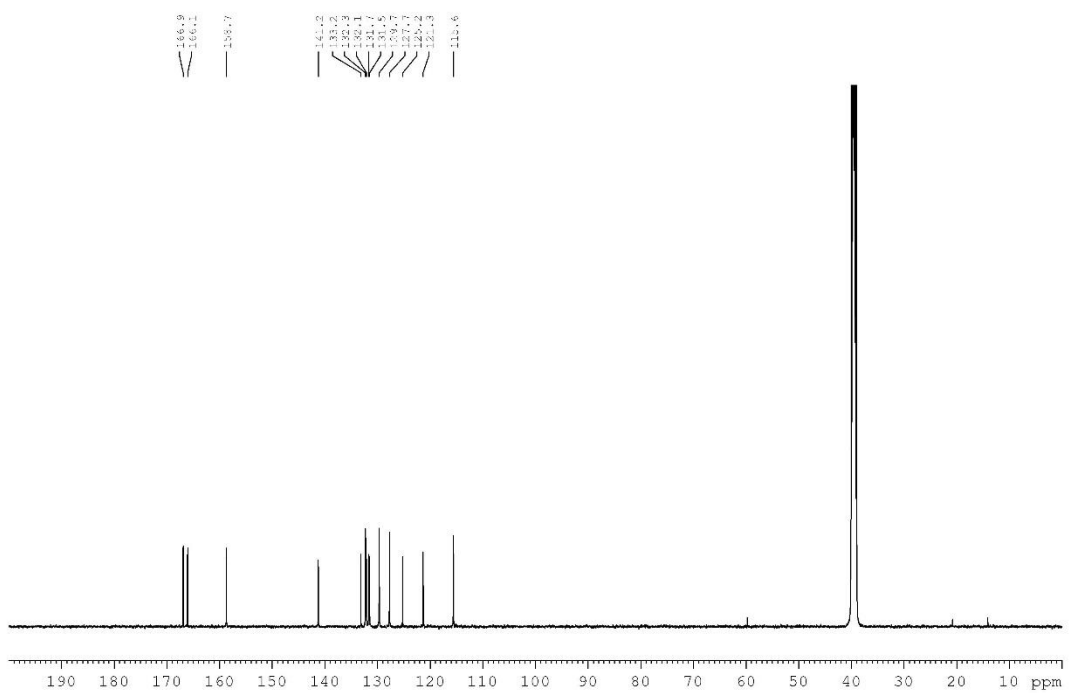
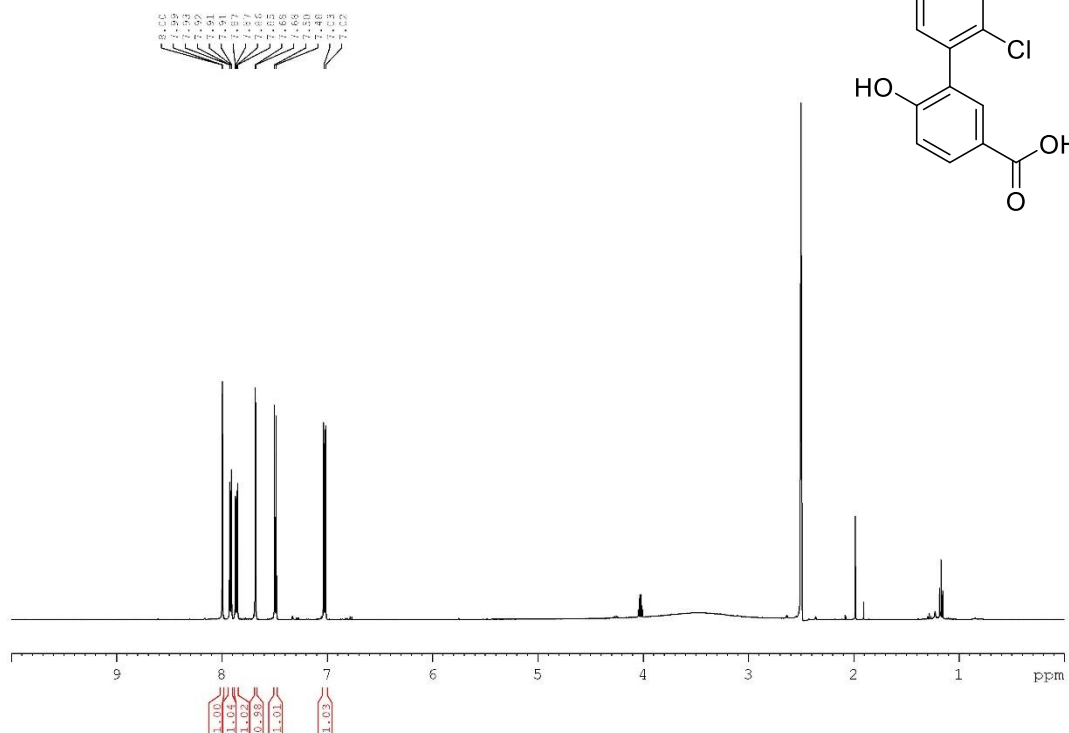
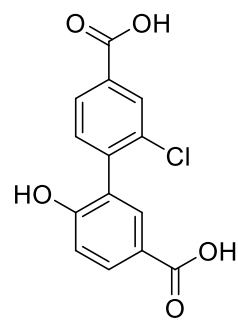
Ethyl 2-chloro-2'-hydroxy-5'-(trifluoromethyl)-[1,1'-biphenyl]-4-carboxylate (76c)



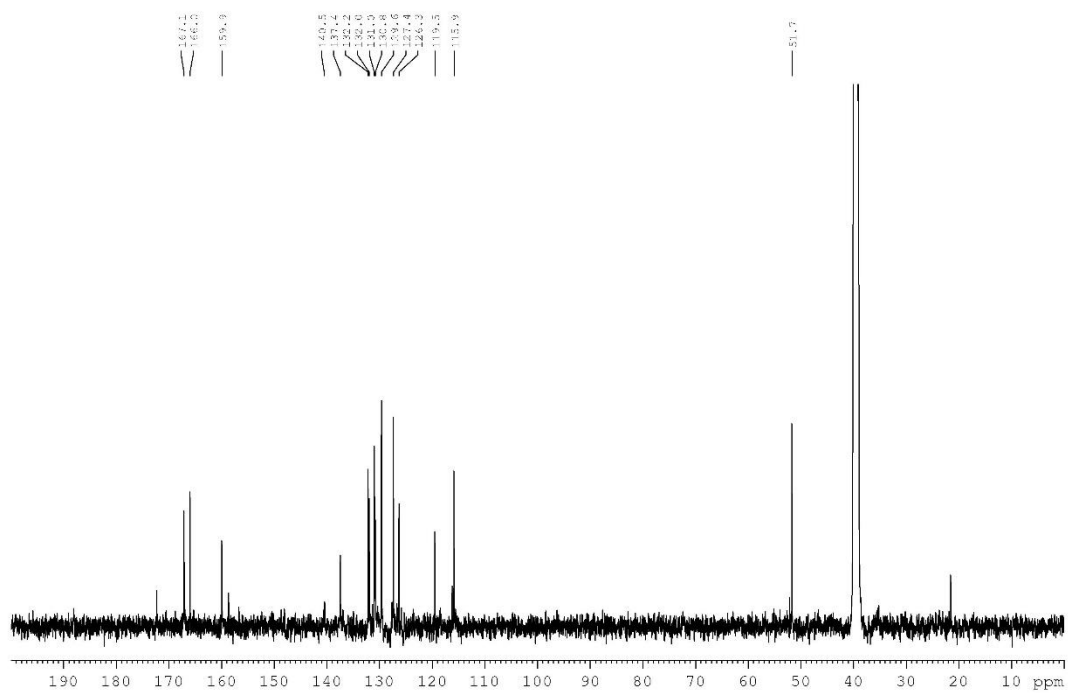
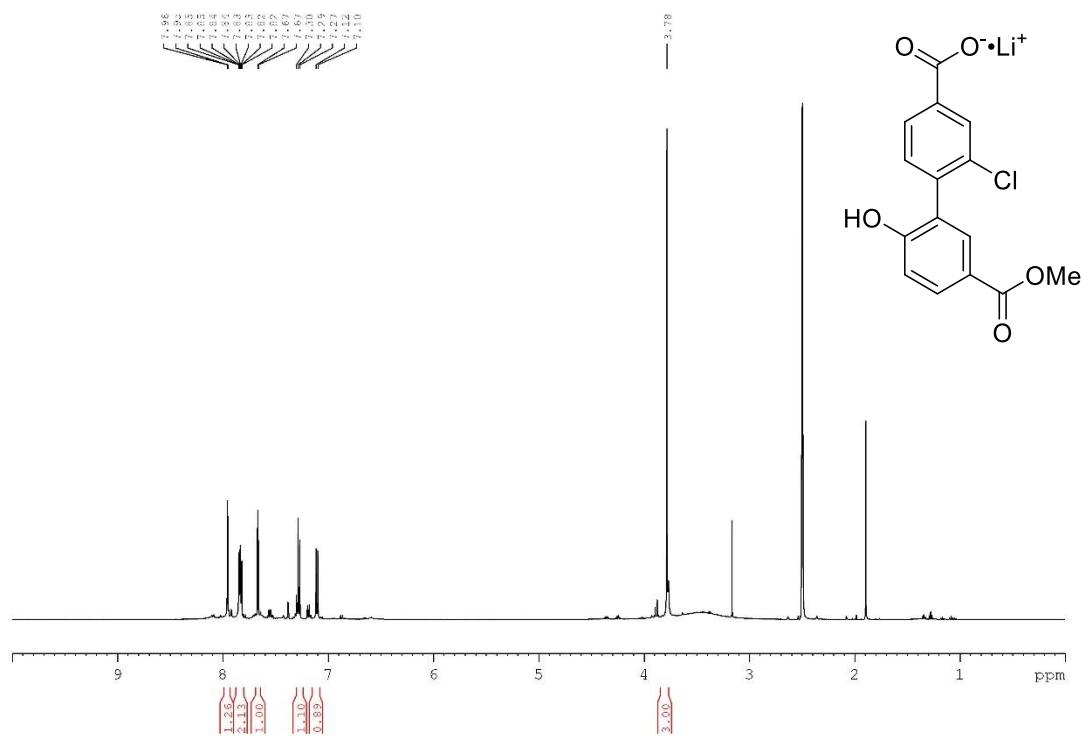
2-Chloro-2'-hydroxy-5'-(trifluoromethyl)-[1,1'-biphenyl]-4-carboxylic acid (76)



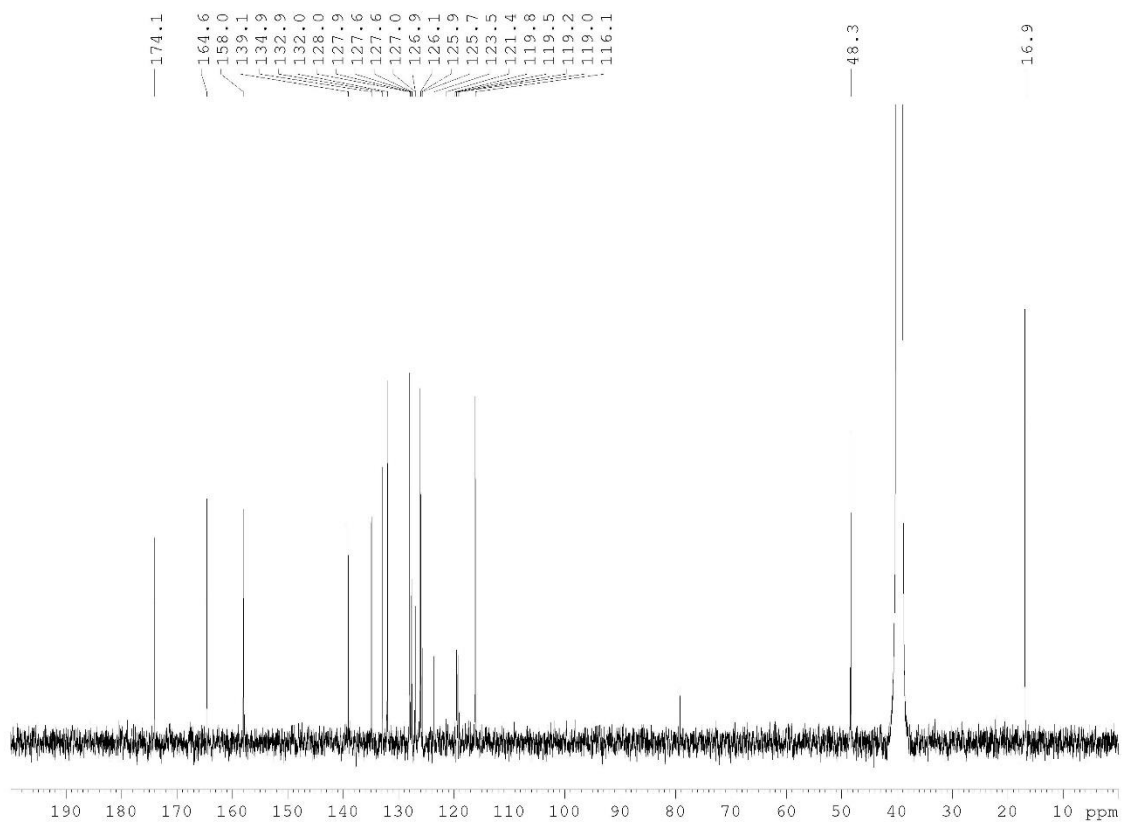
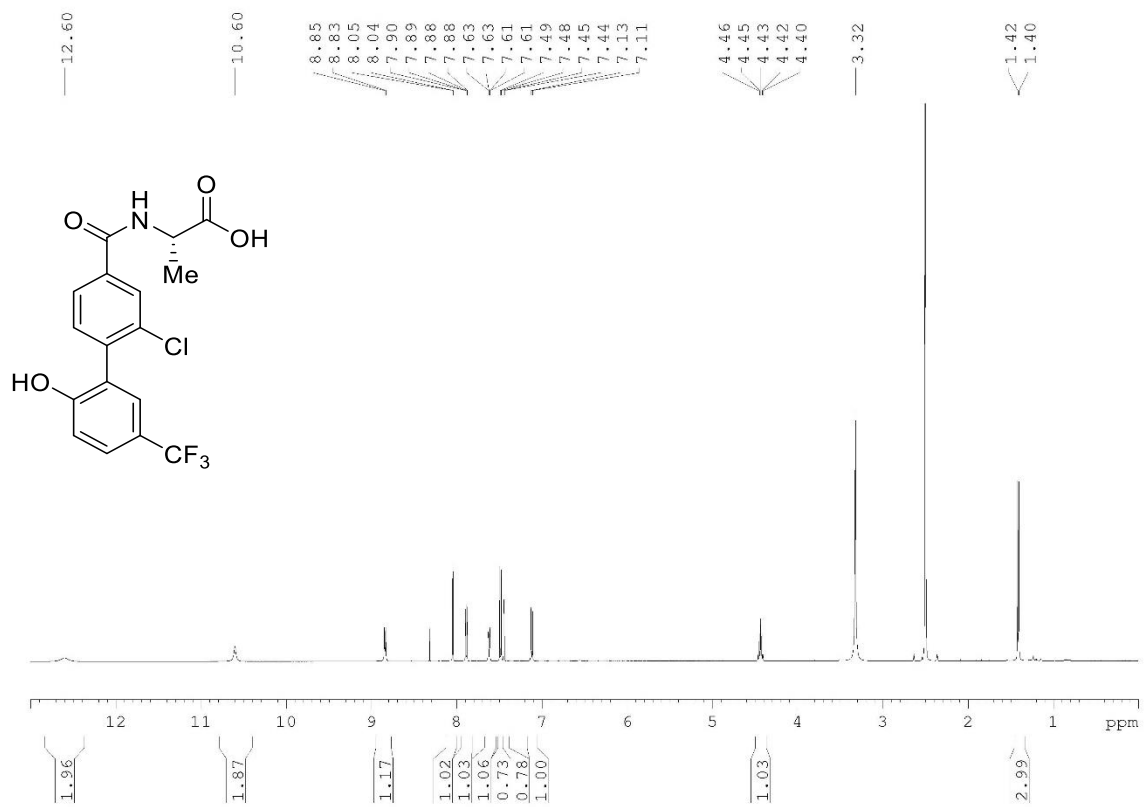
2'-Chloro-6-hydroxy-[1,1'-biphenyl]-3,4'-dicarboxylic acid (77)



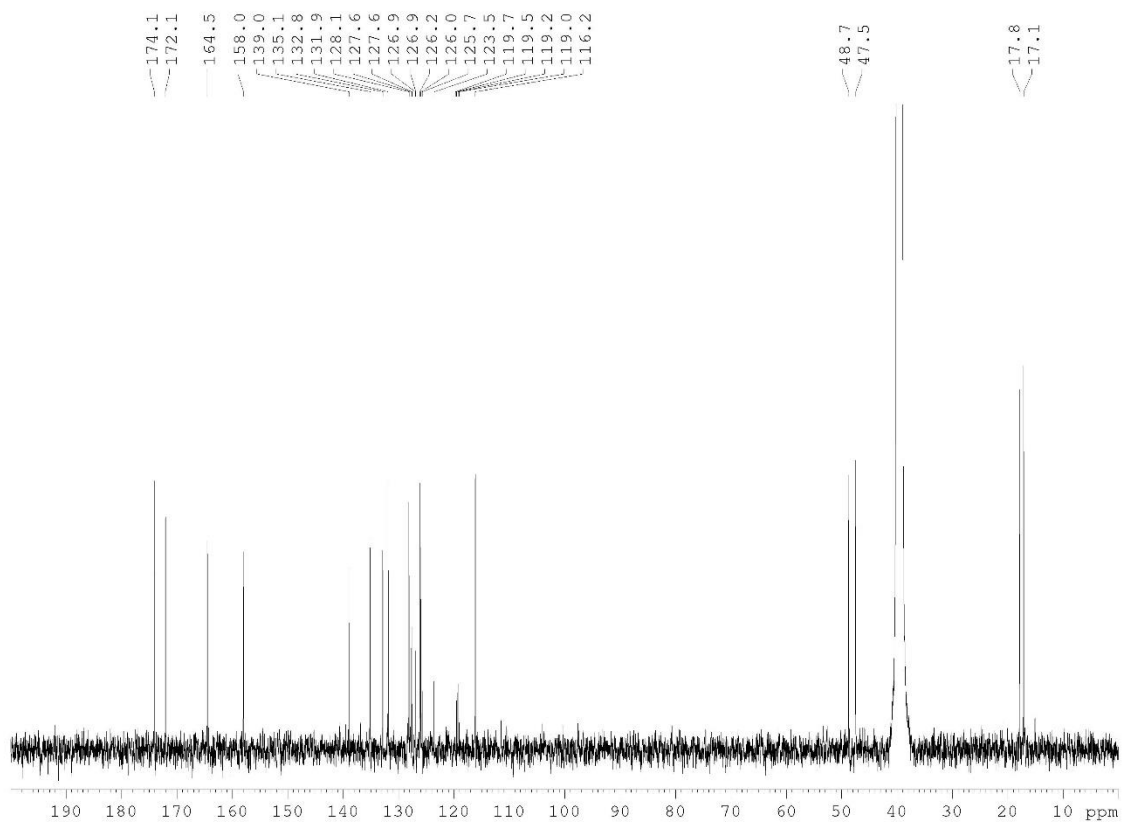
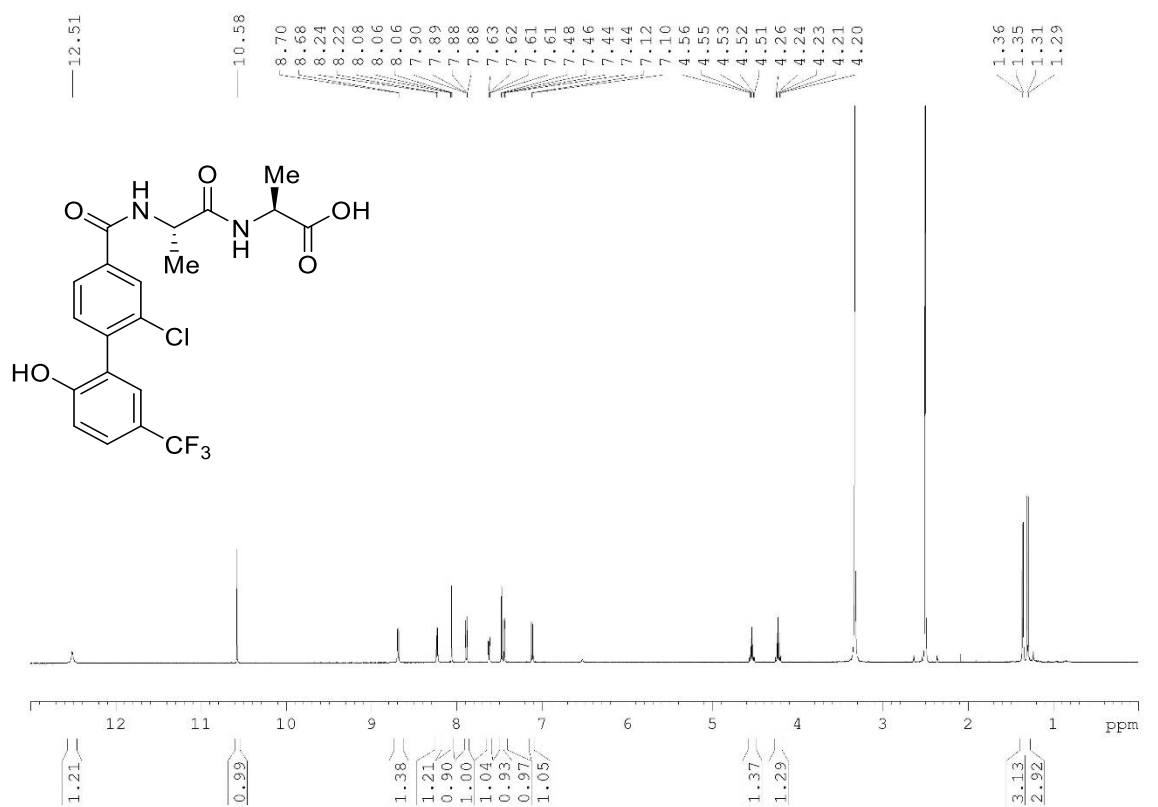
Lithium 2-chloro-2'-hydroxy-5'-(methoxycarbonyl)-[1,1'-biphenyl]-4-carboxylate (79)



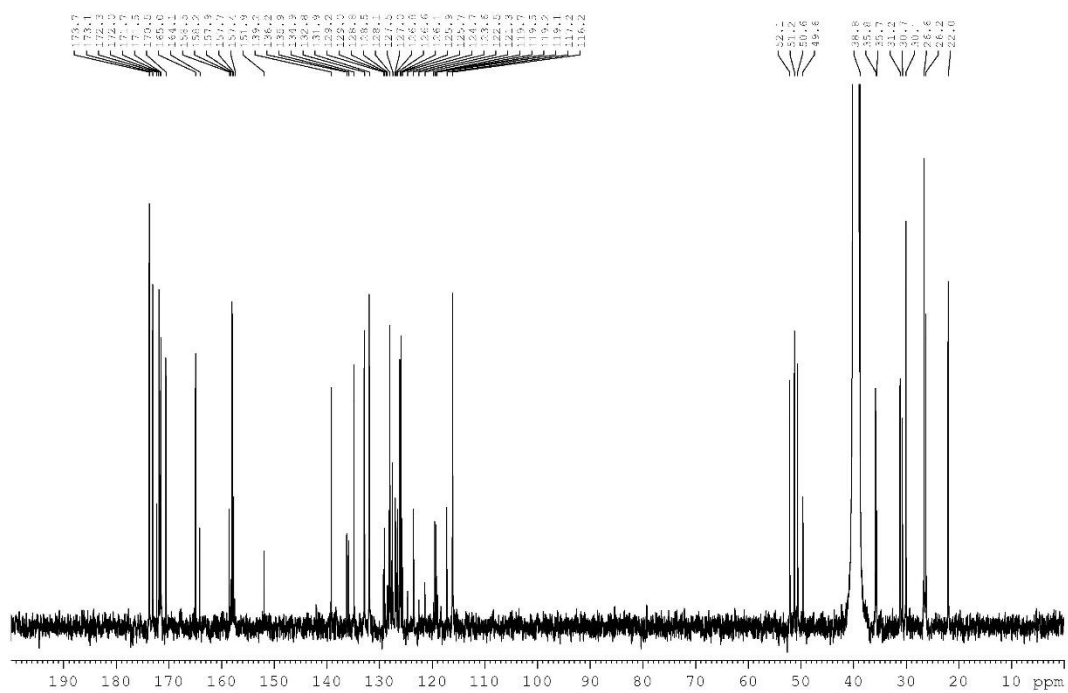
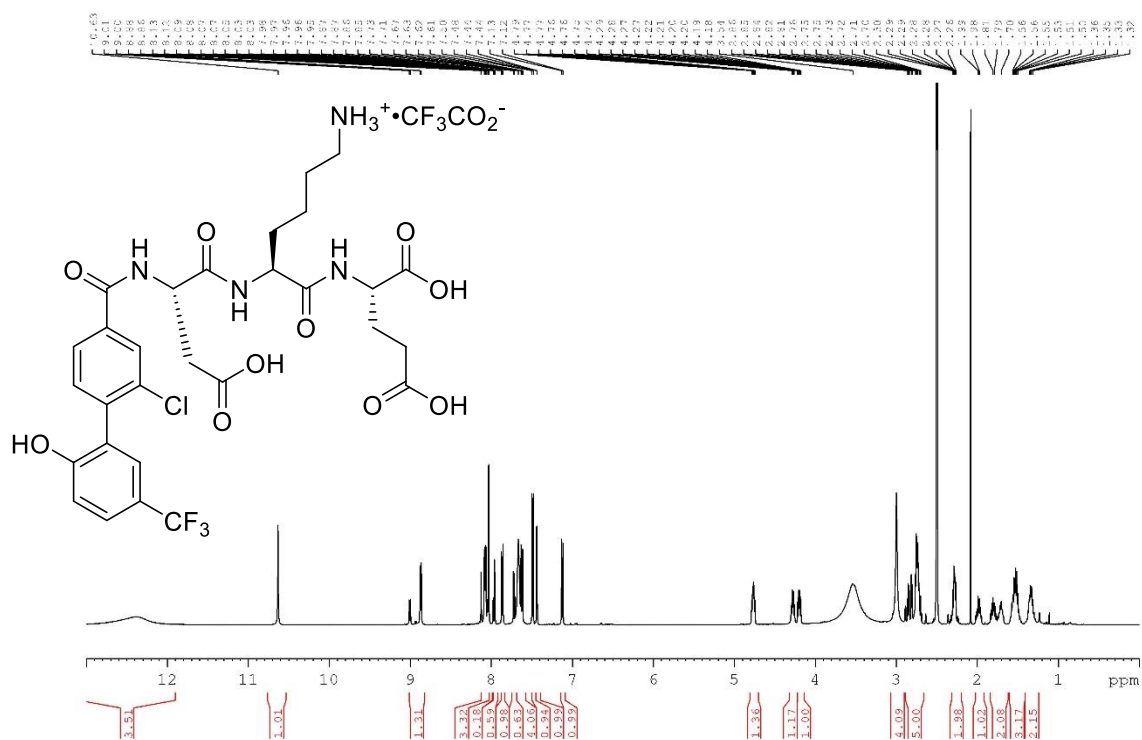
(2-Chloro-2'-hydroxy-5'-(trifluoromethyl)-[1,1'-biphenyl]-4-carbonyl)-L-alanine (92)



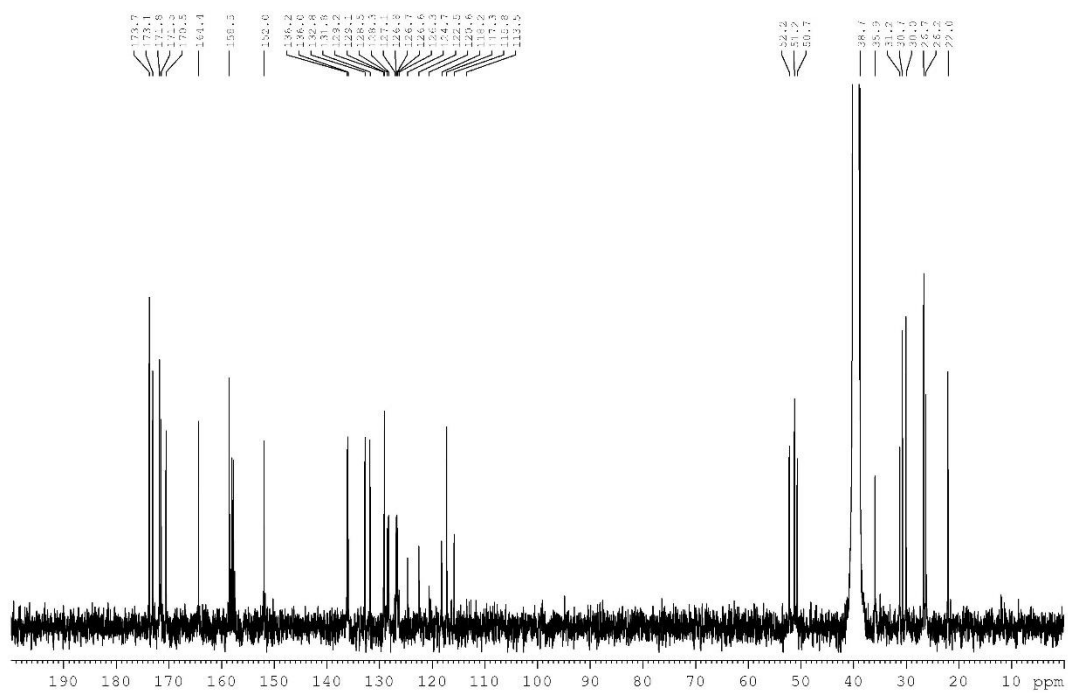
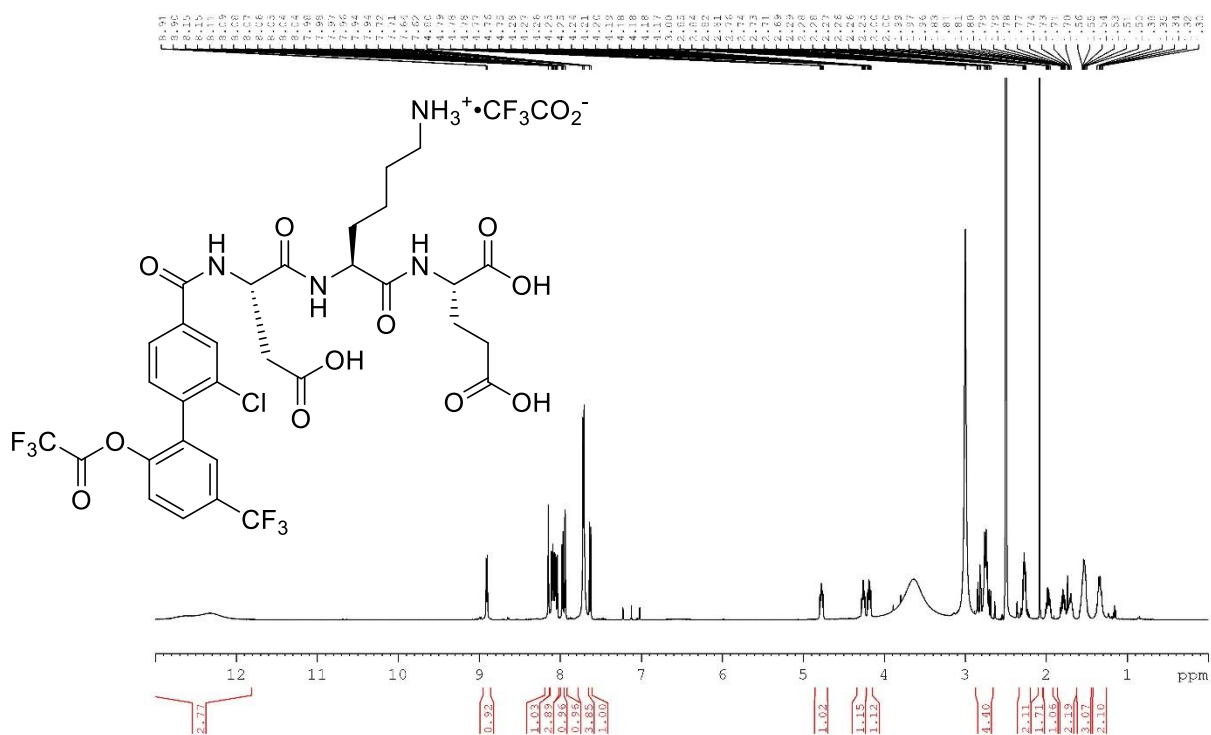
(2-Chloro-2'-hydroxy-5'-(trifluoromethyl)-[1,1'-biphenyl]-4-carbonyl)-L-alanyl-L-alanine (93)



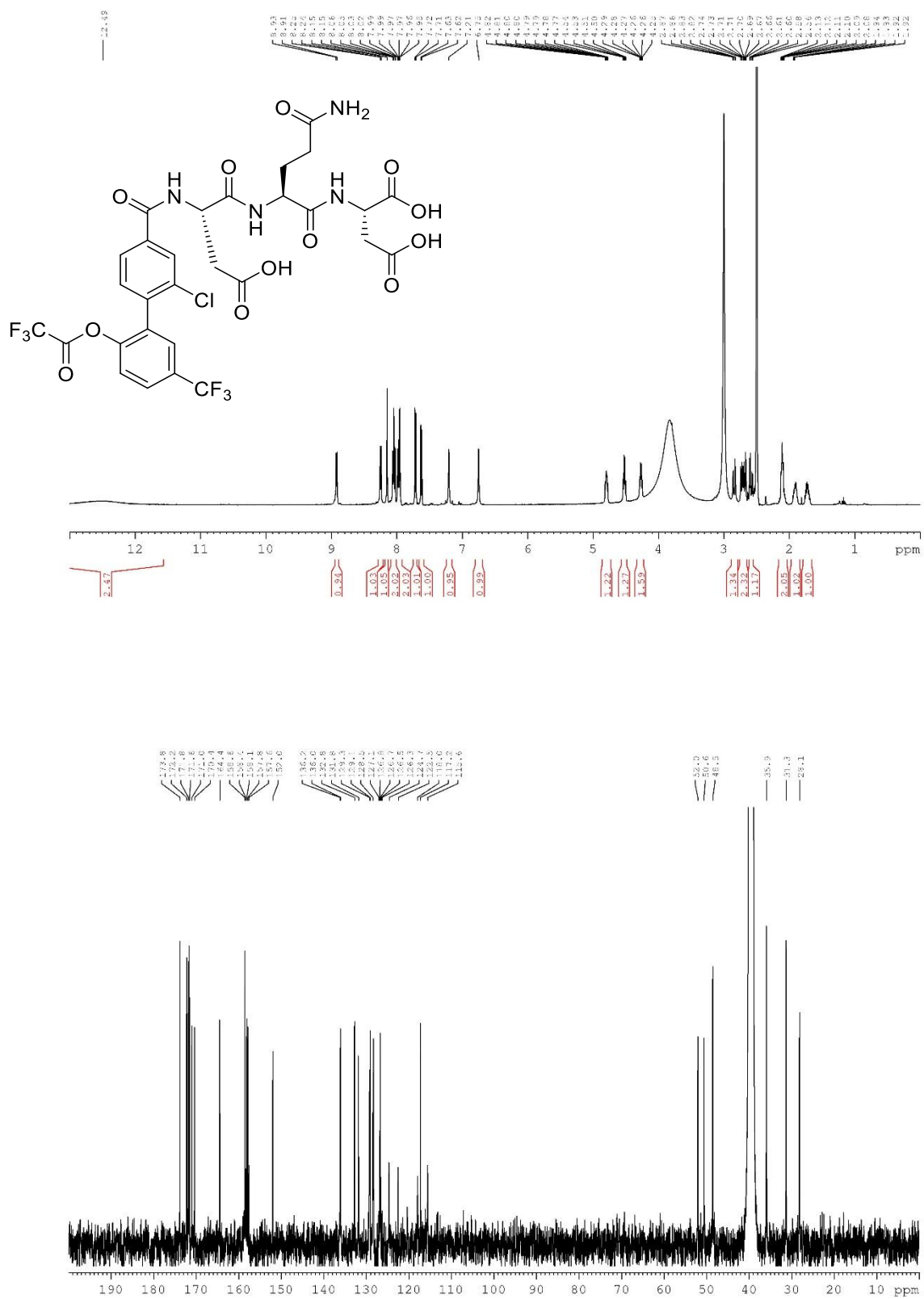
(2-Chloro-2'-hydroxy-5'-(trifluoromethyl)-[1,1'-biphenyl]-4-carbonyl)-L-aspartyl-L-lysyl-L-glutamic acid TFA salt (99)



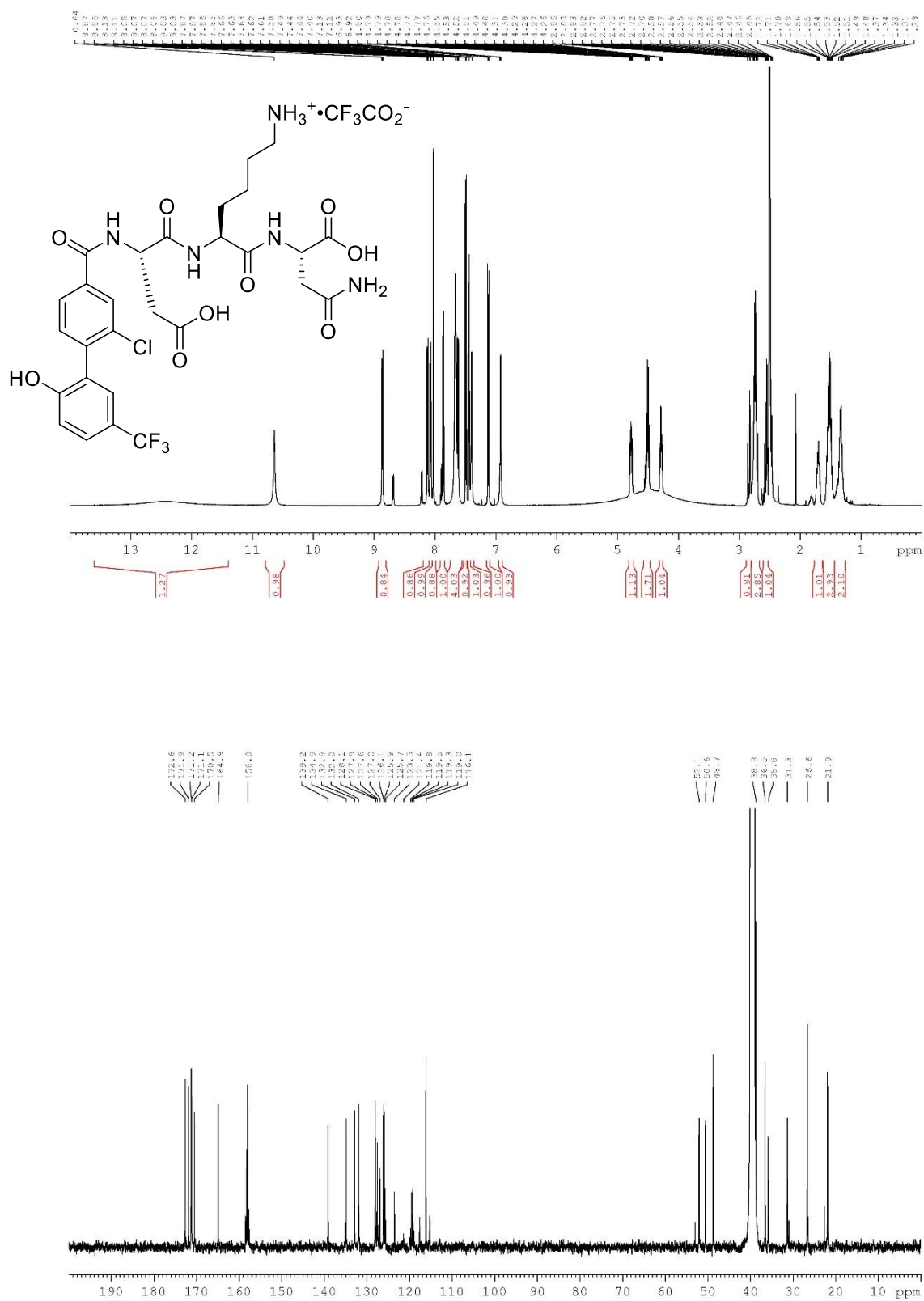
(2-Chloro-2'-(2,2,2-trifluoroacetoxy)-5'-(trifluoromethyl)-[1,1'-biphenyl]-4-carbonyl)-L-aspartyl-L-lysyl-L-glutamic acid TFA salt (99a)



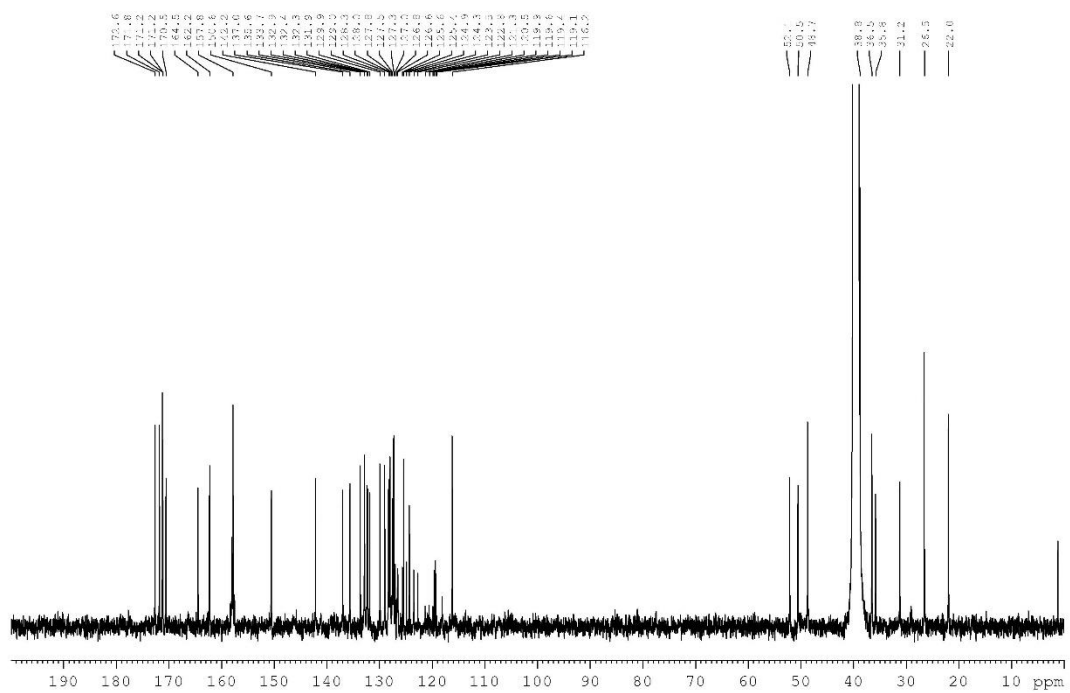
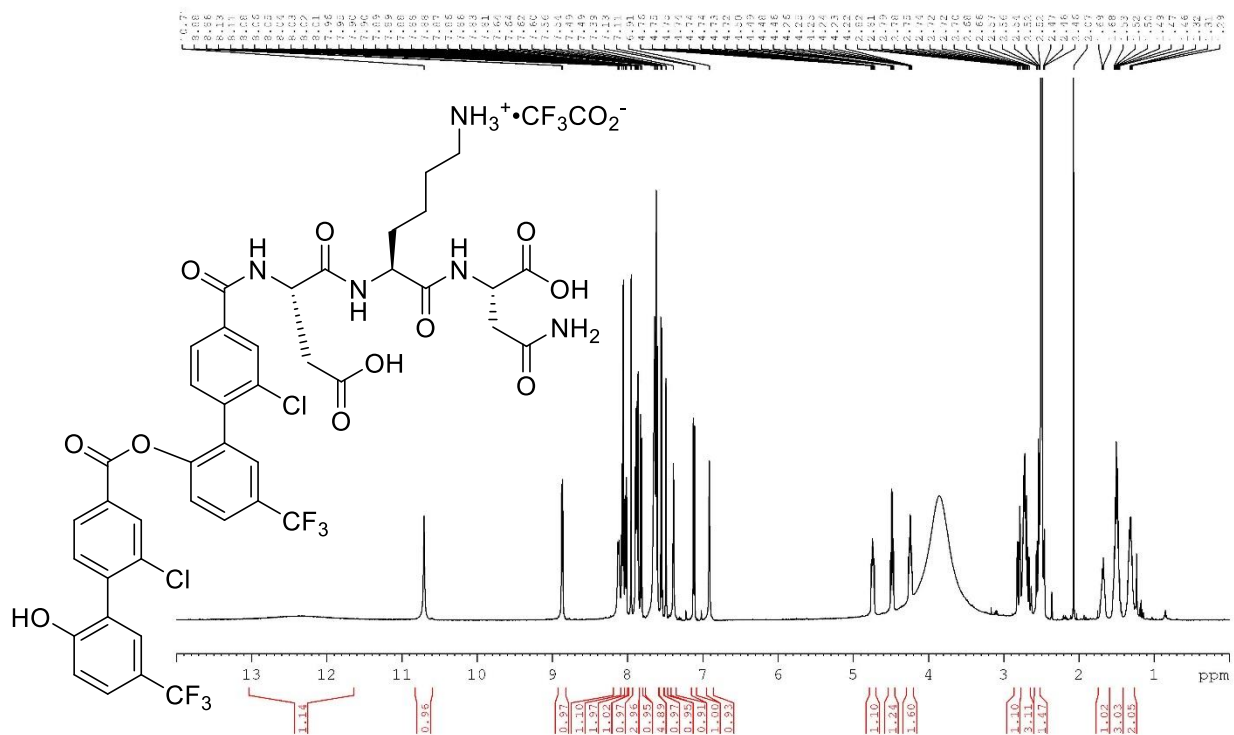
(2-Chloro-2'-(2,2,2-trifluoroacetoxy)-5'-(trifluoromethyl)-[1,1'-biphenyl]-4-carbonyl)-L-aspartyl-L-glutaminy-L-aspartic acid (100a)



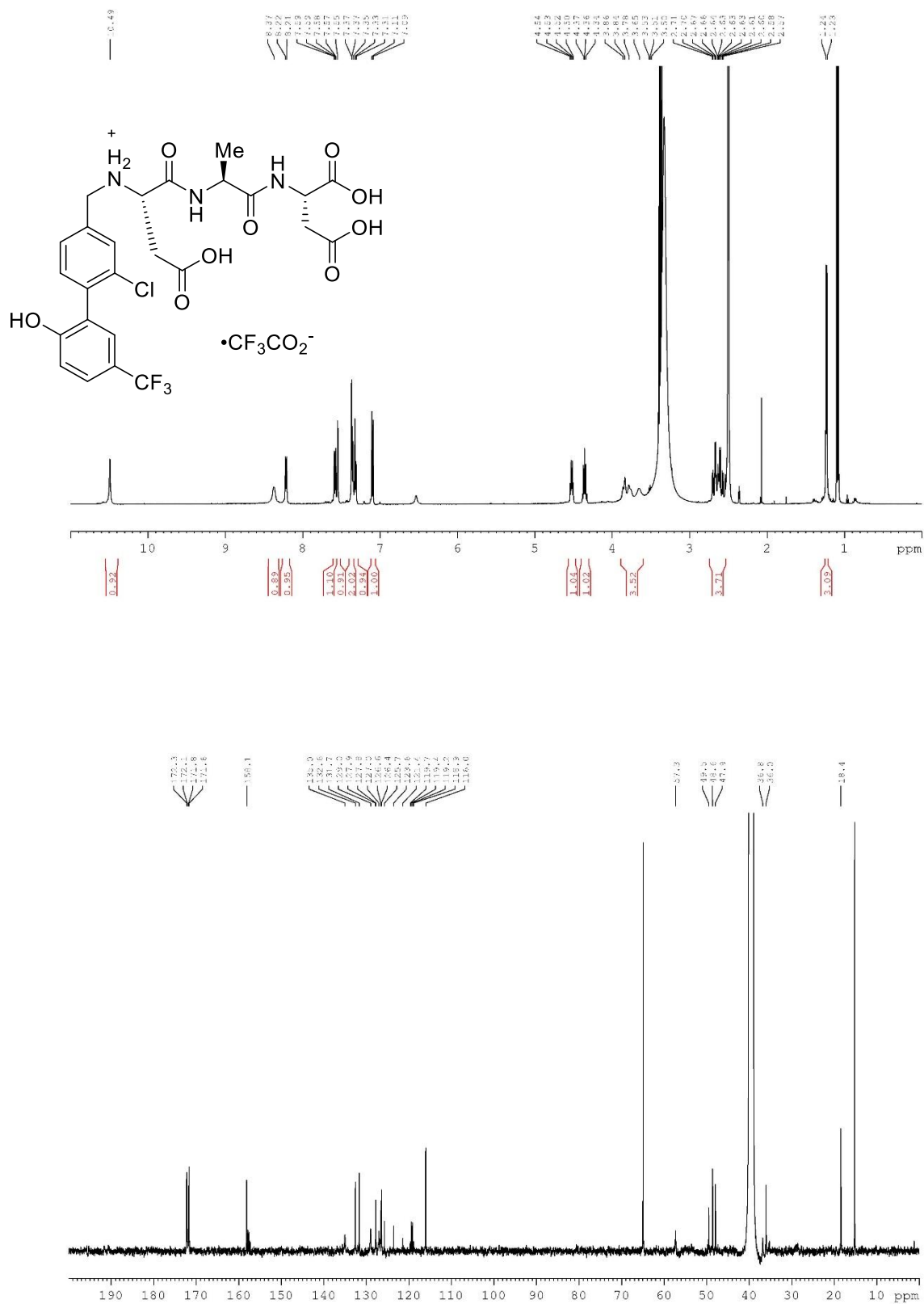
(2-Chloro-2'-hydroxy-5'-(trifluoromethyl)-[1,1'-biphenyl]-4-carbonyl)-L-aspartyl-L-lysyl-L-asparagine TFA salt (101)



(2-Chloro-2'-((2-chloro-2'-hydroxy-5'-(trifluoromethyl)-[1,1'-biphenyl]-4-carbonyl)oxy)-5'-(trifluoromethyl)-[1,1'-biphenyl]-4-carbonyl)-L-aspartyl-L-lysyl-L-asparagine TFA salt (101a)



((2-Chloro-2'-hydroxy-5'-(trifluoromethyl)-[1,1'-biphenyl]-4-yl)methyl)-L-aspartyl-L-alanyl-L-aspartic acid TFA salt (107)

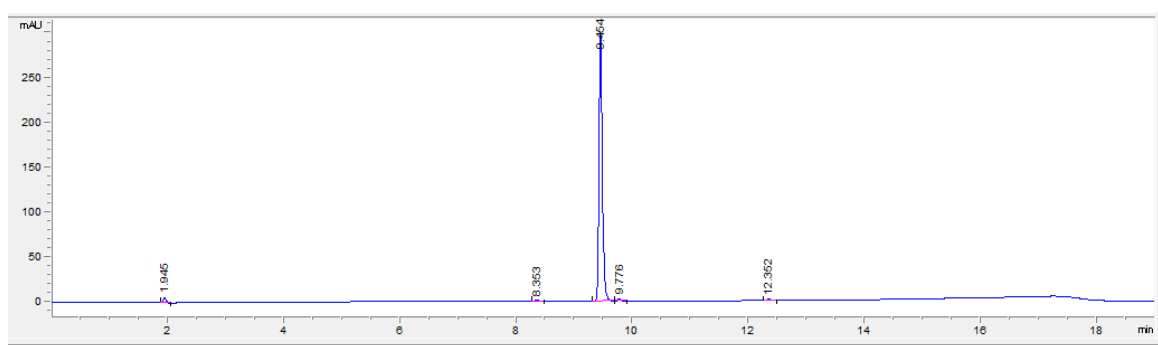


Appendix 1B: Analytical HPLC Traces for Selected Peptides

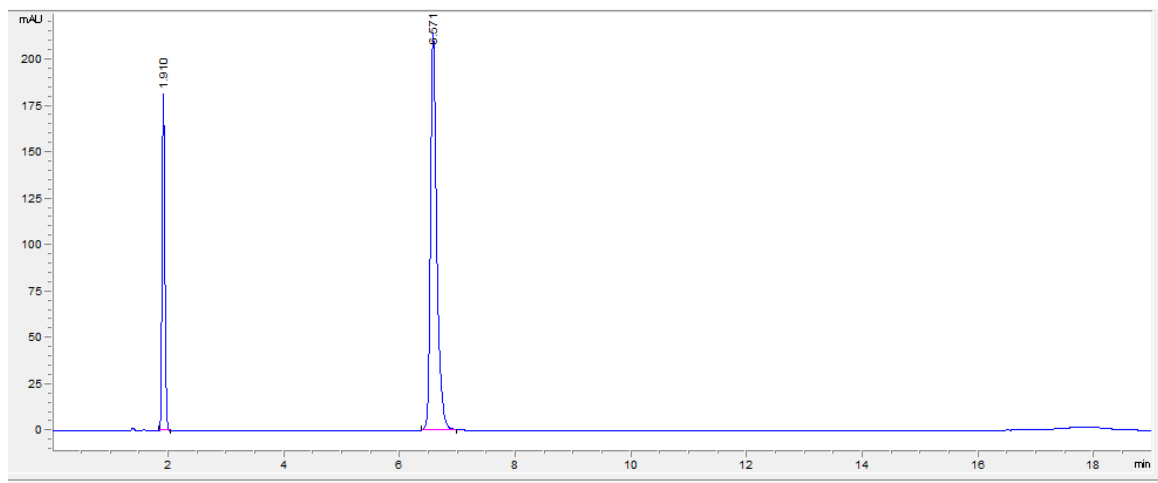
HPLC traces refer to the analytical HPLC trace of purified peptide samples. The percentage in brackets above each trace refers to the linear gradient of solvent B (0.05% (v/v) TFA in acetonitrile) where solvent A is 0.05% (v/v) TFA in water. Data collected over 15 min at a flow rate of 1 mL min⁻¹ and UV detection ($\lambda_{\text{max}} = 220 \text{ nm}$ and 254 nm). Retention times (t_r) are reported in the peptide experimental section.

95 (78-AADD-OH)

(5-95% B)

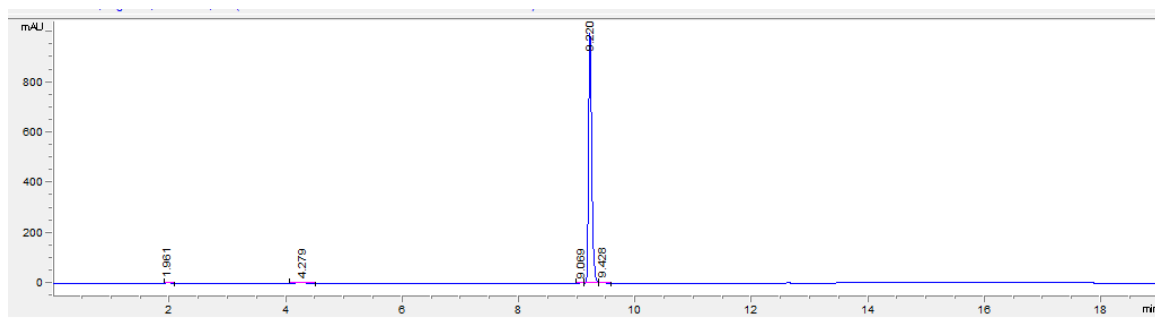


(30-80% B)

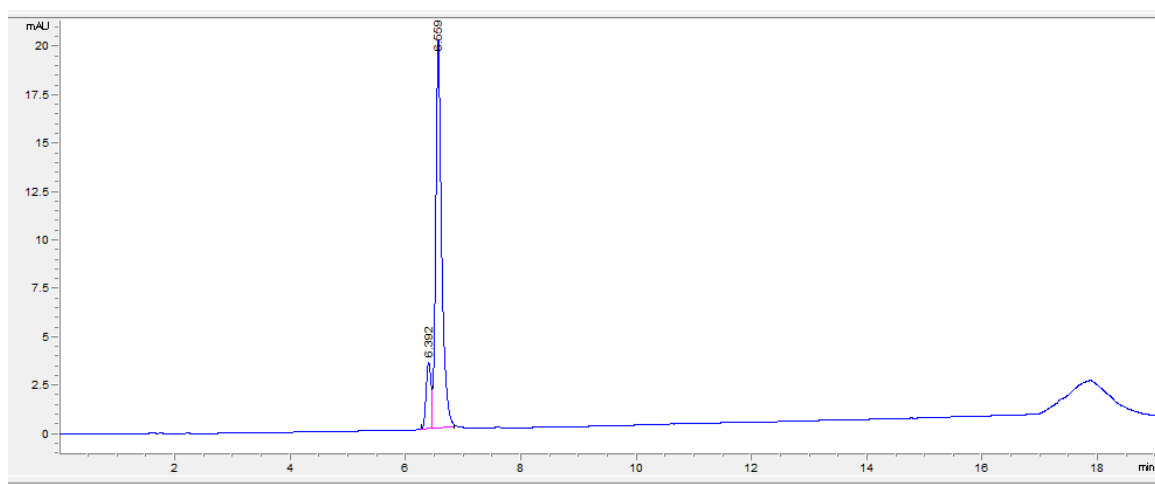


96 (78-AADD-NH₂)

(5-95% B)

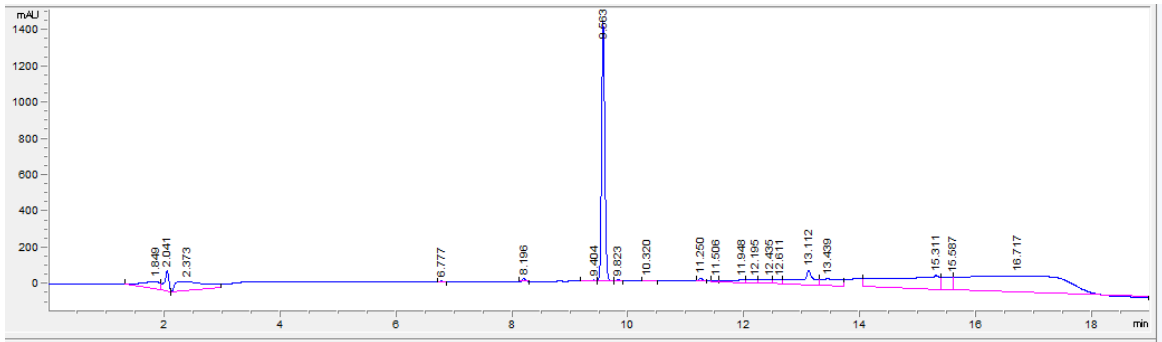


(30-80% B)

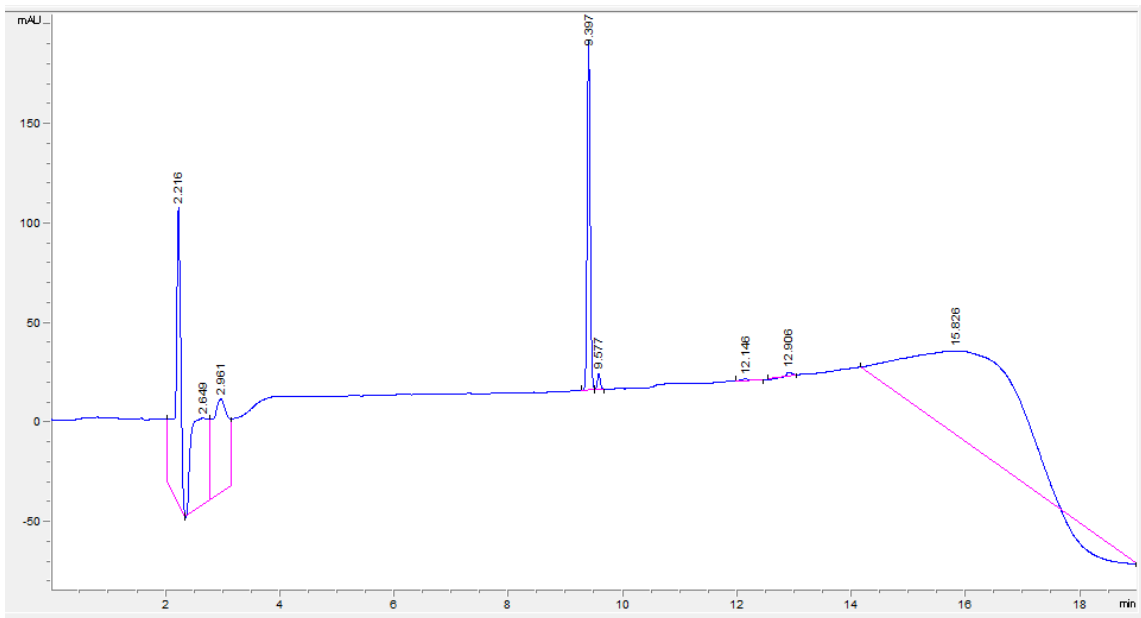


105 (78-PGGD-OH)

(5-95% B)

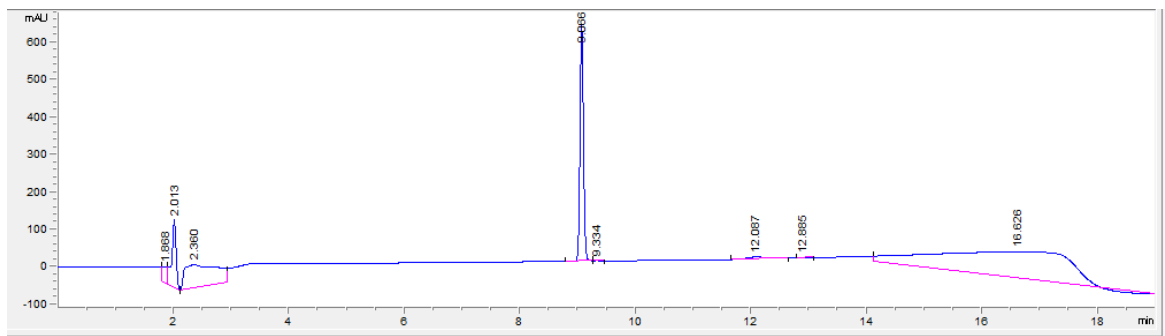


(20-60% B)

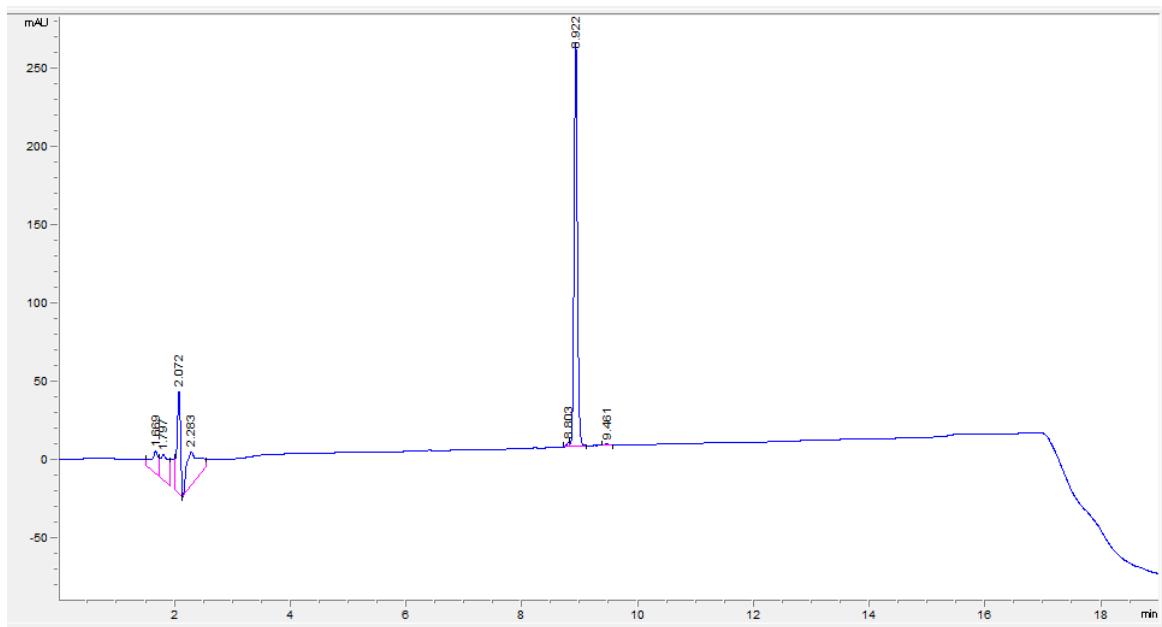


106 (78-PGGN-OH)

(5-95% B)

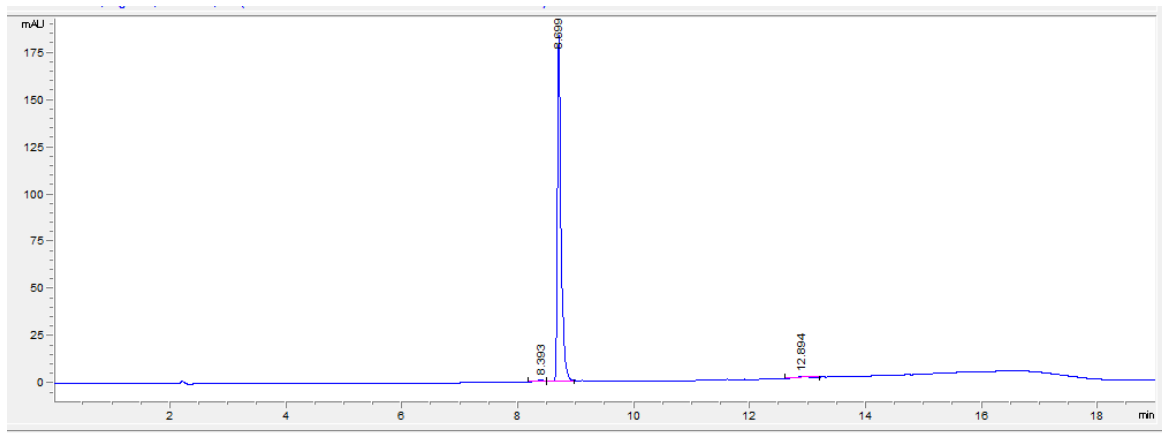


(20-60% B)

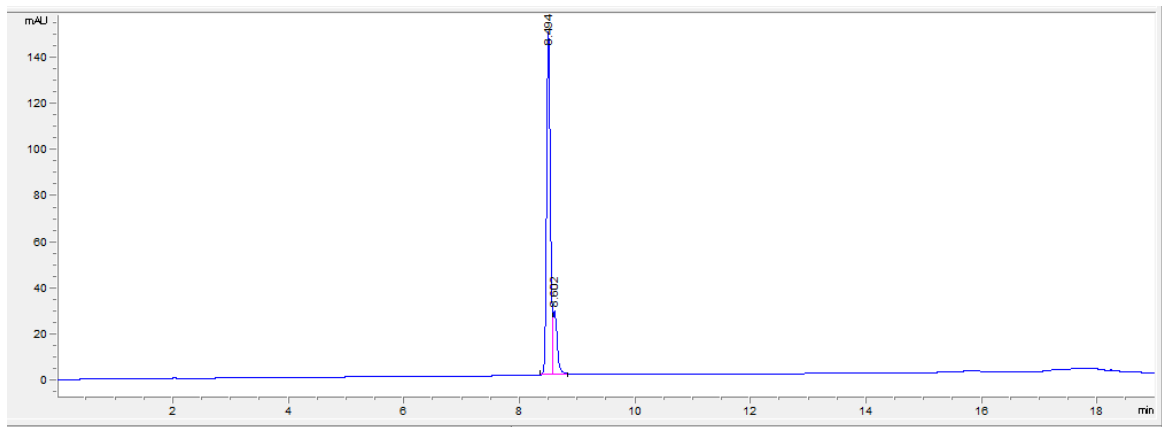


110 (78-dADDDSDDD-OH)

(5-95% B)

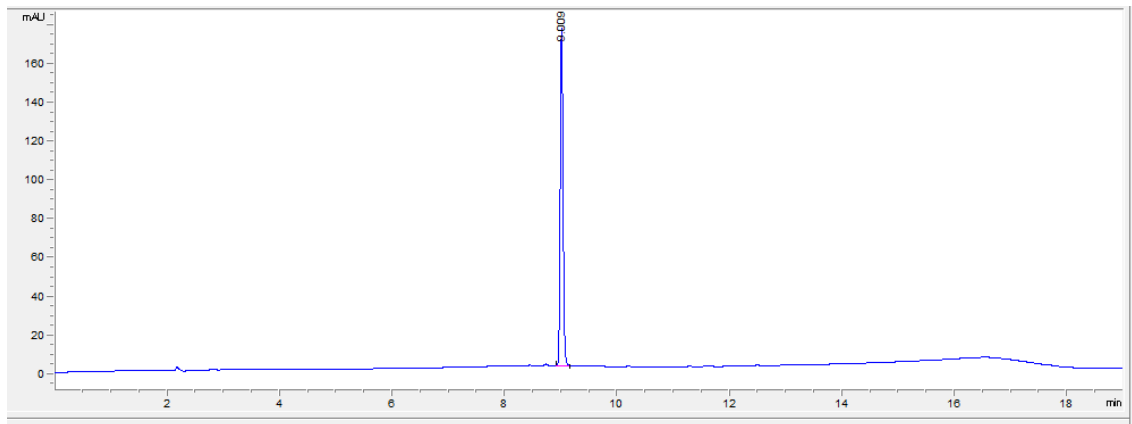


(20-60% B)

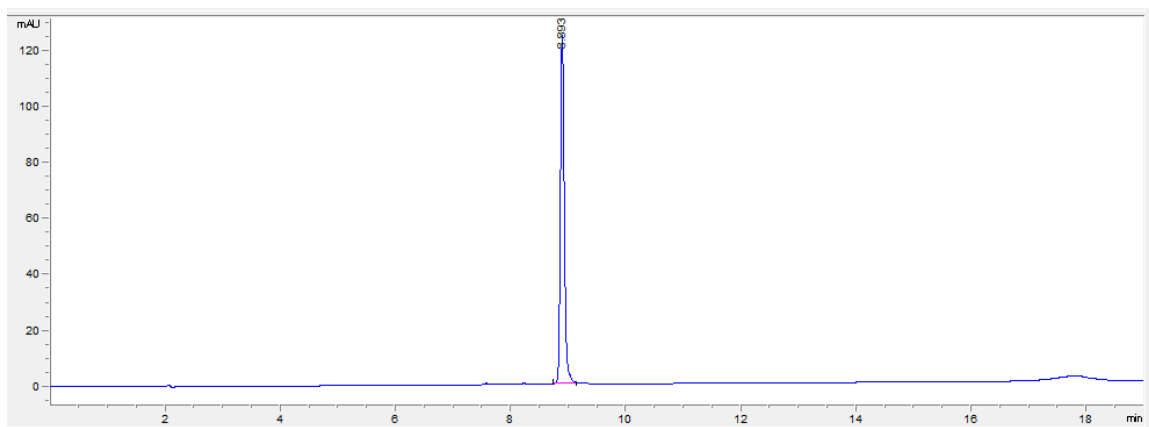


111 (74-dADDDSDDD-OH)

(5-95% B)

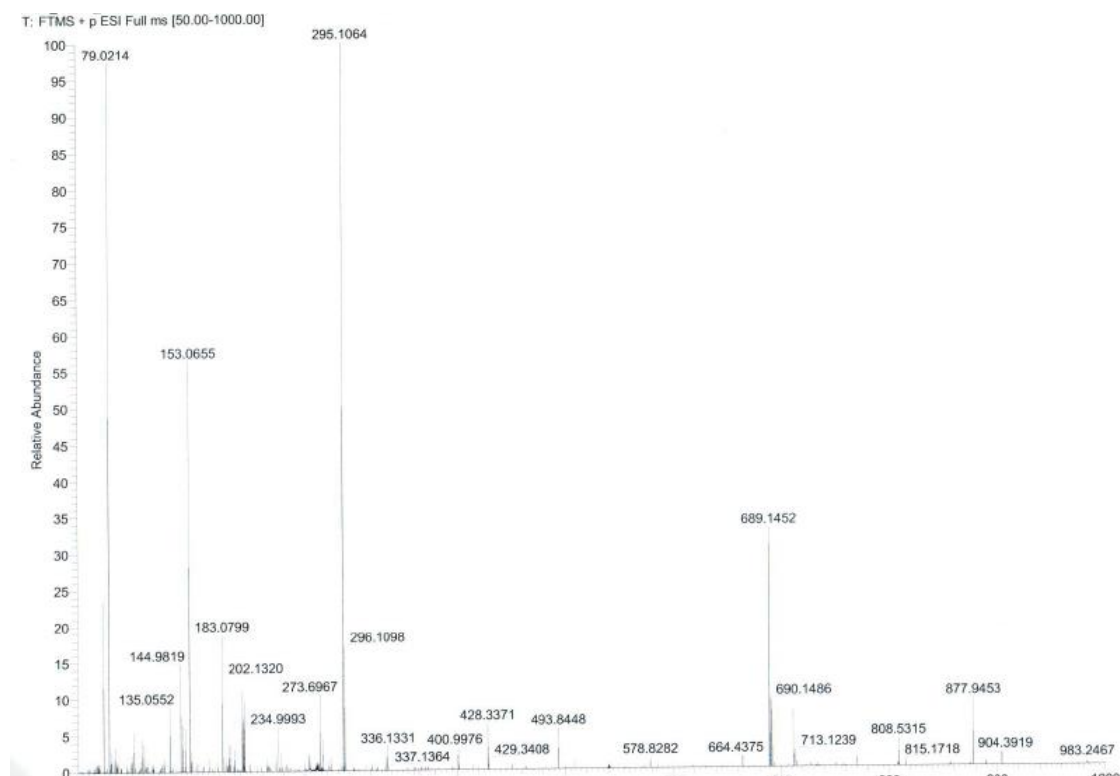


(20-60% B)

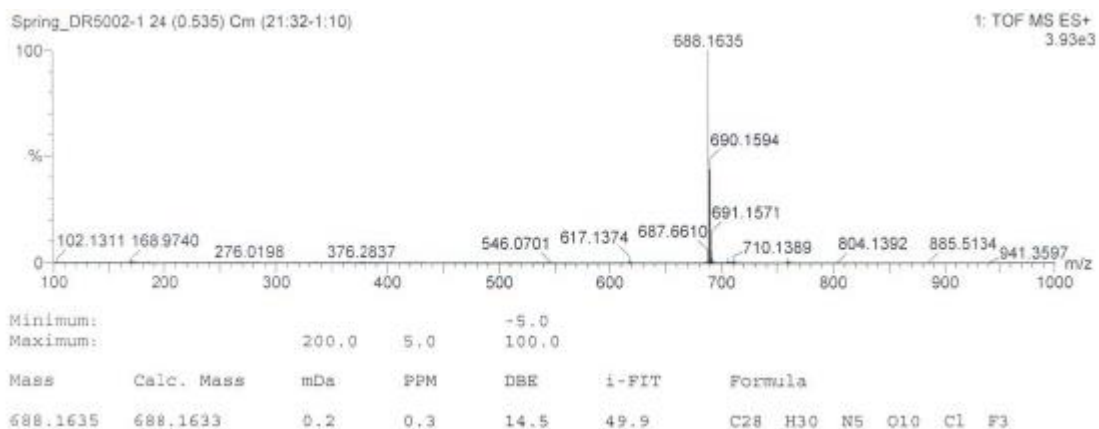


Appendix 1C: Mass Spectra for Selected Peptides

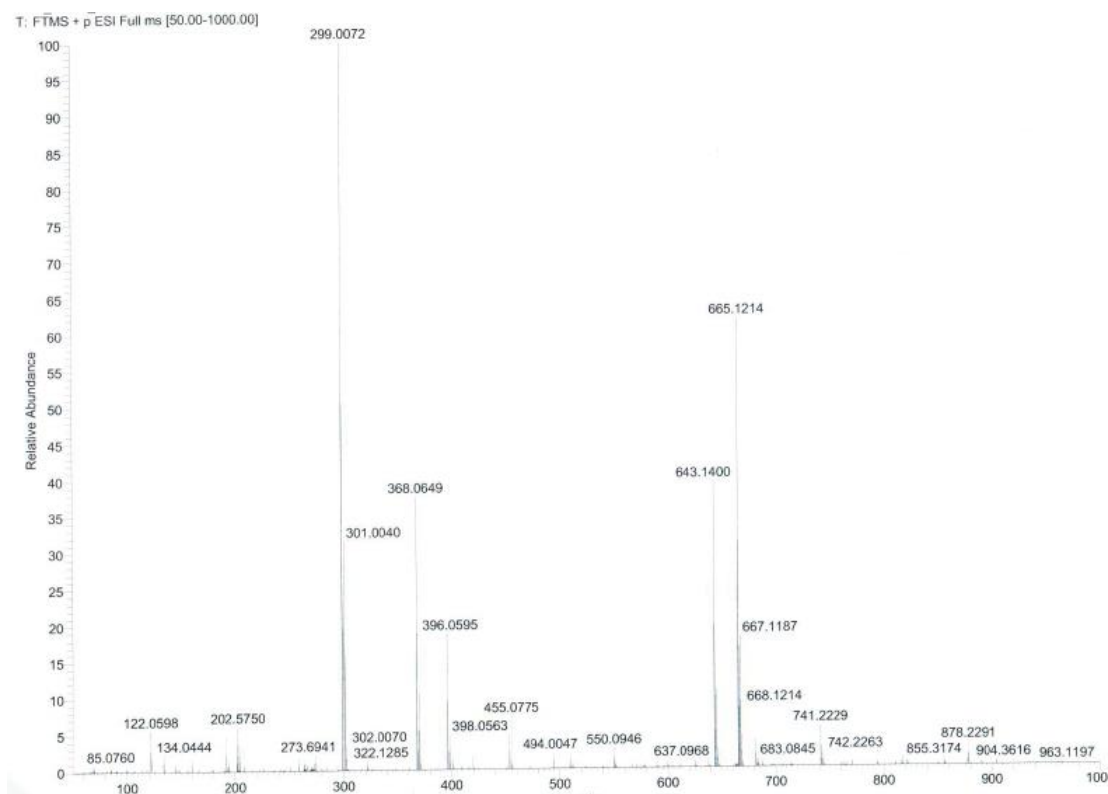
95 (78-AADD-OH) Calculated MW [M+H]⁺ (Da): 689.1468 Found MW [M+H]⁺ (Da): 689.1452



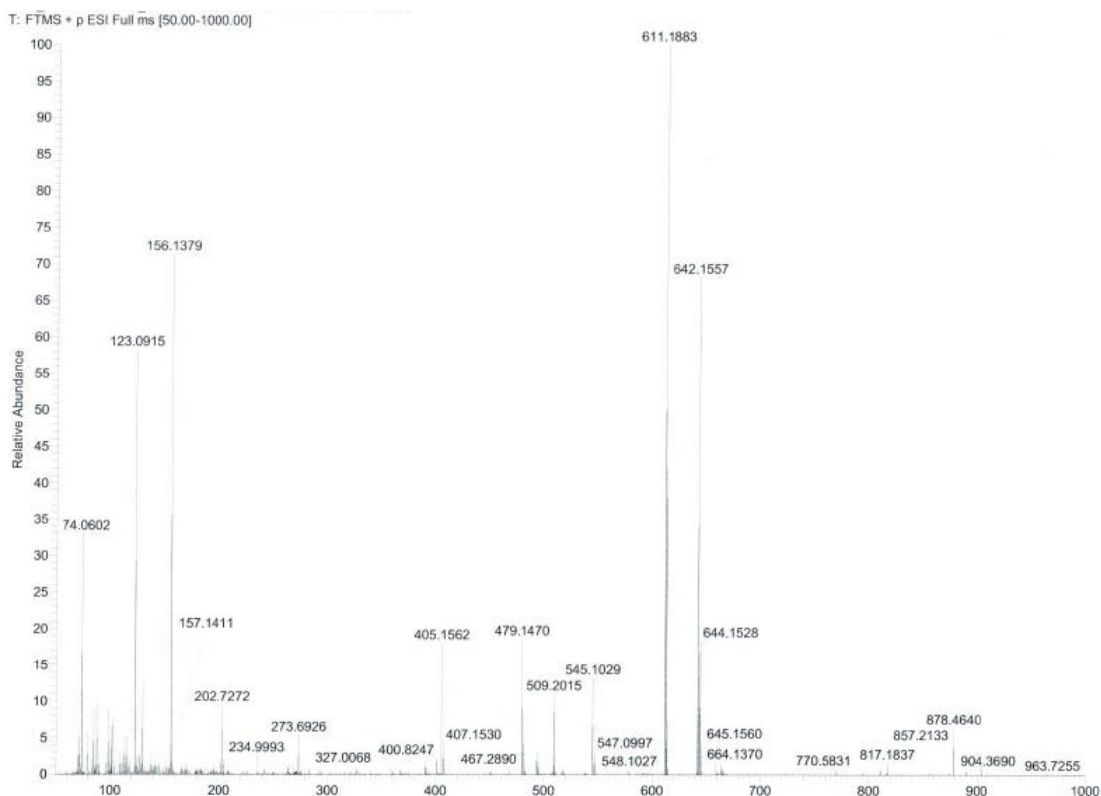
96 (78-AADD-NH₂) Calculated MW [M+H]⁺ (Da): 688.1633 Found MW [M+H]⁺ (Da): 688.1635



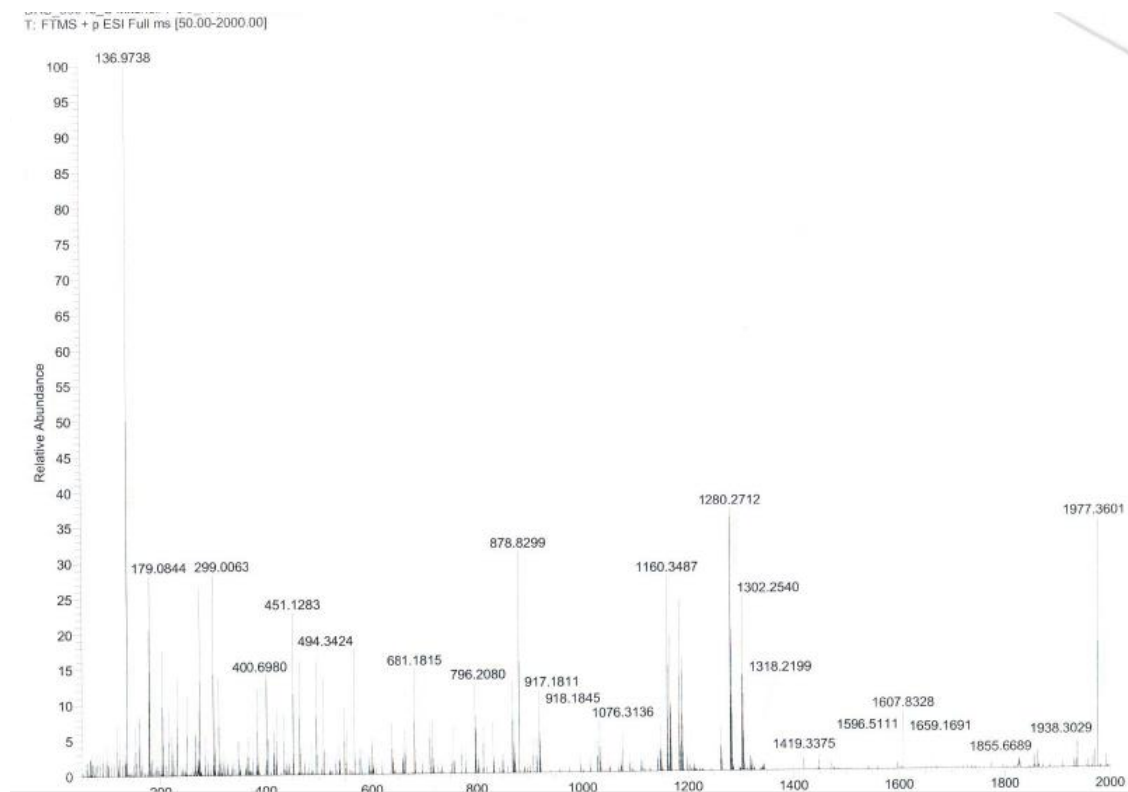
105 (78-PGGD-OH) Calculated MW [M+H]⁺ (Da): 643.1413 Found MW [M+H]⁺ (Da): 643.1400



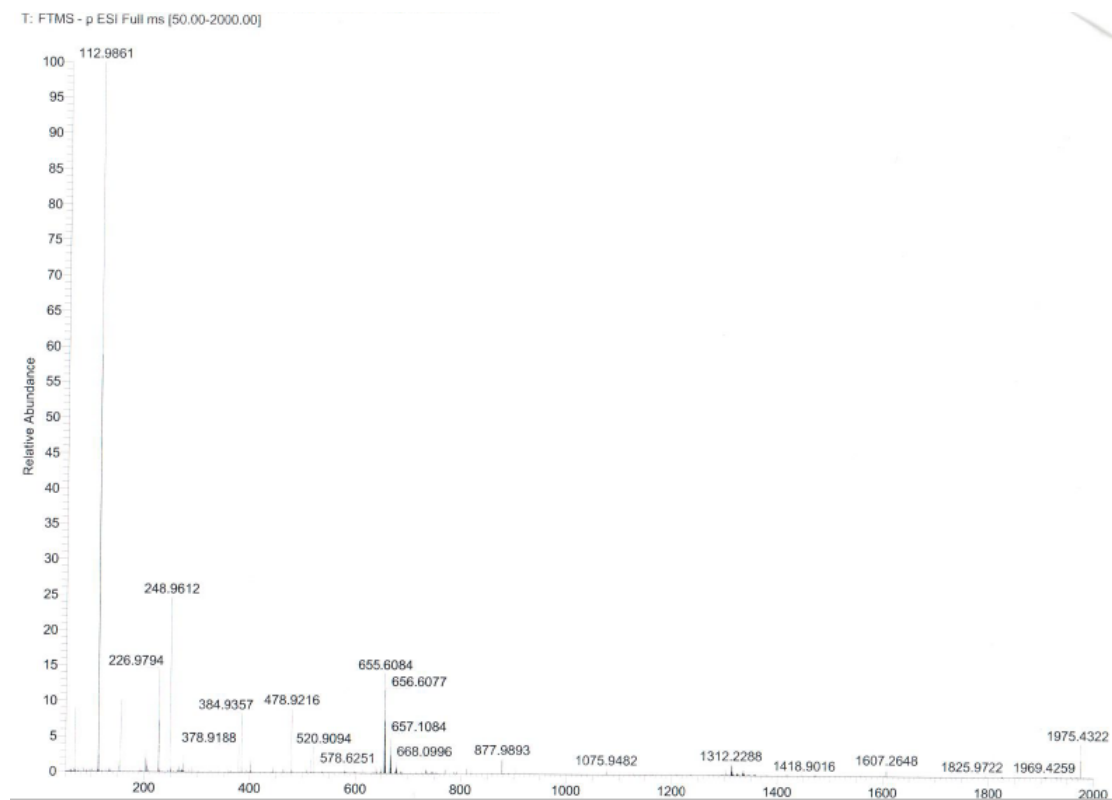
106 (78-PGGN-OH) Calculated MW [M+H]⁺ (Da): 642.1573 Found MW [M+H]⁺ (Da): 642.1557



110 (78-dADDDSDDD-OH) Calc. MW [M+H]⁺ (Da): 1280.2764 Found MW [M+H]⁺ (Da): 1280.2712



111 (74-dADDDSDDD-OH) Calc. MW [M-H]⁻ (Da): 1312.2229 Found MW [M-H]⁻ (Da): 1312.2288



Appendix 2: Publications

Appendix 2A: Second-Generation CK2 α Inhibitors Targeting the α D Pocket

Chem. Sci. 2018, **9**, 3041-3049

Appendix 2B: Partially Saturated Bicyclic Heteroaromatics as an sp³-Enriched Fragment
Collection

Angew. Chem. Int. Ed. 2016, **55**, 12479-12483

Cite this: *Chem. Sci.*, 2018, 9, 3041

Second-generation CK2 α inhibitors targeting the α D pocket†

Jessica Iegre,^{ID ‡^a} Paul Brear,^{ID ‡^b} Claudia De Fusco,^{‡^{a,c}} Masao Yoshida,^{ad} Sophie L. Mitchell,^a Maxim Rossmann,^{ID ^b} Laura Carro,^{ID ^a} Hannah F. Sore,^a Marko Hyvönen,^{ID *^b} and David R. Spring,^{ID *^a}

CK2 is a critical cell cycle regulator that also promotes various anti-apoptotic mechanisms. Development of ATP-non-competitive inhibitors of CK2 is a very attractive strategy considering that the ATP binding site is highly conserved among other kinases. We have previously utilised a pocket outside the active site to develop a novel CK2 inhibitor, **CAM4066**. Whilst **CAM4066** bound to this new pocket it was also interacting with the ATP site: herein, we describe an example of a CK2 α inhibitor that binds completely outside the active site. This second generation α D-site binding inhibitor, compound **CAM4712** (IC₅₀ = 7 μ M, GI₅₀ = 10.0 \pm 3.6 μ M), has numerous advantages over the previously reported **CAM4066**, including a reduction in the number of rotatable bonds, the absence of amide groups susceptible to the action of proteases and improved cellular permeability. Unlike with **CAM4066**, there was no need to facilitate cellular uptake by making a prodrug. Moreover, **CAM4712** displayed no drop off between its ability to inhibit the kinase *in vitro* (IC₅₀) and the ability to inhibit cell proliferation (GI₅₀).

Received 1st December 2017
Accepted 17th February 2018

DOI: 10.1039/c7sc05122k

rsc.li/chemical-science

Introduction

CK2 is a serine/threonine kinase that is a key regulator of many cellular processes and is involved in cellular proliferation and anti-apoptotic mechanisms.¹ *In vivo* it exists mainly as a holoenzyme composed of two catalytic (α and/or α') and a dimer of regulatory (β) subunits, but it can also be found as the isolated subunits.² Unlike most other kinases it is constitutively active and more than 300 proteins have been identified as CK2 substrates, making it probably one of the most pleiotropic proteins in eukaryotic systems.³ Elevated levels of CK2 have been found in a variety of cancers, including leukaemia, breast, lung, prostate, colorectal, renal and glioblastoma brain tumours.^{4,5} It has been shown that cancer cells are particularly susceptible to CK2 inhibition because they rely on high levels of the kinase to survive.⁶ CK2 overexpression has been associated with multi-drug resistance phenotypes and it has been

demonstrated that CK2 α inhibition leads to an increased uptake of known drugs in multidrug resistant cells.^{7,8} It has been shown that CK2 inhibitors are able to limit the growth of a range of cancer cell lines.^{9,10} Hence, CK2 has been recognised as a highly promising target for anti-cancer therapies.

Like the majority of kinase inhibitors, most of the known CK2 inhibitors target the ATP binding site, presenting the issue of poor selectivity over other kinases.^{11–13} This is the case for **CX4945** (known as silmitasertib), the first in class CK2 inhibitor currently in phase II clinical trials.^{14,15} The IC₅₀ of **CX4945** against CK2 is 1 nM but it also inhibits 12 other kinases with nanomolar affinity and it is more potent against Clk2 than against CK2.^{16,17}

Previous work from our groups led to the discovery of a new binding pocket on CK2 α , which is located adjacent to the ATP binding site. This pocket was revealed in a X-ray crystallographic screen, in which several weakly binding fragments were found to occupy this novel site formed through a movement of the α D helix, hence the name of α D pocket.^{18,19} Through fragment growing and linking, we generated a novel selective CK2 inhibitor: **CAM4066** (Fig. 1).

CAM4066 was a valuable tool for validating the concept of using the α D site to develop selective inhibitors of CK2 α ; however, it has several structural features that are undesirable in a lead molecule or chemical tool. These features, shown in Fig. 1, include a long flexible linker (circled in orange), a zwitterionic nature (the amine and the carboxylate are highlighted in green), amide bonds (coloured blue) and a high MW, which is often associated with poor oral bioavailability (Fig. 1).

^aDepartment of Chemistry, University of Cambridge, CB2 1EW, Cambridge, UK. E-mail: spring@ch.cam.ac.uk

^bDepartment of Biochemistry, University of Cambridge, CB2 1GA, Cambridge, UK. E-mail: mh256@cam.ac.uk

^cStructure Biophysics & FBLG, Discovery Sciences, IMED Biotech Unit, AstraZeneca, Cambridge, UK

^dR&D Division, Daiichi Sankyo Co., Ltd., 1-2-58, Hiromachi, Shinagawa-ku, Tokyo 140-8710, Japan

† Electronic supplementary information (ESI) available: All experimental details, crystallographic data collection and refinement statistics, details of chemical synthesis, additional figures and tables. See DOI: 10.1039/c7sc05122k

‡ These authors contributed equally to the work presented here.

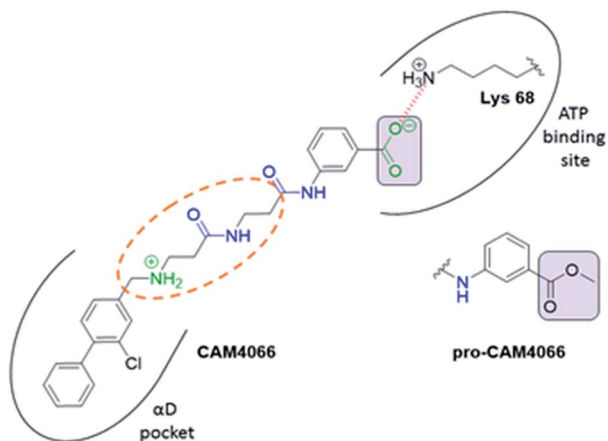


Fig. 1 Structure of CAM4066 and pro-CAM4066. Zwitterionic elements are coloured in dark green, amide bonds in blue and the difference between CAM4066 and its prodrug highlighted in purple. The interaction between CAM4066 and the highly conserved Lys68 is shown as red dashed line. The flexible linker is circled in orange. The α D pocket and ATP binding site are reported as black curves.

Moreover, the carboxylate forms a salt bridge with the conserved Lys68 in the ATP binding site. As expected due to its physicochemical properties, CAM4066 suffers from poor cellular permeability and therefore the methyl ester derivative, pro-CAM4066, was used as a pro-drug to improve cellular activity and target engagement.¹⁸ The aim of this work was to develop enhanced CK2 α inhibitors that have improved physicochemical properties and bind to the α D pocket without reaching deep into the ATP pocket. Our ideal lead-like candidate would have a smaller number of rotatable bonds (<10), not be susceptible to protease action (absence of amide groups), and be cell permeable without resorting to the use of a pro-drug. In addition, we aimed to develop inhibitors that do not rely on any of the conserved interactions within the ATP binding site.

The strategy (shown in Fig. 2) involved a fragment optimisation and a fragment-growing stage, followed by merging of the best compounds. Firstly, we would optimise the α D site fragment further to gain higher affinity and secondly, we would grow the fragment into the upper part of the α D pocket in order to gain inhibition.

Finally, the compounds with the most promising substitution patterns would be combined to provide the final inhibitor that would show inhibition of the kinase activity, good cell permeability and efficacy in cellular assays.

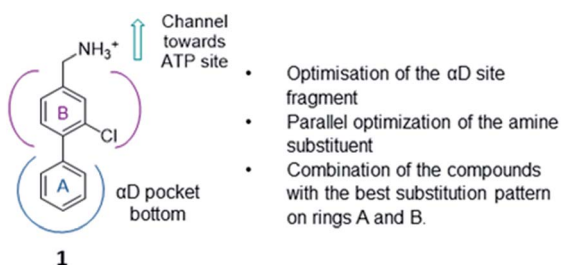


Fig. 2 Optimisation strategy adopted in this project using **1** as the fragment starting point.

Results and discussion

Previously we have reported our preliminary studies on the exploration of the α D pocket, based on the development of primary hits from the crystallographic screen, which led to the identification of compound **1** ($K_d = 267 \mu\text{M}$), shown in Fig. 2. Our strategy to optimise the α D site fragment was to concentrate on ring A of the biaryl structure; however, a brief investigation of ring B was also performed. In parallel, optimisation of the amine substituent was carried out growing in the channel that connects the α D site and the ATP binding pocket.

Optimization of the α D site fragment

Ring A. Ring A effectively fills the bottom of the hydrophobic pocket of the α D site (Fig. 3). However, on closer examination we uncovered a side channel off the main pocket filled by several well-defined water molecules that could be targeted to improve

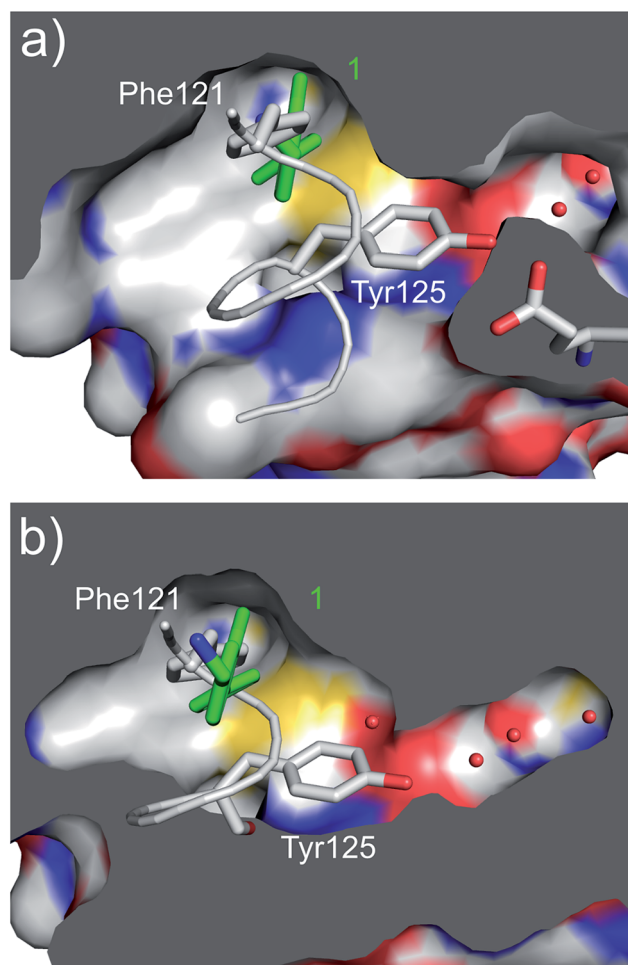


Fig. 3 (a) A cross section of the α D pocket of **1** (green) bound to CK2 α . The first two water molecules in the water channel are shown (PDB: 5CSH). (b) The structure of the α D loop (in grey) in the closed conformation of the apo protein (PDB: 5CSH).¹⁹ Tyr125 fills the mouth of the water channel. The binding mode of **1** (in green) superimposed on the apo structure is shown, with **1** occupying the same position as Phe121.

the affinity. Comparison of the co-crystal structure of CK2 α and **1** (PDB: 5CSH, Fig. 3a) with the closed apo structure (PDB: 5CSP, Fig. 3b) shows that the side channel in the closed structure was occupied by Tyr125. This indicates that this channel can be targeted as it has sufficient volume to accommodate sizable groups, *i.e.* the phenolic ring of the Tyr125, and that the waters can be displaced as this happens in the closed form of the α D loop. Modelling studies indicated that **1** contains the right vectors to grow into the Tyr channel by substitutions on the 2-position of ring A.

A robust crystallographic system for CK2 α enabled us to use X-ray crystallography as our primary screening technique. Therefore, co-crystal structures of all the compounds were attempted. The majority of the structures showed the ligand bound to CK2 and for all the compounds showing a clear electron density K_d was determined *via* ITC (overview of the results of the ITC experiments can be found in Table S1†). Several structures that did not show clear electron density for the ligand were also investigated using ITC to provide SAR data

and controls. A number of mono- and di-substituted rings and bicyclic systems were investigated (Table 1 and 2, Fig. 4).

Substitution in the 2 position of ring A was beneficial when compared to the reference compound **1** ($K_d = 267 \mu\text{M}$); the 2-methyl derivative **2** was promising with a K_d of $41 \mu\text{M}$. The introduction of an ethyl group in the same position (**3**) resulted in the highest affinity ($K_d = 17 \mu\text{M}$) and highest ligand efficiency (LE = 0.39) of the series and the crystal structure (PDB: 5ORJ) showed how the lateral chain grows towards the water channel, displacing the first water molecule on the left (Fig. 4b and c). The presence of the chlorine on ring B and the ethyl group on ring A enforced an almost orthogonal conformation of the biaryl system (Fig. 4c). Expanding the size of the lateral chain did not improve the binding ($K_d = 205 \mu\text{M}$) nor the LE of the isopropyl derivative **4**. The 2-MeO and 2-F derivatives, **5** and **6** respectively, had a comparable K_d to **1** while the 2-OH group (compound **7**) was detrimental to binding even though it formed a hydrogen bond to the conserved water (Fig. S1a,† PDB: 5OSL). Substitution in the 3 position of ring A (compounds **8** to

Table 1 SAR on the bottom ring of **1** (ring A)

Compound	Ring A	K_d^a (μM)	LE ^b	PDB	Compound	Ring A	K_d^a (μM)	LE ^b	PDB
1		267	0.33	5CSH	7		375	0.30	5OSL
2		41	0.38	5ORH	8		>500	—	n.a
3		17	0.39	5ORJ	9		>500	—	5OUL
4		205	0.29	5OS7	10		>500	—	n.a
5		244	0.30	5OQU	11		105	0.33	5OS8
6		234	0.32	5ORK	12		250	0.27	n.a
					13		>500	—	n.a

^a Measured by ITC. ^b LE = ligand efficiency*. *Ligand efficiency is defined as the ratio of the Gibbs free energy of binding of a ligand divided by the number of heavy (non-hydrogen) atoms in the molecule (LE = $\Delta G/[\text{number of heavy atoms}]$).²⁰

Table 2 SAR studies on the bottom ring (ring A) of dichloro derivatives 14 and 15

Compound	Ring A	K_d^a (μM)	LE ^b	PDB
14		12	0.43	5OTR
15		6.5	0.41	5OTZ

^a Measured by ITC. ^b LE = ligand efficiency*. *Ligand efficiency is defined as the ratio of the Gibbs free energy of binding of a ligand divided by the number of heavy (non-hydrogen) atoms in the molecule ($LE = \Delta G/[\text{number of heavy atoms}]$).²⁰

10) appeared not to be tolerated as only the fluoro-derivative 9 yielded a co-crystal structures. The disubstituted 2-Me-4-F derivative 11 was found to have a K_d of 105 μM , marginally

higher than the 2-methyl compound 2, but with a lower ligand efficiency ($LE = 0.33$). Expanding ring A to a naphthyl group 12 improved the affinity only slightly, while the indolyl derivative 13 did not show any significant binding and we were unable to obtain structures of these in complex with CK2 α . Therefore, compound 3 represented the fragment with the best LE and it was chosen as the best optimized fragment as far as the ring A is concerned.

Ring B. In many of the crystal structures of the compounds with different ring A substituents two alternative binding modes were observed for ring B, in which the chlorine atom could be on either side of the pocket. Therefore, the dichloro derivative of 1 (14) was synthesized to fulfil the interactions that both of these chlorine positions made. 14 showed an improved K_d of 12 μM with the highest LE of 0.43 (Table 2). The co-crystal structure is shown in Fig. S1b† (PDB: 5OTR) where 14 (in blue) is overlapped with the two binding poses of 1 (green). The final compound 15, merging both the dichloro functionality on ring B and the 2-ethyl group on ring A, was synthesized and showed an improved K_d of 7 μM ($LE = 0.41$) with its binding mode overlapping well with that of the merged fragments (Fig. 4e, PDB: 5OTZ). Although compounds 3 and 15 showed a comparable LE (0.39 vs. 0.41 respectively), compound 15 was chosen as

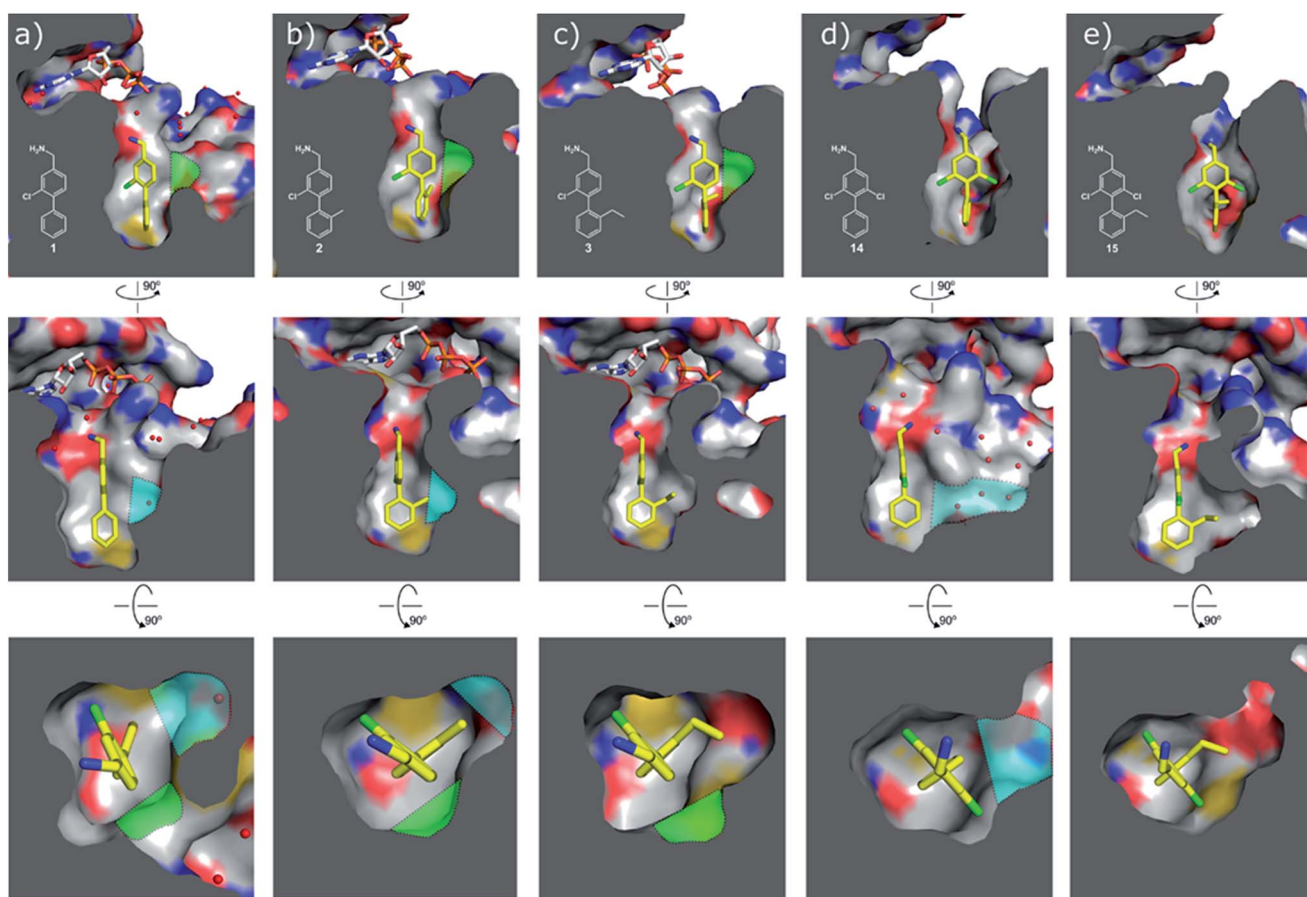


Fig. 4 Cross sections of the αD and ATP pockets: first and second rows are lateral views and last row is a view from the top. The water channel is highlighted in blue and the hydrophobic pocket in green for complexes that are not making the most of the space available. (a) Co-crystal structure of 1 with CK2 α (PDB: 5CSH); (b) co-crystal structure of 2 with CK2 α (PDB: 5ORH); (c) co-crystal structure of 3 with CK2 α (PDB: 5ORJ); (d) co-crystal structure of 14 with CK2 α (PDB: 5OTR); (e) co-crystal structure of 15 with CK2 α (PDB: 5OTZ).

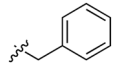
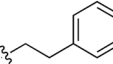
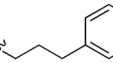
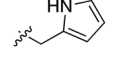
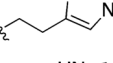
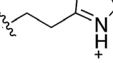
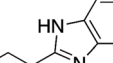
hit to bring forward due to its ability to occupy a larger part of the α D pocket (Fig. 4e).

Growing towards the entrance to the ATP site. The compounds tested so far were not able to effectively inhibit the protein activity as ATP was not displaced. Indeed, most of the co-crystal structures featured a molecule of ATP/ADP in the ATP binding site as well as the ligands bound in the α D pocket (Fig. 4 and 5).

During the development of **CAM4066** a series of flexible linkers were designed and tested to join the α D site fragment to an ATP site fragment. These compounds revealed that it was possible to induce the opening of a small channel between the α D and the ATP sites. Our aim was to induce the opening of the channel with shorter, more rigid compounds than **CAM4066**. The flipping of the side chain of Met163 allows the formation of the channel and results in blocking the ATP site – Met163 is located just underneath the adenine base of ATP. Therefore, these compounds would not need to grow deep into the ATP site to achieve inhibition. The channel from the α D site is lined by Met163 and His160 and we envisioned that compounds with aromatic groups that stacked between these amino acid residues would improve the affinity and cause the conformational change that would lead to inhibition. Toward this end, the effect of several aromatic groups on the amine were investigated using a kinase activity assay (Table 3).

Whilst the reference compound **1**, tested at 500 μ M, inhibited only 21% of the protein activity, the inhibitory activity of the aromatic derivatives **16–19**, were found to be considerably

Table 3 *N*-substituents on the benzylamine^a

Compound	R	Inhibition of the kinase activity @ 500 μ M (%)	PDB
1	H	21	5CSH
16		54	n.a.
17		42	n.a.
18		40	6EII
19		52	5OT6
20		50	5OUE
21		n.d.	5OUM
22		98 (IC ₅₀ 58)	5OUU

^a n.d. = interference with the assay by the test compound.

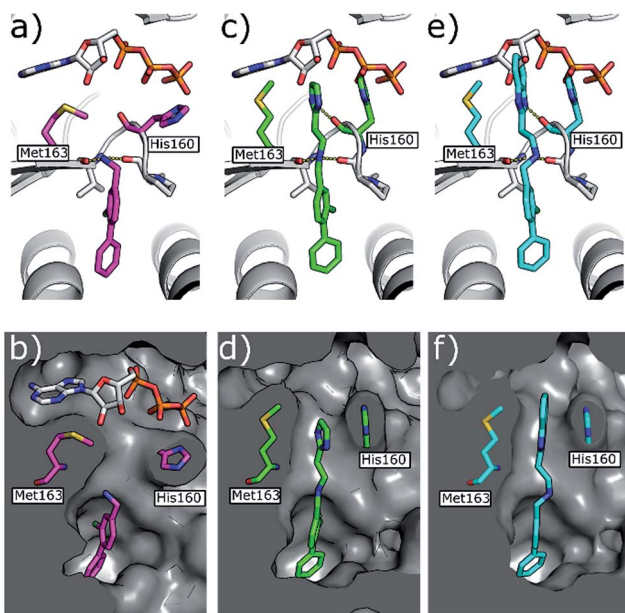
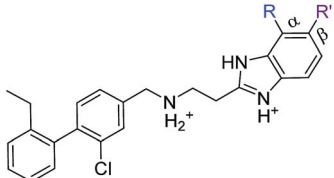


Fig. 5 (a) Co-crystal structure of **1** (in pink) and ATP bound to CK2 α (PDB: 5CSH)¹⁹ and (b) surface representation of CK2 α with **1** bound. (c) Co-crystal structure of **21** (in green) bound to CK2 α . The binding mode of ATP (grey) in the ATP site when **1** is bound is superimposed upon the structure. (d) Co-crystal structure of **21** (in green) bound to the surface representation of CK2 α . (e) Co-crystal structure of **22** (in blue) bound to CK2 α . The binding mode of ATP (grey) in the ATP site when **1** is bound is superimposed upon the structure. (f) Co-crystal structure of **22** (in blue) bound to the surface representation of CK2 α .

improved with compounds **16** and **19** being the most promising (54 and 52% respectively). In order to pick up additional H-bond interactions the pyrrole derivative **19** was chosen over **16** and we hypothesized that the heterocycle should go further up into the channel. Whilst the imidazole derivative **20** did not show significant improvement, the benzimidazole derivative **22** was found to be the most potent compound with an IC₅₀ of 58 μ M. Fig. 5d and f show the co-crystal structure of **21** and **22** with CK2 α , respectively. As expected, Met163 flips upon binding of the more extended compounds compared to the co-crystal structure of **1** (Fig. 5b). This explains the displacement of ATP and therefore activity inhibition even without fragments binding directly in the ATP pocket.

As these compounds showed increased activity, the concentration for the inhibition assay was decreased to 10 μ M and cellular activity was investigated (Table 4). Although **15** had the highest affinity of the α D binders (Table 2), **3** was chosen for further studies for synthetic reasons, with the idea of retrieving the substitution pattern of **15** in the final compound. Merging **3** with **22** provided compound **23**, which featured higher potency than the original fragments in the inhibition assay and a promising GI₅₀ of 10 μ M in HCT116 cells. Therefore, SAR

Table 4 Studies on the benzimidazole substitution



Compound	R	R'	Inhibition @10 μM (%)	GI ₅₀ ^a (μM)	PDB
23	H	H	33 (IC ₅₀ 18)	10	5OSZ
24	Me	H	45	—	5OT5
25	NO ₂	H	50	—	50TD
26	OMe	H	52 (IC ₅₀ 8)	11	5OTH
27	H	Me	38	—	5OTI
28	H	NO ₂	36	—	—
29	H	OMe	64 (IC ₅₀ 7)	11	5OTL
30	H	Cl	50	—	5OTO

^a Inhibition of proliferation tested in HCT116 cell line.

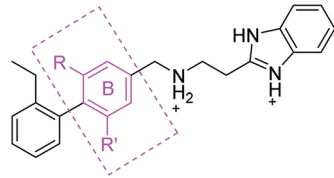
studies around the benzimidazole ring were then performed (compounds 24–30), with both electron withdrawing and donating groups in position α and β of the benzimidazole improving the inhibition activity in respect to the derivative 23. The α and β methoxy derivatives 26 and 29 were found to be the most promising in the respective α and β substituted series with IC₅₀ of 8 and 7 μM , respectively (Table 4, IC₅₀ and GI₅₀ curves are shown in Fig. S4 and S5[†]).

Further modifications of ring B. Alternative substitutions around the middle ring were also investigated and compared to compound 23. Firstly, the dichloro derivative was synthesized as it gave promising results as a fragment (compound 15, Table 2). With an IC₅₀ of 7 μM , CAM4712 was the most potent compound compared to the methyl, trifluoromethyl, methoxy and trifluoromethoxy derivatives (compounds 31, 32, 33 and 34, respectively) (Table 5). Substitution of the chlorine atom in compound 23 (compounds 31–34) was investigated in order to improve the moderate solubility of the related CAM4712 in water. Unfortunately, compounds 31–34 resulted in loss of activity and were therefore not pursued further.

With the optimisation around each aromatic ring in hand, compounds 35 and 36 were designed *via* a merging strategy so that they contained the most promising substitution patterns. The methoxy derivatives 35 and 36 were synthesized and tested but, disappointingly, gave worse results than CAM4712 (Fig. 6).

Validation of CAM4712. As CAM4712 was the most advanced compound in this series a more detailed investigation was performed. Firstly, CAM4712 showed an improved IC₅₀ of 7 μM compared to the compound 22 (58 μM). This data validated our fragment merging strategy to improve upon both affinity and inhibition. Unfortunately, as with the other compounds in the series, once the benzimidazole group had been added CAM4712 was not soluble enough for ITC. Therefore, an ITC competition study was performed to confirm the binding mode and to estimate the affinity of CAM4712 for the αD site (an overview of the results of the ITC experiments can be found in Table S1[†]). In

Table 5 Optimization of ring B



Compound	R	R'	Inhibition @10 μM (%)	PBD
23	Cl	H	33 (IC ₅₀ 18)	5OSZ
CAM4712	Cl	Cl	80 (IC ₅₀ 7)	5OTY
31	Me	H	30	5OYF
32	CF ₃	H	23	6EHU
33	OMe	H	41	5OTQ
34	OCF ₃	H	39	n.a.

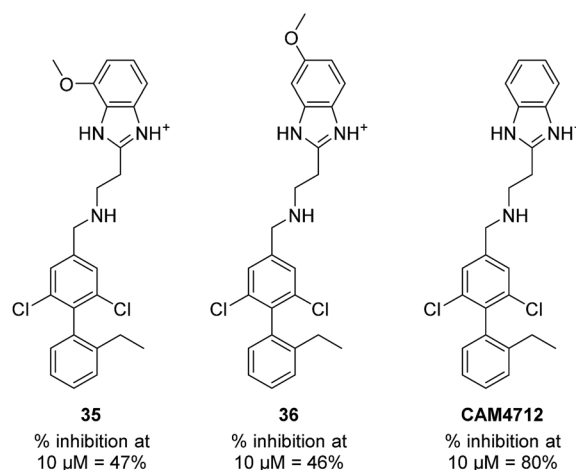


Fig. 6 Compounds 35, 36 and CAM4712 with respective data.

order to achieve this, several probe molecules that have well characterised binding modes and affinities were titrated into CK2 α in the presence of CAM4712. From these experiments, it was possible to determine not only the affinity for the αD site but also which part of the ATP site the benzimidazole group blocks.

Four probes were used for this study in four separate competition experiments, each of them titrated into CK2 α in the presence of and absence 20 μM CAM4712 giving the following results:

(1) Inhibition of binding in the αD or ATP site by CAM4712:

The binding of CAM4066 to CK2 α was inhibited by 20 μM CAM4712. From this the affinity of CAM4712 was estimated to be 4.0 μM (Fig. S2[†]). This experiment confirms that CAM4712 binds to CK2 α but the binding could partially occur in the ATP site.

(2) Inhibition of binding in the αD site:

15 was titrated into CK2 α in the presence of 20 μM CAM4712 (Fig. S3[†]). This showed that CAM4712 was also able to inhibit the binding of 15 to CK2 α and from this the affinity was estimated to be 5.0 μM . As 15 binds in the αD site this experiment confirms that the binding site of CAM4712 is the αD pocket as well as confirming the affinity.

(3) Inhibition of binding to Lys68:

2-Hydroxyl, 5-methyl benzoic acid (37) binds to the conserved Lys68 in the ATP site and occupies the right-hand side of the pocket (PDB: 5CSP). The binding of compound 37 was not inhibited by CAM4712 (Fig. S6†) confirming that the benzimidazole ring does not interact with the right-hand side of the ATP pocket and validates the binding mode derived from the crystal structure (PDB: 5OTZ). This result predicted that it would be possible to generate a crystal structure of CAM4712 and 37 bound simultaneously to CK2 α and this was confirmed by a crystal structure showing both compounds binding simultaneously to CK2 α (Fig. S6d,† PDB: 6EHK).

(4) Inhibition of binding in the ATP site/hinge region:

CX4945, which from the analyses of crystal structures would clash with CAM4712 in the hinge region, was titrated into CK2 α in the presence of CAM4712 (Fig. S7†). CAM4712 was shown to inhibit the binding of CX4945 to CK2 α . The affinity of CAM4712 for CK2 α was estimated to be 3.0 μ M. This confirms that the benzimidazole ring binds in the Met163 channel and blocks access to the ATP site as this would inhibit the binding of CX4945.

In summary, these competition experiments suggest firstly that the K_d of CAM4712 towards CK2 α is approximately 4 μ M. Secondly, they confirm that the binding mode of CAM4712 in the α D pocket and mouth of the ATP site corresponds to that seen in the crystal structure.

The validation experiments of CAM4712 and the crystal structures allowed us to rationalise the difference in *in vitro* potency between CAM4066 and CAM4712 (IC₅₀ 7 μ M and 0.37 μ M respectively). Whilst the binding of both compounds to CK2 resulted in the flipping of the Met163, CAM4712 did not H-bond the conserved Lys68 in the ATP binding site. Instead, a low-energy hydrophobic π - π interaction between the His160 and the benzimidazole was introduced (as shown for the related compound 22 in Fig. 5f) resulting in loss of binding affinity and potency compared to CAM4066.

The efficacy of CAM4712 in cellular assays was tested in HCT116 cell line, which is known to overexpress CK2 α . A cell growth inhibition assay yielded a GI₅₀ for CAM4712 of 10.0 \pm 3.6 μ M, which is similar to that of the clinical trials candidate CX4945 (11.3 \pm 1.2 μ M). It is also similar to pro-CAM4066 (GI₅₀ 9.1 \pm 1.4 μ M, IC₅₀ 0.37 μ M),¹⁸ but, importantly, no drop-off in potency was observed from the functional to the cellular assay. This represents a large step forward compared to CAM4066, which had to be administered as the prodrug pro-CAM4066. The target engagement by CAM4712 was analysed by following the CK2 α dependent phosphorylation of Ser129 of Akt1. This showed good inhibition of the phosphorylation of Ser129 by CAM4712 as well as by its close analogues 23 and 26 which confirms that these compounds inhibit CK2 α in the cellular environment (Fig. 7).

CAM4712 showed a 10-fold decrease in potency compared to CAM4066 and therefore the selectivity of CAM4712 was screened against a panel of 140 kinases at a concentration of 30 μ M (4 \times IC₅₀). CAM4712 showed good selectivity against the 20 closely related CMGC kinases in the panel (Fig. S6a†). However, 4 kinases (CAMK1, SmMLCK, EF2K and SGK1) were inhibited by

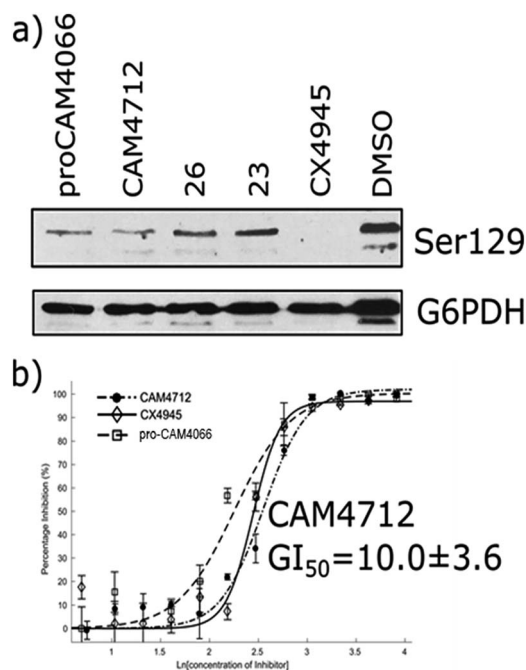


Fig. 7 (a) Western blot analysis showing the specific CK2 phosphorylation target: AKT1 serine 129. HCT116 cells were treated with 2 \times GI₅₀ of CX4945 (20 μ M), CAM4712 (20 μ M) or pro-CAM4066 (20 μ M) for 72 hours (b) dose response curve for the inhibition of the growth of HCT116 cells by CAM4712, pro-CAM4066 and CX4945. All graphs show the mean \pm SEM of not less than three independent experiments with each in triplicate.

CAM4712 for more than 50% (Fig. S8b†) and hence, CAM4712 showed a reduced overall selectivity compared to CAM4066 (which was screened at 2 μ M).¹⁹ This is not surprising considering the high concentration used in the selectivity screen due to CAM4712 being less potent than CAM4066. Nevertheless, CAM4712 showed a more selective profile than other CK2 α inhibitors (Fig. S8b†) and represents, therefore, a good starting point for further development of selective CK2 α inhibitors. Our aim in this work has not been to gain specificity but rather to demonstrate mechanistically that an inhibitor that is not making significant contacts with the conserved active site is able to inhibit the kinase effectively. To fully exploit the

Table 6 Properties and structural features of compound CAM4712 compared to CAM4066^a

	Ideal range	CAM4066	CAM4712
NRB	<10	12	8
HBA	10	4	2
HBD	5	3	2
TPSA	<140 Å ²	101	41
MW	<500	494	453
Conserved interaction		Yes	No
Need of a pro-drug		Yes	No
Amide bonds		Yes	No
Drop in potency		~10 fold	No

^aNRB = number of rotatable bonds; HBA = number of hydrogen bond acceptors; HBD = number of hydrogen bond donors; TPSA = topological polar surface area; MW = molecular weight.²¹

selectivity that α D binding offers, further optimization of CAM4712 is needed to increase its affinity towards CK2 α .

One of the aims of this work was to generate an improved inhibitor compared to the previous compound CAM4066. We managed to design a compound with the physico-chemical properties falling into the range for bioavailable compounds according to Lipinski's rules:²¹ the number of rotatable bonds was reduced, the amide groups were removed and the compound entered the cells and showed activity without the use of a prodrug. Moreover, the number of H-bond donors and acceptors was reduced to 2 and the molecular weight was kept below 500 Da (Table 6). This was all achieved without interacting with the deep and conserved ATP binding site.

Conclusions

In conclusion, we have developed a series of second-generation CK2 α inhibitors that target the α D site. This was achieved by first optimising the fragments that bound in the α D site, followed by identification of groups that grow towards the mouth of the ATP site to provide potent inhibitors of CK2 α . In our previous work we demonstrated that selectivity could be achieved anchoring the inhibitors in the α D pocket and with this work we achieve inhibition with ligands that do not target the active site. CAM4712 showed high cellular activity ($10.0 \pm 3.6 \mu\text{M}$) and target engagement was demonstrated. This second generation of α D pocket inhibitor overcomes the limitations of our first inhibitor, including the fact that it does not need to be administered as a pro-drug to exert anti-proliferative activity. We have also shown that it is not necessary to interact with the ATP site directly, but effective inhibition of the kinase and displacement of ATP can be achieved by blocking the mouth of the ATP site with no need to interact with conserved features of the ATP binding site. These results demonstrate an entirely new approach to CK2 α inhibition and will allow the future development of drug-like molecules, lead compounds and chemical tools that utilise the novel properties of the α D site.

Conflicts of interest

There are no conflicts to declare.

Acknowledgements

We would like to thank the X-ray crystallographic facility and the Biophysics facility at the Department of Biochemistry for support and access to equipment. We thank Diamond Light Source for access to beamlines IO2, IO3, IO4 and I24 (proposals mx9537 and mx9007). We are grateful for academic licence of Instant JChem that was used for structure database management, search and prediction, Instant JChem 16.16.10, 2016, ChemAxon (<http://www.chemaxon.com>). This work was funded by the European Research Council under the European Union's Seventh Framework Programme (FP7/2007-2013)/ERC grant agreement no. [279337/DOS] (to DRS) and the Wellcome

Trust Strategic (090340/Z/09/Z) and Pathfinder (107714/Z/15/Z) Awards (to DRS and MH). In addition, the Spring group research was supported by grants from the Engineering and Physical Sciences Research Council, Biotechnology and Biological Sciences Research Council, Medical Research Council and the Royal Society. CD thanks the Herchel Smith Funds for a postdoctoral fellowship. JI would like to thank Trinity College, University of Cambridge for funding. SLM would like to acknowledge a CASE-EPSRC award in partnership with BASF.

Notes and references

- 1 R. Battistutta and G. Lolli, *Mol. Cell. Biochem.*, 2011, **356**, 67–73.
- 2 K. Niefind, B. Guerra, I. Ermakowa and O. G. Issinger, *EMBO J.*, 2001, **20**, 5320–5331.
- 3 F. Meggio and L. A. Pinna, *FASEB J.*, 2016, **17**(3), 349–368.
- 4 J. Zhang, P. L. Yang and N. S. Gray, *Nat. Rev. Cancer*, 2009, **9**, 28–39.
- 5 R. T. Nitta, S. Gholamin, A. H. Feroze, M. Agarwal, S. H. Cheshier, S. S. Mitra and G. Li, *Oncogene*, 2015, **34**, 3688–3699.
- 6 M. Ruzzene and L. A. Pinna, *Biochim. Biophys. Acta*, 2010, **1804**, 499–504.
- 7 B. Zhou, D. A. Ritt, D. K. Morrison, C. J. Der and A. D. Cox, *J. Biol. Chem.*, 2016, **291**(34), 17804–17815.
- 8 G. Di Maira, F. Brustolon, J. Bertacchini, K. Tosoni, S. Marmiroli, L. A. Pinna and M. Ruzzene, *Oncogene*, 2007, **26**, 6915–6926.
- 9 J. S. Duncan and D. W. Litchfield, *Biochim. Biophys. Acta*, 2008, **1784**, 33–47.
- 10 S. Sarno and L. A. Pinna, *Mol. Biosyst.*, 2008, **4**, 889–894.
- 11 R. Battistutta, G. Cozza, F. Pierre, E. Papinutto, G. Lolli, S. Sarno, S. E. O'Brien, A. Siddiqui-Jain, M. Haddach, K. Anderes, D. M. Ryckman, F. Meggio and L. A. Pinna, *Biochemistry*, 2011, **50**, 8478–8488.
- 12 B. Guerra, J. Hochscherf, N. B. Jensen and O.-G. Issinger, *Mol. Cell. Biochem.*, 2015, **406**, 151–161.
- 13 C. Götz, A. Gratz, U. Kucklaender and J. Jose, *Biochim. Biophys. Acta*, 2012, **1820**, 970–977.
- 14 A. Siddiqui-Jain, D. Drygin, N. Streiner, P. Chua, F. Pierre, S. E. O'Brien, J. Bliesath, M. Omori, N. Huser, C. Ho, C. Proffitt, M. K. Schwaebe, D. M. Ryckman, W. G. Rice and K. Anderes, *Cancer Res.*, 2010, **70**, 10288–10298.
- 15 H. J. Chon, K. J. Bae, Y. Lee and J. Kim, *Front. Pharmacol.*, 2015, **6**(70), 1–5.
- 16 F. Pierre, P. C. Chua, S. E. O'Brien, A. Siddiqui-Jain, P. Bourbon, M. Haddach, J. Michaux, J. Nagasawa, M. K. Schwaebe, E. Stefan, A. Vialettes, J. P. Whitten, T. K. Chen, L. Darjania, R. Stansfield, K. Anderes, J. Bliesath, D. Drygin, C. Ho, M. Omori, C. Proffitt, N. Streiner, K. Trent, W. G. Rice and D. M. Ryckman, *J. Med. Chem.*, 2011, **54**, 635–654.
- 17 H. Kim, K. Choi, H. Kang, S. Y. Lee, S. W. Chi, M. S. Lee, J. Song, D. Im, Y. Choi and S. Cho, *PLoS One*, 2014, **9**, 1–8.

- 18 P. Brear, C. De Fusco, K. H. Georgiou, N. J. Francis-Newton, C. J. Stubbs, H. F. Sore, A. R. Venkitaraman, C. Abell, D. R. Spring and M. Hyvönen, *Chem. Sci.*, 2016, **7**, 6839–6845.
- 19 C. De Fusco, P. Brear, J. Iegre, K. H. Georgiou, H. F. Sore, M. Hyvönen and D. R. Spring, *Bioorg. Med. Chem.*, 2017, **25**, 3471–3482.
- 20 A. L. Hopkins, G. M. Keserü, P. D. Leeson, D. C. Rees and C. H. Reynolds, *Nat. Rev. Drug Discovery*, 2014, **13**, 105–121.
- 21 C. A. Lipinski, F. Lombardo, B. W. Dominy and P. J. Feeney, *Adv. Drug Delivery Rev.*, 1997, **23**, 3–25.

Drug Discovery

International Edition: DOI: 10.1002/anie.201606496
German Edition: DOI: 10.1002/ange.201606496Partially Saturated Bicyclic Heteroaromatics as an sp^3 -Enriched Fragment Collection

David G. Twigg, Noriyasu Kondo, Sophie L. Mitchell, Warren R. J. D. Galloway, Hannah F. Sore, Andrew Madin, and David R. Spring*

Dedicated to Professor Stuart L. Schreiber on the occasion of his 60th birthday

Abstract: Fragment-based lead generation has proven to be an effective means of identifying high-quality lead compounds for drug discovery programs. However, the fragment screening sets often used are principally comprised of sp^2 -rich aromatic compounds, which limits the structural (and hence biological) diversity of the library. Herein, we describe strategies for the synthesis of a series of partially saturated bicyclic heteroaromatic scaffolds with enhanced sp^3 character. Subsequent derivatization led to a fragment collection featuring regio- and stereo-controlled introduction of substituents on the saturated ring system, often with formation of new stereocenters.

Fragment-based drug discovery (FBDD) is a well-established method for generating high-quality hits and leads.^[1] The approval of the B-Raf kinase inhibitor vemurafenib (Zelboraf) in 2011^[2] and the Bcl-2 inhibitor venetoclax (Venclexta) in 2016,^[3] coupled with the ongoing evaluation of over 20 candidates in clinical trials,^[4] validates this approach as a complementary strategy to other hit-discovery techniques such as high-throughput screening.^[5] While the growing prevalence of fragment-based approaches is encouraging, evaluation of many existing fragment libraries shows a predominance of (hetero)aromatic, “flat” compounds, with a deficiency of chiral, sp^3 -rich examples.^[6,7]

Studies by Ritchie et al.^[8] and Lovering et al.^[9] demonstrate improvements in project progression by, for example, increasing the fraction of sp^3 centers within molecules or

restricting the number of aromatic rings. Furthermore, computational analysis demonstrates that greater 3D conformational character is observed in compounds that have been clinically evaluated in humans, compared to those found in commercial libraries.^[10] This indicates the importance of sp^3 -richness in both the design of screening collections and the subsequent development of hits to leads.

Examples of previous studies aiming to synthesize collections of sp^3 -enriched fragments have been limited. Diversity-oriented synthesis^[7,11] and natural product derivatives^[12] have been used to generate 3D fragment collections, but there remains an unmet need to access new scaffold types. Recently there have been calls^[13] for new approaches and methodologies for designing fragments with multiple synthetically accessible growth vectors in three dimensions, to allow rapid and efficient elaboration of hits to leads after initial screening, with some early success.^[14]

With these points in mind, the study described herein was aimed at developing efficient synthetic routes to a series of partially saturated bicyclic heteroaromatic (PSBH) fragments with enhanced sp^3 content relative to existing fragment libraries. Compounds featuring PSBHs have been shown to display bioactivity against a range of targets (Figure 1),^[15] and so a series of related fragments might be expected to serve effectively as a screening collection for FBDD applications.

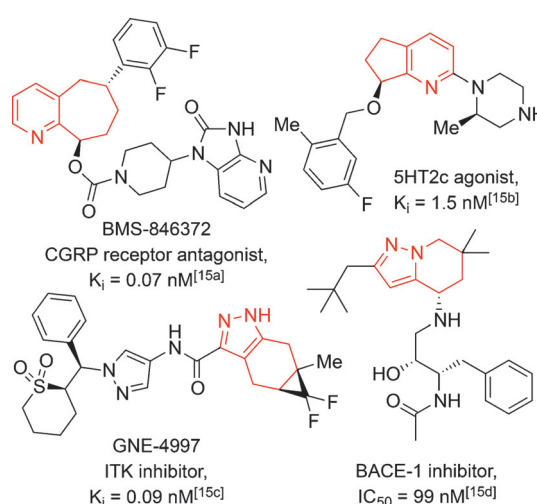


Figure 1. Selected examples of bioactive compounds containing functionalized partially saturated bicyclic heteroaromatics (highlighted in red).

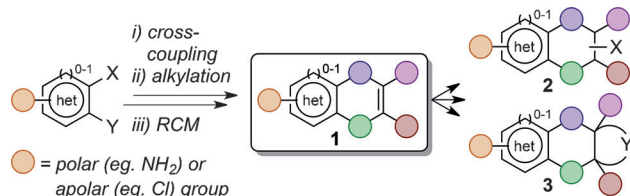
[*] D. G. Twigg, Dr. N. Kondo, S. L. Mitchell, Dr. W. R. J. D. Galloway, Dr. H. F. Sore, Prof. D. R. Spring
Department of Chemistry, University of Cambridge
Lensfield Rd, Cambridge, CB2 1EW (UK)
E-mail: spring@ch.cam.ac.uk

Dr. N. Kondo
Shionogi & Co. Ltd.
1-1, Futaba-cho 3-chome, Toyonaka, Osaka 561-0825 (Japan)

Dr. A. Madin
AstraZeneca UK Ltd.
310 Cambridge Science Park, Milton Rd, Cambridge, CB4 0FZ (UK)

Supporting information for this article (including all data supporting this study) can be found under:
<http://dx.doi.org/10.1002/anie.201606496>.

© 2016 The Authors. Published by Wiley-VCH Verlag GmbH & Co. KGaA. This is an open access article under the terms of the Creative Commons Attribution License, which permits use, distribution and reproduction in any medium, provided the original work is properly cited.



Scheme 1. General synthetic strategy toward PSBH scaffolds **1** and subsequent incorporation of new functionalities (**2**) or rings (**3**).

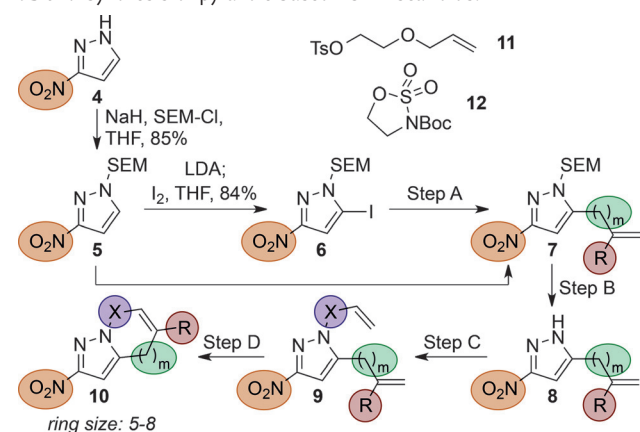
The targets of this study featured a variable aromatic heterocycle fused to a partially saturated carbocycle. The heterocycle could bear either a polar (e.g., amino) group, which should greatly enhance aqueous solubility, a property necessary for fragment screening at higher concentrations,^[7,14] or alternatively a hydrophobic (e.g., chloro) group, which can forge key interactions with protein targets.^[16] The synthetic route (Scheme 1) employed a modular and divergent approach, using simple cross-coupling and alkylation reactions to install a pair of terminal olefins that could be reliably cyclized through ring-closing metathesis (RCM).^[17] This allowed excellent control of the carbocycle ring size and the position and orientation of the resultant endocyclic olefin growth vector, which could undergo subsequent functionalization to produce a range of fragments suitable for screening and/or further elaboration.

We selected pyrazole and pyridine as representative aromatic heterocycles. Whilst previous studies have shown the synthesis of related structures,^[18] they have incorporated less control over the position of the olefin and do not feature the amino group found in many of our compounds. Furthermore, there are only very few examples where the olefin is used as a branch point and further functionalized beyond simple reduction.^[15a,19]

Starting from readily available 3-nitro-1*H*-pyrazole (**4**), 2-(trimethylsilyl)ethoxymethyl (SEM) protection, selective iodination, and subsequent Suzuki coupling with potassium vinyltrifluoroborate gave vinyl derivative **7a** (Table 1). Deprotection followed by N-alkylation with an alkyl bromide of varying C-chain length provided metathesis precursors **9a–c**, which upon treatment with either Grubbs' or Hoveyda-Grubbs' 2nd generation catalysts yielded the desired scaffolds **10a–c**. Inclusion of further heteroatoms in the formation of medium-sized partially saturated rings was achieved through treatment of vinyl intermediate **8a** with either tosylate **11** (leading, after RCM, to O-containing fragment **10d**), or 3-Boc-1,2,3-oxathiazolidine 2,2-dioxide **12**, which gave access to the N-containing scaffold **10e** after allylation and metathesis. Use of a different Suzuki coupling partner gave methyl-substituted product **7f**, which could be elaborated to PSBH fragment **10f**. Alternatively, direct allylation at the C-5 position of SEM-protected intermediate **5** could be achieved upon treatment with lithium diisopropylamide (LDA) and allyl bromide. This led, in an analogous way, to scaffolds **10g–h** with non-conjugated olefins.

A similar approach was used to generate PSBH scaffolds from pyridine **13** (Table 2). Attempts to mask the 2-amino group as a nitro group proved ineffective since, despite

Table 1. Synthesis of pyrazole-based PSBH scaffolds.



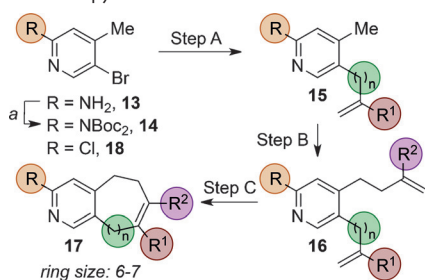
m	R	X	Step			
			A (7)	B (8) ^[c]	C (9) ^[d]	D (10) ^[h]
a	0	H	85% ^[a]	80%	55%	45% ^[h]
b	0	H	–	–	86%	84%
c	0	H	–	–	55%	89%
d	0	H	–	–	59% ^[e]	65%
e	0	H	–	–	29% ^[f]	83%
f	0	Me	76% ^[a]	69%	44%	90%
g	1	H	61% ^[b]	82%	70%	93%
h	1	H	–	–	36%	59% ^[h]

Reaction conditions: [a] R'-BF₃·K (1.5 equiv), Pd(dppf)Cl₂·CH₂Cl₂ (5 mol %), K₂CO₃ (3.0 equiv), THF/H₂O, 70 °C. [b] **5** (1.0 equiv), LDA (1.2 equiv), CuBr (20 mol %), allyl bromide (1.2 equiv), THF, –78 °C to RT. [c] TFA, CH₂Cl₂, RT. [d] NaH (1.5 equiv), alkyl bromide (1.5 equiv), THF or DMF, 70 °C. [e] NaH (1.5 equiv), **11** (1.5 equiv), THF, 70 °C. [f] **12** (2.0 equiv), K₂CO₃ (3.0 equiv), DMF, RT, 43%; then NaH (1.5 equiv), allyl iodide (1.5 equiv), DMF, RT, 68%. [g] Grubbs II (10 mol %), CH₂Cl₂, 40 °C. [h] Hoveyda-Grubbs II (10 mol %), toluene, 110 °C or CH₂Cl₂, RT. THF = tetrahydrofuran, TFA = trifluoroacetic acid, DMF = *N,N*-dimethylformamide.

successful cross-coupling reactions, the 2-nitropyridines were unstable to strong base and did not undergo the desired alkylations at the 4-methyl position. Mono-Boc protection was also unsuitable due to poor yields in the cross-coupling step, possibly due to catalyst chelation. The 2-amino group could be rendered synthetically tractable, however, either through bis-Boc protection or through substitution with a 2-chloro group, which itself can serve as a synthetic handle.^[20]

Bis-Boc substrate **14** (prepared in one step from **13**) was functionalized at the 5-position using either Suzuki coupling (for vinyl substituents) or Stille coupling (for allyl substituents) to produce intermediates **15a,d–f**. Treatment with LDA and trapping of the resultant anion with a variable alkyl bromide electrophile gave a range of metathesis substrates (**16a–f**), which under standard ring-closing metathesis conditions yielded PSBH scaffolds **17a–f**. The 2-chloro substrate **18** could be allylated in the 5-position by using an excess of *i*-PrMgCl·LiCl and trapping the resultant organometallic intermediate with allyl bromide. Allylation at the 4-methyl position and RCM gave scaffold **17g** in superior yields.

Following PSBH synthesis, a series of simple one-, two-, or three-step functionalizations were performed on selected pyrazole and pyridine scaffolds to demonstrate the synthetic

Table 2: Synthesis of pyridine-based PSBH scaffolds.

R	n	R ¹	R ²	A (15) ^[b]	Step B (16) ^[e]	C (17) ^[f]	
a	Boc ₂ N	0	H	H	85 %	60 %	95 %
b	Boc ₂ N	0	H	Me	–	69 %	94 %
c	Boc ₂ N	0	H	CF ₃	–	77 %	54 %
d	Boc ₂ N	0	Me	H	87 %	60 %	94 %
e	Boc ₂ N	0	Ph	H	92 %	68 %	83 %
f	Boc ₂ N	1	H	H	78 % ^[c]	41 %	65 %
g	Cl	1	H	H	73 % ^[d]	79 %	91 %

Reaction conditions: [a] Boc₂O (2.5 equiv), DMAP (0.1 equiv), THF, 70 °C. [b] R¹-BF₃K or R¹-B(MIDA) (1.5 equiv), Pd(dppf)Cl₂·CH₂Cl₂ (10 mol %), K₂CO₃ (3.0 equiv), THF/H₂O, 70 °C. [c] Allyltributyltin (1.1 equiv), Pd(PPh₃)₄ (10 mol %), KF (2 equiv), toluene, 110 °C. [d] *i*-PrMgCl·LiCl (1.5 equiv), allyl bromide (1.2 equiv), THF, –15 °C to RT. [e] LDA (1.2 equiv), alkyl bromide (1.5 equiv), THF, –78 °C to RT. [f] Grubbs II (5 mol %), CH₂Cl₂, 40 °C. DMAP = 4-dimethylaminopyridine.

utility of the olefin π -bond as a growth vector and to generate a variety of new stereocenters (Scheme 2).

Catalytic hydrogenation of nitropyrazoles **10a–d,f** served to reduce both the olefin π -bond and the nitro group in moderate to good yields, revealing the latent amino functionality and, in the case of **19f**, creating a new stereocenter. Other one-step reactions include aziridination, dibromination, allylic oxidation dihydroxylation, difluorocyclopropanation, hydroxybromination, epoxidation, and hydroboration (**20–28**) to introduce functionalities at the 4-, 5- and 6-positions of the fused pyrazole systems. Demonstrating that these initial products can serve as intermediates to other fragments, the products of hydroboration can react further to incorporate Br, F, and N substituents (**30–33**), whilst epoxide **26** can be opened by nucleophiles such as fluoride and hydride to form fluorohydrin **35** and alcohol **36**. Whilst the yields of some reactions were modest, sufficient material was obtained for full characterization and future screening campaigns.

The pyridine-based scaffolds **17a–g** can undergo a similar range of transformations. Catalytic hydrogenation and subsequent acid-mediated deprotection of bis-Boc compounds **17a–f** generated novel fragments, many of which include new stereocenters (**37a–f**). Aziridination, dibromination, dihydroxylation, hydroboration, α -bromoketone formation, and hydroxybromination were also carried out (**38–43**). Further reactions included amino-alcohol (**44**) and epoxide (**45**)

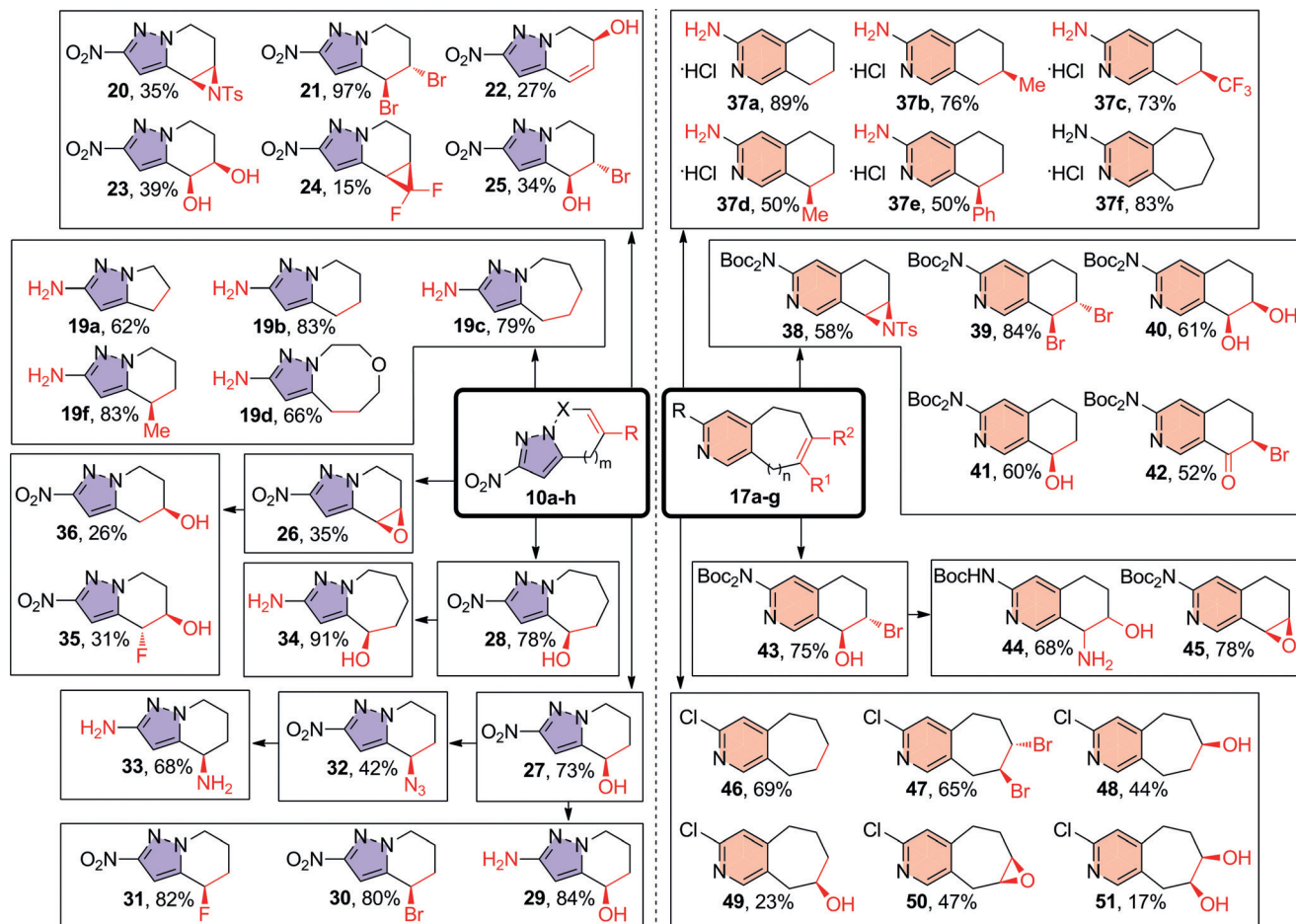
**Scheme 2.** Functionalization of PSBH scaffolds. For reaction conditions, see the Supporting Information.

Table 3: Mean physicochemical properties of fragment collections.

Property ^[a]	Ideal Range ^[b]	This work	Chembridge	Maybridge
SlogP	0-2	1.45	1.31	2.55
MW	140-230	190	222	265
PSA	≤60	58.0	53.9	57.5
HBA	≤3	1.35	1.81	2.12
HBD	≤3	0.55	1.04	0.81
HAC	10-16	12.8	15.5	18.0
RBC	≤3	0.6	3.2	2.8
Chiral centres	0-1	0.88	0.27	0.18
Fraction Aromatic	-	0.43	0.42	0.52

[a] MW = molecular weight, PSA = polar surface area, HBA = number of hydrogen-bond acceptors, HBD = number of hydrogen-bond donors, HAC = heavy atom count, RBC = rotatable bond count. [b] Based on the guidelines used by Astex Pharmaceuticals.^[14,21] Green: within ideal range, orange: at extreme of ideal range, red: outside ideal range. See the Supporting Information for further details.

formation, both from bromohydrin **43**. 3-Chloro fragments **46–51** could also be readily accessed using similar conditions.

Calculation of a range of physicochemical properties was carried out on all of the PSBH products. Almost all fragments were shown to conform to the so-called “Rule of Three”, a set of criteria commonly associated with greater hit rates in fragment screening collections.^[21] Of particular note are the low mean values for molecular weight (190), SlogP (1.45), and “fraction aromatic” (0.43) and the high mean number of chiral centres (0.88), especially when compared to existing commercial libraries (Table 3).

In conclusion, we have developed simple, scalable routes to a series of partially saturated pyrazole- and pyridine-based scaffolds that can readily undergo a range of synthetic transformations to generate a collection of sp³-rich fragments, which are suitable for use either as screening members in a library or as intermediates to “higher-content fragments”. The compounds adhere to recognized guidelines for fragment physicochemical properties, whilst displaying enhanced sp³ character and greater chirality, and providing a range of three-dimensional growth vectors for synthetic development. It is envisioned that the strategy could be applied to a vast range of analogous scaffolds with varied heterocycles and substituents and that several of the functionalization reactions detailed in Scheme 2 could be rendered asymmetric based on related precedents.^[19,22]

Acknowledgements

Our research is supported by the EPSRC, BBSRC, MRC, Wellcome Trust, and ERC (FP7/2007-2013; 279337/DOS). D.G.T. thanks AstraZeneca for funding. S.L.M. thanks BASF for funding. D.R.S. acknowledges support from a Royal Society Wolfson Research Merit award.

Keywords: drug design · drug discovery · fused-ring systems · nitrogen heterocycles · synthetic methods

How to cite: *Angew. Chem. Int. Ed.* **2016**, *55*, 12479–12483
Angew. Chem. **2016**, *128*, 12667–12671

- a) C. W. Murray, D. C. Rees, *Nat. Chem.* **2009**, *1*, 187–192; b) R. E. Hubbard, J. B. Murray in *Methods in Enzymology*, Vol. 493 (Ed.: L. C. Kuo), Academic Press, New York, **2011**, pp. 509–531; c) D. Erlanson in *Fragment-Based Drug Discovery and X-Ray Crystallography* (Eds.: T. G. Davies, M. Hyvönen), Springer, Berlin, **2012**, pp. 1–32; d) E. R. Zartler, *ACS Med. Chem. Lett.* **2014**, *5*, 952–953; e) M. Congreve, G. Chessari, D. Tisi, A. J. Woodhead, *J. Med. Chem.* **2008**, *51*, 3661–3680; f) G. M. Keserü, D. A. Erlanson, G. G. Ferenczy, M. M. Hann, C. W. Murray, S. D. Pickett, *J. Med. Chem.* **2016**, DOI: 10.1021/acs.jmedchem.6b00197.
- a) G. Bollag, J. Tsai, J. Zhang, C. Zhang, P. Ibrahim, K. Nolop, P. Hirth, *Nat. Rev. Drug Discovery* **2012**, *11*, 873–886.
- A. J. Souers, J. D. Levenson, E. R. Boghaert, S. L. Ackler, N. D. Catron, J. Chen, B. D. Dayton, H. Ding, S. H. Enschede, W. J. Fairbrother, D. C. Huang, S. G. Hymowitz, S. Jin, S. L. Khaw, P. J. Kovar, L. T. Lam, J. Lee, H. L. Maecker, K. C. Marsh, K. D. Mason, M. J. Mitten, P. M. Nimmer, A. Oleksijew, C. H. Park, C. M. Park, D. C. Phillips, A. W. Roberts, D. Sampath, J. F. Seymour, M. L. Smith, G. M. Sullivan, S. K. Tahir, C. Tse, M. D. Wendt, Y. Xiao, J. C. Xue, H. Zhang, R. A. Humerickhouse, S. H. Rosenberg, S. W. Elmore, *Nat. Med.* **2013**, *19*, 202–208.
- M. Baker, *Nat. Rev. Drug Discovery* **2013**, *12*, 5–7.
- S. Barelier, I. Krimm, *Curr. Opin. Chem. Biol.* **2011**, *15*, 469–474.
- P. J. Hajduk, W. R. J. D. Galloway, D. R. Spring, *Nature* **2011**, *470*, 42–43.
- A. W. Hung, A. Ramek, Y. Wang, T. Kaya, J. A. Wilson, P. A. Clemons, D. W. Young, *Proc. Natl. Acad. Sci. USA* **2011**, *108*, 6799–6804.
- T. J. Ritchie, S. J. F. MacDonald, *Drug Discovery Today* **2009**, *14*, 1011–1020.
- F. Lovering, J. Bikker, C. Humblet, *J. Med. Chem.* **2009**, *52*, 6752–6756.
- A. D. Morley, A. Pugliese, K. Birchall, J. Bower, P. Brennan, N. Brown, T. Chapman, M. Drysdale, I. H. Gilbert, S. Hoelder, A. Jordan, S. V. Ley, A. Merritt, D. Miller, M. E. Swarbrick, P. G. Wyatt, *Drug Discovery Today* **2013**, *18*, 1221–1227.
- V. S. B. Damerla, C. Tulluri, R. Gundla, L. Naviri, U. Adepalay, P. S. Iyer, Y. L. N. Murthy, N. Prabhakar, S. Sen, *Chem. Asian J.* **2012**, *7*, 2351–2360.
- B. Over, S. Wetzel, C. Grutter, Y. Nakai, S. Renner, D. Rauh, H. Waldmann, *Nat. Chem.* **2013**, *5*, 21–28.
- C. W. Murray, D. C. Rees, *Angew. Chem. Int. Ed.* **2016**, *55*, 488–492; *Angew. Chem.* **2016**, *128*, 498–503.
- N. Palmer, T. M. Peakman, D. Norton, D. C. Rees, *Org. Biomol. Chem.* **2016**, *14*, 1599–1610.
- a) G. Luo, L. Chen, C. M. Conway, R. Denton, D. Keavy, M. Gulianello, Y. Huang, W. Kostich, K. A. Lentz, S. E. Mercer, R. Schartman, L. Signor, M. Browning, J. E. Macor, G. M. Dubowchik, *ACS Med. Chem. Lett.* **2012**, *3*, 337–341; b) K. K.-C. Liu, P. Cornelius, T. A. Patterson, Y. Zeng, S. Santucci, E. Tomlinson, C. Gibbons, T. S. Maurer, R. Marala, J. Brown, J. X. Kong, E. Lee, W. Werner, Z. Wenzel, C. Vage, *Bioorg. Med. Chem. Lett.* **2010**, *20*, 266–271; c) J. D. Burch, K. Barrett, Y. Chen, J. DeVoss, C. Eigenbrot, R. Goldsmith, M. H. A. Ismaili, K. Lau, Z. Lin, D. F. Ortwine, A. A. Zarrin, P. A. McEwan, J. J. Barker, C. Ellebrandt, D. Kordt, D. B. Stein, X. Wang, Y. Chen, B. Hu, X. Xu, P.-W. Yuen, Y. Zhang, Z. Pei, *J. Med. Chem.* **2015**, *58*, 3806–3816; d) C. Sund, O. Belda, N. Borkakoti, J. Lindberg, D. Derbyshire, L. Vrang, E. Hamelink, C. Åhgren, E. Woestenenk, K. Wikström, A. Eneroth, E. Lindström, G. Kalayanov, *Bioorg. Med. Chem. Lett.* **2012**, *22*, 6721–6727.

- [16] Y. S. Tan, D. R. Spring, C. Abell, C. Verma, *J. Chem. Inf. Model.* **2014**, *54*, 1821–1827.
- [17] RCM has been used in many diversity-generating libraries and applications. Selected examples: a) J. W. Herndon, *Coord. Chem. Rev.* **2015**, *286*, 30–150; b) S. Collins, S. Bartlett, F. Nie, H. F. Sore, D. R. Spring, *Synthesis* **2016**, 1457–1473; c) A. Grossmann, S. Bartlett, M. Janecek, J. T. Hodgkinson, D. R. Spring, *Angew. Chem. Int. Ed.* **2014**, *53*, 13093–13097; *Angew. Chem.* **2014**, *126*, 13309–13313; d) D. Morton, S. Leach, C. Cordier, S. Warriner, A. Nelson, *Angew. Chem. Int. Ed.* **2009**, *48*, 104–109; *Angew. Chem.* **2009**, *121*, 110–115.
- [18] a) S. Fustero, R. Román, A. Asensio, M. A. Maestro, J. A. Aceña, A. Simón-Fuentes, *Eur. J. Org. Chem.* **2013**, 7164–7174; b) A. J. Eberhart, C. Cicoira, D. J. Procter, *Org. Lett.* **2013**, *15*, 3994–3997; c) T. A. Moss, *Tetrahedron Lett.* **2013**, *54*, 993–997; d) S. Ahamad, A. K. Gupta, R. Kant, K. Mohanan, *Org. Biomol. Chem.* **2015**, *13*, 1492–1499; e) J. Velcicky, D. Pflieger, *Synlett* **2010**, 1397–1401; f) J. Luo, Z. Huo, J. Fu, F. Jin, Y. Yamamoto, *Org. Biomol. Chem.* **2015**, *13*, 3227–3235; g) A. van den Hoo-
genband, J. A. J. den Hartog, N. Faber-Hilhorst, J. H. M. Lange, J. W. Terpstra, *Tetrahedron Lett.* **2009**, *50*, 5040–5043.
- [19] a) P. Fackler, S. M. Huber, T. Bach, *J. Am. Chem. Soc.* **2012**, *134*, 12869–12878; b) P. Mukherjee, S. J. S. Roy, T. K. Sarkar, *Org. Lett.* **2010**, *12*, 2472–2475.
- [20] G. Pelletier, *e-EROS Encycl. Reagents Org. Synth.* **2011**, 1–5.
- [21] M. Congreve, R. Carr, C. Murray, H. Jhoti, *Drug Discovery Today* **2003**, *8*, 876–877.
- [22] a) J. E. Aaseng, S. Melnes, G. Reian, O. R. Gautun, *Tetrahedron* **2010**, *66*, 9790–9797; b) H. Doucet, E. Fernandez, T. P. Layzell, J. M. Brown, *Chem. Eur. J.* **1999**, *5*, 1320–1330; M. R. Friedfeld, M. Shevlin, G. W. Margulieux, L.-C. Campeau, P. J. Chirik, *J. Am. Chem. Soc.* **2016**, *138*, 3314–3324.

Received: July 5, 2016

Revised: August 1, 2016

Published online: September 6, 2016